

**Mass Transfer from Entrapped DNAPL Sources
Undergoing Remediation: Characterization
Methods and Prediction Tools**

SERDP Project No. CU-1294

Colorado School of Mines

Tissa H. Illangasekare, Principal Investigator

Co-Principal Investigators

Junko Munakata Marr, Robert L. Siegrist and

Kenichi Soga (University of Cambridge)

Contributing Research Team Members

Kent C. Glover, Elena Moreno-Barbero, Jeffery L. Heiderscheidt, Satawat
Saenton, Mini Matthew, Ann R. Kaplan, Youngchoel Kim, Dongping Dai,
Jose L. Gago and John W.E. Page (University of Cambridge)

August 31, 2006

Approved for Public Release, Distribution is Unlimited

REPORT DOCUMENTATION PAGE

*Form Approved
OMB No. 0704-0188*

The public reporting burden for this collection of information is estimated to average 1 hour per response, including the time for reviewing instructions, searching existing data sources, gathering and maintaining the data needed, and completing and reviewing the collection of information. Send comments regarding this burden estimate or any other aspect of this collection of information, including suggestions for reducing the burden, to the Department of Defense, Executive Services and Communications Directorate (0704-0188). Respondents should be aware that notwithstanding any other provision of law, no person shall be subject to any penalty for failing to comply with a collection of information if it does not display a currently valid OMB control number.

PLEASE DO NOT RETURN YOUR FORM TO THE ABOVE ORGANIZATION.

| | | | | | |
|--|--------------------|-----------------------|-----------------------------------|---|--|
| 1. REPORT DATE (DD-MM-YYYY) | | 2. REPORT TYPE | | 3. DATES COVERED (From - To) | |
| 4. TITLE AND SUBTITLE | | | | 5a. CONTRACT NUMBER | |
| | | | | 5b. GRANT NUMBER | |
| | | | | 5c. PROGRAM ELEMENT NUMBER | |
| 6. AUTHOR(S) | | | | 5d. PROJECT NUMBER | |
| | | | | 5e. TASK NUMBER | |
| | | | | 5f. WORK UNIT NUMBER | |
| 7. PERFORMING ORGANIZATION NAME(S) AND ADDRESS(ES) | | | | 8. PERFORMING ORGANIZATION REPORT NUMBER | |
| 9. SPONSORING/MONITORING AGENCY NAME(S) AND ADDRESS(ES) | | | | 10. SPONSOR/MONITOR'S ACRONYM(S) | |
| | | | | 11. SPONSOR/MONITOR'S REPORT NUMBER(S) | |
| 12. DISTRIBUTION/AVAILABILITY STATEMENT | | | | | |
| 13. SUPPLEMENTARY NOTES | | | | | |
| 14. ABSTRACT | | | | | |
| 15. SUBJECT TERMS | | | | | |
| 16. SECURITY CLASSIFICATION OF: | | | 17. LIMITATION OF ABSTRACT | 18. NUMBER OF PAGES | 19a. NAME OF RESPONSIBLE PERSON |
| a. REPORT | b. ABSTRACT | c. THIS PAGE | | | 19b. TELEPHONE NUMBER (Include area code) |

This report was prepared under contract to the Department of Defense Strategic Environmental Research and Development Program (SERDP). The publication of this report does not indicate endorsement by the Department of Defense, nor should the contents be construed as reflecting the official policy or position of the Department of Defense. Reference herein to any specific commercial product, process, or service by trade name, trademark, manufacturer, or otherwise, does not necessarily constitute or imply its endorsement, recommendation, or favoring by the Department of Defense.

Table of Contents

| | |
|---|-------|
| List of Acronyms | viii |
| List of Figures | x |
| List of Tables | xxiii |
| Acknowledgements..... | xxvii |
| | |
| Executive Summary | 1 |
| | |
| 1.0 Introduction..... | 6 |
| 1.1 Objectives | 6 |
| 1.2 Report organization..... | 7 |
| | |
| 2.0 Background..... | 9 |
| 2.1 DNAPL source zone architecture and morphology | 10 |
| 2.1.1 Source-zone development..... | 11 |
| 2.1.2 Source-zone characterization by partitioning tracer techniques | 12 |
| 2.2 Regulatory and Department of Defense requirements related to mass transfer from DNAPL source zones..... | 13 |
| 2.3 Mass transfer from DNAPL source zones | 14 |
| 2.3.1 Natural dissolution and upscaling..... | 14 |
| 2.3.2 Surfactant-enhanced dissolution | 16 |
| 2.3.3 In situ chemical oxidation of DNAPL | 17 |
| 2.3.4 Bioenhanced dissolution | 19 |
| 2.3.5 Thermal treatment of DNAPL | 21 |
| | |
| 3.0 Materials, experiments and modeling methods | 23 |
| 3.1 Approach..... | 23 |
| 3.2 Materials and methods | 25 |
| 3.2.1 Chemicals and materials | 25 |
| 3.2.2 Sampling methods..... | 29 |
| 3.2.3 Analytical methods | 31 |
| 3.2.4 Gamma and x-ray attenuation systems | 33 |

| | | |
|-------|---|-----|
| 3.3 | Experimental design and methods for investigation of partitioning tracers | 35 |
| 3.3.1 | Batch tests | 36 |
| 3.3.2 | Column tests..... | 48 |
| 3.3.3 | Large-tank experiments | 53 |
| 3.4 | Experimental design and methods for investigation of natural dissolution | 65 |
| 3.4.1 | Column experiments with pure or field DNAPLs | 65 |
| 3.4.2 | Two-dimensional flow-cell experiments with pure TCE or field DNAPLs..... | 66 |
| 3.4.3 | Two-dimensional horizontal flow-cell experiments with pure PCE..... | 70 |
| 3.4.4 | Large-tank experiments of natural dissolution | 78 |
| 3.5 | Experimental design and methods for investigation of surfactant-enhanced dissolution | 80 |
| 3.5.1 | Column experiments with surfactants Tween 80 and Aerosol 80I | 80 |
| 3.5.2 | Two-dimensional flow-cell experiments with pure TCE or field DNAPLs..... | 86 |
| 3.5.3 | Two-dimensional horizontal flow-cell experiments with pure PCE..... | 88 |
| 3.5.4 | Two-dimensional experiment with spatially correlated random field | 91 |
| 3.5.5 | Large-tank experiment of surfactant-enhanced dissolution | 103 |
| 3.6 | Experimental design and methods for investigation of in situ chemical oxidation | 107 |
| 3.6.1 | Flow-through reactor experiments | 107 |
| 3.6.2 | Intermediate-scale experiments | 114 |
| 3.6.3 | Large-tank experiments | 136 |
| 3.7 | Experimental design and methods for investigation of biologically-enhanced dissolution | 144 |
| 3.7.1 | Batch and column experiments | 144 |
| 3.7.2 | Flow cell experiments..... | 147 |
| 3.7.3 | Large tank experiments..... | 155 |
| 3.8 | Experimental design and methods for investigation of thermal treatment | 172 |
| 3.8.1 | Batch experiments – temperature dependence of PCE solubility | 172 |
| 3.8.2 | Column experiments – temperature dependence of PCE mass transfer .. | 173 |
| 3.8.3 | Two-dimensional flow-cell experiments | 177 |
| 3.9 | Modeling tools | 183 |
| 3.9.1 | Groundwater flow model | 183 |

| | | |
|-------|--|-----|
| 3.9.2 | Reactive transport model | 183 |
| 3.9.3 | Multiphase flow code..... | 189 |
| 3.9.4 | Inverse modeling algorithms..... | 190 |
| 3.9.5 | Multiple tracer test module..... | 191 |
| 3.9.6 | Chemical oxidation model..... | 194 |
| 3.9.7 | Bioremediation model..... | 207 |
| 3.10 | Design and methods for three dimensional simulation..... | 211 |
| 4.0 | Results and Accomplishments | 213 |
| 4.1 | Investigation of partitioning tracers..... | 213 |
| 4.1.1 | Batch tests | 213 |
| 4.1.2 | Column tests..... | 214 |
| 4.1.3 | Large-tank experiments | 215 |
| 4.1.4 | Summary of key results | 223 |
| 4.2 | Investigation of natural dissolution..... | 225 |
| 4.2.1 | Column experiments with pure or field DNAPL..... | 225 |
| 4.2.2 | Two-dimensional horizontal flow-cell experiments with pure PCE..... | 228 |
| 4.2.3 | Large-tank experiments of natural dissolution | 233 |
| 4.2.4 | Upscaling natural dissolution..... | 235 |
| 4.2.5 | Phenomenological model for an upscaleable mass transfer correlation | 243 |
| 4.2.6 | Evaluation of upscaleable mass transfer model with synthetic data..... | 247 |
| 4.2.7 | Validation of upscaleable mass transfer model with results of large tank experiment..... | 252 |
| 4.2.8 | Summary of key results | 259 |
| 4.3 | Investigation of surfactant-enhanced dissolution..... | 259 |
| 4.3.1 | Simulation of column experiment with surfactant-enhanced dissolution model..... | 259 |
| 4.3.2 | Large-tank experiment of surfactant-enhanced dissolution..... | 263 |
| 4.3.3 | Summary of key results | 263 |
| 4.4 | Investigation of in situ chemical oxidation..... | 266 |
| 4.4.1 | Flow-thru reactor (FTR) experiments..... | 266 |
| 4.4.2 | Intermediate-scale cell experiments..... | 266 |
| 4.4.3 | Large-scale tank experiments | 267 |

| | | |
|--|--|-----|
| 4.4.4 | Modeling study of column experiments | 268 |
| 4.4.5 | Summary of key results | 277 |
| 4.5 | Investigation of biologically enhanced dissolution..... | 278 |
| 4.5.1 | Column experiments | 278 |
| 4.5.2 | Modeling of flow cell experiments | 279 |
| 4.5.3 | Modeling of large-tank experiments | 296 |
| 4.5.4 | Summary of key results | 316 |
| 4.6 | Investigation of thermal treatment | 317 |
| 4.7 | Three dimensional simulation of mass transfer during remediation..... | 317 |
| 4.7.1 | IDEAL aquifer characterization..... | 318 |
| 4.7.2 | AQ9 aquifer characterization | 325 |
| 4.7.3 | Summary of key results | 336 |
| 5.0 | Conclusions and Implications | 337 |
| 5.1 | Key accomplishments | 337 |
| 5.2 | Limitations | 338 |
| 5.3 | Application of results to source-zone remediation and future research..... | 340 |
| References | | 342 |
| Appendix 1 – Large tank experiments with high heterogeneity | | 359 |
| Appendix 2 – Large tank experiments with low heterogeneity | | 384 |
| Appendix 3 – Large tank experiments with multiple hydrogeologic units..... | | 396 |
| Appendix 4 – List of technical publications | | 402 |

List of Acronyms

| | |
|---------|---|
| 1-D | one-dimensional |
| 2-D | two-dimensional |
| 2M1B | 2-methyl-1-butanol |
| 6M2H | 6-methyl-2-heptanol |
| ATSDR | Agency for Toxic Substances and Disease Registry |
| CERCLA | Comprehensive Environmental Response, Compensation, and Liability Act |
| CESEP | Center for the Experimental Study of Subsurface Environmental Processes |
| CMC | critical micelle concentration |
| DCE | dichloroethene |
| DMP | 2, 2-dimethyl-3-pentanol |
| DNAPL | dense nonaqueous phase liquids |
| HEX | hexanol |
| GC | gas chromatograph |
| IC | ion chromatograph |
| ICP-AES | inductively coupled plasma-atomic emission spectroscopy |
| ISCO | in situ chemical oxidation |
| LPM | low permeability media |
| MCL | maximum contaminant level |
| MTE | Molar treatment efficiency |
| NAPL | nonaqueous phase liquids |
| NCP | Final National Oil and Hazardous Substances Pollution Contingency Plan |
| NOD | natural oxidant demand |
| NRC | Nuclear Regulatory Commission |
| PCE | tetrachloroethylene |
| PITT | partitioning interwell tracer test |
| PPB | parts per billion |
| PPM | parts per million |
| SEAR | surfactant-enhanced aquifer remediation |
| TCE | trichloroethylene |

TOC total organic carbon
USEPA United States Environmental Protection Agency
USHHS United States Department of Health and Human Services.
VC vinyl chloride

List of Figures

| | | |
|-------------|---|----|
| Figure 2.1 | Generic Contaminated Site Conceptual Model..... | 10 |
| Figure 2.2 | Regions of Potential Permeability Reduction..... | 19 |
| Figure 3.1 | Soil Coring Devices..... | 30 |
| Figure 3.2 | Batch tests to determine partition coefficient of Tween 80 in a TCE DNAPL-water system..... | 37 |
| Figure 3.3 | Batch Tests to Determine Partition Coefficient of Cyclodextrin in a TCE DNAPL-water system..... | 37 |
| Figure 3.4 | Isotherms for Selected Tracers Partitioning Between Water and KMnO ₄ -Treated PCE..... | 41 |
| Figure 3.5 | Tracer Partition Coefficients at Different Initial Tracer Concentrations for PCE after Treatment with KMnO ₄ | 42 |
| Figure 3.6 | Schematic of Serial Dilution Used to Make Tracer Solutions, Batch Partitioning Tracer Experiments with Biological Treatment..... | 43 |
| Figure 3.7 | Baseline partitioning coefficient determination for (a) DMP and (b) Hexanol, Batch Partitioning Tracer Experiments with Biological Treatment..... | 45 |
| Figure 3.8 | Columns for Partition Tracer Tests with Surfactant Treatment..... | 49 |
| Figure 3.9 | Breakthrough Curves for Partitioning Tracer Test in Columns Before Surfactant Treatment..... | 50 |
| Figure 3.10 | Breakthrough Curves for Partitioning Tracer Test in Columns After Surfactant Treatment..... | 50 |
| Figure 3.11 | Source-Zone Architecture, Large Tank Experiment with High- Heterogeneity Aquifer..... | 56 |
| Figure 3.12 | Source-Zone Architecture, Large Tank Experiment with Low- Heterogeneity Aquifer..... | 57 |
| Figure 3.13 | Source-Zone Architecture after Surfactant Flushing, Large Tank Experiment with High-Heterogeneity Aquifer..... | 58 |
| Figure 3.14 | Source-Zone Architecture after Surfactant Flushing, Large Tank Experiment with Low-Heterogeneity Aquifer..... | 59 |
| Figure 3.15 | Travel Times to Selected Sample Locations in Sampling Array A, Partitioning Tracer Test Prior to Source Creation, Large Tank Experiment with High-Heterogeneity Aquifer..... | 60 |
| Figure 3.16 | Actual PCE DNAPL Saturation (line) and Saturation Calculating from Tracer Data Using the Method of Moments (dots), Large Tank Experiment with High-Heterogeneity Aquifer..... | 61 |

| | | |
|-------------|---|----|
| Figure 3.17 | Comparison of Actual DNAPL Saturation with Saturation Calculating from Tracer Data Using the Method of Moments, Large Tank Experiment with Low-Heterogeneity Aquifer..... | 62 |
| Figure 3.18 | Average DNAPL Saturation Estimated by the Method of Moments from Tracer Data Collected at Various Distances from the Source Zone, Large Tank Experiment with High-Heterogeneity Aquifer | 62 |
| Figure 3.19 | Actual PCE DNAPL Saturation and Saturation Calculating from Tracer Data Using the Method of Moments, Large Tank Experiment with High-Heterogeneity Aquifer after Surfactant Flushing | 64 |
| Figure 3.20 | Comparison of Actual DNAPL Saturation with Saturation Calculating from Tracer Data Using the Method of Moments, Large Tank Experiment with Low-Heterogeneity Aquifer after Surfactant Flushing..... | 64 |
| Figure 3.21 | Comparison of experimental and model-fitted breakthrough concentration of TCE columns with pure and field DNAPL | 66 |
| Figure 3.22 | Schematic of Flow Cell Experiments to Compare Pure and Field DNAPL..... | 67 |
| Figure 3.23 | DNAPL Source Entrapments for Flow Cell Experiments Comparing Pure and Field DNAPL..... | 67 |
| Figure 3.24 | Partition Tracer Breakthrough Curves from Small Cell Tracer Tests with TCE Source and Field DNAPL Source | 68 |
| Figure 3.25 | Breakthrough Curves of TCE from Natural Dissolution Tests in a Two-Dimensional Flow Cell with a Pure TCE Source and a Field DNAPL Source | 68 |
| Figure 3.26 | Model fit for TCE Natural Dissolution Tests in a Two-Dimensional Flow Cell with a Pure TCE Source (Top) and a Field DNAPL Source..... | 69 |
| Figure 3.27 | Two Dimensional Bench-Scale Dissolution Cell with One Source Zone | 71 |
| Figure 3.28 | Transient Concentration of PCE at Selected Monitoring Ports, One-Source Experiment..... | 72 |
| Figure 3.29 | Steady-State PCE Concentration as a Function of Flow Rate at Four Monitoring Ports, Horizontal Flow Cell Experiments with One Source | 73 |
| Figure 3.30 | Steady-State PCE Concentration at Various Flow Rates for Nine Sampling Ports, Horizontal Flow Cell Experiments with One Source | 75 |
| Figure 3.31 | Steady-State Mass Depletion as a Function of Flow Rate, Horizontal Flow Cell Experiments with One Source..... | 76 |
| Figure 3.32 | Steady-State Mass Transfer Coefficient as a Function of Flow Rate, Horizontal Flow Cell Experiments with One Source | 76 |
| Figure 3.33 | Vertical Distribution of Concentration, Mass flux and Saturation at Flow Rate of $2.42 \times 10^{-8} \text{ m}^3 \text{ sec}^{-1}$, Horizontal Flow Cell Experiments with One Source..... | 77 |
| Figure 3.34 | Transient Dissolution of PCE in Two-Source Experiment: Experimental Data and Model Simulated Values | 77 |

| | | |
|-------------|--|----|
| Figure 3.35 | Design for Experimental Tank Showing Heterogeneous Packing, Constant Head Devices, Head Monitoring Ports, and Sampling Ports | 79 |
| Figure 3.36 | Steady-State PCE Concentration Profiles at Sample Arrays A, C and E during the Natural Dissolution Experiment, High Heterogeneity Tank | 79 |
| Figure 3.37 | Steady-State PCE Concentration Profiles at Sample Arrays A, C and E during the Natural Dissolution Experiment, Low Heterogeneity Tank | 80 |
| Figure 3.38 | Setup for Column Experiments with Surfactants..... | 81 |
| Figure 3.39 | Effluent PCE Concentration during Aerosol Flushing in Column Experiments at Selected Flow Rates..... | 83 |
| Figure 3.40 | Effluent PCE Concentration using Continuous and Stepped Flushing with Tween 80..... | 84 |
| Figure 3.41 | Relationship of Aqueous PCE Concentration to NAPL saturation in Column Experiments with Tween 80 and Two Injection Strategies | 84 |
| Figure 3.42 | Setup for Column Experiments with SEAR Comparing Mass Transfer from Pure TCE-DNAPL and a Field DNAPL | 85 |
| Figure 3.43 | Difference in Column Effluents During Surfactant Flushing for Field DNAPL and Pure TCE-DNAPL..... | 85 |
| Figure 3.44 | Plots of TCE Concentration vs. Tween 80 Concentration in Batch Equilibrium Tests of Pure TCE and Field DNAPL | 86 |
| Figure 3.45 | Breakthrough of TCE from Pure and Field DNAPL During Surfactant Flushing..... | 86 |
| Figure 3.46 | Remobilization of Field DNAPL during Surfactant Flushing | 87 |
| Figure 3.47 | Breakthrough Curves for TCE, Flow-Cell Experiments of Surfactant-Enhanced Dissolution with Pure DNAPL (Left) and Field DNAPL..... | 87 |
| Figure 3.48 | Breakthrough Curves for Surfactant-Enhanced Dissolution in the One-Source Experiment..... | 89 |
| Figure 3.49 | Steady-State PCE Concentration in Effluent vs. Percent Mass Removal, Flow-Cell Experiment with One-Source Configuration | 90 |
| Figure 3.50 | Breakthrough Curves for Surfactant-Enhanced Dissolution in Two-Source Experiment..... | 90 |
| Figure 3.51 | Steady-State PCE Concentration at the Effluent as a Function of Percent Mass Removal with the Two-Source Configuration | 91 |
| Figure 3.52 | Source Zone Heterogeneity Field Designed for the Surfactant-Enhanced Dissolution Experiment with Spatially Correlated Random Field | 92 |
| Figure 3.53 | Source Zone Heterogeneity Field as Packed for the Surfactant-Enhanced Dissolution Experiment with Spatially Correlated Random Field | 93 |
| Figure 3.54 | Flow of Dyed Water through the Heterogeneous Source, Surfactant-Enhanced Dissolution Experiment with Spatially Correlated Random Field..... | 94 |

| | | |
|-------------|---|-----|
| Figure 3.55 | Final PCE Source Architecture, Surfactant-Enhanced Dissolution Experiment with Spatially Correlated Random Field..... | 95 |
| Figure 3.56 | PCE Breakthrough Curves at Sampling Ports, Surfactant-Enhanced Dissolution Experiment with Spatially Correlated Random Field | 96 |
| Figure 3.57 | Steady-State Natural Dissolution, Surfactant-Enhanced Dissolution Experiment with Spatially Correlated Random Field: (a) Aqueous PCE Concentrations, (b) Cumulative Mass Removed Over the Same Time Period..... | 97 |
| Figure 3.58 | Changes in PCE Source Architecture During Surfactant Flushing, Surfactant-Enhanced Dissolution Experiment with Spatially Correlated Random Field..... | 99 |
| Figure 3.59 | Aqueous-Phase PCE Concentrations as a Function of Time After Start of Surfactant Flushing, Surfactant-Enhanced Dissolution Experiment with Spatially Correlated Random Field..... | 100 |
| Figure 3.60 | Effluent Aqueous PCE Concentrations during and after Surfactant Flushing (a) Cumulative Mass Removed Over the Same Time Period (b) Surfactant-Enhanced Dissolution Experiment with Spatially Correlated Random Field..... | 102 |
| Figure 3.61 | Breakthrough Curves Obtained from Large-Tank Experiment of Surfactant-Enhanced Dissolution, High Heterogeneity, Sampling Arrays A and C | 104 |
| Figure 3.62 | Vertical Profile of PCE Concentration at Sampling Array A during and after Surfactant Flushing, Large-Tank Experiment with High Heterogeneity | 105 |
| Figure 3.63 | Breakthrough Curves for Large-Tank Experiment of Surfactant-Enhanced Dissolution, Low Heterogeneity, Sampling Arrays A and C, and Effluent..... | 106 |
| Figure 3.64 | Vertical Profile of PCE Concentration at Array A Before, During and After Large-Tank Experiment of Surfactant-Enhanced Dissolution, Low Heterogeneity..... | 107 |
| Figure 3.65 | Schematic of Flow-Through Reactor Used in ISCO Experiments | 108 |
| Figure 3.66 | Example Cumulative Mass Flux Curve, FTR Experiments..... | 111 |
| Figure 3.67 | Example Mass Flux Slope Regions, FTR Experiments..... | 111 |
| Figure 3.68 | Photo and Diagram of Intermediate-Scale Cell for ISCO Experiments | 116 |
| Figure 3.69 | Sources with PCE, Intermediate-Scale ISCO Experiment | 118 |
| Figure 3.70 | Water Head Measurement System, Intermediate-Scale ISCO Experiment..... | 119 |
| Figure 3.71 | PCE Concentrations at Vertical Sampling Array G, Intermediate-Scale ISCO Experiment..... | 120 |
| Figure 3.72 | PCE Concentrations at Vertical Sampling Array N, Intermediate-Scale ISCO Experiment..... | 121 |
| Figure 3.73 | PCE Concentrations along Horizontal Centerline, Intermediate-Scale ISCO Experiment..... | 121 |
| Figure 3.74 | Aqueous PCE Distribution Downgradient of Array G during Pre-Oxidation Natural Dissolution, Intermediate-Scale ISCO Experiment | 123 |

| | | |
|-------------|--|-----|
| Figure 3.75 | Aqueous PCE Distribution Downgradient of Array G during Oxidation Flush, Intermediate-Scale ISCO Experiment..... | 124 |
| Figure 3.76 | Aqueous PCE Distribution Downgradient of Array G during Post-Oxidation Natural Dissolution, Intermediate-Scale ISCO Experiment..... | 125 |
| Figure 3.77 | Cumulative PCE Mass Depleted from Intermediate-Scale ISCO Cell..... | 126 |
| Figure 3.78 | PCE Mass Depletion Rate from Intermediate-Scale ISCO Cell..... | 126 |
| Figure 3.79 | Estimated PCE Mass Depletion Rate from Each Source, Intermediate-Scale ISCO Experiment..... | 127 |
| Figure 3.80 | Estimated Cumulative PCE Mass Depleted from Each Source, Intermediate- Scale ISCO Experiment..... | 128 |
| Figure 3.81 | MnO ₂ (s) Distribution in the Intermediate-Scale ISCO Experiment..... | 130 |
| Figure 3.82 | MnO ₂ (s) Distribution around Sources in the Intermediate-Scale ISCO Experiment..... | 132 |
| Figure 3.83 | Water-Level Hydrographs in the Intermediate-Scale ISCO Experiment..... | 133 |
| Figure 3.84 | Hydrographs of Head Drop across Source Zones, Intermediate-Scale ISCO Experiment..... | 134 |
| Figure 3.85 | Comparison of Model Simulated Heads to Observed Heads Prior to Oxidation, Intermediate-Scale ISCO Experiments..... | 135 |
| Figure 3.86 | Observed and Simulated Head Drop across Sources Prior to Oxidation, Intermediate-Scale ISCO Experiment..... | 135 |
| Figure 3.87 | Comparison of Model Simulated Heads to Observed Heads after Oxidation, Intermediate-Scale ISCO Experiment..... | 136 |
| Figure 3.88 | Observed and Simulated Head Drop across Sources after Oxidation, Intermediate-Scale ISCO Experiment..... | 137 |
| Figure 3.89 | DNAPL PCE Saturation Distribution Prior to Chemical Oxidation, High Heterogeneity Experiment..... | 138 |
| Figure 3.90 | DNAPL PCE Saturation Distribution Prior to Chemical Oxidation, Low Heterogeneity Experiment..... | 138 |
| Figure 3.91 | Oxidation during ISCO High Heterogeneity Experiment..... | 139 |
| Figure 3.92 | Oxidation during ISCO Low Heterogeneity Experiment..... | 140 |
| Figure 3.93 | Mass of PCE Removed during ISCO High Heterogeneity Experiment..... | 141 |
| Figure 3.94 | Mass of PCE Removed during ISCO Low Heterogeneity Experiment..... | 141 |
| Figure 3.95 | DNAPL PCE Saturation Distribution Following Chemical Oxidation, ISCO High Heterogeneity Experiment..... | 143 |
| Figure 3.96 | DNAPL PCE Saturation Distribution Following Chemical Oxidation, ISCO Low Heterogeneity Experiment..... | 143 |
| Figure 3.97 | Flow Cell Used in Bioenhanced Mass Transfer Experiments..... | 148 |

| | | |
|--------------|---|-----|
| Figure 3.98 | Effect of Solution Composition on PCE Mass Flux from a DNAPL Pool, Flow-Cell Experiments of Bioenhanced Dissolution | 149 |
| Figure 3.99 | Distribution of DNAPL in a Pool with Average Saturation of 50 Percent, Flow Cell Experiments of Bioenhanced Dissolution..... | 150 |
| Figure 3.100 | Steady-State Concentration and Mass Flux of PCE in Abiotic Experiments | 152 |
| Figure 3.101 | Steady-State Mass Flux of Chlorinated Ethenes for Flow-Cell Experiments of Bioenhanced Dissolution with Excess Methanol | 154 |
| Figure 3.102 | Effects of Variations in Methanol Flux on Degradation and Dissolution, Series #2 Flow-Cell Experiments of Bioenhanced Dissolution..... | 155 |
| Figure 3.103 | Configuration of CF Tank, Large Tank Experiments of Bioenhanced Dissolution | 159 |
| Figure 3.104 | Configuration of RF Tank, Large Tank Experiments of Bioenhanced Dissolution | 160 |
| Figure 3.105 | DNAPL Saturation Distribution in Four Sources, Large-Tank Experiments of Bioenhanced Dissolution | 162 |
| Figure 3.106 | Observed PCE Concentration in the CF Tank at the End of Abiotic Dissolution Experiments..... | 165 |
| Figure 3.107 | Observed Concentration of Dissolved Ethene Chemicals in the CF Tank During the Bioenhanced Dissolution Experiment | 167 |
| Figure 3.108 | Observed PCE Concentration in the RF Tank at the End of Abiotic Dissolution Experiments..... | 168 |
| Figure 3.109 | Observed Concentration of Dissolved Ethene Chemicals in the RF Tank One Month after Inoculation..... | 170 |
| Figure 3.110 | Observed Concentration of Dissolved Ethene Chemicals in the RF Tank Two Month after Inoculation | 171 |
| Figure 3.111 | PCE Solubility as a Function of Temperature | 173 |
| Figure 3.112 | Relationship of Mass Transfer Rate Coefficient to Sand Grain Size and Water Temperature for a Flow Rate of 5.5 mL/min, Column Experiments with Thermal Treatment | 175 |
| Figure 3.113 | Relationship of Mass Transfer Rate Coefficient to Sand Grain Size and Water Temperature for a Flow Rate of 10.0 mL/min, Column Experiments with Thermal Treatment | 175 |
| Figure 3.114 | Relationship of Sherwood Number to Flow Rate and Sand Grain Size, Column Experiments with Thermal Treatment at 25°C | 176 |
| Figure 3.115 | Relationship of Mass Transfer Rate Coefficient to Sand Grain Size and Flow Rate, Column Experiments with Thermal Treatment at 25°C | 176 |
| Figure 3.116 | Steady-State Distribution of Aqueous-Phase PCE during Flow Cell Experiments with Thermal Treatment (source length is 1 cm, flow rate is 25 mL/min) | 178 |

| | | |
|--------------|---|-----|
| Figure 3.117 | Steady-State Distribution of Aqueous-Phase PCE during Flow Cell Experiments with Thermal Treatment (source length is 1 cm, temperature is 25°C) | 179 |
| Figure 3.118 | Steady-State Distribution of Aqueous-Phase PCE during Flow Cell Experiments with Thermal Treatment (source length is 1 cm, temperature is 55°C) | 179 |
| Figure 3.119 | Steady-State Distribution of Aqueous-Phase PCE during Flow Cell Experiments with Thermal Treatment (source length is 2 cm, flow rate is 25mL/min) | 180 |
| Figure 3.120 | Steady-State Distribution of Aqueous-Phase PCE during Flow Cell Experiments with Thermal Treatment (source length is 2 cm, temperature is 25°C) | 180 |
| Figure 3.121 | Steady-State Distribution of Aqueous-Phase PCE during Flow Cell Experiments with Thermal Treatment (source length is 2 cm, temperature is 55°C) | 181 |
| Figure 3.122 | Steady-State Distribution of Aqueous-Phase PCE during Flow Cell Experiments with Thermal Treatment (source length is 4 cm, flow rate is 25 mL/min)..... | 181 |
| Figure 3.123 | Steady-State Distribution of Aqueous-Phase PCE during Flow Cell Experiments with Thermal Treatment (source length is 4 cm, temperature is 25°C) | 182 |
| Figure 3.124 | Steady-State Distribution of Aqueous-Phase PCE during Flow Cell Experiments with Thermal Treatment (source length is 4 cm, temperature is 55°C) | 182 |
| Figure 3.125 | Simulation Procedures and Execution Sequences of Program Units for Dissolution Simulation..... | 185 |
| Figure 3.126 | Hypothetical NAPL Column Used to Verify the Dissolution Model..... | 188 |
| Figure 3.127 | Numerical and Analytical Solutions of Steady-state PCE Dissolution from a Column | 189 |
| Figure 3.128 | Breakthrough Curves Obtained from MODTRACER Simulation of a Partitioning Tracer Test in a Column..... | 193 |
| Figure 3.129 | Retardation Factors Obtained from Simulated Breakthrough Curves, MODTRACER Verification Exercise | 194 |
| Figure 3.130 | NOD Oxidation Rates for Mines Park Soil..... | 199 |
| Figure 3.131 | Analytical and Model Results for PCE in a Short Column, CORT3D Model Verification..... | 203 |
| Figure 3.132 | Analytical and Model Results for MnO ₄ ⁻ in a Short Column, CORT3D Model Verification..... | 204 |
| Figure 3.133 | Schematic of Two-Dimensional Aquifer Scenario Used to Verify the CORT3D Model..... | 205 |

| | | |
|--------------|---|-----|
| Figure 3.134 | Analytical and Model Results for PCE in the Two-Dimensional Verification Exercise of the CORT3D Model | 206 |
| Figure 3.135 | Chemical and Biomass Components in the PCE Reductive Dechlorination Model of Fennell and Gossett (1998) | 208 |
| Figure 3.136 | Concentration Breakthrough Curves at the Outflow of a Column Obtained with the RT3D and Brusseau Models | 210 |
| Figure 3.137 | Biomass Concentration at the Outflow of a Column Obtained with the RT3D and Brusseau Models | 211 |
| Figure 3.138 | Three-Dimensional Hypothetical Aquifer Used in Field-Scale Simulation Study | 212 |
| Figure 4.1 | Conceptualization of the Source Zone used for Inverse Modeling, Large-Tank Tracer Tests, High Heterogeneity | 216 |
| Figure 4.2 | Comparison of the Saturation Distributions Obtained by Inverse Modeling and Actual Data, Large Tank Tracer Test, High Heterogeneity | 217 |
| Figure 4.3 | Comparison of the Saturation Distributions Obtained by Inverse Modeling, Moment Analysis, and Actual Data, Large Tank Tracer Test, Low Heterogeneity | 218 |
| Figure 4.4 | Experimental and Simulated Breakthrough Curves for Sample Ports A16 and A17, Large Tank Tracer Test, High Heterogeneity | 219 |
| Figure 4.5 | Experimental and Simulated Breakthrough Curves for Selected Sample Ports, Large Tank Tracer Test, Low Heterogeneity | 220 |
| Figure 4.6 | Fractional Change of the Second Moment in Sampling Array A, Large Tank Tracer Test, High Heterogeneity | 222 |
| Figure 4.7 | K_p as a Function of Time for DMP, Batch Partitioning Tracer Tests | 222 |
| Figure 4.8 | Comparison of Observed Saturation Distribution with the Saturation Distribution Obtained by Inverse Modeling with Effective Partitioning Coefficients, Large Tank Tracer Test, High Heterogeneity | 223 |
| Figure 4.9 | Comparison of Observed and Simulated Natural Dissolution of PCE in Column Experiments | 227 |
| Figure 4.10 | Comparison of Observed and Simulated PCE Dissolution under Natural Conditions, Horizontal Flow-Cell Experiments with One Source Zone | 229 |
| Figure 4.11 | Comparison of Observed and Simulated Steady-State PCE Concentration for a Range of Flow Rates, Horizontal Flow-Cell Experiments with One Source Zone..... | 230 |
| Figure 4.12 | Comparison of Observed and Simulated PCE Dissolution Fronts, Horizontal Flow-Cell Experiments with One Source Zone | 231 |
| Figure 4.13 | Comparison of Observed and Simulated Steady-State Mass Depletion Rates as a Function of Flow Rate, Horizontal Flow-Cell Experiments with One Source Zone | 232 |

| | | |
|-------------|--|-----|
| Figure 4.14 | Comparison of Observed and Simulated PCE Dissolution under Natural Conditions, Horizontal Flow-Cell Experiments with Two Source Zones | 233 |
| Figure 4.15 | Comparison of Observed and Simulated Steady-State PCE Concentration, Large Tank Experiment with High Heterogeneity..... | 234 |
| Figure 4.16 | Comparison of Observed and Simulated Steady-State PCE Concentration along Three Vertical Sampling Arrays, Large Tank Experiment with High Heterogeneity..... | 234 |
| Figure 4.17 | Comparison of Observed and Simulated Steady-State PCE Concentration along Three Vertical Sampling Arrays, Large Tank Experiment with Low Heterogeneity and a Total Head Difference of 5.7 cm | 235 |
| Figure 4.18 | Comparison of Observed and Simulated Steady-State PCE Concentration along Two Vertical Sampling Arrays, Large Tank Experiment with Low Heterogeneity and a Total Head Difference of 3 cm | 235 |
| Figure 4.19 | Heterogeneous Test Tank used in Monte Carlo Study of Natural Dissolution | 237 |
| Figure 4.20 | PCE Distribution in the Source Zone for Realization #1, Monte Carlo Simulations of Natural Dissolution..... | 239 |
| Figure 4.21 | PCE Distribution in the Source Zone for Realization #11, Monte Carlo Simulations of Natural Dissolution..... | 239 |
| Figure 4.22 | PCE Distribution in the Source Zone for Realization #54, Monte Carlo Simulations of Natural Dissolution..... | 239 |
| Figure 4.23 | Vertical Distribution of Steady-state Dissolved PCE Concentration and Mass Flux Downstream of the Source Zone for Realization #1, Monte Carlo Simulations of Natural Dissolution..... | 241 |
| Figure 4.24 | Total Steady-State Mass Flux vs. Normalized First and Second Moments for Realizations 1, 11, and 54, Monte Carlo Simulations of Natural Dissolution..... | 242 |
| Figure 4.25 | Finite-Difference Grid Used in the Upscaling Analysis for Natural Dissolution | 244 |
| Figure 4.26 | PCE DNAPL Distribution for Realization #16, Upscaling Analysis of Natural Dissolution | 251 |
| Figure 4.27 | Comparison of Observed and Simulated Concentration Using Small-Scale and Upscaleable Gilland-Sherwood Correlation, Upscaling Analysis of Natural Dissolution | 253 |
| Figure 4.28 | Comparison of Observed and Simulated Mass Flux Using Small-Scale and Upscaleable Gilland-Sherwood Correlation, Upscaling Analysis of Natural Dissolution | 254 |
| Figure 4.29 | Comparison of Observed and Simulated Mass Flux (top) and Concentration Using Upscaleable Gilland-Sherwood Correlation for Spill Realization #16, Upscaling Analysis of Natural Dissolution..... | 255 |

| | | |
|-------------|---|-----|
| Figure 4.30 | Grid Systems 1, 2 and 3 Used in Simulations of Natural Dissolution with the Upscaleable Gilland-Sherwood Correlation, Large Tank Experiment with High Heterogeneity | 256 |
| Figure 4.31 | Grid Systems 4, 5 and 6 Used in Simulations of Natural Dissolution with the Upscaleable Gilland-Sherwood Correlation, Large Tank Experiment with High Heterogeneity | 257 |
| Figure 4.32 | Comparison of Observed and Simulated PCE Concentration Using Small-Scale and Upscaleable Gilland-Sherwood Correlation, Large-Tank Experiment of Natural Dissolution with High Heterogeneity | 258 |
| Figure 4.33 | Comparison of Observed and Simulated PCE Mass Flux Using Small-Scale and Upscaleable Gilland-Sherwood Correlation, Large-Tank Experiment of Natural Dissolution with High Heterogeneity | 258 |
| Figure 4.34 | Comparison of Observed to Simulated Effluent PCE Concentration, Surfactant-Flushing Column Experiment | 259 |
| Figure 4.35 | Comparison of Observed to Simulated PCE Concentration, Surfactant-Flushing Experiment in a Two-Dimensional Flow Cell with One DNAPL Source Zone | 261 |
| Figure 4.36 | Comparison of Observed to Simulated PCE Concentration, Surfactant-Flushing Experiment in a Two-Dimensional Flow Cell with Two DNAPL Source Zones..... | 262 |
| Figure 4.37 | Comparison of Observed and Simulated Breakthrough Curves for Sampling Ports A14 to A27, Large-Tank Experiment of Surfactant Flushing with High Heterogeneity | 264 |
| Figure 4.38 | Comparison of Observed and Simulated Breakthrough Curves for Sampling Ports A29 to C31, Large-Tank Experiment of Surfactant Flushing with High Heterogeneity | 265 |
| Figure 4.39 | Observed Water Head for a Column Experiment with TCE Oxidation | 269 |
| Figure 4.40 | Comparison of Observed and Simulated TCE Concentration (a) and TCE Mass Remaining (b) for the Column Dissolution Experiment of Schroth et al. (2001)..... | 270 |
| Figure 4.41 | Simulated Water Head during TCE Oxidation, Column Experiment of Schroth et al. (2001)..... | 271 |
| Figure 4.42 | Comparison of Simulated and Observed Results for Column Experiments of Schnarr et al. (1998) with PCE Oxidation and Low Oxidant Concentration | 273 |
| Figure 4.43 | Comparison of Simulated and Observed Results for Column Experiments of Schnarr et al. (1998) with PCE Oxidation and High Oxidant Concentration | 273 |

| | | |
|-------------|--|-----|
| Figure 4.45 | Comparison of Simulated and Observed Results for Column Experiments of Schnarr et al. (1998) with Alternative Descriptions of Mass Transfer Enhancement..... | 275 |
| Figure 4.46 | Comparison of Simulated and Observed Results for Column Experiments of Schnarr et al. (1998) with Alternative Descriptions of NOD..... | 276 |
| Figure 4.47 | Comparison of Simulated and Observed Results for Column Experiments of Schnarr et al. (1998) with Alternative Descriptions of Permeability Changes..... | 277 |
| Figure 4.48 | Alternative Representations of DNAPL Saturation in Flow-Cell Model of Bioenhanced Dissolution..... | 280 |
| Figure 4.49 | Cross Sections of Simulated Tracer Plume and PCE Plume for Abiotic Experiment A6 with Two-Layer Pool Model, Flow-Cell Model of Bioenhanced Dissolution..... | 282 |
| Figure 4.50 | Comparison of Simulated and Observed PCE Mass Load for Abiotic Experiments, Flow-Cell Model of Bioenhanced Dissolution..... | 283 |
| Figure 4.51 | Comparison of Gilland-Sherwood Correlations for Flow-Cell Experiments with an Average Source Zone Saturation of 55 Percent, Flow-Cell Model of Bioenhanced Dissolution..... | 284 |
| Figure 4.52 | Relative Permeability as a Function of Biomass Concentration for Several Biomass-Clogging Models..... | 287 |
| Figure 4.53 | Relationship of Degradation-Product Load to (a) Available Methanol Load and (b) Available Methanol Concentration, Flow Cell Experiments of Bioenhanced Dissolution..... | 288 |
| Figure 4.54 | Relationship of Sum of Squared Residuals to Mass Transfer Rate Coefficient and PCE Degradation Rate Coefficient, Bioenhanced Dissolution Model of Flow-Cell Experiment B1-3..... | 291 |
| Figure 4.55 | Relationship of Sum of Squared Residuals to Calibration Parameter Ratios, Bioenhanced Dissolution Model of Flow-Cell Experiment B1-3..... | 292 |
| Figure 4.56 | Simulated Steady State Concentration Profiles (mg/L), Flow-Cell Model of Bioenhanced Dissolution..... | 294 |
| Figure 4.57 | Simulated Steady-State PCE Concentration in the CF Tank during Abiotic Dissolution, Large Tank Experiments of Bioenhanced Dissolution..... | 299 |
| Figure 4.58 | Simulated PCE Concentration and Mass Flux Profiles Downgradient of DNAPL Sources during Abiotic Dissolution in the CF Tank, Large Tank Experiments of Bioenhanced Dissolution..... | 300 |
| Figure 4.59 | Concentration Profiles in Upper Unit, CF Tank, for Four Simulation Scenarios, Large-Tank Modeling of Bioenhanced Dissolution..... | 305 |
| Figure 4.60 | Concentration Profiles in Lower Unit, CF tank, for Four Simulation Scenarios, Large-Tank Modeling of Bioenhanced Dissolution..... | 306 |

| | | |
|-------------|--|-----|
| Figure 4.61 | Comparison of Critical Ethene Concentration for Gas Formation with Simulated Ethene Concentration after 11 Source Pore Volumes, Large Tank Modeling of Bioenhanced Dissolution | 307 |
| Figure 4.62 | Concentration Profiles in the CF Tank for the Base Scenario with Kinetic Gas Partitioning, Large Tank Bioenhanced Dissolution Experiments | 309 |
| Figure 4.63 | Schematic Diagram of Sub-Grid Heterogeneity Due to Pool Morphology | 310 |
| Figure 4.64 | Aquifer System and Finite Difference Grids Used to Evaluate Upscaling Strategy for Bioenhanced Dissolution | 313 |
| Figure 4.65 | Comparison of PCE Concentrations Simulated with Abiotic Dissolution Model Using Fine and Coarse Grids, Upscaling Simulations of Bioenhanced Dissolution | 315 |
| Figure 4.66 | Comparison of Total Ethene Concentrations Simulated Using Fine and Coarse Grids, Upscaling Simulations of Bioenhanced Dissolution..... | 316 |
| Figure 4.67 | Hypothetical Aquifer Used in Three-Dimensional Study of Mass Transfer | 318 |
| Figure 4.68 | Hydraulic Conductivity Distribution for IDEAL Simulations, Three-Dimensional Study of Mass Transfer..... | 319 |
| Figure 4.69 | PCE DNAPL Distribution Based on UTCHEM Simulation, Three-Dimensional Study of Mass Transfer..... | 320 |
| Figure 4.70 | Locations of Observation Wells and Steady-State Dissolved PCE Plume, Three-Dimensional Study of Mass Transfer..... | 321 |
| Figure 4.71 | Locations of Pumping and Observation wells, Three-Dimensional Study of Mass Transfer | 322 |
| Figure 4.72 | Water-Table Configuration for IDEAL Simulation After 0.2 Days of Pumping at PW1, Pumping Rate is 25 m ³ /day, Three-Dimensional Study of Mass Transfer | 322 |
| Figure 4.73 | Water-Table Configuration for IDEAL Simulation After 0.2 Days of Pumping at OW4, Pumping Rate is 25 m ³ /day, Three-Dimensional Study of Mass Transfer | 323 |
| Figure 4.74 | Type-Curve Matching for Pumping Well PW1, Three-Dimensional Study of Mass Transfer | 323 |
| Figure 4.75 | Type-Curve Matching for Pumping Well OW4, Three-Dimensional Study of Mass Transfer | 324 |
| Figure 4.76 | Multi-Level Sampling Wells and Injection-Extraction System used in the Multiple Tracer Test, Three-Dimensional Study of Mass Transfer..... | 325 |
| Figure 4.77 | Examples of Breakthrough Curves at Two Multi-Level Sampling Wells, Three-Dimensional Study of Mass Transfer..... | 326 |
| Figure 4.78 | Point Estimates of PCE Saturation Based on the Method of Moments Analysis, Three-Dimensional Study of Mass Transfer..... | 327 |

| | | |
|-------------|--|-----|
| Figure 4.79 | Tracer Breakthrough Curves at the Extraction Well, Three-Dimensional Study of Mass Transfer | 328 |
| Figure 4.80 | Borehole Logs of Soil Types and Spatial Distribution of Boreholes Used in AQ9 Aquifer Characterization, Three-Dimensional Study of Mass Transfer | 328 |
| Figure 4.81 | Histogram of Log Hydraulic Conductivity Obtained from Borehole Well-Log Analysis, Three-Dimensional Study of Mass Transfer | 329 |
| Figure 4.82 | Example distributions of soil materials in layers 6 and 12, AQ9 Aquifer Characterization, Three-Dimensional Study of Mass Transfer | 329 |
| Figure 4.83 | Soil-Type Distribution, AQ9 Aquifer Characterization, Three-Dimensional Study of Mass Transfer | 330 |
| Figure 4.84 | Observed (IDEAL) and Simulated (AQ9) Time-Drawdown Plots for Pumping Tests, Three-Dimensional Study of Mass Transfer | 331 |
| Figure 4.85 | Measured Steady-State PCE Concentration at Sampling Wells, Three-Dimensional Study of Mass Transfer | 333 |
| Figure 4.86 | PCE Source Zone Estimated by Inverse Modeling, AQ9 Aquifer Characterization, Three-Dimensional Study of Mass Transfer | 334 |
| Figure 4.87 | Comparison of steady-state dissolved PCE plume from the IDEAL and AQ9 Aquifer Characterizations, Three-Dimensional Study of Mass Transfer..... | 334 |
| Figure 4.88 | Particle Tracking Simulation of the Surfactant Delivery System, AQ9 Aquifer Characterization, Three-Dimensional Study of Mass Transfer | 335 |
| Figure 4.89 | SEAR Simulation Results, AQ9 Aquifer Characterization, Three-Dimensional Study of Mass Transfer | 336 |

List of Tables

| | | |
|------------|---|----|
| Table 3.1 | Physical and Chemical Properties of Pure DNAPL..... | 25 |
| Table 3.2 | Partition Coefficients of Tracers..... | 26 |
| Table 3.3 | Properties of Tween-80..... | 26 |
| Table 3.4 | Tap Water Chemical Composition..... | 27 |
| Table 3.5 | Chemical Composition of Simulated Groundwater..... | 27 |
| Table 3.6 | Properties of Porous Media..... | 30 |
| Table 3.7 | Average Chemical Analysis of Porous Media..... | 31 |
| Table 3.8 | GC Method Summaries..... | 31 |
| Table 3.9 | Partition Coefficients for Surfactant-Treated TCE DNAPL Estimated from Batch Tests..... | 38 |
| Table 3.10 | Partition Coefficients for Surfactant-Treated DNAPL Mixture of PCE/TCE Estimated from Batch Tests..... | 38 |
| Table 3.11 | Partition Coefficients for Surfactant-Treated Field DNAPL Estimated from Batch Tests..... | 39 |
| Table 3.12 | Tracer Partition Coefficients for Oxidant and Water Treated DNAPLs..... | 40 |
| Table 3.13 | Partitioning Coefficients for Baseline Systems with Water, Batch Partitioning Tracer Experiments with Biological Treatment..... | 46 |
| Table 3.14 | Partitioning Coefficients for Baseline Systems with Abiotic Nutrient Medium, Batch Partitioning Tracer Experiments with Biological Treatment..... | 46 |
| Table 3.15 | Partitioning Coefficients for Water-Treated Systems, Batch Partitioning Tracer Experiments with Biological Treatment..... | 47 |
| Table 3.16 | Partitioning Coefficients for Bio-Treated Systems, Batch Partitioning Tracer Experiments with Biological Treatment..... | 48 |
| Table 3.17 | Characteristics of Partitioning Tracer Tests in Columns with Surfactant Treatment..... | 49 |
| Table 3.18 | Comparison of Entrapped DNAPL Volumes, Partitioning Tracer Tests in Columns Before and After Surfactant Treatment..... | 51 |
| Table 3.19 | Characteristics of Partitioning Tracer Tests in Columns with Biological Treatment..... | 52 |
| Table 3.20 | Results of Partitioning Tracer Tests in Columns with Biological Treatment..... | 53 |
| Table 3.21 | Statistical Properties of Hydraulic Conductivity Used in Designing Large Tank Experiments of Heterogeneous Test Aquifers..... | 54 |

| | | |
|------------|---|-----|
| Table 3.22 | Volume of PCE Injected During Source Zone Creation, Large Tank Experiments of Heterogeneous Test Aquifers | 56 |
| Table 3.23 | Summary of Partitioning Tracer Tests during Natural Dissolution, Large Tank Experiments of Heterogeneous Test Aquifers | 58 |
| Table 3.24 | Properties of Sands Used in Two-Dimensional Horizontal Flow-Cell Experiments with Pure PCE..... | 70 |
| Table 3.25 | Summary of Column Experiments at Selected Orientations | 81 |
| Table 3.26 | Summary of Column Experiments with the Surfactant Aerosol 80I at Selected Flow Rates | 82 |
| Table 3.27 | Summary of Column Experiments with Tween 80 Using Two Injection Strategies..... | 83 |
| Table 3.28 | Summary of Mass Transfer Coefficients of TCE Present as Pure DNAPL and Field DNAPL During Column and Flow-Cell Experiments..... | 88 |
| Table 3.29 | Aquifer Properties Used in Surfactant-Enhanced Dissolution Experiment with Spatially Correlated Random Field..... | 92 |
| Table 3.30 | Summary of PCE Injection Volumes in Selected Sand Lenses | 94 |
| Table 3.31 | Comparison of Steady State PCE Dissolution Concentrations, Surfactant-Enhanced Dissolution Experiment with Spatially Correlated Random Field..... | 101 |
| Table 3.32 | FTR Experimental Conditions | 110 |
| Table 3.33 | FTR Experimental Results..... | 115 |
| Table 3.34 | Description of Source Zones for Intermediate-Scale ISCO Experiment | 118 |
| Table 3.35 | Chronology of Intermediate-Scale ISCO Experiment | 119 |
| Table 3.36 | Estimated PCE Mass Removal from Sources during Each Phase | 128 |
| Table 3.37 | Oxidant Injection Summary for Tank Experiments with ISCO..... | 139 |
| Table 3.38 | Oxidation Performance Summary..... | 142 |
| Table 3.39 | Characteristics Column Experiments of Bioenhanced Dissolution | 144 |
| Table 3.40 | Mass Flux of Chlorinated Ethenes in Abiotic and Biotic Column Experiments | 145 |
| Table 3.41 | PCE Biodegradation Rate Constants for Batch and Column Experiments..... | 146 |
| Table 3.42 | Observed Mass Load of Dissolved Ethene Chemicals at Groundwater Withdrawal Locations in the RF Tank Experiment of Bioenhanced Dissolution | 168 |
| Table 3.43 | Important Processes Captured by the ISCO Model | 195 |
| Table 4.1 | Empirical Gilland-Sherwood Coefficients Resulted from Inverse Modeling of Natural Dissolution Experiments | 226 |

| | | |
|------------|--|-----|
| Table 4.2 | Optimized Gilland-Sherwood Parameters for Natural Dissolution, Horizontal Flow-Cell Experiments with pure PCE | 228 |
| Table 4.3 | Properties of Sands used to Represent the Random Field, Monte Carlo Study of Natural Dissolution | 237 |
| Table 4.4 | Properties of PCE DNAPL at 25 °C used in Monte Carlo Simulations of Natural Dissolution | 238 |
| Table 4.5 | Summary of the Spatial Moments Calculated for Realizations 1, 11, and 54, Monte Carlo Simulations of Natural Dissolution | 240 |
| Table 4.6 | Finite-Difference Grids Used in Upscaling Analysis for Natural Dissolution | 248 |
| Table 4.7 | Optimized Empirical Parameters, Upscaling Analysis of Natural Dissolution ... | 252 |
| Table 4.8 | Optimization Parameter Estimates for the Upscaleable Gilland-Sherwood Correlation Obtained for the Large-Tank Experiment of Natural Dissolution with High Heterogeneity..... | 252 |
| Table 4.9 | Empirical Parameters of Gilland-Sherwood Expression Obtained by Inverse Modeling, Surfactant-Flushing Column Experiment..... | 260 |
| Table 4.10 | Estimation of Expected Mass Transfer Increase due to Oxidation, Column Experiments of Schnarr et al. (1998)..... | 275 |
| Table 4.11 | Parameter Estimates used in Abiotic Simulations, Flow-Cell Model of Bioenhanced Dissolution | 281 |
| Table 4.12 | Experimental Conditions Used in Flow-Cell Model of Bioenhanced Mass Transfer..... | 285 |
| Table 4.13 | Prior Information for Parameters of Flow-Cell Model of Bioenhanced Dissolution | 286 |
| Table 4.14 | Values for Calibration Parameters in Bioenhanced Dissolution Model of Flow-Cell Experiment B1-3 | 290 |
| Table 4.15 | Sensitivity Coefficients for Calibration Parameters in Bioenhanced Dissolution Model of Flow-Cell Experiment B1-3 | 291 |
| Table 4.16 | Sensitivity Coefficients for Calibration Parameters in Bioenhanced Dissolution Model of Flow-Cell Experiment B2-3 | 293 |
| Table 4.17 | Parameter Estimates Used to Simulate Groundwater Flow and Abiotic Dissolution in the CF Tank, Large Tank Experiments of Bioenhanced Dissolution | 298 |
| Table 4.18 | Mass Flux of Aqueous Phase Ethene Chemicals in the CF Tank, Large Tank Experiments of Bioenhanced Dissolution..... | 301 |
| Table 4.19 | Estimated Ratios of Effective First Order Degradation Coefficients for Chlorinated Ethenes | 303 |
| Table 4.20 | Estimates of Effective First-Order Degradation Coefficients Used in Sensitivity Analysis of Bioenhanced Dissolution in the CF Tank..... | 303 |

| | | |
|------------|---|-----|
| Table 4.21 | Flow-System and Source-Zone Characteristics Used to Evaluate Upscaling Strategy for Bioenhanced Dissolution | 314 |
| Table 4.22 | Calibrated Flow Parameters, AQ9 Aquifer Characterization, Three-Dimensional Study of Mass Transfer..... | 331 |
| Table 4.23 | Calibrated Transport Parameters, AQ9 Aquifer Characterization, Three-Dimensional Study of Mass Transfer | 332 |

Acknowledgements

A number of individuals and organizations contributed to this research project and the generation of this report. Dr. Dongping Dai coordinated experimental efforts during the initial years of the project, developed most of the analytical methods used for chemical analysis of samples, and contributed to studies of partitioning tracers and surfactant-enhanced remediation at batch, column and flow-cell scales. Four graduate students at the Colorado School of Mines (CSM), Division of Environmental Science and Engineering and two graduate students at Cambridge University were involved in the project. Satawat Saenton completed his PhD degree in 2003 and continued to contribute to the project as a post-doctoral research associate. His research focused on surfactant enhanced dissolution and source zone characterization. The modeling methods developed in his research provided the framework for models and up-scaling methods for other treatment technologies. Ann Kaplan conducted research related to biological treatment of DNAPL at batch and column scales and received a MS degree in 2004. Air Force Major Jeff Heiderschidt completed his PhD on in situ chemical oxidation focusing on intermediate-scale testing and modeling. Kent Glover completed his Ph.D. degree in 2006 and conducted research involved flow-cell and large tank experiments and modeling, including upscaling, associated with biological treatment of DNAPL. Jose Gago is a PhD student and has focused on thermal treatment technology. Indu Kulasooriya and John Page completed their doctoral degrees at Cambridge University in 2005. Both students contributed to research presented in this report related to surfactant treatment technology. In addition, Y-C Kim, a doctoral student from the Seoul National University visited CSM from February to August 2003, to participate in the project. His work focused on surfactant enhanced remediation and tracer methods. After completing his degree work, he returned to CSM as a post-doctoral research associate where his work focused on completing several large-tank experiments. The research on in situ chemical oxidation of chemical oxidation is done in collaboration with the research group project ER-1290.

Complex and labor-intensive experiments at a range of scales were fundamental to this research. These experiments could not have been completed successfully without the assistance of many additional people in the form of sampling, development of instrumentation, and other tasks. The assistance of undergraduate students Gareth Middleton, Kris Middleton, Pam Russell and Tushani Illangasekare, graduate students Shiloh Hernandez, Derrick Rodriguez and Anil Waduge, and postdoctoral researcher Ed Hill is greatly appreciated.

The research team gratefully acknowledges the generous provision of the KB-1 culture by Dr. Elizabeth Edwards, University of Toronto, and the assistance of Dr. Melanie Duhamel in its initial cultivation at CSM. Growth of the KB-1 culture was monitored and maintained at CSM through the diligent efforts of Casey Ramey. Dr. James Gossett, Cornell University, provided advise in the growth of anaerobic cultures capable of dechlorination as well as his design for growing and maintaining large volumes of culture. Samples of DNAPL from field sites were provided by URS Corporation and SAIC.

The research team also wishes to acknowledge the programmatic support provided by SERDP program managers and the staff of HydroGeoLogic, Inc., as well as the advise provided by the SERDP DNAPL Scientific Advisory Board.

Executive Summary

Organic chemicals such as chlorinated solvents in the form of dense nonaqueous phase liquid (DNAPL) exhibit complex flow and entrapment behavior in naturally heterogeneous subsurface systems. Technologies that remove mass, change or stabilize DNAPL through controlled physical, chemical or biological activity are designed ultimately to reduce mass flux emission from aquifer zones where DNAPL is present. An understanding of mass transfer that occurs from heterogeneous DNAPL sources is fundamental to determine both the pre- and post-remediation status of the downgradient solute plume. The spatial distribution of saturation and morphology of entrapment (referred to as DNAPL architecture) contributes to the spatial and temporal distribution of mass emission. Non-invasive partitioning tracer techniques used for DNAPL source characterization have the potential to evaluate post-treatment DNAPL entrapment architecture.

The primary research goal was to understand and characterize mass transfer and tracer partitioning in DNAPL sources undergoing remediation. Four source zone treatment technologies were evaluated: (1) bio-treatment, (2) in situ chemical oxidation (ISCO), (3) surfactant enhanced dissolution and (4) thermal treatment. The focus was to generate fundamental knowledge needed to improve and develop tools that can evaluate the impact of remediation technologies on DNAPL distribution. The research approach emphasized (1) evaluations of partitioning tracer techniques for characterizing pre- and post-treatment DNAPL distribution, (2) modeling tools for evaluating effective pre- and post-remediation mass transfer, and (3) strategies for upscaling mass transfer models from laboratory to field scale.

Approach

Objectives were addressed within seven areas of technical focus: (1) characterization by partitioning tracer techniques, (2) mass transfer by natural dissolution, (3) surfactant enhanced dissolution, (4) effects of in-situ chemical oxidation on mass transfer, (5) bioenhanced dissolution, (6) effects of thermal treatment on mass transfer, and (7) three dimensional test simulations. As a fundamental part of this investigation, experimental and modeling approaches were designed to address the issue of upscaling the model parameters from laboratory to the field.

Experimental methods and modeling approaches for the first six focus areas shared common characteristics. Batch and column experiments of partitioning tracer behavior were performed to determine partitioning coefficients for selected test DNAPLs and field samples undergoing transformations associated with remediation, and to evaluate the tracer partitioning coefficients change during remediation. Column and flow-cell experiments of mass transfer behavior were undertaken to test the hypothesis that mass transfer coefficients for entrapped DNAPL sources change during remediation, to determine the “point-scale” mass transfer coefficients from entrapped NAPL sources undergoing remediation, and to upscale the “point-scale” mass transfer coefficients to multi-dimensional flow fields. Large-tank experiments were designed to generate accurate data sets suitable for model validation, to obtain insight to mass transfer processes in source zones undergoing remediation, and to test upscaling methodologies. In conjunction with batch, column, flow-cell and large-tank experiments, mass transfer models were developed, validation studies were undertaken, and models were modified as needed.

A three-dimensional simulation study, was undertaken to demonstrate the use of mass transfer models as decision tools for source-zone management. The purpose of this demonstration was to evaluate if it is possible to accurately characterize, design and monitor remediation of NAPL source zones based on realistic conditions of data availability.

Key Findings

Research in each area of technical focus has significantly enhanced understanding of mass transfer from DNAPL sources in heterogeneous media. After listing the key findings in each area, basic contributions and findings that are common to all areas are identified and implications for future application are discussed.

Partitioning Tracers

The partitioning interwell tracer test (PITT) uses the laboratory-measured equilibrium partitioning coefficient of the tracer to DNAPL and the information contained in the breakthrough curve observed down gradient of the source zone. The breakthrough data could be analyzed either computing the moments or using inverse modeling.

Equilibrium partitioning behavior for pure trichloroethene (TCE) or tetrachloroethene (PCE) NAPL determined from laboratory experiments was linear with respect to tracer concentration and remained unchanged by remediation. The sole exception to this behavior was partitioning behavior for PCE-NAPL following ISCO, which was nonlinear. For NAPL mixtures obtained at field sites, partition coefficients changed following remediation.

The method of moments for analysis of partitioning interwell tracer tests (PITT) is unreliable in heterogeneous source zones where knowledge of vertical distribution of NAPL is needed. Although widely used, this method provided little accurate information to describe source-zone heterogeneity.

Analysis of PITT by inverse modeling can provide more accurate description of source architecture. However, in sources dominated by pools (i.e. low ganglia-to-pool ratio) this method also proved inaccurate due to hydrodynamic inaccessibility of pools for tracer partitioning.

Natural Dissolution

Mass transfer in heterogeneous source zones can be simulated as a kinetic process with effective mass transfer rate coefficients estimated by empirical Gilland-Sherwood correlations that relate a dimensionless form of mass transfer rate coefficient (Sherwood number) to other dimensionless groups that characterize the dominant physical processes that contribute to mass transfer (e.g. Reynolds number, Schmidt's number, etc.). These correlations characterizing dissolution from pure PCE- or TCE-NAPL are incorporated into models to simulate natural dissolution of NAPL mixtures at field sites. Empirical coefficients in the Gilland-Sherwood correlations obtained from 1-D column, 2-D cell, and 2-D large tank experiments were similar suggesting that correlations obtained from 1-D column experiments may be used to simulate dissolution at larger scales by incorporating appropriate parameters of the multi-dimensional flow field.

A new numerical modeling approach was developed to upscale mass transfer. The upscaled Gilland-Sherwood correlation is based on a local-scale Gilland-Sherwood expression in combination with geostatistical descriptions of aquifer heterogeneity and DNAPL entrapment

architecture. The upscaling technique was successfully verified using natural dissolution data obtained from large-scale 2-D test tank experiments.

Inverse modeling techniques can be used to determine the vertical distribution of NAPL saturation from water samples obtained along vertical profiles downgradient of the source zones. The upscaling technique emphasizes the importance of installing multi-level monitoring wells downgradient of suspected NAPL source zones. This suggests the need to develop monitoring methods that are different from the conventional methods that are used on most DNAPL sites.

Surfactant-Enhanced Dissolution

Effectiveness of surfactant-enhanced remediation decreases as source-zone heterogeneity increases. This was demonstrated by comparing remediation effectiveness for experiments in 1-D columns, 2-D bench-scale flow cells, and 2-D large tanks. In experiments with greater source heterogeneity, groundwater bypassing due to relative permeability contrasts caused DNAPL mass removal efficiency to diminish significantly.

The empirical parameters of Gilland-Sherwood correlations during surfactant-enhanced dissolution changed with changes in experimental test scale. Parameter estimates showed little change among 2-D experiments but were significantly different from 1-D column tests. This suggests that Gilland-Sherwood correlations obtained from 1-D column tests undergoing surfactant-enhanced remediation may not be appropriate for use in multidimensional experiments or at field sites.

In Situ Chemical Oxidation

Two-dimensional tank experiments with a physically heterogeneous source demonstrated the dependence of effectiveness of ISCO on the configuration of NAPL. Sources with low ganglia-to-pool ratios resulted in significantly lower mass transfer during remediation and less mass depletion.

Heterogeneous NAPL sources underwent a gradual decline in mass depletion rate as oxidation proceeded. Several sources returned to pre-treatment rates of mass depletion as a result of manganese oxide buildup and changes in flow patterns as remediation proceeded. Manganese oxide formation did not noticeably affect permeability until the mass fraction of manganese oxide exceeded 0.1 mg MnO₂(s) / kg aquifer material.

A reactive transport model based on the widely used RT3D code was developed to simulate effects of in situ chemical oxidation (ISCO) on mass transfer. The model simulates PCE-DNAPL oxidation, TCE-DNAPL oxidation, natural oxidant demand (NOD) based on multiple NOD fractions, kinetic NOD oxidation of each fraction, and permeability reduction due to manganese oxide formation

Bioenhanced Dissolution

Column, flow-cell and large-tank experiments showed significantly enhanced mass transfer from DNAPL sources with an average saturation of 60 percent or less. Bioenhanced dissolution occurred by biodegradation of PCE within source zones to less chlorinated but toxic daughter products with rapid degradation in adjacent downgradient areas to nontoxic ethene.

A numerical model of bioenhanced DNAPL dissolution based on the widely used RT3D code was developed and applied to experimental results. The resulting model is suitable for use as a remediation screening tool at sites contaminated with chlorinated DNAPL.

In source zones dominated by pools, accurate simulation of bioenhanced dissolution requires inclusion of saturation transition zones at pool boundaries. Bioenhanced dissolution depends on an adequate supply of electron donor within pool transition zones. Electron-donor advection within transition zones promotes rapid PCE degradation, lower aqueous-phase PCE concentrations, enhanced dissolution gradients, and increased rates of pool depletion. Therefore, recognition of transition-zone hydrodynamics is critical to characterization and modeling of bioenhanced dissolution.

Simulations of experimental results showed that scale-dependent Gilland-Sherwood correlations developed for pre-remediation conditions are suitable for simulating bioenhanced dissolution. Biodegradation is a local-scale process that can be modeled with parameter estimates derived at batch or column scales. A numerical simulation study suggests that dual-domain approaches can be effective for addressing sub-grid heterogeneity associated with pool transition zones.

Thermal Treatment

Mass transfer during thermal treatment was characterized and modeled as a kinetic process with effective mass transfer rate coefficients estimated by Gilland-Sherwood correlations. Research focused on understanding how thermal treatment affects solubility of PCE-DNAPL and empirical coefficients of Gilland-Sherwood correlations. Hot-water flooding was selected for study as representative of the broader range of thermal technologies. Results presented here were obtained with batch and column experiments. Research to upscale these results to multi-dimensional flow systems in flow cells and large tanks is continuing.

Column experiments with PCE-DNAPL at residual saturation were conducted for a range of temperatures typically used in thermal technologies. Variations in temperature resulted in large variations in effluent concentration of aqueous-phase PCE. Higher temperature resulted in higher PCE concentration. Variations in flow rate also affected PCE concentration, but this effect was secondary to that of temperature. This implies that thermal-treatment designs may be optimized for temperature with optimization for flow rate being a secondary goal.

Temperature affects fluid viscosity and diffusion coefficients and therefore directly affects several dimensionless numbers used as a basis for Gilland-Sherwood correlations. Statistical analysis of changes in empirical coefficients with temperature demonstrated that the use of Gilland-Sherwood correlations developed at one temperature could be used to simulate mass transfer at greater temperatures.

Three-Dimensional Simulation Study

A numerical experiment demonstrated the ability to characterize mass transfer from a heterogeneous source in conditions with limited data. Key findings of this research project in conjunction with inverse modeling techniques were used to evaluate DNAPL mass distribution and mass depletion on the basis of hydraulic and chemical data at a limited number of wells located downgradient of the source. In the heterogeneous geological setting considered, characterization of source-zone configuration, mass transfer and remediation effectiveness required an understanding of plume and tracer distribution transverse to the primary direction of groundwater flow. In field settings, this type of data would be obtained by constructing monitoring wells with multi-level sampling capabilities.

Conclusions and Implications

Characterizing and modeling mass transfer from a DNAPL source where saturation is distributed in a spatially heterogeneous manner and predicting effectiveness of source remediation can be a challenging task considering the many uncertainties in available data and knowledge gaps in the understanding of fundamental processes. The research presented in this report attempts to provide a technically defensible basis for addressing the task of using pre-remediation mass-flux information supplemented by limited laboratory-scale study of remediation processes. Conceptual and numerical models of pre- and post-remediation mass transfer and partitioning tracer behavior were developed for several remediation technologies. These models were developed within the framework of widely used groundwater flow and reactive transport codes. Controlled experiments in large tanks provided high-quality data sets for model validation. This level of comprehensive and accurate data collection is not feasible at field sites for model validation. Even though the intermediate scale test systems do not have the ability to capture all complexities of field systems, as a first step, these types of model validation studies provide a much higher degree of confidence for models to be used in field studies.

A strategy for evaluating mass transfer from heterogeneous sources was developed that can simplify and decrease the amount of site data needed for source-zone characterization and remediation. At the same time, research results point to the importance of using monitoring wells as multi-level samplers to accurately understand mass transfer from heterogeneous sources and to generate required data input for inverse modeling techniques.

Common trends and patterns occur in the key research results presented in this report. These trends are listed below.

- For ISCO, bioremediation and thermal treatment, Gilland-Sherwood correlations describing pre-remediation mass transfer processes can be used with acceptable accuracy to predict mass transfer during and after remediation.
- Procedures for upscaling estimates of mass-transfer rate coefficients from bench to intermediate scales were developed and evaluated. For pre-remediation dissolution, the upscaled Gilland-Sherwood correlation is based on a local-scale Gilland-Sherwood expression in combination with geostatistical descriptions of aquifer-property heterogeneity and DNAPL entrapment architecture. For bioremediation and ISCO, upscaling of pre-remediation dissolution and hydrodynamic processes is required while no upscaling is required to parameterize reaction processes.
- Accurate characterization of mass transfer and tracer partitioning in sources dominated by pools requires simulation of hydrodynamics and remediation processes within saturation transition zones at pool boundaries.
- Flow paths through heterogeneous sources can be highly irregular resulting in water bypassing some high-saturation zones. For surfactant-enhanced remediation, ISCO, and bioremediation, this can limit delivery of chemicals to sites of active DNAPL dissolution and reaction, and adversely impact remediation effectiveness. Research to develop protocols for optimizing delivery of reactants in highly heterogeneous sources is needed.

1.0 Introduction

Organic chemicals such as chlorinated solvents that are in the form of dense nonaqueous phase liquids (DNAPL) exhibit complex flow and entrapment behavior in naturally heterogeneous aquifers. After a spill, the spatial distribution of DNAPL is controlled by unstable fingering, preferential channeling and subsurface geologic heterogeneities. The final DNAPL distribution is present as heterogeneous zones of entrapment at low saturation (residual, ganglia and blobs) and high saturation (pools at permeability barriers and macro-scale entrapment zones resulting from capillary barriers). The contamination problem associated with these heterogeneous sources is a result of slow dissolution of entrapped DNAPL into the flowing groundwater, thus creating a downstream contaminant plume. Technologies that remove, change or stabilize the free phase in the source zone through controlled physical, chemical or biological activity are designed ultimately to reduce the net mass emission from the zone of the aquifer where the DNAPL is entrapped. To determine the effectiveness of remediation, risk analysis must consider the spatial and temporal distribution of concentrations in the solute plume generated through the mass transfer from entrapped DNAPL. An understanding of mass transfer that occurs from heterogeneous DNAPL sources is fundamental to determine both the pre- and post-remediation status of the solute plume. The basic focus of this research is to understand, quantify and model the process of mass transfer from source zones where DNAPLs are distributed in complex configurations due to unstable behavior and natural geologic heterogeneity.

1.1 Objectives

The primary goal of this research was to understand and characterize the processes that affect mass transfer and tracer partitioning in the source zone where DNAPL is entrapped as a free phase during both pre- and post-treatment. Four source zone treatment technologies were evaluated: (1) bio-treatment, (2) in situ chemical oxidation, (3) surfactant enhanced dissolution and (4) thermal treatment.

The specific objectives included:

- Conducting a fundamental study of how partitioning tracers interact with free-phase chlorinated organic solvents undergoing treatment,
- To conduct a fundamental study of how mass transfer occurs from organic solvents in free phase undergoing transformations during treatment,
- To conduct experiments in large soil tanks to generate data on temporal and spatial distribution of multiple tracer concentrations downstream of DNAPL entrapment zones with different distribution morphologies (residual, ganglia and pools),
- To conduct experiments in large soil tanks to generate data on temporal and spatial distribution dissolved concentrations downstream of DNAPL sources created in heterogeneous formations,
- To validate numerical models that could be used as decision tool to predict of temporal and spatial distribution of solute concentrations of dissolved

contaminants downstream of DNAPL entrapment zones undergoing treatment, and

- To develop upscaling methodologies to estimate model input parameters for field applications, from parameters estimated in the laboratory from batch or column tests.

Four research tasks were designed to meet these objectives. Task-specific goals are summarized as follows.

Task 1 – Batch and column experiments on partitioning tracer behavior. The goals of this research task were: (1) to test the hypothesis that the tracer partitioning coefficients change during chemical and biological transformations; and (2) to develop partitioning coefficients for testing DNAPLs and field samples undergoing physical, chemical and biological transformations as characterized by remediation technologies.

Task 2 – Column and bench-scale experiments to determine mass transfer coefficients. The goals of this research task were: (1) to test the hypothesis that the mass transfer coefficients for entrapped DNAPL sources change during remediation, (2) to determine the “point-scale” mass transfer coefficients from entrapped NAPL sources undergoing physical, chemical or biological transformation and (3) to upscale “point-scale” mass transfer coefficients to multi-dimensional flow fields.

Task 3 – Large tank experiments. The primary goal of this research task was to generate an accurate data set under controlled conditions that could be used to develop insight into mass-transfer processes in heterogeneous system, to validate numerical modeling tools and to test upscaling methodologies for heterogeneous field systems.

Task 4 – Model development, validation and modification. The goal of this research task was to use data generated in Task 3 to validate numerical modeling tools and validate upscaling methodologies for field systems with the goal of using the models as decision tools for source zone management.

1.2 Report organization

Research described in this report included numerous experimental and modeling activities related to DNAPL characterization and effects of several remediation technologies on DNAPL mass transfer at a range of investigative scales. The organization of chapters within this report is consistent with SERDP final technical report guidance.

- Chapter 1 – Introduction. Provides a brief problem statement and identifies research objectives that address this problem.
- Chapter 2 – Background. Provides a discussion of problems that DNAPL source zone characterization and remediation pose in terms of Department of Defense and regulatory requirements and identifies past research that has focused on this issue.
- Chapter 3 – Materials, Experiments and Modeling Methods. Provides descriptions of the experimental design and testing methods, presentations of basic data

obtained during experiments, and descriptions of numerical models developed and used to address research objectives.

- Chapter 4 – Results and Accomplishments. Provides detailed interpretation of experimental results and descriptions of models developed from those results to address research objectives. Key findings and accomplishments for specific technical focus areas are summarized.
- Chapter 5 – Conclusions. Identifies key accomplishments of this research and provides a discussion of the utility of the research for application to field sites. Identifies unresolved issues that need further investigation in order to fully resolve problems associated with DNAPL mass transfer at sites undergoing remediation.

Within each chapter, the report is organized to address project objectives in seven areas of technical focus: (1) DNAPL characterization by partitioning tracer techniques, (2) Mass transfer by natural dissolution from DNAPL source zones, (3) Surfactant enhanced dissolution, (4) Effects of in-situ chemical oxidation, (5) Bioenhanced dissolution, (6) Thermal treatment of DNAPL source zones, and (7) Three dimensional simulation study. Although experimental methods and modeling approaches for these focus areas shared common characteristics, presenting information within this framework permits a clear understanding of key research accomplishments and how this research met project objectives.

DNAPL mass transfer experiments were conducted in large tanks as part of research efforts for most of the focus areas identified in the previous paragraph. Designing and implementing these experiments is a complex and lengthy undertaking. For improved efficiency, tank experiments were design to address objectives for several focus areas either simultaneously or in sequence. For this reason, report appendices have been prepared providing documentation of experimental conditions and history, as well as a presentation of the resulting raw data, with minimal data interpretation and modeling. Additional appendices include a listing of publications, and Master's and Ph.D. Theses resulting from this project.

2.0 Background

Chlorinated solvents such as trichloroethylene (TCE) and tetrachloroethylene (PCE) are contaminants of concern in groundwater at many hazardous-waste sites. Each are present at about 60% of National Priority List sites and are ranking 16th and 30th respectively on the 2003 CERCLA Priority List of Hazardous Substances (ATSDR 2003). These chemicals have been used extensively since the early 20th century as cleaning solvents in the dry-cleaning, metal cleaning, vapor degreasing, and textile processing industries (ATSDR 2004, USHHS 2002). Widespread use of chlorinated solvents has resulted in accidental release and improper disposal of these compounds in the subsurface. The aqueous solubility of these organic liquid contaminants is low enough for them to exist in the subsurface as non-aqueous phase liquids but large enough to exceed safe drinking water standards. Chlorinated solvents such as tetrachloroethene (PCE) and trichloroethene (TCE) have densities greater than water and are classified as dense non-aqueous phase liquids (DNAPL).

Chlorinated solvent form primary source zones when present in the form of dense non-aqueous phase liquid (DNAPL) and secondary source zones when present as dissolved and/or sorbed contaminants in low permeability media (LPM) (Johnson and Pankow 1992, Pankow and Cherry 1996, USEPA 1993, USEPA 2004b). Contaminants are termed non-aqueous because they are present as a separate immiscible liquid phase having low solubilities in water, typically on the order of 10^2 - 10^3 mg/L or parts-per-million (ppm). On the other hand, the drinking water maximum contaminant levels (MCLs) of these contaminants are typically on the order of 10^0 - 10^2 µg/L or parts-per-billion (ppb). The combined result is that aqueous phase concentrations exceed MCLs by several order of magnitude, and the DNAPL source can persist for decades producing risk to human health at downgradient receptor points.

When released into the subsurface, DNAPL tend to migrate downward through the unsaturated zone and penetrate the water table (Mercer and Cohen, 1990). DNAPL migration in the subsurface is affected by (1) volume of DNAPL released, (2) area of infiltration, (3) time duration of the release, (4) properties of the DNAPL, (5) properties of the porous media, and (6) subsurface flow conditions (Mercer and Cohen, 1990). After a spill, the spatial distribution of DNAPL is controlled by unstable fingering, preferential channeling and subsurface geologic heterogeneities. The final DNAPL distribution is present as zones of entrapment at low saturation (residual, ganglia and blobs) and high saturation (pools at permeability barriers and macro-scale entrapment zones resulting from capillary barriers). In virtually all geologic settings, the resulting subsurface distribution of DNAPL is a combination of pools and residual zones (Illangasekare et al., 1995a; Illangasekare et al., 1995b). Figure 2.1 shows a generic site conceptual model of a groundwater system contaminated by DNAPLs.

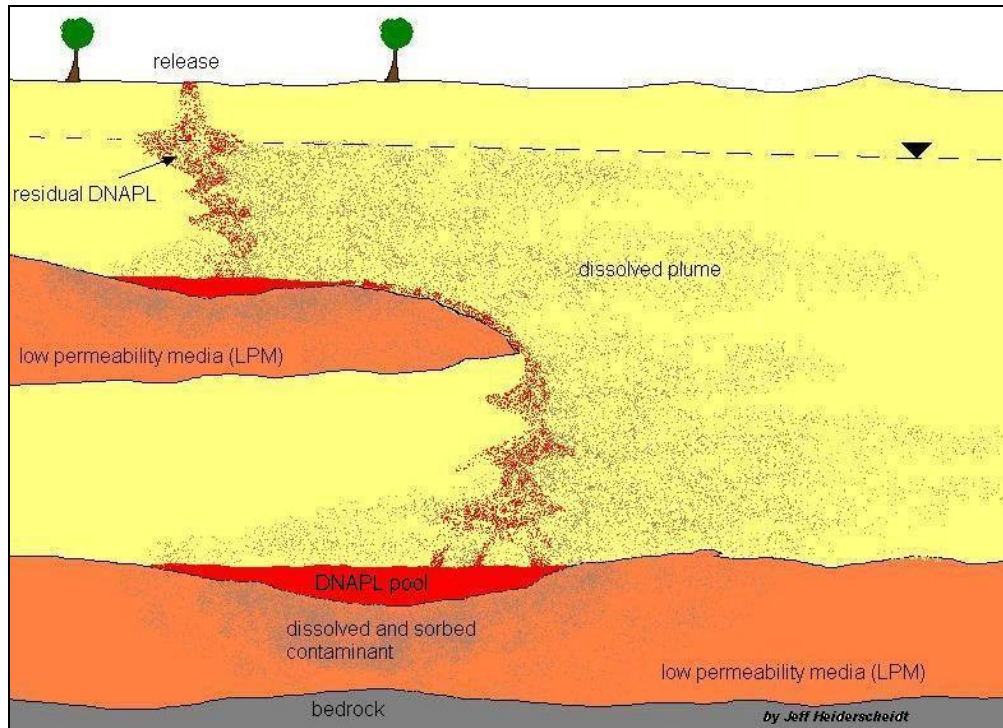


Figure 2.1. Generic Contaminated Site Conceptual Model

Feenstra and Cherry (1996) noted that actual free-phase DNAPL has not been found at most sites strongly suspected of having DNAPL contamination. In many cases, the existence of a DNAPL source can only be inferred from indirect evidence such as aqueous contaminant concentrations exceeding 1% of the aqueous solubility of the chemical (USEPA 1992, USEPA 2003). Parker et al. (2003) demonstrated the difficulty in locating actual subsurface DNAPL sources by performing extensive soil coring and water sampling at five sites (three that had free-phase DNAPL in monitoring wells) with DNAPL contaminated sandy aquifers. They found the DNAPL to be present in sporadic, thin layers only identifiable by taking continuous soil cores, sub-sampling them on small (5 cm or less) vertical intervals, and applying a hydrophobic red dye (Sudan IV) to the cores.

Entrapped DNAPL dissolves slowly into flowing groundwater and serves as a long-term source of contamination (Mackay and Cherry, 1989; Schuille 1988). As a result, conventional pump-and-treat remediation of DNAPL source zones has not been effective in decreasing contaminant concentrations to regulatory cleanup levels in acceptable times (MacDonald and Kavanaugh, 1994).

A number of innovative technologies have been developed to enhance mass transfer and contaminant removal from DNAPL source zones (National Research Council, 1994). Although significant technical advances in DNAPL remediation have been achieved, remediation strategies at most sites consist of DNAPL containment technologies coupled with long-term monitoring. This strategy is effective in limiting spread of contaminants and decreasing the risk of human and ecological exposures to chemicals, but the failure to remove a DNAPL source from groundwater requires the imposition of long-term institutional controls and assurances of sufficient financial resources to maintain these controls (Kavanaugh and Rao, 2003).

In contrast, strategies for active source-zone remediation (Jackson 2001) are based on the contention that mass removal from a source zone will result in decreased long-term mass flux, shortened source longevity, and reduced risk. While a decrease in mass flux may not eliminate needs for further treatment, it could decrease concentrations to levels where natural attenuation becomes feasible. Over the past decade, a number of innovative technologies have been developed that show promise for recovering a large fraction of the DNAPL mass at a given site. These technologies include air sparging (Unger et al., 1995), chemical oxidation (Siegrist et al., 2001), thermal treatment (Udell, 1997), co-solvent flushing (Falta, 1998), surfactant-enhanced aquifer remediation (Dwarakanath et al. 1999; Shiau et al. 1994), and bioremediation (Adamson et al., 2003; Mravik et al., 2003).

Success of source-zone remediation has been mixed, regardless of technology selected (McGuire et al., 2006). Field studies of complete removal of DNAPL from source zones have not been documented. Therefore, risk analysis to determine the effectiveness of remediation has to be conducted using the spatial and temporal distribution of concentrations in the solute plume generated through the mass transfer from entrapped DNAPL. A key component of any risk analysis is characterization and modeling of mass transfer that occurs from entrapped DNAPL sources both prior and after remediation.

The need to understand effects of active source-zone remediation technologies on mass transfer of chlorinated DNAPL entrapped in the subsurface provided the underlying motivation for the research described and reported in this report. This chapter of the report summarizes background information relevant to this research.

2.1 DNAPL source zone architecture and morphology

A DNAPL source zone at a spill or waste site includes the entire portion of an aquifer in which DNAPL is present (Feenstra and Cherry, 1996). DNAPL saturation of a source zone rarely is expected to be homogeneous. Rather, a source zone is composed of multiple sub-zones containing DNAPL that are separated from one another by portions of the aquifer that are entirely free of DNAPL (Schwille, 1988; Kueper et al., 1989; Kueper et al., 1993; Kueper and Frind, 1991a, 1991b). Each sub-zone may contain DNAPL entrapped at continuous and/or residual saturation. Because migration of DNAPL is highly sensitive to subtle, small-scale heterogeneity, the distribution of DNAPL within a source zone is complex and highly variable (Illangasekare et al., 1995a; Illangasekare et al., 1995b). For DNAPL such as PCE with relatively high density, sub-zones often take the geometry of thin, horizontal lenses and pools, interconnected by vertical fingers at residual or near-residual saturation. The term architecture is used to collectively refer to the distribution and saturations of DNAPL sub-zones that comprise the overall source zone. In contrast, morphology refers to the extent and distribution of saturation within a particular sub-zone.

2.1.1 Source-zone development

The source-zone architecture formed by a particular DNAPL release depends upon the volume of DNAPL released, area of infiltration, time duration of the release, properties of the DNAPL, types of geologic units encountered during DNAPL migration, and variability of the hydraulic and capillary properties of those units (Mercer and Cohen, 1990; Kueper and Frind,

1991a, 1991b). As DNAPL migration proceeds, a portion of the mass is retained by pore-scale capillary forces and macro-scale capillary barriers. As a result, the flow of DNAPL slows until a condition of mechanical equilibrium is approached. Rates of dissolution once entrapment occurs suggest that source-zone architecture changes very slowly, particularly in sub-zones with high saturation (Hunt et al., 1988; Johnson and Pankow, 1992; Imhoff et al., 1994; Voudrias and Yeh, 1994; Mayer and Miller, 1996).

2.1.2 Source-zone characterization by partitioning tracer techniques

The tasks of delineating and characterizing source zones can be a challenge. If the morphology and distribution of DNAPL are unknown, implementation of an effective remediation technique becomes difficult. Traditional soil-coring methods have proven to be ineffective as a result of remobilization during sampling (Rao et al. 2000) as well as the large number of discrete samples needed to resolve the spatial distribution of DNAPL (Dai, et al., 2001). Partitioning tracer tests provide a technique for characterizing DNAPL source zones using information integrated over scales greater than can be provided by discontinuous, discrete measurements of the system. Specifically, partitioning tracer tests are conducted to detect and locate DNAPL contamination, estimate the DNAPL volume present, and assess remediation performance.

Tracers are chemicals that can be used to follow fluid movement without changing chemical properties or affecting water movement. Partitioning tracer tests consist of simultaneous injection of several tracers with different partition coefficients. Typically, a tracer solution consists of at least one tracer which migrates without partitioning into DNAPL, called a conservative tracer, and a mixture of chemicals with different partition coefficients, called partitioning tracers. Partitioning tracers undergo retardation, while the conservative tracer will not be affected by the presence of DNAPL. The chromatographic separation of the conservative and partitioning tracer pulses depends on the fraction of time that the tracer spends in the DNAPL phase compared to time spent in water.

Partitioning interwell tracer test (PITT) technique adapts and extends several existing tracer-test methods from the fields of groundwater hydrology and petroleum reservoir engineering (Allison et al., 1991). The technique has been used in petroleum engineering for reservoir description in enhanced oil recovery (Allison, 1988). The PITT technique also has been adapted for environmental applications to detect and characterize DNAPL distribution in subsurface environments (Jin et al., 1995). In most cases, the technique has been used to assess remediation performance in DNAPL source zones at residual saturation (Rao et al., 1997; Annable et al., 1998; Jawitz et al., 1998; Meinardus et al., 2002).

Although the PITT technique and its extensions have been applied with success at a number of sites, its limitations under complex DNAPL entrapment morphologies had not been fully evaluated at the start of this research project. Dai et al. (2001) demonstrated the sole influence of NAPL distribution in tracer performance in one-dimensional column experiments. Tracer tests are expected to result in underestimation of DNAPL volume in certain conditions where the hydrodynamic accessibility is constrained or non-equilibrium mass transfer occurs (Rao et al., 2000).

Successful application of PITT before and after remediation depends on the accuracy of partitioning coefficients used in data analysis. However, effects of surfactant remediation, chemical oxidation, and bioremediation on partitioning tracer behavior on tracer partitioning coefficients were poorly understood at the start of this research project.

2.2 Regulatory and Department of Defense requirements related to mass transfer from DNAPL source zones

The research described in this report focuses on mass transfer of chlorinated contaminants from DNAPL source zones undergoing remediation. Nationally, the dominant regulatory requirement for groundwater considered to be a potential source of drinking water is restoring or achieving drinking water standards in source zones, such as Maximum Contaminant Levels (MCL). The CERCLA statute requires remedial actions to attain drinking water standards established under the Safe Drinking Water Act, or water quality criteria established under the Clean Water Act, "...where such goals or criteria are relevant and appropriate under the circumstances of the release." Superfund regulations, contained in the NCP (Final National Oil and Hazardous Substances Pollution Contingency Plan) establish that the cleanup goal for contaminated ground water is: "...to return usable ground waters to their beneficial uses wherever practicable, within a timeframe that is reasonable given the particular circumstances of the site." Superfund guidance identifies drinking-water standards as cleanup levels for groundwater determined to be current or potential sources of drinking water. For sites regulated under RCRA Corrective Action, similar final cleanup goals are established, although the point of compliance and various short-term and intermediate goals may be defined for the site (U.S. EPA, 2004b).

Source control is a critical part of remediation strategies at many Department of Defense hazardous-waste sites. The aqueous solubility of these organic liquid contaminants is low enough for them to exist in the subsurface as non-aqueous phase liquids but great enough to exceed safe drinking water standards. Efforts to attain safe drinking water standards require effective source control. Unfortunately, for most remediation technologies, complete removal of DNAPL and elimination of mass flux is not feasible (McGuire et al., 2006).

Kavanaugh and Rao (2003) note that new federal and state regulatory policies and practices include implementing alternative approaches to groundwater cleanup such as establishment of management zones where cleanup goals other than drinking water standards may be applied, groundwater classification schemes that permit alternative remedial action goals, and other flexible regulatory approaches that do not impose non-degradation requirements or drinking water standards in source zones. In these situations, partial depletion of DNAPL sources may be deemed an acceptable intermediate goal as a part of phased site cleanup. On the other hand, regulatory policies are constrained by public concerns over leaving contamination in place and concerns over natural resource damages. There is currently no accepted regulatory definition of qualitative terms such as "mass removal to the extent practicable." This results in significant uncertainty as to the extent of mass depletion that may be required in a DNAPL source zone. The research described in this report is designed to provide an understanding of mass transfer, as well as characterization and modeling tools that can be used to assess and where possible decrease this uncertainty.

In addition to regulatory criteria, remedial actions in source zones may be undertaken to eliminate long-term liability. Analysis of risks associated with long-term liability requires an

understanding of mass transfer that occurs from entrapped DNAPL sources both before and after remediation. The understanding of mass transfer from heterogeneous source zones, as well as characterization and modeling tools, developed during this research project provide a fundamental basis for risk analyses of this type.

2.3 Mass transfer from DNAPL source zones

Because DNAPLs have low solubility in water, they dissolve slowly and provide long-term sources for downstream contaminant plumes. Downstream contaminant migration can be contained without addressing continuing mass transfer from a DNAPL source. However, efforts to remove or minimize the effects of such a contaminant source require an understanding of the mass transfer process. Extensive research has been conducted during the past decade in an effort to understand interphase mass transfer under ambient abiotic conditions. Relatively less research on mass transfer from source zones undergoing remediation has been undertaken.

2.3.1 Natural dissolution and upscaling

Dissolution from DNAPL sources at residual saturation has been studied in great detail using one-dimensional columns with single component DNAPL (Miller et al., 1990; Imhoff and Pinder, 1994; Powers et al., 1992; Powers et al., 1994; Imhoff et al., 1998; Bradford et al., 2000). Experimental results from column experiments show aqueous-phase concentration of effluent that increases toward the solubility limit with increasing column length, suggesting a kinetic process. Kinetic mass transfer from a residual zone to flowing groundwater generally has been represented as the macroscopic result of diffusion across pore-scale boundary layers at water-DNAPL interfaces. At a macroscopic scale, the diffusion process can be simulated with a first-order rate coefficient using a lumped mass transfer rate constant.

Removal rates in dissolution experiments depend on flow rate, DNAPL saturation, porous media grain size and porous media wettability. Several empirical power functions have been proposed to correlate these characteristics with apparent first-order rate coefficients for mass transfer. These correlations referred to as Gilland-Sherwood models relate the mass transfer coefficient, expressed in dimensionless form using a modified form of Sherwood number (Sh), to other non-dimensional groups such as Reynolds number (Re) and Schmidt number (Sc) that capture the fundamental processes that contribute to mass transfer [Bird et al., 1960]. However, it is recognized these laboratory determined mass transfer coefficients are not directly applicable to predict inter-phase mass transfer of entrapped NAPLs at field scales [Mayer and Miller, 1996; Khachikian and Harmon, 2000].

In heterogeneous systems, dissolution behavior is highly dependent on spatial DNAPL distribution (Bradford et al., 2003). Spatial distributions of soil texture and wettability that produced strong capillary barriers and higher DNAPL saturations tend to exhibit longer dissolution times than comparable homogeneous systems. Empirical mass transfer correlations are usually developed from experimental data for homogeneous soils in columns or two-dimensional dissolution cells at scales that are much smaller than the grid block sizes used in field-scale numerical simulations [Miller et al., 1990; Geller and Hunt, 1993; Powers et al., 1994; Nambi, 1999]. Without correctly including subsurface hydrodynamics controlled by the

heterogeneous permeability field at the spill site scale, and distribution of NAPL saturation to the simulation, accurate prediction of field scale mass transfer is not possible.

Saba and Illangasekare [2000] demonstrate that flow tends to bypass a DNAPL source in two-dimensional flow fields due to reduction of water permeability from DNAPL entrapment. As a result, mass flux observed in two-dimensional flow fields is orders of magnitude less than would be predicted with Gilland-Sherwood models developed from one-dimensional experiments. Experimental and model results of Saba and Illangasekare (2000) were used to develop scalable mass transfer coefficients in the form of a Gilland-Sherwood expression for dissolution in multidimensional flow systems. This expression related the mass transfer coefficient to a characteristic length parameter for a source zone.

Saba (1999) conducted numerical simulation studies to upscale the dissolution of entrapped *p*-xylene in heterogeneous aquifers. In this work, he attempted to develop a general relationship between the large-scale overall mass transfer coefficient (\bar{k}_{La}) of the entire NAPL source zone and the small-scale mass transfer coefficient (k_{La}) based on a Gilland-Sherwood mass transfer correlation fitted using laboratory data. Although an empirical relationship between \bar{k}_{La} and k_{La} was successfully developed, without the explicit inclusion of aquifer heterogeneity and the entrapment architecture, the relationship could not be generalized. However, it was found that the relationships between \bar{k}_{La} and k_{La} were different for all three spill configurations that were considered (i.e. different entrapment architectures). This difference could be attributed to variability in effective hydraulic conductivity associated with NAPL entrapment zones that was not considered in the analysis.

Nambi (1999) attempted to include the effect of soil heterogeneity in large-scale mass transfer correlations. In her work, NAPL dissolution data in a simple heterogeneous two-dimensional flow system was analyzed using a simplified analytical solution and regression analysis to obtain an expression for the mass transfer rate coefficient. A Gilland-Sherwood relationship was developed that accounted for soil heterogeneity, as described by the variance and average of hydraulic conductivity, as well as the vertical correlation length. However, the applicability of this technique to simulate mass transfer in a heterogeneous field site is still in doubt, since in her analysis, NAPL was assumed to distribute homogeneously in the entrapment zone. Consequently, the effect of entrapment architecture on mass transfer was ignored. Entrapment architecture is expected to significantly affect mass transfer at field scales.

Parker and Park (2004) developed an empirical expression for predicting field-scale effective mass transfer coefficient for a residually saturated entrapped DNAPL source zone based on a theoretical study of a high-resolution three-dimensional domain. They found that field-scale mass transfer coefficient is much lower than laboratory-scale mass transfer coefficients and depends on the relative ground water velocity, DNAPL mass, and the modes of DNAPL distribution, either finger- or lens-like entrapment modes. Although the proposed empirical expression was able to simulate field-scale DNAPL dissolution, the quantified effect of source zone heterogeneity and the DNAPL entrapment architecture was not explicitly included in the relationship.

2.3.2 Surfactant-enhanced dissolution

Surfactant-enhanced aquifer remediation (SEAR), also known as in situ surfactant flooding, is designed to enhance the removal of NAPL from the subsurface by increasing the effective aqueous solubility of NAPL and reducing interfacial tension between the water and NAPL phases. Above a critical concentration, surfactant monomers self-aggregate into micelles and the surfactant concentration above which micelles form is known as the critical micelle concentration (CMC). When surfactant concentrations exceed the CMC, the incremental surfactant goes almost totally to formation of additional micelles resulting in an emulsion phase (Bedient et al., 1999). In a micelle, individual monomers are oriented with hydrophilic moieties in contact with the aqueous phase and hydrophobic moieties clustered together in the interior of the aggregate.

There are two general mechanisms by which surfactants can enhance the removal of NAPL sources from groundwater. The first, enhanced solubilization, results in micelle formation and partitioning of DNAPL molecules into the hydrophobic interiors (Sabatini et al., 1995, 2000). Theoretically, as total aqueous solubility of a DNAPL component increases, less water flush is required for attainment of a target remediation level. The greater the surfactant concentration is above the CMC, the greater the solubility enhancement (Jawitz et al., 1998; Dwarakanath et al., 1999). The second mechanism, enhanced mobilization of NAPL, occurs because surfactants tend to lower interfacial tension and decrease the capillary forces responsible for trapping DNAPL at residual saturation. Mobilization has greater potential than solubilization to increase rates of remediation but also can pose greater risk if entrapped DNAPL is remobilized to undetectable locations.

The use of surfactants to enhance the solubility and increase mobility of DNAPL contaminants has been studied in detail by many researchers. There are clear differences in remediation efficiency for different experimental conditions. Zhou and Rhue (2000) screened 42 surfactants to examine their efficiency and mode of action. Using a range of surfactant combinations, 92 to 98 percent of PCE was removed from a test area by a method which increased DNAPL solubility. Earlier experiments by Pennell et al. (1994) reported the removal of more than 99 percent of residual PCE if mobilization was the dominant removal mechanism. However, concerns have since been raised about the adverse effects caused by remobilized DNAPL migrating into previously uncontaminated aquifer regions. These two studies considered residual DNAPL in homogeneously packed columns experiencing uniform flow. Dwarakanath et al. (1999) also used homogeneous soil columns to identify anionic surfactants that recovered at least 99 percent of the contaminant during flooding. One of the most effective surfactants was identified as sodium sulfosuccinate, or Aerosol OT.

Although the above levels of remediation efficiency might initially appear satisfactory, the test environments were very different from conditions at many sites. Only in rare cases will a NAPL spill occur in homogeneous aquifer material, and even then, a uniform groundwater flow will almost certainly never exist. At actual field sites, the aquifer is likely to display varying degrees of heterogeneity. Furthermore, for any remediation technique to be effective, it is necessary to characterize the source zone completely (Mackay and Cherry 1989). Current techniques used to undertake this have only a limited degree of accuracy and reliability.

Research that highlights the limitations of remediation at the field scale was conducted by Holzmer et al. (2000). They used sodium sulfosuccinate to investigate PCE removal in a shallow,

low-permeability sand aquifer beneath a dry-cleaning facility. The ground at this site consisted of two zones of differing permeability and although the surfactant-enhanced remediation technique removed 92 percent of free-phase PCE from the saturated zone, only 72 percent of DNAPL mass was recovered from the entire soil volume above an aquitard. Hence, 28% of the source volume remained within the low permeability layers. Issues concerning mobilized NAPL were studied by Lunn and Kueper (1999) who investigated the possibility of decreasing the density of the DNAPL prior to reducing its interfacial tension. Using an up-gradient flow cell (1.25m by 0.2m by 0.03m) with 50ml PCE pooled above a fine sand lens, NAPL recoveries ranged from 56.6 to 97.6 percent, with only 1.2 percent by mass removed by natural dissolution.

Although there are several experimental studies of surfactant-enhanced dissolution of entrapped NAPL, relatively few numerical modeling studies have been published. Examples of numerical models for surfactant-enhanced dissolution are those of Abriola et al. (1993), Brown et al. (1994), Mason and Kueper (1996), and Delshad et al. (1996). These models differ from each other in the complexity of the formulation (e.g., multi-dimensional vs. one dimensional, consideration of multiple phase behavior, ability to simulate complex boundary conditions, and simulation of spatially variable permeability). The program UTCHEM, a three-dimension multi-phase, multi-component finite-difference chemical flood simulator, is among the complex models developed specifically for simulating surfactant-enhanced aquifer remediation. The program simulates multi-phase flow and complex phase behavior when surfactants interact with NAPL. A disadvantage of this model is long execution time due to the fact that many process equations are solved for each time step.

Saba (1999) developed a surfactant enhanced dissolution model that is based on the advection-dispersion model, MT3D. The advantage of this model is its relative simplicity while still accounting for complex mass transfer processes in heterogeneous formations. However, this model assumes that NAPL is completely accessible by the surfactant solution. The significance of possible errors resulting from this assumption was shown by Saenton et al, 2002. This assumption is not always realistic. One goal of the SERDP project was to modify the model of Saba (1999) to account for effects of soil heterogeneity that result in the incomplete delivery of surfactants. Hence, more realistic simulations can be performed and more accurate results can be obtained.

2.3.3 In Situ Chemical Oxidation of DNAPL

Chemical oxidation, specifically with permanganate, has been used to treat water and waste water for over 50 years. In the last fifteen years or so, chemical oxidation has become a promising in situ remediation technique for sites where groundwater and soil are contaminated by chlorinated solvents, especially where contaminants are not present in DNAPL form. Field-scale pilot tests have shown encouraging results for sites contaminated with low levels of chlorinated solvents (Cline et al. 1997, Hood 2000, Lowe et al. 2002, Schnarr et al. 1998, Siegrist et al. 1999). Additionally, laboratory research has provided an understanding of many fundamental details of the technology. The reaction pathways and kinetics of permanganate oxidation of alkenyl halides, specifically chlorinated ethenes such as PCE and TCE have been elucidated (Huang et al. 1999, Huang et al. 2001, Huang et al. 2002, Schnarr et al. 1998, Yan and Schwartz 1999, Yan and Schwartz 2000). Struse et al. (2002) demonstrated the ability of permanganate to diffuse into LPM, destroying DNAPL TCE and preventing diffusion of aqueous

TCE from the LPM. A number of researchers have also studied the impacts of water chemistry and porous media constituents on the reaction (Gates-Anderson et al. 2001, Glaze and Kang 1988, Li and Schwartz 2000, Urynowicz 2000, Vella and Veronda 1994). However, limited research of chemical oxidation in the presence of greater than residual DNAPL saturation has shown inconclusive results (MacKinnon and Thomson 2002, NATO/CCMS 2003, Reitsma and Marshall 2000, Schroth et al. 2001, Siegrist et. al. 1999, Urynowicz and Siegrist 2000, USEPA 1998).

Application of in situ chemical oxidation (ISCO) to a source zone with DNAPL is designed to speed up remediation by inducing increased mass transfer (and subsequent destruction) from the source. Based on experimental results, Schnarr et al. (1998) suggest that NAPL dissolution and oxidation are processes that occur in parallel with increased mass transfer during oxidation occurring primarily as a result of an increased aqueous concentration gradient. Reitsma and Dai (2001) performed a theoretical study to estimate the maximum expected NAPL mass transfer enhancement resulting from chemical oxidation. They estimated a maximum of five times increase in dispersive mass transport from a PCE NAPL pool resulting from the increased concentration gradient; however, they predict little enhancement in local-scale mass transfer from NAPL to aqueous phase suggesting no change in dissolution mass transfer parameters. Further, they suggest that actual enhancement is likely to be less, because permeability reduction and decreased interfacial contact area were not accounted for in the estimate. On the contrary, MacKinnon and Thomson (2002) calculated a ten times initial increase in PCE mass transfer from a NAPL pool during a 2-D oxidation experiment, with decreasing mass flux over time attributed to $MnO_2(s)$ formation.

Studies of the effects of permanganate oxidation on porous media permeability have been largely qualitative (Conrad et al. 2002, Lee et al. 2003, Li and Schwartz 2000, Reitsma and Randhawa 2002, Siegrist et al. 2002). For example, research has shown that oxidation of a high DNAPL saturation source using permanganate can result in permeability reductions at the DNAPL perimeter due to precipitation of manganese dioxide thereby reducing the ability for oxidant to be transported to the source, but also possibly reducing the mass flux of aqueous contaminant from the DNAPL source (Lee et al. 2003, Siegrist et al. 2002). On the other hand, research into permeability effects from permanganate oxidation of DNAPL source zones at lower saturations is more ambiguous. Nelson et al. (2001) concluded that the manganese oxides produced during oxidation of a PCE DNAPL present at approximately 4 to 7 percent saturation had negligible effect on the permeability in a system under neutral pH conditions. However, Lee et al. (2003) found that permanganate oxidation of a TCE DNAPL source zone at 8 percent saturation, under slightly acidic conditions, resulted in generation of up to 4900 mg $MnO_2(s)$ /kg of porous media, with a six-fold decrease in velocity of the oxidation front over the two-month experiment, attributed to reductions in permeability. Further research is necessary to better understand how well ISCO will work under different site and source conditions, including the effects of ISCO on source zone porous media (Ibaraki and Schwartz 2001, Seol et al. 2003, Stroo et al. 2003). Figure 2-2 depicts the various subsurface regions that may undergo permeability reductions due to manganese oxide formation.

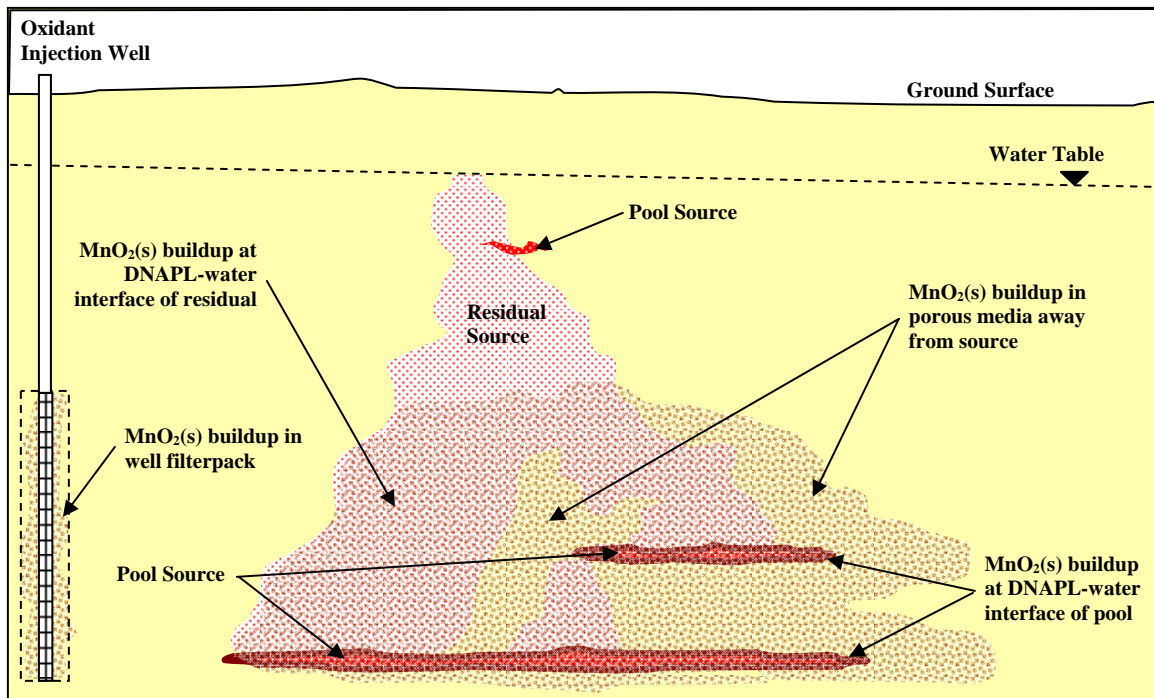


Figure 2.2. Regions of Potential Permeability Reduction

2.3.4 Bioenhanced dissolution

Biotransformation of separate-phase hydrocarbons generally requires compound dissolution into the aqueous phase. If the biodegradation rate for a dissolved hydrocarbon is greater than the DNAPL dissolution rate under abiotic conditions, microbial activity may accelerate dissolution by increasing the concentration gradient near the DNAPL–water interface. Research demonstrating the ability of bioremediation to enhance dissolution of DNAPL has been conducted at laboratory and field scales. However, relatively few studies have been conducted to understand how physical transport processes interact with microbial reaction processes to control and/or enhance mass transfer and removal of contaminants from DNAPL.

Under reducing conditions, aquifer microorganisms can reductively dechlorinate PCE and TCE to the less chlorinated daughter products 1,2-cis-dichloroethene (DCE) and vinyl chloride (VC) by sequential replacement of chlorine substituents with hydrogen. Reductive dechlorination occurs in anaerobic environments at reduction potentials of +580 mV for PCE degradation and +490 mV for TCE degradation (Loeffler et al., 1999; Vogel et al. 1987; Vogel and McCarty 1987). These reduction potentials correspond approximately with manganese- and iron-reducing conditions. Reduction of the more highly chlorinated compounds (PCE, TCE) occurs more readily than reduction of DCE and VC due to a higher available energy yield (Tandoi et al. 1994).

Microbes utilizing reductive dechlorination as a strategy for growth are common at PCE- and TCE-contaminated sites throughout North America and Europe (Hendrickson et al., 2002) and rates of degradation by this method typically are several orders of magnitude greater than for other degradation strategies (Fetzner, 1998). Most laboratory isolates are only capable of dechlorination to the DCE intermediate (Krumholz et al., 1996; Sharma and McCarty, 1996). A

single bacterium *Dehalococcoides etheneogenes* (Maymo-Gatell et al., 1997) has been isolated that degrades PCE completely to ethene. However, sustaining growth of *Dehalococcoides etheneogenes* as an isolate is extremely difficult.

Reductive dechlorination in the environment typically is catalyzed by interdependent communities of anaerobic bacteria. Several mixed cultures of dechlorinating microbes have been enriched from wastewater, soil or groundwater (Freedman and Gossett 1989; Edwards and Cox 1997; Nielsen and Keasling, 1999). One of the more extensively characterized cultures of dechlorinators was enriched by Dr. Gossett and his associates at Cornell University (Freedman and Gossett, 1989). In the Cornell culture, sources of energy for metabolism and growth are simple organics such as alcohols or fatty acids. Fermentative bacteria within the consortia generate molecular hydrogen (H_2), and bacteria capable of reductive dechlorination use H_2 as an electron donor (DiStefano et al. 1992). The presence of other microbes including methanogens and sulfate reducers both enhances and inhibits the activity of dehalogenators by supplying necessary nutrients and by establishing competition for H_2 (Maymo-Gatell et al. 1995).

Researchers from the University of Toronto have developed a mixed culture, designated KB-1 (Edwards and Cox, 1997), that has proven to be highly robust and well suited for use in bioremediation of chlorinated ethene plumes at field locations (Major et al., 2002; Morrill et al., 2005). The culture degrades PCE to ethene using methanol as an electron donor. KB-1 includes microbes that are phylogenetically similar to those of the Cornell culture including *Dehalococcoides ethenogenes* that degrades PCE completely to ethene (Duhamel et al. 2002). The KB-1 culture is used throughout the research described in this report.

Research related to bioremediation of chlorinated DNAPL has focused primarily on demonstrating feasibility either at laboratory or field scales. Results of batch (Nielsen and Keasling, 1999) and column (Isalou et al, 1998) experiments indicate that cultures can be acclimated to grow at PCE concentrations that approach solubility. Biologically enhanced dissolution of DNAPL containing PCE have been demonstrated in batch tests (Yang and McCarty, 2000; Carr et al., 2000). Biodegradation was assumed to occur in the aqueous phase and bioactivity was reported at PCE concentration that approached equilibrium solubility. Adamson et al. (2004) determined that biological systems produced mass fluxes of degradation products that were similar to each other regardless of the initial PCE mole fraction within a mixed DNAPL. Yang and McCarty (2000, 2002) and Cope and Hughes (2001) reported biologically enhanced dissolution in column experiments with DNAPL containing PCE at residual saturation. Mass flux from DNAPL was increased by factors of 2 to 6 at residual saturation of less than 5 percent PCE-DNAPL with excess electron-donor supply. Effectiveness of PCE mass transfer depended on electron donor substrate. Biodegradation and enhanced dissolution has been demonstrated in an intermediate-scale tank (5.5 m x 2.1 m x 1.8 m) with homogeneous sand containing PCE-DNAPL at residual saturation (Adamson et al., 2003). However, dechlorination within the source zone stopped at DCE, indicating that complete dechlorination may be limited in source zones. Field-scale bioremediation of a DNAPL source areas containing PCE or TCE at residual saturation has been demonstrated (Song et al., 2002; Macbeth et al., 2004; Bloom et al, 2005; Dennis, et al., 2005; Elder et al., 2005; Lackovic et al., 2005; Macbeth and Sorenson, 2005; Martin et al., 2005; McGuire et al., 2006; Miller et al., 2005; Seguiti et al., 2005; Vidumsky et al., 2005). Efforts to quantify bioenhanced mass transfer at these sites are ongoing.

No experiments of biologically enhanced dissolution from DNAPL source zones containing PCE at high saturation (pools) have been reported. However, mapping of DNAPL pools by x-ray attenuation techniques (Moreno-Barbero and Illangasekare, 2006) has shown that saturation increases with distance into a pool. If PCE-degrading microbes remain active within this transition zone, dissolution gradients may be greatly increased and dissolution greatly enhanced. Studies of this hypothesis have not been reported. Because long-term persistence of PCE in groundwater is closely tied to dissolution from pools, evaluation of this hypothesis is an important part of the research described later in this report.

Few studies have been conducted to understand how physical transport processes interact with microbial reaction processes to control and/or enhance mass transfer and removal of contaminants from DNAPL. Yang and McCarty (2002) and Chu et al. (2003) suggest that source-zone biodegradation acts as a local-scale aqueous-phase sink for PCE as it dissolves from DNAPL. Biodegradation increases the PCE dissolution gradient and enhances mass transfer. Although bio-clogging at high electron-donor concentration may decrease permeability (Baveye et al., 1998) and DNAPL interfacial area (Chu et al., 2003), the mass transfer process described by these researchers is an abiotic one with a superposed local-scale sink. Therefore, first-order rate expressions, commonly used to model abiotic mass transfer (Saba and Illangasekare, 2000; Saenton et al., 2002), may be useful to describe enhanced mass transfer during bioremediation. Furthermore, because biodegradation is thought to occur in the aqueous phase rather than at the DNAPL surface, estimated values of kinetic rate coefficients used to model abiotic mass transfer of PCE may remain unchanged due to biological activity. This is equivalent to stating that abiotic Gilliland-Sherwood expressions can be used to parameterize mass transfer rate coefficients during source-zone bioremediation. Evaluation of this hypothesis is an important part of the research described in later in this report.

Aqueous-phase biodegradation is fundamentally a local-scale process that depends on biomass concentration and mixing of electron donor and acceptor. In field-scale applications, microbe population, groundwater chemistry and biodegradation kinetics are site specific. Typically, estimates of biodegradation parameters are obtained in a laboratory at batch or column scales. Estimation at larger scales typically is impractical. Biodegradation modeling of a field-scale dissolved gasoline plume showed that laboratory-derived kinetic parameters can adequately describe field scale degradation, provided advective–dispersive transport of electron donors and acceptors, and large-scale spatial heterogeneities are incorporated in a field-scale model (Schirmer et al., 2000). A similar hypothesis for upscaling bioenhanced mass transfer was evaluated as part of the research described in this report.

2.3.5 Thermal treatment of DNAPL

Thermal technologies are used to either enhance DNAPL dissolution, or remove and destroy entrapped DNAPL contaminants in the subsurface (Heron et al. 2005). These technologies include hot-water flooding, steam injection, resistive heating, and microwave heating (Smith et al. 1993). Hot-water flooding is designed to enhanced DNAPL dissolution. Most other heating technologies are designed to promote in situ destruction of contaminants. However, technologies other than hot-water flooding also may enhance dissolution. In many situations, the location and distribution of DNAPL is not precisely known. Flow of DNAPL in the subsurface is sensitive to small variations in capillary properties of a porous medium. This

translates into a wide distribution of DNAPL saturation in the soil as well as a source- zone architecture that is both uncertain and apparently random (Kueper et al., 1991a and 1991b; Illangasekare et al., 1995a and 1995b). As a result, efforts to apply a destructive treatment to a DNAPL source zone may not be effective in reaching the totality of the source. Cold spots with temperatures less than that needed for complete destruction of the DNAPL may develop, but which may cause enhanced dissolution of the NAPL into flowing water (Newmark et al. 1997).

To understand and model the behavior of a source zone undergoing any kind of thermal remediation it is important to understand how mass transfer of NAPL into water is affected by increased temperatures. Therefore, the goal of thermal research described in this report is to understand, quantify and model the effects of temperature on mass transfer rates from DNAPL sources to flowing water. The thermal technology that is used in this research is hot-water flooding.

Very little research has been undertaken to understand dissolution behavior of contaminants for the range of temperatures expected during thermal treatment of DNAPL and at different scales of interest. Several empirical expressions, called Gilland-Sherwood correlations, have been developed that relate apparent first-order rate coefficients for mass transfer with other system parameters (Miller et al., 1990; Powers et al., 1992; Imhoff et al., 1994; Powers et al., 1994; Imhoff et al., 1998; Powers et al., 1998; Saba and Illangasekare, 2000; Saenton et al., 2002; Imhoff et al., 2003; Nambi et al., 2003). Generally, these correlations have been developed from experiments conducted under isothermal conditions. Imhoff et al. (1997) proposed that the correlations be extended to variable-temperature conditions by adjusting thermally dependent parameters such as fluid densities, water viscosity, molecular diffusion, etc. To evaluate this hypothesis, results of column experiments were used to fit a Gilland-Sherwood correlation. Other experimental studies of the effects of temperature on mass transfer from NAPL in otherwise water-saturated porous media are scarce and limited in temperature range. Most thermal remediation studies have focused on the effectiveness of a particular thermal technology (Udell et al. 1988; Udell et al. 1994; Heron et al. 1998; Udell and Itamura, 1998; Udell and McCarter, 1998; Kaslusky and Udell, 2002 and 2005) or on mass transfer by volatilization (van der Ham et al. 1998).

Increases in temperature also produce decreases of NAPL-water interfacial tension (Imhoff et al. 1997) and viscosity (Sleep et al. 1997). Changes in interfacial tension produce changes in capillary pressure saturation curves. These factors may create conditions for DNAPL remobilization, producing a new source configuration. Mass transfer characteristics of the new configuration may be either beneficial or detrimental to achieving remediation objectives. Theoretical studies based on basic NAPL properties and empirical relationships suggest that no displacement occurs under normal conditions of groundwater flow and thermal treatment (Sleep et al. 1997; Heron et al. 1998). Column experiments in which a thermal gradient was established along a homogeneous water saturated medium with residual DNAPL saturation have shown evidence of changes in fundamental properties of the NAPL and water (interfacial tension, viscosity, density, contact angle) resulting in remobilization of NAPL ganglia.

3.0 Materials, Experiments and Modeling Methods

The research described in this report represents an effort to characterize and understand the fundamental processes that govern mass transfer from complexly distributed DNAPL after application of source zone removal/destruction technologies. These technologies were: (1) surfactant enhanced dissolution, (2) chemical oxidation, (3) bioremediation and (4) thermal treatment. It also was designed to test the effectiveness of tracer technologies for evaluating DNAPL distribution in complex, heterogeneous systems undergoing remediation and hence to predict mass transfer behavior in the field. As such, the goal of this research was to improve and develop tools that can measure the impact of remediation technologies on DNAPL distribution in heterogeneous systems. The study did not research the effectiveness of remediation technologies to treat DNAPL sites. Instead, the focus was on how characterization methods and tools can be used to understand and evaluate source zone removal. Therefore, experimental methods emphasized (1) evaluations of partitioning tracer techniques for characterizing DNAPL distribution both before and after remediation, (2) modeling tools for evaluating effective mass transfer rates during and after remediation, and (3) strategies for upscaling mass transfer parameters from laboratory to field scale.

This chapter of the report includes a description of the overall approach used in the research, discussions of materials and methods used in laboratory experiments along with presentations of fundamental data obtained in those experiments, and modeling approaches. Detailed interpretation of experimental results and application of models to those results are described in chapter 4 entitled “Results and Accomplishments.”

3.1 Approach

Project objectives were addressed within the context of seven areas of technical focus: (1) DNAPL characterization by partitioning tracer techniques, (2) Mass transfer by natural dissolution from DNAPL source zones, (3) Surfactant enhanced dissolution, (4) Effects of in-situ chemical oxidation, (5) Bioenhanced dissolution, (6) Thermal treatment of DNAPL source zones, and (7) Three dimensional simulation study. Experimental methods and modeling approaches for the first six focus areas shared common characteristics. Therefore parallel technical approaches and objectives were used in each. Specifically, research was conducted within the context of four major tasks:

Task 1 – Batch and column experiments of partitioning tracer behavior. The goals of this task were: (1) to determine partitioning coefficients for test DNAPLs and field samples undergoing transformations associated with remediation technologies, and (2) to test the hypothesis that the tracer partitioning coefficients change during remediation.

Task 2 – Column and bench-scale experiments of mass transfer behavior. The goals of this task were (1) to test the hypothesis that mass transfer coefficients for entrapped DNAPL sources change during remediation, (2) to determine the “point-scale” mass transfer coefficients from entrapped NAPL sources undergoing remediation, and (3) to upscale the “point-scale” mass transfer coefficients to multi-dimensional flow fields.

Task 3 – Large-tank experiments. The goals of this task were (1) to generate accurate data sets under controlled conditions suitable for model development and validation, (2) to obtain insight to mass transfer processes in heterogeneous system undergoing remediation, and (3) to test upscaling methodologies for heterogeneous systems.

Task 4 – Model development, validation and modification. The goal of this task was to use data generated in Task 3 to validate numerical modeling tools and upscaling methodologies for field systems.

The seventh area of technical focus for research described in this report, a three-dimensional simulation study, was undertaken to demonstrate the use of mass transfer models as decision tools for source-zone management. Application of modeling tools and site characterization methods developed during this research was demonstrated using a hypothetical but realistic aquifer system where only limited data were available at specified locations. The purpose of this demonstration was to evaluate if it is possible to accurately characterize, design and monitor remediation of NAPL source zones in realistic conditions of data density.

Experiments were conducted at a fully equipped intermediate-scale test facility at the Center for the Experimental Study of Subsurface Environmental Processes (CESEP) at Colorado School of Mines. This facility contains a number of two- and three- dimensional test tanks of various sizes. Two-dimensional test tanks were used in the research described in this report in order to facilitate accurate non-destructive measurement of source-zone architecture and temporal changes in DNAPL saturation as experiments proceeded. The largest tank used in this research was approximately 1.2 m in height and 4.9 m long. Instrumentation for each tank experiment included an automated pressure measurement system, a dual-gamma or x-ray attenuation system to measure fluid saturations in multi-phase porous media systems, and equipment for chemical analysis (GC, HPLC, IC).

Large-tank experiments are difficult to setup, costly and time consuming. Therefore, each experiment was designed to meet multiple project objectives while obtaining comprehensive data sets. Experiments consisted of the following primary steps: (1) pack the tank with a designed heterogeneity field and control the water table gradient to obtain the desired discharge and velocity through the tank, (2) record the steady state pressure distribution at pressure ports distributed throughout the tank, and use the pressure data to calibrate a groundwater flow model, (3) inject conservative tracer and obtain tracer break through curves to calibrate a transport model for effective porosity and macro-scale dispersivity coefficients, (4) scan the tank with the automated gamma-ray or x-ray system to provide a baseline for subsequent mapping of DNAPL saturation, (5) conduct a controlled DNAPL spill within the upstream portion of the tank and map pre-remediation distribution of DNAPL with the gamma-ray or x-ray system, (6) monitor downgradient distribution of dissolved DNAPL compounds to evaluate effective mass transfer prior to remediation and conduct a pre-treatment partitioning tracer test, (7) implement the remediation scheme and monitor downgradient distribution of aqueous-phase DNAPL compounds including reaction products, (8) scan the tank with the gamma-ray or x-ray system at periodic intervals to monitor DNAPL mass depletion, (9) conduct a post-treatment partitioning tracer test, and (10) core the tank at the conclusion of the experiment to determine final DNAPL saturations in the tank and distribution of immobile-phase reaction products associated with remediation technologies.

In the model development and validation phase of this research, results of batch, column and bench-scale experiments were used to provide inputs to numerical models of intermediate-scale experiments. If the model simulated intermediate-scale observations within acceptable degrees of accuracy it could be concluded that the model accurately captured the basic processes. However, calibration using a suitable inverse-modeling tool typically was required to match observations. Any significant deviation of the fitted parameter estimates from those measured at batch, column or bench scales, suggests that the model may not have captured the basic processes accurately. This does not necessary imply that the model can not be used in practical problem solving as data accuracy achievable in a laboratory setting rarely can be met in the field. Rather, validation exercises served to identify model limitations, guide model improvements, and evaluate the accuracy that can be expected in field applications. Modeling of intermediate-scale experiments also provided assessments of model sensitivity for mass-transfer parameters and other important model parameters such as NAPL saturations and distribution or remediation reaction rates under upscaled conditions.

3.2 Materials and methods

This report describes a large number of experiments at multiple scales. Many of the experiments were conducted used similar materials and testing methods. These materials and methods are described in the following sections.

3.2.1 Chemicals and materials

Test DNAPL. Both pure (single component) DNAPL and mixtures were used in this research. These included (1) tetrachloroethene (PCE), (2) trichloroethene (TCE), (3) a 50/50 mixture of PCE and TCE, and (4) two complex DNAPL mixtures obtained from field sites. Physical and chemical properties of the pure DNAPL are listed in Table 3.1.

Table 3.1. Physical and Chemical Properties of Pure DNAPL

| Property | TCE | PCE |
|--|----------------------|----------------------|
| Density (g/mL) | 1.46 | 1.62 |
| Viscosity (cp) | 0.58 | 0.90 |
| Interfacial tension (dynes/cm) | 34.5 | 47.5 |
| Contact angle (degrees) | 38 | 66 |
| Solubility (mg/L) | 1100 | 170-200 |
| Molecular weight (g/mole) | 131.4 | 165.83 |
| 2 nd order oxidation rate (L/mole—sec)* | 6.7×10^{-1} | 4.5×10^{-2} |

*(Zhang and Schwartz, 2000)

Tracers. Long-chained alcohols selected as partitioning tracers for this study were 2-methyl-1-butanol (2M1B), 2, 2-dimethyl-3-pentanol (DMP), hexanol (HEX) and 6-methyl-2-heptanol (6M2H). The partition coefficients of these tracers within a DNAPL-water system were determined by conducting a set of batch equilibrium tests (Table 3.2). Sodium bromide was used as a conservative tracer. All aqueous solutions were prepared using DI water (>18.2M Ω -cm).

Table 3.2. Partition Coefficients of Tracers

| DNAPL | Partition Coefficient (dimensionless) | | | |
|-----------------|---------------------------------------|--------------------------|---------|---------------------|
| | 2-Methyl-1-Butanol | 2, 2-Dimethyl-3-Pentanol | Hexanol | 6-Methyl-2-Heptanol |
| PCE | 2.47 | 27.51 | 8.49 | 71.92 |
| TCE | 3.98 | 62.01 | 20.87 | 193.2 |
| Mixture PCE/TCE | n/a | 34.13 | 10.84 | n/a |

Surfactants. The surfactant used in this research was Polyoxyethylene (20) sorbitan monooleate, commercially known as Tween-80 (Aldrich Chemicals). Tween-80 is a non-toxic and bio-degradable food-grade additive used in food and pharmaceutical industries. It was selected because of it has a low critical micelle concentration and has the potential to enhance PCE solubility up to 100 times when used as a solution of 5 percent by mass. The properties of Tween-80 are listed in Table 3.3.

Table 3.3. Properties of Tween-80 (Lide and Frederikse, 2003)

| Property | Value |
|---|------------------------|
| Molecular weight (kg/mol) | 1.310 |
| Density (kg/m ³) | 1.064x10 ³ |
| Viscosity (Pa s) | 1.177x10 ⁻³ |
| Critical micelle concentration (kg/m ³) | 1.30x10 ⁻² |

Chemical oxidant and tap water. Permanganate obtained as granular potassium permanganate (technical grade) from Carus Chemical was used in chemical oxidation experiments. Tap water was de-aired and used to provide flow during tank experiments. Therefore, oxidant was mixed with tap water instead of DI water. This ensured that background chloride levels in the tank remained constant prior, during and after oxidation. Chemical composition of tap water used in experiments is provided in Table 3.4.

Table 3.4. Tap Water Chemical Composition

| Anions (mg/L) | | Cations (mg/L) | |
|---|--------------------------------|----------------|-------|
| Fluoride | 1.5 +/- 0.2 | Calcium | 27.39 |
| Chloride | 25.0 +/- 1.3 | Sulfur | 25.53 |
| Bromide | below detection | Sodium | 25.45 |
| Nitrate | 0.89 +/- 0.16 | Magnesium | 7.85 |
| Phosphate | below detection | Potassium | 5.66 |
| Sulfate | 75.3 +/- 1.0 | Silicon | 4.50 |
| Alkalinity | 35.2 mg/L as CaCO ₃ | Phosphorus | 1.01 |
| General Water Quality Parameters | | | |
| pH | 7.41 | Boron | 0.21 |
| Conductivity | 348 µS at 22.6 °C | Zinc | 0.19 |
| Total solids | 200 mg/L | Strontium | 0.18 |
| Suspended solids | 15 mg/L | Iron | 0.04 |
| Dissolved solids | 185 mg/L | Copper | 0.03 |
| Total organic carbon | 1.14 mg/L | Manganese | 0.02 |
| | | Lithium | 0.02 |
| | | Barium | 0.01 |

Chemical oxidation experiments also were conducted in a one-dimensional flow-through reactor. In these experiments, water was used that represented typical groundwater conditions (Struse et al. 2002). The resulting water was referred to as simulated groundwater. Table 3.5 lists the chemical composition of the simulated groundwater.

Table 3.5. Chemical Composition of Simulated Groundwater

| Chemical Component | Concentration (mg/L) |
|---|------------------------------|
| Potassium | 0.44 |
| Sodium | 0.27 |
| Iron | 0.44 |
| Magnesium | 17.56 |
| Calcium | 41.23 |
| Chloride | 52.47 |
| Nitrate | 0.73 |
| Sulfate | 98.77 |
| General Water Quality Parameters | |
| pH | 7 |
| Alkalinity | 40 mg/L as CaCO ₃ |
| Conductivity | 277 µohms |
| Total dissolved solids | 211.9 mg/L |

Microbial culture. All experiments described in this report that were designed to investigate effects of biological activity on mass transfer used the KB-1 mixed culture (Edwards and Cox, 1997). The KB-1 culture has proven to be highly robust and well suited for use in bioremediation of chlorinated ethene plumes at a number of locations (Major et al. 2002). The culture degrades PCE to ethene using methanol as an electron donor. KB-1 includes microbes that are phylogenetically similar to those of the Cornell culture including *Dehalococcoides ethenogenes* that degrades PCE completely to ethene (Duhamel et al. 2002). Several mixed and pure cultures were grown and evaluated before selecting KB-1 for subsequent tests. However, the ability of KB-1 to adapt to porous-media environments proved to be greater than other cultures (Kaplan, 2004). Protocols for growing the KB-1 culture in batch mode at high PCE concentration are described by Kaplan (2004). Large volumes of KB-1 culture were needed to conduct experiments in large tanks. Protocols for developing the required volumes of culture are described by Glover (2006).

Porous media. Experiments were conducted using clean white silica sands and bentonite (Table 3.6). Estimates of saturated hydraulic conductivity, K_s , are approximate values that can vary greatly depending on packing procedure. The parameters d_{50} and U are the median grain diameter and uniformity index, respectively. $S_{r,w}$ is the residual or irreducible saturation of water, and TOC is the total organic carbon. Table 3.7 lists the typical chemical analysis for silica sands obtained from Unimin and Wedron. Natural oxidant demand (NOD) for the silica sands, measured by batch studies, was below detection levels (S. Jackson, personal communication, Oct 2003). Total carbon, measured by procedures given later in this chapter, also was below detection levels.

Table 3.6. Properties of Porous Media

| Property | Sand | | | | | | | Bentonite clay |
|----------------------|--------|--------|--------|--------|--------|-------------|--------------|----------------|
| | #8 | #16 | #30 | #50 | #70 | #110 | #140 | |
| K_s (cm/min) | 101.3 | 37.500 | 11.800 | 2.267 | 1.458 | 0.383 | 0.126 | n/a |
| d_{50} (cm) | 0.125 | 0.088 | 0.049 | 0.030 | 0.019 | 0.010 | 0.010 | 0.0045 |
| U (-) ¹ | 1.56 | 1.72 | 1.50 | 1.94 | 1.86 | 2.00 | 1.92 | n/a |
| $S_{r,w}$ | 0.11 | 0.070 | 0.260 | 0.290 | 0.30 | 0.260 | 0.26 | n/a |
| pH ³ | 7.39 | 7.39 | 7.39 | 7.39 | 7.39 | 7.39 | 7.39 | 9.1 |
| TOC ³ | 0.019 | 0.019 | 0.019 | 0.019 | 0.019 | 0.019 | 0.019 | n/a |
| Bulk density (g/ml) | 1.6 | 1.6 | 1.6 | 1.8 | 1.6 | 1.8 | 1.6 | 0.83 |
| Grain density(g/ml) | 2.65 | 2.65 | 2.65 | 2.65 | 2.65 | 2.65 | 2.65 | 2.55 |
| Supplier | Unimin | Unimin | Unimin | Wedron | Unimin | U.S. Silica | Manley Bros. | Wyo-Ben |

¹Barth et al. (2001), ²Saenton et al. (2002), ³Seitz (2004)

Table 3.7. Average Chemical Analysis of Porous Media (percent by weight)

| Mineral | #8, #16 Sand | #30, #70 Sand | #50 Sand |
|--|-----------------|------------------|-------------|
| Silicon Dioxide (SiO ₂) | 90.484 | 87.263 | 99.88 |
| Iron Oxide (Fe ₂ O ₃) | 0.095 | 0.113 | 0.025 |
| Aluminum Oxide (Al ₂ O ₃) | 5.451 | 7.244 | 0.050 |
| Calcium Oxide (CaO) | 0.358 | 0.609 | 0.010 |
| Titanium Dioxide (TiO ₂) | 0.016 | 0.018 | - |
| Magnesium Oxide (MgO) | 0.021 | 0.024 | 0.003 |
| Potassium Oxide (K ₂ O) | 2.536 | 2.819 | 0.003 |
| Sodium Oxide (Na ₂ O) | 0.714 | 1.672 | 0.007 |
| Loss on Ignition (LOI) | 0.325 | 0.238 | 0.15 |

3.2.2 Sampling methods

Aqueous samples were collected at multiple locations during most flow-cell and large-tank experiments. Sampling locations consisted of a permanently installed stainless steel needle reaching to the centerline of the tank or flow cell, and a valve on the tank exterior. Before collecting an aqueous sample, 0.1 to 0.5 mL was purged from the sampling port to eliminate stagnant water from the last sampling episode. All aqueous samples were collected by opening the sampling port valve and collecting liquid in a 1.5 mL glass vial. In experiments where volatilization was a concern or the number of samples was very large, vials were fitted with 0.5 mL glass inserts.

Immediately after collection, vials were capped with a Teflon-lined septa cap and analyzed, immediately if possible, or refrigerated until analytical equipment was available. Methods for sample preservation depended on the intend method of chemical analysis. No special procedures were needed for preservation during natural dissolution, surfactant-enhanced dissolution and partitioning tracer tests.

During oxidation experiments, aqueous samples were sub-sampled for a variety of analyses. A portion was placed into a 1.5 mL glass vial containing hexane and capped, shaken for one minute, and allowed to settle for at least 60 minutes prior to analysis for PCE using a gas chromatograph (GC). Another portion was placed into a 15 mL glass tube (Hach) containing DI water, capped, shaken, and analyzed on a UV-spectrophotometer (UV/Vis-Spec) for MnO₄⁻ within three hours. A third portion was added to a 1.5 mL glass vial containing sodium bisulfite (to stop oxidation by reducing any permanganate in the sample), capped, shaken, and allowed to rest for six hours to settle out any manganese oxides prior to analysis for chloride using an ion chromatograph (IC). For select aqueous samples obtained during the intermediate-scale 2D experiments, another portion was added to a 15 mL polypropylene conical vial containing DI water, acidified with nitric acid to pH less than 2, capped, shaken, and analyzed for Mn⁺² using inductively coupled plasma-atomic emission spectroscopy (ICP-AES). Finally, for aqueous samples obtained during the oxidation phase of each experiment, pH was measured in the remaining original sample.

During large-tank experiments with biological activity, sample preservation and treatment depended on the method planned for chemical analysis. Samples intended for analysis

of soluble constituents were stored without headspace in a 1.5mL glass vial capped with a Teflon-lined septa cap, or transferred to a 5mL vial capped with a Mininert valve. Liquid samples stored without headspace were analyzed by gas chromatography for PCE, TCE and cis-DCE within 7 days of collection. If collected as part of a tracer test, liquid samples also were analyzed by ion chromatograph for bromide. Samples intended for analysis of highly volatile constituents were stored in 5mL vials with headspace and placed on a shaker table for 18 to 30 hours to equilibrate. The headspace was sub-sampled for GC analysis of PCE, TCE, cis-DCE, VC, ethene, and methanol. Air temperature at time of analysis was recorded and temperature-corrected Henry's constants, along with precisely measured sample and headspace volumes, were used to calculate the concentration of the original liquid sample. Henry's constants were obtained from Gossett (1987).

Upon completion of select tank experiments, soil cores were obtained from throughout the tank using manual coring devices such as those shown in Figure 3.1. Cylindrical samplers were used to obtain cores at representative locations, along the tank centerline, through much of a tank. Soil coring grids such as those shown in Figure 3.1 were used to core source zones such that the entire source could be extracted while subdividing it into rectangular cores 2.0cm x 2.6cm. When obtaining a core, the water level was lowered to the desired core level, and the tank was excavated to that point. The coring device was then pushed into the soil at the desired location and sand was excavated around the device. The device was then removed and the soil sample pushed into a sample-storage vial containing hexane. The vial was capped, shaken for 30 seconds, and left to rest for 24 hours before transferring some of the hexane into a glass vial for PCE analysis using a GC.



Figure 3.1. Soil Coring Devices

Additional sample preparation was required for soil cores obtained following chemical oxidation experiments. After analyzing for PCE, the hexane remaining in soil core vials was evaporate for 48 hours under an exhaust hood, and hydroxylamine hydrochloride (0.2M) and nitric acid (0.1M) were added to the vials to reduce and dissolve any $MnO_2(s)$. The vials were placed on a wrist-action shaker (60rpm) for two hours and then centrifuged for 10min at 1150G before transferring liquid into 15mL polypropylene conical vials to be analyzed for Mn^{+2} by ICP-

AES. Following ICP-AES analysis, the remaining liquid was drained and the core dried at 103°C for four hours before determining the dry weight, so PCE and MnO₂(s) content could be expressed as mass fractions.

3.2.3 Analytical methods

Gas chromatography. Aqueous samples intended for analysis of PCE, TCE, DCE, and partitioning tracer concentration were analyzed on a Hewlett-Packard (HP) 6890 gas chromatograph (GC) equipped with an HP7683 auto-sampler/injector and DB-624 column, utilizing a flame ionization detector (FID). Aqueous sub-samples extracted into hexane were analyzed for PCE using an HP GC equipped with an HP7683 auto-sampler/injector and DB-5 column, utilizing an electron capture detector (ECD). Soil cores that had been extracted into hexane were analyzed for PCE using an HP GC equipped with an HP7683 auto-sampler/injector and DB-624 column, utilizing an FID. Six-point calibration curves were used for each method. Table 3.8 provides method summaries.

Table 3.8. GC Method Summaries

| Parameter | Aqueous Samples, water | Aqueous Samples with Hexane Extraction | Soil Cores |
|---------------------------|------------------------|--|------------|
| Initial Oven Temp (°C) | 55 | 120 | 55 |
| Oven Ramp (°C/min) | 12 | 45 | 26 |
| Final Oven Temp (°C) | 150 | 200 | 120 |
| Injector Mode | Splitless | Split (50:1 ratio) | Splitless |
| Injection Volume (µL) | 1.0 | 0.2 | 1.0 |
| Detector | FID | ECD | FID |
| Detector Temperature (°C) | 250 | 250 | 250 |

Headspace samples collected during tank experiments with biological activity were intended for analysis of PCE, TCE, cis-DCE, VC, ethene, and methanol. Gas chromatograph analysis of headspace was done by obtaining a 0.4 mL sub-sample with a gas-tight syringe. The sub-sample was injected manually into the GC injection port to start a GC sample run. Conditions for the headspace analytical method were the same at those used for liquid analyses with one exception. Inlet temperature for the headspace method started at 35°C for three minutes, ramped at 15 °C/min to 120 °C where it was held for 2 minutes. This procedure provided adequate separation of target compounds for most samples obtained during flow cell and large-tank experiments. When monitoring degradation progress of KB-1 batch cultures, ethene mass in headspace typically would increase to a high concentration. This resulted in large GC peaks for ethene and poor resolution of VC and methanol peaks.

Ion chromatography. Samples collected during tracer tests were analyzed for bromide. Samples collected during oxidation phases of chemical oxidation experiments were analyzed for

chloride. In both cases, analyses were performed using a Dionex AS50 ion chromatograph/high performance liquid chromatograph (IC/HPLC) with Dionex IonPac AS-14A ion exchange analytical (4mm x 150mm) and IonPac AG-14A (4mm x 50mm) guard columns, AS50 auto-sampler, AS50 gradient pump, and CD25 conductivity detector. A sodium carbonate (8.0 mM) and sodium bicarbonate (1.0 mM) effluent, at a flow rate of 1.2 mL/min, was used with this carbonate-selective anion exchange column. Calibration was performed daily using a 7-point (for chloride) or 8-point (for bromide) calibration curve.

UV-spectrophotometer. Experiments in small sand-filled flow cells were conducted to characterize mass transfer from DNAPL pools undergoing bioremediation. Because these experiments were conducted with flow cells of small volume and correspondingly low flow rates, they provided an ability to focus on processes that dominate at NAPL pool interfaces. However, they limited the number and frequency of conventional water samples that could be obtained. Therefore, a computer controlled monitoring system was developed to supplement information obtained by conventional sampling of effluent.

The system consisted of an in-line UV spectrometer (Waters model 486) and data logger (Campbell Scientific model CR10X) that were calibrated to monitor total concentration of chlorinated ethane compounds. While this system did not provide the accuracy or chemical specificity possible in gas-chromatograph analysis of effluent samples, it did provide a more detailed description of temporal changes in effluent chemistry. By connecting the data logger to a PC computer, the system also provided data results in real time as an experiment proceeded.

Effluent from the sand-filled flow cell was routed by Teflon tubing through a cell in the spectrometer that is equipped with UV energy source and a photodiode detector. The spectrometer can be tuned to a specified wavelength. For detection of total chlorinated ethenes, the spectrometer was set at a wavelength of 220 μm . Measured absorbance was transmitted continuously to the data logger and average absorbance for 10 sec intervals was stored. Periodically, absorbance information was downloaded from the data logger and a calibration curve was applied to determine total ethene concentration. The relationship between the quantity of light of a particular wavelength arriving at the detector and the concentration of the sample is described by the Lambert-Beer law.

Calibration involved preparing standards of known ethene concentration, running the standards through the spectrometer, and noting the instrument response. Calibration standards included de-ionized water, microbe nutrient medium known to be free of ethene compounds, de-ionized water containing specified concentrations of PCE, and nutrient medium with specified concentration of PCE. Standards containing PCE were created initially for PCE at saturation. Serial dilutions were performed to create additional PCE standards at lower concentrations. The PCE concentration in standards was verified by analyzing samples by gas chromatograph methods.

Total organic carbon (TOC) analyzer. Total organic carbon in soil samples was determined with a carbon dioxide coulometer (UIC Inc. model CM5014). The standard method for use of this coulometer involved calibrating the instrument prior to running environmental samples. Samples were air dried, weighed and placed within a combustion chamber. Carbon dioxide released by combustion was measured by a UV spectrometer. Calibration of the coulometer involved running blank and calcium carbonate standards. Sand that had been heated to 500C to drive off organic carbon also was used as a calibration blank. Detection limit of the

method typically was in the range of 10^{-6} to 10^{-5} g C / g dry soil. As a result, the method was suitable for measuring biomass concentration in samples but was not suitable for measuring DNAPL or sorbed concentration of highly volatile compounds such as chlorinated ethenes.

Hydrogen ion activity. During oxidation phases, pH was measured using an Orion 98-63BN micro-pH probe and Orion 420A+ meter. A 3-point calibration was performed daily.

Inductively coupled plasma-atomic emission spectroscopy (ICP-AES). Analysis for Mn^{+2} was performed using a Perkin Elmer Optima 3000 ICP-AES, utilizing internal and external standards and triplicate measurements.

3.2.4 Gamma and x-ray attenuation systems

Gamma Ray spectroscopy is used to obtain the saturation of the contaminant in the porous media. It is based on the fact that different materials will attenuate photons of certain energy by different amounts, and this attenuation will be proportional to the path length of the material. If the photon attenuation of the contaminant for a specific energy is known then, from the comparison of the spectrums before and after the contaminant was introduced in the porous media, it is possible to predict the volume or mass of the contaminant.

The rate of energy transmitted is described by the number of photons that reach the detector in a determined amount of time (counts per unit of time). For our application this rate is the number of counts over a certain energy range per unit of time. The transmitted photons through the system can be obtained using the Beer-Lambert equation

$$I = I_0 e^{-[(\mu_n - \mu_w)x_n]} \quad (3.1)$$

where I_0 corresponds to the initial number of counts obtained before the contaminant was added to the porous media, μ are the mass attenuation coefficient of the NAPL (n) and water (w) divided by their corresponding densities and x_n is the path length through NAPL. A modified form of this equation can be used to obtain the saturation of the NAPL phase

$$S_{NAPL} = \frac{\ln\left(\frac{I_0}{I}\right)}{(\mu_n - \mu_w) \cdot L \cdot \phi} \quad (3.2)$$

where L is the inner thickness of the container of the porous medium and ϕ is the porosity.

The attenuation coefficient of the different materials is calculated using the following procedure. First the total number of counts through five one-centimeter wide precision vials is obtained (I_0). Then the vials are successively filled with the material of interest (water, NAPL, etc.) and the corresponding number of counts recorded. Since only one substance is being analyzed and the path length is known we have from the Beer-Lambert equation

$$\ln\left(\frac{I_0}{I}\right) = \mu \cdot x \quad (3.3)$$

Then, plotting of $\ln\left(\frac{I_0}{I}\right)$ vs. the path length x will result in a straight line in which the slope corresponds to the attenuation coefficient of the material.

The Gamma System used in this research consists of a 200 millicuries Americium 241 (Am) source housed in a cylindrical lead container. The gamma photons pass through a collimation port to create a 5 mm collimated beam. The detector is a 5 x 5 x 5 mm Cadmium-Zinc-Tellurium crystal detector with an included preamplifier to minimize the noise to signal ratio. The source and the detector are in opposing platforms separated 43 cm. A second amplifier (Ortec 575A) is used to increase the amplification and shape the signal into a Gaussian pulse with a 10 μ second shaping time. An ORTEC 918A multi-channel analyzer is used to select the pulses of the desired energy (~60 KeV).

The Source and detector platforms can be moved vertically, and the whole system can be displaced horizontally, allowing for a complete scan of the tank or column positioned between the two platforms. A custom computer program written in LabView controls the movement of the system as well as the data acquisition from the multi-channel analyzer, this allows for a complete automation of the scan. The data is processed using a MatLab script and the Plotting software Surfer.

X-ray attenuation techniques are non-destructive methods for monitoring the spatial distribution and temporal change in NAPL saturation. The techniques are applicable to laboratory settings with columns, and two dimensional flow cells and sand tanks. Attenuation of photon radiation by porous media is used to determine differential path lengths of sand, water and NAPL within a sample. Material path lengths are measures of porosity and fluid saturation. With single-energy gamma-radiation sources, a single unknown can be determined. With multiple-energy sources, independent path lengths can be determined for multiple materials. X radiation differs from gamma radiation by having a broad energy spectrum allowing for simultaneous determination of multiple unknown material path lengths. X-ray sources also provide relatively high photon flux rates that can improve measurement quality and/or reduce measurement time. An x-ray source is tunable in the sense that the photon spectrum can be adjusted to match specific needs of a given experiment or measurement.

Procedures for collecting X-ray attenuation data and processing results to determine DNAPL saturation are provided by Hill et al. (2002). The x-ray source strength used in flow cell and tank experiments typically was 70 kV and 10 mA. However, deviations from these values were used in some experiments in order to obtain optimum measurement of X-ray attenuation. Deviations are noted in descriptions of individual experiments. Spectral filters (barium carbonate salt and samarium carbonate solution at the solubility limit) were used to create x-ray spectra with three distinct peaks.

During typical operation, X-ray scans of the flow cell were conducted before and after DNAPL injection and differences in spectral intensity were used to determine DNAPL saturation. Spatial resolution in terms of both the X-ray beam width and the grid spacing used to gather data typically was 2 mm. Temporal drift in X-ray spectra was determined by repeated scanning of an aluminum control block and areas outside the flow cell.

Analyses of photon attenuation spectra are based on an application of the Beer-Lambert law written for multiple materials and an equivalent number of lumped-energy ranges over which photon count rates are recorded. The resulting matrix expression can be solved for a vector of path lengths given a set of attenuation coefficients, typically determined by a calibration procedure with samples of known path length, and a vector of photon count rates.

Attenuation coefficient values are defined for specific wavelengths and are material dependent. In this research, the materials of interest include water, quartz sand, and PCE. For a particular wavelength, an attenuation coefficient relates photon attenuation to the thickness of a specified material. The calibration procedure used to estimate attenuation coefficients is essentially identical for each material. Therefore, only PCE calibration is described here.

Calibration consisted of placing a set of five square glass vials, each with an internal thickness of 1.00 cm, within the X-ray path. Spectra, measured in terms of photon count rate, were recorded with no PCE in the vials. Additional spectra were recorded after each glass vial was filled with PCE solvent. The difference in photon count rate as each glass vial was filled represents the photon attenuation due to an increased path length through PCE of 1 cm. The amount of photon attenuation varies as a function of wavelength. However, a good set of calibration spectra will show a log-linear increase in attenuation as path length increases. The resulting data pairs of photon attenuation and path length were then fit to the Beer-Lambert equation to determine attenuation coefficients.

3.3 Experimental design and methods for investigation of partitioning tracers

Partitioning tracer tests are used to detect and locate NAPL contamination, estimate the NAPL volume present and assess remediation performance. A partitioning tracer test is conducted by injecting several tracers with different water-NAPL partition coefficients upgradient of a NAPL source zone and monitoring tracer migration at downgradient locations. Typically, a tracer solution includes at least one conservative, non-partitioning tracer designed to move as if it were water, and a mixture of chemicals with different partition coefficients. Partitioning tracers undergo retardation, while the conservative tracer is not affected by the presence of DNAPL. The observed chromatographic separation of the various tracers at downgradient locations depends on the fraction of total travel time from injection to sampling locations that each tracer spends in the NAPL phase. In field settings wells typically are used as injection and sampling locations and the technique is called a partitioning inter-well tracer test (PITT).

The technique has been adapted from the fields of groundwater hydrology and petroleum reservoir engineering (Allison et al., 1991) and extended for use in detecting and characterizing the distribution of NAPL contaminants in subsurface environments (Jin et al., 1995). In most cases, this technique has been used to assess remediation performance (Rao et al., 1997; Annable et al., 1998; Jawitz et al., 1998; Meinardus et al., 2002). However, PITT techniques have not

been completely evaluated under complex DNAPL entrapment morphologies that can occur in heterogeneous porous media. Partitioning tracer tests also are expected to underestimate DNAPL volume in certain conditions where the hydrodynamic accessibility is constrained or non-equilibrium mass transfer occurs (Rao et al., 2000).

The focus of this research study was to evaluate the use of partitioning tracer tests as a tool for characterizing NAPL sources in heterogeneous source zones undergoing remediation. Laboratory studies were conducted at batch, column and large-tank scales to access quantitatively the performance of current tracer methods both before and after remediation. In this way, fundamental processes, hypotheses and data analysis of partitioning tracer methods were investigated. Specific objectives were (1) to identify causes of estimation error, (2) to refine tracer methods, and (3) to obtain information about the architecture of NAPL source zones. The knowledge gained from these investigations can be used to improve design protocols for field characterization of NAPL entrapment morphologies encountered at geologically complex field sites.

Successful application of PITT depends on the accuracy of partitioning coefficients (K_p) used in data analysis. This section of the report describes the effect of three remediation methods, surfactant flushing, chemical oxidation and bioremediation, on partitioning-tracer behavior, and evaluates changes in tracer partitioning coefficients during and after remediation.

3.3.1 Batch tests

Surfactant Treatment. Batch tests were conducted to understand how partitioning tracers interact with free-phase chlorinated organic solvent and solvent mixtures undergoing surfactant treatment. Batch tests were completed for three water-DNAPL systems including pure TCE DNAPL, a 50/50 mixture of PCE and TCE, and a DNAPL obtained at a field site. A 2:1 volume ration of surfactant solution to DNAPL was used in these experiments. Surfactants used in the tests were Tween 80 at concentrations ranging from 0.17 to 5 percent and cyclodextrin at concentrations ranging from 0.33 to 10 percent. As a control, tests also were conducted with batch reactors that did not include surfactants. After equilibration, water samples from each batch were analyzed by GC methods and tracer isotherms were developed. Figures 3.2 and 3.3 are typical examples of tracer isotherms obtained for batch tests with pure TCE DNAPL. Tracer partitioning coefficients were estimated from the slope of isotherm plots.

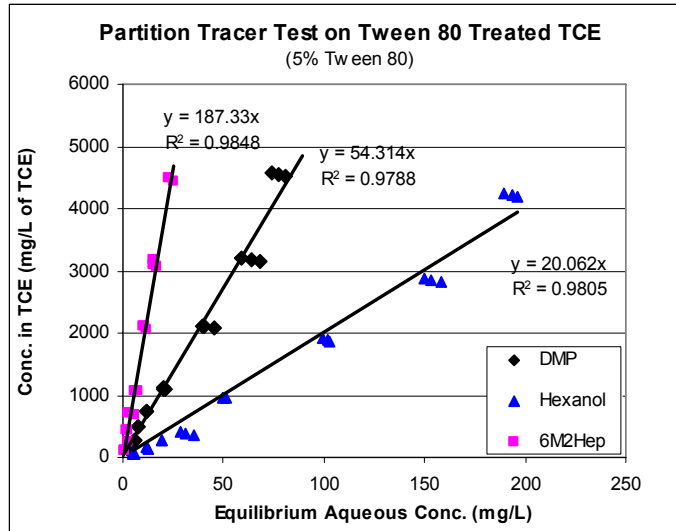


Figure 3.2. Batch tests to determine partition coefficient of Tween 80 in a TCE DNAPL-water system

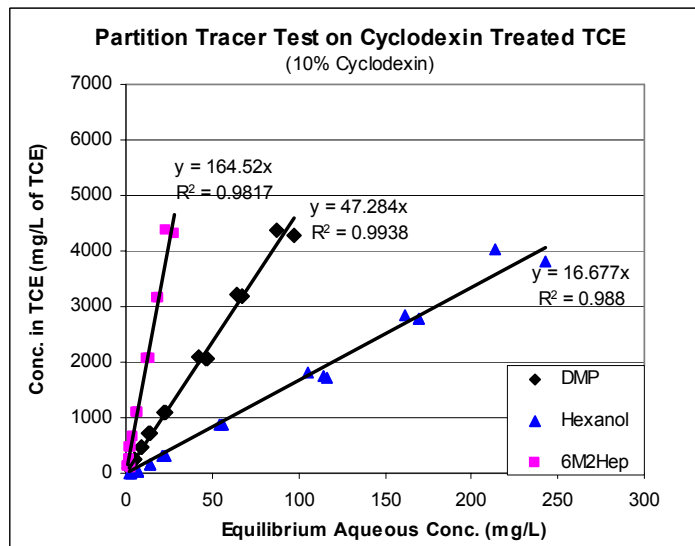


Figure 3.3. Batch Tests to Determine Partition Coefficient of Cyclodextrin in a TCE DNAPL-water system

Surfactant treatments showed no significant effect on partitioning behavior and tracer partition coefficients for the pure phase DNAPL and the PCE/TCE DNAPL mixture. However, partition coefficients for the field DNAPL mixture decreased with a single surfactant treatment. Partition coefficients for TCE DNAPL are summarized in Table 3.9. Partition coefficients for the DNAPL with a 50/50 mixture of PCE and TCE are summarized in Tables 3.10. Partition coefficients for the field DNAPL are summarized in Tables 3.11.

Table 3.9. Partition Coefficients for Surfactant-Treated TCE DNAPL Estimated from Batch Tests

| Surfactant Type | Surfactant Concentration | <u>2, 2-Dimethyl-3-Pentanol</u> | | <u>Hexanol</u> | | <u>6-Methyl-2-Heptanol</u> | |
|-----------------|--------------------------|---------------------------------|----------------|----------------|----------------|----------------------------|----------------|
| | | K _p | R ² | K _p | R ² | K _p | R ² |
| No Surfactant | 0% | 53.00 | 0.978 | 19.350 | 0.982 | 192.93 | 0.967 |
| | 5% | 54.314 | 0.979 | 20.062 | 0.981 | 187.33 | 0.985 |
| Tween 80 | 2.5% | 51.112 | 0.975 | 19.196 | 0.984 | 174.72 | 0.895 |
| | 0.5% | 53.109 | 0.983 | 19.226 | 0.984 | 190.57 | 0.955 |
| | 0.17% | 56.408 | 0.998 | 19.622 | 0.991 | 208.65 | 0.993 |
| | 10% | 47.284 | 0.994 | 16.677 | 0.988 | 164.52 | 0.982 |
| | 5% | 50.38 | 0.999 | 17.82 | 0.996 | 185.08 | 0.994 |
| Cyclodextrin | 1% | 50.65 | 0.997 | 17.42 | 0.995 | 178.67 | 0.989 |
| | 0.33% | 54.913 | 0.992 | 19.07 | 0.994 | 179.94 | 0.924 |

Table 3.10. Partition Coefficients for Surfactant-Treated DNAPL Mixture of PCE/TCE Estimated from Batch Tests

| Surfactant Type | Surfactant Concentration | <u>2M1B</u> | | <u>DMP</u> | | <u>Hexanol</u> | | <u>6M2Hep</u> | |
|-----------------|--------------------------|----------------|----------------|----------------|----------------|----------------|----------------|----------------|----------------|
| | | K _p | R ² |
| No Surfactant | 0% | 2.76 | 0.92 | 42.95 | 0.99 | 13.35 | 0.99 | 130.75 | 0.97 |
| | 0.5 % | 2.34 | 0.99 | 40.35 | 0.99 | 12.81 | 0.99 | 130.87 | 0.98 |
| Tween 80 | 2.5 % | 2.94 | 0.84 | 42.46 | 0.99 | 13.24 | 0.99 | 133.78 | 0.98 |
| | 5 % | 2.45 | 0.99 | 41.06 | 0.99 | 12.99 | 0.99 | 131.32 | 0.98 |
| Cyclo-dextrin | 5 % | 2.78 | 0.83 | 41.00 | 0.99 | 12.83 | 0.98 | 128.46 | 0.98 |
| | 10 % | 2.16 | 0.99 | 35.43 | 0.99 | 11.24 | 0.99 | 102.59 | 0.98 |

Table 3.11. Partition Coefficients for Surfactant-Treated Field DNAPL
Estimated from Batch Tests

| Surfactant Type | Surfactant Concentration | <u>2M1B</u> | | <u>DMP</u> | | <u>Hexanol</u> | | <u>6M2Hep</u> | |
|-----------------------------|--------------------------|----------------|----------------|----------------|----------------|----------------|----------------|----------------|----------------|
| | | K _p | R ² |
| No Surfactant | 0% | 5.63 | 0.94 | 33.82 | 0.99 | 12.5 | 0.99 | 112.28 | 0.99 |
| Tween 80 | 5% | 4.95 | 0.85 | 30.33 | 0.99 | 11.24 | 0.99 | 84.32 | 0.91 |
| Cyclo-dextrin | 10% | 5.04 | 0.89 | 29.26 | 0.99 | 10.90 | 0.99 | 94.56 | 0.94 |
| Tween 80, multiple washings | 5% | | | 20.57 | 0.99 | 8.13 | 0.99 | | |

The effect of multiple washings by surfactant was evaluated by conducting an additional set of batch experiments with the field DNAPL. These tests may more closely replicate conditions that would occur in column or field-scale settings and were used to estimate changes in partition coefficients following surfactant remediation. In these batch tests, a total of 300 ml of 5 percent Tween was used to wash 20 mL of filed DNAPL in 6 consecutive steps, and then followed by two additional washes with 60 mL of water wash. The TCE concentration in the surfactant solution and in the post-surfactant water wash was measured on the GC. Total TCE removed from the DNAPL was about 4.0 g. This surfactant-treated DNAPL was used in batch tracer tests to evaluate the effect of treatment on the partition coefficients.

The partitioning tracer tests were conducted in the same way as previous batch tests. However, only DMP and Hexanol were utilized as partitioning tracers. The resulting partition coefficients are summarized in Table 3.11. The DMP and Hexanol partition coefficients changed significantly after multiple surfactant washes. If unrecognized in a column or field application, this change in partition coefficients could significantly affect the accuracy of DNAPL volume estimated following surfactant remediation.

Chemical Oxidation. Batch tests were conducted to determine if tracer partitioning coefficients change during chemical oxidation and to estimate partitioning coefficients for test DNAPLs and field samples undergo chemical oxidation. The DNAPL used in these tests were pure PCE and pure TCE. Partitioning tracers were hexanol, 2,2- DMP and 6M2Hep.

Experiments were conducted for water-DNAPL systems and oxidant solution-DNAPL systems. The chemical oxidant was potassium permanganate as 0.3 and 3 percent solutions. Two treatment methods were used. In the first, oxidant was added to DNAPL in a volume ratio of 50 mL 3% KMnO₄ to 20 mL DNAPL. Tests were conducted for contact times of 48 and 120 hours. In the second, oxidant was added in several consecutive steps for contact times similar to the resident time expected in column test at a specified flow rate. The DNAPL remaining after oxidant treatment were used in batch partitioning tracer tests and results were compared with similar batch tests conducted with DNAPL in water.

The tracer partitioning between water and 3 percent KMnO_4 treated PCE DNAPL showed unexpected behavior. When PCE contacted KMnO_4 for either 48 or 120 hours, all tracer isotherms showed nonlinear behavior (Figure 3.4). Partition coefficients for all tracers also increased following oxidant treatment. When compared with partition coefficients for systems without oxidant treatment, changes were greater at lower tracer concentrations and smaller at higher concentrations. Figure 3.5 shows the relationship between the tracer partition coefficients and initial concentration of tracer. For oxidant-treated TCE, there was no significant increase in tracer partitioning coefficients. The tracer partitioning coefficients did not show significant changes with 0.3 percent KMnO_4 treated DNAPLs. The results of partitioning-tracer tests with the DNAPL for different oxidant treatments are summarized in Table 3.12.

Table 3.12. Tracer Partition Coefficients for Oxidant and Water Treated DNAPLs (correlation coefficient shown in parentheses)

| DNAPL | KMnO_4 (%) | Time (hour) | Oxidant Treated | | | DI Water Treated | | |
|-------|---------------------|--------------------|------------------|------------------|-------------------|------------------|------------------|-------------------|
| | | | Hexanol | DMP | 6M2Hep | Hexanol | DMP | 6M2Hep |
| TCE | 0.3 | 1 hr 5 times | 18.58 (0.996) | 54.37 (0.997) | 196.18 (0.988) | 18.06 (0.990) | 52.59 (0.998) | 192.02 (0.998) |
| | 3 | 48 | 17.0 (0.998) | 47.9 (0.977) | 178.6 (0.990) | 16.3 (0.998) | 46.9 (0.992) | 173.7 (0.993) |
| | 3 | 120 | 17.5 (0.994) | 51.0 (0.988) | 165.9 (0.983) | 16.7 (0.999) | 47.4 (0.998) | 175.8 (0.968) |
| PCE | 0.3 | 1 hr 5 times 24 | 7.13 (0.999) | 25.51 (0.999) | 76.87 (0.999) | | | |
| | 3 | 48 | 6.9-17.7 | 23-150 | 66-173 | 6.06 (0.999) | 21.8 (0.997) | 66.2 (0.999) |
| | 3 | 120 | 6.6-17.0 | 23.8-80 | 72-190 | 6.312 (0.997) | 22.3 (0.997) | 65.5 (0.995) |

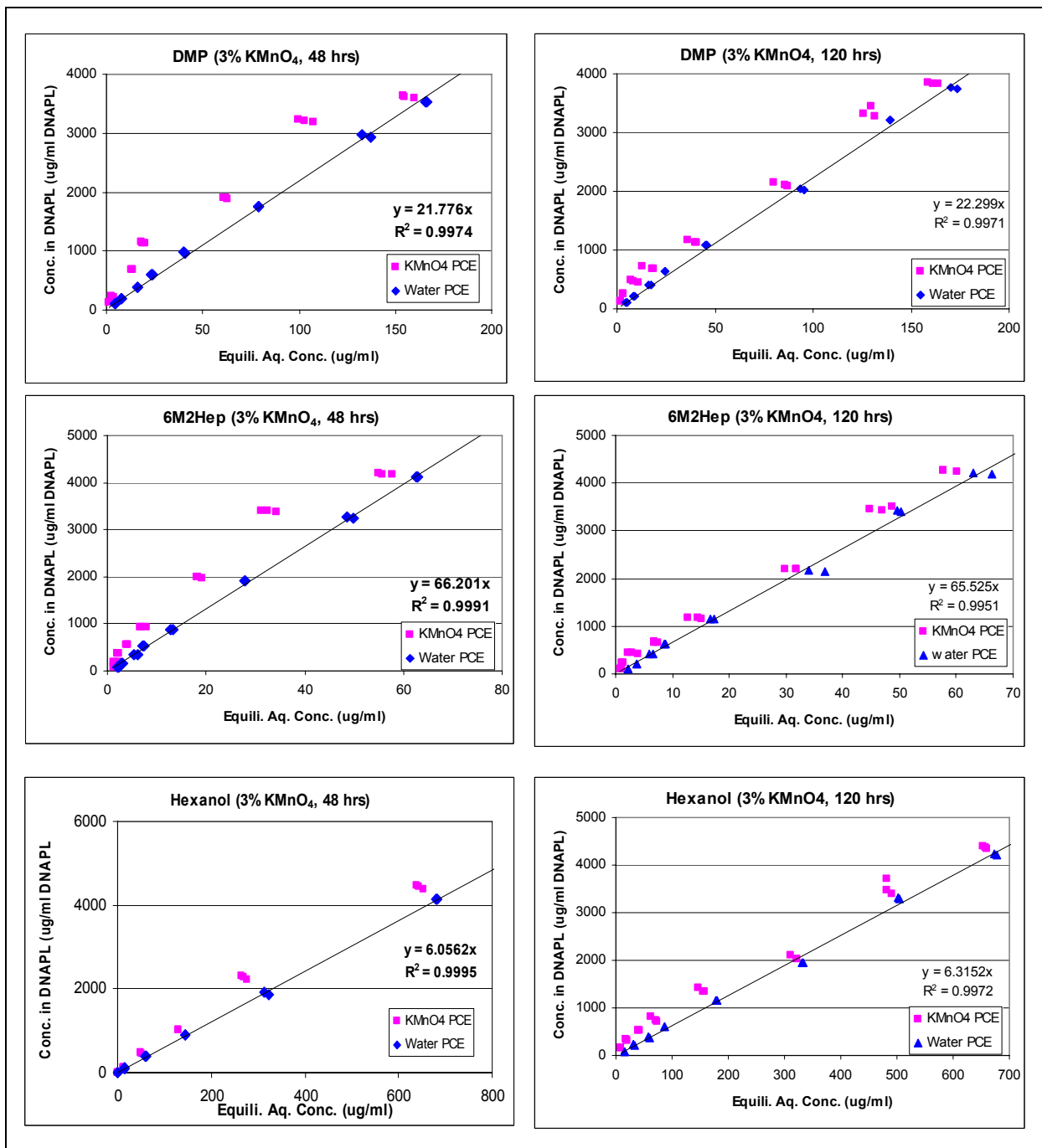


Figure 3.4. Isotherms for Selected Tracers Partitioning Between Water and KMnO₄-Treated PCE

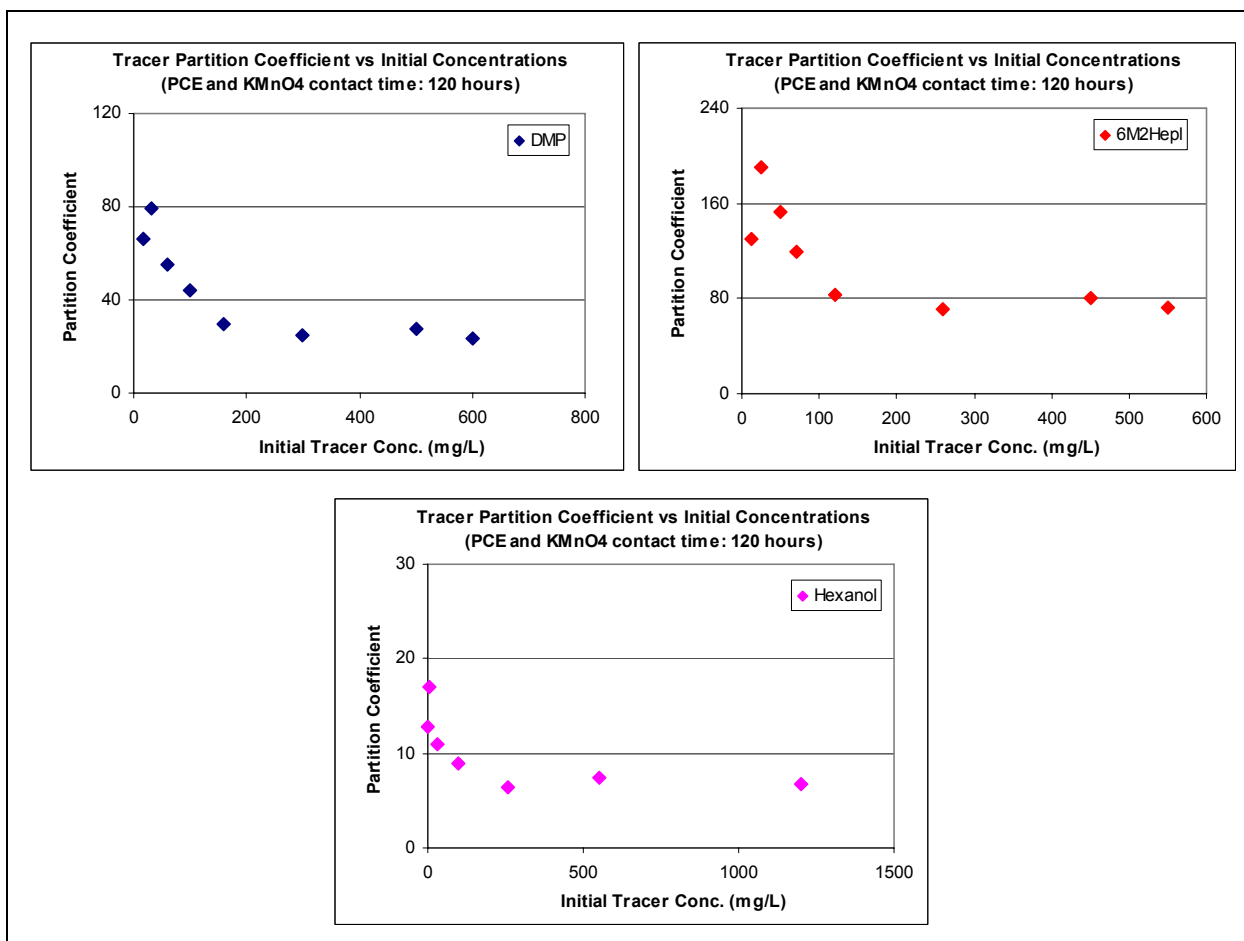


Figure 3.5. Tracer Partition Coefficients at Different Initial Tracer Concentrations for PCE after Treatment with KMnO_4

Biological Treatment. Bioremediation of DNAPL source zones may affect partitioning tracers by biological clogging, formation of biological surfactants and/or changes in solution chemistry associated with nutrient injection. Batch tests were conducted to characterize these factors for three DNAPL, pure PCE, pure TCE, and a 50/50 mixture of PCE and TCE. For each DNAPL, batch tests were conducted to prepare partitioning isotherms for 4 tracer solution-DNAPL systems. These systems included (1) fresh DNAPL added to a tracer solution made from water, (2) fresh DNAPL added to a tracer solution made from KB1 nutrient medium that had been autoclaved to prevent biological growth. (3) DNAPL equilibrated with water for selected times, extracted and added to a tracer solution made from water, and (4) DNAPL equilibrated with an actively growing culture of KB-1 for selected times, extracted and added to a tracer solution made with KB1 nutrient medium. In this section of the report, batch systems that included fresh DNAPL are called baseline systems. The system that included DNAPL equilibrated with water is called the water-treated system. The system that included DNAPL equilibrated with the actively growing culture of KB-1 is called the bio-treated system.

Tests for each DNAPL and tracer concentration were conducted in triplicate with two controls. A tracer solution containing n-hexanol (400ppm), dimethylpentanol (DMP) (300ppm), 6-methyl, 2-heptanol (MH) (300ppm), and potassium bromide (KBr) (300ppm) was subjected to

serial dilution to obtain seven solutions of varying concentrations. The parent solution was mixed and allowed to equilibrate overnight, stirring constantly, before dilutions were made. Figure 3.6 shows the serial dilution schematic. For each experimental replicate, 2 mL microvials were filled with 1.6 mL of tracer solution and 0.2 mL of DNAPL, and allowed to equilibrate on a shaker table overnight. In addition, two microvials containing 1.8 mL of each solution without DNAPL were used as controls. After microvials equilibrated, they were centrifuged to promote phase separation, and the aqueous phase was sampled by GC-FID. Analytical results were then used to create tracer partitioning isotherms. Partition coefficients were estimated as the slope of a line fitted to the isotherm data.

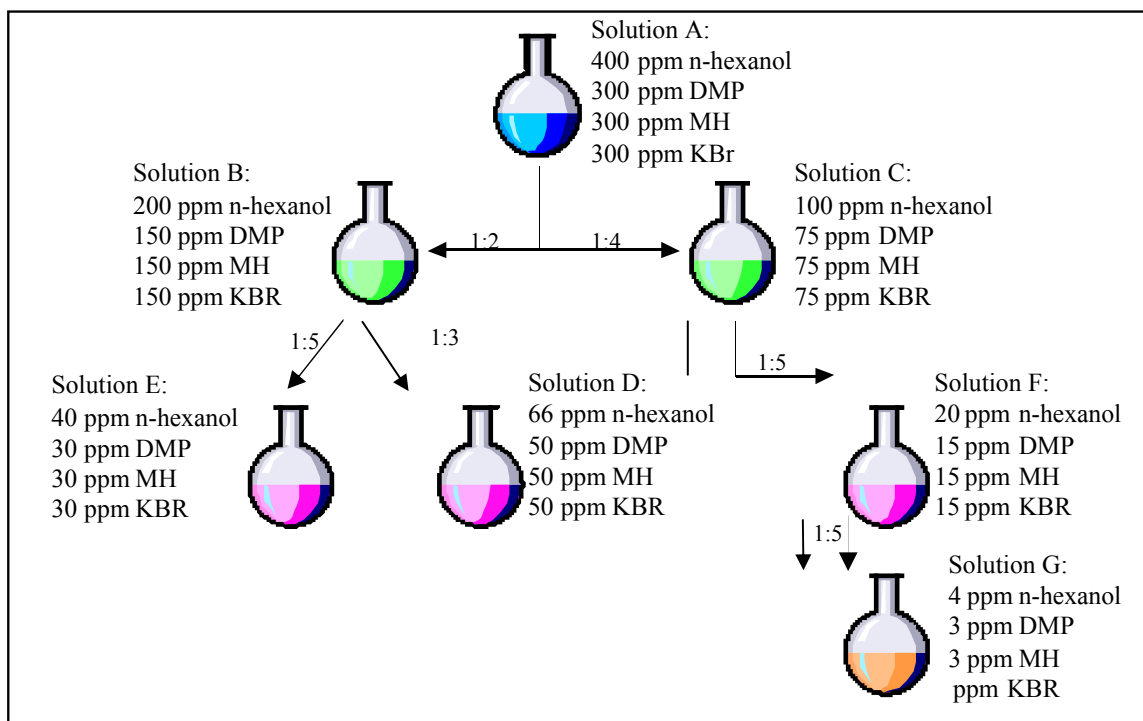


Figure 3.6. Schematic of Serial Dilution Used to Make Tracer Solutions, Batch Partitioning Tracer Experiments with Biological Treatment

In order to evaluate the effects of KB-1 nutrient medium on partition coefficients, the set of batch tests were repeated using tracer solutions made with nutrient medium instead of pure water. To keep tracers from being degraded by naturally occurring microbes in the presence of nutrient medium, the solutions were made in the anaerobic chamber and were autoclaved immediately after being made. The test was also conducted in the anaerobic chamber using sterile techniques according to the protocol previously described. Microvials were wrapped in foil and autoclaved prior to use, vial caps and the inside of the chamber were sprayed with ethanol and all instruments were handled only with gloves that had been sprayed with ethanol as well.

Water treatment of DNAPL was included in the experimental design to verify that the partitioning behavior of the tracers did not change over time in absence of biological activity. The treatment protocol for each DNAPL consisted of injecting 20 mL of the selected DNAPL into sealed 100 mL serum bottles containing 50 mL milli-Q water. All bottles were placed on their sides on a shaker table. Five mL of DNAPL was extracted from the bottles every 24 hours for four days and used in microvial batch tests to evaluate partition coefficients.

Biological treatment of DNAPL was analogous to water treatment, except that active KB-1 culture was used instead of pure water. Treatment for each DNAPL consisted of injecting 20 mL of DNAPL into a sealed 100 mL serum bottle that contained 80 mL of KB-1 culture and 33 μ L of methanol as electron donor for PCE biodegradation. For each DNAPL, control and bio-active treatments were prepared. The control treatments were identical to the bio-active treatments except that controls were autoclaved. For both control and bio-active treatments, KB-1 was obtained from batch cultures that had degraded available aqueous PCE completely to ethene since its last feeding. The amount of methanol provided a 1:5 electron-equivalent ratio of PCE aqueous solubility to methanol. Partitioning tracer tests following bio-active treatment were conducted in microvials as at selected times by extracting DNAPL from the bio-active treatment bottles after 24 hours, 14 days, and 30 days. Partitioning tracer tests using the control treatments were conducted after 30 days. Headspace samples also were taken at the same times as DNAPL was extracted from treatment bottles and analyzed by GC-FID for PCE and biodegradation products to determine if the culture remained active during treatment.

Partitioning isotherms for the baseline systems of DNAPL and water were developed for three DNAPL, and the tracers Hexanol and DMP (Figure 3.7). The third tracer (6M2Hep) was not added to the testing protocol for the baseline system with water but was added to subsequent systems. Resulting partitioning coefficients and correlation coefficients (R^2) are summarized in Table 3.13. Results for baseline DNAPL systems with abiotic nutrient medium indicate an increase in partitioning with nutrient medium compared to pure water (Table 3.14).

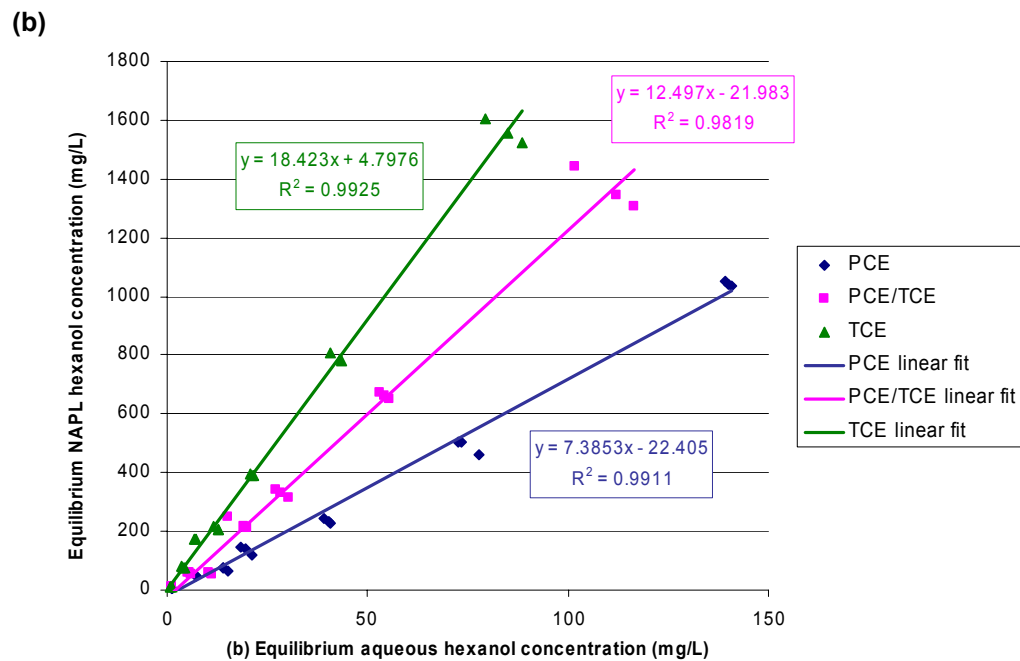
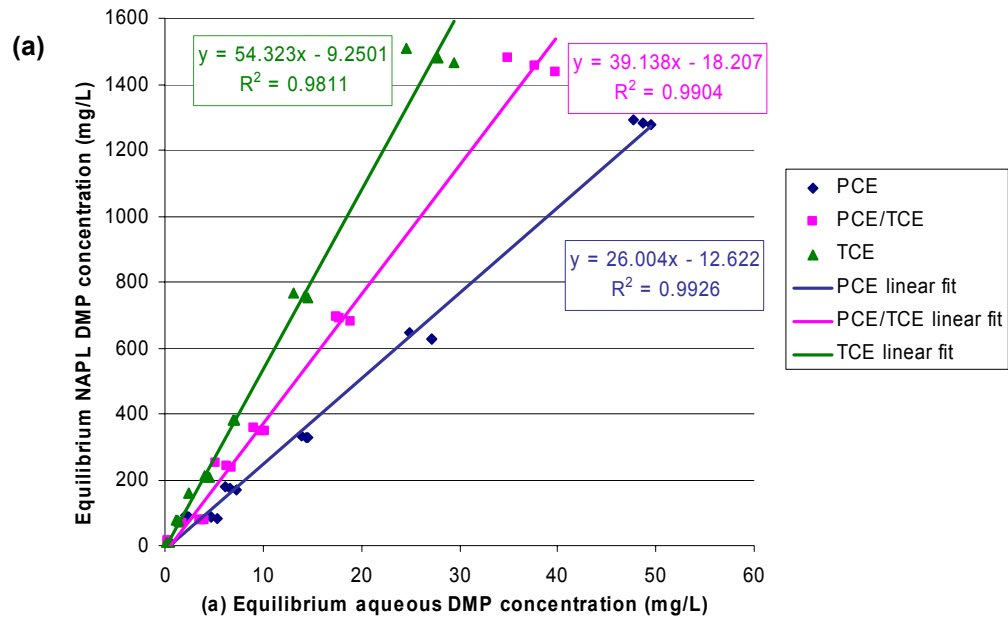


Figure 3.7. Baseline partitioning coefficient determination for (a)DMP and (b)Hexanol, Batch Partitioning Tracer Experiments with Biological Treatment

Table 3.13. Partitioning Coefficients for Baseline Systems with Water, Batch Partitioning Tracer Experiments with Biological Treatment

| DNAPL | DMP | | | Hexanol | | |
|---------|----------------|----------------|----------------|----------------|----------------|----------------|
| | K _p | R ² | Standard Error | K _p | R ² | Standard Error |
| PCE | 26.0 | 0.99 | 0.52 | 7.39 | 0.99 | 0.16 |
| PCE/TCE | 39.1 | 0.99 | 0.88 | 12.5 | 0.98 | 0.39 |
| TCE | 54.3 | 0.98 | 1.8 | 18.4 | 0.99 | 0.38 |

Table 3.14. Partitioning Coefficients for Baseline Systems with Abiotic Nutrient Medium, Batch Partitioning Tracer Experiments with Biological Treatment

| | DMP | | | Hexanol | | | 6M2Hep | | |
|---------|----------------|----------------|----------------|----------------|----------------|----------------|----------------|----------------|----------------|
| | K _p | R ² | Standard Error | K _p | R ² | Standard Error | K _p | R ² | Standard Error |
| PCE | 32.3 | 0.98 | 0.92 | 8.40 | 0.99 | 0.22 | 85.1 | 0.92 | 5.8 |
| PCE/TCE | 51.1 | 0.89 | 4.1 | 14.7 | 0.99 | 0.35 | 142 | 0.92 | 9.5 |
| TCE | 70.8 | 0.91 | 5.2 | 24.2 | 0.90 | 1.9 | 230 | 0.76 | 29 |

Partition coefficients for the water-treated systems are shown in Table 3.15. As expected, water treatment had no statistically significant effect on the partitioning coefficients. There was also no statistically significant trend in coefficients over time. Statistical analyses of these results are provided in the M.S. thesis of Kaplan (2004). Partition coefficients for the bio-treated systems are shown in Table 3.16. Headspace measurements showed no biodegradation. Statistical analysis showed no significant difference in K_p with time compared to the baseline measurement. Visually, all batches were either pink, indicating aerobic conditions or all sulfides had been consumed by the end of the experiments. Rubber stoppers used with DNAPL treatment bottles also were noticeably disintegrated by the presence of DNAPL.

Table 3.15. Partitioning Coefficients for Water-Treated Systems, Batch Partitioning Tracer Experiments with Biological Treatment

| DNAPL | Time (hrs) | Replicate | DMP | | Hexanol | | 6M2Hep | | |
|-------------|------------|----------------------------|----------------|----------------|----------------|----------------|----------------|----------------|--|
| | | | K _p | R ² | K _p | R ² | K _p | R ² | |
| PCE | 24 | 1 | 26.6 | 1.0 | 7.2 | 1.0 | | | |
| | 24 | 2 | 25.4 | 1.0 | 6.9 | 1.0 | | | |
| | 48 | 1 | 22.5 | 0.99 | 6.5 | 1.0 | | | |
| | 48 | 2 | 26.5 | 1.0 | 7.1 | 1.0 | | | |
| | 72 | 1 | 27.7 | 0.99 | 7.2 | 0.98 | | | |
| | 72 | 2 | 26.5 | 1.0 | 7.0 | 1.0 | | | |
| | 96 | 1 | 26.3 | 1.0 | 6.9 | 1.0 | | | |
| | 96 | 2 | 25.3 | 1.0 | 6.6 | 1.0 | | | |
| | | Average | | 25.8 | | 6.9 | | | |
| | | Standard Deviation control | | 0.75 | | 0.22 | | | |
| | | | 25.4 | 1.0 | 6.8 | 1.0 | | | |
| PCE/ TCE | 24 | 1 | 55.5 | 0.99 | 16.0 | 0.99 | 180 | 0.98 | |
| | 24 | 2 | 39.5 | 0.97 | 13.6 | 1.0 | 147 | 1.0 | |
| | 48 | 1 | 54.1 | 1.0 | 14.9 | 1.0 | 177 | 1.0 | |
| | 48 | 2 | 62.3 | 0.99 | 16.5 | 0.99 | 195 | 0.99 | |
| | 72 | 1 | 52.3 | 0.99 | 15.5 | 1.0 | 178 | 1.0 | |
| | 72 | 2 | 49.1 | 0.99 | 13.7 | 0.99 | 157 | 1.0 | |
| | 96 | 1 | 47.0 | 0.99 | 14.1 | 1.0 | 156 | 1.0 | |
| | 96 | 2 | 49.7 | 1.0 | 13.4 | 1.0 | 156 | 1.0 | |
| | | Average | | 52.2 | | 14.8 | | 169 | |
| | | Standard Deviation control | | 2.1 | | 0.47 | | 6.5 | |
| | | | 60.3 | 1.0 | 15.4 | 1.0 | 175 | 0.99 | |
| TCE | 24 | 1 | 72.2 | 0.99 | 21.3 | 1.0 | 240 | 0.99 | |
| | 24 | 2 | 77.2 | 0.99 | 20.5 | 1.0 | 248 | 0.99 | |
| | 48 | 1 | 67.6 | 0.97 | 20.5 | 0.99 | 237 | 0.98 | |
| | 48 | 2 | 70.6 | 0.98 | 21.0 | 0.99 | 242 | 0.99 | |
| | 72 | 1 | 76.5 | 0.97 | 21.7 | 1.0 | 254 | 0.98 | |
| | 72 | 2 | 68.3 | 0.97 | 20.1 | 0.99 | 233 | 0.99 | |
| | 96 | 1 | 58.8 | 1.0 | 18.6 | 1.0 | 209 | 1.0 | |
| | 96 | 2 | 68.1 | 0.99 | 19.7 | 1.0 | 234 | 0.99 | |
| | | Average | | 71.6 | | 20.8 | | 242 | |
| | | Standard Deviation control | | 4.4 | | 0.62 | | 11 | |
| | | | 85.6 | 0.98 | 23.4 | 1.0 | 283 | 0.99 | |

Table 3.16. Partitioning Coefficients for Bio-Treated Systems, Batch Partitioning Tracer Experiments with Biological Treatment

| DNAPL | Time | DMP | | Hexanol | | 6M2Hep | |
|-------------|--------------------|-------|-------|---------|-------|--------|-------|
| | | K_p | R^2 | K_p | R^2 | K_p | R^2 |
| PCE | 24 hrs | 31.2 | 1.0 | 8.27 | 0.99 | 90.3 | 0.99 |
| | 1 wk | 30.5 | 0.99 | 7.96 | 0.98 | 90.5 | 0.99 |
| | 30 d | 36.8 | 0.99 | 9.43 | 0.99 | 109 | 0.95 |
| | Average | 33.2 | | 8.61 | | 97.7 | |
| | Standard Deviation | 1.4 | | 0.41 | | 7.6 | |
| | control | 34.3 | 0.99 | 8.79 | 1.0 | 101 | 0.96 |
| PCE/ TCE | 24 hrs | 44.0 | 0.98 | 13.5 | 1.0 | 146 | 0.99 |
| | 1 wk | 46.0 | 1.0 | 13.9 | 1.0 | 159 | 0.99 |
| | 30 d | 48.5 | 1.0 | 12.0 | 0.99 | 134 | 0.93 |
| | Average | 48.5 | | 14.2 | | 153 | |
| | Standard Deviation | 2.2 | | 0.65 | | 22 | |
| | control | 55.3 | 1.0 | 17.4 | 1.0 | 170 | 0.90 |
| TCE | 24 hrs | 64.1 | 1.0 | 21.3 | 1.0 | 230 | 0.99 |
| | 1 wk | 71.2 | 1.0 | 23.4 | 0.99 | 259 | 0.99 |
| | 30 d | 80.4 | 0.99 | 17.4 | 0.95 | 145 | 0.91 |
| | Average | 72.5 | | 20.8 | | 206 | |
| | Standard Deviation | 3.4 | | 1.6 | | 30 | |
| | control | 74.5 | 0.99 | 21.1 | 0.99 | 190 | 0.77 |

3.3.2 Column tests

Surfactant Treatment. Two 15 cm long and 5 cm ID glass columns with Teflon -metal fittings and valves were used in these tests. The columns were packed with well-characterized #70 test sand and residually saturated with either pure TCE or a field DNAPL. Figure 3.8 shows column set up and Table 3.17 gives basic parameters and DNAPL saturations for both test columns. Partition tracer tests were performed for pre and post treatment with surfactant. A tracer solution containing Hexanol, DMP and 6M2Hep was injected at a flow rate of 1.2 ml/min for approximately one pore volume for each column and effluent samples were taken at 10 to 30 minutes intervals. The samples were analyzed with GC/FID for concentrations of tracers and TCE. Then both columns were flushed with about 300 ml of 5 percent Tween 80 and followed by water flushing until the effluent TCE concentration reached steady state. Again, the tracer solution was injected at the same flow rate and similar volumes as were used in pre-surfactant tracer tests. The samples were collected the same way and analyzed with GC/FID.



Figure 3.8. Columns for Partition Tracer Tests with Surfactant Treatment (pure TCE DNAPL, dyed at right and field DNAPL at left)

Table 3.17. Characteristics of Partitioning Tracer Tests in Columns with Surfactant Treatment

| Sand (#70) | Volume of DNAPL (mL) | Pore Volume (mL) | DNAPL Saturation |
|--------------------|----------------------|------------------|------------------|
| TCE Column | 16 | 130 | 0.123 |
| Field DNAPL Column | 16 | 125 | 0.128 |

Tracer breakthrough curves for Hexanol and DMP with both columns are shown in Figure 3.9 prior to surfactant flushing and Figure 3.10 after surfactant flushing. The breakthrough curves for 6M2Hep are not presented due to extremely high partitioning with TCE.

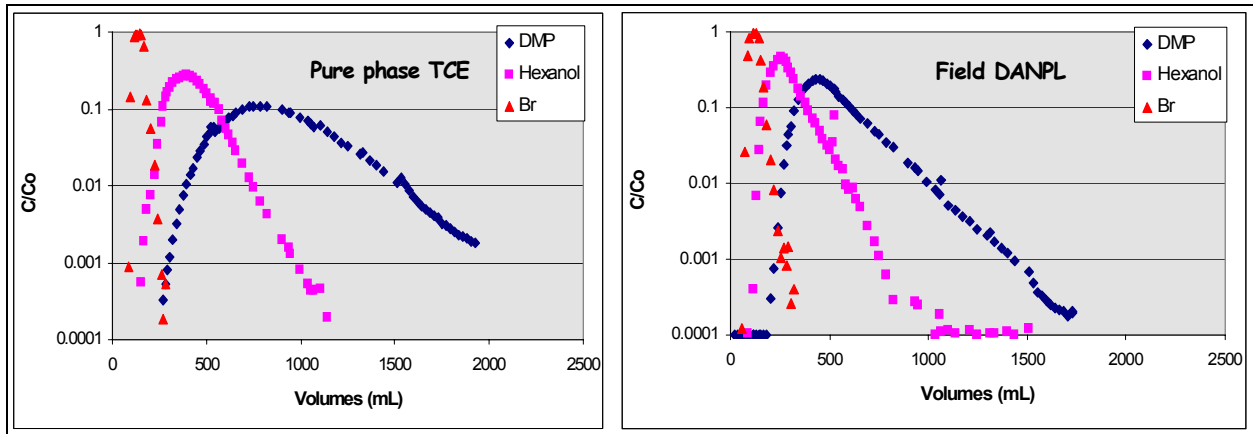


Figure 3.9. Breakthrough Curves for Partitioning Tracer Test in Columns Before Surfactant Treatment

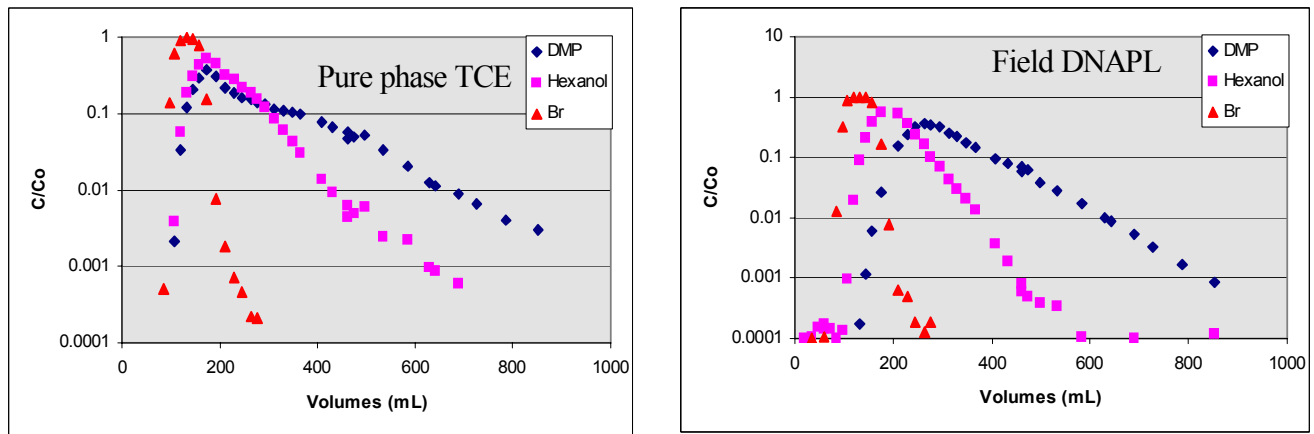


Figure 3.10. Breakthrough Curves for Partitioning Tracer Test in Columns After Surfactant Treatment

Partitioning tracer tests conducted before surfactant treatment were able to detect 85 percent of the TCE and 87 percent of the field DNAPL entrapped in the columns. Hexanol, with a relatively lower partition coefficient, gave better estimates than other tracers because Hexanol breakthrough was essentially complete for both column tests within the test period while breakthrough of DMP was not complete. Surfactant flushing removed 11.7 mL of TCE from the column with pure TCE DNAPL and 3.44 mL of TCE from the column with the field DNAPL. Total DNAPL removal from the column with the field DNAPL was 8.6 mL. Partitioning tracer tests conducted after surfactant treatment estimated that 4.4 mL (Hexanol) to 2.96 mL (DMP) of TCE still remained in the column with pure TCE DNAPL. This was 70 to 102 percent of the actual volume estimated based on mass balance. However, for the column with the field DNAPL, partition tracer tests estimated that less than 2.1 ml (Hexanol) to 5.1 ml (DMP) of field DNAPL remain following surfactant treatment. This was 28 to 69 percent of the actual volume estimated based on mass balance. The tracer-test estimates of DNAPL volume depletion are based on an assumption that partitioning coefficients did not change after surfactant treatment. If corrected partition coefficients measured after surfactant treatment in the batch test were used,

the tracer-estimated field DNAPL volumes were about 70 to 108% of remaining volumes based on mass balance. This indicates that changes in tracer partition coefficients after surfactant remediation was significant for the field DNAPL. Table 3.18 summarizes residual DNAPL volumes estimated by partition tracer tests for pre and post surfactant flushing.

Table 3.18. Comparison of Entrapped DNAPL Volumes, Partitioning Tracer Tests in Columns Before and After Surfactant Treatment (values in parentheses estimated using partition coefficients from batch testing after surfactant treatment)

| DNAPL | Initial DNAPL Volume (mL) | Partitioning Tracer Test Before Treatment | | | | Partitioning Tracer Test After Treatment | | | | Final DNAPL Volume (mL) |
|-------------|---------------------------|---|-------------------|-------------|-------------------|--|-------------------|----------------|-------------------|-------------------------|
| | | Hexanol | | DMP | | Hexanol | | DMP | | |
| | | Volume (mL) | Percent of Actual | Volume (mL) | Percent of Actual | Volume (mL) | Percent of Actual | Volume (mL) | Percent of Actual | |
| Dyed TCE | 16 | 13.6 | 84.9 | 11.8 | 73.4 | 4.44 | 103 | 2.96 | 69 | 4.3 |
| Field DNAPL | 16 | 13.9 | 86.7 | 12.6 | 79.0 | 2.07 (5.10) | 28 (69) | 5.11 (8.05) | 69 (109) | 7.4 |

Biological Treatment. A series of partitioning tracer tests were conducted in columns. Detailed descriptions of packing, column setup and testing methodology are provided in the M.S. thesis of Kaplan (2004). A summary of column and tracer test characteristics is provided in Table 3.19. Column tests 1 and 2 were run as trials and used to adjust the column set-up, operation, and sampling protocols. Effluent from both columns indicated that oxygen leakage occurred and no degradation daughter products were observed. Redox conditions for subsequent column tests were sufficiently reduced to promote dechlorination. Column 3 was run with residual PCE throughout the entire column, while Columns 4 and 5 were run with residual PCE in the bottom quarter of the column only.

Table 3.19. Characteristics of Partitioning Tracer Tests in Columns with Biological Treatment

| Column | Type of Test | NAPL Configuration | Flow Rate (mL/min) | Gravimetric Porosity (-) |
|--------|--------------|--------------------|--------------------|--------------------------|
| 1 | abiotic | throughout | 0.02 | 0.473 |
| 2 | biotic | throughout | 0.02 | 0.500 |
| 3a | abiotic | throughout | 0.264 | 0.471 |
| 3b | abiotic | throughout | 0.016 | 0.471 |
| 3c | biotic | throughout | 0.016 | 0.471 |
| 4a | abiotic | lower quarter | 0.264 | 0.505 |
| 4b | abiotic | lower quarter | 0.017 | 0.505 |
| 4c | biotic | lower quarter | 0.017 | 0.505 |
| 5a | abiotic | lower quarter | 0.023 | 0.451 |
| 5b | biotic | lower quarter | 0.023 | 0.451 |

Glass chromatography columns (1 in x 12 in.) were packed within an anaerobic chamber with #30 sand. Prior to packing the sand was mixed in the anaerobic chamber with a sodium sulfide solution until redox conditions were sufficiently reduced for dechlorination to occur. For each test, the column was sealed, removed from the chamber and attached to a gas-tight syringe pump and tubing containing anaerobic water and/or medium. Valves and tubing were used to allow the removal of the inflow syringe reservoirs for refilling with anaerobic fluids without compromising the redox status of the column. After conducting abiotic tests with a column, the column was inoculated with KB-1. Inoculation consisted of pumping one pore volume of nutrient medium through the column, followed by two pore volumes of KB-1 inoculum. Following inoculation, mass transfer tests were conducted and additional biotic tests were conducted.

Differences in volume of DNAPL estimated by partitioning tracer tests before and after inoculation provide an estimate of DNAPL mass removed during the mass transfer experiments. This estimate can be compared with results of effluent sampling for aqueous phase PCE, and associated degradation daughter products to provide an evaluation of the partitioning tracer test method.

Partitioning tracer tests were conducted using an anaerobic solution containing 200 μ L of each partitioning tracer and 20 mg of KBr per 100 mL de-ionized water. Approximately 1/2 pore volume of tracer solution was used in each tracer test. Following tracer injection, 15 pore volumes of de-ionized water was pumped through the column. Column effluent samples were taken every 0.25 pore volumes by an air-tight glass syringe and analyzed for the partitioning tracers and bromide. After conducting tracer tests in Columns 3 and 4, it was apparent that NAPL volume was being underestimated. This was attributed to high pore velocity (\sim 35 m/d). At faster velocities, the tracers probably did not have equilibrate or interact fully with entrapped NAPL in the column and therefore NAPL volume was underestimated. Subsequent tracer tests were run at a lower velocity more representative of literature values used in PITT (1.5 m/d) (Jin et al. 1995).

Tracer data were analyzed using the method of moments (Jin et al., 1995) in order to estimate NAPL saturation, mass, and column porosity (Table 3.20). Partitioning tracer tests gave results that were the same order of magnitude as volumetric estimates but differed by as much as 48 percent. In most cases the test estimate was lower than the volumetric estimate. Although most tests provided lower estimates of NAPL mass following inoculation and a period of biologically-treated mass transfer, mass removal estimated by column effluent data was orders of magnitude lower than that estimated by the partitioning tracer data. Mass removal estimated from several partitioning tracer tests was significantly higher than that estimated from effluent data. Furthermore, several tests provided estimates of NAPL mass that were higher after inoculation. Once significant figures were taken into account, several tests also detected no change in NAPL volume or mass.

Table 3.20. Results of Partitioning Tracer Tests in Columns with Biological Treatment

| Column Test | Effective Porosity | Disper-sivity (cm) | DNAPL Volume Before Biological Treatment | | DNAPL Volume Removed by Biological Treatment (mL) | DNAPL Volume After Biological Treatment | |
|-------------|--------------------|--------------------|--|------------------|---|---|------------------|
| | | | Actual (mL) | Tracer Test (mL) | | Calculated** (mL) | Tracer Test (mL) |
| 1 | ND | ND | ND | 6.0 | 0.040 | 6.0 | 8.5 |
| 2 | 0.530 | 0.34 | ND | 5.8 | 0.19 | 5.7 | 9.7 |
| 3a | 0.478 | 0.30 | ND | 8.2 | 0.070 | 8.1 | 6.3 |
| 3b | | | | 6.3 | 0.020 | 6.3 | 6.7 |
| 3c | | | | 6.7 | 0.030 | 6.7 | 5.2 |
| 4a | 0.431 | ND | 7.10 | 3.4 | 0.080 | 3.3 | 2.2 |
| 4b | | | | 2.2 | 0.12 | 2.0 | 1.7 |
| 4c | | | | 1.7 | 0.020 | 1.7 | 1.5 |
| 5a | ND | ND | 5.91 | 5.8 | 0.020 | 5.7 | 4.8 |
| 5b | | | | 4.8 | 0.030 | 4.8 | 5.3 |

ND Not determined

** Calculated as (tracer test estimate before mass transfer) – (volume removed by biological treatment)

3.3.3 Large-tank experiments

This investigation filled a gap between the relatively simplistic homogeneous aquifer conditions evaluated in most bench-scale laboratory experiments of partitioning tracers and the complex heterogeneous conditions that occur in full-scale DNAPL contamination problems. Intermediate scale tanks packed with several sands with known properties were used to create

two artificial two-dimensional test aquifers. The design of each test aquifer was based on spatially correlated random fields of hydraulic conductivity with specified geostatistical parameters. Spatial distributions of hydraulic conductivity were discretized and well characterized sands of known hydraulic conductivity were assigned to each discrete hydraulic-conductivity interval. The resulting sand patterns were then used to pack the tanks. Because aquifer properties of the sands were known with a high degree of accuracy, and exact DNAPL architecture could be mapped *in situ* using a gamma-ray attenuation system, it was possible to evaluate tracer test performance quantitatively to a degree not possible in field settings.

The main objective of this study was to conduct two-dimensional experiments in large tanks that emulate real DNAPL spills and perform partitioning interwell tracer tests (PITT) to estimate DNAPL architecture. The resulting comprehensive data sets were then used to evaluate the performance of PITT for DNAPL architecture estimation. Analysis of PITT results was conducted within the context of specific modeling goals. These included:

1. Calibrating tracer-test results with a selected numerical model and performing sensitivity analysis of model parameters that may affect effectiveness of partitioning tracer test.
2. To evaluate the capability of the selected numerical model for simulation of tracer transport and partitioning behavior
3. To compare the performance of this numerical model to a traditional method of tracer test analysis called the method of moments (Jin et al., 1995), and
4. To evaluate effects of heterogeneity on the effectiveness of PITT for estimation of DNAPL architecture.

Experimental Methods. Experiments were conducted with a large-scale tank having dimensions of 4.88 m × 1.22 m × 0.05 m. was named as low heterogeneous (Experiment 2) with respect to the variance of the heterogeneity field which was selected to fill the tank. The tank was packed with six silica sand having high degrees of uniformity. In the first experiment, the tank was packed with #16, #30, #50, #70, and #110 sands to produce a test aquifer having a high degree of heterogeneity. In the second experiment, the tank was packed with #16, #30, #50, #70, and #140 sands to produce a test aquifer having a low degree of heterogeneity. Table 3.21 shows the statistical properties of hydraulic conductivity used to create the two test aquifers.

Table 3.21. Statistical Properties of Hydraulic Conductivity Used in Designing Large Tank Experiments of Heterogeneous Test Aquifers

| Statistical Property of Hydraulic Conductivity | High Heterogeneity | Low Heterogeneity |
|--|--------------------|-------------------|
| Mean, log transformed - $\mu_{\ln K}$ (m/day) | 4.18 | 4.18 |
| Variance - $\sigma_{\ln K}^2$ (m/day) | 1.22 | 0.25 |
| Horizontal correlation length (m) | 0.50 | 0.50 |
| Vertical correlation length (m) | 0.05 | 0.05 |

Prior to packing the tank, spatially correlated random fields were generated using the turning bands algorithm (Tompson et al., 1989) to produce continuous distributions of log-normally distributed hydraulic conductivity values ($\ln K_s$). Multiple random field realizations were generated for each set of design parameters and one realization was selected for packing each experiment. The chosen configurations included zones within the planned DNAPL source area that were likely to produce a complex entrapment morphology while minimizing the possibility of vertical DNAPL migration to the bottom of the tank. In this way, an adequate vertical distribution of DNAPL in the source zone for testing could be achieved while protecting the bottom of the tank from DNAPL that could deteriorate the seals and result in leaks. Each realization was discretized into five categories of sand spanning the range of hydraulic conductivity as mentioned earlier. Categories were associated with laboratory sands having known hydraulic properties.

The test aquifers consisted of a homogeneous section of #8 sand (60 cm long) at the upgradient end of the tank designated for tracer injection, a heterogeneous section designated for creation of the DNAPL source zone, and a downgradient heterogeneous section. Gravel-packed wells were located at each end of the tank and connected to external head reservoirs to control overall hydraulic gradient across the tanks. Additional details of design and packing procedures are provided in Appendix 1 for the high-heterogeneity aquifer and in Appendix 2 for the low-heterogeneity aquifer. This includes schematic sketches of the experimental setup, permeability fields and head monitoring locations (Figure A1.1 and A1.2 for high heterogeneity and Figure A2.1 for low heterogeneity).

Flow System Characterization and Partitioning Tracer Test Prior to Creation of DNAPL Sources. After packing the tanks, steady-state flow was established using constant-head reservoirs at inflow and outflow ports located at opposite ends of the tank. Hydraulic head data were obtained at numerous sampling ports located throughout the tank. Details of experimental procedures are provided in Appendix 1 and 2. Prior to creating the DNAPL sources, the planned source zones were scanned by the gamma-ray attenuation system to provide baseline data for subsequent scans after DNAPL injection.

Head distribution was monitored continuously throughout all tracer tests. A tracer test was conducted in the high-heterogeneity experiment prior to DNAPL source-zone creation. The objectives of this test were (1) to evaluate the uniformity of tracer injection through all the ports, (2) to evaluate if the partitioning tracers were subject to retardation due to sorption, (3) to improve the design of subsequent tracer tests conducted after creation of the DNAPL sources, and to obtain a data set for a conservative tracer that could be used for estimation of solute transport parameters.

The tracer test began by injecting a solution of 500 ppm NaBr, 300 ppm hexanol and 300 ppm DMP upgradient of the planned source zones using a multi-syringe pump. Injection was through 32 sampling ports equally spaced along a vertical plane in the homogeneous portion of the tank. The flow rate of the injected solution was 0.25 mL/min per injection port providing a total injection rate of 8 mL/min.

Source-Zone Creation. In each experiment, the PCE DNAPL source zones were created by injecting PCE slowly through multiple injection ports. PCE injection was performed under constant head conditions using a Marriott bottle. Multiple injection locations were used to ensure that PCE stayed within the planned source zone without migrating too far laterally. The

injection locations and volumes also were selected in order to provide source-zone architectures with pools as well as portions at residual saturation (Table 3.22).

Table 3.22. Volume of PCE Injected During Source Zone Creation, Large Tank Experiments of Heterogeneous Test Aquifers

| Injection Port | PCE Volume (mL) | |
|----------------|--------------------|-------------------|
| | High Heterogeneity | Low Heterogeneity |
| 1 | 272.0 | 61.0 |
| 2 | 71.9 | 103.1 |
| 3 | 41.4 | 60.0 |
| 4 | 93.3 | 60.0 |
| 5 | 93.2 | - |
| Total | 586.7 | 284.1 |

After the source zones were created, DNAPL distributions were determined using gamma-ray attenuation techniques. The visual distributions of PCE are compared with distributions obtained by gamma attenuation for the high-heterogeneity aquifer in Figure 3.11, and for the low-heterogeneity aquifer in Figure 3.12.

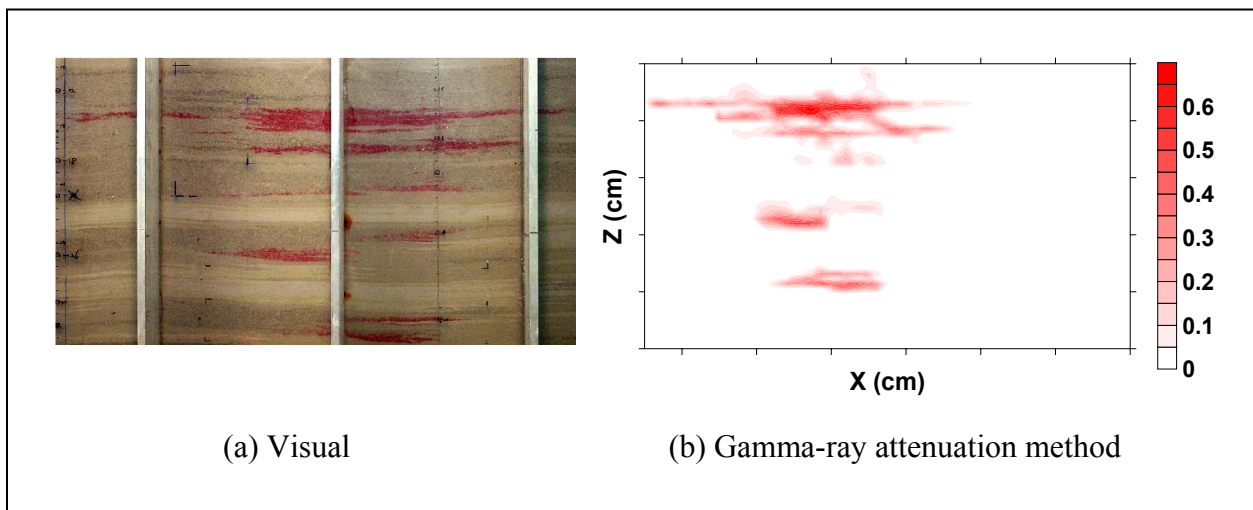


Figure 3.11. Source-Zone Architecture, Large Tank Experiment with High-Heterogeneity Aquifer

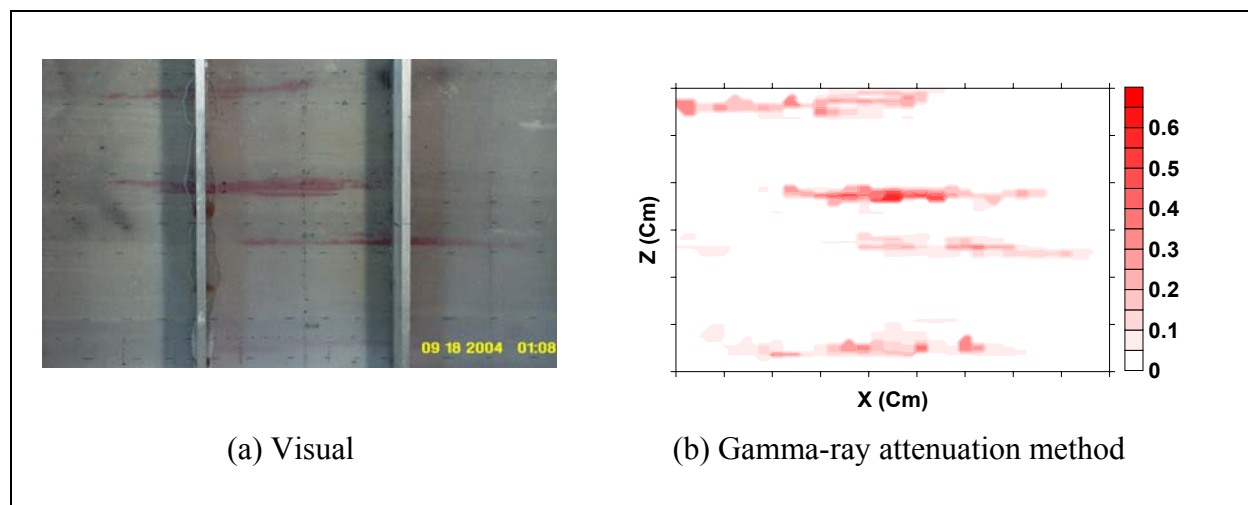


Figure 3.12. Source-Zone Architecture, Large Tank Experiment with Low-Heterogeneity Aquifer

Partitioning Tracer Tests during Natural Dissolution. In each experiment, partitioning tracer tests were created once source zones were created and steady-state flow conditions were reestablished. During the tests, flow was monitored at the tank outlet to verify steady state flow conditions throughout the experiment. Water samples also were obtained to characterize natural dissolution. However, in this section, results of partitioning tracer tests are emphasized. Results of natural dissolution monitoring are described in section 3.4 of this report. Conditions during tests were similar for the two experiments (Table 3.23). Sample collection and analysis procedures are provided in section 3.2 of this report.

Partitioning Tracer Tests after Surfactant Remediation. Surfactant flushing was used in both experiments to remove DNAPL from the source zones. After remediation, additional gamma scans were conducted and new DNAPL entrapment architectures were observed (Figures 3.13 and 3.14). A partitioning tracer test was then conducted with the same design parameters as the previous ones. Data from these tests were used to evaluate the partitioning tracer technique as a tool for assessing remediation performance.

Table 3.23. Summary of Partitioning Tracer Tests during Natural Dissolution, Large Tank Experiments of Heterogeneous Test Aquifers

| Test Condition | High Heterogeneity Experiment | Low Heterogeneity Experiment |
|--|--|--|
| Tracers | Bromide, DMP, HEX | Bromide, DMP, HEX |
| Duration of injection | 10.0 hrs | 11.5 hrs |
| Injection rate | 32 ports at 0.25 mL/min | 32 ports at 0.25 mL/min |
| Sampling ports | A7, A12, A15, A17, A21, A26, A31, B7, B12, B14, B17, B21, B26, B31, C7, C12, C17, C21, C26, C31, D7, D12, D17, D21, D28, E7, E12, E17, E21, E28, F7, F12, F17, F21 | A11, A13, A15, A17, A19, A21, A23, A25, A27, A29, A31, A33, A35, A37, C11, C13, C15, C17, C19, C21, C23, C25, C27, C29, C31, C33, C35, C37 |
| Initial tracer concentration (mg/L) | Br = 977.5, DMP= 715.2, HEX= 1318.7 | Br = 605.2, DMP= 905.4, HEX= 770.1 |
| Duration and interval of tracer concentration measurements | 2hr intervals for first 40hrs and 4 hr intervals from 40hrs to 4days. | 2hr interval for first 40hrs and 4 hr interval from 40hrs to 80 hrs |

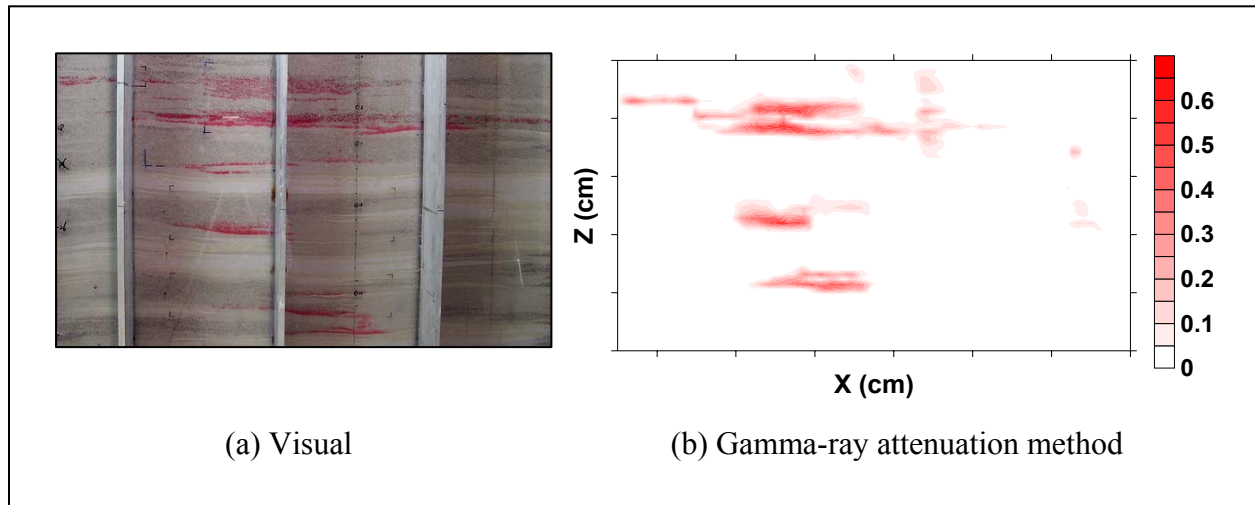


Figure 3.13. Source-Zone Architecture after Surfactant Flushing, Large Tank Experiment with High-Heterogeneity Aquifer

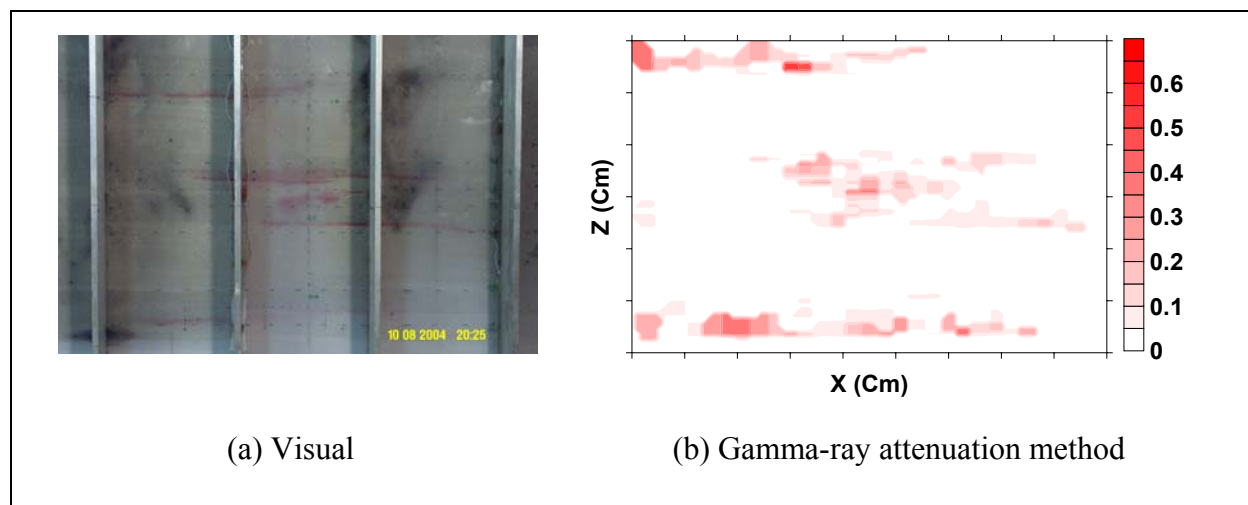


Figure 3.14. Source-Zone Architecture after Surfactant Flushing, Large Tank Experiment with Low-Heterogeneity Aquifer

Observed Tracer Behavior before Creation of DNAPL Source. In a flow system where no DNAPL is present, breakthrough curves for ideal non-partitioning and partitioning tracers should be identical. However, for the tracer test conducted in the high-heterogeneity aquifer prior to source-zone creation, some discrepancies were noted between the non-partitioning bromide tracer and partitioning tracers. To evaluate if the difference in concentration values between the different tracers affected travel time, the first centralized moments of the breakthrough curves were calculated. Breakthrough data for this test are provided in Appendix 1. As it is shown in Figure 3.15 the travel time to selected sampling ports in sampling array A were very similar for all tracers. Differences in travel time between sample ports were expected and can be attributed to effects of aquifer heterogeneity. The similarity of travel times among the tracers suggests that tracers were not affected by adsorption to any measurable extent. Results of this test also suggested that a similar tracer test design would prove sufficient to meet project objectives. The tracer data set also was suitable for estimation of transport parameters for numerical models.

Observed Tracer Behavior after Source Creation. Tracer breakthrough data are provided in Appendix 1 for the high-heterogeneity aquifer and Appendix 2 for the low-heterogeneity aquifer. Breakthrough curves were able to detect the presence of high saturation zones of PCE in both experiments. Tailing was particularly evident for the high-heterogeneity aquifer at sample ports A16 and A17 and for the low-heterogeneity aquifer at A13, A25 and A35. The vertical distribution of breakthrough curves along sampling array A for the two aquifers indicated that DNAPL was not distributed uniformly since a uniform distribution would produce uniform offsets (Brooks et al., 2002; Jawitz et al., 1998).

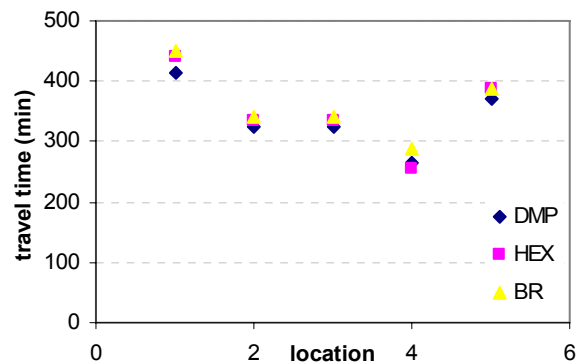


Figure 3.15. Travel Times to Selected Sample Locations in Sampling Array A, Partitioning Tracer Test Prior to Source Creation, Large Tank Experiment with High-Heterogeneity Aquifer

Breakthrough data for the two experiments were analyzed by the method of moments and compared to actual PCE saturation measured by gamma-ray attenuation methods (Figures 3.16 and 3.17). At locations where the breakthrough curve was not complete, the tail of the curve was extrapolated using an exponential decay function (Pope et al., 1994; Annable et al., 1998). In both test aquifers, retardation values estimated by the method of moments decreased with increasing distance from the source. For the high-heterogeneity aquifer, data obtained from sampling arrays A, B and C contained information about the vertical DNAPL architecture. However, data obtained at arrays D, E and F also reflected affects of mixing and dispersion associated with heterogeneous flow patterns. Therefore, data from these sampling arrays did not contain enough information about the DNAPL vertical distribution. For the low-heterogeneity aquifer, tracer concentration was observed only at arrays A and C. These figures show that the method of moments generally provided a poor match to the actual DNAPL saturation, and did not consistently over or underestimate the actual vertical profile.

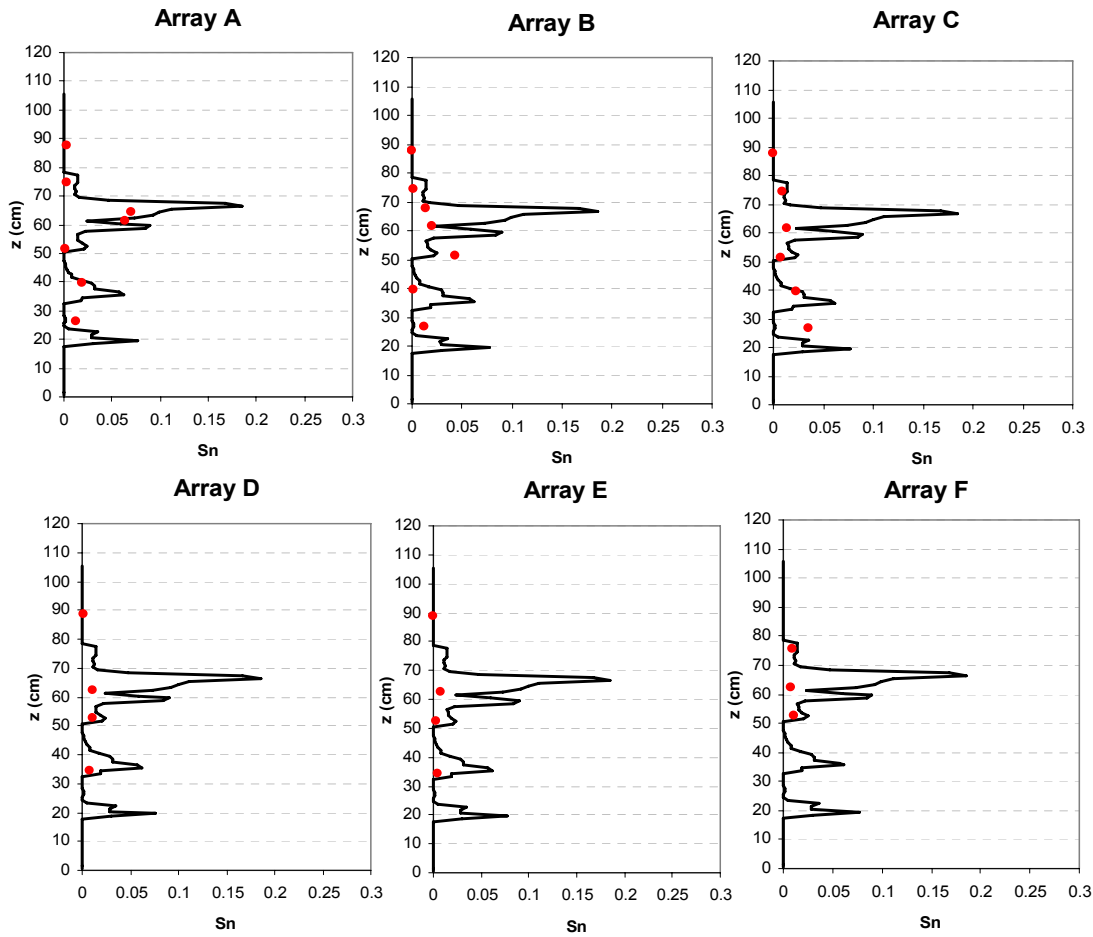


Figure 3.16. Actual PCE DNAPL Saturation (line) and Saturation Calculating from Tracer Data Using the Method of Moments (dots), Large Tank Experiment with High-Heterogeneity Aquifer

Figure 3.18 shows the average saturation values estimated by the method of moments for the high-heterogeneity experiment as a function of distance from the source. Error bars represent the estimated variability of saturation along a vertical profile. Average saturation estimated from data at sampling array A, located closest to the source zone, had more variability than was estimated at more distant since the Array A ports collected strong signals with information about the vertical architecture of source zone. As the distance from the source zone increases, the signal attenuated and the information about vertical architecture dissipated. Based on the results presented in Figure 3.18, water sampling locations for tracer tests in the subsequent low-heterogeneity experiment were limited to Arrays A and C located near the source zone.

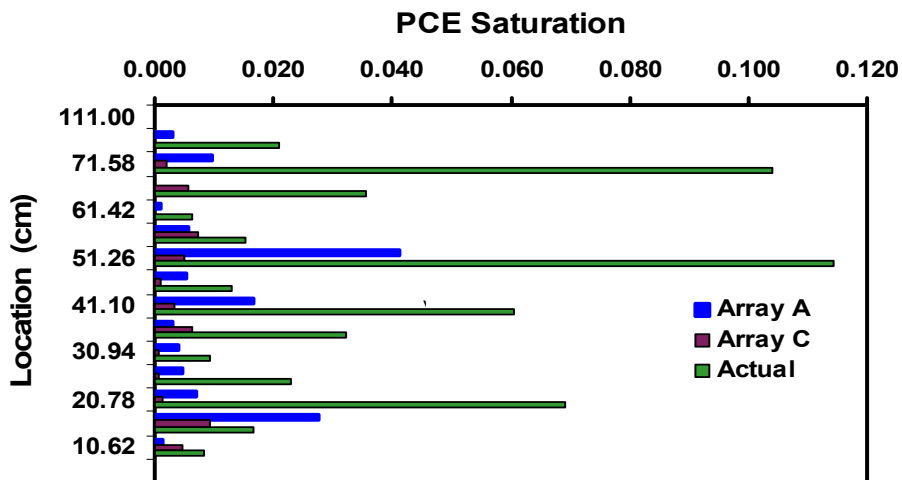


Figure 3.17. Comparison of Actual DNAPL Saturation with Saturation Calculating from Tracer Data Using the Method of Moments, Large Tank Experiment with Low-Heterogeneity Aquifer

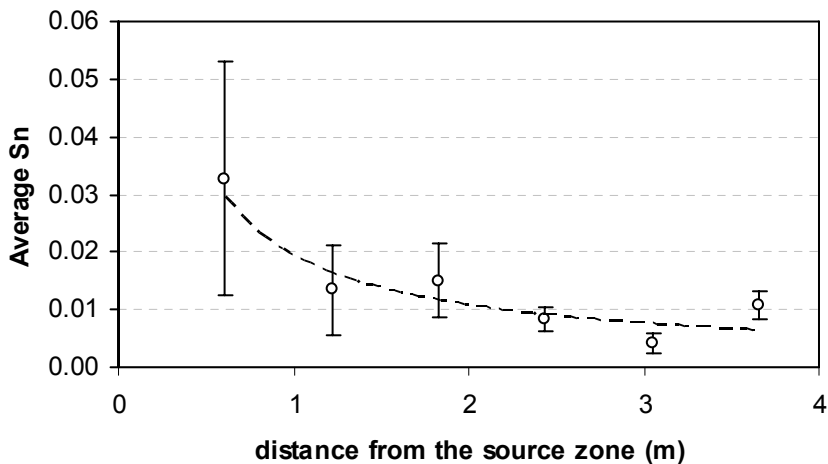


Figure 3.18. Average DNAPL Saturation Estimated by the Method of Moments from Tracer Data Collected at Various Distances from the Source Zone, Large Tank Experiment with High-Heterogeneity Aquifer

In both high- and low-heterogeneity experiments, average DNAPL saturation within the source zones was underestimated by tracer breakthrough data and the method of moments. Underestimation probably reflected limited hydrodynamic accessibility of some DNAPL within the source zone. This may have been caused by rate-limited tracer partitioning or irregular flow paths associated with aquifer heterogeneity. These possible causes were investigated during numerical modeling of the tracer tests, described in chapter 4 of this report. Errors in estimating

retardation factors due to incomplete breakthrough curves and/or insufficiently low detection limits for analytical instruments also may have contributed to the underestimates.

Observed Tracer Behavior after Surfactant Flushing. Breakthrough curves for the tracer test conducted in the high-heterogeneity aquifer after surfactant flushing shows little difference between partitioning and non-partitioning tracers. This may reflect water flowing predominantly around rather than through portions of the source zone with DNAPL. If bypassing of high-saturation pools occurred and portions of the source zone with residual saturation were minimal, tracer partitioning would be limited and retardation would not occur. Breakthrough curves for the tracer test conducted in the low-heterogeneity aquifer showed some tailing effects at some locations. Effects of flow bypassing pools appeared to be less important for low-heterogeneity conditions.

Figures 3.19 and 3.20 compare DNAPL saturation measured by gamma-ray attenuation with saturation estimated by the method of moments. The method of moments generally provided poor estimates of the actual vertical saturation profile. Saturation measured by gamma-ray attenuation showed decreases in saturation at some locations after surfactant flushing. As expected locations of pools also appeared to be different than observed prior to surfactant remediation.

Results of the tracer tests analyzed by the method of moments provided poor estimates of remediation effectiveness. For the high-heterogeneity experiment, the percentage of DNAPL removed during surfactant flushing estimated by tracer data and the method of moments varied from 47 to 79 percent depending on the sample location used in the analysis (Table 3.16). Actual decrease in DNAPL mass was 39 percent. For the low-heterogeneity experiment, DNAPL mass removal was estimated by the method of moments to be 22 to 34 percent of the original mass. Actual reduction of DNAPL mass was 5 percent.

Overestimation of remediation effectiveness probably reflected limited hydrodynamic accessibility of some DNAPL within the source zone. This may have been caused by rate-limited tracer partitioning or irregular flow paths associated with aquifer heterogeneity. DNAPL mass within high saturation pools would be particularly insensitive to detection by partitioning tracer data analyzed by the method of moments. These possible causes were investigated during numerical modeling of the tracer tests, described in chapter 4 of this report. Errors in estimating retardation factors due to incomplete breakthrough curves and/or insufficiently low detection limits for analytical instruments also may have contributed to the overestimation of remediation effectiveness.

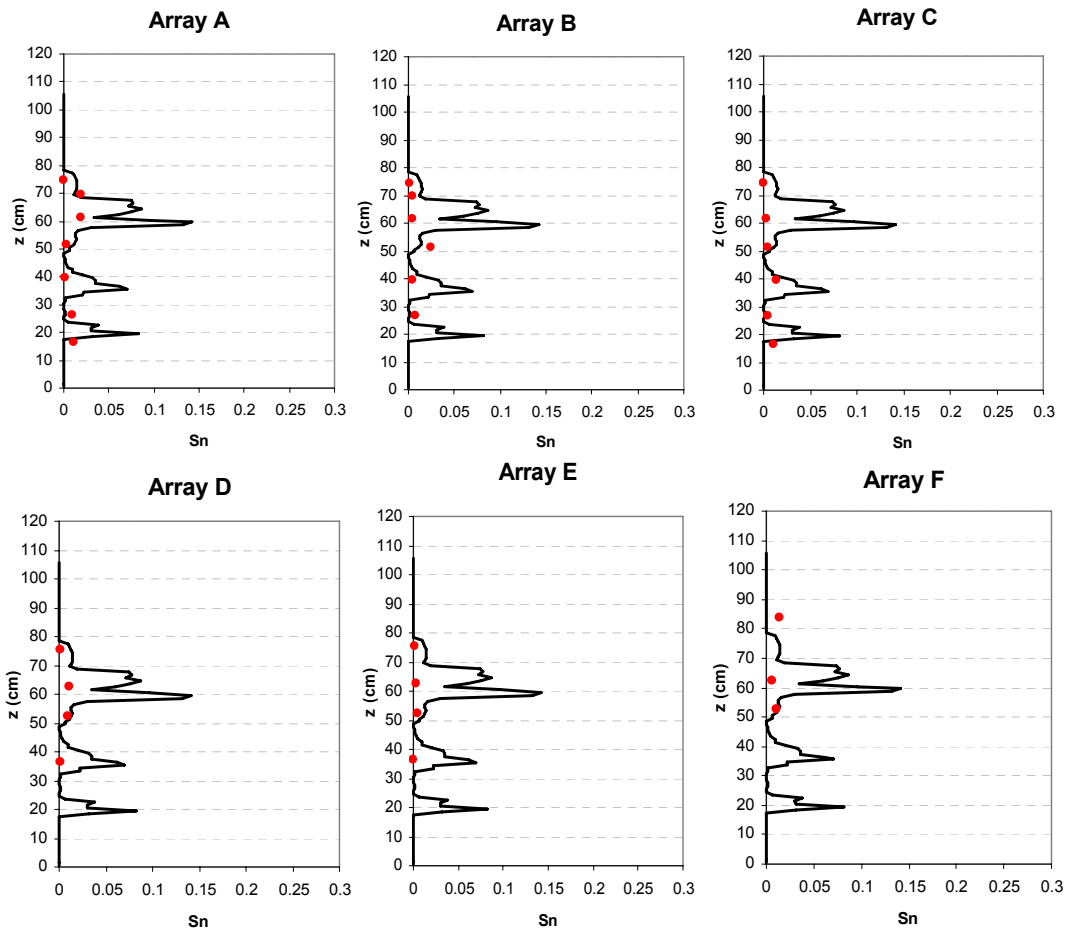


Figure 3.19. Actual PCE DNAPL Saturation (line) and Saturation Calculating from Tracer Data Using the Method of Moments (dots), Large Tank Experiment with High-Heterogeneity Aquifer after Surfactant Flushing

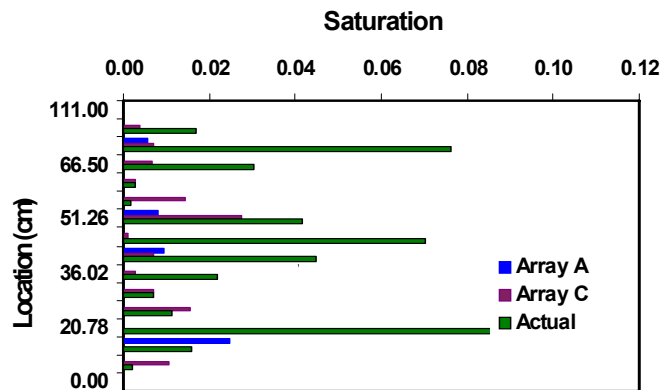


Figure 3.20. Comparison of Actual DNAPL Saturation with Saturation Calculating from Tracer Data Using the Method of Moments, Large Tank Experiment with Low-Heterogeneity Aquifer after Surfactant Flushing

3.4 Experimental design and methods for investigation of natural dissolution

Dissolution experiments were conducted at three scales: one-dimensional columns, bench-scale two-dimensional flow cells, and large two-dimensional tanks. Initial experiments were designed to investigate and compare mass transfer characteristics of pure and multi-component field DNAPL. Due to the complex multi-component nature of field DNAPL, mass transfer study of the field DNAPL focused on TCE dissolution. Subsequent dissolution experiments in 1-D column and 2-D test cells and tanks considered dissolution of pure PCE. Data generated from these experiments were used to calibrate and validate mass transfer models and to validate an upscaling method for simulating natural dissolution of entrapped NAPL at larger scales.

3.4.1 Column experiments with pure or field DNAPLs

Column experiments were conducted to evaluate and compare mass transfer characteristics of a pure phase DNAPL and a DNAPL obtained at a field site that consisted of a mixture of components. Trichloroethene was a major component of the field DNAPL and therefore was used to characterize dissolution.

Two 15.0-cm long and 5.0-cm ID glass columns with Teflon-metal fittings and valves were used in these tests. The columns were packed with #70 test sand and residually saturated with either pure TCE or the field DNAPL. Figure 3.8 shows column set up and Table 3.17 gives basic characteristics and DNAPL saturations for both test columns. A natural dissolution experiment was conducted at a flow rate of 0.6 cm³/min. The breakthrough curves resulting from natural dissolution were analyzed to obtain average mass transfer coefficients.

Transient dissolution data for TCE were used to estimate average mass transfer coefficients (\bar{k}_{La}) for each experiment based on the following equation:

$$\frac{\partial c}{\partial t} = D_x \frac{\partial^2 c}{\partial x^2} - \bar{v}_x \frac{\partial c}{\partial x} - \bar{k}_{La} (c - c_s) \quad (3.4)$$

A Fortran-90 program was written to solve Equation 3.4 using a fully implicit finite difference scheme. The inverse modeling algorithm UCODE was coupled with the transport model to estimate the average mass transfer coefficient. Figure 3.21 shows the experimental data and model fit for both columns. Average mass transfer coefficients were 14.21 d⁻¹ for the column with pure TCE DNAPL and 22.83 d⁻¹ for the column with field DNAPL.

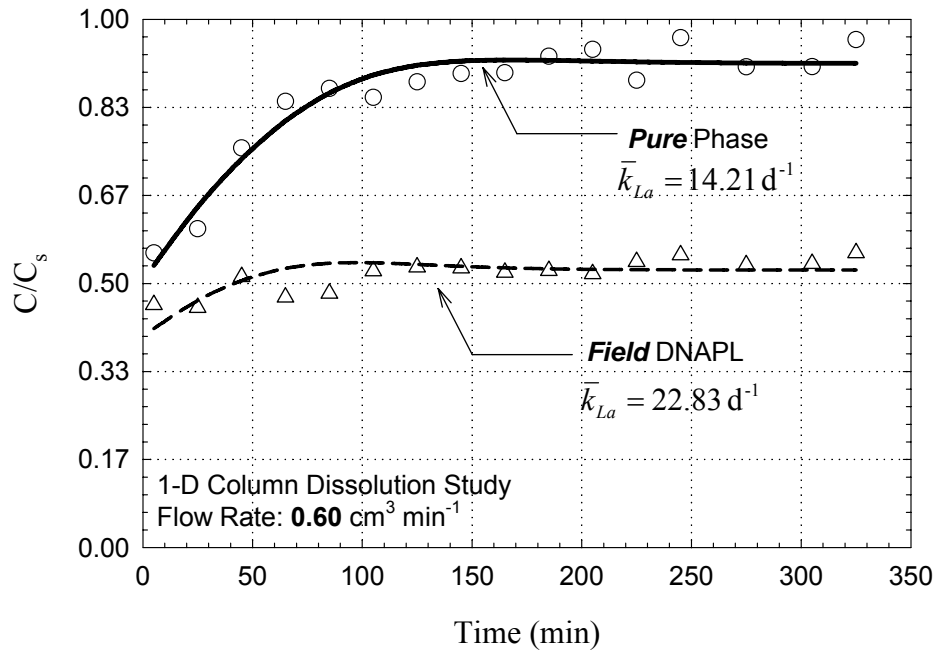


Figure 3.21. Comparison of experimental and model-fitted breakthrough concentration of TCE columns with pure and field DNAPL

Column experiments also were conducted with PCE as a pure phase DNAPL. Separate experiments were conducted using three different sands (#16, #30 and #70) as packing material. Protocols for these experiments were the same as used in previous column experiments. Results of these tests are presented in chapter 4 of this report.

3.4.2 Two-dimensional flow-cell experiments with pure TCE or field DNAPLs

Experiments were conducted in a two-dimensional flow cell to estimate and compare mass transfer coefficients for TCE from pure and a field DNAPL with a large fraction of TCE. The resulting estimates of mass transfer coefficients also were compared with estimates obtained from column tests. The flow cell consisted of a front glass wall to allow visualization and a back aluminum plate to allow sampling at different locations of the domain (Figure 3.22). The cell had an internal volume of $9.0 \times 6.56 \times 1.0 \text{ in}^3$. Test cell was wet-packed using #70 sand. A zone of coarse-grained sand (#16) was imbedded within the #70 sand to promote DNAPL entrapment. The coarse entrapment zone, was 7.5-cm long and 3.0-cm tall. This porous media configuration represents a contaminant zone entrapped in a two dimensional confined flow domain.

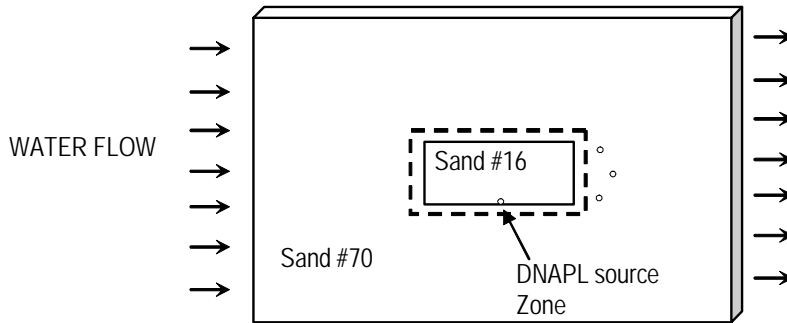


Figure 3.22. Schematic of Flow Cell Experiments to Compare Pure and Field DNAPL

Separate flow-cell experiments were conducted with known volumes of TCE or field DNAPL. In each experiment, DNAPL was injected slowly through a port near the base of coarse sand to create a source zone. Due to the capillary barrier effect of the fine sand, the DNAPL was fully contained within this area (Figure 3.23). The DNAPL volume entrapped in the source were 6.5 cm^3 for dyed TCE, and 8 cm^3 for field DNAPL, respectively. After allowing time for DNAPL to redistribute and achieve static conditions, natural TCE dissolution and partitioning tracer tests were conducted. An HPLC (Acuflow Series II) pump was used to provide constant water flow of $3.6 \text{ cm}^3/\text{min}$ through the tank. Throughout the tests, effluent samples were taken at 10- to 30-min intervals. TCE concentration of the samples was analyzed using HP GC/FID.

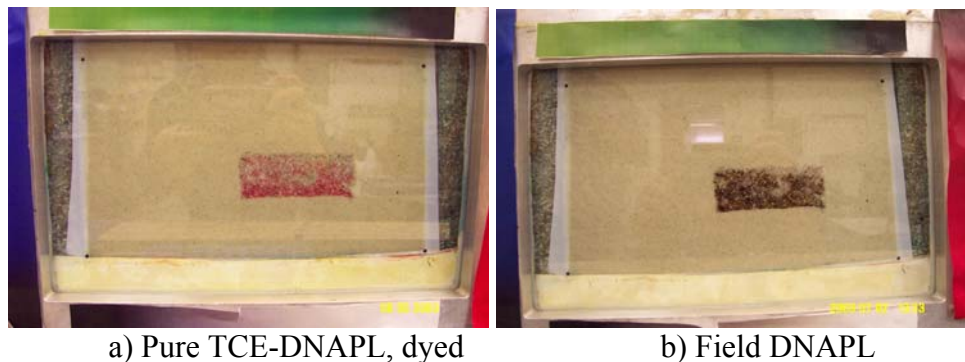


Figure 3.23. DNAPL Source Entrapments for Flow Cell Experiments Comparing Pure and Field DNAPL

Breakthrough curves from the tracers (Figure 3.24) were used to estimate entrapped DNAPL volumes in the cells. The tracer method significantly underestimated DNAPL volumes in the cells due to formation of a DNAPL pool in the source zone and a high water flow rate in the transition zone of the pool (strong non-equilibrium).

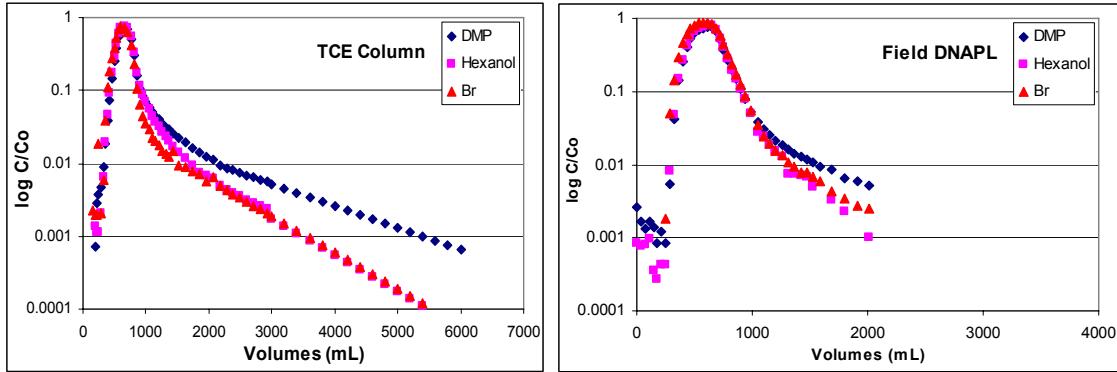


Figure 3.24. Partition Tracer Breakthrough Curves from Small Cell Tracer Tests with TCE Source (left) and Field DNAPL Source (right)

Breakthrough curves for TCE natural dissolution (Figure 3.25) were used to estimate average mass transfer coefficients \bar{k}_{La} (i.e. average over the entire DNAPL source block) in two-dimensional flow fields. Estimates were obtained using the solute transport model and inverse modeling algorithms described in Section 3.10. Figure 3.26 shows experimental data and model fit for both DNAPLs (pure and field). Generally concentrations associated with the experiment using pure-phase DNAPL were higher than those associated with the experiment using the field DNAPL mixture. This is due to the fact that, according to Raoult's Law, aqueous solubility of a component in a mixture is smaller than pure phase solubility. However, the average mass transfer coefficient (\bar{k}_{La}) obtained with pure phase TCE (3.17 d^{-1}) was slightly smaller than \bar{k}_{La} obtained with field DNAPL (4.09 d^{-1}). This finding supports a hypothesis that mass transfer correlations developed from pure phase dissolution study can be used to simulate field DNAPL dissolution.

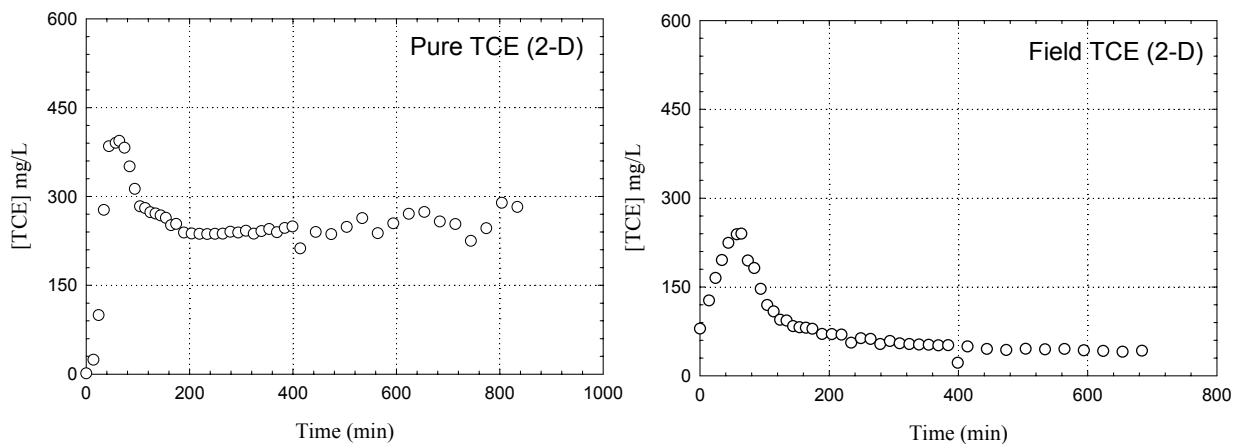


Figure 3.25. Breakthrough Curves of TCE from Natural Dissolution Tests in a Two-Dimensional Flow Cell with a Pure TCE Source (Left) and a Field DNAPL Source (Right)

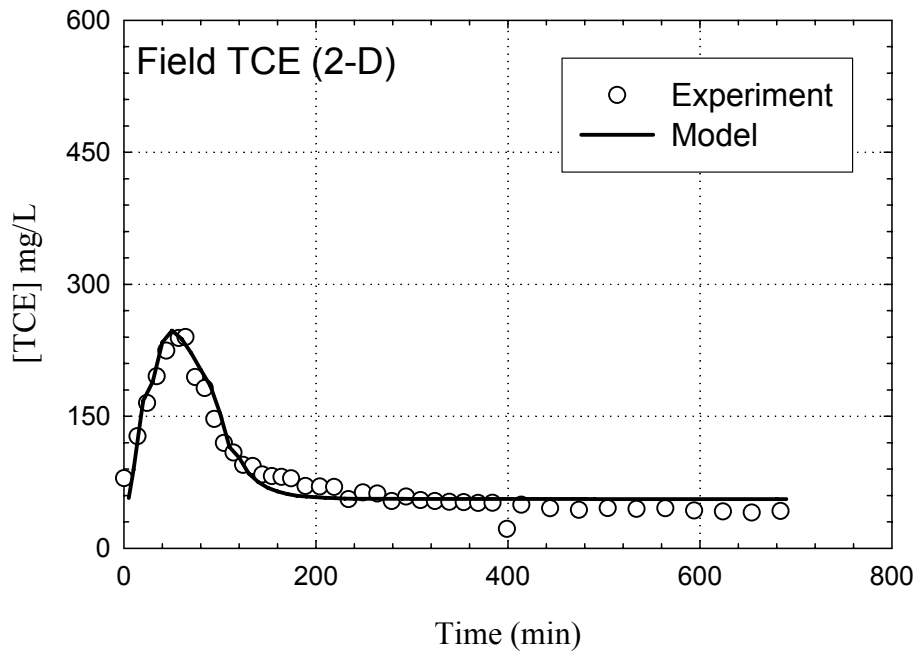
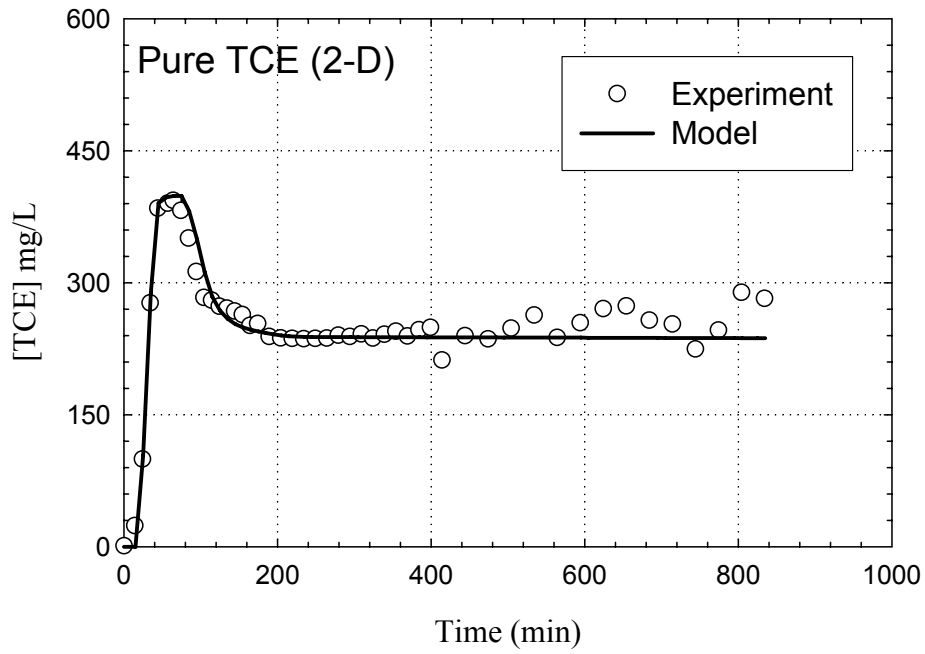


Figure 3.26. Model fit for TCE Natural Dissolution Tests in a Two-Dimensional Flow Cell with a Pure TCE Source (Top) and a Field DNAPL Source (Bottom)

3.4.3 Two-dimensional horizontal flow-cell experiments with pure PCE

The goal of experiments conducted in a 2-D bench-scale test cell was to evaluate the effect of dimensionality on mass transfer coefficients. This was accomplished by comparing coefficient estimates for the flow cell experiments with those estimated from one dimensional column experiments. Separate experiments were conducted for packing arrangements with one and two source zones.

The bench-scale, two-dimension test cell consisted of clear Plexiglas walls for top and bottom plates, and aluminum metal pieces for sides. Internal volume of the tank was nominally 0.65-m \times 0.45-m \times 0.05-m. The flow cell was packed with a simple heterogeneous system consisted of a coarse sand lens surrounded by a finer medium. Coarse and fine sands were #16 and #70 (Unimin Corporation), respectively, and their properties are listed in Table 3.24. These sand properties were determined previously in our research group using sieve analysis and flow-pump to determine hydraulic conductivity and residual water saturation.

Table 3.24. Properties of Sands Used in Two-Dimensional Horizontal Flow-Cell Experiments with Pure PCE

| Property | #16 | #30 | #50 | #70 | #110 |
|---------------------------------|------|------|-------|-------|-------|
| K_s (10^{-3} m s $^{-1}$) | 8.03 | 1.98 | 0.406 | 0.243 | 0.053 |
| d_{50} (mm) | 1.08 | 0.50 | 0.32 | 0.20 | 0.12 |
| $S_{r,w}$ (-) | 0.07 | 0.26 | 0.29 | 0.30 | 0.26 |

In the one-source experiment, the source zone was 0.105-m long and 0.05-m wide (Figure 3.27). Source zone was filled to approximately one-third of total thickness with red-dyed PCE, injected into the source zone using a glass syringe. The total volume of PCE in the source zone was 31.0 cm 3 . The tank was then inverted one day to allow PCE redistribution within the source zone. After one day, the tank was returned to the original position for a second 24 hour period. In this way, a fully developed saturation profile was generated where NAPL saturation ranged from residual at the top of the source to high saturation in a pool at the base of the source. Two-constant head reservoirs are installed upstream and downstream of the tank to maintain a continuous and steady flow of de-ionized water (ROPure $^{\text{®}}$, Barnstead/Thermolyne Corporation) through the tank. Three injection ports located upstream were used for tracer's solution injection. A multi-channel syringe pump was used to provide a constant injection rate of the tracer solution. Nine sampling ports located downstream were used to extract aqueous solution samples. The outlet also was used as a sampling port to monitor both total flow rate and mass balance.

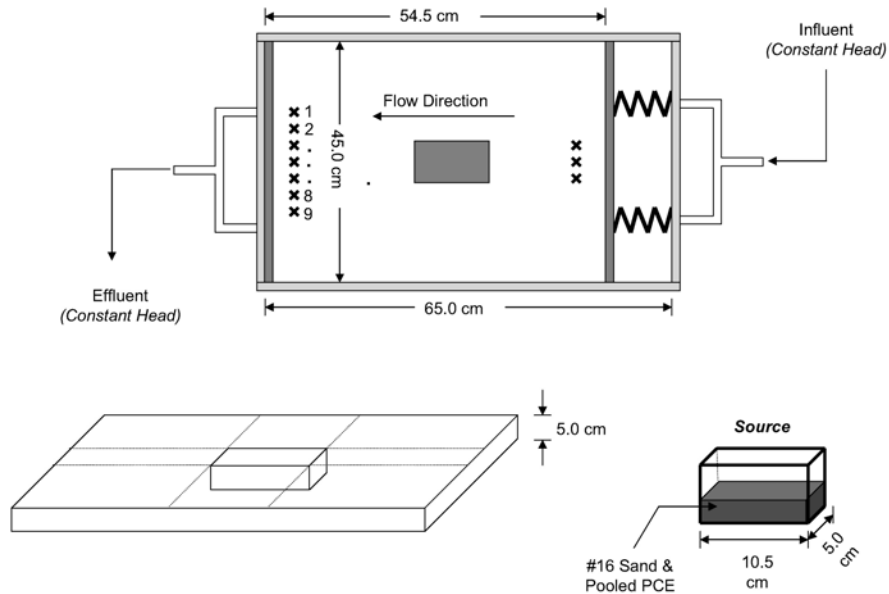


Figure 3.27. Two Dimensional Bench-Scale Dissolution Cell with One Source Zone

Dissolution experiments were conducted at specified flow rates that ranged from $2.42 \times 10^{-8} \text{ m}^3 \text{ sec}^{-1}$ to $1.50 \times 10^{-7} \text{ m}^3 \text{ sec}^{-1}$. For each experiment, PCE concentration was monitored under transient and steady-state conditions. As soon as the hydraulic gradient was applied to the tank that produced the desired flow, PCE concentration was monitored at ports No. 4, 5, 6, and the outlet (i.e. port O). Figure 3.28 shows the experimental data for transient dissolution of PCE for the single-source setup. Typical transient breakthrough curves of NAPL dissolution were observed at all monitoring ports. This type of breakthrough curve is characterized by a rise in concentration from zero or background value at the dissolution front followed by a steady-state plateau. Highest steady-state concentration was observed at the central port (#5) where $C_{\infty} = 117.0 \text{ mg/L}$. The dissolved PCE in the effluent (port O) also reaches steady-state value of 27.0 mg/L .

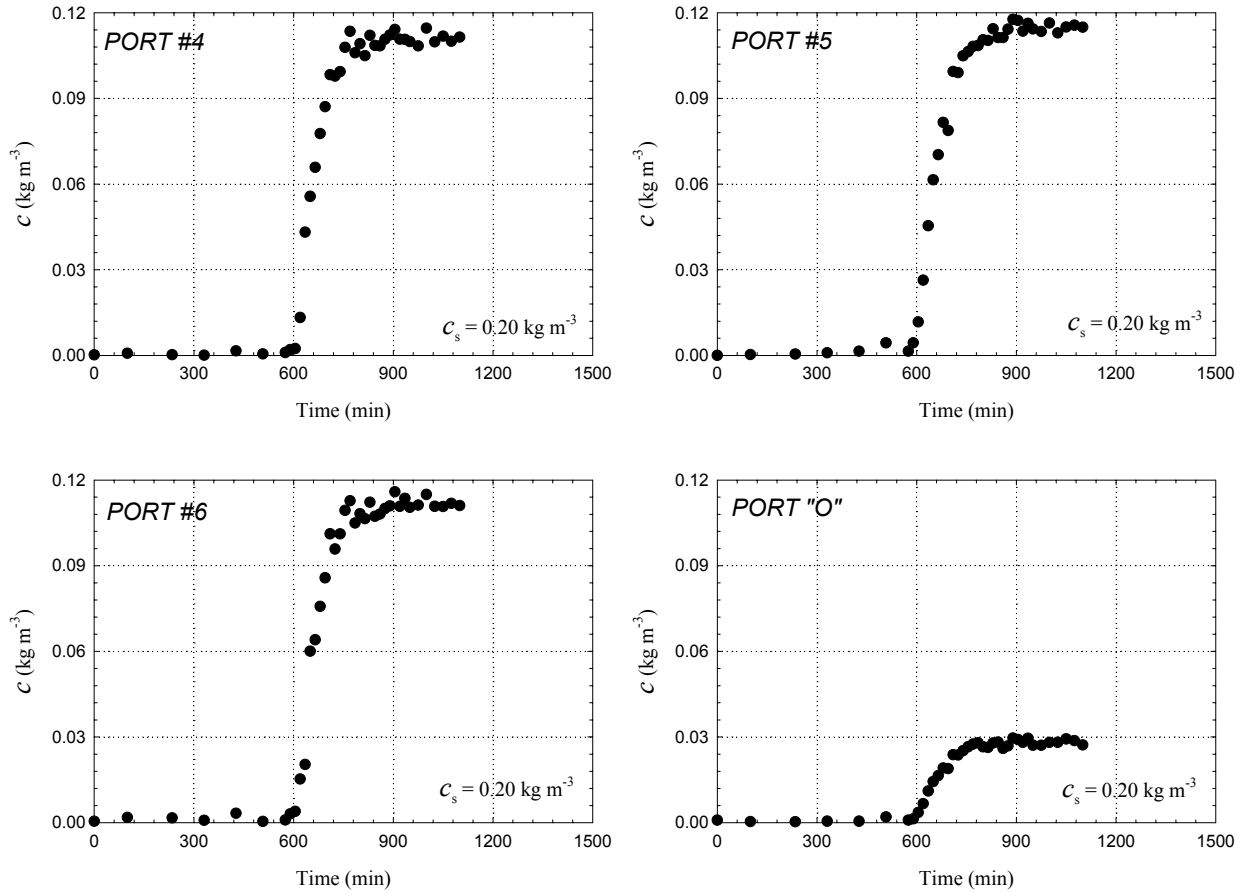


Figure 3.28. Transient Concentration of PCE at Selected Monitoring Ports, One-Source Experiment

Effective mass transfer coefficient under steady-state condition $\bar{k}_{La,\infty}$ can be determined using the steady-state concentration measured at the effluent. This effective mass transfer coefficient is the average value that represents k_{La} of the entire source zone. Equation 3.5, derived from the general linear driving-force interphase mass transfer equation, was used to calculate the value of $\bar{k}_{La,\infty}$ and is given by

$$\bar{k}_{La,\infty} = -\frac{Q}{V_0} \left(1 - \frac{C^*}{C_\infty} \right) \quad (3.5)$$

where Q is the total effluent flow rate, V_0 is the volume of the porous medium that comprises the source zone (in this case $V_0 = 10.5 \times 5.0 \times 5.0 \text{ cm}^3$), C^* is the apparent aqueous solubility of

PCE (in this normal dissolution case, $C^* = C_s$), and C_∞ is steady-state concentration of dissolved PCE measured at the effluent.

Figure 3.29 shows steady-state PCE concentration as a function of flow rate at four monitoring ports (#4, 5, 6, and O). As the flow rate increases, the effluent concentration decreases due to dilution. However the steady-state mass depletion rate, which is the product of the steady-state concentration at the effluent (port O) and the total flow rate, increases almost linearly with the flow rates. As the seepage velocity increased, the rate of mass transfer also increased since the modified Sherwood number that represents the mass transfer rate is proportional to the Reynolds number (Bird et al., 1960; Schwille, 1988; Miller et al., 1990; Powers et al., 1994).

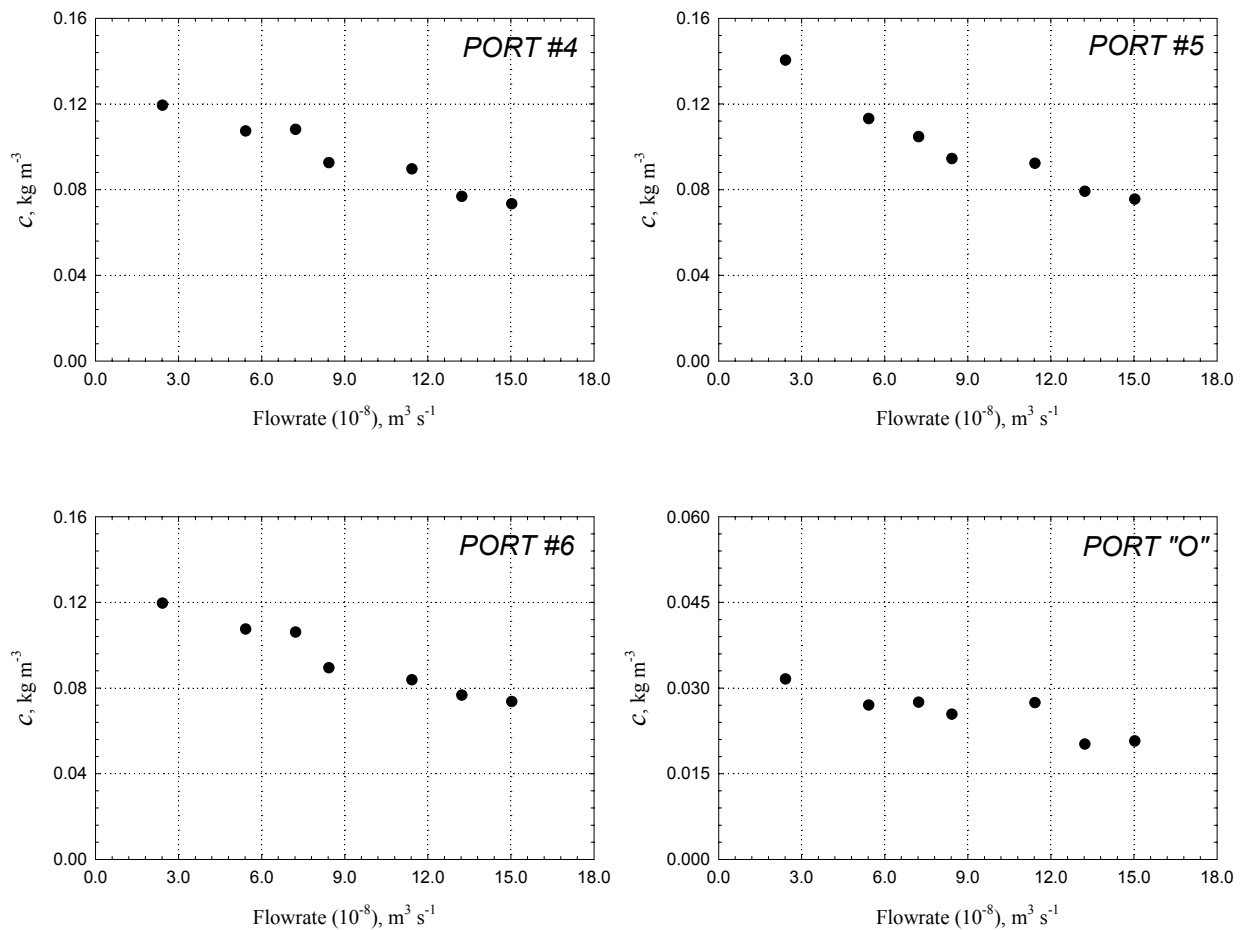


Figure 3.29. Steady-State PCE Concentration as a Function of Flow Rate at Four Monitoring Ports, Horizontal Flow Cell Experiments with One Source

The largest effluent concentration was observed at the lowest flow rate (Figure 3.29). This suggests that the concentration alone may not be a good indicator of the characteristic of a

DNAPL source zone. Figure 3.30 shows the steady-state PCE concentration distribution at various flow rates for all sampling ports. PCE concentration distributed approximately evenly about the middle port. Ports #4, 5, and 6 showed higher concentrations than the others due to the architecture of the entrapment zone where these three ports lined up with the source zone (Figure 3.27).

Steady-state mass depletion increased with increasing flow rate (Figure 3.31). A similar trend was observed for effective mass transfer coefficients under steady-state condition $\bar{k}_{La,\infty}$ (Figure 3.32). For comparison purposes, the overall mass transfer coefficient of NAPL undergoing dissolution in column experiments was on the order of 10^1 to 10^4 day⁻¹ depending on the type of NAPL and the experimental condition, especially the Darcy velocity (Miller et al., 1990). However, the overall mass transfer coefficient estimated from flow cell experiments presented in this report, as well as those of Saba (1999) and Nambi (1999), were on the order of 10^{-1} to 10^2 day⁻¹.

Vertical concentration profiles were evaluated in one flow cell experiment. At the flow rate of 2.42×10^{-8} m³ sec⁻¹, aqueous samples were taken at five different depths, 0.5 cm downstream of the source (Figure 3.33a). The vertical profile was located at the mid-point of the source's axis with samples were taken at 0.5 cm intervals, providing the mass flux J_a and concentration profiles shown in Figures 3.33b and 3.33c. Mass flux J_a was calculated based on measured concentration and flow rates obtained from a calibrated flow model. The DNAPL saturation profile is presented in Figure 3.33d. The profiles show that measured steady-state mass flux of dissolved PCE was higher in the transition zone than in the pool at the bottom. Maximum mass flux was at mid-depth where intermediate PCE saturation was present. Dissolved mass flux from the high saturation pool at the base of the source zone was smaller than the flux emanating from the saturation transition zone above the pool. However, concentration downstream of the pool is significant. Therefore, it can be concluded that although a large fraction of DNAPL mass resides in the pool, a much small fraction of mass present in the transition zone contributes to a majority of flux producing a down-gradient plume.

A second set of experiments was conducted using the horizontal flow cell packed with two source zones. Protocols for conducting this test were essentially the same as those used in the one-source experiments and therefore are not presented in detail. The independent set of data obtained from the two-source dissolution experiments was used to verify or test the validity of a dissolution model calibrated from data obtained from the one-source experiments. Transient breakthrough curves monitored at ports B and O (effluent) were used in this model verification. Figure 3.34 illustrates the experimental data as well as the model prediction for natural dissolution of PCE in two-source experiment. The developed dissolution module for natural dissolution was validated and verified, and can readily be used in subsequent theoretical studies.

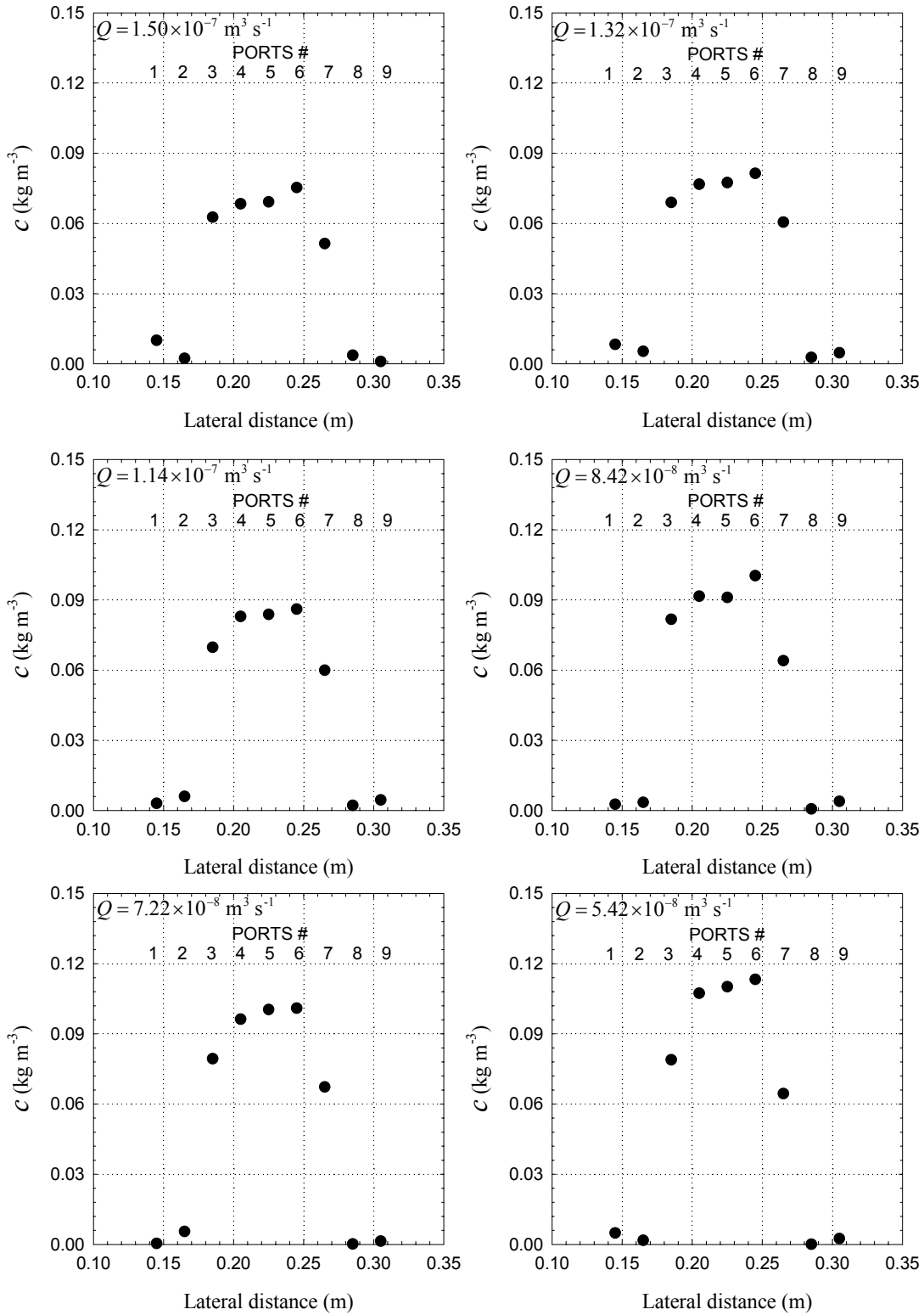


Figure 3.30. Steady-State PCE Concentration at Various Flow Rates for Nine Sampling Ports, Horizontal Flow Cell Experiments with One Source

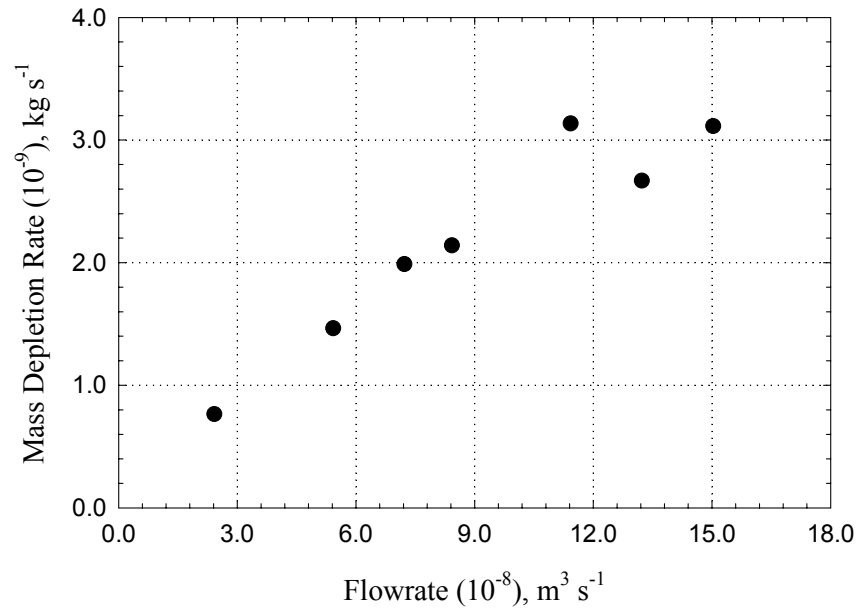


Figure 3.31. Steady-State Mass Depletion as a Function of Flow Rate, Horizontal Flow Cell Experiments with One Source

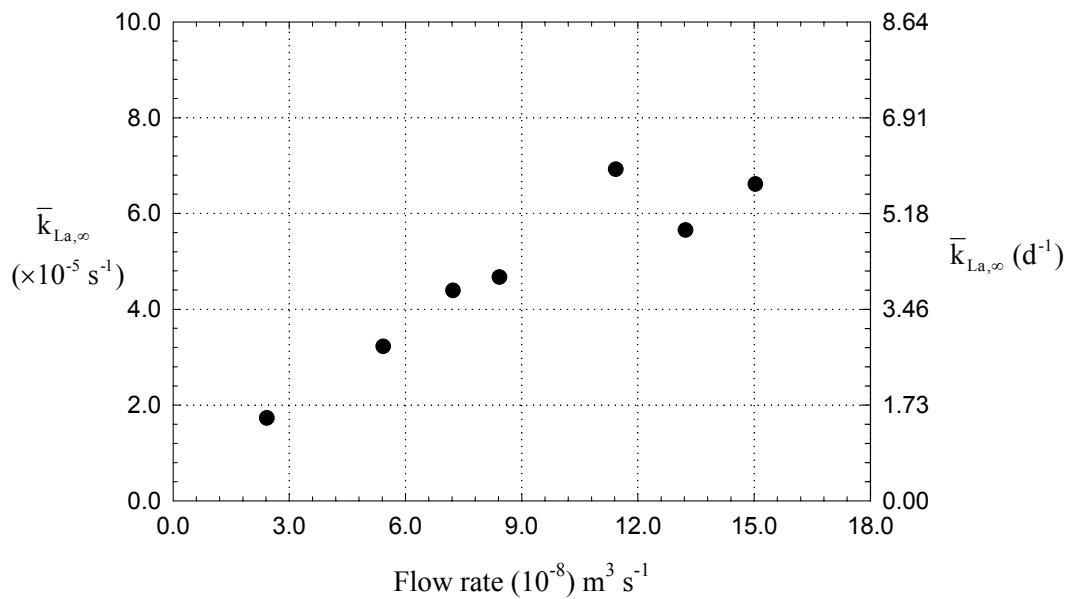


Figure 3.32. Steady-State Mass Transfer Coefficient as a Function of Flow Rate, Horizontal Flow Cell Experiments with One Source

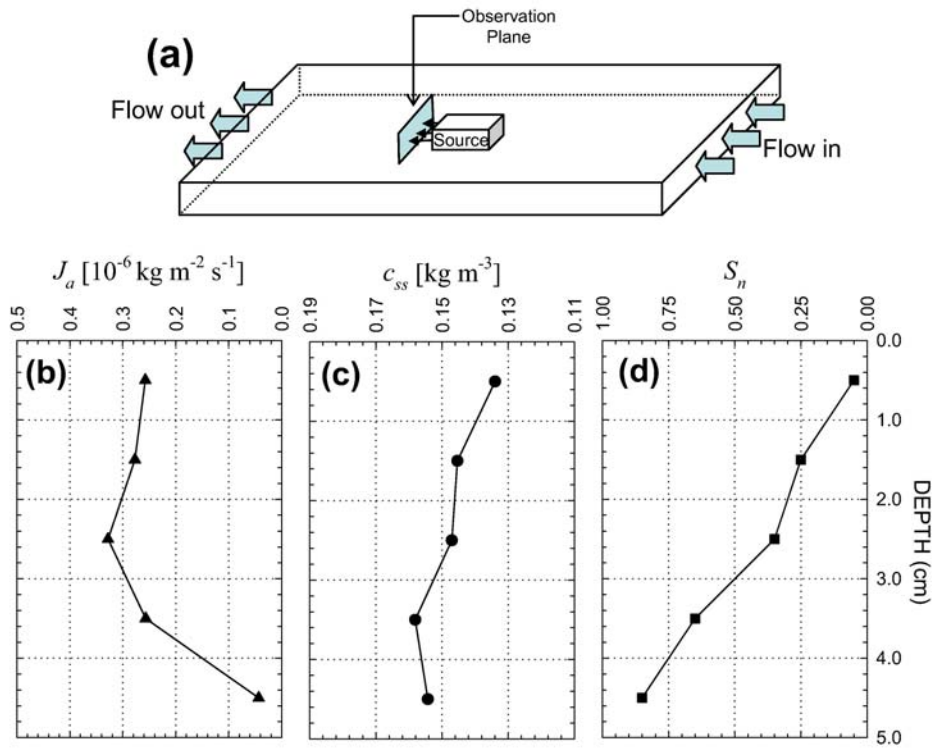


Figure 3.33. Vertical Distribution of Concentration, Mass flux and Saturation at Flow Rate of $2.42 \times 10^{-8} \text{ m}^3 \text{ sec}^{-1}$, Horizontal Flow Cell Experiments with One Source

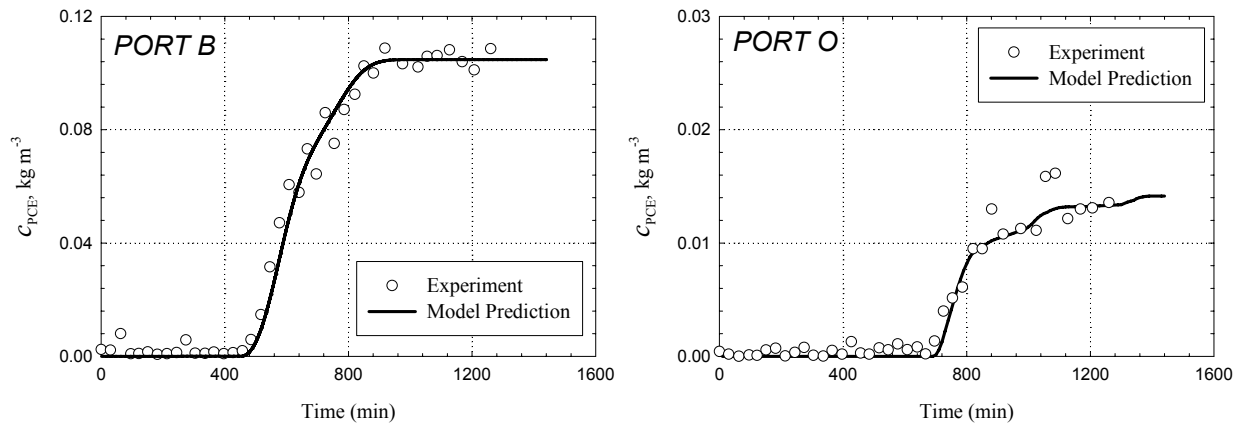


Figure 3.34. Transient Dissolution of PCE in Two-Source Experiment: Experimental Data and Model Simulated Values

3.4.4 Large-tank experiments of natural dissolution

Three sets of large tank experiments were conducted to generate data associated with each of the technologies studied. The first and second sets were conducted after packing the tank to represent an aquifer with high and low degrees of soil heterogeneity. Experiments in these tanks focused on partitioning tracers, natural dissolution, surfactant enhanced dissolution, and *in situ* chemical oxidation. The third tank was packed to represent three aquifer units. Each unit was separated from the others by bentonite-Teflon confining units to assure hydraulic isolation. Experiments in this tank focused on bioenhanced dissolution and thermal treatment. Each set of experiments was conducted in a tank with dimensions of 4.88 m × 1.22 m × 0.05 m.

Large-tank experiments are difficult to setup, costly and time consuming. Therefore, each experiment was designed to meet multiple project objectives while obtaining comprehensive data sets. The large tank experiments generated a large amount of data. Materials and methods used to generate these data also were extensive. Appendices 1, 2 and 3 provide detailed descriptions of these experiments.

In addition to providing a basis of comparison with post-remediation mass transfer, natural dissolution experiments were conducted in order to (1) confirm the mass transfer model obtained from column and cell studies, (2) validate a methodology for determining entrapped NAPL architecture using mass flux data, and (3) validate a methodology for upscaling models of natural dissolution (Saenton, 2003). By conducting experiments with both high and low degrees of heterogeneity, it also was possible to study the effect of permeability heterogeneity on mass transfer rate coefficients associated with natural dissolution.

Two large tank experiments were conducted to evaluate natural dissolution from source zones in complexly heterogeneous porous media. The first experiment was designed with high aquifer heterogeneity (variance of $\ln K = 1.22$) and the second experiment was designed with low aquifer heterogeneity (variance of $\ln K = 0.25$). Detailed descriptions of design and packing procedures are provided in Appendix 1 for the high heterogeneity tank and in Appendix 2 for low heterogeneity tank. The large tank experimental setup is shown in Figure 3.35 Natural dissolution experiments were conducted in conjunction with flow system characterization and partitioning tracer tests (section 3.3). Detailed descriptions of DNAPL distribution within source zones are provided in appendix sections A1.4 and A2.4.

Natural dissolution experiments were conducted after a static PCE entrapment architecture had been obtained and saturation distribution was mapped by gamma-ray attenuation methods. During natural dissolution tests, down-gradient distributions of dissolved PCE were monitored and results were used to evaluate effective mass transfer prior to remediation. Procedures for sample collection and analysis are provided in section 3.2.

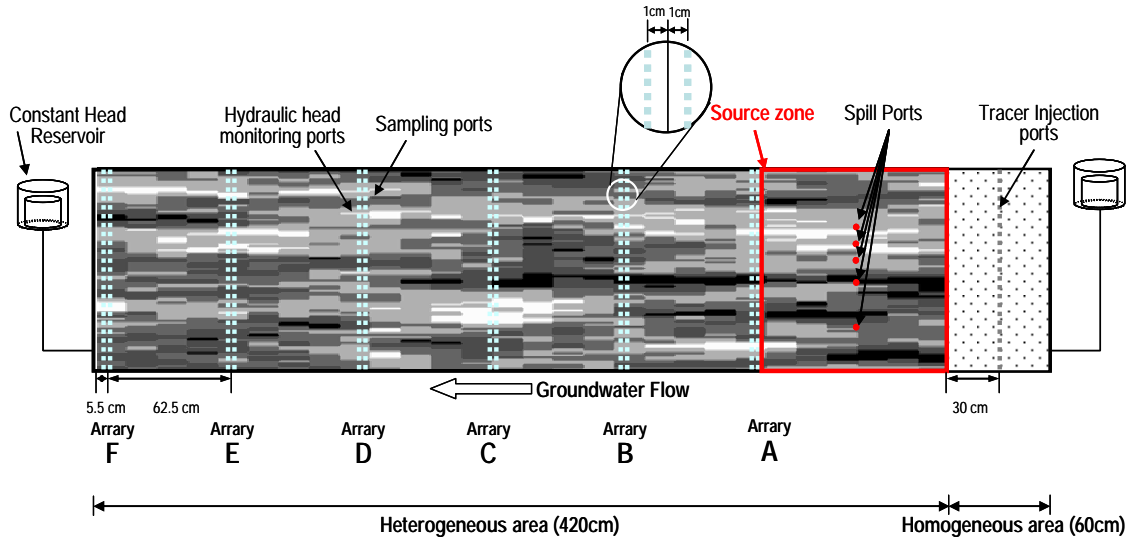


Figure 3.35. Design for Experimental Tank Showing Heterogeneous Packing, Constant Head Devices, Head Monitoring Ports, and Sampling Ports

High Heterogeneity Tank. Once the static PCE entrapment architecture had been established, four different hydraulic gradients were applied to the test tank. Aqueous samples were taken at every other port (in the vertical direction) for three arrays (A, C, and E). The example shown below (Figure 3.36) illustrates the distribution of PCE concentration in the vertical direction for head difference of 8 cm.

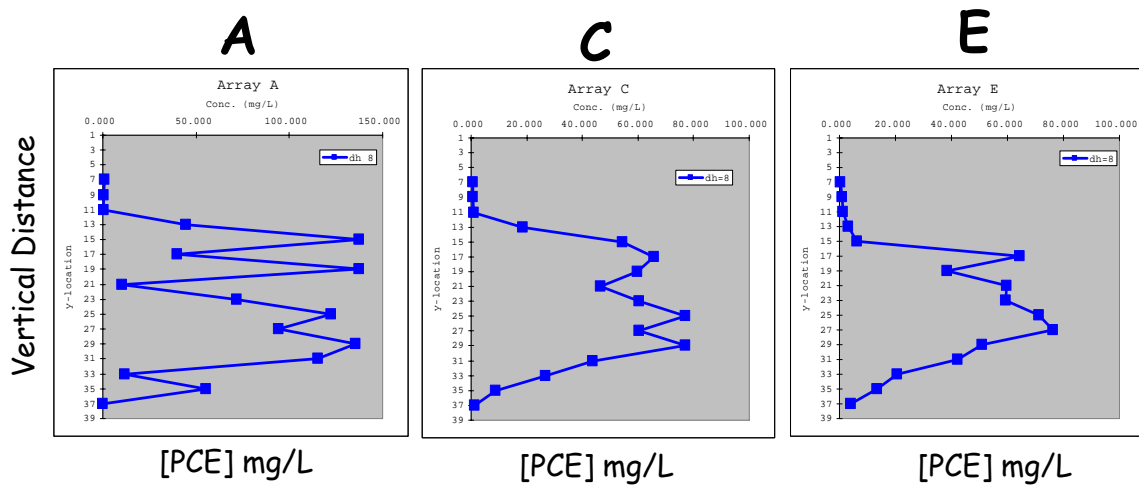


Figure 3.36. Steady-State PCE Concentration Profiles at Sample Arrays A, C and E during the Natural Dissolution Experiment, High Heterogeneity Tank

Low Heterogeneity Tank. Once the static PCE entrapment architecture had been established, three different hydraulic gradients were applied to the test tank and the concentration of PCE were monitored at different locations. Aqueous samples were taken at every other port (in the vertical direction) for three arrays (A, C, and E). Figure 3.37 shows the distribution of PCE concentration in the vertical direction for the three different head gradients.

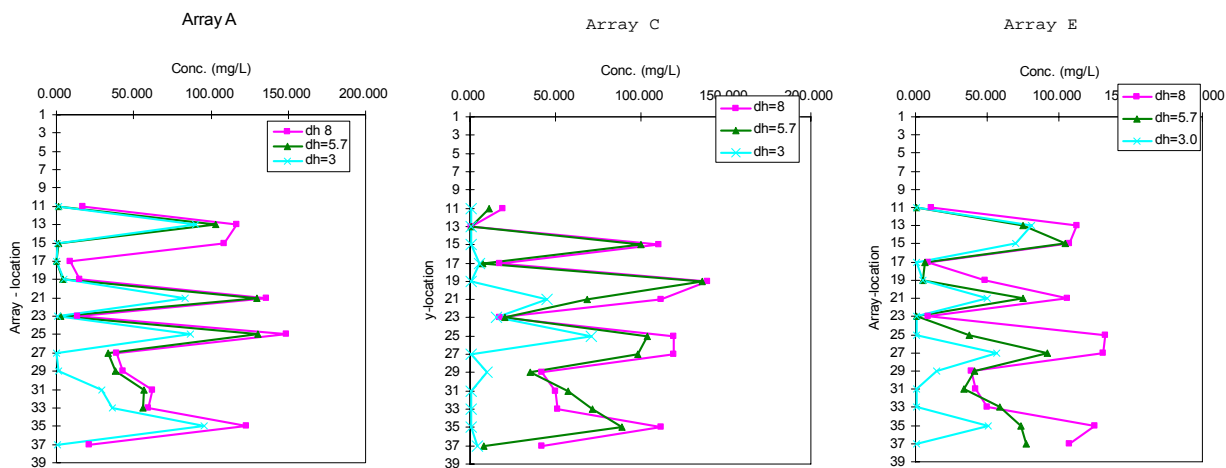


Figure 3.37. Steady-State PCE Concentration Profiles at Sample Arrays A, C and E during the Natural Dissolution Experiment, Low Heterogeneity Tank

3.5 Experimental design and methods for investigation of surfactant-enhanced dissolution

Mass transfer experiments with surfactant-enhanced aquifer remediation (SEAR) were conducted in order (1) to evaluate how experimental scale affects SEAR efficiency, (2) to demonstrate the capability of a modeling tool for simulating SEAR, and (3) to determine how flow system dimensionality affects SEAR efficiency. Experiments were conducted with one-dimensional columns, bench-scale two-dimensional flow cells, and a large two-dimensional tank.

3.5.1 Column experiments with surfactants Tween 80 and Aerosol 80I

Column tests were conducted to determine (1) mass transfer rates from DNAPL after surfactant had been applied, (2) the effect of flow rate on DNAPL mass transfer and depletion, and (3) the effect of DNAPL removal on mass transfer. Separate tests were conducted to evaluate effects of column orientation on SEAR effectiveness, and effects of flow rate and injection strategy. Additional tests were conducted to compare effects of SEAR on mass transfer from pure TCE-DNAPL and a field DNAPL with a large component of TCE.

A set of column tests was conducted using horizontal, vertical and inclined column orientations to evaluate the effects of flow direction on mass transfer with surfactants. Column

experiments were conducted with two surfactants, Tween 80 & Aerosol 80I, which have different dominant mechanisms for mobilization and enhanced dissolution of DNAPL. Tween 80 is an anionic surfactant and solubilization is the dominant removal mechanism. Aerosol 80I is ionic and mobilization is the dominant removal mechanism. By using two surfactants, it was possible to examine relative effectiveness of mobilization and solubilization during PCE removal.

Surfactant flushing was performed in a soil column with PCE at residual saturation of approximately 15 percent. Effects of mobilization were examined by placing the soil column at different inclinations. Figure 3.38 showed experiment set up and the details of the experiments are provided in Table 3.25. The PCE removal was larger in the vertically placed column compared to the horizontally placed column, especially for Aerosol 80I. This is mainly due to mobilization of residual PCE, in which mobilized PCE accumulates at the bottom boundary of the horizontally placed column.



Figure 3.38. Setup for Column Experiments with Surfactants

Table 3.25. Summary of Column Experiments at Selected Orientations

| Experimental Parameter | Tween 80 | | | Aerosol 80I | |
|-------------------------|--------------|----------------|--------------|--------------|----------------|
| | Vertical PCE | Horizontal PCE | Inclined PCE | Vertical PCE | Horizontal PCE |
| Flow rate (mL/min) | 0.66 | 0.66 | 0.66 | 2 | 2 |
| Porosity | 0.36 | 0.36 | 0.36 | 0.48 | 0.43 |
| Pore volume (mL) | 217 | 210 | 215 | 320 | 288 |
| NAPL volume | 42.53 | 32.97 | 32.89 | 36.8 | 45.8 |
| NAPL saturation (%) | 19.6 | 15.7 | 15.3 | 11.5 | 15.9 |
| Surfactant pore volumes | 14.7 | 17.49 | 19.8 | 3.2 | 4.6 |
| Total Removal (%) | 89 | 77.2 | 87 | 85 | 25.8 |
| Solubilization (%) | 65.2 | 58.3 | 74.8 | 8.2 | 10.1 |
| Mobilization (%) | 23.8 | 18.8 | 12.2 | 76.8 | 15.7 |

The effect of flow rate on DNAPL removal mechanisms and resulting mass transfer rate was investigated by conducting a series of column experiments with DNAPL placed in a soil column at residual saturation. The column was 30 cm long and 10 cm in diameter. In each experiment, the column was flushed with water to obtain the steady state aqueous DNAPL concentration and then the column was flushed with surfactant solution in vertical downward direction. After surfactant flushing, water was flushed and the steady aqueous phase concentration was measured. In some tests, the surfactant flushing was performed in multiple stages and the aqueous DNAPL concentration was measured at the end of each stage. Two different surfactant solutions (8% Aerosol 80-I with 15000mg/L NaCl and 4% Tween 80) were used for the investigation.

Three tests were performed to evaluate PCE removal with Aerosol 80-I at three different surfactant injection rates. The parameters of the experiments are given in Table 3.26. Figure 3.39 shows the effluent PCE concentration with different surfactant injection rates. The test with a high injection rate of 6 mL/min showed rate-limited behavior and low removal efficiency compared to tests with slower injection rates. The aqueous PCE concentration after remediation was approximately 10 percent of the original PCE concentration. However, flow rate had little effect on steady-state effluent concentration after remediation.

Two column tests were conducted to evaluate PCE removal with Tween 80. Surfactant flushing rate in both tests was 6 mL/min. In the first test, surfactant was injected continuously. In the second test, surfactant flushing was conducted in three stages and each stage was followed by water flushing at a rate of 0.5 mL/min. The experimental details are summarized in Table 3.27. Figure 3.40 shows the effluent PCE concentration for both tests. Removal rates were similar for continuous and alternative flushing. However, continuous flushing was able to remove PCE better than alternative flushing. Figure 3.41 shows the steady state PCE aqueous concentration as a function of the average free phase PCE saturation in the soil column. It shows the mass transfer behavior at different levels of PCE removal. Large removal of PCE was required in these soil columns to reduce the PCE aqueous phase concentration.

Table 3.26. Summary of Column Experiments with the Surfactant Aerosol 80I at Selected Flow Rates

| Experimental Parameter | Column 1 | Column 2 | Column 3 |
|--|----------|----------|----------|
| Flow rate (mL/min) | 6 | 2 | 0.5 |
| Porosity | 0.34 | 0.35 | 0.4 |
| Pore volume (mL) | 204 | 236 | 269 |
| NAPL volume | 40.5 | 41.5 | 37.8 |
| NAPL saturation (%) | 19.8 | 17.58 | 14.05 |
| Surfactant pore volumes | 9.7 | 8.5 | 5.8 |
| Total removal (%) | 78 | 85.3 | 77.7 |
| Solubilization (%) | 38 | 23.9 | 37.7 |
| Mobilization (%) | 40 | 61.4 | 39.9 |
| Initial aqueous PCE concentration (mg/L) | 49.54 | 47.60 | 49.73 |
| Final aqueous PCE concentration (mg/L) | 5.4 | 1.07 | 3.29 |

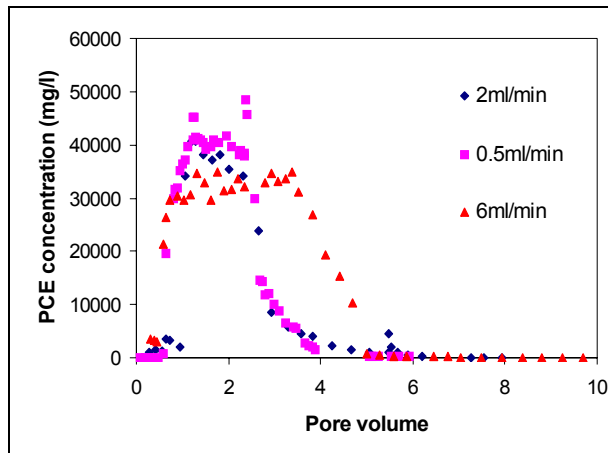


Figure 3.39. Effluent PCE Concentration during Aerosol Flushing in Column Experiments at Selected Flow Rates

Table 3.27. Summary of Column Experiments with Tween 80 Using Two Injection Strategies

| Experimental Parameter | Column 1 | Column 2 |
|--|------------|----------|
| Flow | Continuous | Stepped |
| Porosity | 0.31 | 0.31 |
| Pore volume (mL) | 186.8 | 184.2 |
| NAPL volume | 33.75 | 34.5 |
| NAPL saturation (%) | 18.06 | 18.72 |
| Surfactant pore volumes | 28.9 | 29.3 |
| Total removal (%) | 94.13 | 84.8 |
| Solubilization (%) | 88.8 | 77.3 |
| Mobilization (%) | 5.3 | 7.5 |
| Initial aqueous PCE concentration (mg/L) | 71.1 | 72.1 |
| Final aqueous PCE concentration (mg/L) | 9.55 | 27.28 |

A set of column tests was conducted to characterize and compare surfactant-enhanced dissolution of pure TCE-DNAPL and a field DNAPL containing a significant fraction of TCE. The tests were conducted in two 15 cm long and 5 cm diameter glass columns (Figure 3.42). The columns had exclusively Teflon tubing, and metal fittings and valves. The columns were packed with #70 sand and DNAPL sources were created at residual saturation. Residual DNAPL saturation of the columns was estimated with partitioning tracer tests at the beginning of the dissolution process and at the end of the surfactant dissolution. Prior to surfactant dissolution, a set of natural dissolution experiments were conducted using a range of flow rates (0.6 to 4.4 mL/min). All tests were conducted in parallel.

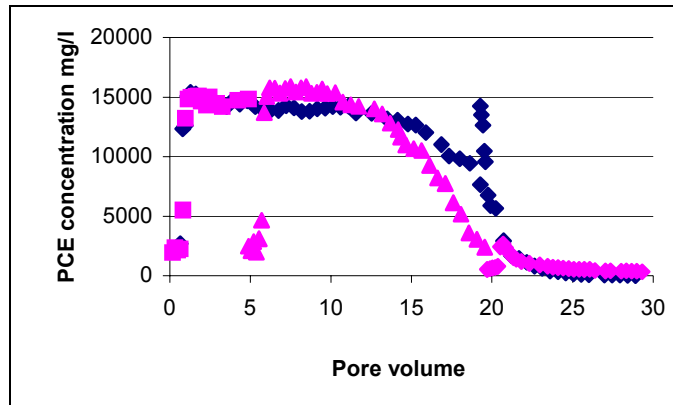


Figure 3.40. Effluent PCE Concentration using Continuous and Stepped Flushing with Tween 80

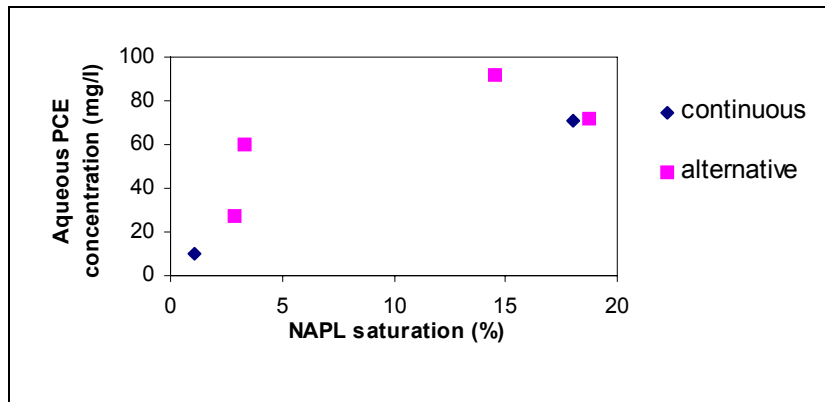


Figure 3.41. Relationship of Aqueous PCE Concentration to NAPL saturation in Column Experiments with Tween 80 and Two Injection Strategies

During surfactant treatment with 5 percent Tween 80, effluents from the columns were noticeable different (Figure 3.43). For the column with pure phase TCE, effluent started to turn very cloudy after surfactant injection of approximately one pore volume, and continued to discharge as a cloudy emulsion solution during surfactant injection and two subsequent pore volumes of water injection. This result indicated that there is a strong emulsion forming when the surfactant is in contact with pure phase DNAPL. For the column contaminated with field DNAPL, the effluent stayed clear throughout the test.



Figure 3.42. Setup for Column Experiments with SEAR Comparing Mass Transfer from Pure TCE-DNAPL and a Field DNAPL



Figure 3.43. Difference in Column Effluents During Surfactant Flushing for Field DNAPL (Left Volumetric Cylinder) and Pure TCE-DNAPL (Right Volumetric Cylinder)

The breakthrough curves resulting from both natural and surfactant enhanced dissolutions were analyzed to obtain mass transfer rate coefficients using the solute transport model and parameter estimation algorithm described in section 3.4.1. Mass transfer rate in the transport model depends on the difference between TCE solubility and the ambient aqueous-phase concentration. During surfactant flushing, solubility was expected to vary with surfactant concentration. Therefore, TCE solubility was estimated from results of batch experiments (Figure 3.44). Fitting the transport model to the observed effluent concentration data provided estimates of the average mass transfer coefficient during surfactant flushing. The mass transfer coefficient was estimated to be 23.27 day^{-1} for field DNAPL and 18.09 day^{-1} pure TCE (Figure 3.45).

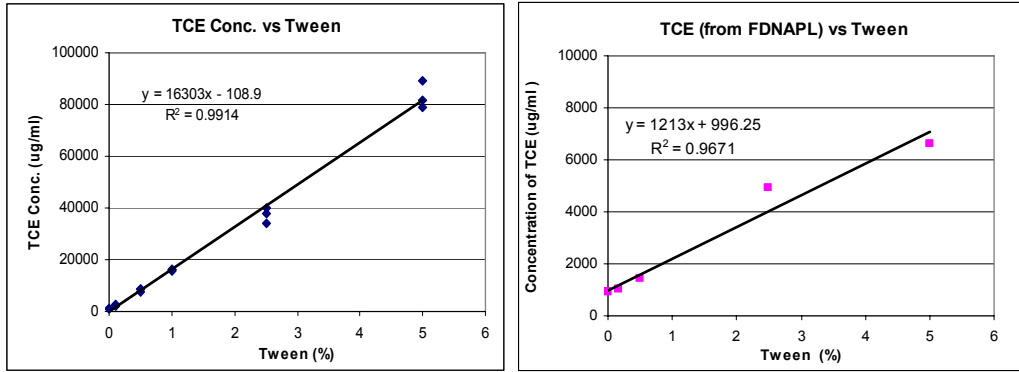


Figure 3.44. Plots of TCE Concentration vs. Tween 80 Concentration in Batch Equilibrium Tests of Pure TCE and Field DNAPL

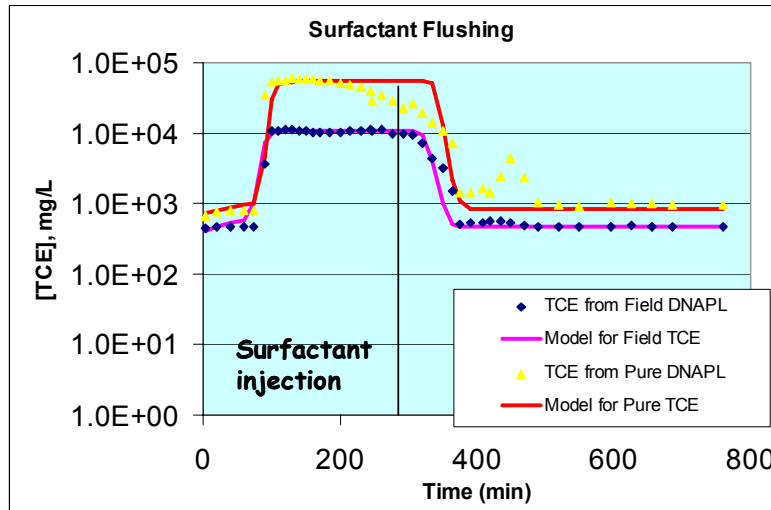


Figure 3.45. Breakthrough of TCE from Pure and Field DNAPL During Surfactant Flushing

3.5.2 Two-dimensional flow-cell experiments with pure TCE or field DNAPLs

Two-dimensional flow-cell experiments were designed to estimate mass transfer coefficients for TCE from pure and field DNAPL, to compare these estimates with those obtained from one dimension columns, and to evaluate the effect of flow-system dimensionality on the mass transfer coefficients. The flow cell was identical to the cell used in experiments described in section 3.4.2. The experiments described here were conducted following the natural dissolution tests described in section 3.4.2.

Following natural dissolution, the cells were flushed with about 630 mL (pure TCE-DNAPL source) and 750 mL (field DNAPL source) of 5 percent Tween 80 at 3.6 mL/min. Flow was interrupted for a short period when the surfactant solution was refilled. Water was flushed for 16 hours after surfactant injection stopped. A TCE volume of 3.84 mL was removed from the pure DNAPL source during the surfactant flush. A TCE volume of 4.582 mL was removed from the field DNAPL source. A significant amount of TCE remained in the flow cell at the end of both experiments.

During surfactant flushing, the source zone had noticeable changes in DNAPL distribution. For the field DNAPL source, DNAPL was mobilized and entered the fine sand zone (Figure 3.46). Transient dissolution data from surfactant enhanced dissolutions were used to estimate overall mass transfer coefficients k_{La} based on the mathematical model described in section 3.4.1 and inverse modeling. Figure 3.47 shows the experimental data and model fit for both DNAPLs (pure and field) during surfactant enhanced dissolution. Table 3.28 summarizes the lumped mass transfer coefficient of TCE from pure TCE and field DNAPL during column and flow-cell experiments.



Figure 3.46. Remobilization of Field DNAPL during Surfactant Flushing

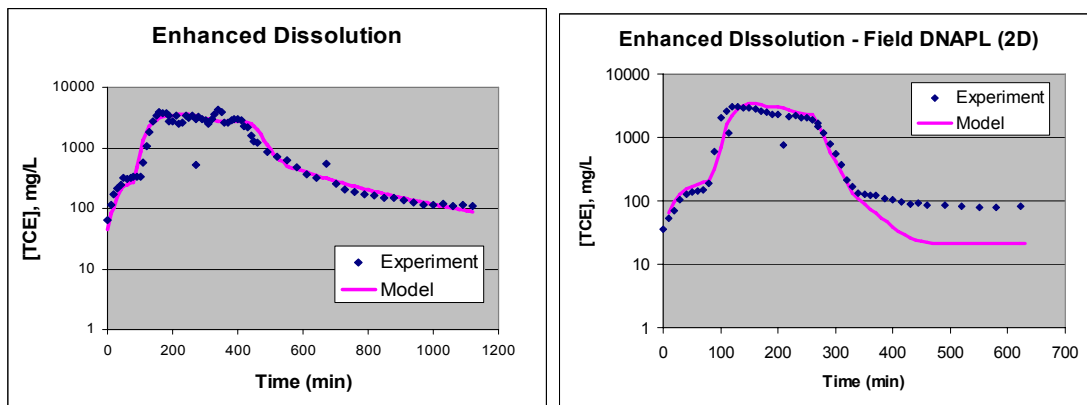


Figure 3.47. Breakthrough Curves for TCE, Flow-Cell Experiments of Surfactant-Enhanced Dissolution with Pure DNAPL (Left) and Field DNAPL (Right)

Table 3.28. Summary of Mass Transfer Coefficients (Day⁻¹) of TCE Present as Pure DNAPL and Field DNAPL During Column and Flow-Cell Experiments

| DNAPL Type | <u>Natural Dissolution</u> | | <u>Surfactant-Enhanced Dissolution</u> | |
|-------------|----------------------------|-----------|--|-----------|
| | Column | Flow Cell | Column | Flow Cell |
| Pure TCE | 14.21 | 3.17 | 18.09 | 13.12 |
| Field DNAPL | 22.83 | 4.09 | 23.27 | 7.12 |

3.5.3 Two-dimensional horizontal flow-cell experiments with pure PCE

Two-dimensional flow-cell experiments with pure PCE DNAPL provided set of high quality laboratory data to be used in model calibration and validation. The flow cell was identical to the cell used in experiments described in section 3.4.3. The experiments described here were conducted following the natural dissolution tests described in section 3.4.3. As with the natural dissolution tests, surfactant-enhanced dissolution experiments were conducted using the flow-cell packed with a one-source and a two-source configuration.

The surfactant-enhanced dissolution experiment with the one-source configuration began by injecting 50.0 g/L of Tween 80 solution into the dissolution cell. At the time of injection the flow system was at steady state with a total flow rate of $1.36 \times 10^{-7} \text{ m}^3 \text{ s}^{-1}$. Injection was through three ports located upstream of the source with a combined injection rate of $4.62 \times 10^{-8} \text{ m}^3 \text{ s}^{-1}$. The reservoir was flooded for 865 min (14.4 hr) and the concentration of PCE was monitored downstream. Figure 3.48 shows PCE concentration at the four monitoring time periods for the first surfactant flushing. It can be seen that Tween 80 effectively enhances the dissolution of PCE and removes PCE free phase from the source zone. This is confirmed by comparing the resultant steady-state effluent concentration before and after surfactant flushing which decreases from 27.0 to 17.0 mg/L. This surfactant flushing experimental data was used to calibrate the surfactant-enhanced dissolution numerical model described in the modeling section. From mass balance calculated using data from port O, this first surfactant flushing removed 5.67 cm³ (or 18.3%) of free-phase PCE.

After the first surfactant flooding, one to two pore volumes of de-ionized water were used to flush the source zone and to obtain a steady-state concentration of PCE in the effluent. Then, the next surfactant flushing was initiated. These alternate processes were repeated four times. In each cycle, the duration of surfactant injection was 14.4 to 30.0 hr. Mass of PCE left in the system was calculated based on mass balance using monitored effluent concentrations. A plot of steady-state PCE concentration vs. percent PCE removal (Figure 3.49) shows that PCE mass was removed from the source zone with each treatment cycle. However, the steady-state PCE concentration at the effluent did not drop at the same rate of mass removal. This suggests that it is necessary to remove a large amount of free-phase PCE in order to significantly lower the observed PCE concentration downstream.

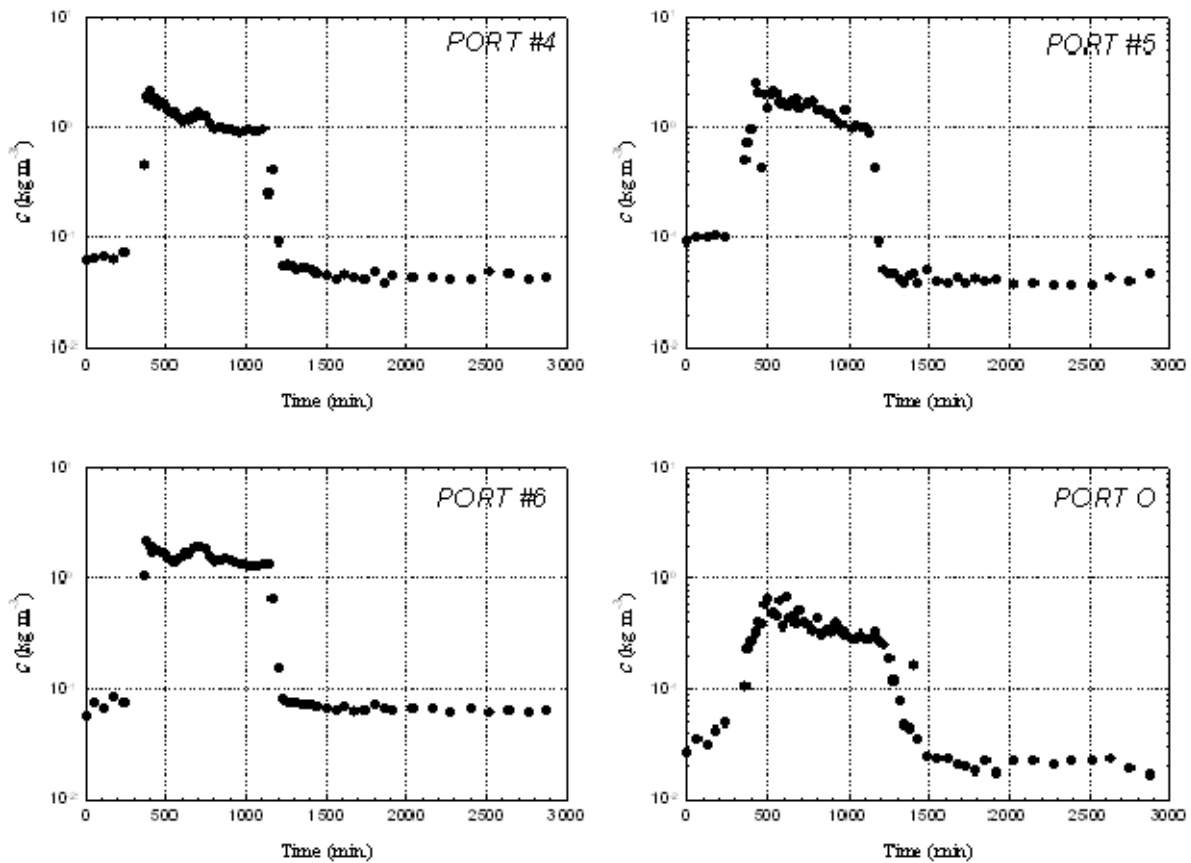


Figure 3.48. Breakthrough Curves for Surfactant-Enhanced Dissolution in the One-Source Experiment

The surfactant-enhanced dissolution experiment with the two-source configuration began by injecting a 50.0 kg m^{-3} Tween 80 solution. At the time of injection the flow system was at steady state with a total flow rate of $6.64 \times 10^{-8} \text{ m}^3 \text{ s}^{-1}$. Injection was through three ports located upstream of the source with a combined injection rate of $1.67 \times 10^{-8} \text{ m}^3 \text{ s}^{-1}$. The tank was flooded with surfactant for 1075 min (17.9 hr) and PCE concentrations were monitored at two ports, B and O. Figure 3.50 shows the breakthrough curves for the first surfactant flood for both monitoring ports. Although a batch experiment of enhanced dissolution showed that equilibrium dissolution of PCE in the presence of Tween 80 can increase almost 100 fold ($\sim 20,000 \text{ mg/L}$), the maximum concentration of PCE observed in port B is less than $3,000 \text{ mg/L}$. The steady-state concentrations at port O prior to and after surfactant flushing are 26.1 and 14.5 mg/L , respectively. This observation confirms that the removal of the accessible free-phase by solubilization can reduce the downstream concentration of dissolved PCE. However, based on mass balance calculation, this first surfactant flushing removed only 9.42 cm^3 of PCE (or 19.2 percent removal).

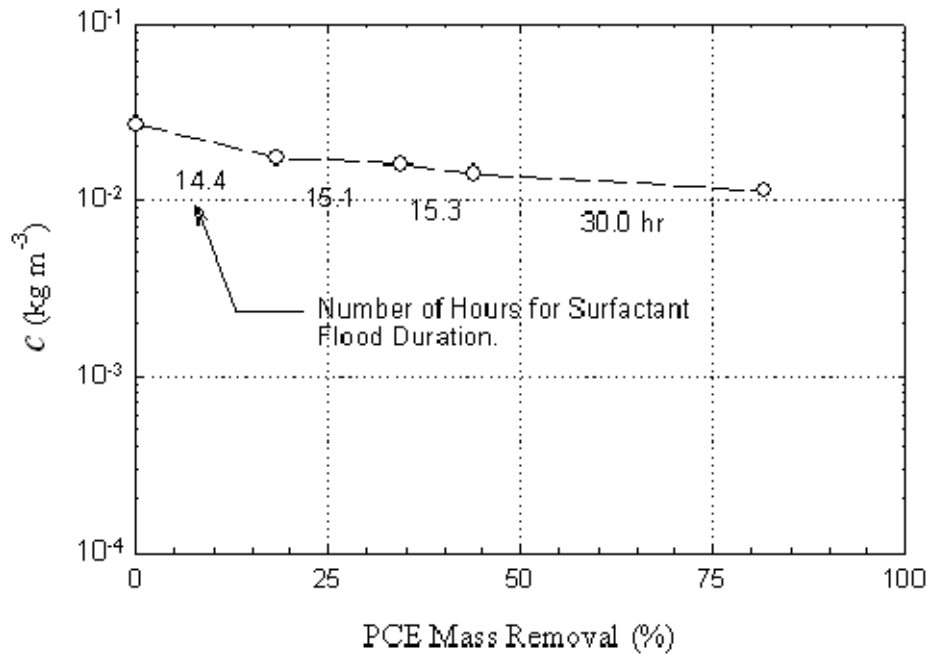


Figure 3.49. Steady-State PCE Concentration in Effluent vs. Percent Mass Removal, Flow-Cell Experiment with One-Source Configuration

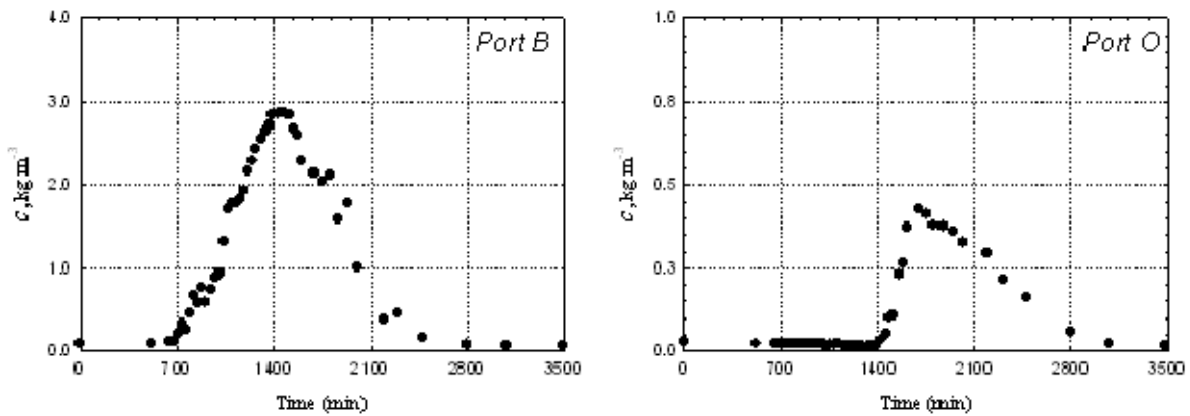


Figure 3.50. Breakthrough Curves for Surfactant-Enhanced Dissolution in Two-Source Experiment

Similar to the one-source experiment, three additional cycles of surfactant flushing and water flooding were conducted. The duration of surfactant flushing ranged from 18 to 36 hr. Mass of PCE removed from the system was calculated based on a mass balance at the effluent concentration (port O). Steady-state concentration of PCE corresponding to the mass removed

from the source (Figure 3.51) shows that it became more difficult in later treatment cycles to remove free-phase DNAPL. This occurred even though the final flush lasted 36 hr. This suggests the injected surfactant solution almost completely bypassed the source zone once the readily accessible DNAPL was removed from the system. This partial source zone removal experiment indicates that although PCE mass removal exceeded 80 percent, the downstream concentration did not drop significantly to a target or regulated value. Addition remediation of the plume would have been required to decrease the concentration of dissolved PCE.

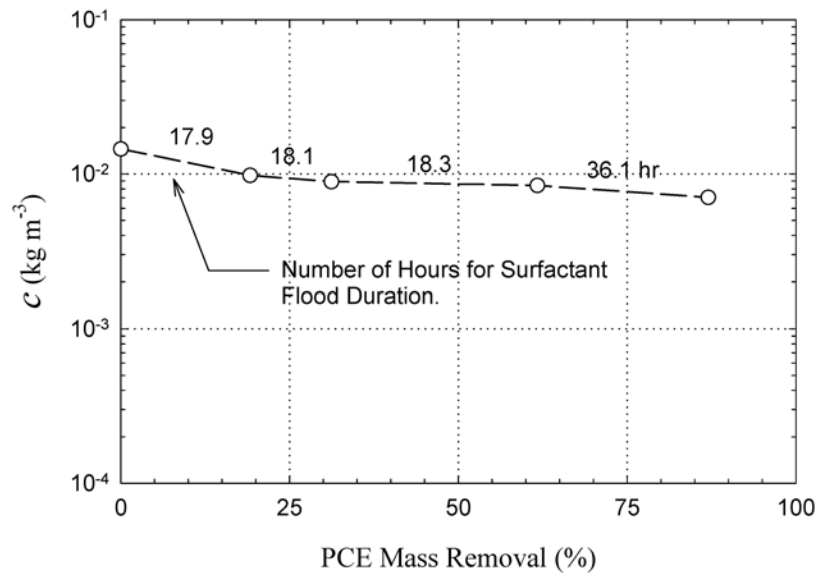


Figure 3.51. Steady-State PCE Concentration at the Effluent as a Function of Percent Mass Removal with the Two-Source Configuration

3.5.4 Two-dimensional experiment with spatially correlated random field

The purpose of this experiment was to examine the natural and enhanced dissolution and mass transfer behavior of a heterogeneous DNAPL source zone, as well as the response obtained from a commonly used site characterization procedure – the partitioning interwell tracer technique. A heterogeneous source zone was designed using a random field generator and a two-dimensional tank was filled accordingly. Following DNAPL injection, groundwater flow was initiated and the aqueous PCE concentrations were monitored under natural dissolution conditions. A pre-remediation tracer test was carried out to assess the efficiency of the technique for estimating the DNAPL source zone volume and distribution. A surfactant flood was then implemented with continued monitoring of downstream PCE aqueous concentrations and this was followed by a second tracer test in an attempt to quantify the volume of PCE removed during remediation. An independent measure of the PCE volume remaining is obtained by calculating the total PCE mass removed from the system due to source zone mass transfer.

A heterogeneous source zone was created in one section of the tank, and the remaining volume was homogeneously filled with sand. The heterogeneity was created using the turning bands method which generates a random, yet spatially correlated, hydraulic conductivity field. To achieve this, a number of aquifer parameters must be supplied, and these are the mean and variance of the source zone, as well as the correlation lengths of the soil units in both the horizontal and vertical directions. The values chosen for this experiment were based on the sands available (Table 3.29).

Table 3.29. Aquifer Properties Used in Surfactant-Enhanced Dissolution Experiment with Spatially Correlated Random Field

| Aquifer Parameter | Value |
|--|--------------|
| Mean of ln (hydraulic conductivity-m/day) | 5.05 |
| Variance of ln (hydraulic conductivity- m/day) | 1.2 |
| Horizontal correlation length | 20 cm |
| Vertical correlation length | 4 cm |

The experimental tank was 220cm by 40cm by 8cm and the source zone was planned as a 60cm by 40cm by 8cm region, so there would be 10 vertical and 3 horizontal correlation scales within the test region. The hydraulic conductivity values were binned into five categories (#16, #30, #50, #70 and #110), each one representing a sand fraction. The #50 fraction represented the mean of the conductivity distribution and the final ‘binned’ source zone conductivity distribution is shown in Figure 3.52 below. Although multiple random field realizations were generated, the chosen configuration was selected because the coarser sand lenses were in locations which would generate satisfactory aqueous PCE concentrations following DNAPL injection.

The tank was filled with sand in accordance with the designed heterogeneity field. However, the discrete, ‘blocky’ geometry was avoided to establish more realistic sand contacts. To achieve this, the sand volumes were tapered at boundaries to create a more gradual transition zone, rather than a sharp vertical front. The final experimental source zone is shown in Figure 3.53 and the remainder of the tank was filled with #70 sand. All sand was poured into the tank at a constant rate and with a constant drop height in order to eliminate any trapped air. After packing and establishing flow through the tank, the groundwater flow pattern through the source zone was characterized by injection of a dyed tracer pulse (Figure 3.54).

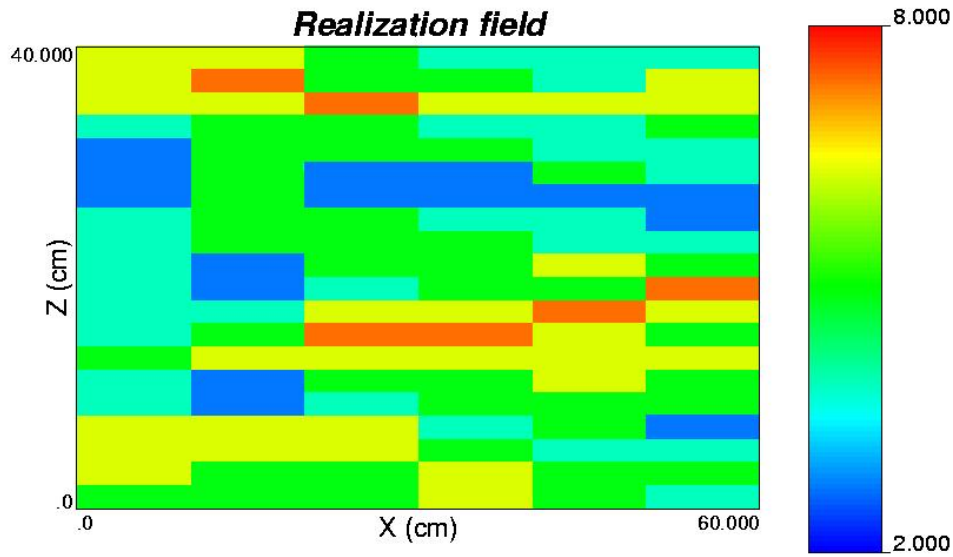


Figure 3.52. Source Zone Heterogeneity Field Designed for the Surfactant-Enhanced Dissolution Experiment with Spatially Correlated Random Field

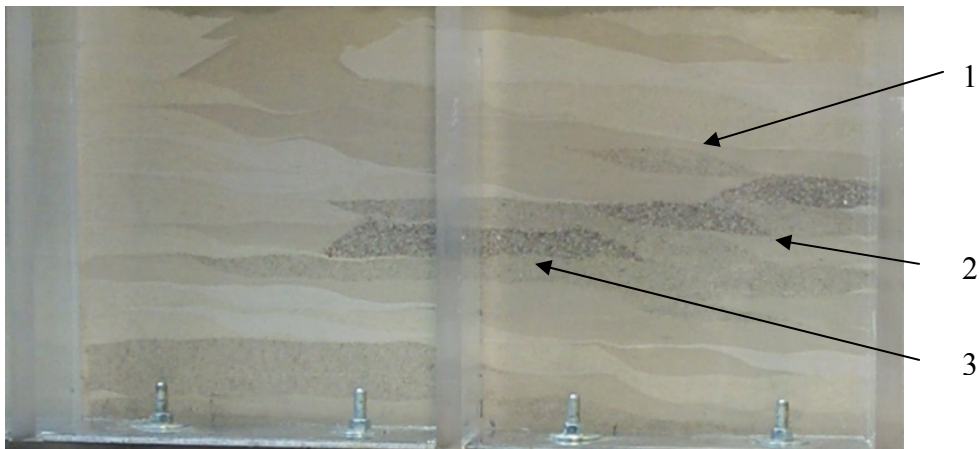


Figure 3.53. Source Zone Heterogeneity Field as Packed for the Surfactant-Enhanced Dissolution Experiment with Spatially Correlated Random Field

A representative DNAPL entrapment morphology was created by injecting PCE dyed with 0.1 g /L Sudan IV red under static groundwater flow conditions into the three coarse sand lenses shown on Figure 3.54. Total injected volume was 146mL. A summary of the individual injection volumes is presented in Table 3.30.

Table 3.30. Summary of PCE Injection Volumes in Selected Sand Lenses

| Location | PCE Volume (mL) | Approximate Lens Pore Volume (mL) | Estimated Initial Saturation | PCE Mass (g) |
|------------------|-----------------|-----------------------------------|------------------------------|--------------|
| Lens #1 (n=0.4) | 35.86 | 64 | 0.560 | 58.5 |
| Lens #2 (n=0.36) | 50.00 | 77.6 | 0.7644 | 97.9 |
| Lens #3 (n=0.33) | 60.01 | 108.8 | 0.552 | 81.56 |

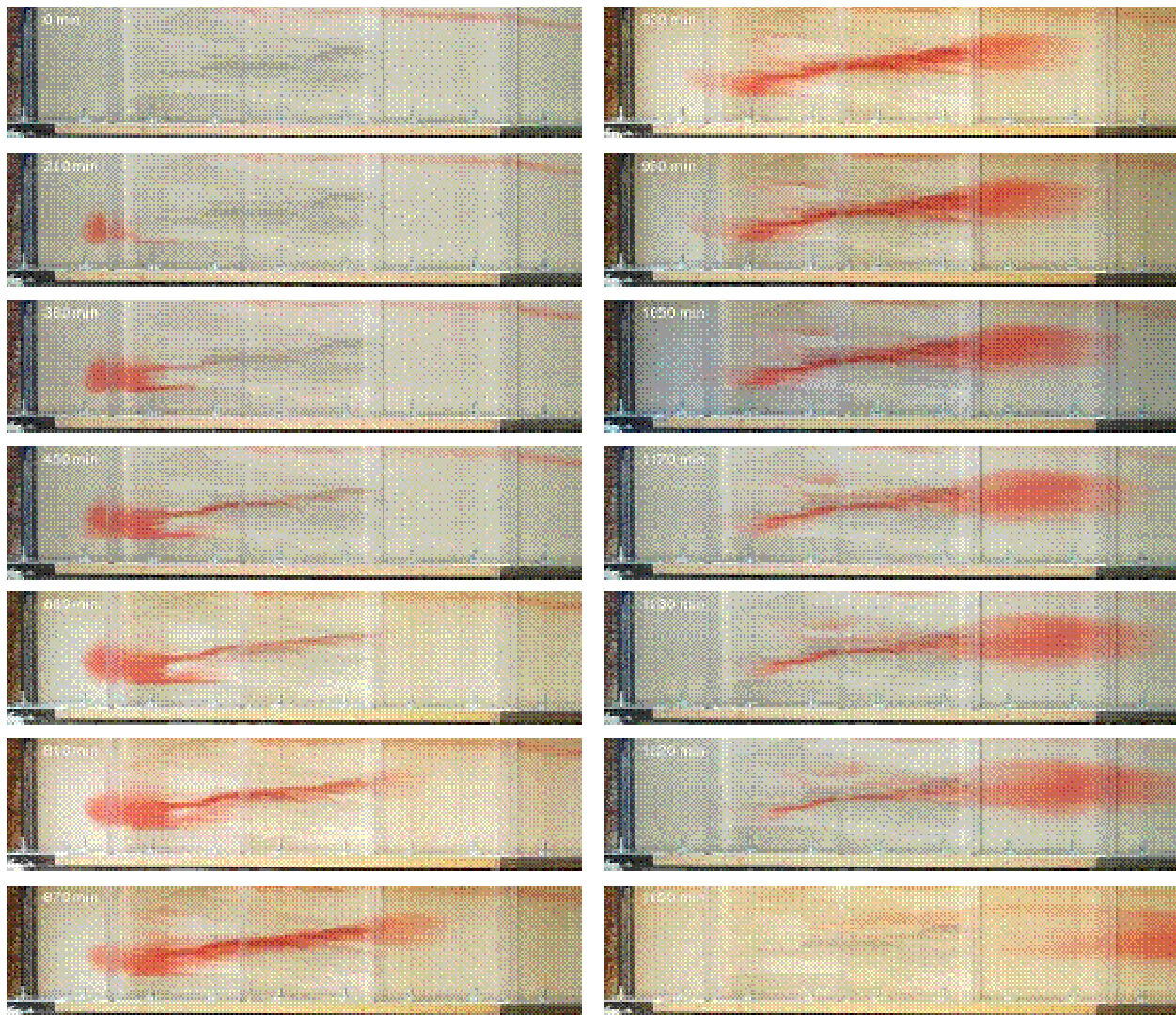


Figure 3.54. Flow of Dyed Water through the Heterogeneous Source, Surfactant-Enhanced Dissolution Experiment with Spatially Correlated Random Field

On completion of injection, the PCE was allowed to redistribute for 24 hours yielding the architecture shown in Figure 3.55. It is clear that the DNAPL had migrated into some of the surrounding coarse sands, either directly from the down gradient tip of a lens, or by fingering through the sand pore space within the tank interior. The final source zone occupied almost half of the tank depth, representing a significant distribution perpendicular to flow within this groundwater regime. However, the PCE morphology is generally at quite high initial saturations (Table 3.30) and comparable to pooled conditions.

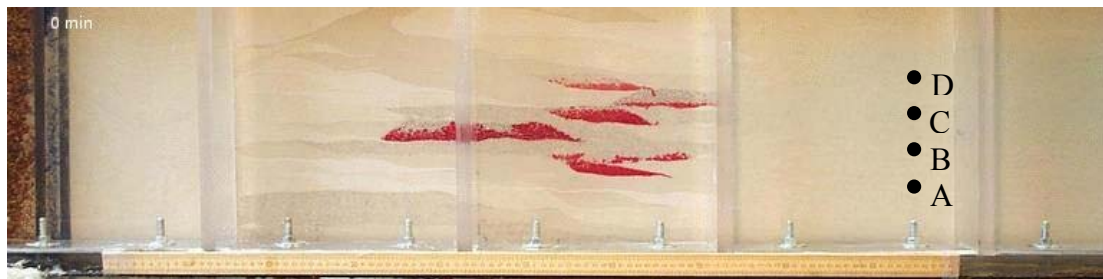


Figure 3.55. Final PCE Source Architecture, Surfactant-Enhanced Dissolution Experiment with Spatially Correlated Random Field (meter ruler at base for scale)

Constant head devices at the upgradient and down-gradient tank boundaries were adjusted to create a hydraulic gradient required for a groundwater flow rate of 10 mL/min. This value is equivalent to a linear Darcy velocity of 0.5 m/day and the rate of effluent discharge was periodically recorded to ensure that this flow velocity was maintained for the duration of the experiment.

To examine mass transfer from the heterogeneous PCE source zone prior to remediation, aqueous samples were collected at regular intervals for the duration of the experiment. Samples were collected at four sampling ports immediately downgradient of the source (labeled A-D in Figure 3.55) and a tap in the tank effluent connection. Results showed significant variation in aqueous phase PCE concentration with depth, reflecting the heterogeneous DNAPL distribution (Figure 3.56). Over a depth of 5cm, the peak PCE concentration changed from 16.16 mg/L (Port A) to 125.86 (Port B), and then decreased to 41.49 mg/L at the uppermost sampling location (Port D). However, all four plots display the same general trend of increasing concentrations in the early stages of dissolution with a degree of stability developing at later time. The data from sampling ports are useful for understanding the localized mass transfer and magnitude of local PCE concentration values, they only provide a part of the overall picture and relate to the source zone immediately up-gradient of the sampling points. Due to significant profile variation over short distances, some dissolution information for calculating mass flux and PCE removal rates were incomplete. The effluent sample may provide overall dissolution behavior of the source.

Figure 3.57a presents temporal variations in aqueous phase PCE concentrations leaving the test domain. The first contaminant mass was detected 1200 minutes after the initiation of groundwater flow conditions. Neglecting the limited dissolution and diffusion of PCE during the redistribution stage, this represents the time taken for contaminated water to travel the length of the tank. The aqueous PCE levels rose at a near constant rate until 3000 minutes, when a 'steady-state' condition was reached. After this time, the dissolution rate appeared to level off with

concentration fluctuating around 35 mg/L. The observed fluctuations at this stage were not unexpected. The tank had been filled in a heterogeneous manner and the various flow routes result in different travel lengths and dispersed arrival times at the effluent port located 1.5 m downstream.

If steady-state dissolution is occurring within the source zone, then the rate of contaminant mass removal should be constant. By multiplying the aqueous PCE concentrations by the effluent outflow rate and the time interval between samples, it is possible to find the cumulative mass of PCE removed under natural dissolution conditions. These data have been plotted in Figure 5-57b. Once again, this plot shows no mass removal before 1200 minutes, but from that point until 2950 minutes, the relationship between mass removed and time is non-linear. This is because the cumulative mass removed is increasing at an increasing rate and represents dissolution that occurs until a steady state is reached. From 3000 minutes onwards, the data are essentially linear with a constant rate of PCE removal from the source zone, justifying the previous steady-state assumption. The fitting of a linear equation to this data generates a very strong positive correlation, and the gradient is equivalent to the rate of PCE mass removal.

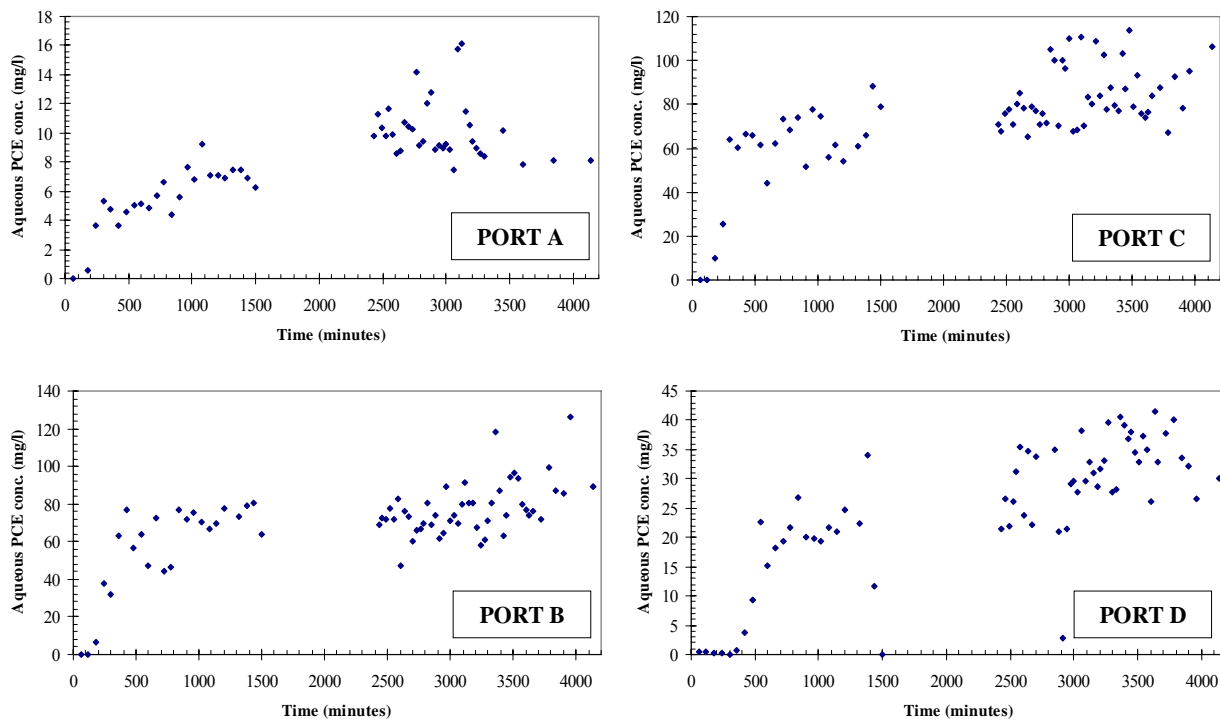


Figure 3.56. PCE Breakthrough Curves at Sampling Ports, Surfactant-Enhanced Dissolution Experiment with Spatially Correlated Random Field

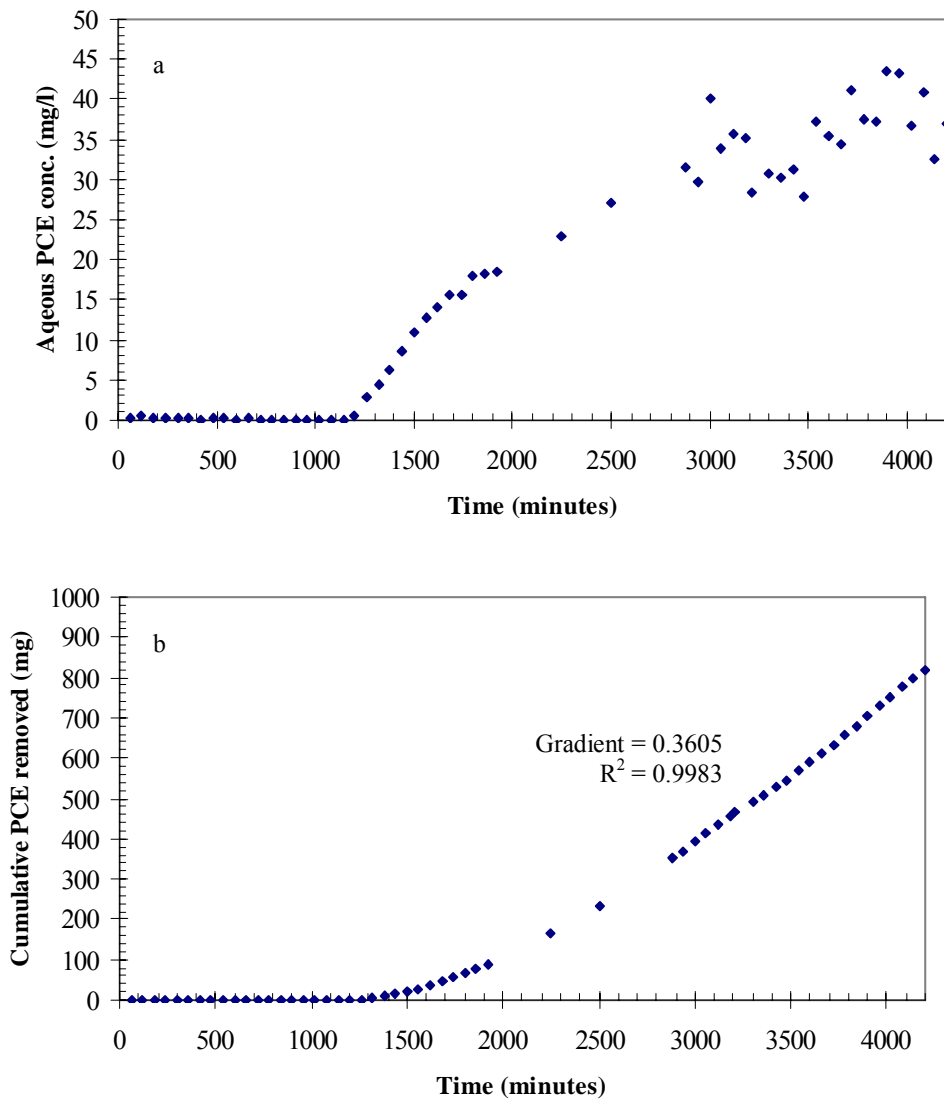


Figure 3.57. Steady-State Natural Dissolution, Surfactant-Enhanced Dissolution Experiment with Spatially Correlated Random Field: (a) Aqueous PCE Concentrations, (b) Cumulative Mass Removed Over the Same Time Period

Less than 1g of PCE had been removed by natural dissolution after 4500 minutes of dissolution (approximately three days). This occurred despite localized aqueous concentrations at the sampling ports exceeding 100mg/L. From the rate established in Figure 3.57, 457 days would be required for the entire PCE mass to be removed.

Surfactant enhanced removal of DNAPL can either mobilize DNAPL by preferentially reduce the interfacial tension or increase the solubility of the DNAPL, these two properties are intrinsically related and both processes were occurred in this test during surfactant injection.

Surfactant remediation began by injecting 4 L of an 8 percent solution of Aerosol-OT at 2.5 mL/min through the injection ports. Digital images of the source zone were taken at regular time intervals to record the changing source architecture. Selections of these images are presented in Figure 3.58 to illustrate the observed PCE remobilization.

The effect of the surfactant on PCE was significant and immediate. Substantial DNAPL mobilization occurred during the flushing period, and the resultant source zone architecture was very different from the initial situation. Induced PCE migration resulted from two distinct processes. Initially, as contact occurred between surfactant and DNAPL source, very rapid PCE mobilization was observed. Comparing the images taken at 200 and 210 minutes, some PCE fingered very rapidly into the finer sands upgradient of the initial source zone. This movement actually took place against the groundwater flow direction, and highlights the uncertainties associated with fingering, particularly in DNAPL modeling and migration prediction. By 240 minutes, additional vertical fingering had created a higher saturation pool at the base of the flow domain. As a consequence of this remobilization, the largest coarse sand lens had effectively been drained of PCE.

Although the properties of the Aerosol-OT surfactant preferentially promote PCE remobilization, a degree of increased dissolution will occur concurrently. To investigate the enhanced mass transfer that happened during (and after) surfactant flushing, aqueous samples were collected from Ports A-D and the tank effluent in a manner identical to that used during the previous natural dissolution assessment. These results and their implications are discussed next.

The aqueous phase PCE concentration profile from Port A (Figure 3.59) clearly displays evidence of the increased contaminant solubility associated with surfactant flushing. The mass of PCE per liter of water increased by two orders of magnitude and source zone mass transfer continued at this rate for almost 500 minutes. The PCE concentrations then begin to decline and after 5500 minutes were similar in magnitude to pre-remediation levels. This drop was due to changes in the source zone conditions. Prior to remediation, the PCE saturation was quite high upgradient of Port A and this limited dissolution. During flushing, the concentrations increased with the greater mass transfer rate while contaminant volume decreased greatly as a result of remobilization. After surfactant has flowed through the entire source zone, subsequent dissolution occurs from PCE entrapped in the pore spaces at residual conditions. Although a similar pattern is observed in the data from Port B and can be explained in a similar manner, it is interesting to note that the maximum concentration during flushing was recorded after only 270 minutes. This is considerably shorter than the 1470 minutes required at Port A, and is further evidence for the locally greater groundwater flow velocities through the coarsest sand lenses, with Port B located directly downgradient.

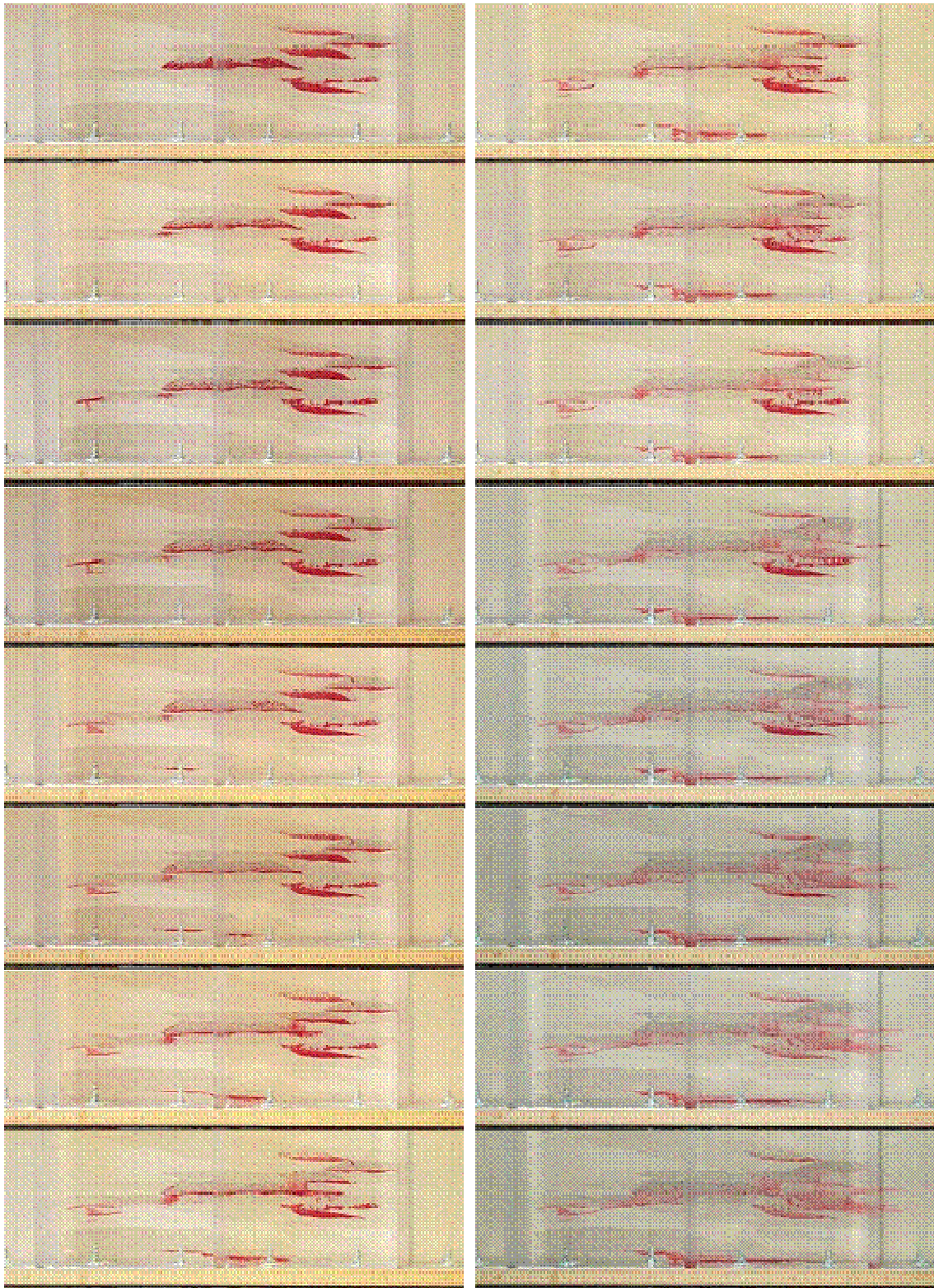


Figure 3.58. Changes in PCE Source Architecture During Surfactant Flushing, Surfactant-Enhanced Dissolution Experiment with Spatially Correlated Random Field

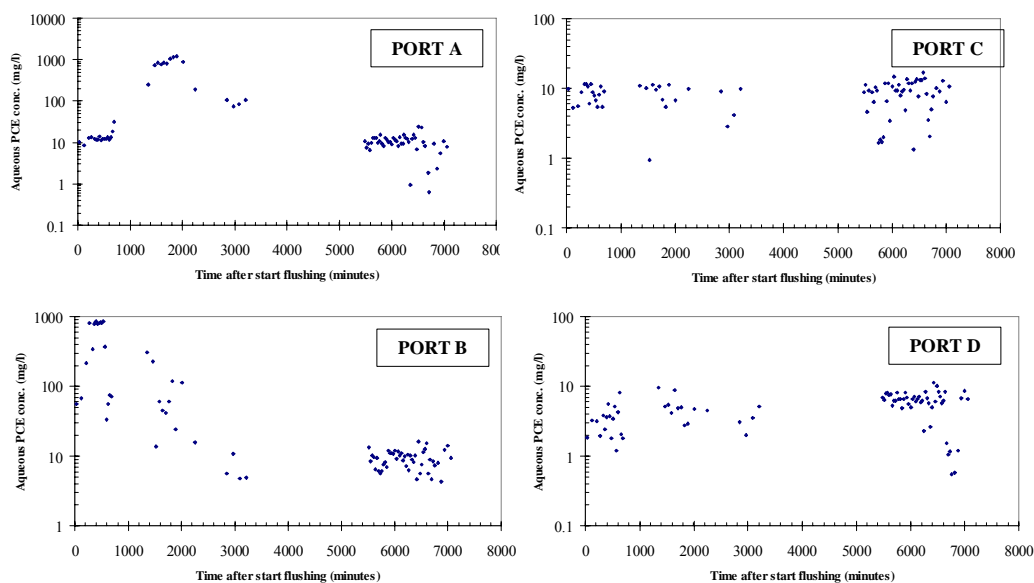


Figure 3.59. Aqueous-Phase PCE Concentrations as a Function of Time After Start of Surfactant Flushing, Surfactant-Enhanced Dissolution Experiment with Spatially Correlated Random Field

The data from Ports C and D are somewhat contrasting and surprising. There is no obvious peak in the concentrations recorded during flushing, and no significant differences exist between those and the levels measured 10 hours later. Examination of these data alone reveals no evidence of any surfactant flushing or associated increases in dissolution. In fact, it is only by comparing these values with the concentrations recorded at the same locations during the pre-flushing, steady state dissolution (Table 3.31) that the effects of remediation become apparent. The concentrations at Ports C and D during and after surfactant injection were less than pre-remediation values, considerably so in the case of Port C. This suggests that the PCE mobilized significantly faster than any enhanced mass transfer processes occurred. This could be misinterpreted as extreme contaminant removal, rather than remobilization, so care should be taken when interpreting field data from similar treatment processes. The average PCE concentration at Port D during post-surfactant water flushing was actually greater than the average during flushing, and this is most likely due to diffusion and the proximity of remobilized PCE that had pooled at the base of the flow domain.

Further evidence of enhanced PCE dissolution during surfactant flushing can be observed in the aqueous phase contaminant concentrations measured at the tank effluent. The PCE concentrations plotted in Figure 3.60 are representative of temporal variations in the mass transfer behavior of the entire source zone. The initial concentrations were of a similar order of magnitude to those recorded 14 hours previously and the actual values display much less scatter. Both of these observations support the assumption of steady-state dissolution within the source

zone, at least until the time of initial contact between PCE and surfactant. Elevated aqueous PCE concentrations were first detected at the effluent approximately 2250 minutes after the start of flushing, with values increasing by an order of magnitude from ~25 mg/L to 180 mg/L. Soil heterogeneity and associated differential localized flow velocities were responsible for different arrival times at the effluent port; hence the concentration breakthrough curve did not display a smooth peak. Although surfactant was only injected for 240 minutes, the elevated concentrations occurred over a 1000 minute time interval, reflecting dispersion and other flow-associated processes.

Table 3.31. Comparison of Steady State PCE Dissolution Concentrations, Surfactant-Enhanced Dissolution Experiment with Spatially Correlated Random Field

| Port | Range of PCE Concentrations (mg/L) | | |
|------|------------------------------------|--------------------|------------------|
| | Pre-Remediation | During Remediation | Post-Remediation |
| A | 12 – 16.16 | 950 – 1470 | 14 – 24.26 |
| B | 80 – 125.86 | 800 – 856.96 | 11 – 16.18 |
| C | 90 – 113.95 | 9 – 11.91 | 8 – 16.76 |
| D | 32 – 41.49 | 4 – 9.69 | 7 – 11.21 |

Once the enhanced PCE concentrations passed through the effluent port, subsequent data represents mass transfer occurring within and around the post-surfactant source zone architecture. The amount of DNAPL dissolved in the water fell below the pre-remediation level. From 5900 minutes to 7770 minutes, concentrations generally were 25 to 50 percent of pre-flushing data, and in subsequent daily samples fell further. After 11070 minutes (approximately 7.5 days), steady-state conditions appeared to have been re-established with an average PCE concentration is 0.8645 mg/L, significantly less than the equivalent pre-remediation value. This reduction was due predominantly to surfactant flushing. The contribution from enhanced dissolution and elevated mass removal was negligible. Rather, the contaminant remobilization highlighted in Figure 3.58 resulted in a source-zone architecture with DNAPL-water contact area that severely limited PCE mass transfer. However, despite the substantial reduction in aqueous phase PCE concentrations and mass flux leaving the source zone, a value of 0.8645 mg/L is still two orders of magnitude above the US EPA MCL for PCE.

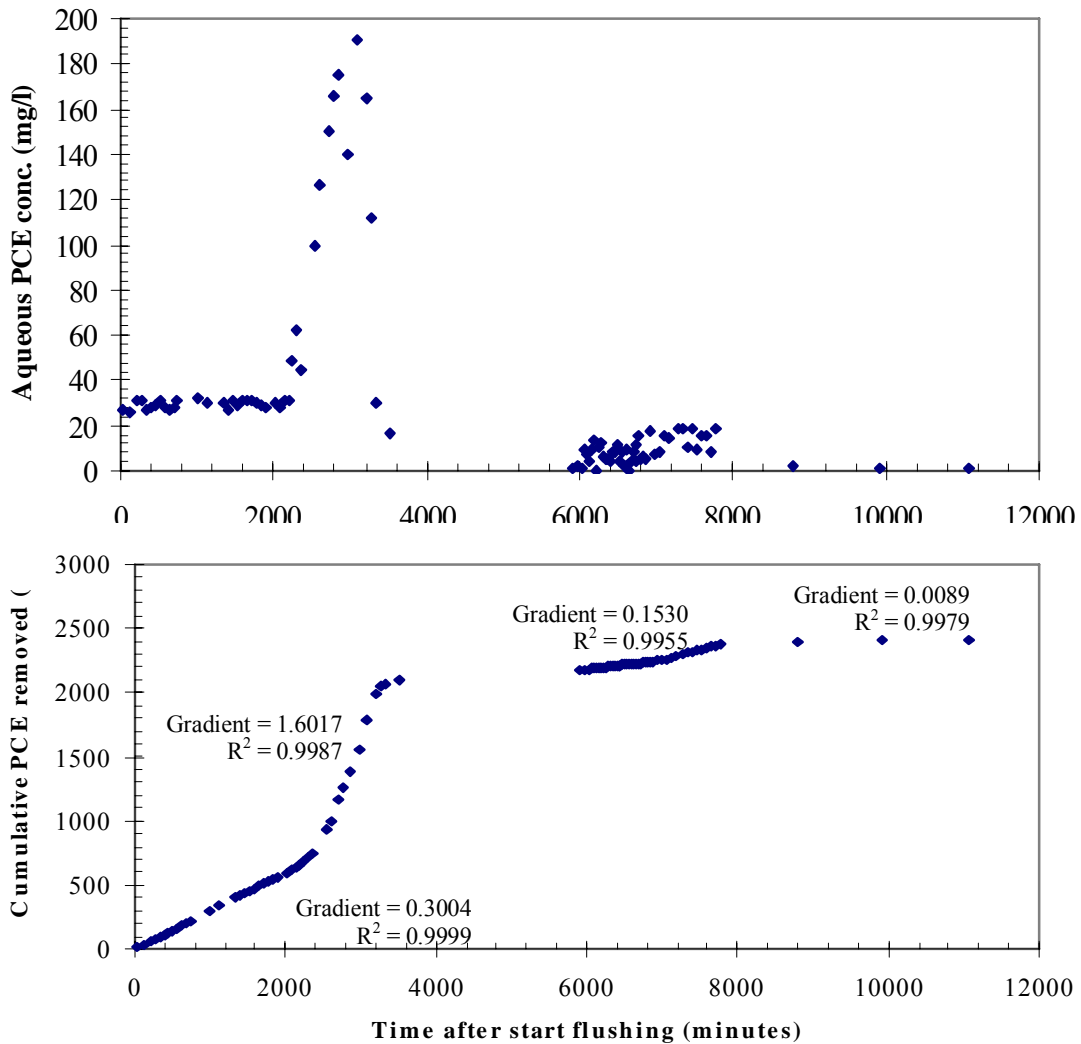


Figure 3.60. Effluent Aqueous PCE Concentrations During and After Surfactant Flushing (a) and Cumulative Mass Removed Over the Same Time Period (b), Surfactant-Enhanced Dissolution Experiment with Spatially Correlated Random Field

In Figure 3.60b, the cumulative mass of PCE removed from the source zone during and after flushing has been annotated with rates of contaminant mass removal. The changes in gradient of the graph can be used to define a number of ‘linear’ regions which are all related to source zone mass transfer processes. Initially, PCE mass was removed from the source zone under steady-state conditions and at a similar rate to that observed previously. This removal continued at a constant rate until the effects of surfactant flushing reached the effluent port. The result of surfactant flushing on PCE mass removal is illustrated by the large amount of PCE removed between 2190 and 2550 minutes. The gradient of the graph between these points is equivalent to a rate that is five times greater than the previous steady-state condition.

3.5.5 Large-tank experiment of surfactant-enhanced dissolution

The large-tank experiments of surfactant enhanced dissolution were conducted to determine if empirical estimates of mass transfer coefficients obtained from column and flow-cell experiments can be used to simulate SEAR at larger scales. The removal of entrapped PCE by SEAR also can result in changes in entrapment architecture. These changes can be used for validation of a concentration/flux matching technique for estimating DNAPL architecture, and validation of characterization methodologies based on partitioning tracers tests.

Large-tank experiments of surfactant-enhanced dissolution were conducted using the same tank as was used for large-tank experiments of natural dissolution (section 3.4.4). The experiments described here were conducted following natural dissolution tests. Surfactant-enhanced dissolution tests were conducted in tanks that had been packed to form complexly heterogeneous flow fields. The first experiment was designed with high aquifer heterogeneity (variance of $\ln K = 1.22$) and the second experiment was designed with low aquifer heterogeneity (variance of $\ln K = 0.25$). Detailed descriptions of design and packing procedures, flow system characterization, source creation and initial architecture, and natural dissolution tests are provided in Appendix 1 for the high heterogeneity experiment and in Appendix 2 for the low heterogeneity experiment.

The surfactant-dissolution experiment with high heterogeneity began by injecting a 50.0 g/L solution of Tween 80 into the test tank at the injection array of 32 ports for 10 hours. The aqueous samples were taken every two hours downgradient of the source at sampling arrays A and C. Plume concentration was monitored for four consecutive days. Figure 3.61 shows breakthrough curves of PCE concentration for monitored ports at arrays A and C. Figure 3.62 shows a vertical profile of PCE concentration in array A. The peak concentration of PCE was as high as 4000 mg/L, twenty times larger than the aqueous solubility limit during natural dissolution.

A gamma-ray attenuation scan was completed after surfactant injection to map changes in source zone architecture. Based on a mass balance calculation from both the effluent breakthrough curve and the gamma data, total PCE removal was found to be approximately 24 percent of the original spill mass.

The surfactant-dissolution experiment with low heterogeneity began by injecting a solution of 50.0 g/L Tween 80 through the tank at 57.0 ml/min for 11.75 hrs. Aqueous samples were taken every two hours at arrays A, C, and at effluent. Plume concentration was monitored for four consecutive days. The tank was then scanned by the gamma-ray attenuation system to map DNAPL distribution.

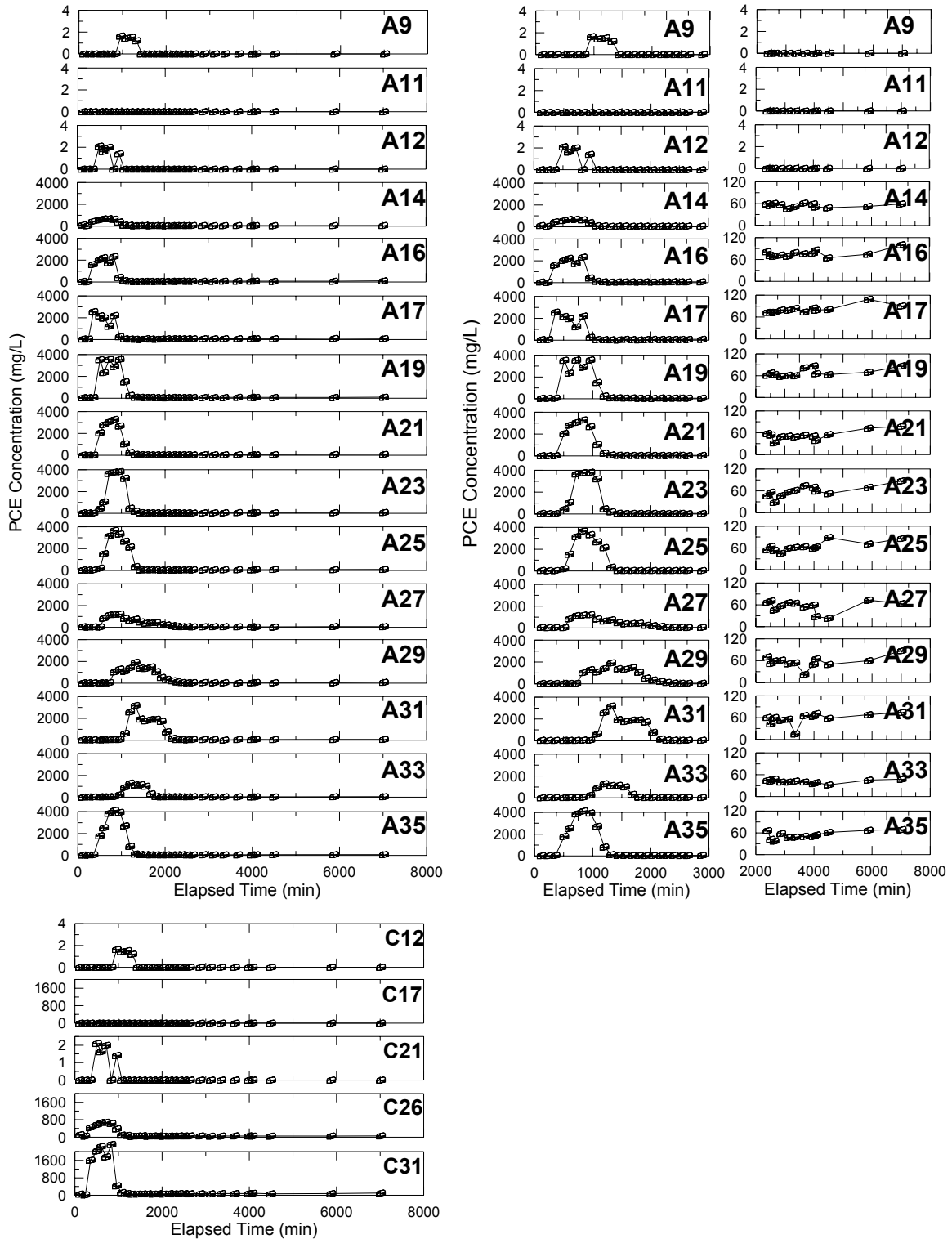


Figure 3.61. Breakthrough Curves Obtained from Large-Tank Experiment of Surfactant-Enhanced Dissolution, High Heterogeneity, Sampling Arrays A and C

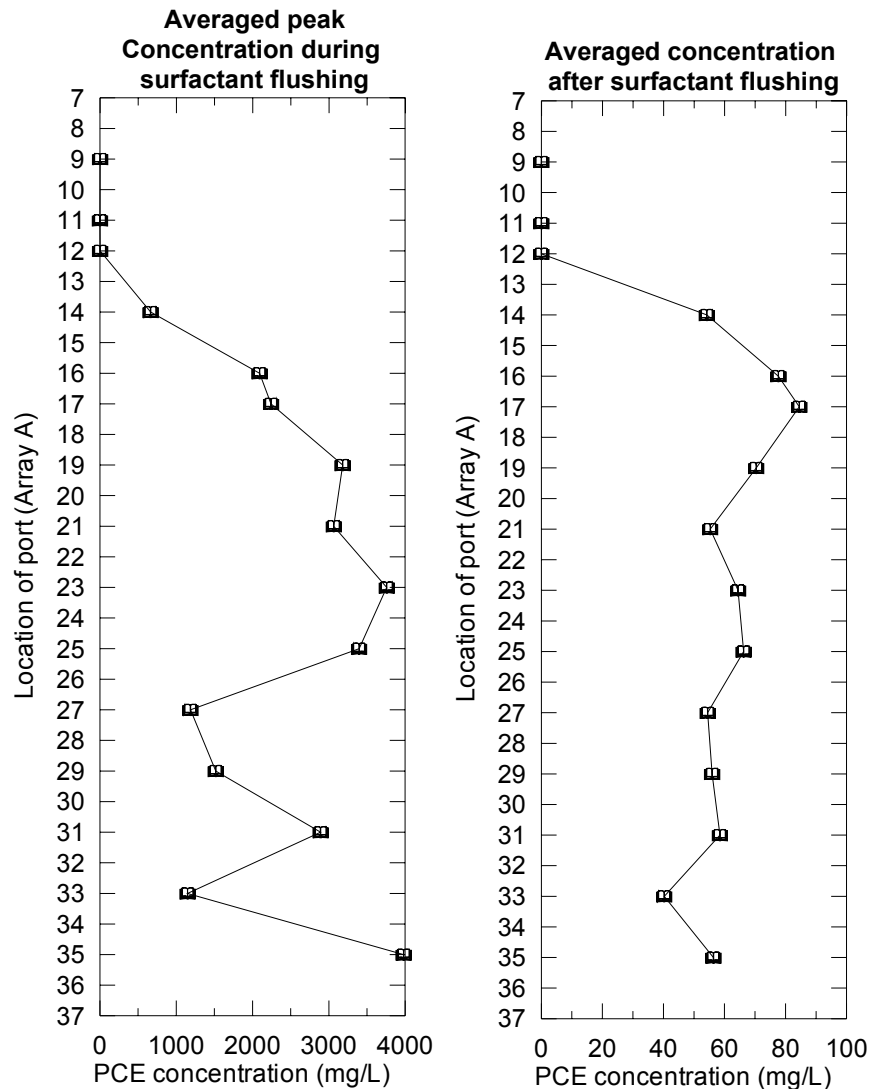


Figure 3.62. Vertical Profile of PCE Concentration at Sampling Array A during and after Surfactant Flushing, Large-Tank Experiment with High Heterogeneity

Figure 3.63 shows breakthrough curves of PCE concentration for monitored ports at arrays A, C, and at effluent. The peak concentration of PCE is as high as 7000 mg/l. The injected surfactants removed approximately 5 percent of the PCE mass predominantly from portions of the source zone where DNAPL was entrapped at residual saturation. This result was based on both visual observation and gamma data. No re-mobilization of PCE-DNAPL mass was observed during surfactant flushing. After surfactant flushing, steady-state effluent PCE concentrations were slightly higher than were observed before remediation. The steady state concentrations were below the solubility limit for PCE.

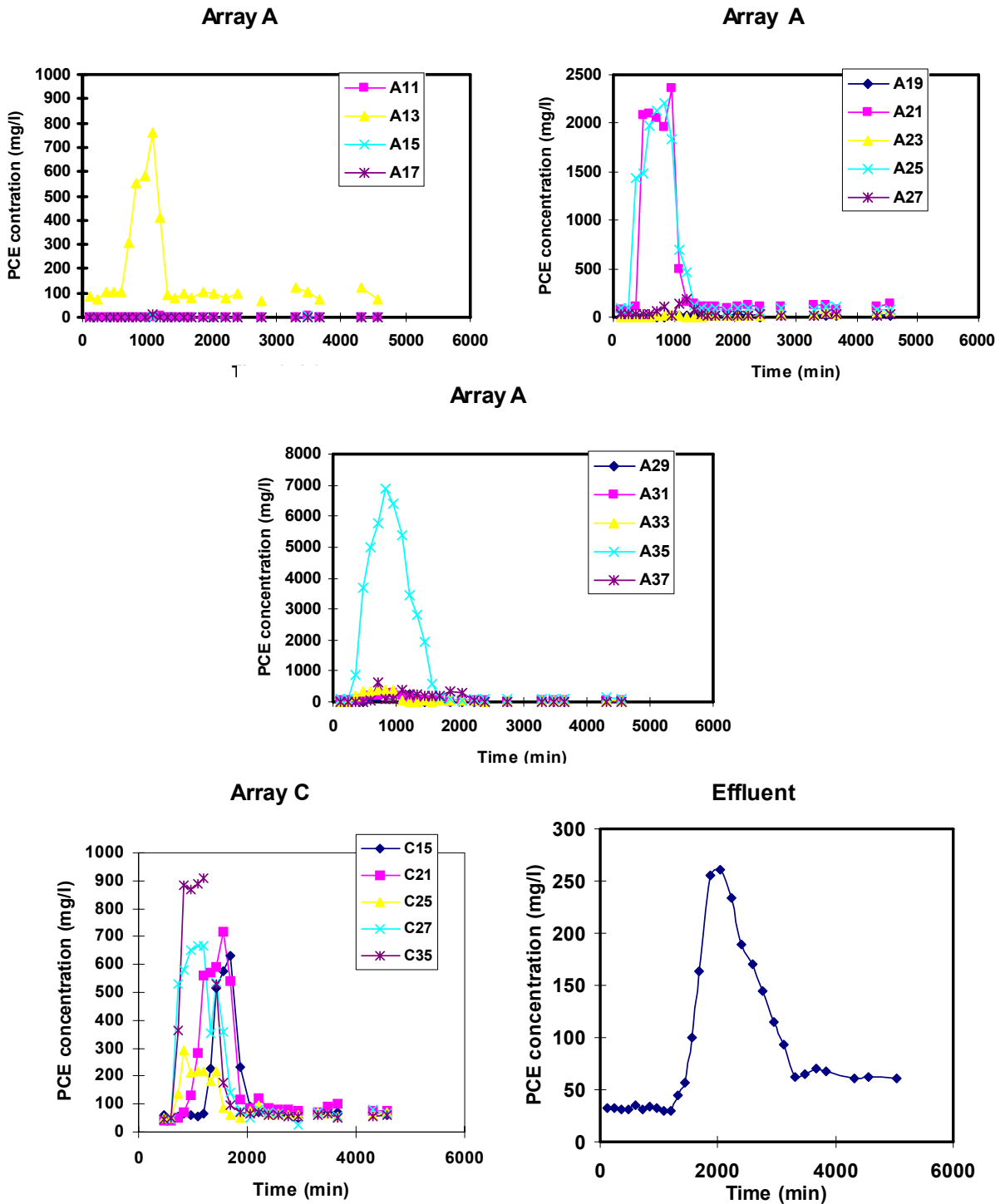


Figure 3.63. Breakthrough Curves for Large-Tank Experiment of Surfactant-Enhanced Dissolution, Low Heterogeneity, Sampling Arrays A and C, and Effluent

Once surfactant remediation ended, natural dissolution continued to be monitored. Monitoring was conducted for three hydraulic-gradient scenarios. Total head differences across

the tank for the three scenarios was 3.0 cm, 5.7 cm, and 8 cm. Figure 3.64 shows the PCE concentration distribution at array A measured before and after the SEAR during natural dissolution. This figure also shows the vertical PCE concentration at sampling array A during surfactant flushing.

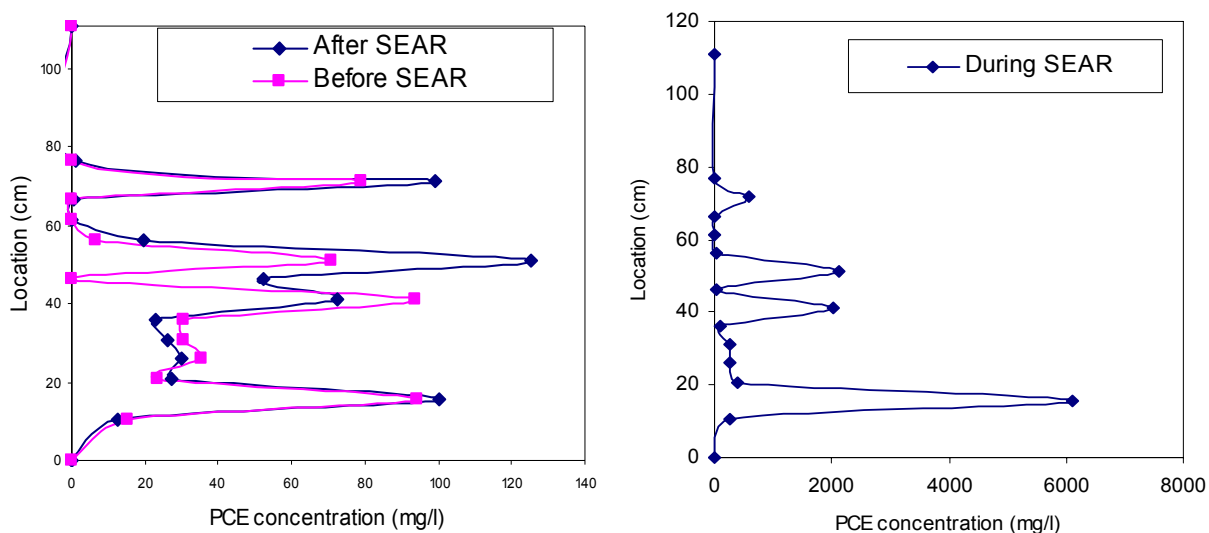


Figure 3.64. Vertical Profile of PCE Concentration at Array A Before, During and After Large-Tank Experiment of Surfactant-Enhanced Dissolution, Low Heterogeneity

3.6 Experimental design and methods for investigation of *in situ* chemical oxidation

In situ chemical oxidation (ISCO) experiments were conducted (1) to evaluate the effect of ISCO on DNAPL source depletion, (2) to evaluate the effect of source zone complexity on ISCO, and (3) to develop comprehensive experimental data sets that can be used for numerical model evaluation and/or validation. Experiments were conducted at a laboratory bench scale using custom-designed flow-through reactor, a two-dimensional intermediate scale using a large flow cell packed with discrete source zones, and a large two-dimensional tank packed with a complex heterogeneous source zone.

3.6.1 Flow-through reactor experiments

A series of bench-scale flow-through reactor (FTR) experiments were conducted to examine how ISCO impacts DNAPL mass transfer rates under various delivery conditions. This work was performed and reported in detail under SERDP project CU-1290. However, the experiments are summarized here because the results were used to design intermediate-scale ISCO tests described in this report. Refer to the CU-1290 report for greater detail on materials and methodology.

A full factorial design was used in the FTR experiments to test the effects of ISCO against three primary conditions (1) oxidant flushing velocity, (2) oxidant concentration, and (3) DNAPL type. Three oxidant flushing velocities, four oxidant concentrations, and two DNAPL chemicals were tested. All experiments within the factorial design were tested using DNAPL at residual saturation. Several additional experiments were conducted outside of the factorial design to evaluate the effect of large DNAPL ganglia instead of residual as well as to provide duplicate experiments for evaluation of experimental error. Table 3.32 describes specific conditions tested. Note that oxidant concentrations are reported as KMnO_4 .

The FTR vessels consisted of 18 in. long, 1/2 in. inner diameter glass tubing, equipped with five Mininert™ syringe valves (Figure 3.65). Two valves, located in the center of the tube, allowed for injection of DNAPL into the source zone. The other valves allowed for aqueous phase sampling up-gradient of the source zone, slightly down-gradient of the source, and farther down-gradient of the source. These sampling locations are labeled A, B and C, respectively. FTRs were wet-packed with a matrix that consists of inert glass beads, saturated with simulated groundwater (consisting of de-ionized water with a number of salts, metals, nitrate, and sulfate added) which was also used as the flow medium. Glass beads simulated the flow properties of a homogenous sandy media without introducing other media related interactions such as sorption or natural oxidant demand (NOD). The FTR packing consisted of course-grained DNAPL source zone (approximately 2.5cm long) in the center of the reactor, with fine-grained transport zones on either side of the source zone. The resulting capillary barrier between the two grain sizes retained DNAPL within the desired source zone. Near-residual DNAPL saturation was accomplished by saturating the source zone with DNAPL using a syringe and then withdrawing as much DNAPL as possible, without pulling water into the syringe. Alternately, large DNAPL ganglia sources were approximated by injection of a fixed quantity of DNAPL saturating the bottom portion of source zone.

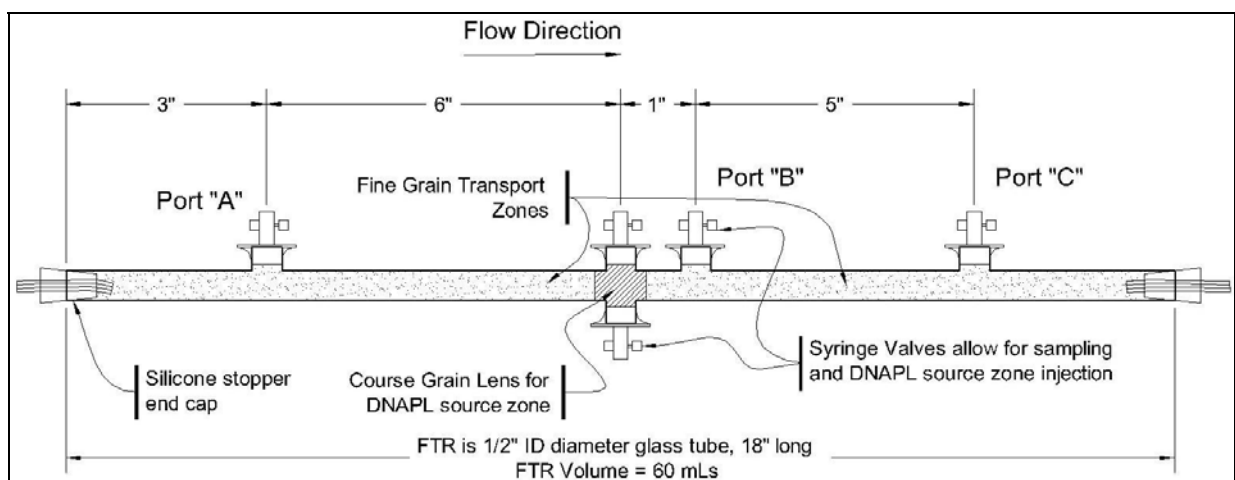


Figure 3.65. Schematic of Flow-Through Reactor Used in ISCO Experiments

Flow was provided to the FTR using a syringe pump for low flow rate experiments, or a peristaltic pump for medium and high flow rates. Flexible silicone tubing was used for all connections between the influent containers, pump, FTR, and constant head effluent device. All

influent solutions were degassed with a vacuum pump prior to introduction to the FTR, to avoid gas accumulation in the reactor.

Each FTR experiment included three phases following DNAPL emplacement: natural dissolution, oxidation, and post-oxidation dissolution. Flow rate was monitored during each experiment with effluent volume measurements. During each phase, samples were regularly withdrawn from ports A, B and C, as well as the effluent. Samples were analyzed by GC for aqueous contaminant, IC for chloride and organic acids (intermediary products of contaminant oxidation), by UV/Vis-Spec for permanganate, and pH. At the conclusion of the experiment, porous media was analyzed by ICP-AES for manganese oxide deposition within the FTR.

From each FTR experiment, chloride and aqueous contaminant concentrations were analyzed, to yield a mass flux of PCE from the FTR. Since this was a one-dimensional flow system, DNAPL mass flux was equivalent to DNAPL mass transfer. Chloride concentrations above background levels were used to determine the amount of contaminant oxidized based on a reaction stoichiometry of one mole of PCE completely oxidized to produce 4 moles of chloride. Temporal trends in aqueous contaminant and chloride concentrations were used along with the flow rate to produce a cumulative mass flux curve. Figure 3.66 is an example curve showing data for samples from ports B and C.

From the mass flux curves, it is possible to identify changes in the mass flux (and therefore mass transfer) rate for each of the phases of the experiment. A change in the rate of mass flux between different experimental phases appears as a change in the slope of the cumulative mass flux curve. A steeper slope means that DNAPL mass is being depleted more quickly, and a shallower slope indicates a slower mass depletion rate. The slope (β) of the cumulative mass flux curve during a particular phase is determined by linear regression. This β represents a quantifiable lumped rate of mass transfer in experimental system, having units of 1/time, similar to a first order rate coefficient. An example is shown in Figure 3.67. It should be noted that β values are specific to an experimental system, because they are dependent on the immeasurable DNAPL-water interfacial area. Separate β values are calculated for each experimental phase: β_{pre-ox} , β_{ox} and $\beta_{post-ox}$.

Table 3.32. FTR Experimental Conditions

| Experimental Conditions | | | | | | | |
|-------------------------|-------|---------------|-------------|------------|----------------------------|-----------------|---------|
| FTR | DNAPL | | | | Oxidant Conc. (mg/L) | Linear Velocity | |
| | Type | Geometry | Mass (g) | Saturation | | Range | (m/day) |
| 1 | TCE | residual | 0.365 | 16.5% | 100 | High | 16.63 |
| 2 | TCE | residual | 0.435 | 19.6% | 1000 | High | 18.01 |
| 3 | TCE | residual | 0.531 | 24.0% | 10000 | High | - |
| 4 | TCE | large ganglia | 0.231 | 10.4% | 1000 | High | 15.91 |
| 5 | TCE | large ganglia | 0.221 | 10.0% | 10000 | High | 14.86 |
| 6 | PCE | residual | 0.443 | 18.2% | 10000 | High | 16.64 |
| 7 | PCE | large ganglia | 0.326 | 13.3% | 1000 | High | 15.40 |
| 8 | PCE | residual | 0.348 | 14.3% | 1000 | High | 14.62 |
| 9 | PCE | large ganglia | 0.399 | 16.3% | 10000 | High | 14.50 |
| 10 | PCE | residual | 0.404 | 16.5% | 100 | High | 15.08 |
| 11 | TCE | residual | 0.353 | 15.9% | 100 | Medium | 1.17 |
| 12 | TCE | residual | 0.381 | 17.2% | 1000 | Medium | 1.42 |
| 13 | TCE | residual | 0.313 | 14.1% | 10000 | Medium | 1.31 |
| 14 | PCE | residual | 0.705 | 21.6% | 1000 | Medium | 1.04 |
| 15 | PCE | residual | 0.952 | 38.5% | 100 | Medium | 1.28 |
| 16 | TCE | residual | 0.347 | 15.7% | 100 | Low | 0.16 |
| 17 | TCE | residual | 0.453 | 20.5% | 1000 | Low | 0.16 |
| 18 | TCE | residual | 0.385 | 17.4% | 10000 | Low | 0.16 |
| 19 | TCE | residual | 0.325 | 14.7% | 1000 | Medium | 1.10 |
| 20 | PCE | residual | 0.521 | 21.4% | 10000 | Medium | 1.06 |
| 21 | PCE | residual | 0.482 | 19.8% | 100 | Low | 0.16 |
| 22 | PCE | residual | 0.515 | 21.2% | 1000 | Low | 0.16 |
| 23 | PCE | residual | 0.475 | 19.5% | 10000 | Low | 0.16 |
| 24 | TCE | residual | 0.387 | 17.5% | 10000 | Low | 0.16 |
| 25 | TCE | residual | 0.374 | 16.9% | 10000 | High | 17.24 |
| 26 | TCE | residual | 0.329 | 14.9% | 0 | Low | 0.16 |
| 27 | PCE | residual | 0.449 | 18.4% | 0 | Low | 0.16 |
| 28 | PCE | residual | 0.395 | 16.2% | 0 | Medium | 1.05 |
| 29 | TCE | residual | 0.599 | 22.0% | 0 | Medium | 0.98 |
| 30 | TCE | residual | 0.395 | 17.9% | 0 | Medium | 1.05 |
| 31 | TCE | residual | 0.321 | 14.5% | 0 | High | 14.78 |
| 32 | PCE | residual | 0.614 | 25.2% | 0 | High | 17.23 |

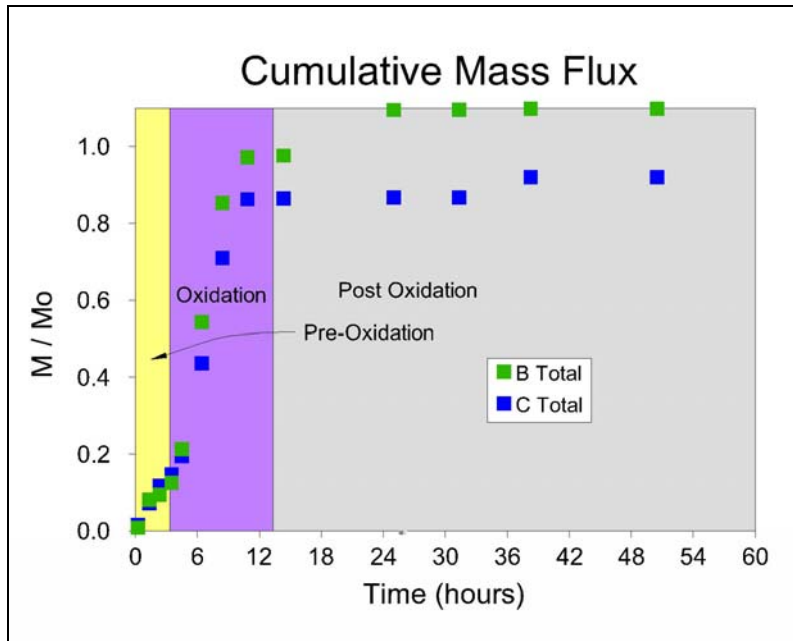


Figure 3.66. Example Cumulative Mass Flux Curve, FTR Experiments

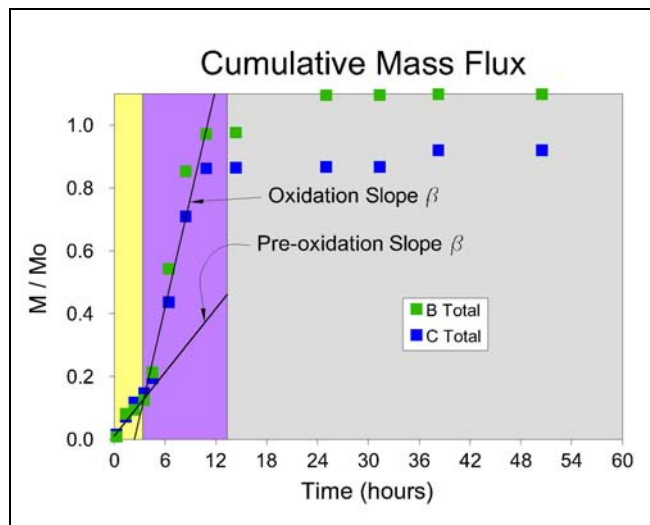


Figure 3.67. Example Mass Flux Slope Regions, FTR Experiments

In order to better compare systems to each other, the ratio of β values between experimental phases was considered. For example, the ratio of the oxidation phase slope (β_{ox}) to the pre-oxidation slope (β_{pre-ox}) indicates whether net DNAPL mass transfer was impacted by the presence of permanganate. This ratio is denoted as the oxidation slope ratio (SR_{ox}), which is given by equation 3.6. In some experiments, the DNAPL mass was substantially depleted prior

to completion of the oxidation flush resulting in the cumulative mass flux curve beginning to level off in the later stages of the oxidation phase as shown in Figure 3.67. Therefore, in computing the SR_{ox} , only those data points falling on the linear increasing portion of the curve are included in the regression. Similar to the oxidation slope ration, the post-oxidation slope ratio ($SR_{post-ox}$) is determined using equation 3.7. The post-oxidation slope ratio indicates whether source zone mass flux was decreased by ISCO, describing the effectiveness of ISCO. An oxidation or post-oxidation slope ratio greater than one indicates increased mass transfer within the system due to oxidation, during oxidation or following oxidation, respectively. Conversely, a value less than one suggests mass transfer was hindered or reduced. A slope ratio of one suggests no impact to mass transfer.

$$SR_{ox} = \frac{\beta_{ox}}{\beta_{pre-ox}} \quad (3.6)$$

$$SR_{post-ox} = \frac{\beta_{post-ox}}{\beta_{pre-ox}} \quad (3.7)$$

The primary advantage of the SR value is that it compares changes in mass flux rates within the same FTR system. The β value dependence on the interfacial surface area is effectively canceled out, as it impacts the rate regardless of the phase of the experiment. As such, SR values can be better compared between experiments in addition to indicating enhanced mass transfer.

Molar treatment efficiency (MTE) is the ratio of moles of contaminant destroyed to the molar amount of oxidant flushed through the system. It includes all permanganate that has been flushed into the reactor, thus including permanganate that may have passed through the source zone, but did not react. The MTE is expressed as a percentage of the theoretical reaction stoichiometry between contaminant and oxidant. The MTE is calculated using

$$MTE = \frac{\alpha_{DNAPL}}{\alpha_{ox}} \frac{n_{DNAPL,Cl}}{n_{ox}} \times 100\% \quad (3.8)$$

where, $n_{DNAPL,Cl}$ is the molar amount of DNAPL destroyed over the entire FTR trial, based on a chloride mass balance, n_{ox} is the molar amount of oxidant flushed through the FTR for each trial, α_{DNAPL} is the contaminant molar coefficient for the reaction with permanganate, and α_{ox} is the molar coefficient for the oxidant. The chloride mass balance is calculated as the value of chloride measured in the up-gradient sample relevant sample, with the background chloride value measured at sample port A subtracted out. For TCE, $\alpha_{DNAPL} = 1$ and $\alpha_{ox} = 2$, and for PCE, $\alpha_{DNAPL} = 3$ and $\alpha_{ox} = 4$. If reaction occurs exactly at the theoretical stoichiometric ratios, then the MTE will be 1.0 and the efficiency will be 100%. A higher MTE is desirable as less permanganate is required to destroy the DNAPL, indicating efficient flushing and use of oxidant.

The volumetric depletion efficiency (*VDE*) considers how much DNAPL is depleted from the system, relative to the total volume of solution flushed through the FTR and normalized by solubility limit of the DNAPL. Depletion of the DNAPL includes both oxidized contaminant present as chloride, as well as aqueous phase contaminant. *VDE* is important to consider, as conditions that result in the fastest mass transfer, highest enhancement, or best *MTE*, may still be disadvantageous from a flushing perspective. For example, since flushing large field sites may require large pumping systems and large volumes of flushing fluid, maximizing DNAPL depletion while minimizing flushing volume requirements may be desirable from a remediation standpoint. *VDE* is calculated from

$$VDE = \frac{m_{DNAPL \text{ removed}}}{Q \times t_{tot}} \times \frac{1}{C_{sat}} \quad (3.9)$$

where, $m_{DNAPL \text{ removed}}$ is the total mass of DNAPL removed from the FTR during each experimental phase, Q is the flow rate through the FTR, and t_{tot} is the total time duration of the experimental phase. The *VDE* can be calculated separately for each phase of the FTR trials and represents an average effluent concentration for each phase, normalized by the solubility limit of the DNAPL. A higher *VDE* is desirable as it will result in depletion of the DNAPL phase with lower flushing volumes.

Several experiments suffered data loss due to various malfunctions. For example, FTR3 experienced a pump head failure so that the precise flow rate is unknown. Another example is that port C of FTR10 and port B of FTR12 became plugged early in the experiment so aqueous samples could not be drawn. Despite these malfunctions, enough data remained so that all desired conditions were tested and a full factorial analysis was possible. Table 3.33 shows the β , *SR*, *MTE*, and *VDE* values calculated for the various phases, and sample ports B and C, as appropriate. A dash line for a particular value indicates that missing data due to a malfunction prevented calculation of that value. Gray cells indicate that no value was calculated since no oxidant was injected and the oxidation molar treatment efficiency is therefore undefined.

Results of this work confirm that oxidant delivery and DNAPL configuration conditions are important factors determining the affect oxidation has on mass transfer. The following discussion does not focus on result for individual sampling ports (B or C), since results for Ports B and C generally agree.

In the case of DNAPL present as large ganglia or pools, the DNAPL chemical was very important. Under the high oxidant delivery flow conditions tested, and considering oxidation slope ratio, molar treatment efficiency, and volumetric depletion efficiency, a high oxidant concentration provided the greatest increase in mass transfer during oxidation of PCE. However, with TCE as the DNAPL, a low oxidant concentration provided the greatest mass transfer increase during oxidation. However, to attain the greatest decrease in post-oxidation mass transfer, a low oxidant concentration would be optimum for PCE and a high oxidant concentration would be optimum for TCE.

For DNAPL present as near-residual saturation, the optimum oxidant delivery varied with DNAPL composition. The greatest increase in mass transfer during oxidation, indicated by large SR_{ox} , occurred with high oxidant concentration delivered at low to medium flow rates for PCE

and TCE as well as high flow rates for TCE. Generally, TCE had similar or greater increases in mass transfer during oxidation for all conditions; however, the greatest increase in mass transfer during oxidation was seen for PCE under high oxidant concentration delivered at low flow.

Just as with the large ganglia or pools, the optimum delivery conditions appeared to reverse when the goal was to decrease post-oxidation mass transfer rate, indicated by a $SR_{post-ox}$ much less than one. For low and medium flow oxidant delivery to PCE DNAPL and low flow delivery to TCE DNAPL, the post-oxidation mass transfer rate was nearly the same as the pre-oxidation rate regardless of oxidant concentration. However, the post-oxidation mass transfer rate dropped by about two orders of magnitude for high flow oxidant delivery to PCE, or medium and high flow oxidant delivery to TCE. This may be due to complete DNAPL removal by dissolution and oxidation at the higher flow rates and/or manganese oxide formation at the DNAPL-water interface.

3.6.2 Intermediate-scale experiments

Experiments to evaluate effects of ISCO on DNAPL depletion and mass transfer were conducted at a two-dimensional intermediate scale using a large flow cell packed with discrete source zones. Three initial experiments were conducted to examine interactions of PCE dissolution, aqueous PCE diffusion, permanganate diffusion, and oxidation by systematically adding each process to an otherwise duplicated system. A fourth experiment utilizing a number of sources was then completed. Only the final experiment is described in this report. Detailed descriptions of the three initial experiments are provided in Appendix A4.3 of the Ph.D. thesis of Heidersheidt (2005).

The initial experiments with a single source served to refine cell assembly and sampling protocols, as well as pointing out the value of using a larger, complex, constructed source zone for this research. These experiments also demonstrated the need to have tapered ends on the sources to prevent abrupt hydraulic conductivity changes resulting in significant vertical flow. The first experiment involved dissolution of a small PCE DNAPL residual zone overlying a pool. The second experiment duplicated the DNAPL source configuration, but added a layer of low permeability material (LPM) beneath the source to look at diffusion of aqueous PCE into the LPM. The third experiment used the source zone that remained at the end of the second experiment and involved flushing the flow cell with permanganate after residual PCE DNAPL was depleted.

Intermediate-scale experiments with ISCO were conducted in a two-dimensional flow cell ($L \times W \times H = 243.5\text{cm} \times 8.0\text{cm} \times 45.5\text{cm}$) that was constructed of clear acrylic, with 1.5mm diameter sampling ports distributed throughout the cell. The cell included influent and effluent end wells filled with clean pea gravel to promote mixing. Figure 3.68a shows a photo of the packed cell and Figure 3.68b shows a diagram labeling sources and sampling locations. A peristaltic pump was used to provide a constant flow rate of tap water into the cell after passing through sediment and carbon filters and a vacuum de-gassing system. A constant head reservoir was connected to the outlet of the cell. Analytical grade PCE (>99% purity) dyed with Sudan IV hydrophobic organic red dye was used as the DNAPL. Technical grade potassium permanganate was used as the oxidant.

Table 3.33. FTR Experimental Results

| FTR | Experimental Conditions | | | β | | | | | | SR | | | | MTE | | VDE | | | | | | | | |
|-----|-------------------------|---------------|----------------------|----------------|------------------|------------------|-------------------|------------------|------------------|-------------------|------------------|------------------|--------|--------|--------|--------|-------------------|---------------|---------------|----------------|--------|------|---------|--------|
| | DNAPL | | Oxidant Conc. (mg/L) | Velocity Range | Port B | | Port C | | Port B | | Port C | | Port B | Port C | Port B | Port C | Port B | | Port C | | Port B | | Port C | |
| | Type | Geometry | | | β_{pre-ox} | $\beta_{ox,max}$ | $\beta_{post-ox}$ | β_{pre-ox} | $\beta_{ox,max}$ | $\beta_{post-ox}$ | β_{pre-ox} | $\beta_{ox,max}$ | | | | | $\beta_{post-ox}$ | SR_{pre-ox} | $SR_{ox,max}$ | $SR_{post-ox}$ | Pre-ox | Ox | Post-ox | Pre-ox |
| 27 | PCE | residual | 0 | Low | 0.004 | 0.003 | 0.003 | 0.003 | 0.003 | 0.003 | 0.003 | 0.90 | 0.92 | 0.99 | | 0.79 | 0.79 | 0.90 | 0.77 | 0.86 | 0.90 | 0.77 | 0.86 | 0.90 |
| 21 | PCE | residual | 100 | Low | 0.003 | 0.005 | 0.004 | 0.003 | 0.004 | 0.003 | 1.36 | 1.12 | 1.066 | 1.947 | 1.00 | 1.293 | 1.13 | 0.93 | 1.171 | 0.65 | 1.171 | 0.93 | 1.171 | 0.65 |
| 22 | PCE | residual | 1000 | Low | 0.003 | 0.015 | 0.004 | 0.003 | 0.011 | 0.004 | 4.69 | 3.58 | 1.263 | 1.442 | 1.08 | 4.133 | 1.35 | 0.95 | 3.411 | 0.79 | 3.411 | 0.95 | 3.411 | 0.79 |
| 23 | PCE | residual | 10000 | Low | 0.003 | 0.064 | 0.003 | 0.003 | 0.044 | 0.003 | 18.40 | 12.81 | 1.015 | 0.590 | 0.99 | 12.999 | 0.83 | 1.01 | 12.192 | 0.66 | 12.192 | 0.83 | 1.01 | 0.66 |
| 15 | PCE | residual | 0 | Medium | 0.027 | 0.029 | 0.026 | 0.022 | 0.029 | 0.024 | 1.07 | 0.98 | 1.11 | | 0.98 | 0.93 | 0.95 | 0.82 | 0.98 | 0.83 | 0.98 | 0.82 | 0.98 | 0.83 |
| 14 | PCE | residual | 100 | Medium | 0.009 | 0.008 | 0.006 | 0.010 | 0.009 | 0.007 | 0.88 | 0.655 | 0.700 | 0.052 | 0.65 | 0.502 | 0.40 | 0.71 | 0.612 | 0.48 | 0.612 | 0.71 | 0.612 | 0.48 |
| 14 | PCE | residual | 1000 | Medium | 0.015 | 0.020 | 0.014 | 0.013 | 0.019 | 0.014 | 1.30 | 0.942 | 1.43 | 0.244 | 0.95 | 1.149 | 0.91 | 0.90 | 1.086 | 0.91 | 1.086 | 0.90 | 1.086 | 0.91 |
| 20 | PCE | residual | 10000 | Medium | 0.024 | 0.100 | 0.022 | 0.022 | 0.074 | 0.021 | 4.11 | 0.894 | 3.41 | 0.974 | 1.13 | 4.423 | 1.02 | 0.94 | 3.095 | 0.99 | 3.095 | 0.94 | 3.095 | 0.99 |
| 32 | PCE | residual | 0 | High | 0.246 | 0.265 | 0.273 | 0.265 | 0.259 | 0.246 | 1.08 | 1.11 | 0.93 | | 0.82 | 0.89 | 0.92 | 0.90 | 0.86 | 0.83 | 0.86 | 0.90 | 0.86 | 0.83 |
| 10 | PCE | residual | 100 | High | 0.156 | 0.314 | 0.001 | - | - | - | 2.01 | 0.007 | - | 0.013 | 0.40 | 0.251 | 0.00 | - | - | - | - | - | - | - |
| 8 | PCE | residual | 1000 | High | 0.171 | 0.370 | 0.003 | 0.152 | 0.255 | 0.002 | 2.16 | 0.017 | 1.68 | 0.006 | 0.40 | 0.349 | 0.01 | 0.37 | 0.247 | 0.01 | 0.247 | 0.37 | 0.247 | 0.01 |
| 6 | PCE | residual | 10000 | High | 0.142 | 0.075 | 0.013 | 0.128 | 0.049 | 0.002 | 0.53 | 0.093 | 0.38 | 0.006 | 0.36 | 0.143 | 0.04 | 0.33 | 0.091 | 0.01 | 0.091 | 0.33 | 0.091 | 0.01 |
| 7 | PCE | large ganglia | 1000 | High | 0.224 | 0.260 | 0.015 | 0.217 | 0.168 | 0.023 | 1.16 | 0.066 | 0.77 | 0.105 | 0.48 | 0.195 | 0.03 | 0.41 | 0.148 | 0.05 | 0.148 | 0.41 | 0.148 | 0.05 |
| 9 | PCE | large ganglia | 10000 | High | 0.092 | 0.214 | 0.182 | 0.142 | 0.164 | 0.180 | 2.31 | 1.972 | 1.15 | 1.266 | 0.23 | 0.587 | 0.48 | 0.34 | 0.406 | 0.47 | 0.406 | 0.34 | 0.406 | 0.47 |
| 26 | TCE | residual | 0 | Low | 0.029 | 0.027 | 0.028 | 0.027 | 0.030 | 0.027 | 0.92 | 0.95 | 1.00 | | 0.84 | 0.72 | 0.80 | 0.64 | 0.79 | 0.79 | 0.79 | 0.64 | 0.79 | 0.79 |
| 16 | TCE | residual | 100 | Low | 0.028 | 0.031 | 0.031 | 0.026 | 0.028 | 0.027 | 1.10 | 1.093 | 1.08 | 1.557 | 0.85 | 0.733 | 0.91 | 0.74 | 0.797 | 0.70 | 0.797 | 0.74 | 0.797 | 0.70 |
| 17 | TCE | residual | 1000 | Low | 0.021 | 0.029 | 0.023 | 0.021 | 0.028 | 0.024 | 1.41 | 1.113 | 1.33 | 1.164 | 0.82 | 0.992 | 0.91 | 0.77 | 1.042 | 0.77 | 1.042 | 0.77 | 1.042 | 0.77 |
| 18 | TCE | residual | 10000 | Low | 0.025 | 0.136 | 0.003 | 0.023 | 0.066 | 0.003 | 5.46 | 0.111 | 2.81 | 0.119 | 0.78 | 1.576 | 0.11 | 0.71 | 1.319 | 0.09 | 1.319 | 0.71 | 1.319 | 0.09 |
| 24 | TCE | residual | 10000 | Low | 0.025 | 0.232 | 0.022 | 0.024 | 0.148 | 0.023 | 9.23 | 0.884 | 6.17 | 0.964 | 0.88 | 5.502 | 0.73 | 0.81 | 4.135 | 0.51 | 4.135 | 0.81 | 4.135 | 0.51 |
| 29 | TCE | residual | 0 | Medium | 0.090 | 0.125 | 0.080 | 0.098 | 0.098 | 0.071 | 1.39 | 0.89 | 1.01 | 0.72 | 0.76 | 0.83 | 0.68 | 0.81 | 0.69 | 0.59 | 0.69 | 0.81 | 0.69 | 0.59 |
| 30 | TCE | residual | 100 | Medium | - | - | - | - | - | - | - | - | - | - | - | - | - | - | - | - | - | - | - | - |
| 11 | TCE | residual | 1000 | Medium | 0.211 | 0.201 | 0.054 | 0.188 | 0.161 | 0.058 | 0.95 | 0.257 | 0.85 | 0.308 | 0.85 | 0.497 | 0.23 | 0.79 | 0.445 | 0.24 | 0.445 | 0.79 | 0.445 | 0.24 |
| 12 | TCE | residual | 10000 | Medium | - | - | - | 0.241 | 0.385 | 0.004 | - | - | 1.59 | 0.015 | - | - | 0.65 | 0.355 | 0.01 | - | 0.355 | 0.65 | 0.355 | 0.01 |
| 19 | TCE | residual | 10000 | Medium | 0.228 | 0.224 | 0.002 | 0.206 | 0.135 | 0.001 | 0.98 | 0.008 | 0.65 | 0.004 | 0.91 | 0.587 | 0.01 | 0.83 | 0.379 | 0.00 | 0.379 | 0.83 | 0.379 | 0.00 |
| 13 | TCE | residual | 10000 | Medium | 0.236 | 2.903 | 0.001 | 0.190 | 1.384 | 0.001 | 12.30 | 0.005 | 7.27 | 0.005 | 0.78 | 0.912 | 0.00 | 0.61 | 0.600 | 0.00 | 0.600 | 0.61 | 0.600 | 0.00 |
| 31 | TCE | residual | 0 | High | 1.551 | 1.686 | 0.340 | 1.605 | 0.999 | 0.439 | 1.09 | 0.22 | 0.62 | 0.27 | 0.47 | 0.41 | 0.10 | 0.47 | 0.26 | 0.12 | 0.26 | 0.47 | 0.26 | 0.12 |
| 1 | TCE | residual | 100 | High | 2.421 | 2.020 | 0.010 | 2.501 | 2.212 | 0.017 | 0.83 | 0.004 | 0.88 | 0.007 | 0.72 | 0.229 | 0.00 | 0.71 | 0.242 | 0.01 | 0.242 | 0.71 | 0.242 | 0.01 |
| 2 | TCE | residual | 1000 | High | 1.609 | 2.805 | 0.003 | 1.429 | 1.522 | 0.004 | 1.74 | 0.002 | 1.06 | 0.003 | 0.53 | 0.522 | 0.00 | 0.48 | 0.287 | 0.00 | 0.287 | 0.48 | 0.287 | 0.00 |
| 3 | TCE | residual | 10000 | High | - | - | - | - | - | - | - | - | - | - | - | - | - | - | - | - | - | - | - | - |
| 25 | TCE | residual | 10000 | High | 2.583 | 11.932 | 0.035 | 2.483 | 12.300 | 0.036 | 4.62 | 0.014 | 4.95 | 0.014 | 0.76 | 1.267 | 0.01 | 0.72 | 1.085 | 0.01 | 1.085 | 0.72 | 1.085 | 0.01 |
| 4 | TCE | large ganglia | 1000 | High | 0.808 | 3.524 | 0.053 | 0.980 | 2.677 | 0.025 | 4.36 | 0.065 | 2.73 | 0.025 | 0.16 | 0.320 | 0.01 | 0.19 | 0.255 | 0.00 | 0.255 | 0.19 | 0.255 | 0.00 |
| 5 | TCE | large ganglia | 10000 | High | 1.455 | 1.002 | 0.009 | 1.186 | 0.534 | 0.004 | 0.69 | 0.006 | 0.45 | 0.003 | 0.29 | 0.087 | 0.00 | 0.22 | 0.047 | 0.00 | 0.047 | 0.22 | 0.047 | 0.00 |

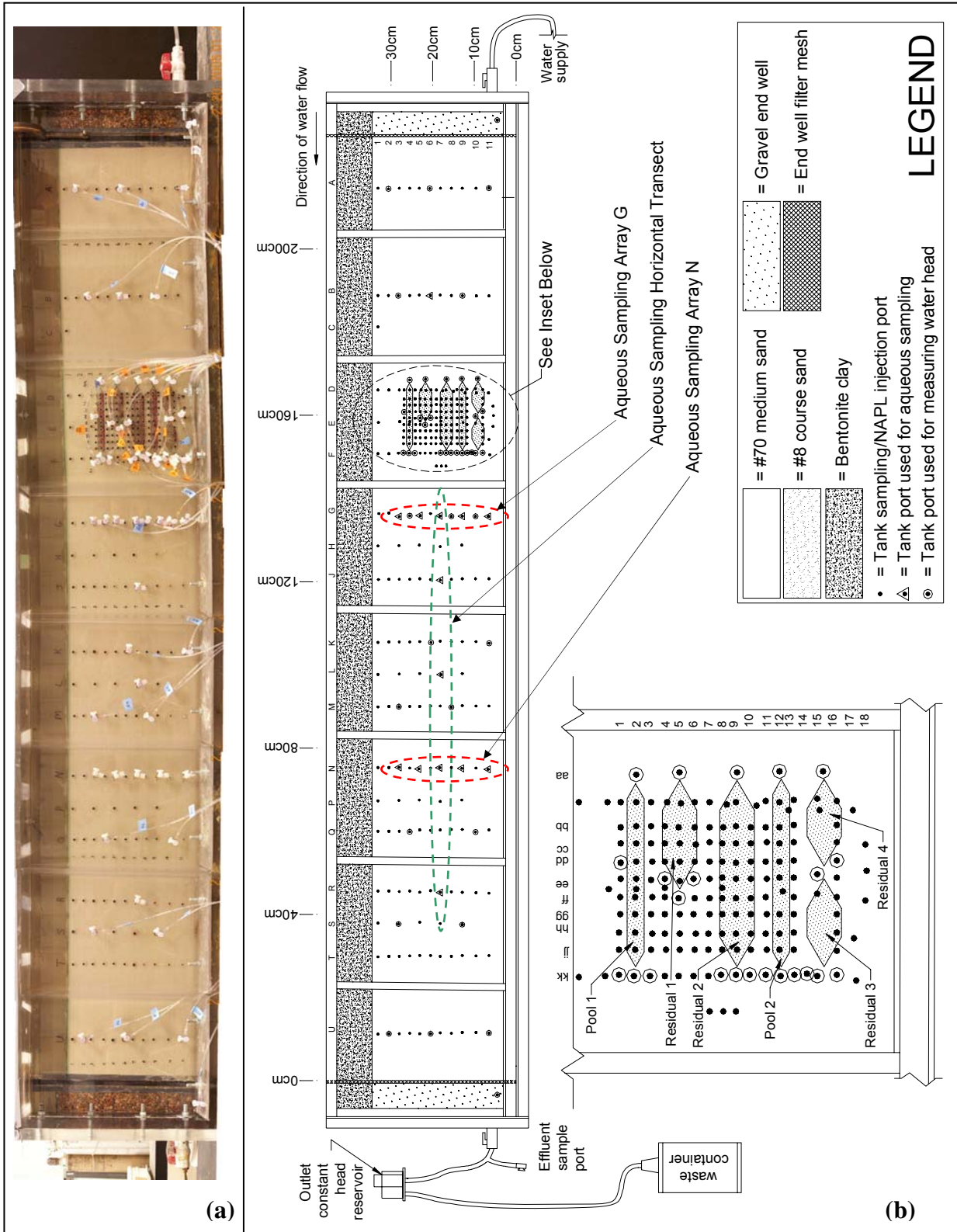


Figure 3.68. (a) Photo and (b) Diagram of Intermediate-Scale Cell for ISCO Experiments

Flow through the cell was maintained during the experiment at 14.6mL/min providing a Darcy velocity of 77.14cm/day. This Darcy velocity was chosen to represent the flow that might be expected near the center of a source zone, halfway between an injection and extraction well. The selected velocity could also represent ambient groundwater flow conditions in an aquifer with a moderately fast flow rate. At this flow rate it took about 29 hours for fluid to transit the cell. Flow rate through the cell was monitored at least daily by weighing the cell effluent volume generated over a period of at least 30 minutes.

The cell was wet-packed by hand to prevent air entrapment, clean #70 silica sand to an approximate bulk density of 1510mg/mL, except for the DNAPL source cells. Each source lens was wet-packed with clean #8 silica sand to an approximate bulk density of 1570mg/mL. The packed cell had a porosity of 0.41. The fine-grained sand surrounding the coarse-grained source lens creates a capillary barrier to keep the PCE DNAPL within the well-defined source lens. After packing the cell, it was flushed with water for five days before PCE emplacement, to ensure removal of fines or air bubbles that may have been trapped despite wet-packing. During this period, a dye tracer test was performed, injecting water with red food dye into the inlet to visually determine that the flow front of injected dye was uniform from the cell bottom to top, and that flow accessed all areas of the cell from inlet to outlet. The test verified there were no preferential flow paths or stagnant zones. Following the dye tracer test, no residual dye was visible in the cell; however, any remaining was expected to have no impact on the subsequent oxidant injection based on batch studies by Dugan (personal communication, Jan 2005)

The source zone consisted of six different discrete sources—two configured as pools and four at near-residual saturation. The layout of the sources (Figure 3.69 and inset of Figure 3.68b) was chosen so that oxidation of DNAPL sources under a variety of conditions could be investigated. Specifically, pool 1 and residual 1 were expected to be mostly unaffected by each other or any other source. Residual 2 and pool 2 were expected to show the interaction of a residual source overlying a pool. Residuals 3 and 4 were expected to show the interaction that occurs as oxidant passes through successive residual sources. Table 3.34 describes each source. The ganglia-to-pool (GTP) ratio describes the architecture of the source. It is a ratio of the mass of DNAPL present at less than residual saturation to the mass present at residual or greater saturation (Lemke et al. 2004). This ratio was estimated visually because no method to directly measure the DNAPL distribution was available. PCE emplacement was performed by slowly injecting PCE into each source near the bottom, until the coarse-grained lens was nearly full without breaching the capillary barrier. Next, PCE was slowly withdrawn from the four residual sources until no more PCE could be removed.

Following PCE emplacement, the experiment commenced with eight days of natural dissolution. On the second day of the natural dissolution phase, a transient conservative tracer test using bromide (200.0mg/L as Br⁻) was performed by changing the influent to a solution containing sodium bromide for one hour. The natural dissolution phase was followed by two and a half days of oxidant flushing with potassium permanganate (2120mg/L as MnO₄⁻). The mass of oxidant added was deliberately less than needed to destroy all the PCE because the goal was to destroy enough PCE and generate enough MnO₂(s) to result in measurable changes in permeability and mass depletion rates, while leaving enough DNAPL PCE so that post-oxidation dissolution could be compared to pre-oxidation. Following the oxidant flush, the post-oxidation dissolution phase began and continued for another eleven days. Following the experiment, flow was maintained at a reduced rate for another 19 days until cell shutdown and soil coring, with

effluent samples taken and flow rate measured every several days to track continued dissolution. Table 3.35 summarizes the chronology of the experiment.

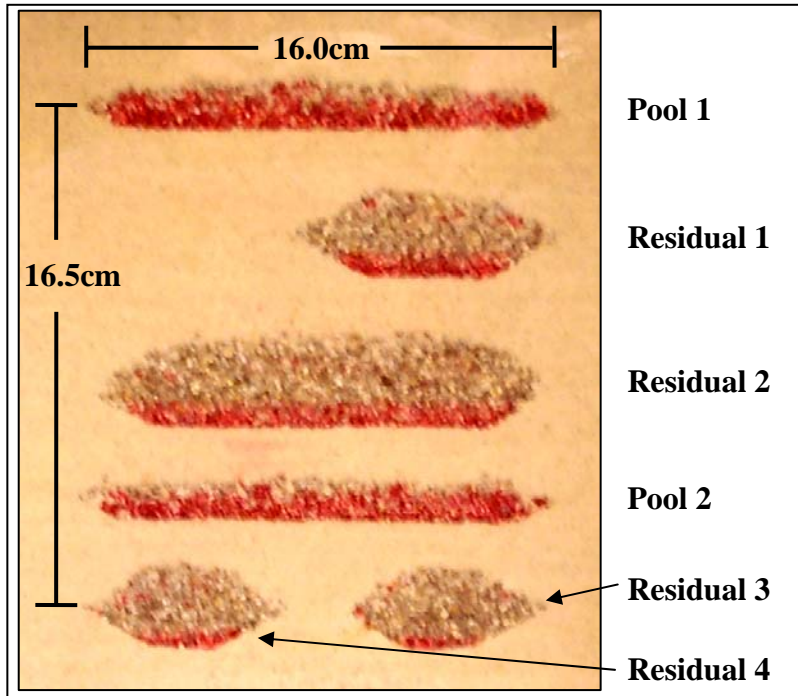


Figure 3.69. Sources with PCE, Intermediate-Scale ISCO Experiment

Table 3.34. Description of Source Zones for Intermediate-Scale ISCO Experiment

| DNAPL Source | | | | | | |
|---------------------|--------------------------------|------------------------|---------------------------|-------------------------------|-----------------------------|----------------------------|
| Name | Volume (cm³) | PCE Volume (mL) | Average Saturation | Ganglia -to-Pool Ratio | Initial PCE Mass (g) | Mass of Ganglia (g) |
| Pool 1 | 174.20 | 29.93 | 0.43 | 0.00 | 48.78 | 0.0 |
| Pool 2 | 178.95 | 28.79 | 0.40 | 0.00 | 46.92 | 0.0 |
| Residual 1 | 163.58 | 6.79 | 0.10 | 0.36 | 11.07 | 2.93 |
| Residual 2 | 324.74 | 15.79 | 0.12 | 0.11 | 25.73 | 2.55 |
| Residual 3 | 118.55 | 2.79 | 0.06 | 1.05 | 4.55 | 2.33 |
| Residual 4 | 120.92 | 3.85 | 0.08 | 0.33 | 6.28 | 1.56 |
| TOTAL | 1080.94 | 87.94 | - | - | 143.33 | 9.37 |

Table 3.35. Chronology of Intermediate-Scale ISCO Experiment

| Activity | Duration (hrs) | Cell Pore Volumes |
|--|----------------|-------------------|
| Pre-DNAPL Emplacement Flushing | 117 | 4.0 |
| Pre-Oxidation Natural Dissolution | 199 | 6.9 |
| Oxidant Flushing | 59 | 2.0 |
| Post-Oxidation Dissolution | 245 | 8.4 |
| Reduced Flow until Shutdown and Coring | 472 | 9.4 |

Throughout all phases of the experiment, water head was monitored at 21 locations concentrated around the sources and 23 additional locations dispersed across entire cell to quantify changes in permeability (Figure 3.68). This was performed using a custom-built automated head measurement device, shown in Figure 3.70 capable of measuring heads at up to 20 locations per minute with an accuracy $\pm 0.088\text{mm}$ around the source zone and $\pm 0.14\text{mm}$ in the rest of the cell.

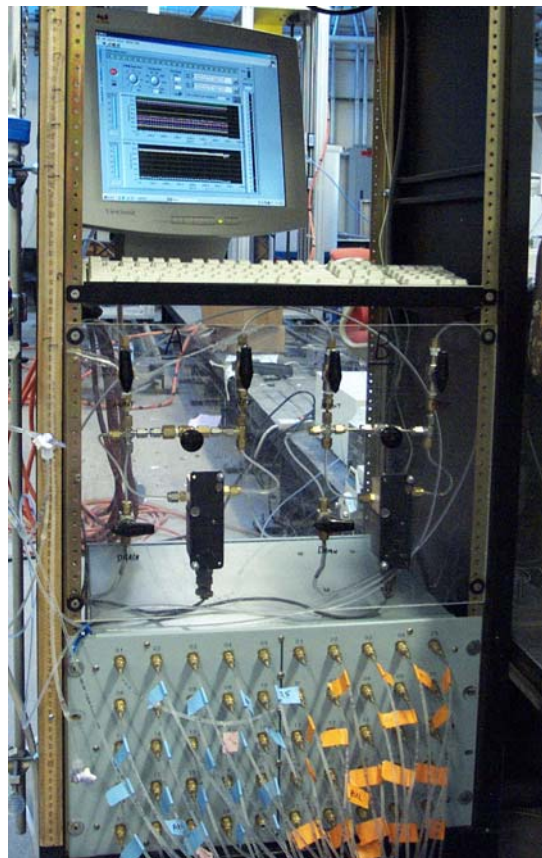


Figure 3.70. Water Head Measurement System, Intermediate-Scale ISCO Experiment

Aqueous samples were collected during the bromide tracer test along two vertical transects down-gradient of the source area, providing a total of 8 sample locations. During natural dissolution, chemical oxidation, and post-oxidation dissolution, aqueous samples were obtained along two vertical transects, along the horizontal cell centerline shown in Figure 6.6, and at the cell effluent, providing a total of 14 sample locations. Upon completion of the experiment, soil cores were obtained from throughout the cell to determine the distribution of manganese oxides and remaining mass of DNAPL PCE. A total of 168 cores were obtained from within sources and 44 were obtained from the rest of the tank.

This experiment provided insight into several important aspects of DNAPL mass transfer related to chemical oxidation. Overall oxidation performance will be discussed first, followed by the effects on source depletion. Last, manganese oxide formation and related permeability reductions will be discussed.

Oxidation Performance. Aqueous PCE concentrations were measured at a vertical transect (array G) about 16cm downgradient of the source zone, at a vertical transect (array N) about 77cm down-gradient, along the cell centerline (about every 15-30cm), and at the cell outlet. Plots of PCE concentration vs. time are shown in Figures 3.71 through 3.73. Aqueous PCE concentrations reached a steady state throughout the cell within approximately 40 hours. As expected, PCE concentrations drop below the method detection level (0.05mg/L) during the oxidant flush. The complex nature of the source zone, along with flushing less mass of MnO_4^- than needed to destroy all the PCE, resulted in varying degrees of post-oxidation concentration rebound. However, it is interesting that concentrations in port G3 and N3 (downgradient of pool 1) returned to only 10 percent of pre-oxidation levels while concentrations in ports G9 and N9 (downgradient of pool 2) rebounded to 117 percent of pre-oxidation levels. This may have occurred because flow paths interacting with pool 1 did not interact with any other sources, whereas pool 2 was purposely located so that flow paths interacting with it also would interact with nearby residual sources (see Figure 3.69).

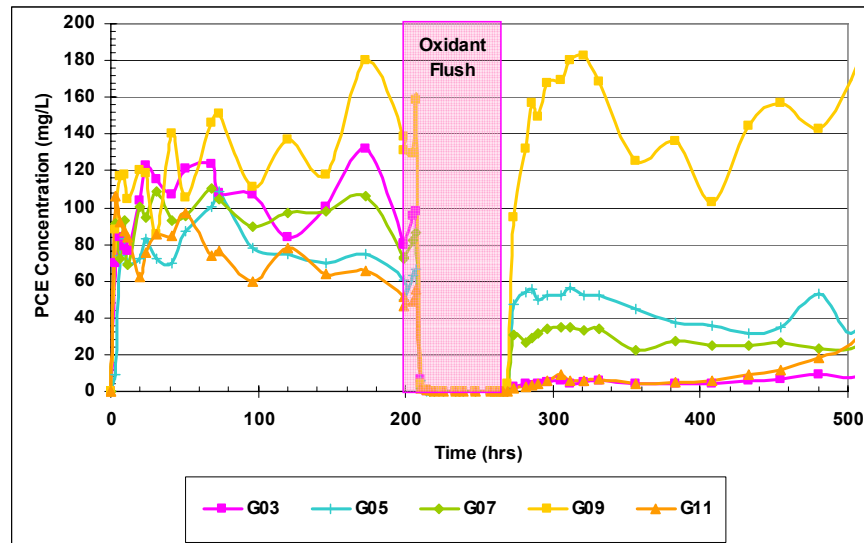


Figure 3.71. PCE Concentrations at Vertical Sampling Array G, Intermediate-Scale ISCO Experiment

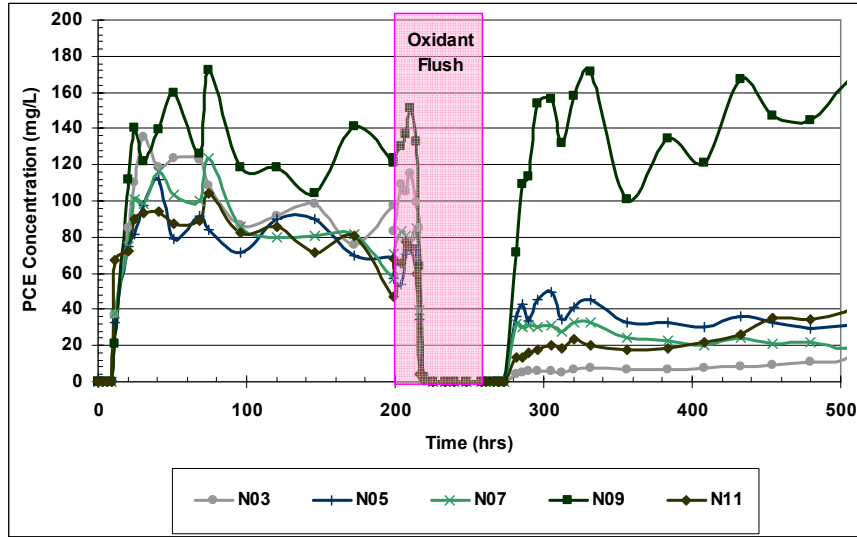


Figure 3.72. PCE Concentrations at Vertical Sampling Array N, Intermediate-Scale ISCO Experiment

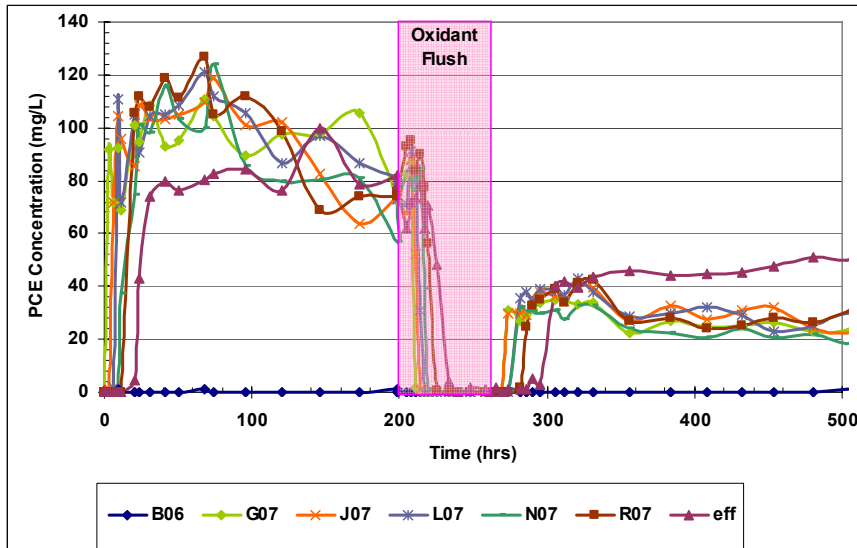


Figure 3.73. PCE Concentrations along Horizontal Centerline, Intermediate-Scale ISCO Experiment

Figures 3.74 through 3.76 show PCE concentrations as steady-state conditions developed through the cell during the three experiment phases: pre-oxidation, oxidation, and post-oxidation. Once steady-state was reached during pre-oxidation, the bottom half of the cell had concentrations roughly 50 percent higher than the top half of the cell. During oxidation, aqueous PCE concentrations throughout the cell dropped to zero indicating the oxidant was destroying

PCE as fast as it could transfer to the aqueous phase. When the post-oxidation phase reached steady-state, concentrations in the top half of the cell had dropped by roughly 75 percent compared to pre-oxidation. However, the bottom half of the cell had concentrations higher than during pre-oxidation. Despite adding less oxidant than necessary for complete destruction, ISCO succeeded in substantially decreasing plume concentrations down-gradient of pool 1 and residual 1, but appears to have created a hotspot down-gradient of pool 2. The different effect on pool 1 and pool 2 again appears to be a result source zone configuration. Flow paths interacting with pool 1 did not interact with other sources, so that $\text{MnO}_2(\text{s})$ appears to have formed at the DNAPL-water interface effectively cutting off mass flux from pool 1. Conversely, pool 2 had residual sources around it that resulted in more complex flow patterns increasing mixing and maintaining flow in contact with pool 2.

Changes in plume concentration following oxidation likely resulted from a combination of source mass depletion as well as changes in source mass depletion rates. Changes in mass depletion rates could have resulted from manganese oxide formation at the DNAPL-water interface reducing the interfacial contact area for mass transfer from the DNAPL to aqueous phases. Alternately, mass depletion rates could have changed as a result of manganese oxide formation inducing flow changes—either flow-bypassing or increased mixing, depending on the complexity of the source zone.

Source-Depletion Effects. As a next step it was useful to evaluate how the PCE DNAPL mass was depleted during oxidation. Chloride concentrations were measured, at the same locations as aqueous PCE, during and following oxidation as an indirect measure of PCE oxidation because oxidized PCE was the only source of chloride. The chloride concentrations were converted to effective oxidized PCE concentrations based on the stoichiometric mole ratio and molecular weights, assuming PCE was completely oxidized to chloride and carbon dioxide.

Figure 3.77 shows cumulative mass of PCE depleted from the cell, based on flow rate and effluent concentrations of PCE and chloride. The shaded region indicates injection of oxidant at the cell inlet and the dashed line represents the period during which measurable chloride was present in effluent (indicating PCE oxidation). Flow rate was constant, so the line slope represents an average mass depletion rate from the source zone. The average mass depletion rate increased most significantly at the beginning of the oxidant flush, indicated by the increased slope of the “Total PCE Removed” line, and diminished as the flush continued so by the end of oxidation it returned approximately to pre-oxidation levels.

Variation in mass depletion rate as oxidation progresses can be seen more clearly in Figure 3.78 which shows mass depletion rate versus time, estimated from effluent concentrations and flow rate. The shaded region and dashed line are the same as in Figure 3.77. Shortly after oxidation began, as indicated by chloride arrival at the effluent, the mass depletion rate increased to nearly three times the natural dissolution rate. However, this rate was only sustained for 10-15 hours before quickly dropping to 2 times the pre-oxidation rate and continued to drop more slowly until reaching pre-oxidation levels. Following conclusion of the oxidant flush, as indicated by lack of detectable permanganate in effluent, the mass depletion rate dropped approximately 80 percent further to pre-oxidation levels. By the end of the experiment it had dropped to about 50 percent of pre-oxidation levels.

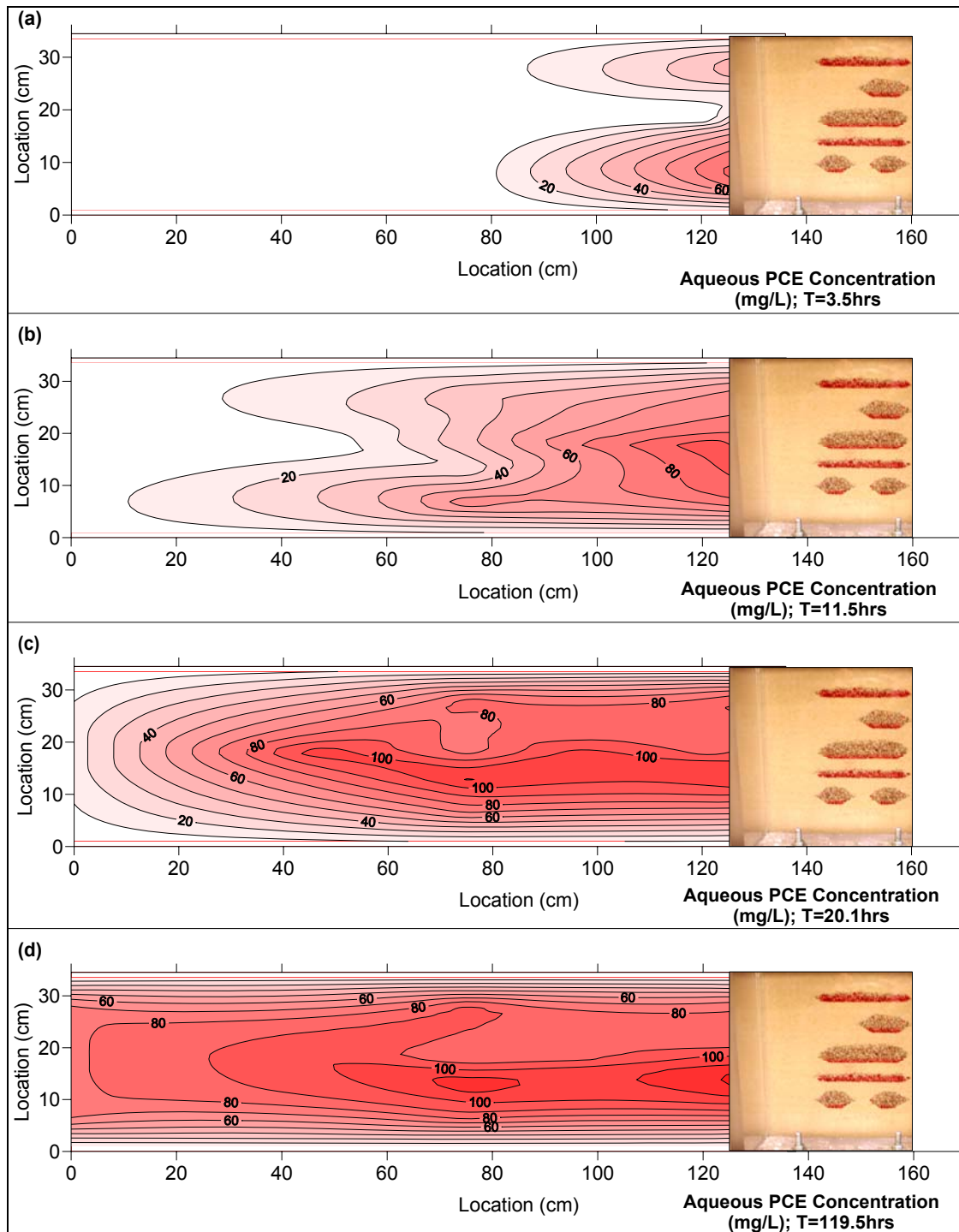


Figure 3.74. Aqueous PCE Distribution Downgradient of Array G during Pre-Oxidation Natural Dissolution, Intermediate-Scale ISCO Experiment

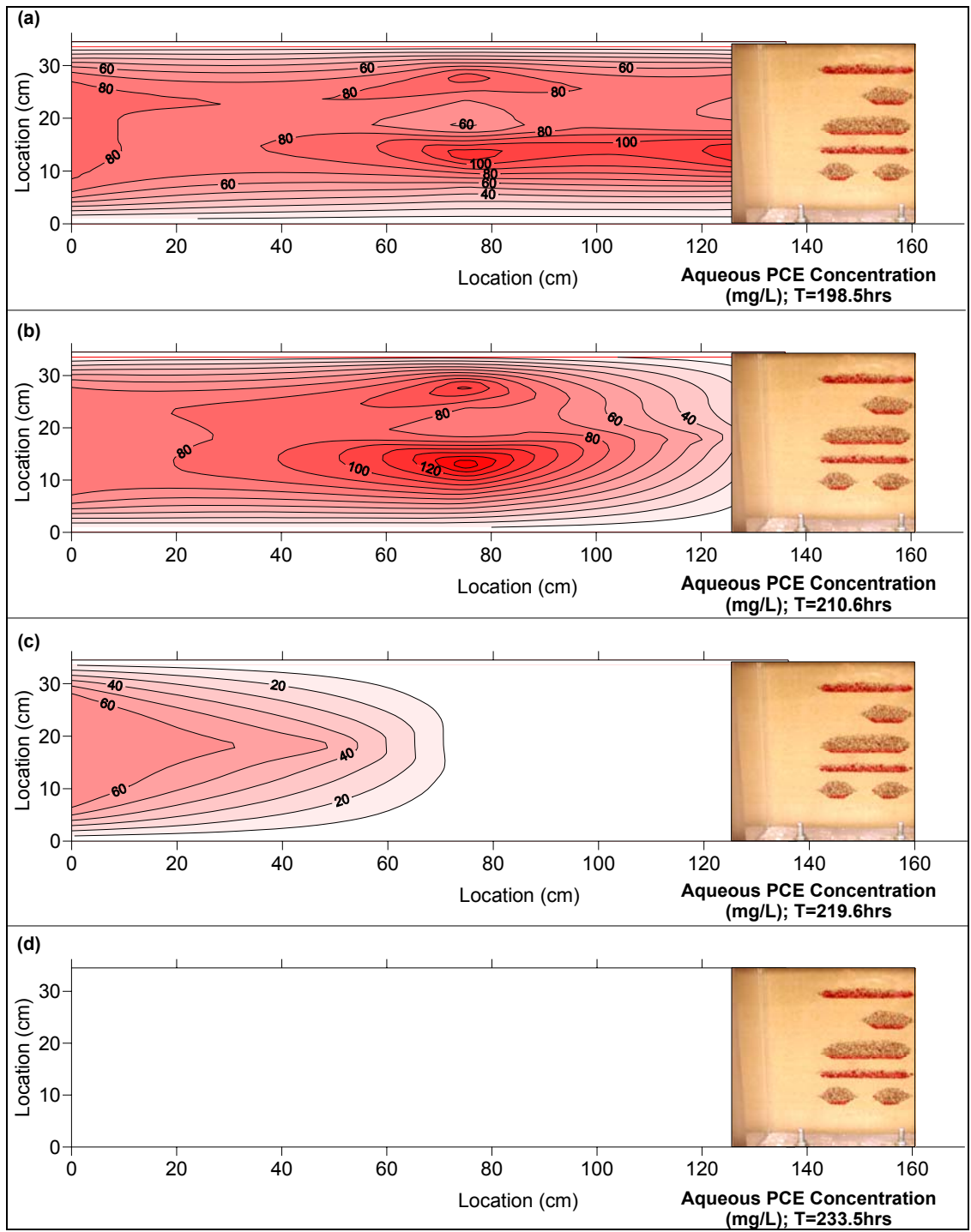


Figure 3.75. Aqueous PCE Distribution Downgradient of Array G during Oxidation Flush, Intermediate-Scale ISCO Experiment

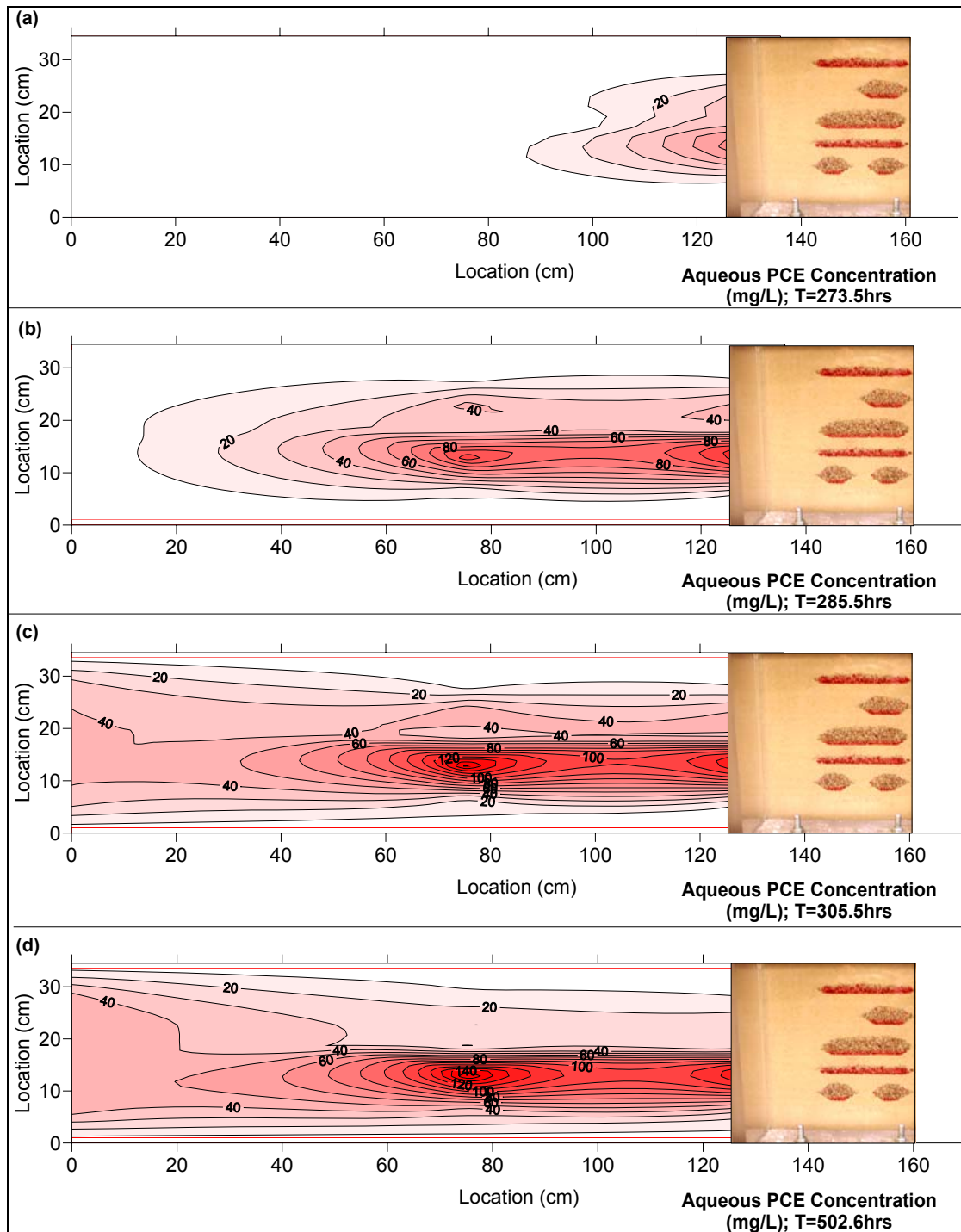


Figure 3.76. Aqueous PCE Distribution Downgradient of Array G during Post-Oxidation Natural Dissolution, Intermediate-Scale ISCO Experiment

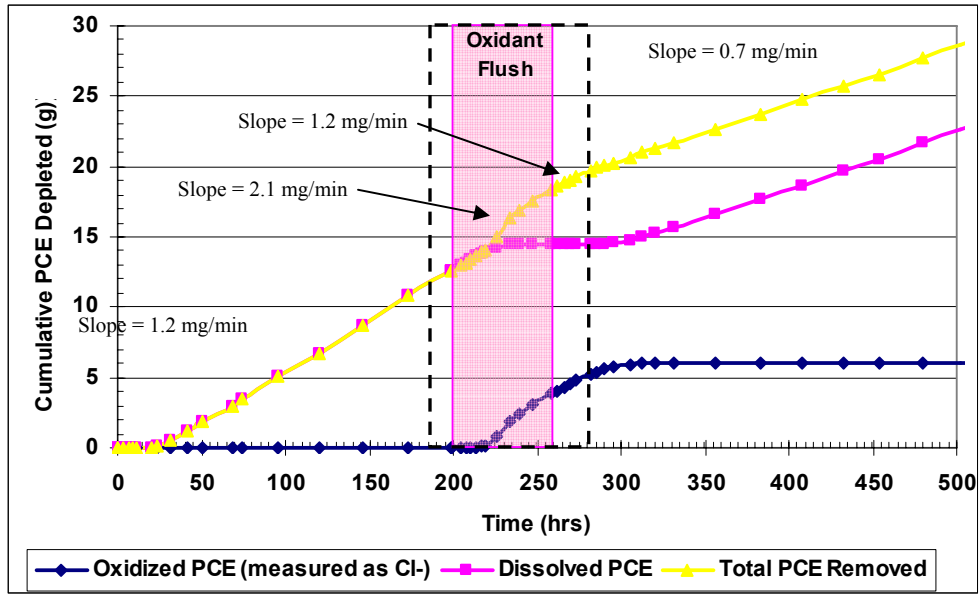


Figure 3.77. Cumulative PCE Mass Depleted from Intermediate-Scale ISCO Cell (shaded region represents oxidant injection, dashed region represents chloride in effluent)

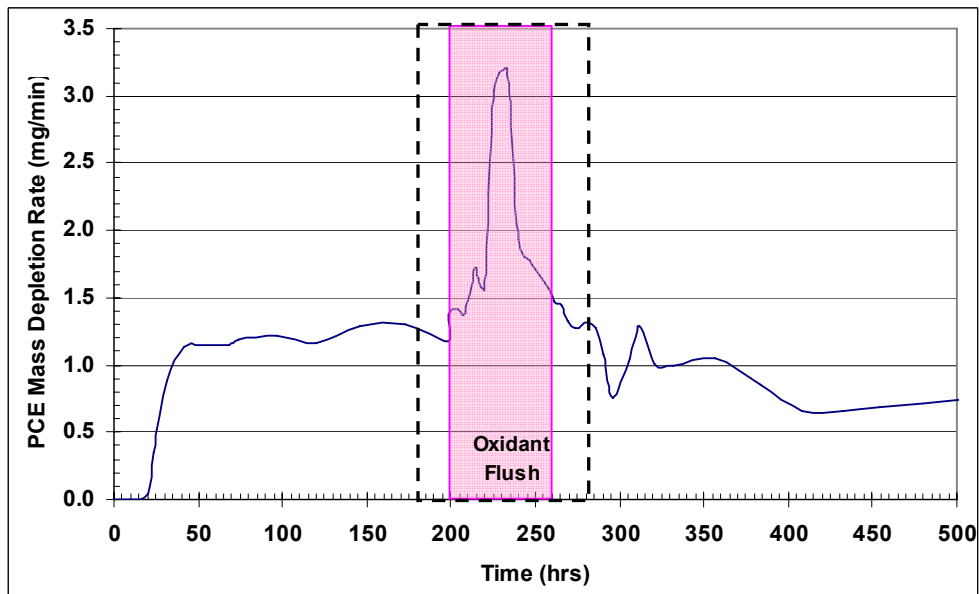


Figure 3.78. PCE Mass Depletion Rate from Intermediate-Scale ISCO Cell (shaded region represents oxidant injection, dashed region represents chloride in effluent)

The drop off in PCE mass depletion rate while still undergoing oxidation suggests a change in mass transfer characteristics of the sources. This could be a result of depletion of PCE originally present as ganglia or deposition of $MnO_2(s)$ at the DNAPL-water interface, decreasing the interfacial contact area, thereby reducing mass transfer of PCE from the DNAPL to aqueous phase for subsequent oxidation. Alternately, or additionally, permeability reductions from $MnO_2(s)$ deposition could have caused flow to bypass some of the sources.

In order to gain insight into what was limiting the overall oxidation mass-depletion rate, mass depletion rates for each source were estimated. The vertical sampling arrays were essentially multilevel samplers, with the port at each level roughly corresponding to a particular source zone. As such, the concentration profiles provided an indication as to what was happening at each source. Mass depletion rates from each source were estimated from concentrations at the corresponding array G port multiplied by the approximate flow rate through the source, based on the cross-sectional area of each source. These estimated source mass depletion rates are not exact, but are useful approximations for comparative purposes.

Figure 3.79 shows the estimated PCE mass depletion rate from each source versus time, except for residual sources 4 and 5 which are combined into a single mass depletion rate. Because no samples were obtained from between these two sources, it was not possible to determine how much of each of them contributed to the concentrations measured at array G. The shaded region and dotted line are again the same as in Figure 3.77, except the dotted line represents measurable chloride present in array G samples. Cumulative mass depleted from each source was estimated by summing the area under the mass depletion rate curve for each source. Figure 3.80 shows the cumulative PCE mass depleted from each source and Table 3.36 summarizes the PCE mass depleted from each source, during each experimental phase.

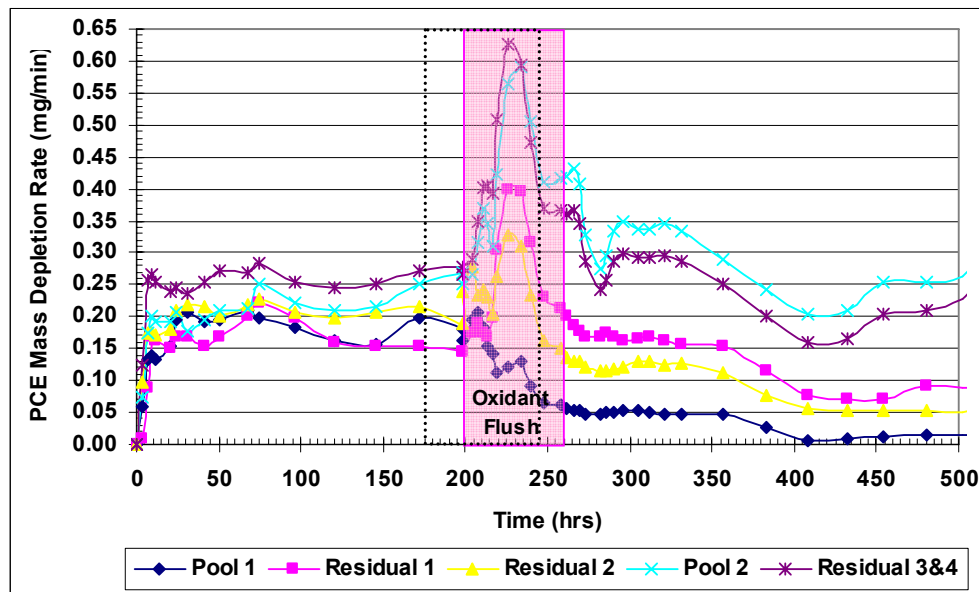


Figure 3.79. Estimated PCE Mass Depletion Rate from Each Source, Intermediate-Scale ISCO Experiment (shaded region represents oxidant injection, dotted region represents chloride at array G)

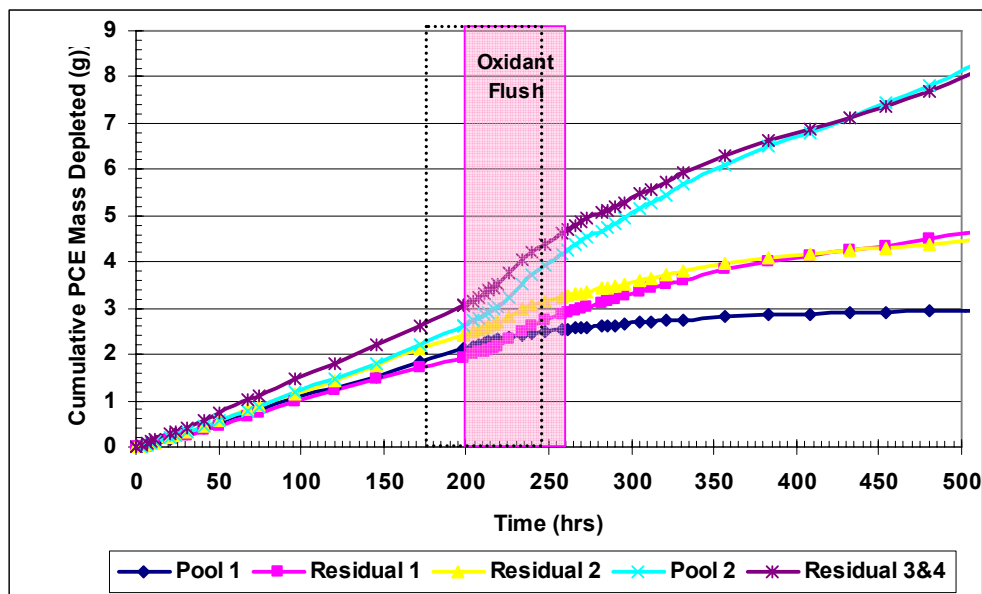


Figure 3.80. Estimated Cumulative PCE Mass Depleted from Each Source, Intermediate-Scale ISCO Experiment (shaded region represents oxidant injection, dotted region represents chloride at array G)

Table 3.36. Estimated PCE Mass Removal from Sources during Each Phase

| Source | Initial PCE Mass (g) | Mass as Ganglia (g) | Mass Removed (g) | | |
|--------------|----------------------|---------------------|------------------|------------|----------------|
| | | | Pre-Oxidation | Oxidation | Post-Oxidation |
| Pool 1 | 48.78 | 0.0 | 2.1 | 0.5 | 0.5 |
| Pool 2 | 46.92 | 0.0 | 2.6 | 1.5 | 4.0 |
| Residual 1 | 11.07 | 2.9 | 1.9 | 1.0 | 1.6 |
| Residual 2 | 25.73 | 2.5 | 2.4 | 0.9 | 1.2 |
| Residual 3 | 4.55 | 2.3 | 3.0 | 1.6 | 3.4 |
| Residual 4 | 6.28 | 1.6 | | | |
| TOTAL | 143.33 | 9.3 | 12.0 | 5.5 | 10.7 |

All the sources apparently experienced a large increase in mass depletion rate following start of the oxidation flush, except pool 1. The mass depletion rate for pool 1 began to steadily decrease when the other sources began to increase. Because there was little or no PCE present as ganglia in this source, the decrease is likely due to $\text{MnO}_2(\text{s})$ formation at the DNAPL-water interface combined with development of flow bypassing around pool 1 from $\text{MnO}_2(\text{s})$ formation. Conversely, the mass depletion rate from pool 2 had one of the highest increases during oxidation, roughly equaling that of combined residuals 3 and 4. The sudden drop in mass

depletion rate from the other sources midway through oxidation appears to occur when mass present as ganglia is estimated to have been depleted. The more gradual decrease following the sudden drop appears similar to the decrease for pool 1 suggesting that the continued decrease was a result of $MnO_2(s)$ formation.

Once the oxidation flush was completed, mass depletion rates from pool 1 and residual 2 both decreased to less than pre-oxidation levels, while mass depletion rates from residual 1 and combined residuals 3 and 4 returned to pre-oxidation levels. The mass depletion rate from pool 2 remained higher following oxidation than during pre-oxidation. Because residuals 3 and 4 had the greatest ganglia-to-pool ratio, it is not surprising they had a large increase in mass depletion rates during oxidation; however, their rebound after oxidation to pre-oxidation levels may be a little surprising because they also had the largest estimated percent removal as shown in Table 3.36. Based on soil coring results, as well as visual observations of the source zone following oxidation, it appears that the PCE mass in residual source 3 was nearly completely depleted during oxidation and the rebound of mass flux was a result of PCE remaining as ganglia in residual source 4. Similarly the rebound of residual 1, when residual 2 did not rebound, may be because residual 1 had a larger mass originally present as ganglia and more $MnO_2(s)$ appears to have formed around residual 2. It appears the ganglia mass in residual 1 was not quite completely removed during oxidation allowing the mass depletion rate to return to pre-oxidation levels. The decreased mass depletion rate in pool 1 following oxidation appears to be due to flow by-passing and decreased interfacial DNAPL-water contact area that resulted from high levels of manganese oxide formed at the NAPL-water boundary. The formation of manganese oxides may also partly account for the rebounds in mass depletion rates for residual 1 and combined residual 3 and 4. As shown in Figure 3.81, $MnO_2(s)$ formation was most prevalent in pools 1 and 2 followed by residual 2. As a result some flow initially through these sources is expected to have been re-directed through residuals 1, 3 and 4, increasing mass depletion rates from them.

Mass depletion rate from pool 2 increased substantially after oxidation compared to the pre-oxidation rate. A possible explanation appears to lay in the configuration of the source zone. Specifically, pool 2 was positioned with a residual source above it, along with two residual sources below it. A more complex flow pattern resulted around pool 2 because each source was constructed of coarse sand with a higher hydraulic conductivity than the surrounding sand. As manganese oxides formed in each of the sources, it is likely that flow patterns became even more complex resulting in increased mixing in and around pool 2 enhancing the mass depletion rate.

Regarding overall mass depletion, as Table 3.36 indicates, only 5.5g of DNAPL PCE were oxidized. This was less than theoretically possible based on oxidant mass delivered, partly due to oxidant delivery. In this experiment, it was estimated that at most 50 percent of injected oxidant would pass through sources because oxidant was flushed through the entire cross-sectional area of the cell while the source zone cross-sectional area was less than 50 percent that of the cell. This is typical of any flushing scheme, including field applications; some portion of the injected solution is expected to bypass sources due to subsurface flow and delivery characteristics. The other factor resulting in lower mass depletion than theoretically possible was that not all of the oxidant passing through the source zone participated in oxidation of PCE, evidenced by visible permanganate exiting the sources. This may be due to limitations in mass transfer from the DNAPL to aqueous phase or local flow bypassing within the source zone.

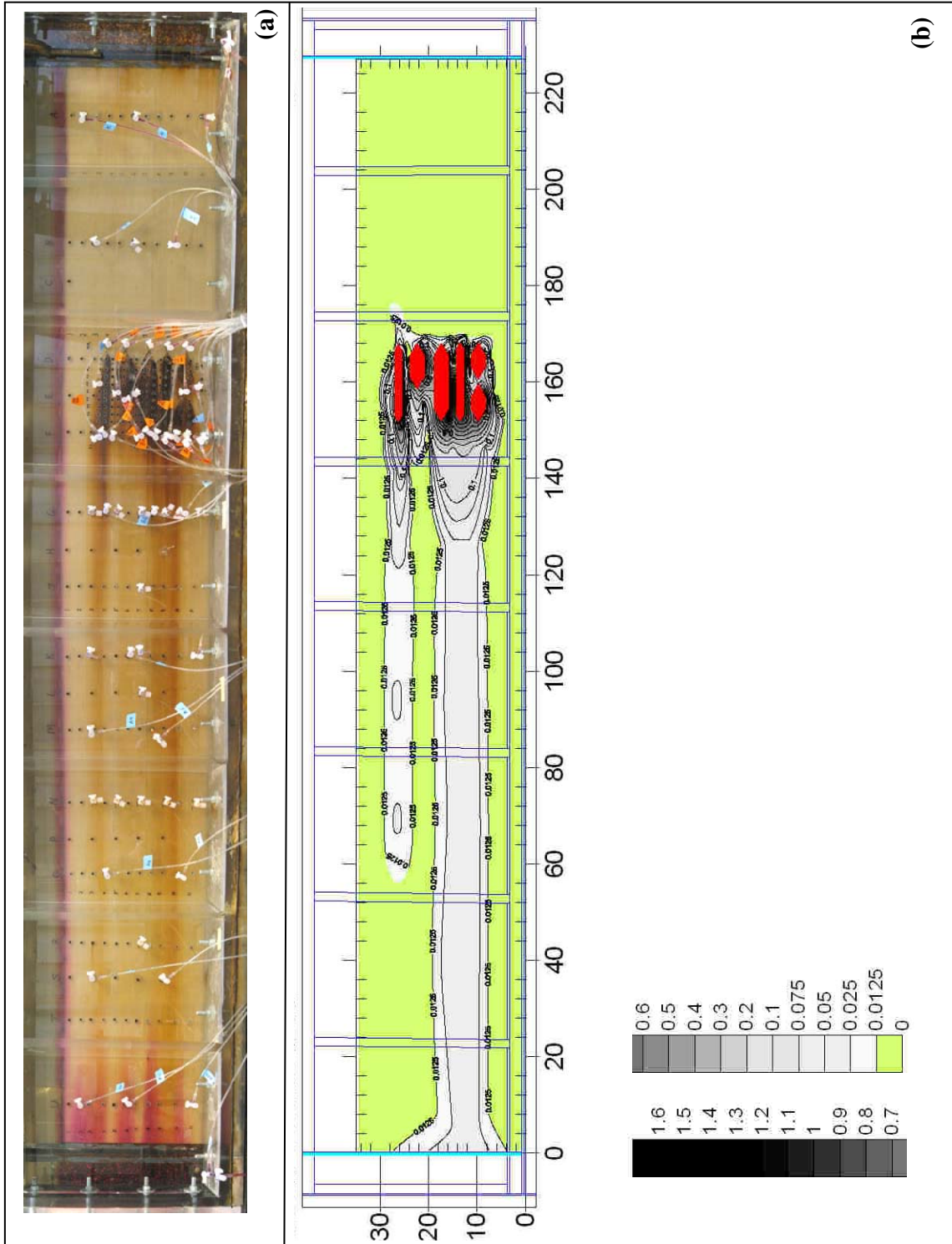


Figure 3.81. $\text{MnO}_2(\text{s})$ Distribution in the Intermediate-Scale ISCO Experiment (g $\text{MnO}_2(\text{s})/\text{kg}$ soil)

Once the cell was shut down, it was destructively sampled, obtaining 168 cores from the sources and 44 from the rest of the cell. Soil cores from sources were extracted using hexane to measure remaining DNAPL PCE. Despite every effort to extract intact cores and transfer them into the hexane quickly (less than five minutes), the mass balance suggested that a more than 50 percent of PCE mass was lost during the coring procedure. Fortunately, mass balances on chloride, aqueous PCE, permanganate, and $\text{MnO}_2(\text{s})$ were performed and provided good agreement. The soil core and effluent sample analyses show that 4.08g $\text{MnO}_2(\text{s})$ were generated, equating to 5.87g of PCE oxidized and matching the mass of PCE estimated to have been oxidized based on effluent chloride concentrations. Similarly, 110.4g of permanganate were flushed through the cell, with approximately 5.61g consumed in oxidation of PCE and 97.73g exiting the cell in effluent. Overall the mass balance accounted for 93.6 percent of injected permanganate. The slight difference is likely due to a combination of the high dilution factor used for sample analysis on the spectrophotometer as well as oxidation of a small amount of oxidizable material on the pea gravel used at the cell inlet and outlet. A small amount of $\text{MnO}_2(\text{s})$ was visible within the first 10cm of sand adjacent to the inlet end well, as seen in Figure 3.81.

Of the oxidant flushed through the cell only 5.1 percent was consumed in oxidizing PCE. As alluded to in the preceding discussion, this appears to be due to oxidant bypassing sources and decreased mass transfer resulting from reduced interfacial surface area caused by $\text{MnO}_2(\text{s})$ formation at DNAPL-water interfaces. Because aqueous PCE concentrations dropped to zero during oxidation, and oxidant was still visible passing through sources, it seems that mass transfer from the DNAPL to aqueous phase was a limiting factor. Because so much excess oxidant was exiting the system, it suggests that a lower oxidant concentration or lower flow rate may have been suitable. Although a lower concentration would reduce the kinetic rate of PCE oxidation, it would be acceptable as long as the oxidation rate still exceeded the dissolution rate. Decreasing the oxidation rate sufficiently may also allow more of the reaction to occur further down-gradient of the source possibly decreasing the $\text{MnO}_2(\text{s})$ buildup at the source.

Permeability Reduction. Manganese oxides were formed and deposited throughout the cell as shown in Figure 3.81a and the contour map of soil core results (Figure 3.81b). Figure 3.82 is a close-up and $\text{MnO}_2(\text{s})$ contour map of the source zone.

Water head was monitored continuously throughout the cell as a measure of the permeability. Because fluid properties were not changing, and a constant flow was maintained through the cell, any observed changes in water head distribution were a result of changes to the permeability of the porous media. Figure 3.83 shows the measured head at each port during the experiment. No data are available from approximately 294-340 hours due to an equipment malfunction. The heads fluctuated daily, presumably due to the daily temperature fluctuations in the lab of 4-6°C. The individual ports are not labeled on this graph as it is just meant to provide an overview. However, the cell inlet head, outlet head, and source zone heads have been labeled. It can be seen that during oxidation, the spread of the source zone heads increased so that after oxidation the head drop through the source was approximately double what it had been before oxidation. Further, the heads down-gradient of the source zone did not change, while those up-gradient did. This suggests that while $\text{MnO}_2(\text{s})$ was distributed through the length of the cell at various mass fractions, only the higher mass fractions found in and around the sources significantly altered permeability.

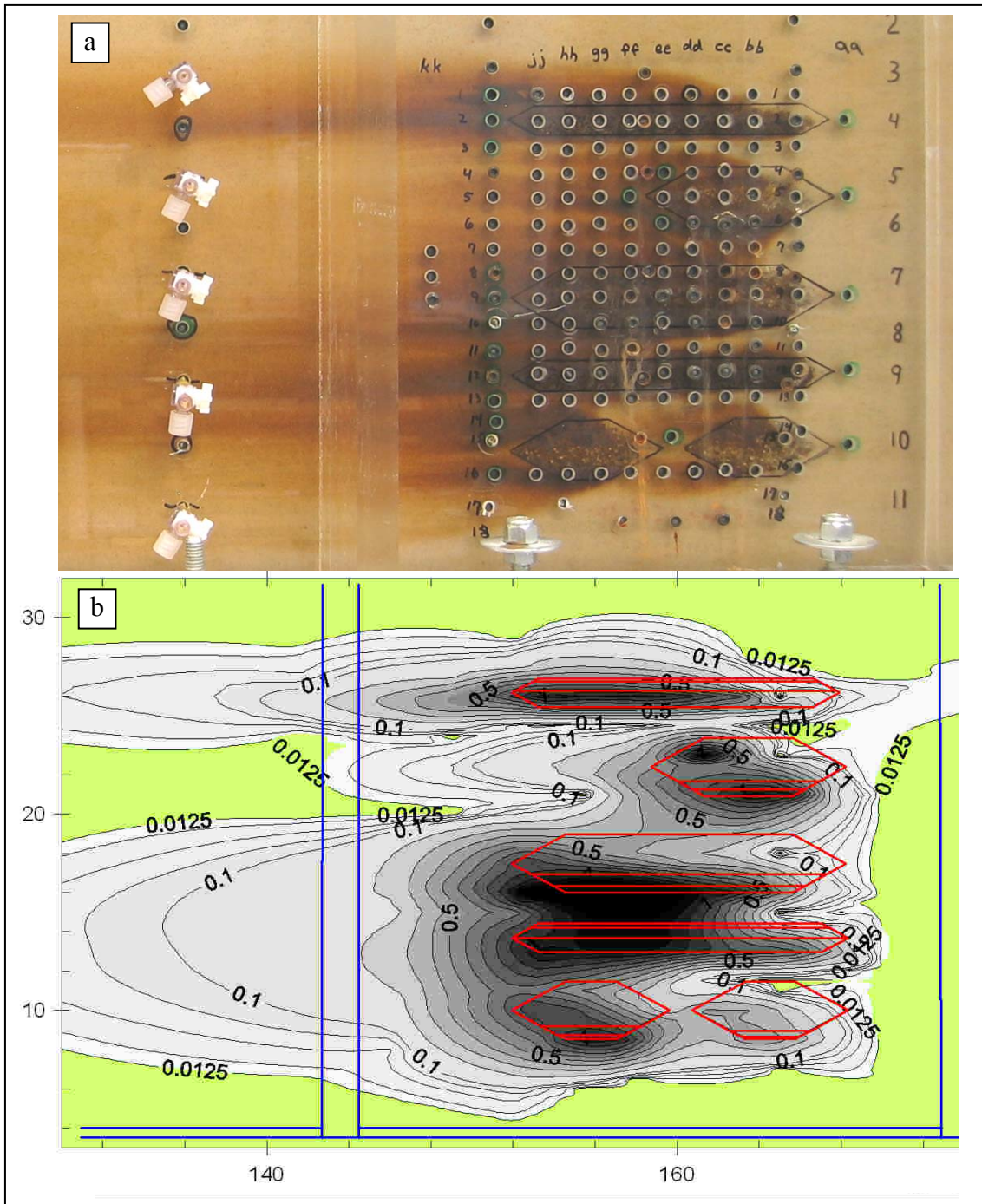


Figure 3.82. MnO₂(s) Distribution around Sources in the Intermediate-Scale ISCO Experiment (g MnO₂(s)/kg soil)

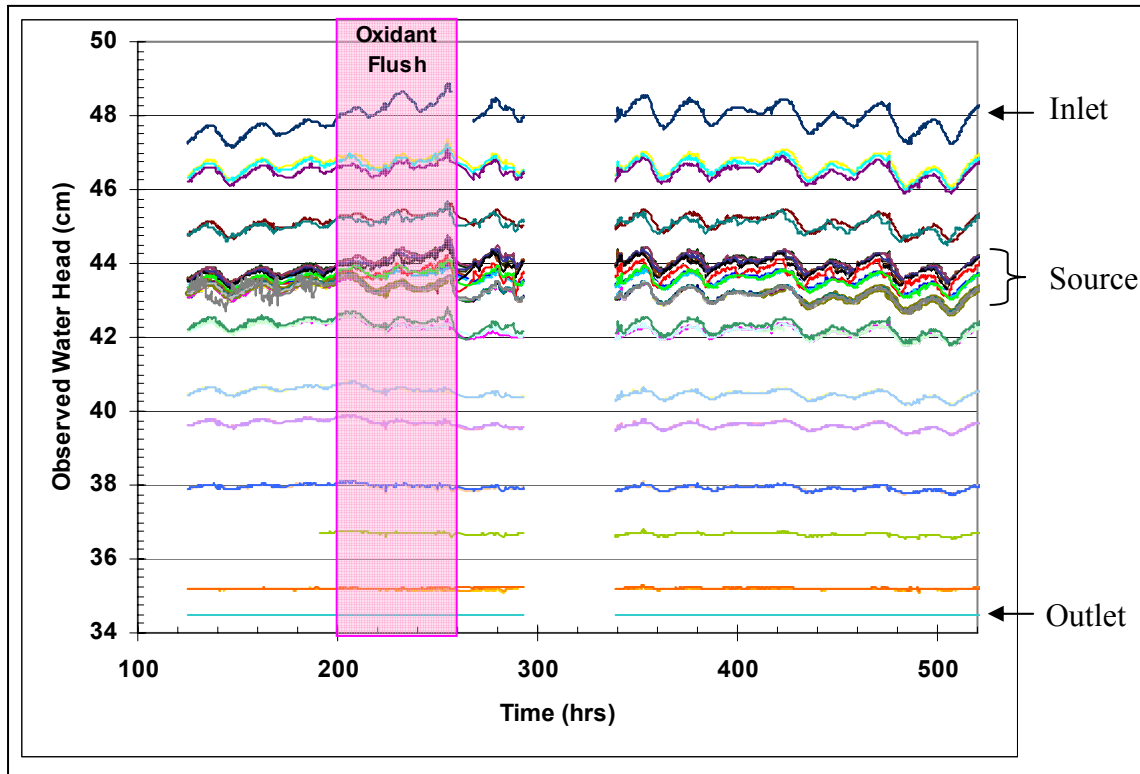


Figure 3.83. Water-Level Hydrographs in the Intermediate-Scale ISCO Experiment

The effect of permeability reductions around the sources is clearly visible in Figure 3.84 which graphs the head drop across each source zone over time. The markers are data points selected to eliminate the daily fluctuation effects. The lines represent moving 3-point averages of the data to improve visualization. Pool 2 had the greatest increase in head drop (and decrease in permeability), at approximately three times, in agreement with visual observations of heavier and darker $\text{MnO}_2(\text{s})$ buildup around this source. This is interesting because pool 2 also showed the greatest apparent rebound in mass depletion rate and down-gradient plume concentration. Conversely, pool 1 had the smallest increase in head drop (and decrease in permeability) at approximately 1.8 times, despite having the greatest decrease in mass depletion rate and down-gradient plume concentration. All of the residual sources showed slightly higher permeability reductions (roughly two times). Another interesting observation was that following oxidation the head drop across residual 3 continued to decrease while that across residual 4 continued to increase. This may have been a result of $\text{MnO}_2(\text{s})$ generated in residual 3 being flushed into residual 4 where it is combined with the high amount of $\text{MnO}_2(\text{s})$ already present there and became immobilized.

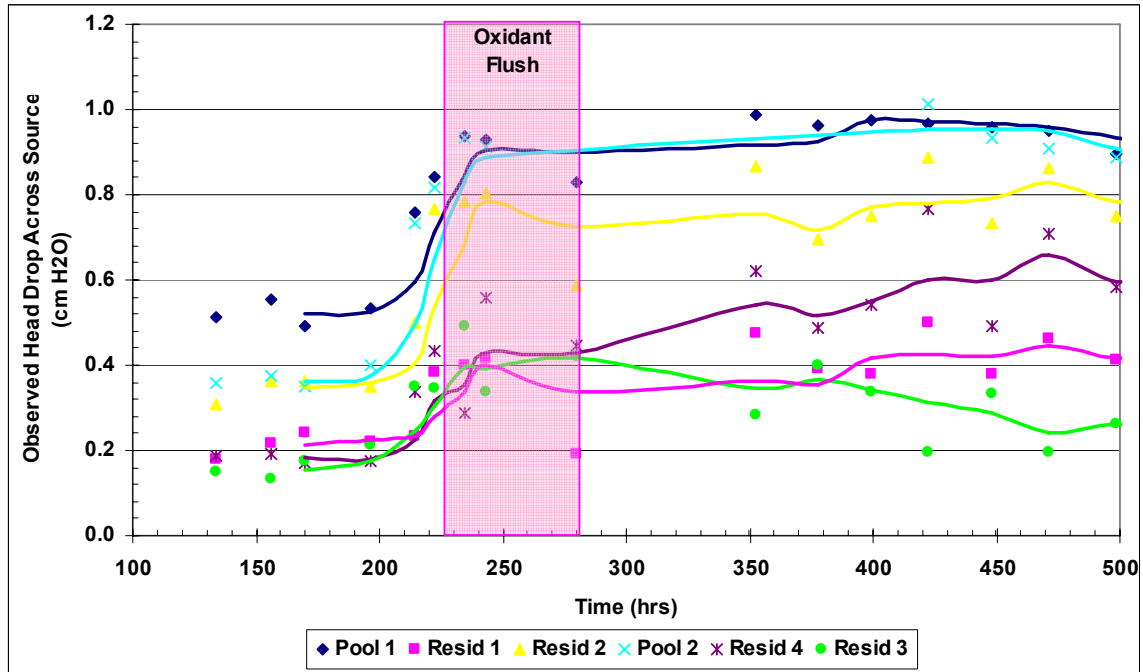


Figure 3.84. Hydrographs of Head Drop across Source Zones, Intermediate-Scale ISCO Experiment

Observed changes in hydraulic head were used to estimate changes in hydraulic conductivity through inverse modeling using the CORT3D model code developed as part of this research. First, a simulation of the experiment was calibrated to observed head and flow rate values for pre-oxidation conditions. Figure 3.85 shows scatter plots of the simulated versus observed head values for (a) locations throughout the cell and (b) locations around the source zones. As indicated by R^2 values greater than 0.94 for both data sets good calibration was achieved. The apparent variability of Figure 3.85b is a result of the small axes scales magnifying normal daily head fluctuations. Figure 3.86 shows the head drop across each source, where markers (without lines) represent observed values and lines represent simulated values.

Post-oxidation conditions were simulated using the $MnO_2(s)$ distribution determined from soil cores (Figure 3.81b). The apparent $MnO_2(s)$ density was varied to achieve the best fit of simulated and observed head values throughout the cell. An apparent density of 9.5mg/mL was found to provide the best fit. Although this value is 530 times less than the density of dry, solid manganese oxide it is not surprising because it represents both the decreased density of the hydrous $MnO_2(s)$ as well as the pore-throat blocking mechanism of permeability reduction. Interestingly, it was found that not all the $MnO_2(s)$ deposited in the cell affected permeability. Only those areas of the cell with $MnO_2(s)$ mass fractions greater than 0.1g $MnO_2(s)$ /kg soil (generally in, around, and within 15cm down-gradient of the sources) saw reductions in permeability.

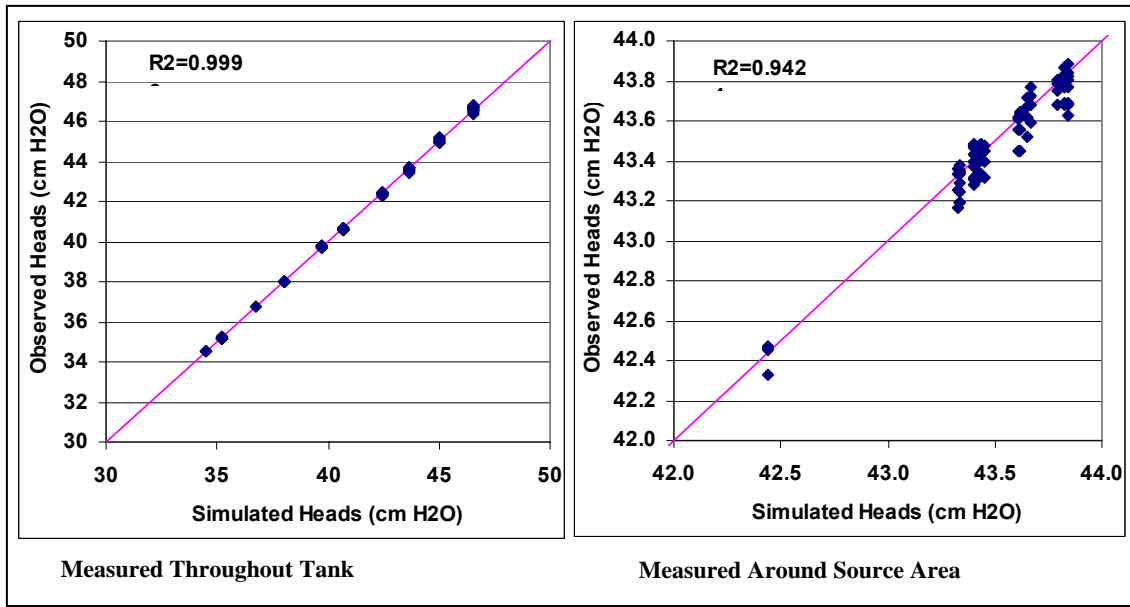


Figure 3.85. Comparison of Model Simulated Heads to Observed Heads Prior to Oxidation, Intermediate-Scale ISCO Experiments

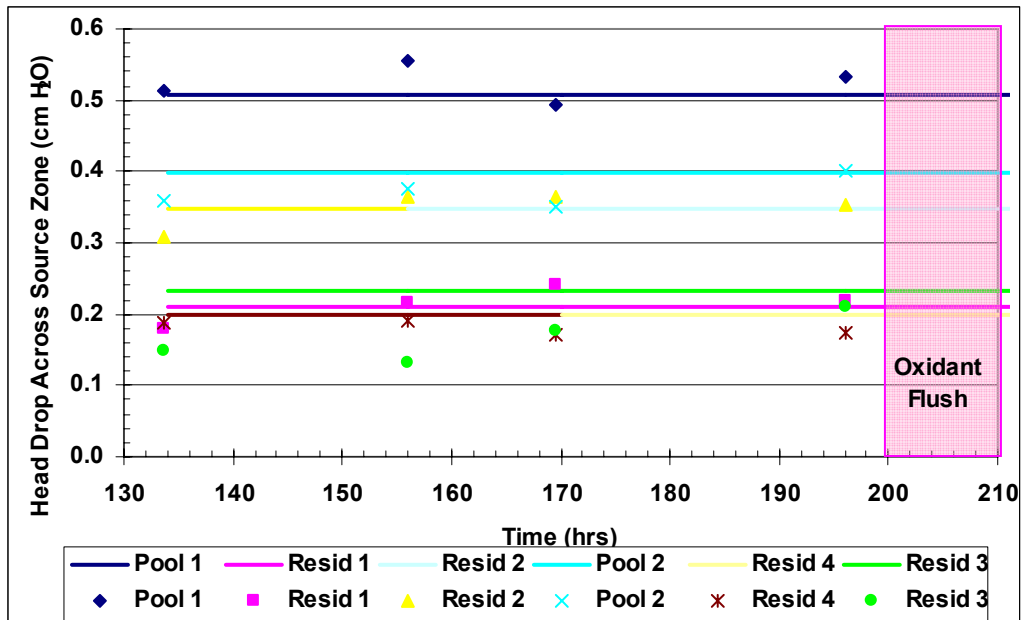


Figure 3.86. Observed and Simulated Head Drop across Sources Prior to Oxidation, Intermediate-Scale ISCO Experiment

Figure 3.87 again shows scatter plots of the simulated versus observed head measurements. The fit is still good across the entire cell, with reasonably good fit ($R^2 > 0.88$)

around the source. The slightly decreased fit in the source area compared to pre-oxidation may be a result of small scale variations in $MnO_2(s)$ or DNAPL PCE mass fractions that could not be measured and incorporated in the modeling effort. Finally, Figure 3.88 shows the head drop across each source. Again markers without lines represent observed values and lines represent simulated values.

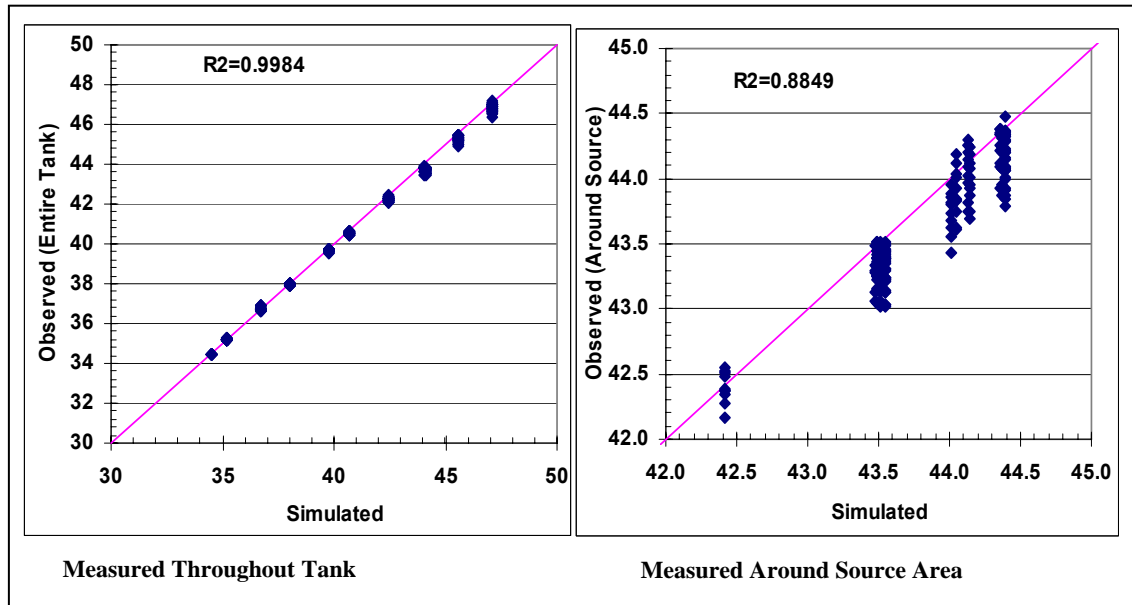


Figure 3.87. Comparison of Model Simulated Heads to Observed Heads after Oxidation, Intermediate-Scale ISCO Experiment

3.6.3 Large-tank experiments

Large-tank experiments with ISCO were conducted to determine if understanding of the ISCO process developed in intermediate-scale experiments with discrete source zones could be extended to systems with complex heterogeneous source architecture. The large-tank experiments were conducted in conjunction with experiments of natural dissolution (section 3.4.4) and surfactant-enhanced dissolution (section 3.5.5) described previously. Two large-tank ISCO experiments were conducted. The first experiment was designed with high aquifer heterogeneity (variance of $\ln K = 1.22$) and the second experiment was designed with low aquifer heterogeneity (variance of $\ln K = 0.25$). Detailed descriptions of design and packing procedures, flow system characterization, source creation and initial architecture, and natural dissolution tests are provided in Appendix 1 for the high heterogeneity experiment and in Appendix 2 for the low heterogeneity experiment. The chemical oxidation phase occurred after surfactant-enhanced dissolution experiments were completed.

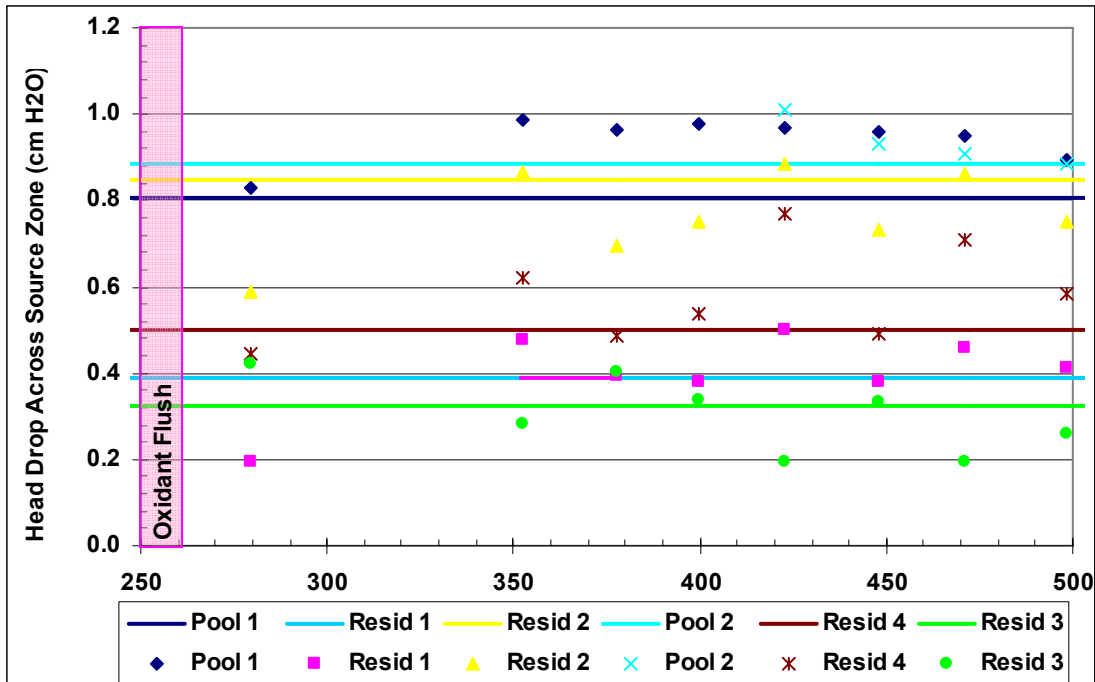


Figure 3.88. Observed and Simulated Head Drop across Sources after Oxidation, Intermediate-Scale ISCO Experiment

Water flow through the tank was maintained for several weeks after the conclusion of the surfactant remediation experiments. Five weeks elapsed for the high heterogeneity experiment and three for the low heterogeneity experiment between surfactant flushing and the start of chemical oxidation phase. This was intended to provide sufficient time to ensure little or no residual surfactant remained in the tank; however, surfactant was still present up to 1000 mg/L. Tween 80 is readily oxidized by permanganate, so any remaining surfactant exerts a non-productive oxidant demand similar to NOD. As a result, increased manganese oxide generation was expected beyond that from oxidation of PCE alone.

After the surfactant flush, the source zone was scanned with the gamma-ray attenuation system to map DNAPL saturation. Figure 3.89 is a plot of the PCE DNAPL distribution at the beginning of the ISCO high heterogeneity experiment and Figure 3.90 is a plot of the PCE DNAPL distribution at the beginning of ISCO low heterogeneity experiment.

Analysis of DNAPL saturation data suggested that the source zones for the two experiments did not differ greatly in a statistical sense. The ganglia-to-pool (GTP) ratio was 3.5 for the high heterogeneity experiment and 4.7 for the low heterogeneity experiment. This represents a difference of 35 percent. This slight difference was supported by visual examination of the source zone photos. It appeared that the low heterogeneity experiment had a little less pooling corresponding to a slightly higher initial ganglia-to-pool ratio. While the high heterogeneity experiment had approximately 85 percent greater initial mass of PCE, the PCE source also had 60 percent greater cross-sectional area. As a result, source zone configuration differences do not appear to account for the dramatic differences in dissolution.

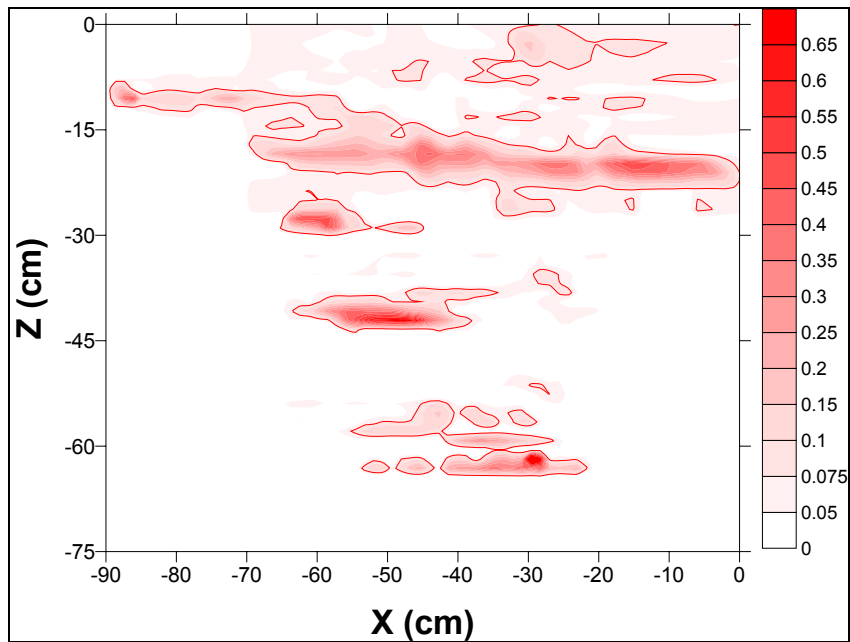


Figure 3.89. DNAPL PCE Saturation Distribution Prior to Chemical Oxidation, High Heterogeneity Experiment (axes are distance from origin of gamma scan)

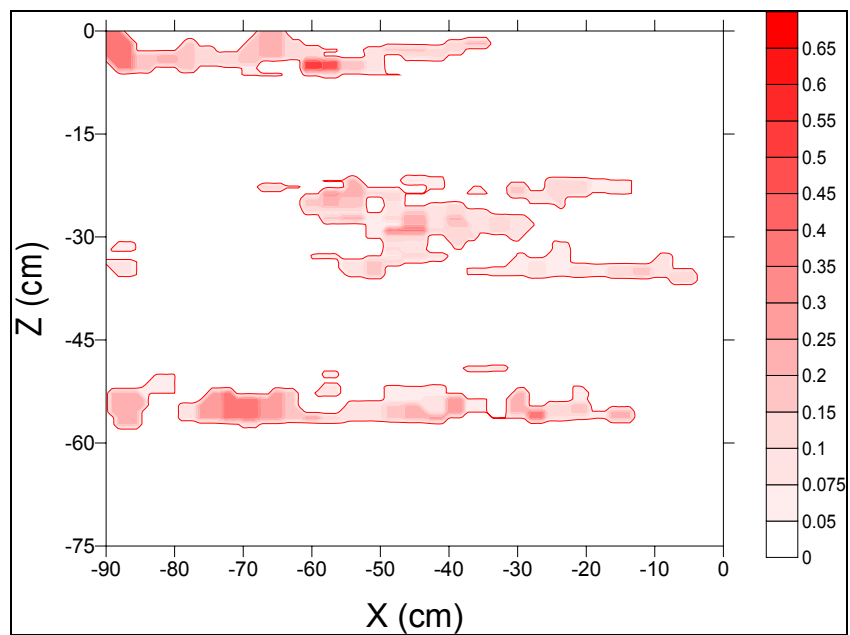


Figure 3.90. DNAPL PCE Saturation Distribution Prior to Chemical Oxidation, Low Heterogeneity Experiment (axes are distance from origin of gamma scan)

Calculations the ganglia-to-pool ratio for these experiments assumed a residual DNAPL saturation of 0.3 because a measured value was not available for the sands used. It is expected that each of the five sands used may have slightly different residual saturation levels. However, based on visual observation of photos of the source zones as well as the DNAPL saturation contour plots generated from the gamma data, 0.3 appeared to be a reasonable average saturation value. Using a value of 0.3 also resulted in calculated DNAPL volumes that matched volumes obtained by mass balance calculations during prior natural dissolution and surfactant-enhanced dissolution experiments. Calculation of GTP ratios using residual saturation values that ranged from 0.10 to 0.40 showed that the calculated differences in GTP ratios between the two experiments was highly sensitive to the assumed value of residual saturation.

The ISCO large-tank experiments were initiated by injecting potassium permanganate into the homogeneous region upgradient of the source zone (Table 3.37). The total injection rate, divided among 32 injection ports vertically spaced through the tank was approximately 1/8 the ambient flow rate through the tank, so the concentration flowing in the tank was expected to be approximately 1/8 of that injected. Aqueous samples were obtained frequently from sampling arrays A and C, as well as from the tank effluent. Figure 3.91 is a representative photo of the oxidation flush during the ISCO high heterogeneity experiment, and Figure 3.92 shows the oxidation flush during the ISCO low heterogeneity experiment. The distribution of DNAPL was mapped by the gamma-ray attenuation system at the end of the ISCO experiment.

Table 3.37. Oxidant Injection Summary for Tank Experiments with ISCO

| Parameter | High Heterogeneity Experiment | Low Heterogeneity Experiment |
|--|-------------------------------|------------------------------|
| KMnO ₄ Concentration (mg/L) | 8000.0 | 5000.0 |
| Injection Duration (hrs) | 48.5 | 24.5 |
| Total Injection Rate (mL/min) | 8.0 | 8.0 |
| KMnO ₄ Mass Injected (g) | 186.24 | 58.8 |
| Approximate PCE Mass at Start of Oxidation (g) | 509.2 | 273.3 |
| Maximum PCE Oxidation Possible (g) | 146.6 | 46.3 |



Figure 3.91. Oxidation during ISCO High Heterogeneity Experiment



Figure 3.92. Oxidation during ISCO Low Heterogeneity Experiment

Despite the build-up of manganese oxides, mass transfer from the DNAPL was enhanced during oxidation for both experiments as suggested by Figures 3.93 and 3.94. These figures show the mass of PCE removed from the tank via dissolution and oxidation, based on flow rate and effluent concentrations of PCE and chloride. The shaded region indicates the duration of oxidant injection. The slope of the “Total PCE” line represents an average mass depletion rate from the source zone, with slopes indicated on each figure for the pre-oxidation, oxidation, and post-oxidation phases. The slope of the “Dissolved PCE” line decreases as a result of oxidation, while the slopes of the “Oxidized PCE” and “Total PCE” lines are much greater than the “Dissolved PCE” line was originally, indicating mass-transfer from the DNAPL has been enhanced by the presence of oxidant. The enhancement is much more dramatic in the high heterogeneity experiment, possibly because of differences in source zone configuration, the much higher oxidant concentration, or greater flow field heterogeneity. However, the relatively small differences in GTP ratio for source zones in the two experiments are not consistent with the dramatic differences in observed mass depletion.

The higher oxidant concentration of the high heterogeneity experiment may not explain the dramatic differences in oxidation mass transfer increase. Table 3.38 summarizes the overall oxidation performance, and shows that the increase in mass transfer during oxidation was 2.5 times greater for the high heterogeneity experiment than for the low heterogeneity experiment although oxidant concentration was only 1.6 times greater. The intermediate-scale cell experiment suggested that a higher degree of source zone heterogeneity resulted in greater increase in DNAPL mass depletion during oxidation for the same oxidant concentration. However, higher oxidant concentration and duration of flush are suspected to be a main reason a greater change in GTP ratio occurred in the high heterogeneity experiment following oxidation. This makes sense, because enough oxidant was added during the experiment to potentially destroy 29 percent of the PCE, while oxidant added during the low-heterogeneity experiment was sufficient to potentially destroy 17 percent.

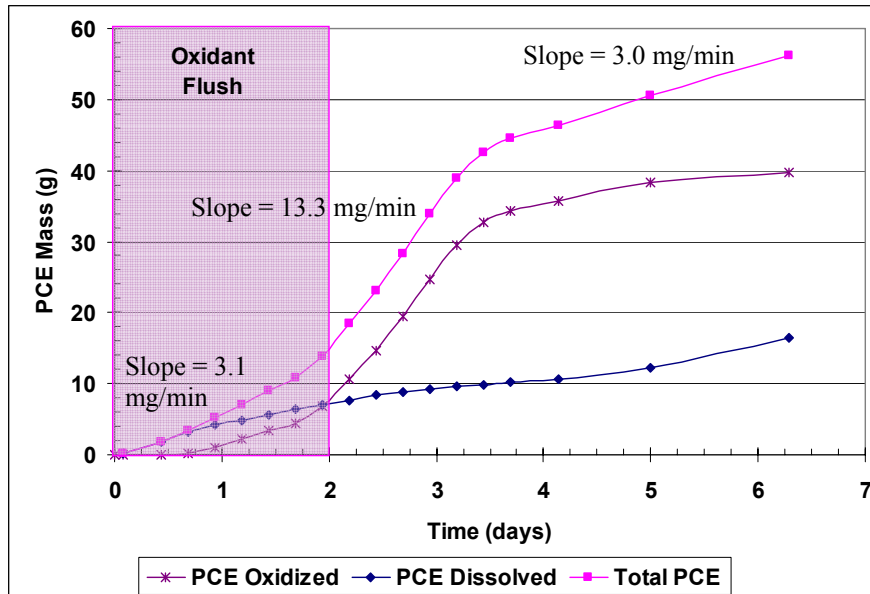


Figure 3.93. Mass of PCE Removed during ISCO High Heterogeneity Experiment

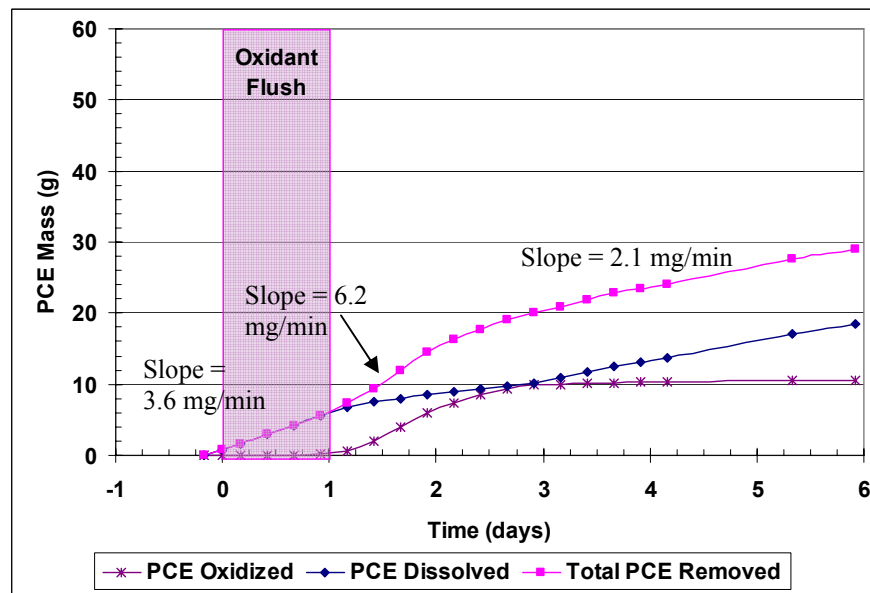


Figure 3.94. Mass of PCE Removed during ISCO Low Heterogeneity Experiment

Table 3.38. Oxidation Performance Summary

| Parameter | High Heterogeneity Experiment | Low Heterogeneity Experiment |
|--|--------------------------------------|-------------------------------------|
| Approximate PCE Mass at Start of Oxidation (g) | 509.2 | 273.3 |
| Approximate Cross-sectional Area of All Sources (cm ²) | 225 | 150 |
| Ganglia-to-pool Ratio at Start of Oxidation | 3.45 | 4.67 |
| Percent Change in GTP Following Oxidation | 87% | 70% |
| Maximum PCE Oxidation Possible (g) | 146.6 | 46.3 |
| PCE Oxidized (measured as Cl ⁻ at effluent) (g) | 40.2 | 10.6 |
| Percent of Possible PCE Oxidized | 27.4% | 22.9% |
| Change in Mass Depletion Rate (oxidation compared to pre-oxidation) | 4.4 times | 1.7 times |
| Change in Mass Depletion Rate (post-oxidation compared to pre-oxidation) | 1.0 times | 0.6 times |

The post-oxidation GTP for both experiments was actually higher than the pre-oxidation GTP. The PCE DNAPL distribution following chemical oxidation is shown in Figure 3.95 for the high heterogeneity experiment and Figure 3.96 for the low heterogeneity experiment. Comparing these images to pre-oxidation (Figures 3.89 and 3.90) it appears that although much of the ganglia source regions were reduced, the pool regions were reduced even more resulting in the higher post-oxidation GTPs. Mixing of oxidant with DNAPL may have been greater in the high heterogeneity experiment and resulted in greater dissolution and destruction of PCE from pooled regions than occurred in the low heterogeneity experiment.

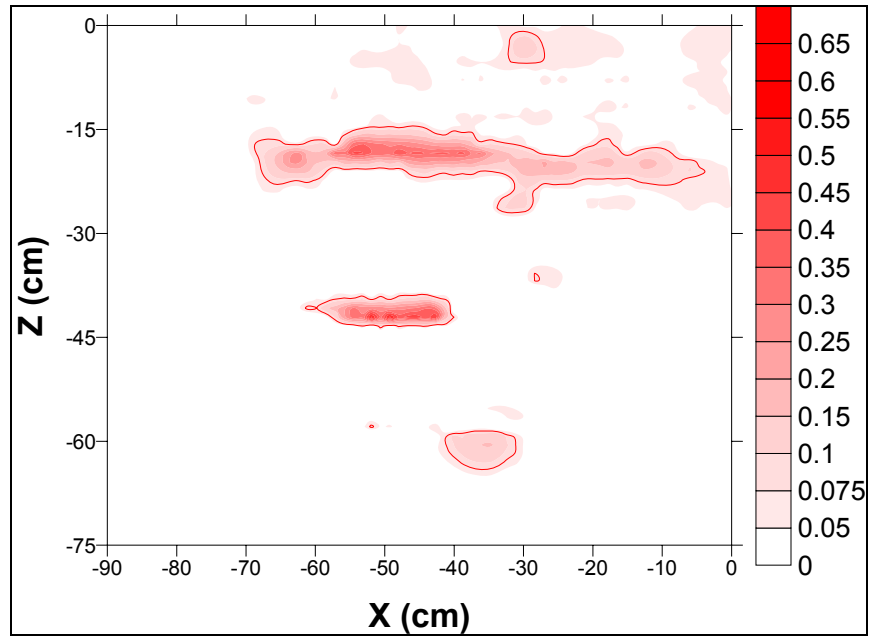


Figure 3.95. DNAPL PCE Saturation Distribution Following Chemical Oxidation, ISCO High Heterogeneity Experiment (axes are distance from origin of gamma scan)

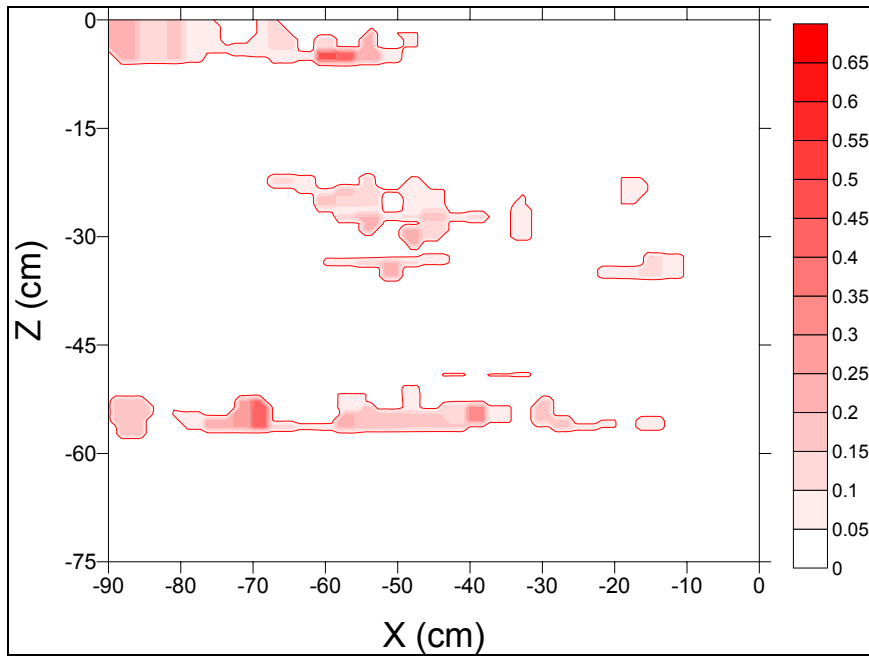


Figure 3.96. DNAPL PCE Saturation Distribution Following Chemical Oxidation, ISCO Low Heterogeneity Experiment (axes are distance from origin of gamma scan)

3.7 Experimental design and methods for investigation of biologically-enhanced dissolution

Bioenhanced dissolution experiments were conducted to understand and characterize mass transfer from PCE DNAPL undergoing bioremediation. Experiments at scales ranging from batch to large tanks were conducted to generate accurate data under controlled conditions that are suitable for hypothesis testing, model development and validation. Specific objectives were (1) to determine if biological activity can enhance mass transfer (2) to determine how biological activity changes mass transfer rate coefficients, (3) to identify how experimental scale affects mass transfer during bioremediation, and (4) to develop methods for upscaling models of mass transfer during bioremediation from point scale to multi-dimensional flow fields. These objectives were addressed by conducting experiments at batch, column, flow-cell and large tank scales. This section of the report describes the designs and methods used in bioenhanced dissolution experiments. Resulting basic data also are presented. Detailed interpretation and modeling of experimental results is presented in chapter 4.

3.7.1 Batch and column experiments

A series of mass transfer experiments were conducted in columns. Detailed descriptions of packing, column setup and testing methodology are provided in the M.S. thesis of Kaplan (2004). A summary of column characteristics is provided in Table 3.39. Column tests 1 and 2 were run as trials and used to adjust the column set-up, operation, and sampling protocols. Effluent from both columns indicated that oxygen leakage occurred and no degradation daughter products were observed. Redox conditions for subsequent column tests were sufficiently reduced to promote dechlorination. Column 3 was run with residual PCE throughout the entire column, while Columns 4 and 5 were run with residual NAPL in the bottom quarter of the column only.

Table 3.39. Characteristics Column Experiments of Bioenhanced Dissolution

| Test Number | Type of Test | NAPL Configuration | Flow (mL/min) | Pore Velocity (cm/d) | Porosity (-) |
|-------------|--------------|--------------------|---------------|----------------------|--------------|
| 1 | abiotic | throughout | 0.02 | 13.7 | 0.473 |
| 2 | biotic | throughout | 0.02 | 12.6 | 0.500 |
| 3a | abiotic | throughout | 0.264 | 164 | 0.471 |
| 3b | abiotic | throughout | 0.016 | 10.0 | 0.471 |
| 3c | biotic | throughout | 0.016 | 9.91 | 0.471 |
| 4a | abiotic | lower quarter | 0.264 | 166 | 0.505 |
| 4b | abiotic | lower quarter | 0.017 | 10.5 | 0.505 |
| 4c | biotic | lower quarter | 0.017 | 10.5 | 0.505 |
| 5a | abiotic | lower quarter | 0.023 | 15.0 | 0.451 |
| 5b | biotic | lower quarter | 0.023 | 15.0 | 0.451 |

Glass chromatography columns (1 x 12 in.) were packed within an anaerobic chamber with #30 sand. Prior to packing the sand was mixed in the anaerobic chamber with a sodium sulfide solution until redox conditions were sufficiently reduced for dechlorination to occur. For each test, the column was sealed, removed from the chamber and attached to a gas-tight syringe pump and tubing containing anaerobic water and/or medium. Valves and tubing were used to permit removing the inflow syringe reservoirs for refilling with anaerobic fluids without compromising the redox status of the column. For each column, an abiotic mass transfer experiments was conducted at a selected flow rate using KB-1 medium as the inflow fluid. Flow through the column was continued until effluent PCE concentration reached a steady state or until ten pore volumes were pumped.

After conducting abiotic mass transfer tests with a column, the column was inoculated with KB-1. Inoculation consisted of pumping one pore volume of nutrient medium through the column, followed by two pore volumes of KB-1 inoculum. After the inoculum was in place, flow through the column was stopped overnight to allow attachment of the bacteria to the sand. Following inoculation, additional mass transfer tests were conducted and results were compared with those obtained previously for abiotic conditions. The biotic experiments were conducted in a similar manner to the abiotic ones but ran for approximately 1 month each, as this was the time required for effluent concentrations to become relatively stable. For both abiotic and biotic experiments, column effluent was sampled at least daily and analyzed by GC-FID for PCE and daughter products.

Three column tests provided data for evaluating mass transfer during bioremediation. For each column test, effluent data obtained after flow of one pore volume were used to calculate average mass flux of chlorinated ethenes. Data from the first pore volume were neglected to account for degradation daughter products that may have been present in the inoculum. In addition, after one pore volume, the column effluent concentrations stabilized and may have reached pseudo-steady-state conditions. Mass fluxes were calculated separately for PCE, TCE, DCE, etc. and added on a molar basis to give overall mass flux (Table 3.40).

Table 3.40. Mass Flux of Chlorinated Ethenes in Abiotic and Biotic Column Experiments

| Column Test | Pore Velocity (cm/d) | NAPL Configuration | Mass Flux (mol/hr) | | Percent Difference |
|-------------|----------------------|--------------------|--------------------|----------|--------------------|
| | | | Abiotic | Biotic | |
| 3b, 3c | 10 | throughout | 5.16E-07 | 1.02E-06 | 198 |
| 4b, 4c | 10.5 | lower quarter | 7.68E-07 | 1.80E-06 | 234 |
| 5a, 5b | 15 | lower quarter | 1.18E-06 | 2.18E-06 | 185 |

The comparison between the abiotic and biotic runs of all three columns showed that the presence of dechlorinating bacteria enhanced mass flux from the NAPL zone. Although degradation daughter products were observed in effluent of each test, the greatest contributor to

increase mass flux during biotic experiments was due to a higher PCE effluent concentration than occurred in abiotic experiments. This may have been due to production of surfactants by the culture, but additional studies are necessary to verify this. Other studies have shown that microorganisms secrete surfactant or emulsifying agents when growing on NAPLs (Einsele et al. 1975). Solubilization caused by these secretions accounts for the utilization of the insoluble substrate at rates greater than their solubilities would predict (Cameotra et al. 1983; Goswami and Singh 1991).

Bioenhanced mass flux from NAPL zones has been shown in other studies but most previous column work that investigated mass flux either did not use pure PCE as a DNAPL (Carr and Hughes 1998; Carr et al. 2000; Cope and Hughes 2001; Adamson et al. 2003) or used PCE at a much lower saturation than used in the experiments reported here (Yang and McCarty 2000).

Effluent from column 5 had the highest mass flux observed in all experiments. This was true in both abiotic and biotic experiments. The increased mass flux is a reflection of the greater velocity used in this experiment.

PCE degradation in the column experiments appeared to be first order (data shown in Kaplan, 2004). Therefore, a first order degradation rate constant was calculated for each column experiment by using a first order decay function to estimate moles of PCE degraded, which was then converted to moles of daughter product generated. Calculated moles of daughter products was then compared to moles of daughter products observed in column effluent and the rate constant was adjusted to fit the function to the observations. Resulting degradation rate constants are compared to the rate constant determined from batch tests for PCE degradation by KB-1 at saturated PCE concentrations (Table 3.41).

Table 3.41. PCE Biodegradation Rate Constants for Batch and Column Experiments

| Experiment | First-Order Rate Constant (1/d) |
|-------------------|--|
| Batch | 0.10 |
| Column 3c | 0.0044 |
| Column 4c | 0.024 |
| Column 5b | 0.0040 |

Assumed that the biomass concentration present in the columns was similar to that in the batches, the rate of PCE degradation in the columns appears to be slower than in batch systems. The smaller decay constant in the columns indicates that upscaling can affect degradation kinetics. This is contrary to the findings Major et al. (2002) where KB-1 was used in a field-scale application. Degradation rate constants from that site were estimated to be 24.0 1/d. Major et al. (2002) also found that TCE degradation rates in the field were an order of magnitude higher than those found in the microcosm studies. However, the application was to a zone with PCE and TCE concentrations around 5 μM , significantly lower than the PCE levels used in this research (PCE saturation is approximately 900-1200 μM), and therefore any inhibitory effects of high PCE concentrations were not observed.

3.7.2 Flow cell experiments

Preliminary Abiotic Experiments. At the time that this research began (2002), previous studies of chlorinated ethene mass transfer from DNAPL sources undergoing bioremediation were very limited and focused on demonstrating enhanced mass transfer in batch and column experiments at very low residual DNAPL saturation (Carr et al., 1998; Cope and Hughes, 2000; Yang and McCarty, 2000; Yang and McCarty, 2002). A model involving equilibrium partitioning and first-order biodegradation had been applied to batch experiments (Carr et al., 1998). However, no efforts to validate this model using results of column experiments were reported. No bioremediation experiments with PCE at high DNAPL saturation or with heterogeneous source zones had been reported.

In contrast, research described in this report was conducted with the general goal of understanding, quantifying and modeling the process of biologically enhanced mass transfer from source zones containing DNAPL at both residual and high saturation (pools). Broadly stated, transformations associated with biological treatment were to be quantified experimentally at scales ranging from columns to large sand tanks, and effects of bioremediation on DNAPL mass transfer rate coefficients were to be tested. Experimental results were to be used to develop methods for upscaling mass transfer rate coefficients to multi-dimensional flow conditions encountered at field sites, as well as to validate numerical modeling tools and upscaling methodologies.

A set of preliminary experiments was conducted to provide insight to processes affecting enhanced mass transfer of chlorinated ethenes from DNAPL source zones undergoing bioremediation. Specifically, these experiments were designed to observe how PCE mass transfer characteristics vary at a DNAPL pool interface as hydrodynamic and biochemical conditions change. Results were used to focus research objectives and hypotheses.

Several flow cells were developed and tested in an effort to focus experiments on conditions in the close vicinity of a DNAPL pool. A custom designed 16.5 ml glass flow cell, circular in cross section and elliptical in profile, was selected for experiments (Figure 3.97). This flow cell provided good detail of water chemistry leaving a source zone and was well suited to creating a DNAPL pool with a specified volume in a layered sand system. Ports at the top and bottom of the flow cell provided access for packing, DNAPL injection and coring, and were sealed with septa or Mininert valves. The remainder of this section of the dissertation proposal describes experiments conducted with this flow cell.

The procedure for each experiment began by packed the small flow cell with two well-characterized sands to create a capillary trap for DNAPL injection. The upper half was packed with fine-grained sand (mesh size #50) while the lower portion consisted of coarse-grained sand (#16). Total porosity of the packed flow cell was determined by gravimetric measurement of water displaced during packing. A DNAPL pool was created by injecting a volume of PCE sufficient to nearly fill the pore space of the lower sand. The high entry pressure of the overlying fine-grained sand prevented DNAPL from entering the upper part of the flow cell. A specified volume of PCE was then withdrawn from the flow cell, leaving a DNAPL pool of known mass. After static conditions were established, a selected solution was pumped through the cell by HPLC pump until PCE concentration in effluent stabilized. The PCE concentration in effluent was monitored continuously by an in-line UV spectrometer and water samples are obtained for chemical analysis by gas chromatography.

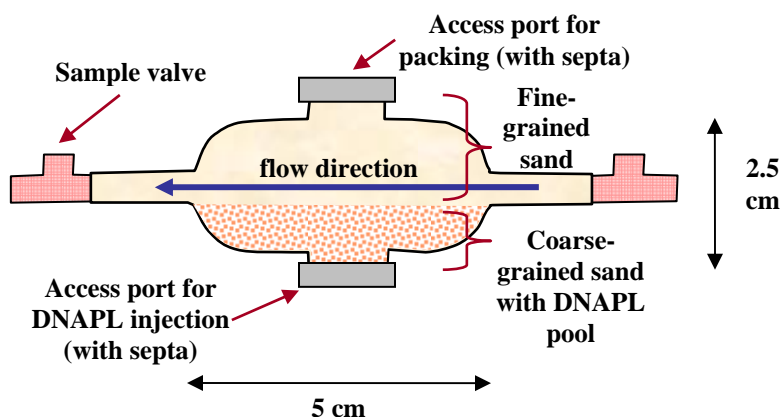


Figure 3.97. Flow Cell Used in Bioenhanced Mass Transfer Experiments

Effect of Solution Chemistry on Mass Transfer from a DNAPL Pool. Several explanations have been postulated for enhanced mass transfer from DNAPLs of non-chlorinated solvents. Explanations include: (1) bacteria that grow at the DNAPL–water interface and use chlorinated substrate directly from the DNAPL so that dissolution into the aqueous phase is not required (Efroymson and Alexander, 1991; Ortega-Calvo and Alexander, 1994), (2) bacteria and/or bacterial metabolic byproducts (e.g., biosurfactants or solubilizing agents) that increase partitioning of chlorinated compounds from the DNAPL to the aqueous phase (Osswald et al., 1996), and (3) microbial activity such as reductive dechlorination that accelerates dissolution by increasing the concentration gradient near the DNAPL–water interface (Ortega-Calvo and Alexander, 1994; Seagren et al., 2002).

Applicability of these explanations to chlorinated solvents has received little study. A theoretical modeling study at the REV scale showed that the first explanation, growth of dechlorinating bacteria directly at the DNAPL-water interface, was unlikely unless the supply of electron donor was very high (Chu et al., 2003). Experimental or modeling studies of the second and third mechanisms applied to mass transfer of chlorinated solvents have not been reported.

Experiments with a DNAPL pool at average saturation of 70 percent were conducted to provide an assessment of the second postulated mechanism, increased partitioning of chlorinated compounds from the DNAPL to the aqueous phase as a result of biosurfactants or solubilizing agents. This assessment could be accomplished relatively quickly by conducting mass transfer experiments with a DNAPL pool entrapped in a flow cell using various aqueous solutions as inflow. For each inflow solution, experiments were conducted with a range of flow rates.

Experiments were not conducted during this phase of the research to assess the third postulated mechanism for enhanced mass transfer, reductive dechlorination that increases the concentration gradient near the DNAPL–water interface and increases the rate of PCE dissolution. Assessing this mechanism would have required establishment of an active microbe population within a flow cell. At the time preliminary experiments were being planned, several microbe cultures were being evaluated for use at CSM (Kaplan, 2004). Ultimately, the KB-1

mixed culture was identified. However, at the time, no suitable culture had been identified and successfully cultured for long-term *in-situ* bioremediation experiments.

Mass transfer experiments were conducted using several flow rates and water compositions. Water compositions included de-ionized water, abiotic microbe growth medium, and solutions containing metabolic by-products and inactive bacteria (from previously active microbe cultures). The Cornell mixed culture of reductive dechlorinators (Fennell and Gossett, 1998) was used for the preliminary experiments. Experiments were run under aerobic conditions to assure that biodegradation by reductive dechlorination would not occur.

Experimental results provided a qualitative assessment of the ability of biosurfactants or solubilizing agents to increase partitioning of chlorinated compounds (Figure 3.98). Experiments using growth medium without microbe inoculation resulted in enhanced dissolution relative to experiments using solely de-ionized water. Introduction of a solution containing metabolic byproducts and inactive microbes increased PCE dissolution from dissolution observed with inflow of de-ionized water. In both cases, mass transfer increased by a factor of less than 2.

While results of this qualitative assessment indicate that PCE solubility may increase due to biosurfactants or solubilizing agents in bacterial solutions, this increase is significantly less than the 5 to 6-fold increase in mass transfer observed by column experiments with actively degrading microbe cultures (Cope and Hughes, 2000; Yang and McCarty, 2000). Because much of the chlorinated ethane flux observed in column experiments was attributed to degradation daughter products (TCE and DCE), it is more likely that enhanced mass transfer during bioremediation is caused primarily by microbial activity that increases concentration gradients near DNAPL–water interfaces and increases dissolution.

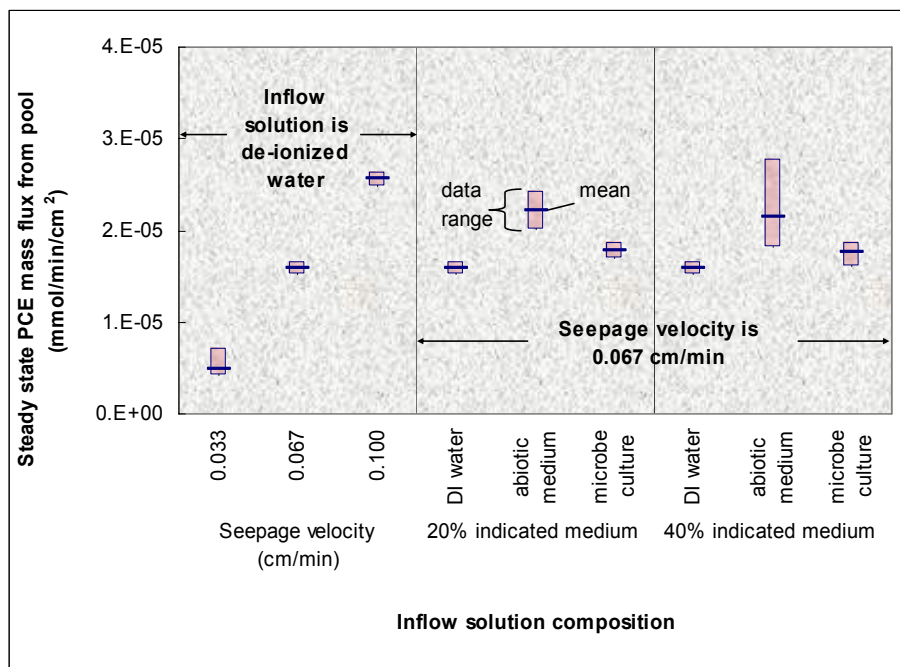


Figure 3.98. Effect of Solution Composition on PCE Mass Flux from a DNAPL Pool, Flow-Cell Experiments of Bioenhanced Dissolution

Effect of DNAPL Pool Morphology on Mass Transfer. Traditionally, interfaces between high saturation DNAPL pools and adjacent water-filled pores have been treated as sharp interfaces. However, the density difference between water and DNAPL results in a capillary head gradient within a pool that leads to a trend of increasing DNAPL saturation with depth in the pool. Moreno-Barbero (2005) has shown that this saturation transition zone has a strong influence on tracer travel times and partitioning characteristics. Effective bioremediation of PCE by reductive dechlorination requires adequate mixing of electron donor with PCE. Therefore, it was considered likely that enhanced mass transfer during bioremediation also might be affected by pool morphology.

Mass transfer experiments with an average DNAPL pool saturation of 50 percent provided a qualitative assessment of how mass transfer during bioremediation might be affected by pool morphology. In addition to mass transfer experiments with an inflow solution of de-ionized water, dye-tracer tests were completed and variations in DNAPL saturation within the pool were mapped by x-ray attenuation techniques. Progress of the tracer fronts were observed visually and recorded photographically to determine relative rates of flow in the upper sand, the upper part of the pool and the deeper part of the pool.

X-ray attenuation mapping of the flow cell showed a trend of increasing DNAPL saturation with depth in the pool (Figure 3.99). Although there was significant spatial variability throughout the pool, the saturation profile obtained by spatial averaging along horizontal strata show a distinct transition zone that was consistent with results obtained by Moreno-Barbero and Illangasekare (2006) for DNAPL pools in a larger flow cell.

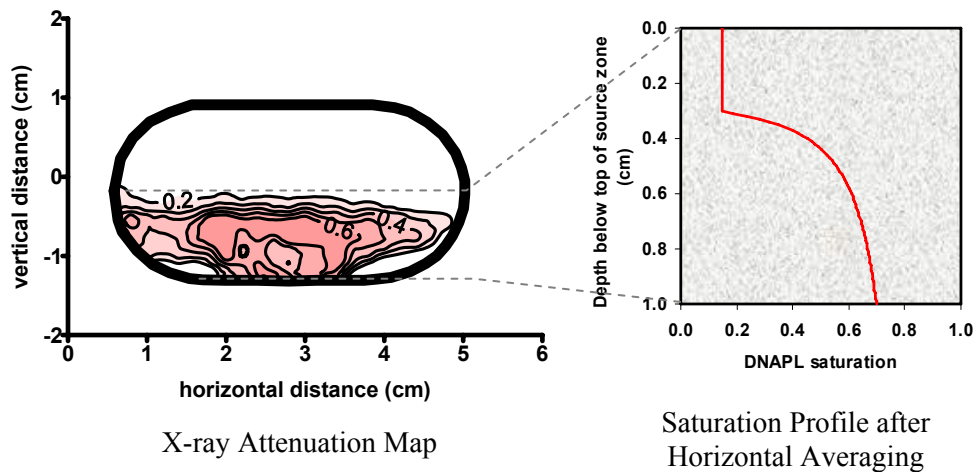


Figure 3.99. Distribution of DNAPL in a Pool with Average Saturation of 50 Percent, Flow Cell Experiments of Bioenhanced Dissolution

Results of dye tracer tests with this flow cell showed that tracer fronts propagated much more rapidly through this transition zone than through either overlying or underlying portions of

the flow cell. Because effective bioremediation of PCE by reductive dechlorination required adequate mixing of electron donor with PCE, results of these preliminary experiments suggest that saturation transition zones are important sites for phase transfer and chemical reaction.

The x-ray attenuation data showed that DNAPL saturation throughout the transition zone in the upper part of the pool was at or near typical values for residual saturation (approximately 20 percent). Previous investigations of mass transfer during bioremediation (Cope and Hughes, 2000; Yang and McCarty, 2000) showed that mass transfer was enhanced at residual saturation. Although PCE saturation in these studies was much lower than 20 percent, the results of the preliminary experiments suggest that mass transfer processes within a pool transition zone may be similar in many respects to mass transfer processes in DNAPL residual zones.

Additional Abiotic Experiments. Abiotic mass transfer in source zones with DNAPL saturation of approximately 30 percent or less is thought to be a first-order kinetic process with a mass transfer rate coefficient that can be parameterized by an appropriate Gilland-Sherwood expression (Nambi and Powers, 2003). From the x-ray attenuation data obtained in the preliminary experiments, abiotic mass transfer in the saturation transition zone of a DNAPL pool also is likely to be a kinetic process. If biological activity affects mass transfer primarily by increasing concentration gradients at DNAPL-water interfaces, then a Gilland-Sherwood expression derived from abiotic experiments with a DNAPL pool should have application in describing mass transfer during bioremediation.

For completeness, two additional sets of abiotic mass transfer experiments were conducted for flow cells packed with a DNAPL pool at average saturation of approximately 30 and 90 percent. Experiments were conducted with an inflow solution of de-ionized water for a range of flow rates. In combination with results of previous tests at 50 and 70 percent average pool saturation, these experiments provided data for developing a Gilland-Sherwood expression that describe relationships between flow cell characteristics and abiotic mass transfer rate coefficients. A total of 12 dissolution experiments were conducted with de-ionized inflow water. Total flow rate through the cell varied between experiments from 0.08 to 0.25 ml/min (nominal seepage velocity, 0.015 to 0.05 cm/min). Average saturation of DNAPL in the lower sand was approximately 30, 50, 70 and 90 percent.

Steady-state PCE concentration in flow-cell effluent and mass flux of PCE from the DNAPL pool (Figure 3.100) and show complex responses to variations in DNAPL saturation and flow rate. For a given average pool saturation, PCE concentration decreases as flow rate increases and residence time of water in the pool decreases. PCE mass flux increases with increasing flow rate. However, effects of flow-rate variations were not as large as those caused by variations in average pool saturation.

The smallest PCE concentrations were recorded in experiments with the highest DNAPL saturation. At high average pool saturation, the portion of the pool with residual or near residual DNAPL saturation is likely to be small. Hydraulic conductivity of most of the pool is decreased several orders of magnitude from the water-saturated value. Water movement through this part of the pool, as well as PCE dissolution, are correspondingly small. At lower DNAPL saturation, the portion of the pool with near residual saturation is likely to be larger. As a result, water movement through the DNPL source zone is likely to increase, as are interfacial area for DNAPL dissolution and PCE concentration in effluent.

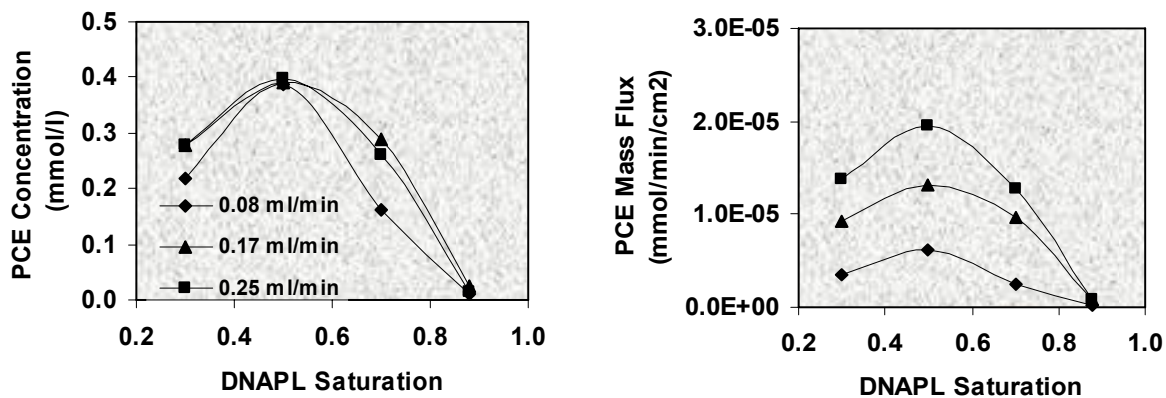


Figure 3.100. Steady-State Concentration and Mass Flux of PCE in Abiotic Experiments

The trend of increasing PCE effluent concentration and mass flux with decreasing average DNAPL saturation was reversed at saturation below 50 percent and may have been a reflection of kinetic dissolution behavior. At low saturation, the effect of increasing interfacial surface area was offset by limitations caused by the increased rate of water movement through the source zone. The higher flow rates that occur at low saturation decreased residence time of water in the source zone and did not provide adequate time for dissolution to approach equilibrium conditions.

Influence of Biological Activity on Mass Transfer from Pools. Flow-cell experiments with bio-treatment were conducted to evaluate the influence of biodegradation on mass transfer of chlorinated ethene compounds in multi-dimensional flow systems with a relatively simple DNAPL source-zone configuration. Results of these experiments were used to test the hypothesis that mass transfer of PCE from DNAPL pools is enhanced by source-zone bioremediation. Specific objectives included:

1. Determine if mass transfer from individual DNAPL pools is enhanced by biological activity. This objective was accomplished by conducting paired flow-cell experiments with and without actively degrading microbe cultures.
2. Determine how variations in the thickness of the saturation transition zone at the top of DNAPL pools affect biologically enhanced mass transfer. This objective was accomplished by conducting flow cell experiments with a specified range of average pool saturations. Thickness of the transition zone was expected to increase with decreasing pool saturation. If biological activity occurred within the transition zone the degree of biological enhancement was expected to increase as the transition-zone thickness increased.

Three series of mass transfer experiments were conducted at the flow-cell scale to assess the influence of biological activity on mass transfer. For each series, a capillary trap for PCE-DNAPL was created by filling the lower part of a 16.5 ml flow cell with coarse-grained sand while filling the overlying volume with medium- to fine-grained sand (Figure 3.97). Average

DNAPL saturation within the lower sand was established as 0.35, 0.60 and 0.85 for the three series. The experimental series at DNAPL saturation of 0.35 provided a pool that was slightly greater than residual saturation and had a relatively thick transition zone. The series at DNAPL saturation of 0.85 provided a pool with a sharp pool interface. The x-ray attenuation system was used to map DNAPL saturation in each series.

Each series consisted of at least 4 biotic experiments and an equal number of abiotic tests (24 total experiments). Experiments were conducted at specified constant-flow rates and electron-donor concentration. Inflow solution for the experiments consisted of KB-1 nutrient medium with methanol added as electron donor. Total flow rate through the cell was selected to provide residence times that promoted significant biodegradation while representing seepage velocities that are typical of field-scale conditions (Adams and Gelhar, 1992; Boggs et al., 1992; Freyberg, 1986; Hess et al., 1992; Mackay et al., 1986; Rehfeldt et al., 1992; Sudicky, 1986).

In series #1, average DNAPL saturation in the lower sand was 0.35 and methanol concentration was held constant at 200 mg/l. In series #2, average DNAPL saturation in the lower sand was 0.60 and methanol concentration was varied between experiments from 50 to 350 mg/l. In series #3, average DNAPL saturation in the lower sand was approximately 0.85 and methanol concentration was held constant at 200 mg/l. Flow rates for each series ranged from 0.005 to 0.025 ml/min (nominal Darcy velocities, 0.001 to 0.005 cm/min).

For each experiment, effluent water was collected until cumulative flow volume exceeded 20 pore volumes. Samples were collected at a rate of approximately 1 sample per pore volume. Effluent concentrations of chlorinated ethenes approached steady-state conditions after 3 pore volumes for abiotic tests and 6 to 10 pore volumes for biotic tests. Pump clogging occurred in some tests due to iron sulfide in the inflow solution. Any tests where cumulative flow volume failed to exceed 12 pore volumes were repeated.

Direct comparison of results for sequential mass transfer tests with and without actively degrading biomass provided a straightforward measure of the significance of bioenhanced dissolution without recourse to model-derived estimates of abiotic dissolution. Therefore, each series of experiments consisted of (1) preparing and inoculating a flow cell with an actively degrading culture, (2) conducting a set of aqueous phase biodegradation experiments (prior to DNAPL injection) at selected steady flow rates and specified concentrations of methanol (electron donor) and PCE (electron acceptor), (3) injecting a known amount of DNAPL as a pool and conducting bioenhanced dissolution experiments at selected flow rates and specified concentrations of methanol, (4) introducing oxygen to the flow system to stop degradation, (5) conducting a set of abiotic dissolution experiments with inactive biomass, run sequentially at the flow rates used in the bioenhanced experiments, and (6) characterizing biomass by destructive sampling. Periodically during the DNAPL mass transfer experiments, x-ray attenuation data were obtained to map saturation profiles through the DNAPL pool. However, given the flow rates and initial DNAPL volumes used in these tests, changes in DNAPL saturation were expected to be small during each series of experiments.

Mass transfer experiments by other researchers suggested that biodegradation of cis-DCE to vinyl chloride and ethene is inhibited by high PCE concentration in the close vicinity of DNAPL (Adamson et al., 2003; Cope and Hughes, 2000; Yang and McCarty, 2000; Yang and McCarty, 2002). Therefore, effluent water was analyzed by gas chromatograph for PCE, TCE and cis-DCE. However, to verify that vinyl chloride and ethene were not formed, 1 ml sub-

samples were obtained periodically and stored in sealed 2 ml vials. After equilibration of gas and water phases, headspace was analyzed by GC-FID method.

Time plots of PCE, TCE, DCE, and total chlorinated ethene concentration demonstrate that local-scale biodegradation kinetics exert a strong control on DNAPL dissolution from a high saturation pool. The majority of chlorinated ethene mass in effluent is in the form of DCE indicating the effectiveness of biodegradation within the flow cell.

Bio-activity enhanced DNAPL dissolution and mass flux relative to the level observed for abiotic dissolution. This was clearly shown by comparing results of biotic and abiotic tests conducted at the same flow rate and DNAPL saturation (Figure 3.101). In many biotic experiments, total chlorinated ethene concentration exceeded 1 mmol/L. In an abiotic system containing PCE-DNAPL, equilibrium dissolution serves as an upper limit for DNAPL mass transfer. The aqueous solubility limit of PCE is approximately 1 mmol/L. However, in an abiotic system with heterogeneous zones of high DNAPL saturation, flow bypass of pools and kinetic dissolution decrease the concentration of chlorinated ethenes leaving the source zone to well below aqueous solubility.

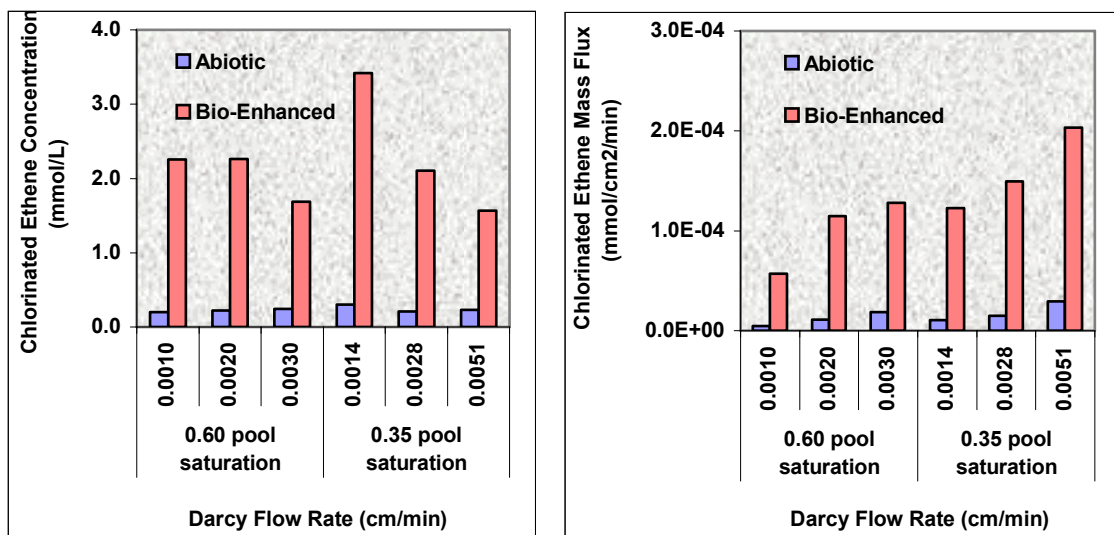


Figure 3.101. Steady-State Mass Flux of Chlorinated Ethenes for Flow-Cell Experiments of Bioenhanced Dissolution with Excess Methanol

Biological activity enhanced DNAPL mass flux from the level expected for abiotic dissolution. Steady-state mass flux rates in experiments with the KB-1 culture were greater than observed in subsequent abiotic dissolution experiments by factors of approximately 7 to 10 (Figure 3.102). The greater enhancement occurred in experiments with slower groundwater seepage velocity. The majority of chlorinated ethene mass in effluent was in the form of DCE.

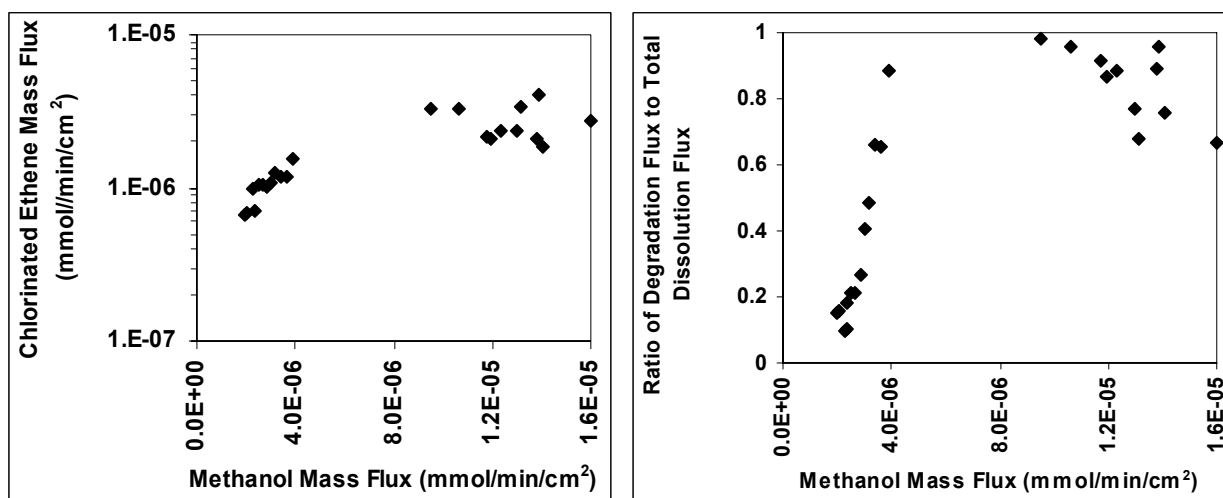


Figure 3.102. Effects of Variations in Methanol Flux on Degradation and Dissolution, Series #2 Flow-Cell Experiments of Bioenhanced Dissolution

The effect of biological activity on mass transfer increased as average pool saturation decreased. At lower average pool saturation, the thickness of the saturation transition zone increased, as did the ratio of biotic to abiotic mass flux of total chlorinated ethenes. The corresponding increase in mass transfer may reflect the presence of a stronger biodegradation sink within the transition zone.

A comparison of results from the first two series of experiments shows that biological enhancement of mass transfer in series #2 may be greater than observed in series #1. The decreased overall pool saturation in series #2 (0.35) compared with series #1 (0.60) results in a larger portion of the pool with residual or near residual DNAPL saturation. A larger saturation transition zone in series #2 and a corresponding increase in mass transfer may indicate that the microbes are present within the transition zone.

The ability to enhance mass transfer by biodegradation was limited by supply of electron donor. Experimental results from series #2 show the effects of limiting the supply of electron donor. When the inflow methanol flux dropped below 2×10^{-4} mmol/min/cm², effectiveness of dechlorination decreased (Figure 3.102). As effectiveness of dechlorination decreased, mass flux of total chlorinated ethenes also declined. This indicates that biologically enhanced mass transfer is electron-donor limited at the scale of individual DNAPL pool interfaces.

3.7.3 Large tank experiments

In this section of the report, a set of intermediate-scale experiments of bioenhanced dissolution in two-dimensional sand-filled tanks are described. The intermediate-scale experiments were designed to address two issues: (1) effectiveness of bioenhanced source depletion from DNAPL pools at intermediate scales, and (2) application a flow-cell scale conceptual model of bioenhanced DNAPL dissolution to source depletion at larger scales.

Biologically enhanced mass transfer from DNAPL source zones occurs in a system with a very large number of reactive transport processes. Flow-cell experiments focused on a limited subset of processes believed to exert primary control on overall system response. Specifically, physical advection-dispersion processes, abiotic mass transfer from DNAPL, and reductive dechlorination have been identified and incorporated in reactive-transport simulations of flow cell experiments.

The intermediate-scale experiments described here were designed primarily to focus on processes characterized during the flow cell experiments. However, during the intermediate-scale experiments, results were affected by several secondary processes not considered in flow-cell experiments. The secondary processes included competition for electron-donor supply between dechlorinators and other members of the microbial consortium, as well as formation, accumulation and migration of gas-phase waste products of biological activity. These processes may be significant in field-scale applications where even less control is possible than with intermediate-scale experiments. Although identified during the experiments, the secondary processes were not studied in detail.

Data summarized by Soga et al. (2004) for several remediation technologies suggest that effectiveness of source-depletion decreases and becomes less certain with increasing source-zone volume. Here, intermediate scale experiments with entrapped DNAPL pools at a range of specified average saturations and groundwater flow-field configurations are described and results are compared with results obtained previously in flow-cell experiments. Source-zone volume in flow cell experiments was 16.5 ml with average saturations that ranged from 0.25 to 0.74. Source-zone volumes in intermediate-scale experiments described in this paper were 350 to 400 ml with average saturations of 0.21 and 0.67.

Effectiveness of surfactant-enhanced dissolution is controlled by delivery of surfactant from injection location to source zone (Saenton et al., 2002). Mass depletion shows greater variability when surfactant delivery is incomplete. For bioenhanced dissolution, incomplete delivery of electron donor may cause similar problems. If electron donor is consumed upstream of a source, biodegradation within the source zone may be limited and effectiveness of bioenhanced dissolution would decline. The intermediate-scale experiments described in this paper address this issue by considering two flow-system configurations that are used in field-scale bioremediation projects. Electron donor loss upstream of a DNAPL source is minimized with one configuration, identified in this paper as continuous flow (CF), although the risk of incomplete degradation of PCE to ethene is increased. The other configuration, identified as recycle flow (RF) promotes dechlorination and electron-donor consumption upstream of the source as part of a strategy to promote complete dechlorination.

Remediation using a CF configuration supplies electron donor at injection wells upstream of a DNAPL source to promote biodegradation of chlorinated ethenes within and downstream of the source zone (Lackovic et al., 2005; Macbeth et al., 2005; Miller et al., 2005). In continuous flow systems, biodegradation within a PCE source zone is expected to stall at DCE. Electron donor that is not utilized in degrading PCE to DCE, or that bypasses PCE sources, is available for subsequent degradation of DCE to ethene in adjacent downstream areas. However, degradation to ethene may not occur if the electron donor does not adequately mix with the transported DCE or a suitable microbe culture is not present where mixing occurs.

The RF configuration combines electron donor injection upstream of a DNAPL source with downgradient withdrawal of groundwater (Bloom et al, 2005; Elder et al., 2005; Seguiti et al., 2005). Chlorinated daughter products and any unused electron donor are pumped to land surface, mixed and recycled through the bio-active source zone for degradation. The RF configuration has the advantage of controlling system hydraulics and preventing transport of chlorinated compounds away from the source zone. Typically, remediation using a RF configuration is preferred if ambient water quality requires manipulation to promote anaerobic conditions suitable for reductive dechlorination or if bioaugmentation is required. However, this strategy may affect the supply of electron donor available for PCE degradation in the source zone. If degradation rates are not sufficient to increase PCE dissolution gradients, mass transfer may not be enhanced.

Two large tanks suitable for mass transfer experiments with biological activity were constructed. One tank, designated the continuous flow (CF) tank, was designed specifically for anaerobic experiments and included many design features that minimized oxygen diffusion. Experiments in this tank were conducted using a continuous flow-system configuration. The second tank, designated the recycle flow (RF) tank, was originally designed for abiotic mass transfer experiments. Experiments in this tank were conducted using a recycle-flow configuration.

A series of tests and procedures were undertaken with each tank following construction and sand packing. Photon-attenuation monitoring provided a baseline for subsequent mapping of DNAPL distribution. DNAPL pools were created and scanned by photon-attenuation techniques to measure DNAPL distribution. Tracer tests and potentiometric-head monitoring confirmed expected flow patterns and results were used to estimate aquifer properties. Tanks were converted to anaerobic conditions suitable for reductive dechlorination and abiotic dissolution experiments were completed to provide a basis for comparison with subsequent bioenhanced dissolution experiments. Bio-active regions were developed that included the DNAPL sources by inoculating the tanks with the KB-1 microbe culture. After sampling to confirm bio-activity, bioenhanced dissolution experiments were conducted. The remainder of this section of the paper includes a description of tank construction followed by summaries of testing methods and protocols.

Construction of CF Tank. The CF tank was 2.43 m long, 0.61 m high and 5 cm thick, and contained flow under confined aquifer conditions. Side walls of the tank were clear acrylic lined with glass to minimize reaction of PCE with tank materials and oxygen diffusion. Ends and bottom were constructed of aluminum. Gasket material was placed between aluminum pieces and the acrylic sides. After bolting, the gasket provided an air- and gas-tight seal. The tank was then wet-packed with sand and sealed with bentonite, Teflon sheeting, and aluminum plate was installed to seal the top of the tank. The top seal permitted experimental conditions where the water head in the tank was greater than the top elevation of the tank producing confined aquifer conditions. This provided further resistance to contact with oxygen in the atmosphere. The tank included influent and effluent end wells (approximately 5 cm x 5 cm x 50 cm) filled with clean pea gravel to promote mixing. The end wells were separated from the rest of the tank with 200 mesh stainless steel screen.

The CF tank was packed with two hydrogeologic units separated by an impermeable Teflon-clay liner (Figure 3.103). The source zone in each unit consisted of a single lens of coarse-grained sand (#16) with an approximate volume of 350 ml. The sand lenses were placed

in a matrix of #50 sand. The downgradient portion of the upper unit was packed with a heterogeneous pattern of fine to coarse-grained sands (#110, #70, #50 and #30). The lower unit was packed as a homogeneous unit (#50 sand). An x-ray attenuation system was used to map DNAPL saturation in this tank.

The downstream portion of the upper unit was packed with a heterogeneous arrangement of sands in order to promote preferential plume migration within the coarse-grained sand lenses. The packing configuration was selected to represent a hydraulic conductivity field with high heterogeneity. Statistics of log transformed hydraulic conductivity in m/day were mean of 4.18, variance of 1.22, horizontal correlation length of 0.5 m and vertical correlation length of 0.05 m. Multiple random-field realizations of hydraulic conductivity were generated using these design parameters and one realization was selected for packing that would promote preferential migration through the unit. This realization was discretized into five categories spanning the range of hydraulic conductivity and categories were associated with laboratory sands with known hydraulic properties (Illangasekare et al., 1995a and 1995b; Compos, 1998; Saba and Illangasekare, 2000; Barth et al, 2001; Sakaki and Illangasekare, 2006).

The tank was filled by hand according to the packing design. Filling involved placing individual sand volumes of approximately 80 cm³ into the tank with the aid of a 5 cm PVC pipe. In this manner, individual sand lenses approximate 15 cm long and 1 cm high were placed at the desired locations. By dropping the sand through the PVC pipe while the pipe was moved laterally along a 15 cm track, a discrete 'blocky' geometry was avoided and more realistic sand contacts were established. The resulting individual sand units were tapered at their boundaries rather than having sharp vertical fronts.

Sample locations were established along several vertical profiles in order to provide detailed descriptions of mass transfer along flow paths at various depths in the DNAPL pool and at several horizontal distances from the source zone (Figure 3.103). Because sides of the tank were glass lined, access for samples was provided by thin-walled Teflon tubes with a nominal diameter of 0.3 mm. The tubes were installed as wells while packing the tank with sand and operated with minimal clogging throughout the experiments. After packing and sealing the tank, each sampling tube was fitted with a three-way valve that provided access for sampling and pressure monitoring. This tubing also provided access for injection of fluids during the experiment.

Separate HPLC pumps (Beckman model 114M) were used to inject water or nutrient medium at controlled rates into the upper aquifer unit, the lower aquifer unit, and the injection end well. Outflow from the tank at the effluent well was controlled by a head reservoir installed at an elevation slightly above the top of the tank. Effluent flow rate was monitored by collecting and weighing all water leaving the tank.

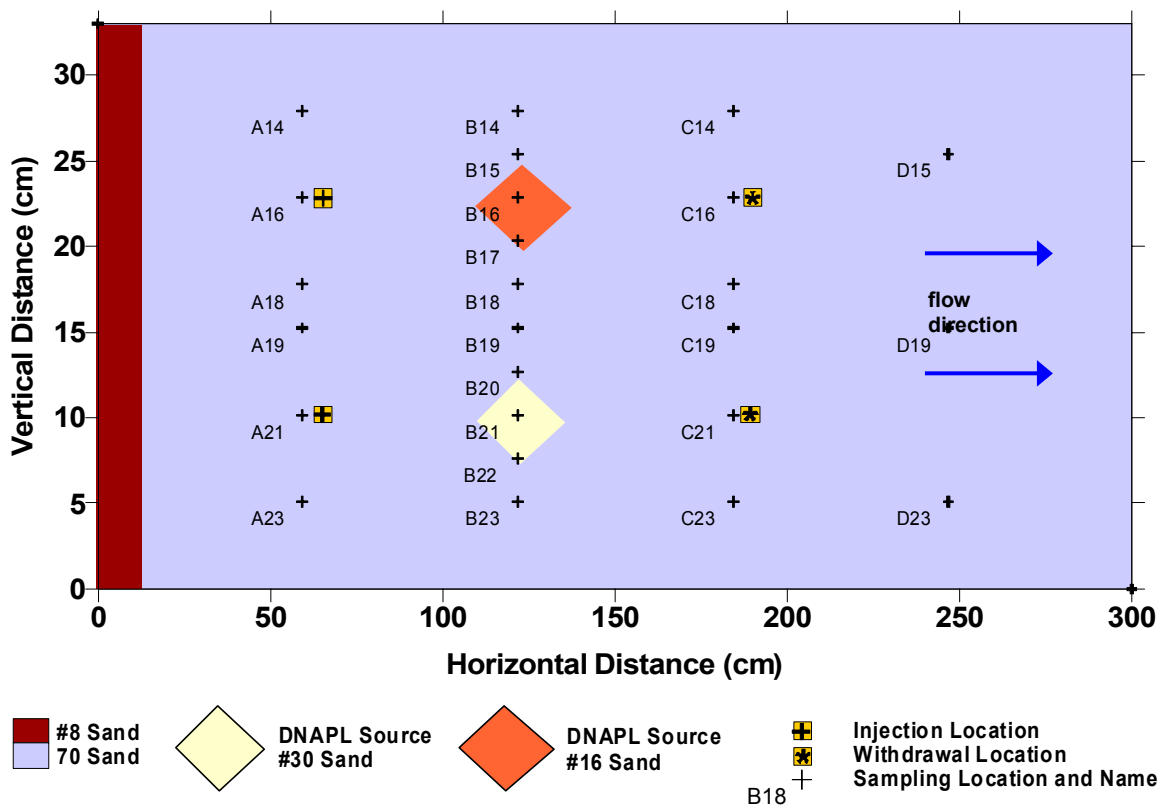


Figure 3.104. Configuration of RF Tank, Large Tank Experiments of Bioenhanced Dissolution

A flow recirculation system was established by withdrawing water at two locations approximately 60 cm downstream of the DNAPL source zones, collecting this water in a 9 L glass bottle held under anaerobic conditions, and injecting water from the bottle at two locations approximately 60 cm upstream of source zones. Withdrawal rate was controlled by a multi-channel peristaltic pump (Ismatec). Injection rate matched withdrawal rate as verified by a constant water volume in the glass bottle. Teflon tubing was used throughout the recirculation system.

Materials. The tanks were packed with clean silica sand obtained from Unimin Corporation. During packing, sand was placed in 2.5 cm lifts and the water level was maintained at 5 cm above the top of the sand to avoid significant grain-size separation as the sand fell through the water. Bentonite was used in combination with Teflon liners to create confining layers within tanks to isolated one flow system from overlying or underlying systems. Hydraulic properties of the sands have been characterized by several investigators conducting laboratory experiments at column to large tank scales (Illangasekare et al., 1995a and 1995b; Compos, 1998; Saba and Illangasekare, 2000; Barth et al., 2001; Sakaki and Illangasekare, 2006).

A single component DNAPL consisting of PCE was used in all experiments. Analytical grade PCE (>99% purity) was obtained from Mallinckrodt Chemicals. In experiments with the RF tank, PCE was dyed with a small concentration of Sudan IV (0.01%). Sudan IV is a hydrophobic organic red dye that was obtained from Aldrich Chemicals.

The KB-1 mixed culture of dechlorinators (Edwards and Cox, 1997) was used in bioenhanced dissolution experiments. KB-1 has proven to be highly robust and well suited for use in bioaugmentation of chlorinated ethene plumes (Major et al., 2002; Morrill et al., 2005). The culture degrades PCE to ethene using methanol as an electron donor. The culture was maintained in an anaerobic nutrient medium using established procedures (Edwards and Grbic-Galic, 1994) and had been adapted to PCE at high aqueous concentration (120 mg/L) approximately 1 yr prior to inoculation of the tanks.

Creation of DNAPL Sources. Source zones were designated during construction of the tanks by placing coarse-grained sand lenses within a matrix of medium to fine-grained sand. To create a DNAPL pool within the source zones, a volume of PCE equal to 85 percent of the coarse-grained sand pore volume was injected at a rate of 0.02ml/min through a sampling port located at the base of the sand lens. The 85 percent value was selected because it is slightly less than the maximum DNAPL saturation reported in laboratory experiments for #16 sand (Illangasekare et al., 1995a). The high entry pressure of the surrounding #50 sand prevented DNAPL migration outside the source zones. The injection and containment due to the barrier effect resulted in nearly complete displacement of water in the coarse-grained sand lenses by the DNAPL. The direction of pumping was reversed and DNAPL was withdrawn until the desired volume remained in the flow cell. This resulted in a saturation profile in the transition zone characteristic of the water-imbibition portion of a DNAPL-water capillary retention function.

DNAPL Characterization. Photon attenuation techniques were used to monitoring the spatial distribution of DNAPL saturation. Attenuation of photon radiation by porous media was used to determine differential path lengths of sand, water and DNAPL within a sample. Material path lengths are measures of porosity and fluid saturation. Analysis of photon attenuation spectra is based on an application of the Beer-Lambert law written for multiple materials and an equivalent number of lumped-energy ranges over which photon count rates are recorded (Illangasekare et al, 1995; Hill et al., 2002; Ferre et al., 2005). The resulting matrix expression can be solved for a vector of path lengths given a set of attenuation coefficients, typically determined by a calibration procedure with samples of known path length, and a vector of photon count rates.

An x-ray attenuation system was used to map DNAPL saturation in the CF tank and a gamma attenuation system was used with the RF tank. The x-ray system consisted of an x-ray source and detector located within a movable frame. The x-ray source (Pantak HF100) was optimized for experimental conditions by selecting source intensity (72 kV, 15 mA) and x-ray filters (barium carbonate salt and samarium carbonate solution at solubility) to produce multiple-peak spectra. The x-ray attenuation system was capable of positioning within a vertical-horizontal plane with a precision of 2 mm. Accuracy of the x-ray system, determined by replicate scans of the source zones, is 2 percent of measured DNAPL saturation. The gamma attenuation system also consisted of a source and detector located within a movable frame. It used a 200 mCi Americium-241 source with a primary peak at 60keV and was capable of positioning with a precision of 5 mm.

Photon attenuation data showed a heterogeneous distribution of DNAPL saturation in each experiment. Average saturation for horizontal strata within source zones showed layered transition zones across pool interfaces (Figure 3.105). Lateral variations in DNAPL saturation were significantly less than vertical variations. Coefficients of variation along horizontal strata were generally less than 10 percent for the CF tank and 20 percent for the RF tank. For each flow

cell, average DNAPL saturation obtained by photon attenuation methods matched DNAPL saturation determined by volumetric measurement of injected mass.

Photon attenuation techniques were used to monitor DNAPL distribution in each tank at the beginning of abiotic DNAPL dissolution, prior to inoculation, and at the end of the bioenhanced dissolution tests. Temporal declines in DNAPL saturation calculated from results of these scans were less than the accuracy of the photon attenuation technique. Accuracy of the x-ray system is 1 to 2 percent of measured saturation. Accuracy of the gamma-ray system is approximately 5 percent (Gago et al., 2002). The relatively small volumes of DNAPL depletion observed by photon attenuation techniques were consistent with total mass flux of DNAPL calculated from results of water samples and flow measurements.

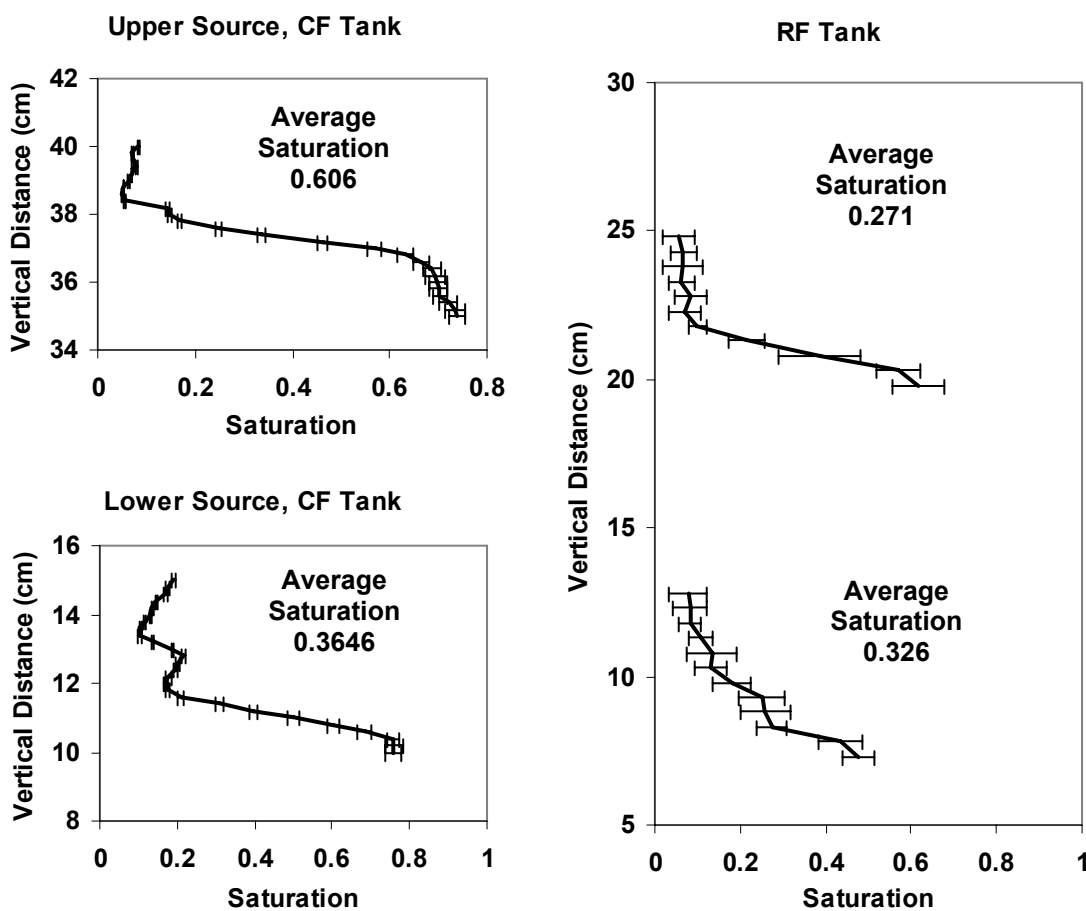


Figure 3.105. DNAPL Saturation Distribution in Four Sources, Large-Tank Experiments of Bioenhanced Dissolution

Hydraulic-Head Monitoring and Natural Gradient Tracer Tests. Hydraulic head distribution was monitored at 48 locations in the CF tank and 24 locations in the RF tank using differential pressure transducers fitted to mechanical multiplexers. Each position in the

multiplexer was connected by 1/16 in. polypropylene tubing to a sample-port valve and cycled at hourly intervals to collect pressure data. Scanning was controlled by a PC with custom-written LabView software. Head differences between upstream and downstream tank boundaries were small (less than 1 cm for CF tank, 2 cm for RF tank) and reflected the low flow rate used in the experiments.

Tracer tests were conducted following tank construction, packing and DNAPL source creation to confirm that desired flow patterns had been established and to estimate effective porosity and longitudinal dispersivity coefficient. In both tanks, natural gradient flow conditions were established by setting upstream and downstream head reservoirs at elevations that resulted in flow rates similar to those used in subsequent abiotic and bioenhanced dissolution experiments. In each tank, known volumes of red food dye and bromide as a conservative tracer at 1000 mg/L were injected for 1 hr at locations shown in Figures 3.103 and 3.104. Dye clouds formed at injection points showed convergence upstream of source zones with preferential movement through the upper part of the sources (saturation transition zones). Dye flow paths also bypassed the lower part of the sources where saturation was high. Flow paths diverged strongly immediately downstream of the source zones. Within the upper unit, downstream migration occurred primarily in coarse-grained sand. Within the lower unit, downstream migration was primarily horizontal, reflecting the homogeneous distribution of sand.

Water samples were collected at locations shown in Figures 3.103 and 3.104 at 2 to 8 hour intervals. Water samples were analyzed for bromide concentration by ion chromatography (Dionex AS50) using an 8-point calibration at bromide concentrations from 0.01 to 1000 mg/L. Results were interpreted with the method of moments (Fernandez-Garcia et al., 2002) to estimate effective porosity (0.50 in the CF tank and 0.52 in the RF tank) and longitudinal dispersivity (approximately 0.1 cm for both tanks). These estimates are consistent with tracer tests conducted in similar tanks (Saba and Illangasekare, 2000; Moreno-Barbero, 2005)

Creation of Anaerobic Conditions. Anaerobic conditions suitable for reductive dechlorination were created in each tank prior to conducting mass transfer experiments. For each tank, a solution of de-ionized water with a sulfide concentration of 3 to 5 mmol/L and adjusted to pH 7 was made in an 18 L glass bottle and injected. Anaerobic conditions were readily observed by the presence of dark green to black precipitate downstream of the injection points. Accumulation was particularly evident in the coarse-grained sands (#30 and #16).

Abiotic Dissolution Experiments. Abiotic dissolution experiments were conducted in each tank to provide a basis of comparison for subsequent bioenhanced dissolution experiments. Inflow solution consisted of anaerobic nutrient medium (Edwards and Grbic-Galic, 1994) augmented with methanol at 200 mg/L. Injection flow rates were 1.0 ml/min in the CF tank (0.5 ml/min per unit) and 1.2 ml/min in the RF tank. Water samples were collected at sample locations throughout each tank and analyzed for PCE, TCE and DCE by gas chromatography. Sampling and analysis methods were identical to those used by Glover et al. (2006). Injection and sampling locations are shown in Figures 3.103 and 3.104. In the CF tank, samples were collected at 2-day intervals from locations near the sources and at 2-week intervals from all locations. In the RF tank samples were collected at 2-day intervals. Sampling continued for one month in the CF tank and 15 days in the RF tank. Sample analysis indicated that quasi-steady state conditions were attained during these times with the exception of locations in the downstream portion of the CF tank (upper unit) that sampled water from fine-grained sand (#110). Degradation products (TCE, DCE) were not detected during abiotic experiments.

Inoculation with KB-1. Following abiotic dissolution experiments, each source zone was inoculated with approximately 900 mL of actively growing KB-1 culture. At the time of inoculation, water samples from the KB-1 cultures showed negligible concentrations of PCE and chlorinated daughter products. The CF tank was inoculated by injecting the KB-1 culture at a rate of 0.05 mL/min through a sampling port located immediately upstream of each source zones. The RF tank was inoculated by injecting the KB-1 culture through a sampling port located near the top of each source zone. The bioactive zones shown in Figures 3.103 and 3.104 have water-saturated pore volumes equal to the volume of KB-1 used during inoculations and were estimated on the basis of simulated groundwater flow patterns. Water samples collected 2-4 days after inoculation showed elevated concentrations of PCE degradation products and indicated that inoculation was successful.

Bioenhanced Dissolution Experiments. Experimental conditions for bioenhanced dissolution experiments were identical to those used in previous abiotic dissolution experiments. Inflow solution consisted of anaerobic nutrient medium (Edwards and Grbic-Galic, 1994) augmented with methanol at 200 mg/L. Injection flow rates were 1.0 ml/min in the CF tank (0.5 ml/min per unit) and 1.2 ml/min in the RF tank. Water samples were collected at sample locations throughout each tank and analyzed for methanol, PCE, TCE, DCE, VC and ethene by gas chromatography. Injection and sampling locations are shown in Figures 3.103 and 3.104. In the CF tank, samples were collected at 2-day intervals from locations near the sources and at 2 week intervals from all locations. In the RF tank samples were collected at 2-day intervals. Sampling continued for one month in the CF tank and two months in the RF tank. Test durations were sufficient to meet study objectives but were not sufficient to establish steady-state conditions. Additional sampling and coring of the CF tank is being conducted by other researchers on a continuing basis.

Water samples (1 mL) were collected by gas-tight syringe, stored with headspace in sealed 5 mL vials, and placed on a shaker table for 18-30 hours to equilibrate. Headspace was sub-sampled for gas-chromatography analysis of PCE, TCE, cis-DCE, VC, ethene, and methanol. Temperature-corrected Henry's constants (Gossett, 1987), along with precisely measured sample and headspace volumes, were used to calculate concentrations in the original liquid sample.

Observed Mass Transfer in the CF Tank. Abiotic experimental results show a complex distribution of PCE concentration downstream of sources (Figure 3.106). This reflects spatial variations in flow paths near sources and downstream, as well as dissolution dynamics within sources. Flow paths inferred from measured hydraulic head data were unreliable because head gradients were very flat relative to measurement resolution. However, flow paths calculated with a groundwater flow modeling showed convergence upstream of sources, rapid movement through transition zones and divergence downstream. Flow rates in deeper portions of the pools were very slow with most water bypassing either through the transition zone or beneath the source. In the upper unit, downgradient flow paths are predominantly horizontal in lenses of highly permeable sand with notable vertical components in low permeable sand.

Comparison of measured PCE distribution with flow paths estimated by groundwater flow modeling shows that PCE concentrations were greater along flow paths that traversed pool transition zones. In the downstream portion of the upper unit, the PCE plume appeared to migrate predominantly within coarse-grained sand lenses. The PCE plume in the lower unit was more regular and reflected a homogeneous distribution of sand. Detailed discussions of the groundwater flow model and abiotic mass flux, as well as quantitative comparisons of abiotic to

bioenhanced mass flux for the CF tank are presented in the modeling section of this report (chapter 4).

Bioactivity was observed in the upper unit within 4 days of inoculation by the presence of DCE and VC at sample locations downstream of sources. With increasing time, PCE concentrations declined and degradation product concentrations increased. Concurrent with increases in degradation products, methanol levels declined downstream of the source. Evidence of bioactivity in the lower unit was not observed until 2 weeks after inoculation. Reasons for the lag were not readily apparent. Throughout the remainder of the experiment, DCE and VC concentrations increased and PCE concentrations decreased in the lower unit.

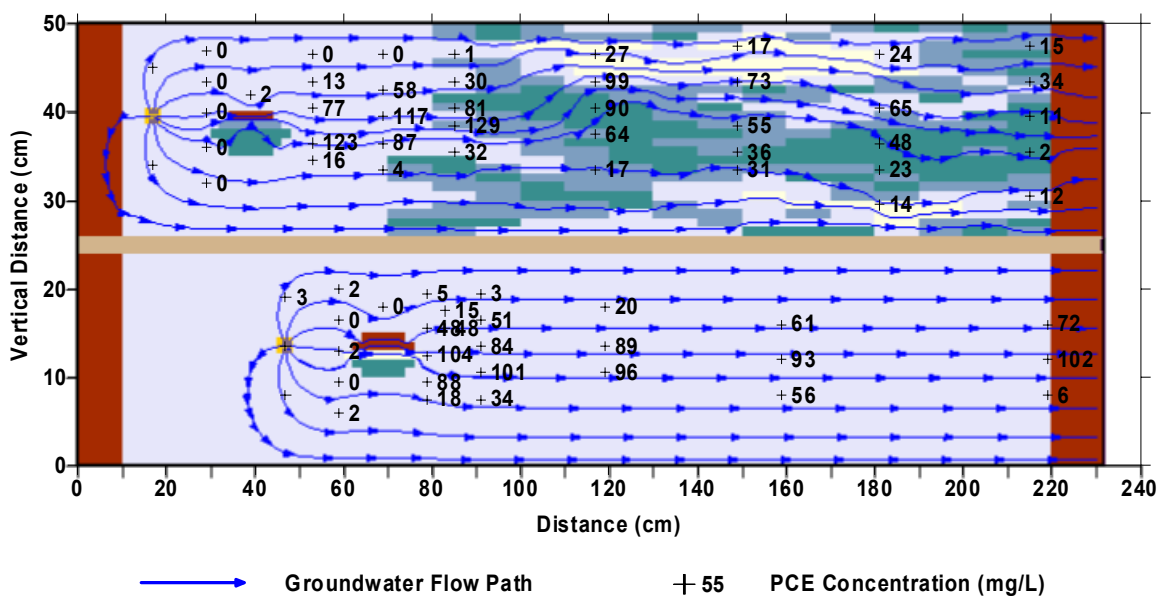


Figure 3.106. Observed PCE Concentration in the CF Tank at the End of Abiotic Dissolution Experiments

Degradation products at sample locations immediately downstream of sources (profiles U6 and L6) were predominantly in the form of DCE with the exception of one sample location in the lower unit where VC was the dominant ethene. At locations in the upper unit downgradient of profile U6, DCE concentration declined, while DCE remained high at downgradient locations in the lower unit. The limited DCE degradation in the lower unit may reflect the delayed response of microbes noted previously.

Bioenhanced dissolution occurred primarily along flow paths that traversed transition zones of the DNAPL pools. This is most clearly illustrated by comparison of total ethene concentration for the bioenhanced dissolution experiment with PCE concentration for the abiotic experiment at individual sample locations (Figure 3.107). Total ethene concentration observed during the bioenhanced dissolution experiment exceeded abiotic concentration for most sample

locations along transition-zone flow paths. Typically, increased dissolution was associated with elevated concentrations of PCE degradation products. In contrast, sample locations along flow paths that bypass the sources provided minimal changes in total ethene concentration from abiotic levels.

Significant gas accumulation occurred in the upper unit during the bioenhanced dissolution experiment. During the first 6-10 days, VC and ethene concentrations increased and reached a level where gas formation was possible. Gas accumulation was observed by visual inspection 2 weeks after inoculation. Initially, gas formed in areas immediately downstream of the source and accumulated at the contact between the top of the upper unit and the overlying bentonite seal where the high air displacement pressure of the bentonite prevented upward migration (Figure 3.107). Analysis of this process in greater detail is provided in the modeling section of this paper. With time, gas accumulation in the upper unit also was noted upstream of the source. After 4 weeks, gas also accumulated within the upper portion of the coarse-grained sand lens that formed the source zone.

Gas accumulation was not anticipated during experimental design and sampling locations were not available to determine the composition of the gases. However, water samples obtained in the vicinity of the upstream gas had an odor consistent with the presence of sulfides. This suggests that methanol injected upstream of the sources may have been partly consumed by sulfate-reducing bacteria. No odors were detected in water samples located near the downstream areas of gas accumulation. Sampling and coring of the CF tank is ongoing as part of other research and may provide more definitive information on the composition of the gases (Pierre Phillip, Ecole Polytechnique Federale de Lausanne, ENAC, written communication, March 2006).

Methanol concentrations downgradient of source areas declined as bioactivity increased. After one month, methanol concentrations in the upper unit were near detection limits. Within the lower unit, methanol concentrations were depressed from levels in the injection solution but remained significantly above detection limit. This result is consistent with delayed biological activity in the lower unit.

Observed Mass Transfer in the RF Tank. Data to characterize dissolution in the RF tank were more limited than in the CF tank, making detailed validation of dissolution models impractical. Nevertheless, experimental results provide useful insights to bioenhanced dissolution at intermediate scales. The amount of data available for the RF tank was more comparable with amounts of data available at field scales.

Because water in the RF tank was withdrawn downstream of the sources and injected upstream, PCE was observed throughout the capture zone (Figure 3.108). PCE concentration downstream of the two sources differed. After withdrawal, mixing and injection, PCE concentration upstream of the sources was similar.

Abiotic mass load of PCE, measured at the two withdrawal points, was greater for the lower source than for the upper source of the RF tank (Figure 3.109 and Table 3.42). This suggests differences in the distribution of DNAPL within the two sources. The thickness of the transition zone was greater for the lower source than for the upper source (Figure 3.105) and reflected differences in the shape of the saturation retention function of #30 sand (lower source) and #16 sand (upper source). As a result, DNAPL-water interfacial surface area within the lower source was greater than within the upper source and mass flux was greater.

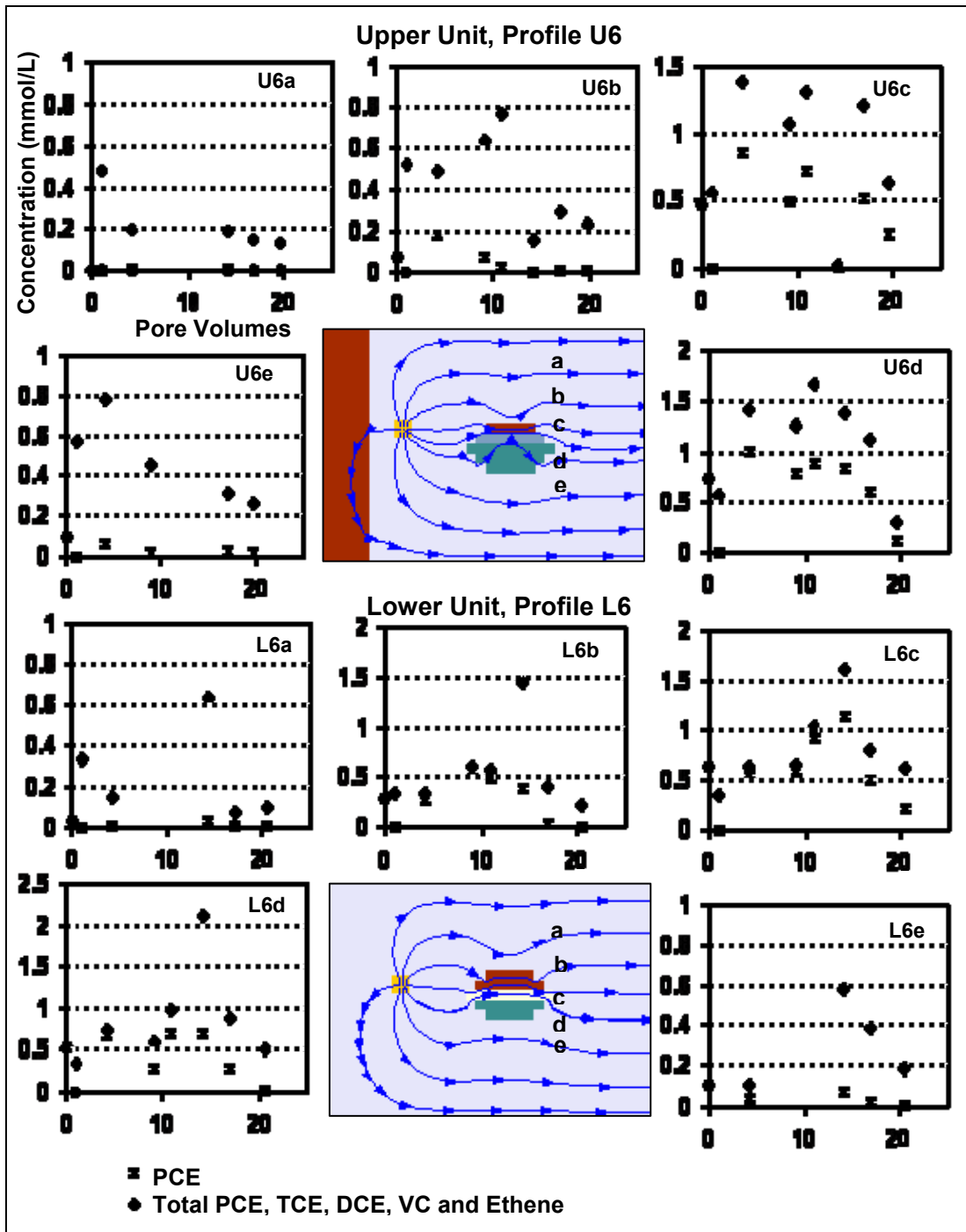


Figure 3.107. Observed Concentration of Dissolved Ethene Chemicals in the CF Tank During the Bioenhanced Dissolution Experiment

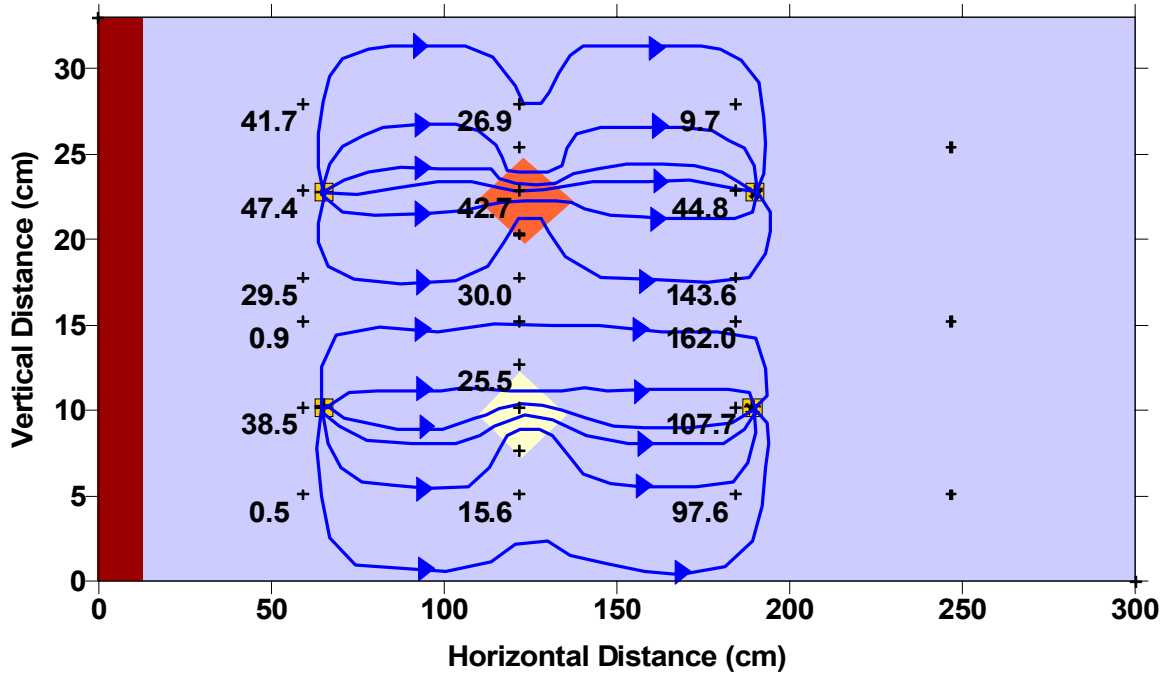


Figure 3.108. Observed PCE Concentration in the RF Tank at the End of Abiotic Dissolution Experiments

Table 3.42. Observed Mass Load of Dissolved Ethene Chemicals at Groundwater Withdrawal Locations in the RF Tank Experiment of Bioenhanced Dissolution

| Source | Abiotic Mass Load (mmol/min) | Mass Load One Month after Inoculation (mmol/min) | Mass Load Two Months after Inoculation (mmol/min) |
|--------|------------------------------|--|---|
| Upper | 4.50×10^{-4} | 2.19×10^{-3} | 1.35×10^{-3} |
| Lower | 1.08×10^{-3} | 4.35×10^{-3} | 2.88×10^{-4} |

High concentrations of PCE at sample locations between the two withdrawal points corresponded with a stagnation point in the flow system (Figure 3.108). Detailed solute-transport modeling to explain these data was not undertaken. However, PCE concentrations in this region of the tank were not elevated during a natural-gradient tracer test. When flow was recycled and stagnation developed, transverse dispersion from adjacent areas with more rapidly flowing water may have contributed to elevated concentrations near the stagnation point.

Effects of bioactivity in the RF tank are most clearly illustrated by comparing PCE mass flux prior to inoculation with the mass flux of total ethene compounds one and two months after inoculation (Table 3.42). One month after inoculation mass flux of ethenes, measured at withdrawal wells, increased by a factor of 4.87 for the upper source and 3.45 for the lower source.

After two months, mass flux from the upper source had declined but remained greater than abiotic levels by a factor of 3.00. Mass flux from the lower source was significantly lower than abiotic levels.

The distribution of ethene compounds one month after inoculation showed that water from the upper source was predominately DCE while data for the lower source presented a more complex distribution (Figure 3.109). Composition of water near the lower source was dominated by DCE and ethene while water near the lower withdrawal location contained significant PCE. Water upstream of the lower source was dominated by DCE.

Two months after inoculation, ethene was the dominant constituent in water upstream and near the sources while ethene and DCE were the dominant constituent of water near withdrawal points (Figure 3.110). PCE also was observed as a secondary constituent in samples located near the downstream stagnation point. The data at two months suggest that the system did not experience significant methanol limitations. If methanol had been strongly limiting, PCE concentrations would have been larger.

Water withdrawn from the RF tank was pumped into a 7 L mixing reservoir with a 3 L headspace. In the reservoir, methanol could be added as needed before injection upstream of the sources. Differences in composition and concentration of total ethene compounds at downstream withdrawal points and upstream injection points can be attributed to biodegradation and gas-phase partitioning within the mixing reservoir. At the start of the bioenhanced dissolution experiment, the mixing reservoir was not inoculated with the KB-1 culture. However, PCE concentration declined between withdrawal and injection locations one month after inoculation. Similarly, DCE concentration declined two months after inoculation. These changes suggest that microbes had been transported into the reservoir and were active during the experiment.

Gas accumulation was noted in the lower source one month after inoculation. By two months, gas had virtually filled the lower source and also had accumulated in the upper source. Gas samples obtained from the upper part of each source were analyzed by gas chromatography and contained extremely high concentrations of VC and ethene. The decline in mass flux from one to two months may have reflected the effects of water bypassing the gas-filled source zones and increased gas saturation that decreased the interfacial surface area available for DNAPL dissolution.

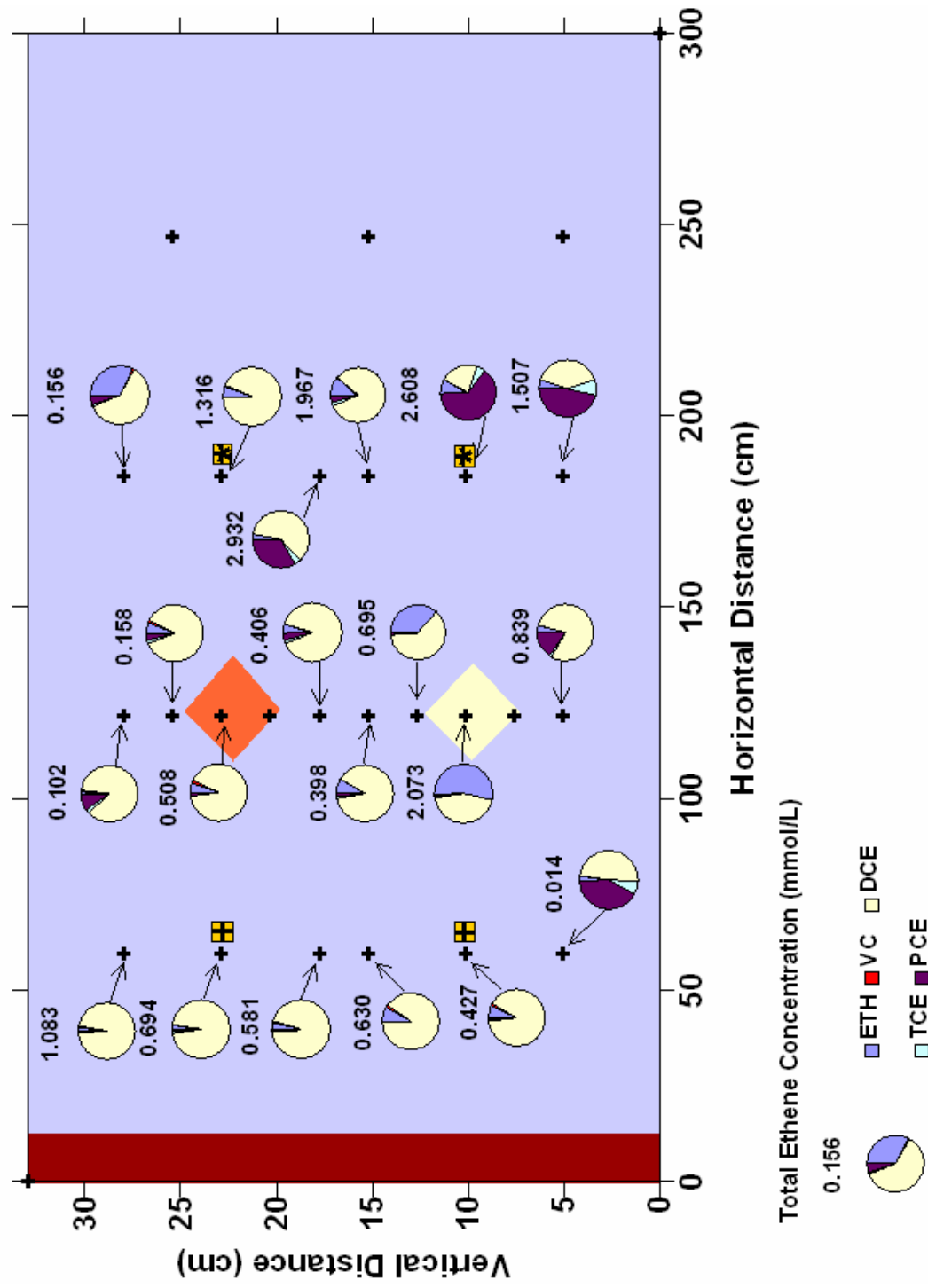


Figure 3.109. Observed Concentration of Dissolved Ethene Chemicals in the RF Tank One Month after Inoculation

3.8 Experimental design and methods for investigation of thermal treatment

Research focused on understanding how thermal treatment affects solubility of PCE-DNAPL and empirical coefficients of Gilland-Sherwood correlations. Hot-water flooding was selected for study as representative of the broader range of thermal technologies. Results presented here were obtained with batch and column experiments. Research to upscale these results to multi-dimensional flow systems in flow cells and large tanks is continuing.

3.8.1 Batch experiments – temperature dependence of PCE solubility

The general objective of batch experiments was to obtain equilibrium dissolution data needed for modeling of subsequent column and flow cell experiments of kinetic mass transfer. Batch tests were conducted for a temperature range of 12 to 85 °C. The lower temperature was selected as the minimum temperature that could be sustained without using a cooling system. The maximum temperature limit of 85 °C was chosen because boiling of the PCE-water system was observed at higher temperature.

Experimental Design. Approximately 5 mL of PCE was added in each of five 20 mL vials. The rest of the volume was filled with water. The vials were then placed in a thermal bath/shaker. Beginning at 12 °C, the temperature of the water was steadily increased to 25, 50, 75 and 85 °C. When one of these temperatures was reached, it was maintained at a steady temperature for at least an hour before sampling. One-mL samples were obtained from each vial with a pre-heated gas tight syringe and in 5 mL vials containing 3 mL of hexane. After collecting the samples the hexane-filled vials placed on a shaker for a day and a half to give time for complete hexane extraction of the PCE. Afterward, the hexane was sampled and analyzed by GC obtain the PCE concentration.

Results. Solubility of PCE increased with temperature over the range of 12 to 85 °C (Figure 3.111). These results are in the same range as the results of Horvath (1982) and Sleep and Ma (1997), but differ significantly from the studies by Stephenson (1992) and Imhoff (1997). Stephenson's results show a decrease in solubility between 20 and 40 °C, while the Imhoff results show a decrease in the solubility between 5 and 20 °C.

A second order polynomial equation was fitted to the data to give

$$S_{PCE} = 0.0368 \cdot T^2 - 1.5293 \cdot T + 202.1400 \quad (3.10)$$

with T in °C and S_{PCE} in (mg/L). The correlation coefficient for the above equation was 0.996.

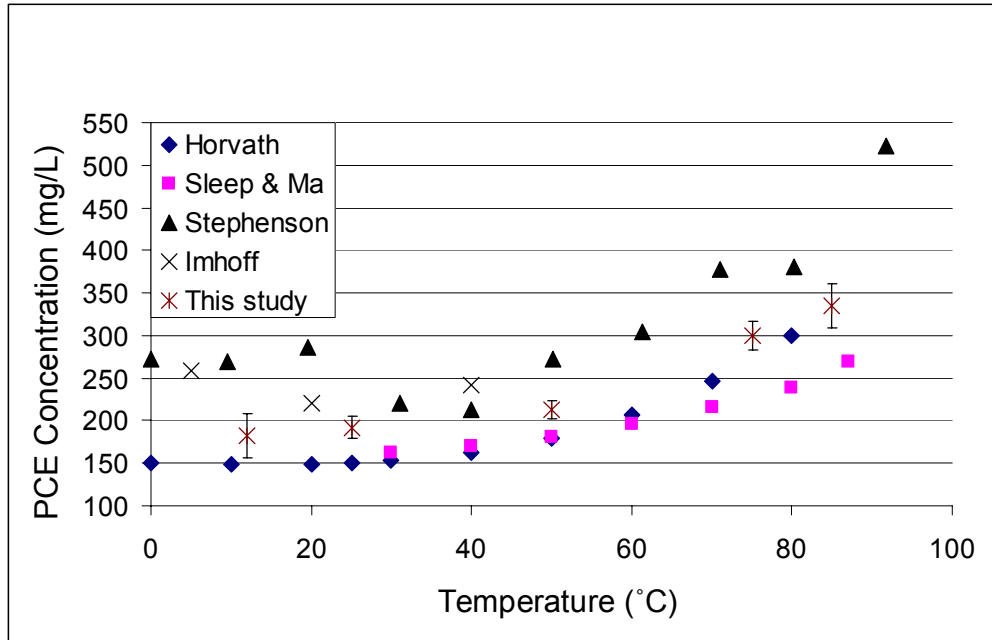


Figure 3.111. PCE Solubility as a Function of Temperature

3.8.2 Column experiments – temperature dependence of PCE mass transfer

Column experiments with PCE-DNAPL at residual saturation were conducted for a range of temperatures typically used in thermal technologies. Column experiments were conducted to determine the dependence of mass transfer on temperature, pore velocity and grain size.

Experimental Design. A total of 30 dissolution experiments were run for five sands with a d_{50} ranging from 0.019 cm to 0.13 cm. The sand was packed in a 2.5 cm diameter by 10 cm long chromatography column. The length of the column was reduced to 1.4 cm using a plunger. A three millimeter thick capillary barrier was created between the sand and the plunger tip using fine sand. For columns packed with sand having d_{50} of 0.13 cm and 0.094 cm, the capillary barrier was created with sand having d_{50} of 0.019 cm. For columns packed with sand having d_{50} of 0.05 cm and 0.028 cm, the barrier was created with a sand having d_{50} of 0.011 cm. For columns packed with sand having d_{50} of 0.019 cm, the barrier was created with a sand having d_{50} of 0.009 cm. The columns were saturated using nanopure de-ionized water.

Residual saturation in each column was created using a methodology similar to the one presented by Powers et al. (1992) and Imhoff et al. (1997). PCE dyed with Sudan IV was injected from the bottom of the column at an approximate flow rate of 0.3 mL/min. The injection was stopped when PCE reached the capillary barrier. Flow direction was then reversed to displace the NAPL. Water was injected at 1 mL/min until no more free phase came out of the column. The flow rate was increased to 15mL/min and approximately 5 pore volumes of water were injected through the column. This method produced a series of disconnected ganglia with residual saturation of approximately 20 percent distributed throughout the sand, except for the capillary barrier.

Water was heated before injection to the column by using a copper coil wrapped with a computer controlled heating tape. Temperature control of the heating tape was achieved with a California Instruments power supply which was used to vary the voltage applied to the heating tape. The voltage required for a specific temperature was calculated with the aid of an analytical solution to the problem of water flowing through a circular pipe with constant heat flux in the walls of the pipe. Temperature of the water was monitored at the inflow and outflow of the column via two type-K thermocouples. The temperature variation was less than 1 °C. To minimize horizontal thermal gradients inside the column due to lateral heat losses the column was wrapped with pipe insulation and fiberglass insulation.

Experiments were conducted within the framework of a 6x10x5 factorial design with temperature, sand grain diameter, and flow rate as factors in the design (Table 1). For each of the five sands, six experiments were run at temperatures of 25, 35, 45, 55, 65 and 75 °C. The minimum temperature was selected to be room temperature, and the highest temperature was selected to be 75 °C because over 80 °C water-vapor bubbles were formed at the inlet of the column that affected water flow. For a given combination of temperature and sand grain diameter, water flow rate was varied from 5.5 ml/min to 10 ml/min in increments of 0.5 ml/min to provide 10 different flow rates. This range of flow rates was selected on the basis of previous experiments by Imhoff et al. (1997). High flow rates were used to assure that PCE concentration in the outflow was less than the solubility limit.

For each experiment, water samples of column outflow were collected after experimental conditions were established. Because flow rates were high, sample intervals were rapid. Five samples were collected for each experiment. Sample treatment and analysis were the same as used in batch experiments described previously. Analytical results showed that steady-state conditions were established during all sampling periods. Only steady-state data are presented in this report.

Experimental Results. The lumped mass transfer rate coefficient (K_{la}) was calculated for all the experiments using methods described previously for column experiments of natural dissolution. Sherwood number was then calculated with molecular diffusion of PCE in water estimated by the method of Tyn and Calus (1975a and 1975b). Figures 3.112 and 3.113 show the difference in mass transfer rate coefficients between 25 and 75 °C for the minimum and maximum flow rates of the experiments.

Sherwood number increased significantly with increasing sand grain size (Figure 3.114). For a given sand-grain size, Sherwood number also increased with increasing flow rate, particularly for sands with larger grain size.

Mass transfer rate coefficient (K_{la}) showed little variation as a function of grain size (Figure 3.115). Flow rate had a small but observable effect on K_{la} . Similar behavior has been observed by Miller et al. (1990). Grain size and shape contribute to the shape, size and distribution of NAPL drops or ganglia within a porous media, which in turn can affect mass transfer rates.

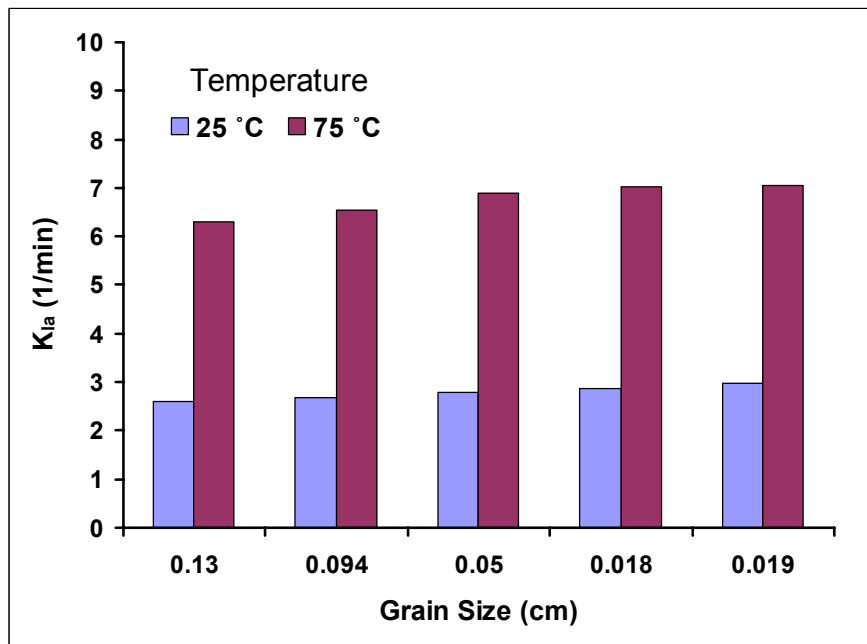


Figure 3.112. Relationship of Mass Transfer Rate Coefficient to Sand Grain Size and Water Temperature for a Flow Rate of 5.5 mL/min, Column Experiments with Thermal Treatment

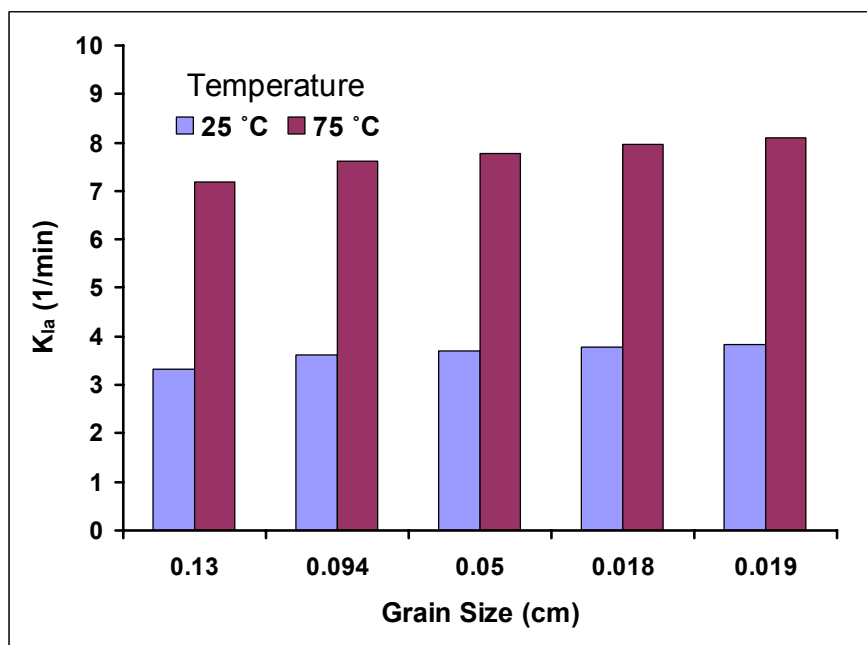


Figure 3.113. Relationship of Mass Transfer Rate Coefficient to Sand Grain Size and Water Temperature for a Flow Rate of 10.0 mL/min, Column Experiments with Thermal Treatment

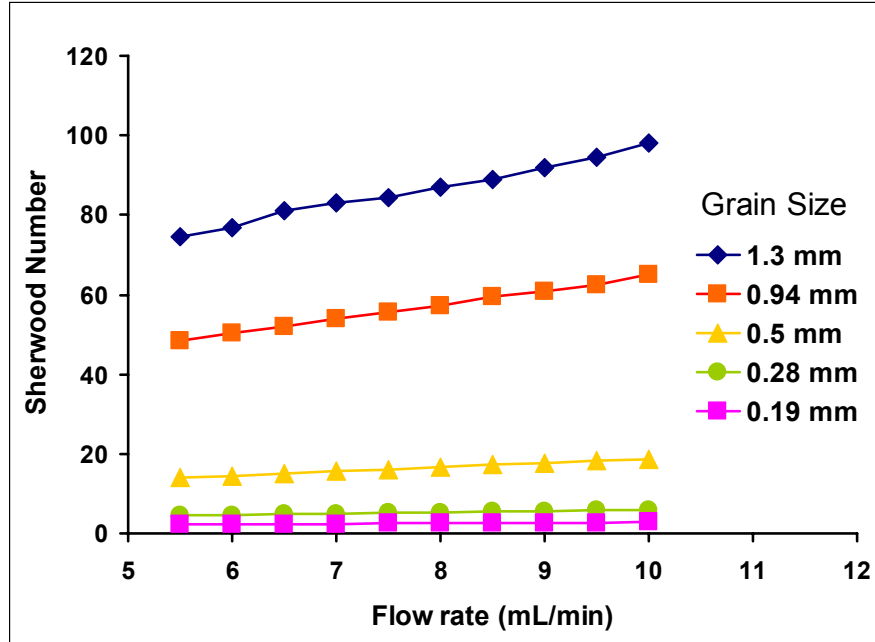


Figure 3.114. Relationship of Sherwood Number to Flow Rate and Sand Grain Size, Column Experiments with Thermal Treatment at 25°C

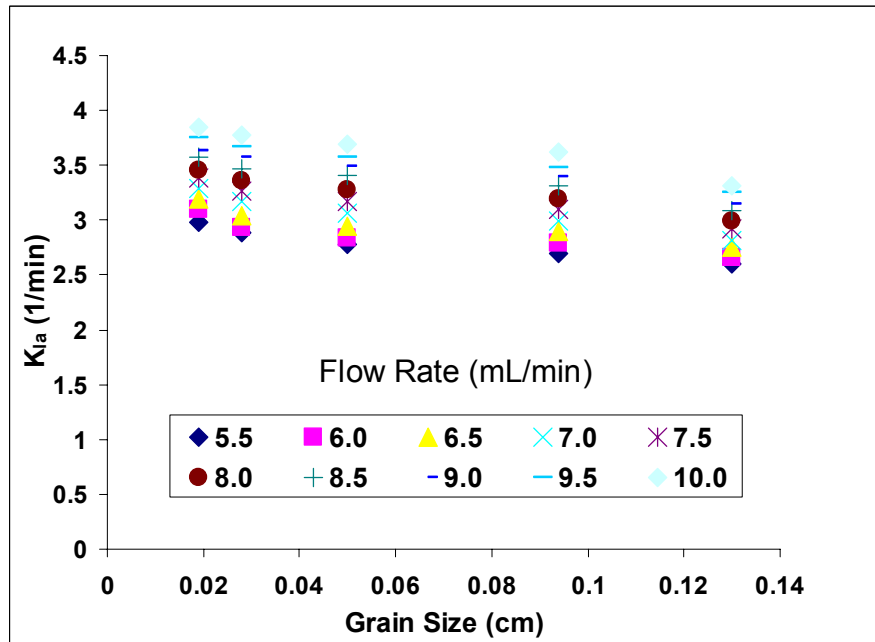


Figure 3.115. Relationship of Mass Transfer Rate Coefficient to Sand Grain Size and Flow Rate, Column Experiments with Thermal Treatment at 25°C

3.8.3 Two-dimensional flow-cell experiments

The goal of the flow-cell experiments was to generate a data set that could be used to test the hypothesis that point-scale Gilland-Sherwood relationships developed from column experiments can be upscaled to multidimensional flow systems.

Experimental Design. Three flow-cell experiments were run, each with a different source length. Internal dimensions of the flow cell were nominally 23 cm long x 17 cm high x 2.54 cm wide. Source lengths for the three experiments were 1 cm, 2 cm and 4 cm. In all experiments, the DNAPL source was 1 cm high and 2.54 cm wide. Three columns of sampling ports are located at 2 cm, 5 cm and 10 cm from the end of the source zone. The first column consist of three ports with 2 cm separation between them, the second column consists of 2 ports separated by 2 cm and vertically centered with the source zone, the third column consists of 3 ports with a vertical separation of 4 cm between them. To keep the cell insulated, it is placed inside a 4 x 2 feet Plexiglas vacuum chamber. The cell was wet-packed with #70 sand ($d_{50} = 0.019\text{cm}$) and the sand used for the source zone was #16 sand ($d_{50} = 0.094\text{ cm}$).

Flow rate through the tank was selected to provide a pore velocity inside the source zone that was in the range of column experiments conducted previously. MODFLOW simulations of the flow cell showed that a flow rate of 25 mL/min would provide a pore velocity of 2.94 cm/min within the source zone. A flow rate of 40 mL/min would provide a pore velocity of 4.74 cm/min. These velocities are equivalent to the pore velocities that occurred in the column experiments at flow rates of 5.6 mL/min and 9.08 mL/min. Therefore, for each packing of the flow cell, experiments were conducted at flow rates of 25 and 40 mL/min.

The residual source zone was created by pumping dyed PCE at a flow rate of 2 $\mu\text{L}/\text{min}$ and then withdrawing a specific amount at the same flow rate to establish a residual source at approximately 20 percent saturation. For example, the amount of PCE injected for the experiment with a source length of 1 cm was 1.1 mL. The amount withdrawn was 0.88 mL. For the source zone with a length of 2 cm, the amount of PCE injected was approximately 1.6 mL. The amount withdrawn was about 1.3 mL.

The water injected into the cell was heated using the same computer controlled system used for the columns experiments. Temperature was monitored using ten thermocouples inserted in the sand through lateral ports in the cell.

For each experiment, water samples were collected at sample locations 2 to 16 cm downstream of the source and at the outflow. Sampling began after flow rate and temperature were established throughout the flow cell at steady conditions. Because flow rates were high, sample intervals were rapid. Three samples were collected at each sample location. Sample treatment and analysis were the same as used in batch experiments described previously. Analytical results showed that steady-state conditions were established during all sampling periods. Only steady-state data are presented in this report.

Experimental Results. Figure 3.116 shows that aqueous-phase PCE concentration increased as temperature increased for the experiment with a source length of 1 cm and a flow rate of 25 mL/min. This result was consistent with results from the column experiments. Higher concentrations occurred at sample locations aligned with the center of the source zone. Flow-cell results in Figure 3.116 for temperatures labeled ~35 and ~45 correspond to the transition period

between 25 °C and 55 °C. All observed PCE concentrations were below the solubility limit for 25 °C.

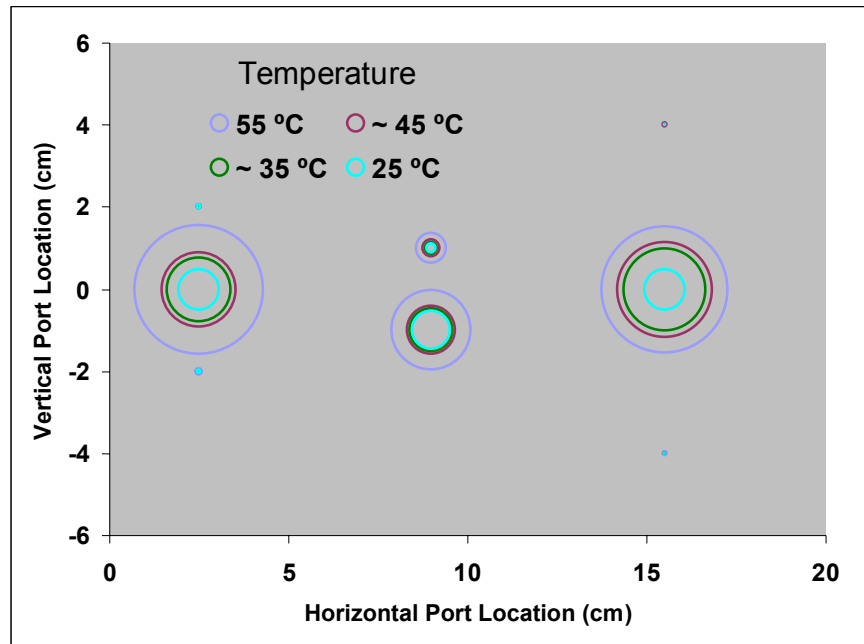


Figure 3.116. Steady-State Distribution of Aqueous-Phase PCE during Flow Cell Experiments with Thermal Treatment (source length is 1 cm, flow rate is 25 mL/min)

For experiments with a source length of 1 cm, Figures 3.117 and 3.118 show the PCE concentration distribution downgradient of the source with flow rates for 25 °C and 55 °C respectively. Figure 3.117 shows that changes in concentration with flow rate at 25 °C were relatively small. This behavior was consistent with results of the column experiments. Comparison of Figures 3.117 and 3.118 also shows that the difference between the concentrations at 25 and at 40 ml/min observed at 55 °C was larger than was observed at 25 °C. A plausible explanation for this behavior is the decrease in PCE content of the source zone. It is possible that smaller ganglia were being totally dissolved at later stages of the experiment, decreasing significantly the NAPL-water interfacial area and thus producing a decrease in concentration.

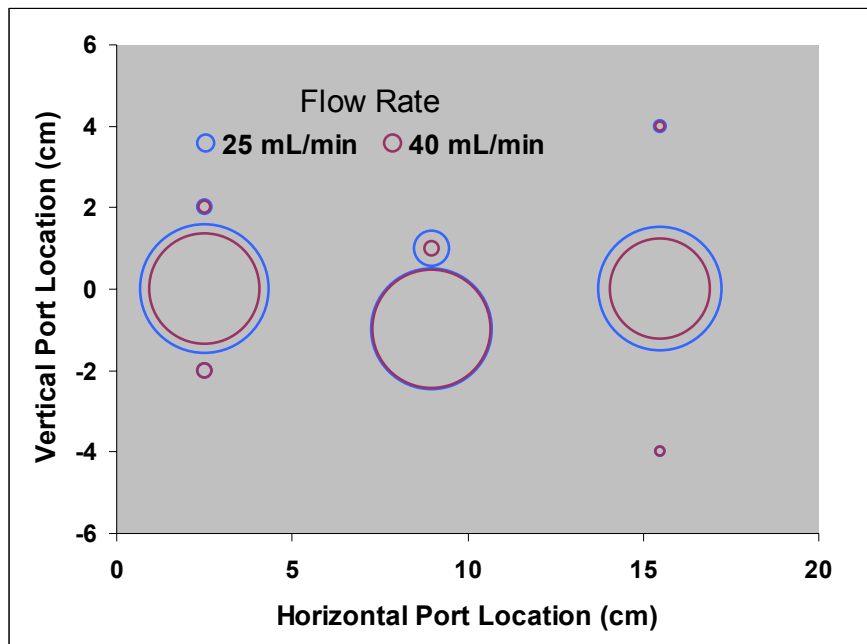


Figure 3.117. Steady-State Distribution of Aqueous-Phase PCE during Flow Cell Experiments with Thermal Treatment (source length is 1 cm, temperature is 25°C)

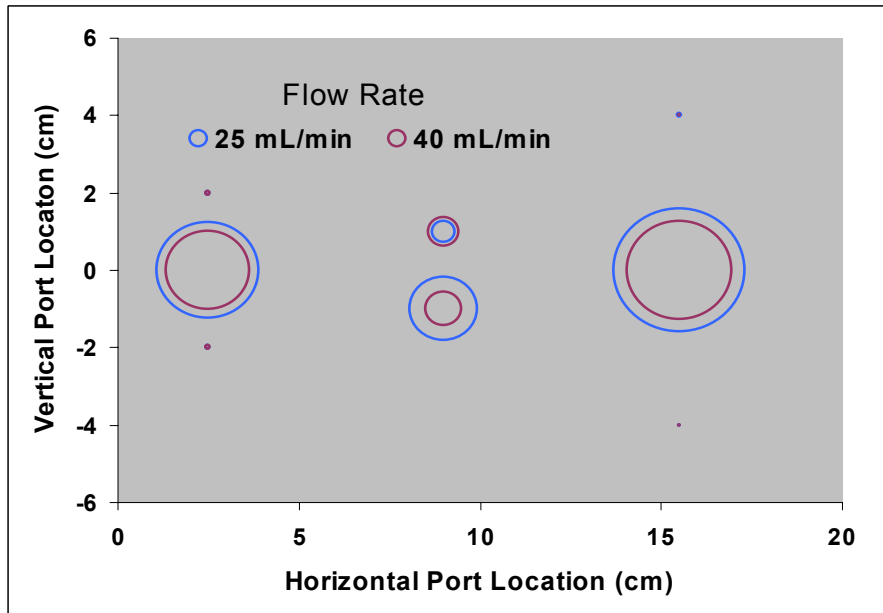


Figure 3.118. Steady-State Distribution of Aqueous-Phase PCE during Flow Cell Experiments with Thermal Treatment (source length is 1 cm, temperature is 55°C)

Mass transfer characteristics observed with a source length of 1 cm also were observed in subsequent experiments with source zone lengths of 2 and 4 cm (Figures 3.119 through 3.124). However, for a given sampling location, aqueous-phase PCE concentration increased as source length increased. This was expected because the longer lengths permitted water to be in contact with residual PCE DNAPL for a longer time resulting in increased amounts of PCE dissolution into the water.

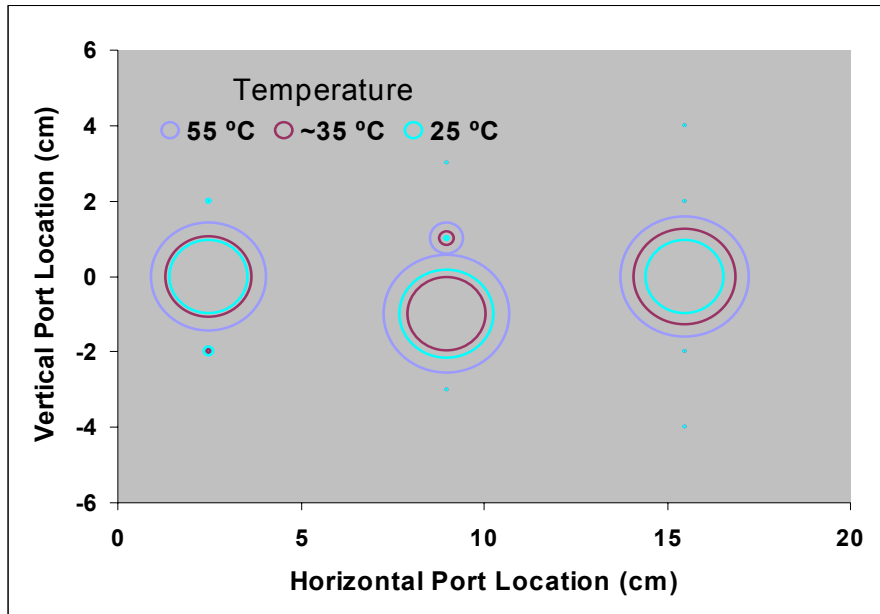


Figure 3.119. Steady-State Distribution of Aqueous-Phase PCE during Flow Cell Experiments with Thermal Treatment (source length is 2 cm, flow rate is 25 mL/min)

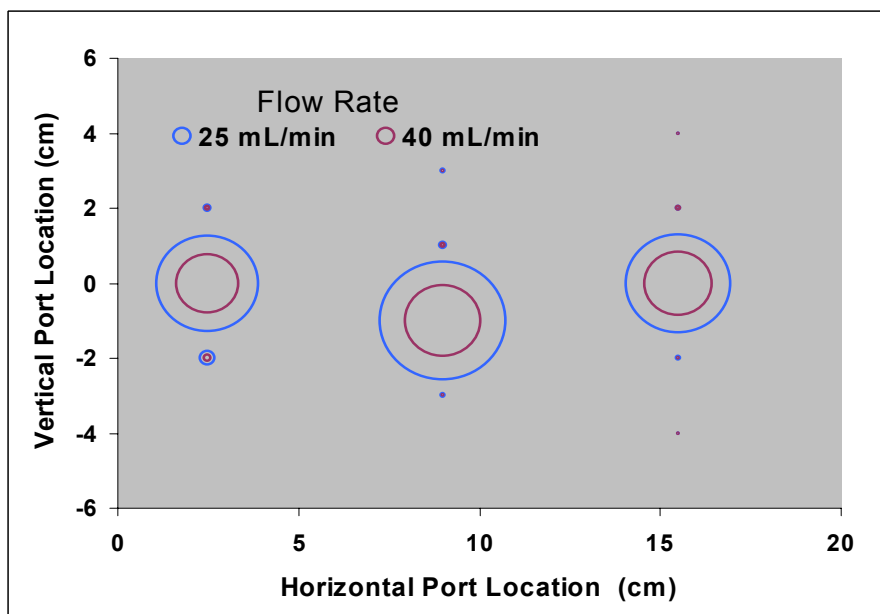


Figure 3.120. Steady-State Distribution of Aqueous-Phase PCE during Flow Cell Experiments with Thermal Treatment (source length is 2 cm, temperature is 25 °C)

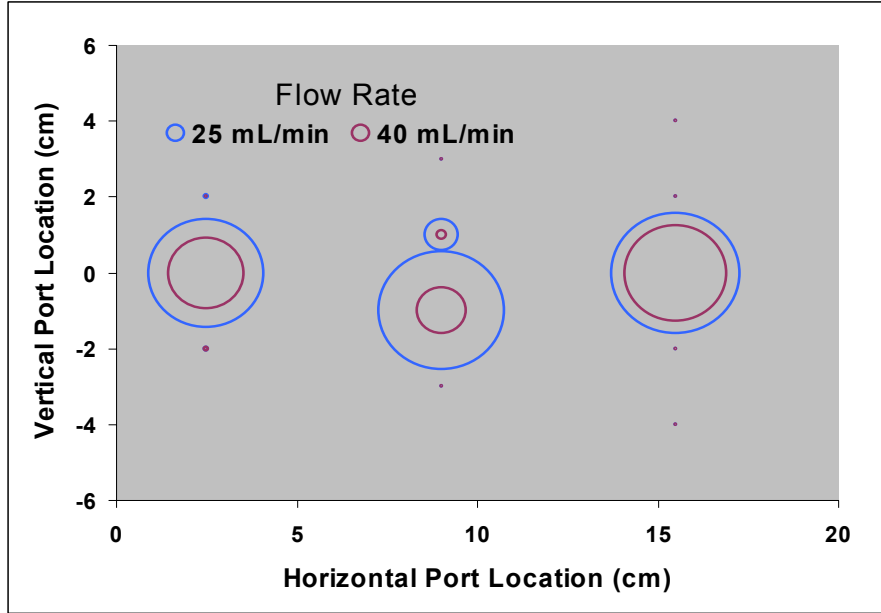


Figure 3.121. Steady-State Distribution of Aqueous-Phase PCE during Flow Cell Experiments with Thermal Treatment (source length is 2 cm, temperature is 55°C)

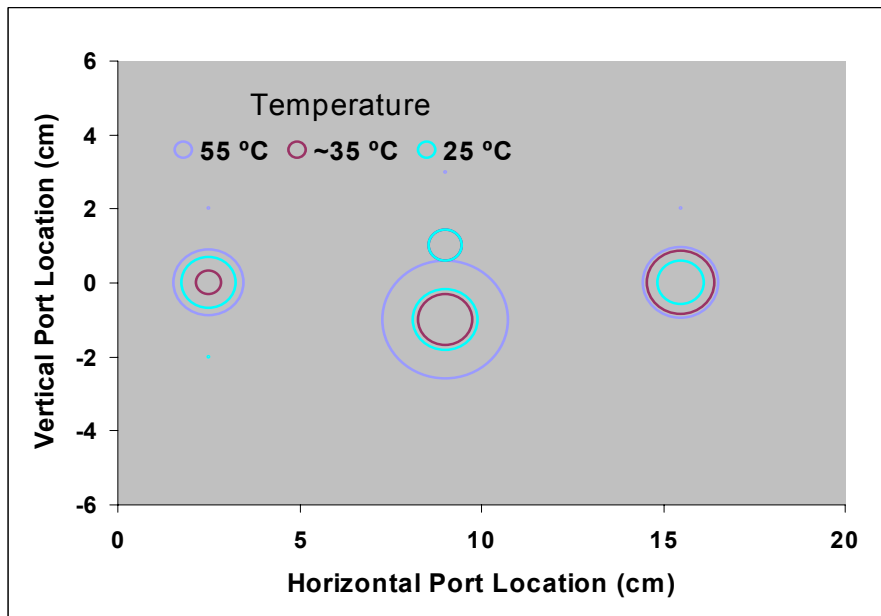


Figure 3.122. Steady-State Distribution of Aqueous-Phase PCE during Flow Cell Experiments with Thermal Treatment (source length is 4 cm, flow rate is 25 mL/min)

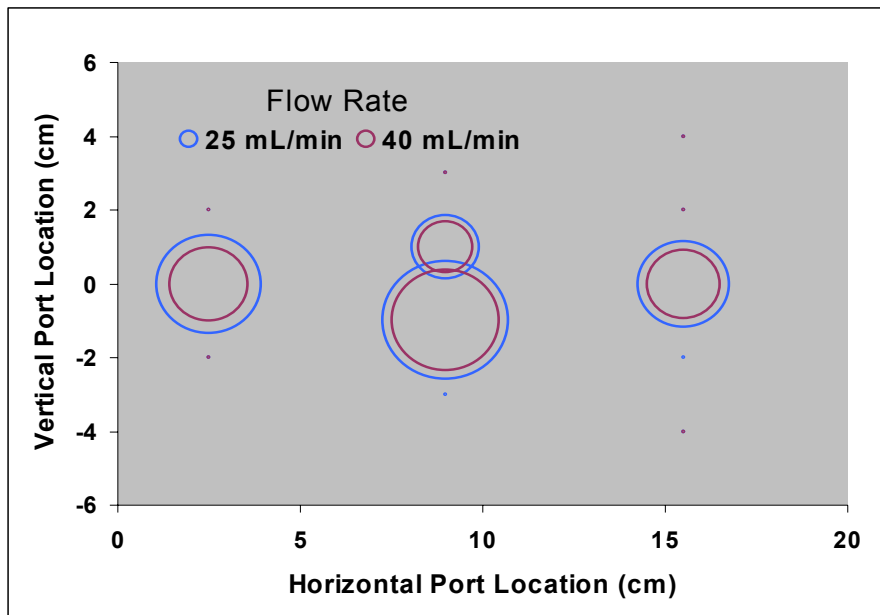


Figure 3.123. Steady-State Distribution of Aqueous-Phase PCE during Flow Cell Experiments with Thermal Treatment (source length is 4 cm, temperature is 25°C)

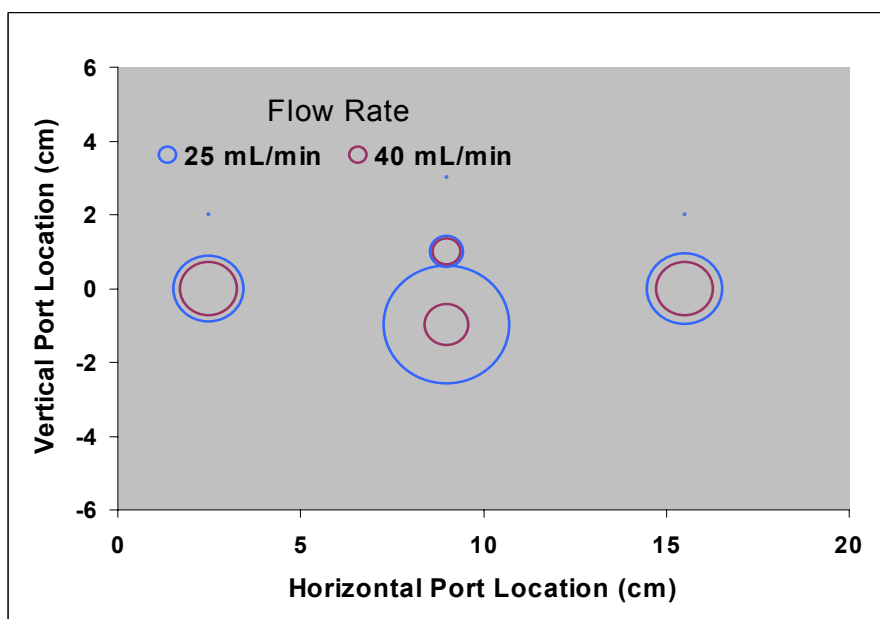


Figure 3.124. Steady-State Distribution of Aqueous-Phase PCE during Flow Cell Experiments with Thermal Treatment (source length is 4 cm, temperature is 55°C)

3.9 Modeling tools

This chapter describes the numerical models that were used to analyze experimental data and perform numerical simulations in this research. In order to accurately predict the fate and transport of chemical species, mass transfer and reactive processes such as chemical and biological transformations that occur in the source zones must be correctly simulated. In recent years, several numerical codes for simulating mass transfer and reactive transport processes have been developed and most of them are available in the public domain. These numerical models include MODFLOW, MT3D, RT3D, UTCHEM, UCODE, and PEST. These codes have been used extensively in both laboratory- and field-scale applications. Specific features of these models are discussed in this section of the report.

3.9.1 Groundwater flow model

MODFLOW is a U.S. Geological Survey three-dimensional, finite-difference groundwater flow model that can simulate both transient and steady-state conditions with different kinds of boundary conditions and stresses that are applied to the heterogeneous (or homogeneous) aquifer (Harbaugh et al., 2000). An inverse modeling algorithm (called Parameter Estimation Process) has been added in a current version of MODFLOW (called MODFLOW-2000). This feature enables easier and more efficient automated calibration process when aquifer hydraulic parameters are to be determined.

The MODFLOW program solves the following groundwater flow equation as shown in Equation 3.11 using a block-centered finite-difference scheme.

$$S_s \frac{\partial h}{\partial t} = \frac{\partial}{\partial \mathbf{x}_i} \left(\mathbf{K}_{ii} \frac{\partial h}{\partial \mathbf{x}_i} \right) + q_s \quad (3.11)$$

The program solves for hydraulic heads and generates budget output files for cell-by-cell flow rates for all finite-difference grids and these values are converted to seepage velocity and/or average linear pore velocity for use in transport models.

3.9.2 Reactive transport model

RT3D (Reactive Transport in 3-Dimensions version 2.5) is a computer code that solves the coupled partial differential equations that describe reactive-flow and transport of multiple mobile and/or immobile species in three-dimensional saturated groundwater systems (Clement, 1997; Clement et al., 1998). RT3D requires the groundwater flow code (in this case, MODFLOW-2000) for computing spatial and temporal variations in groundwater head distribution.

The RT3D code is unique in that it includes an implicit reaction solver that makes the code sufficiently flexible for simulating various types of chemical and biological reaction kinetics. RT3D supports several pre-programmed reaction modules that can be used to simulate

different types of reactive contaminants including benzene-toluene-xylene mixtures (BTEX), and chlorinated solvents such as tetrachloroethene (PCE) and trichloroethene (TCE). In addition, RT3D has a user-defined reaction option that can be used to simulate any other types of user-specified reactive transport systems including the non-equilibrium dissolution from non-aqueous phase liquids. The RT3D code, developed based on the well-known contaminant transport program MT3D (Zheng and Wang, 1999), solves the reactive transport equation as

$$\frac{\partial c}{\partial t} = \underbrace{-\frac{\partial}{\partial \mathbf{x}_i} (\bar{\mathbf{v}}_i c)}_{\text{Advection}} + \underbrace{\frac{\partial}{\partial \mathbf{x}_i} \left(\mathbf{D}_{ij} \frac{\partial c}{\partial \mathbf{x}_j} \right)}_{\text{Dispersion}} - \underbrace{k_{La} (c - c_s)}_{\text{Dissolution}} + \underbrace{\frac{q_s}{\phi} c_{\text{source}}}_{\text{Source/Sink}} - \underbrace{r_k}_{\text{Reaction}} \quad (3.12)$$

In RT3D, this equation is solved using operator-splitting numerical strategy for any number of coupled transport equations. A reaction package is used to formulate the reaction term and can include rate-limited dissolution, chemical oxidation, biological transformations, degradation, non-equilibrium sorption, for chemical species in both aqueous, and sorbed or immobile phases.

Dissolution Module. Non-equilibrium NAPL dissolution is a transient process that can affect spatial and temporal variability of hydraulic properties of the aquifers. During dissolution, NAPL volume decreases with time and relative permeability increases accordingly. Figure 3.125 shows the program sequences describing the algorithm of MODFLOW/RT3D with dissolution module (DSS). The contaminant mass flux per unit volume of porous medium (J_v) in the mass transport equation (Equation 3.12) is calculated using mass transfer expression (Equation 3.13) in RT3D program through a modified reaction or RCT package. The value of c_s is a function of surfactant concentration and can be calculated from the expression that is obtained from the relationship between concentration of PCE vs. surfactant .

$$J_v = -k_{La} (c - c_s) \quad (3.13)$$

Given an initial NAPL saturation in each finite-difference grid block, MODFLOW solves the groundwater flow equation based on modified hydraulic conductivity field resulting from NAPL entrapment. The partially water saturated or modified hydraulic conductivity K can be expressed in terms of the relative permeability k_{rw} , and saturated hydraulic conductivity K_s as:

$$K = k_{rw} K_s \quad (3.14)$$

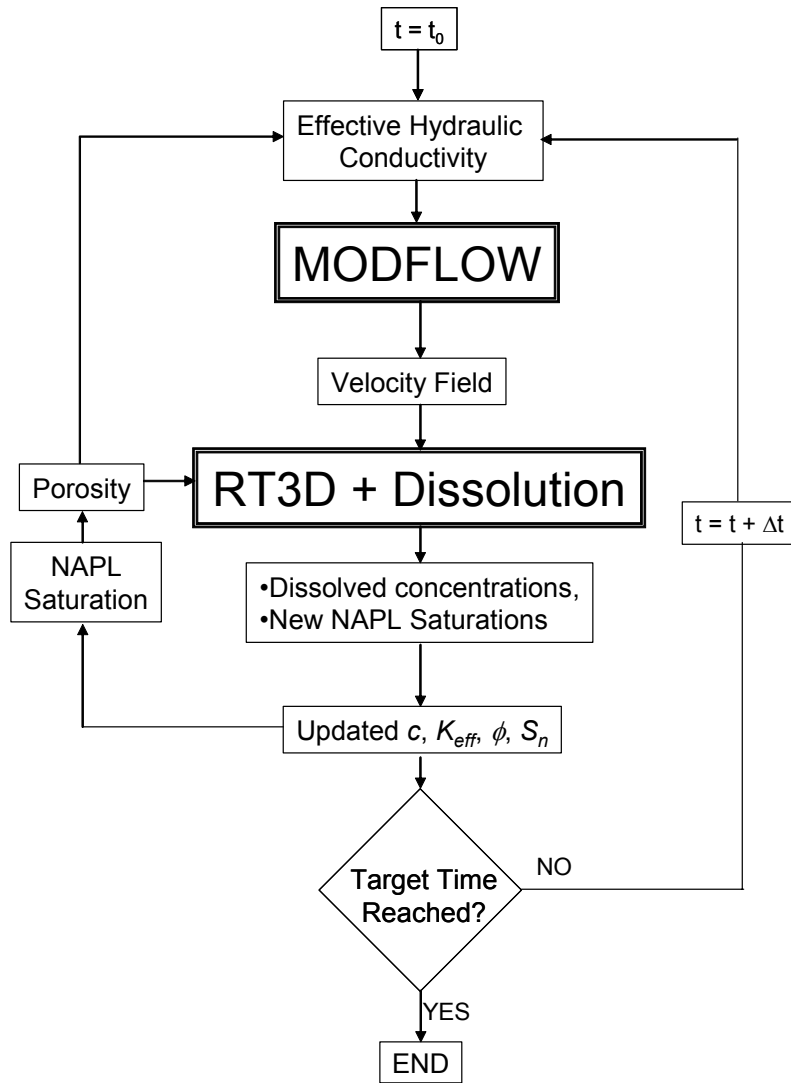


Figure 3.125. Simulation Procedures and Execution Sequences of Program Units for Dissolution Simulation

The relative permeability is a function of water saturation (S_w). Several expressions of this function were proposed in literature (Wyllie, 1962; Brooks-Corey, 1966; van Genuchten, 1980). The developed numerical model also accepts an experimentally derived relative permeability function. Wyllie (1962) proposed the relationship between the relative permeability of the wetting phase and NAPL saturation as

$$k_{rw} = \left(\frac{1 - S_n - S_{r,w}}{1 - S_{r,w}} \right)^3 \quad (3.15)$$

where S_n is the NAPL saturation, and $S_{r,w}$ is the residual saturation of the aqueous phase. Wyllie's equation was chosen in this study because it was found to best describe the relative permeability measurement data for the test sands used in our past laboratory investigations (Saba 1999; Saba and Illangasekare, 2000). The value of hydraulic conductivity is time-dependent since NAPL content decreases during surfactant-enhanced dissolution. Consequently, during the simulation, the flow field within the NAPL entrapment zone will change accordingly with the updated hydraulic conductivity.

Injection of surfactant solution is simulated using the WEL or MNW package of MODFLOW-2000. The delivery of surfactant to the NAPL entrapment zone is simulated by solving the advection-dispersion equation using RT3D for surfactant concentrations. For simplicity, the aqueous phase and the micro-emulsion phase were combined, treating them as a single aqueous phase. In addition, the viscosity and density of the surfactant solution were assumed to be close to those of water. In the absence of surfactant, the dimensionless mass transfer coefficient or a modified Sherwood number is calculated using Equation 3.16. When surfactant is present, the modified Sherwood number takes the relationship shown in Equation 3.17. Note that the modified Sherwood number is related to the overall mass transfer coefficient by $k_{La} = D_m \text{Sh} / d_{50}^2$.

$$\text{Sh} = \alpha_1 (\text{Re})^{\alpha_2} (\text{Sc})^{\alpha_3} \left(\frac{\theta_n d_{50}}{\tau L^*} \right)^{\alpha_4} \quad (3.16)$$

$$\text{Sh} = \beta_1 (\text{Re})^{\beta_2} (\text{Sc})^{\beta_3} \left(\frac{\theta_n}{1 - \theta_n} \right)^{\beta_4} \left(\frac{d_{50}}{\tau L^*} \right)^{\beta_5} \quad (3.17)$$

When the RT3D solves for the mass transfer of NAPL to aqueous phase, it keeps track of the rate of dissolution of the NAPL into the flowing aqueous phase and hence the rate of depletion of the NAPL mass. Variation of NAPL saturation, effective porosity for the aqueous phase, and relative permeability are updated at the end of each simulation time step. With an updated hydraulic conductivity field, MODFLOW simulates the new groundwater flow field within the NAPL source zone. These cyclic processes will be executed until the target time is reached.

Model Implementation. The dissolution module developed in this research is a suite of executable programs written in Fortran-90. Specifically, it consists of MODFLOW (mf2k.exe), RT3D (rt3dv25.exe), modk.exe, dss.exe, and update.exe. The first executable (mf2k.exe) is a regular MODFLOW program while the rt3dv25.exe is a re-compiled RT3D program with a modified reaction package to simulate interphase mass transfer. The last three executables are pre- and post-processors that help MODFLOW and RT3D recognize the presence of entrapped non-aqueous phase. Also, these executables are used to generate and update the necessary values of model inputs (e.g. concentrations, saturation, porosities, and hydraulic conductivities) when the next time step is simulated. These five executables are executed in sequences using a perl command file. Each sequence is a simulation of the steady-state dissolution over a short period

of time (Δt). The sequence is repeated in a do-loop statement in the perl command file until the target time is reached.

The modk.exe program reads input parameters of NAPL saturation, residual water saturation, and saturated hydraulic conductivity on a cell-by-cell basis, and produces output files containing effective hydraulic conductivity for each model layer based on Equations 3.14 and 3.15. This program must be executed prior to running MODFLOW simulation.

The dss.exe program reads output file from MODFLOW (flow-transport link file or FTL), and reads parameters from separate input files that contain NAPL saturation, surfactant concentration, empirical parameters in Equations 3.16 and 3.17, densities, viscosity, initial porosity, tortuosity, characteristic or dissolution length, and critical micelle concentration. It produces the necessary input files for subsequent RT3D simulation. These input files are effective porosities, bulk densities, mass transfer coefficients (k_{La}), and NAPL mass available for dissolution. This program must be executed between MODFLOW and RT3D.

The update.exe program reads output from RT3D, updates concentrations and saturations, and writes these values to files that will be used as input parameters for next time step simulation. The updated values are concentrations of all constituents and NAPL saturations.

Dissolution Model Verification. In this section, the developed dissolution module is verified with the available analytical solution of a one-dimension advection-dispersion-dissolution transport equation. A one-dimension transport equation with dissolution of a homogeneously distributed NAPL in a column can be written as

$$\frac{\partial c}{\partial t} = D_{xx} \frac{\partial^2 c}{\partial x^2} - \bar{v}_x \frac{\partial c}{\partial x} - \bar{k}_{La} (c - c_s) \quad (3.18)$$

where D_{xx} is hydrodynamic dispersion coefficient and $D_{xx} = D_m + \alpha_L \bar{v}_x$, D_m is molecular diffusion coefficient of dissolved NAPL in water, α_L is the longitudinal dispersivity, \bar{v}_x is the average linear pore velocity which is equal to the Darcy's velocity divided by effective porosity ϕ . c is the concentration of dissolved NAPL, c_s is the apparent aqueous solubility of NAPL in water, and \bar{k}_{La} is the average, overall mass transfer coefficient.

Under steady-state condition, concentration c is no longer a function of time t . It is therefore only a function of x . The partial differential Equation 3.18 can reduce to the second-order ordinary differential equation

$$D_{xx} \frac{d^2 c}{dx^2} - \bar{v}_x \frac{dc}{dx} - \bar{k}_{La} (c - c_s) = 0 \quad (3.19)$$

With the following boundary conditions $\left\{ \begin{array}{l} c = 0 \quad \text{at} \quad x = 0 \\ \frac{dc}{dx} = 0 \quad \text{at} \quad x \rightarrow \infty \end{array} \right\}$, the solution to this equation becomes

$$\frac{c(x)}{c_s} = 1 - \exp\left[\left(\frac{x}{2D_{xx}}\right)\left(\bar{v}_x - \sqrt{\bar{v}_x^2 + 4D_{xx}\bar{k}_{La}}\right)\right]. \quad (3.20)$$

In this derivation, it is assumed that \bar{k}_{La} does not vary with either x or t . In addition, the temporal change in NAPL saturation due to natural dissolution is negligibly small, and it does not affect the variation of overall mass transfer coefficient.

Assuming all assumptions are valid, Equation 3.20 can be used to verify the dissolution module. The dissolution simulation of PCE in a one-dimension sand column (100-cm \times 5-cm \times 5-cm, $\phi_0 = 0.4$, $\alpha_L = 0.01$ cm, $K_s = 1.0$ cm/min, $S_{r,w} = 0.0$) containing homogeneously distributed PCE at residual saturation ($S_n = 0.25$, $c_s = 200.0$ mg/L, $D_m = 4.92 \times 10^{-4}$ cm²/min) was simulated. The goal was to obtain a steady-state PCE concentration profile $c = c(x)$ when clean water was injected at one end of the column at the flow rate of $Q = 2.5$ cm³/min (Figure 3.126).

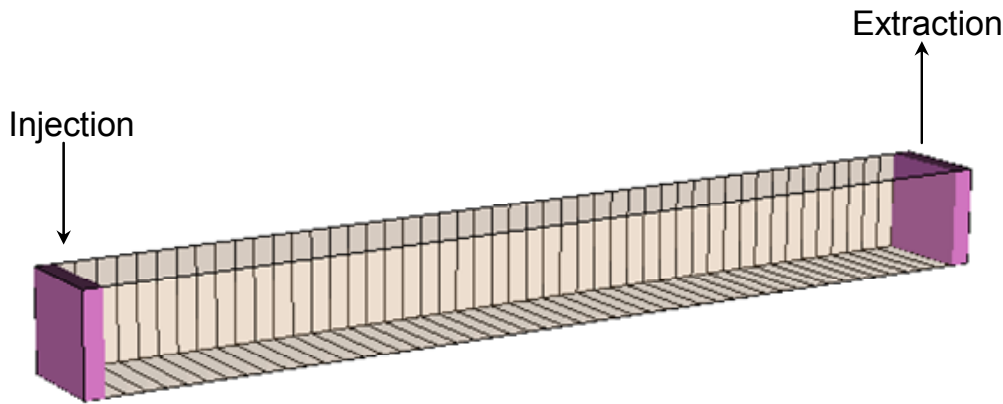


Figure 3.126. Hypothetical NAPL Column Used to Verify the Dissolution Model

The column was discretized into 1 row, 1 layer, and 50 columns (uniform grid size). Clean water was injected at column 1 and the effluent was monitored at column 50; both were represented as wells in the flow simulation. The dissolution model was executed using a constant $\bar{k}_{La} = 0.01$ min⁻¹ for a sufficiently long time to obtain the steady-state concentration without updating PCE saturation. Figure 3.127 shows the comparison of the steady-state concentration profile $c(x)$ obtained from both numerical and analytical solutions. From Figure 3.127, it is

obvious that the numerical solution approaches the analytical solution and, thus, the dissolution module is verified.

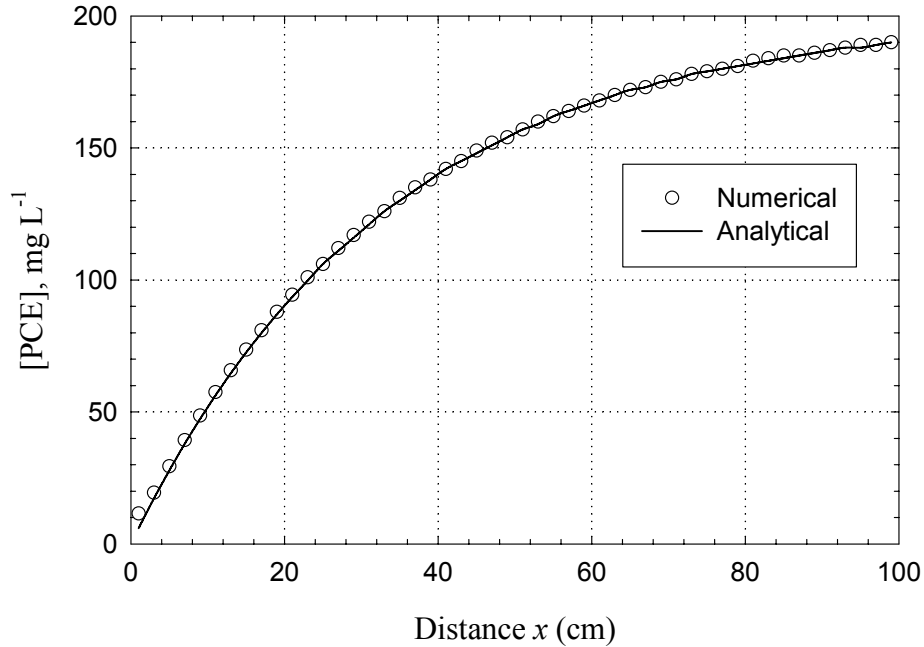


Figure 3.127. Numerical and Analytical Solutions of Steady-state PCE Dissolution from a Column

3.9.3 Multiphase flow code

UTCHEM, version is 9.3, is a highly sophisticated groundwater flow and reactive transport model capable of performing multi-phase simulations (Delshad et al., 1996). UTCHEM was originally developed at the University of Texas at Austin for surfactant flooding of an oil reservoir. It is a three-dimensional, multi-component, multiphase, compositional model of chemical flooding processes which accounts for complex phase behavior, chemical and physical transformations and heterogeneous porous media. It is also capable of simulating the flow and transport under non-isothermal condition. The governing equation for the momentum transport that UTCHEM solves is similar to the following equation.

$$\frac{\partial}{\partial t}(\phi_0 S_i \rho_i) = \bar{\nabla} \cdot \left[\frac{\rho_i k_{r,i}}{\mu_i} \mathbf{k}(\nabla p - \rho_i g \nabla z) \right] + \rho_i q_i \quad (3.21)$$

In addition to the capability of solving multiphase flow problem, UTCHEM includes tracer options where multiple tracers, conservative and partitioning, can be simulated (Jin et al., 1995). The code is also able to simulate the geochemical and biochemical reactions. However, in this research the primary interest in UTCHEM was an ability to simulate multiphase flow and tracer transport.

3.9.4 Inverse modeling algorithms

Model calibration is an important part of any modeling exercises. Before groundwater flow and contaminant transport models are used as predictive tools, they should be calibrated and validated with existing observations. Calibration is a process where by certain parameters of the model such as hydraulic conductivity or mass transfer coefficient are altered in a systematic fashion and the model is repeatedly run until the computed solution matches the observed values within an acceptable level of accuracy.

Trial and error methods can be used to adjust model parameters iteratively until model computed values match observations; but this is a time-consuming process providing little information concerning model uniqueness or parameter uncertainty. Two automated procedures for calibration based on parameter estimation theory from statistics are used in the research described in this report. The two codes are UCODE (Poeter and Hill, 1998) and PEST (Doherty, 1994). UCODE is a universal inverse modeling algorithm. It is used for both calculating parameters sensitivity (using a perturbation method) and non-linear regression (using modified Gauss-Newton iteration). PEST is a more sophisticated non-linear parameter estimation tool which has been widely used by scientists and engineers. With an automatic user intervention (AUI) capability, PEST becomes a more powerful tool when calibration is needed. In short, the AUI process temporarily freezes the insensitive parameters (during regression) so that the regression is performed more efficient and un-freezes these parameters in the next iteration.

UCODE. A computer program UCODE performs inverse modeling posed as a parameter estimation process using nonlinear regression. UCODE consists of algorithms that have been programmed in perl and Fortran-90. The non-linear regression is solved by minimizing a weighted least square objective function with respect to the parameter values using a modified Gauss-Newton method. Parameter sensitivities are calculated using the perturbation method based on forward, backward, or central difference methods. UCODE initializes the problem by reading the initial parameter values and executes the application model. Then, the simulated values are compared with observations to obtain the residuals. To calculate the sensitivities, UCODE executes the application model several times for each perturbed parameter values. Once the residuals and sensitivities are calculated, a computer program MRDRIVE.EXE will update the new parameter values using one-iteration of the Gauss-Newton method. If parameter convergence criteria are not met at the end of an iteration, MRDRIVE is called again with the new sensitivities and residuals values. This process will repeat until the convergence criteria are met or the maximum number of iterations specified by user is reached.

PEST. Similar to UCODE, an inverse algorithm PEST (Parameter Estimation) is a nonlinear parameter estimation package developed by Doherty (1994). The major difference between PEST and UCODE is that, in PEST, optimum parameter values can be constrained to lie between individually-specified upper and lower bounds. This is implemented using a

mathematically advanced algorithm that actually regularizes the parameter estimation problem as bounds are imposed. Many application models will produce nonsensical results or may cease with run-time error if certain input parameters fall outside the permissible range. For example, the estimation of NAPL saturation based on measured mass flux and dissolution model may suffer errors from prematurely terminated program if the updated parameter values fall outside the permissible range where during optimization. Thus, posing the lower and upper bounds for adjustable parameters will eliminate this problem.

3.9.5 Multiple tracer test module

The method of temporal moment and inverse numerical modeling are used in the analysis of multiple tracer test data. The method of temporal moments is widely used to analyze tracer breakthrough data in homogeneous settings. Inverse modeling provides greater capabilities for analyzing heterogeneous systems.

Methods of Temporal Moments. In this method, the average travel times for both conservative and partitioning tracers are compared and the average saturation as well as NAPL volume can then be determined. The average travel time \bar{t}_i for a tracer i can be calculated as

$$\bar{t}_i = \frac{\int t \cdot c_i(t) dt}{\int c_i(t) dt} - \frac{t_0}{2} \quad (3.22)$$

where c_i is the aqueous concentration of tracer i , and t_0 is the tracer injection duration.

Theoretically, the time-domain of integration must be $t \in [0, \infty)$, which is not practical because we cannot run the experiment and take samples indefinitely long. Therefore, the extrapolation of the breakthrough curves to negligible concentrations is sometimes necessary. After the average breakthrough time is obtained, the effective or average NAPL saturation \bar{S}_n within the tracer-swept zone can be calculated from the following relationship of retardation factor R ,

$$\bar{S}_n = \frac{R - 1}{K_p + R - 1} \quad (3.23)$$

where $R = \bar{t}_p / \bar{t}_c$, K_p is NAPL-water partition coefficient, \bar{t}_p and \bar{t}_c are average travel times for partitioning and conservative tracers, respectively. The partition coefficient for partitioning tracer in NAPL-water system is $K_p = c_w / c_{nw}$, where c_w and c_{nw} are the equilibrium concentrations of partitioning tracer (usually, alcohols) in water and non-aqueous phase liquid, respectively. The volume of non-aqueous phase liquid can be calculated as

$$V_n = \frac{m_r}{m_{tot}} \frac{\bar{S}_n Q_{inj} \bar{t}_c}{1 - \bar{S}_n} \quad (3.24)$$

where m_r/m_{tot} is the recovered tracer mass fraction of tracer or the ratio of tracer mass recovered at the well to the total mass injected into the system, and Q_{inj} is the total injection rate of tracer.

Inverse Modeling Method. Multiple tracer test data were analyzed using inverse modeling methods based on the multiple tracers test module (MODTRACER) and inverse algorithm PEST. The partitioning tracer module was developed based on MODFLOW and MT3DMS models. The development of this pre-processor program (MODTRACER) for simulating the equilibrium and/or rate-limited partitioning is described here. It is assumed that the reader is familiar with the programs MODFLOW and MT3DMS.

A preprocessor (PTT.EXE) is used to generate input files necessary for MODFLOW and MT3DMS. It requires an input file (PTT.INP) that contains information on NAPL saturation (S_n), initial reservoir porosity (ϕ_0), and water-saturated hydraulic conductivity (K_s) of the aquifer, partition coefficient (K_p), and the first-order mass transfer coefficient (β). Output files contain information on effective hydraulic conductivity, effective porosity, partition coefficient (K_p), and effective bulk density (ρ_b). The program is capable of simulating several partitioning tracers simultaneously.

In simulating a partitioning tracer test, the MODTRACER program requires four types of input parameters in the basic transport (BTN) and reaction (RCT) packages: effective porosity, bulk density, partition coefficient, and linear mass transfer coefficient (for equilibrium sorption, the mass transfer coefficient is not required). Based on the input NAPL saturation and initial porosity, the model calculates the required parameters from the following equations.

$$\phi = (1 - S_n)\phi_0 \quad (3.25)$$

$$\rho_b = S_n\phi_0\rho_n \quad (3.26)$$

In the method of moments, retardation factor, calculated by $R = 1 + K_p S_n / (1 - S_n)$, is used to calculate the average saturation of the NAPL phase present in a system. The tracers (conservative and partitioning) are assumed to be injected upstream and the breakthrough concentrations are monitored downstream of the NAPL entrapment zone. The average travel times of both tracers are calculated and compared to obtain the retardation factor which can be subsequently converted to average NAPL saturation using the partition coefficient.

In contrast, MODTRACER used in conjunction with an inverse algorithm PEST can be used to analyze the breakthrough curves by matching the measured and simulated breakthrough curves obtained from tracers test. The inverse algorithm can then be used to automatically evaluate the value of NAPL saturation (S_n) in each numerical grid block.

Model Verification. In this section, the proposed numerical scheme for multiple tracers test was verified using analytical solution. A test problem was set up as follows. A one-dimension column of sands ($100\text{-cm} \times 5\text{-cm} \times 5\text{-cm}$) having hydraulic conductivity and initial porosity of 5.0 cm/min and 0.40 , respectively, was contaminated with NAPL ($\rho_n = 1.62\text{ g/cm}^3$, $K_p = 20.0$) at residual saturation of $S_n = 0.20$. Theoretical retardation factor based on $R = 1 + K_p S_n / (1 - S_n)$ is 6.0 . Numerical simulation of flow and *advective* transport of conservative and partitioning tracers in this 1-D column was setup. The domain was discretized into 1 layer, 1 row, and 50 columns (Figure 3.126). Multiple tracers (conservative and partitioning) solution was introduced through an injection well located at column 1, and the effluent at well in column 50 was monitored for the breakthrough concentrations. The injection rate, although it did not affect the retardation factor for equilibrium partitioning, was chosen to be $2.5\text{ cm}^3/\text{min}$. Tracers were injected for 60 min and the total simulation time was 1 day. Breakthrough curves (concentration versus time) of both conservative and partitioning tracers obtained from the simulation are illustrated in Figure 3.128. The average travel times given by the first moment of the breakthrough curves for both tracers were calculated using Equation 3.22 and the retardation factor is calculated accordingly. Figure 3.129 shows the retardation factor calculated from the simulated breakthrough curves for several values of injection duration t_0 . These retardation factor values are close to the analytical solution, hence, the model is verified.

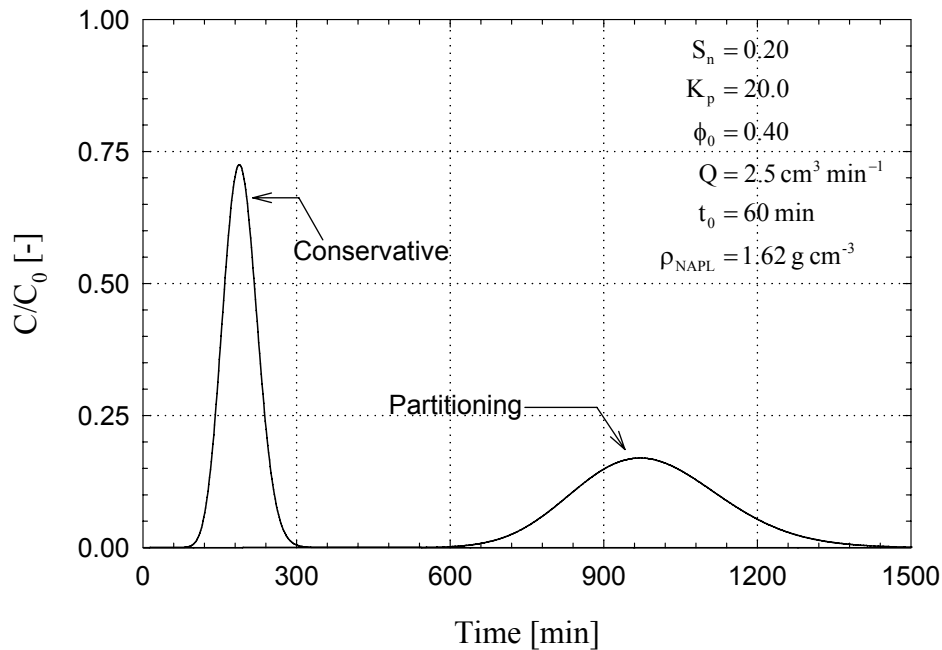


Figure 3.128. Breakthrough Curves Obtained from MODTRACER Simulation of a Partitioning Tracer Test in a Column

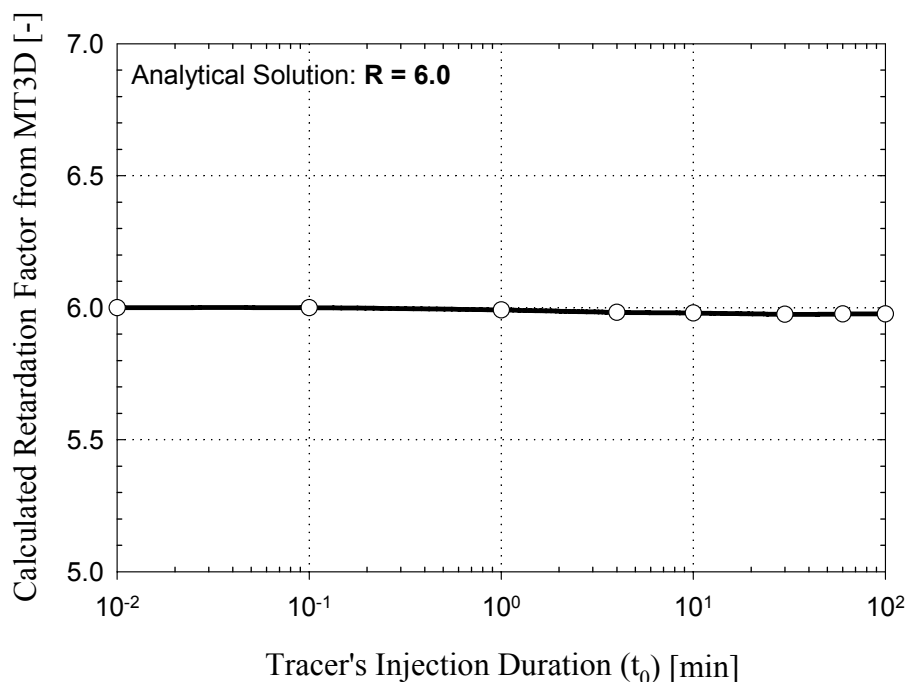


Figure 3.129. Retardation Factors Obtained from Simulated Breakthrough Curves, MODTRACER Verification Exercise

3.9.6 Chemical oxidation model

There are three main applications for a new numerical model code for simulating ISCO.

1. An investigative tool for studying the interaction of site and source conditions with different transport and reactive processes, providing insight into how these factors affect oxidation effectiveness.
2. A decision tool for assessing whether ISCO using permanganate is a feasible technology for further consideration at a specific site based on site and source conditions
3. A design tool to assist in determining the optimal oxidant delivery scheme (what oxidant concentration, at what flow rate, and in what locations?) for a site based on site and source conditions.

Although there is typically a large degree of uncertainty in site characterization, the modeling code described here is useful for comparing effects of different remediation scenarios. Further, by performing simulations using the expected upper and lower limits for site parameters, the effect of the uncertainty can be examined. This may provide insight into the need for additional site characterization.

The chemical oxidation model was designed to be readily available, useable by the average trained environmental modeler, and capable of simulating any combination of processes from Table 3.43. The code utilizes input parameters that are typically available or can be estimated by batch or small column studies using field samples. These include: soil characteristics (porosity, saturated hydraulic conductivity, dispersivity, bulk density, median grain size), contaminant characteristics (density, molecular weight, molecular diffusion coefficient), NOD distribution (mass fraction), oxidation reaction information (contaminant oxidation rate, NOD oxidation rates, reaction stoichiometry), DNAPL dissolution parameters (Gilland-Sherwood parameters), and sorption parameters based on the contaminant and soil. As with any heterogeneous source, additionally, information about the contaminant source distribution (location, DNAPL saturation) and subsurface flow characteristics can improve simulation accuracy.

Table 3.43. Important Processes Captured by the ISCO Model

| Process | Description |
|-------------------|---|
| Advection | 2 nd Order Contaminant Oxidation |
| Dispersion | Kinetic NOD oxidation |
| Sorption | Multiple NOD components |
| Diffusion | Permeability decrease due to MnO ₂ (s) formation |
| DNAPL Dissolution | Permeability Increase due to DNAPL Dissolution |

Development of the Chemical Oxidation Reactive Transport in 3D (CORT3D) model code began by selecting the multi-component reactive transport code RT3D version 2.5 (Clement 1997, Clement 2002, Clement et al. 1998) as a point of departure. The well-documented, widely accepted, and commonly used groundwater flow code MODFLOW-2000, which can simulate the flow regime under both transient and steady-state conditions with a wide variety of boundary conditions and stresses (McDonald and Harbaugh 1988, Harbaugh et al. 2000), was used to generate the underlying spatial and temporal variations in groundwater head distribution. The formulation of each process represented in the model code follows.

DNAPL Dissolution. Mass transfer or dissolution of the DNAPL into the aqueous phase is implemented using the well-known stagnant film model (Sherwood et al. 1975) utilizing a first-order linear driving force

$$\frac{dX_{napl}}{dt} = -\frac{\phi_{eff}}{\rho_B} k_{La} (C_{cont}^* - C_{cont}) \quad (3.27)$$

where X_{napl} is the mass fraction of DNAPL in soil (MM⁻¹), ϕ_{eff} is the effective soil porosity available for water flow, ρ_B is the soil bulk density (L³T⁻¹), C_{cont}^* is the maximum solubility limit of the contaminant (ML⁻³), C_{cont} is the aqueous concentration of the contaminant (ML⁻³), and k_{La} is the DNAPL dissolution rate or lumped mass transfer coefficient (T⁻¹). Mass transfer is a system dependent process, and estimation of k_{La} is system specific and is determined from the

modified Sherwood number (Sh) which relates the mass transfer in a system to the diffusive forces

$$Sh = \frac{k_{La} d_{50}^2}{D_m} \quad (3.28)$$

where d_{50} is the representative (median) grain size (L), and D_m is the molecular diffusion coefficient for a bulk solution of the solute (at an infinitely dilute concentration) (L^2T^{-1}). The same general form of the mass transfer correlation of Saba and Illangasekare (2000), utilized for natural dissolution and surfactant-enhanced dissolution, is used to calculate the modified Sherwood number in the ISCO code

$$Sh = \alpha_1 Re^{\alpha_2} Sc^{\alpha_3} \left(\frac{\theta_n d_m}{\tau L} \right)^{\alpha_4} \quad (3.29)$$

where the empirical coefficients $\alpha_1, \alpha_2, \alpha_3, \alpha_4, \tau$ are unique for a given system, and are determined through inverse modeling. However, the computer model code is written such that any mass transfer correlation can be used.

It has been suggested that chemical oxidation can increase the rate of mass transfer or dissolution from the DNAPL to the aqueous phase. In the presence of chemical reaction, the concentration gradient across the theoretical stagnant film is no longer linear. The resulting increase in mass transfer rate can be estimated using the following relation from Cussler (1997)

$$\frac{k_L^*}{k_L} = \left[\frac{D_m k_1}{(k_L)^2} \right]^{1/2} \coth \left[\left(\frac{k_1 D_m}{k_L^2} \right)^{1/2} \right] \quad (3.30)$$

where k_L^* is the intrinsic mass transfer coefficient with chemical reaction is (MT^{-1}) and k_1 is the first-order or pseudo-first-order kinetic reaction rate constant (T^{-1}). Unfortunately, for DNAPL in porous media, the intrinsic mass transfer coefficient without chemical reaction, k_L (MT^{-1}), can not be determined. Instead it must be estimated from the empirically-determined lumped mass transfer coefficient, assuming some geometry for DNAPL within soil pores.

The model code does not directly account for ISCO effects on mass transfer when calculating the lumped mass transfer coefficient. As currently implemented, if the intrinsic mass transfer coefficient is expected to increase due to fast chemical reaction, the Gilland-Sherwood parameters need to be estimated for dissolution during chemical reaction thru inverse modeling. A forward simulation is then run in phases, using the appropriate Gilland-Sherwood parameters for each phase.

Contaminant Diffusion. The original RT3D version 2.5 computer model code was modified to allow different effective diffusion coefficients to be simulated for each mobile species. Further, the effective diffusion coefficient for each species varies spatially based on soil properties. This modification is important for simulating diffusive transport of permanganate into LPM, where transport is dominated by diffusion (Siegrist et al. 1999, Struse et al. 2002). In

CORT3D, effective diffusion coefficients, D_e , (L^2T^{-1}) are estimated using a modified Millington-Quirk relationship (Jury et al. 1991), relating effective diffusion to water content (θ_w) as well as effective porosity.

$$D_e = D_m \frac{\theta_w^{10/3}}{\phi_{eff}^2} \quad (3.31)$$

In the fully water-saturated case, the water content is equal to effective porosity and Equation 3.31 simplifies to the Millington-Quirk relation (1959, 1961)

$$D_e = D_m \phi_{eff}^{4/3} \quad (3.32)$$

Contaminant Oxidation. A new chemical oxidation reaction module or package was developed for use with the modified RT3D code. The new module tracks a number of mobile and immobile species. The mobile species are: aqueous phase contaminant ($cont$), permanganate (MnO_4^-), and chloride (Cl^-). Contaminant concentrations (resulting from the oxidation reaction) are calculated using the second order reaction (Huang et al. 1999, Siegrist et al. 2001),

$$\frac{dC_{cont}}{dt} = -k_2 C_{cont} C_{MnO_4^-} \quad (3.33)$$

where C_i is the concentration of component i (ML^{-3}), dC_i/dt is the rate of change in concentration of component i with time, and k_2 is the 2nd-order reaction coefficient for degradation of the contaminant by MnO_4^- ($L^3M^{-1}T^{-1}$).

MnO_4^- , and Cl^- concentrations are calculated based on the reaction stoichiometry. The reaction module was written so the stoichiometric ratios are adjustable to accommodate modeling oxidation of different contaminants; however, for oxidation of PCE the stoichiometric reaction given by Equation 2-24 applies. This reaction has been shown to represent the oxidation of PCE by permanganate over the pH range of 3.5-10 expected to be found in the subsurface (Huang et al. 2002, Siegrist et al. 2001, Yan and Schwartz 1999).



In addition to the specified mobile species, the reaction module also tracks a number of immobile species, including: DNAPL phase contaminant, sorbed contaminant, $MnO_2(s)$, and natural oxidant demand (NOD). The $MnO_2(s)$ precipitates are assumed to be immobile and remain at the location they are generated. Treating all the generated $MnO_2(s)$ as immobile

provides a worst-case simulation of generated solids filling pore-space and potentially altering permeability.

Natural Oxidant Demand. The new reaction package also incorporates non-productive oxidant consumption by field soil and aquifer sediment components such as natural organic matter (NOM), reduced metals, and other reductants that can be readily oxidized. These soil constituents are referred to collectively as natural oxidant demand (NOD), or sometimes soil oxidant demand (SOD), and compete with target contaminants for available oxidant. Because NOD is generally a complex mixture of components whose surface area available for oxidant contact varies, NOD oxidation is implemented in the model code as a kinetic process. Further, Because NOD results from a mixture of constituents, the kinetic rate for oxidation of NOD can vary widely for different soils. While kinetic rates for some NOD constituents of a particular soil are often higher than that of the target contaminant, preliminary results related to this research, and that of others, suggest NOD frequently consists of at least two components with markedly different oxidation rates (Crimi and Siegrist 2004, Jackson 2004, Mumford et al. 2005). As an example, Chambers et al. (2000) found two distinct NOD oxidation rates for each of three different field soils in batch tests, with the rate during the first 24 hours being 10 – 20 times faster than the rate during the next 13 days. They also found that the slower rate for the three soils was virtually the same, while the initial fast rate varied by soil type with silt and clay being about twice that of sand. Similar results are shown in Figure 3.130, for a field soil taken from the Mines Park test site near the Colorado School of Mines in Golden CO (Seitz 2004). Because the graph is natural log of oxidant concentration over initial concentration versus time, the slope can be taken directly as a kinetic oxidation rate. From the figure, it can be seen that during the first day, the fraction of NOD oxidized has a high oxidation rate; after the first day, the remaining NOD is oxidized at a much lower rate. The addition of site groundwater increased the overall amount of NOD slightly, but did not change the NOD oxidation rates.

Research on kinetic rates for NOD oxidation to date, has not determined the overall reaction order. Results from the studies already mentioned suggest it is first-order with respect to NOD, but there has been little study of the effect of MnO_4^- concentration. The work of Crimi and Siegrist (2004) utilized two MnO_4^- concentrations, and provided some indication that at least the NOD fraction with the slower kinetic rate is also first-order with respect to MnO_4^- (second-order overall).

In the new model code, NOD is assumed to be immobile, because batch studies so far have suggested the soil NOD is typically far greater than any NOD exerted by dissolved constituents in the groundwater. Further, the volume of NOD oxidized is assumed to be negligible compared to the pore space so that removal of NOD does not increase permeability; however, the oxidation of NOD does consume permanganate generating $\text{MnO}_2(\text{s})$ which in turn can reduce permeability. Due to the absence of second-order NOD kinetic data, at locations where oxidant is present, changes to the mass fraction of fast and slow NOD are calculated using first-order equations. If NOD oxidation is actually second order (or some higher order) reaction instead of first-order, treating it as first-order in the model code will result in simulations overestimating permanganate depletion from NOD oxidation. In a higher order reaction, the kinetic constant is dependent on the concentration of the oxidant as well as the amount of NOD so that as oxidant is consumed the rate of NOD oxidation will decrease. Overestimating the permanganate depletion in the simulation would further cause an underestimation in the contaminant oxidation.

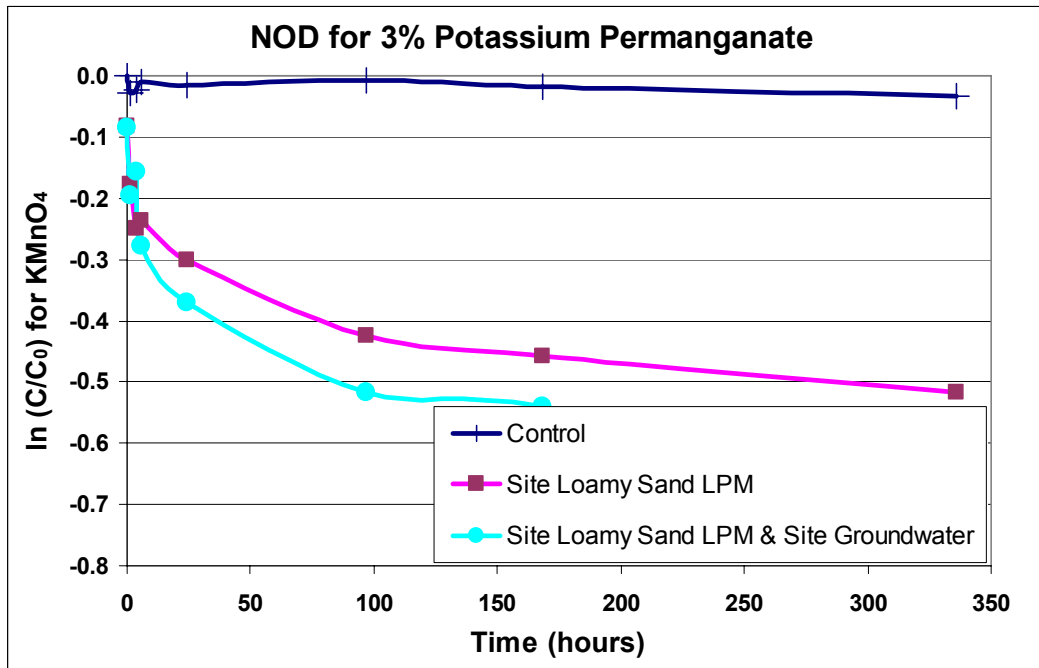


Figure 3.130. NOD Oxidation Rates for Mines Park Soil (Seitz 2004)

Permeability Effects. Research has shown that oxidation of a high DNAPL saturation source using permanganate may result in permeability reductions due to precipitation of manganese oxides (Lee et al. 2003, Schroth et al. 2001, Siegrist et al. 2002). On the other hand, research into permeability effects from permanganate oxidation of DNAPL source zones at lower saturations is more ambiguous. Nelson et al. (2001) concluded that the manganese oxides produced during oxidation of a PCE DNAPL present at approximately 4-7% saturation had negligible effect on the permeability, despite the system remaining at a neutral pH due to natural buffering from the carbonate mineral-containing sands. On the contrary, Lee et al. (2003) found that permanganate oxidation of a TCE DNAPL source zone at 8% saturation resulted in generation of up to 4900mg $MnO_2(s)$ /kg porous media, in an unbuffered silica sand system utilizing de-ionized water. Further, they witnessed a six-fold decrease in velocity of the oxidation front over the two-month experiment, attributing this decrease to reductions in permeability. This is especially interesting because less $MnO_2(s)$ is expected to precipitate at low pH where the reaction favors generation of Mn^{2+} instead of $MnO_2(s)$ (Stewart 1965, Yan and Schwartz 1999).

There are various methods to relate permeability changes to changes in porosity resulting from immobile components in porous media pore spaces, such as a power law model as in Equation 3.35 (Wyllie 1962) or capillary-tube model like the Kozeny-Carman equation in Equation 3.36 (Bear 1972)

$$k_{r,w} = \left(\frac{1 - S_n - S_{r,w}}{1 - S_{r,w}} \right)^3 \quad (3.35)$$

$$k_{r,w} = \frac{\phi_{eff}^3}{K_s (1 - \phi_{eff})^2} \left(\frac{d_m^2}{180} \right) \quad (3.36)$$

where $k_{r,w}$ is the relative water permeability, S_n is the saturation of immobile component in the pore space, $S_{r,w}$ is the residual water saturation for the porous media and K_s is the saturated hydraulic conductivity.

Saenton (2003) found Equation 3.35 provided good agreement to experimentally derived permeability data (Saba 1999) for DNAPL in silica sands like those that are being used in this research. Additionally, Clement et al. (1996) proposed a form of Equation 3.35 for pore-clogging due to microbial growth. These power law and Kozeny-Carman equations may not be perfectly suited to permeability reduction following chemical precipitation in porous media because they significantly under-predict permeability reductions, especially at high levels of plugging (Reis and Acock 1994). However, application of the CORT3D model code is done at a much larger scale than the pore-scale. Although Equations 3.35 and 3.36 may not be applicable to estimating pore-scale permeability reduction due to chemical precipitation, they may be adequate at the much larger modeling scale. For example, Equation 3.35 may estimate a 10 percent permeability reduction; however, in reality pores with the smallest throats may see a nearly 100 percent reduction, while pores with large throats may see virtually no reduction. Because the large throat pores are initially responsible for the greatest transport of water, plugging of the smallest pores has relatively little impact, and the overall change (at a modeling scale) may be well represented by the estimate of Equation 3.35.

Along these lines, CORT3D uses a version of Equation 3.35 to estimate permeability changes

$$k_{r,w} = \left(\frac{1 - S_{mno2} - S_n - S_{r,w}}{1 - S_{r,w}} \right)^3 \quad (3.37)$$

where S_{mno2} is a pseudo-saturation representing the volume of total pore space filled with manganese oxide solids. This pseudo-saturation is estimated by converting the mass fraction of solids produced to a volume using an effective manganese oxide precipitate density. The effective density is essentially a fitting parameter, and not an actual density of manganese oxide particles generated. This is because $MnO_2(s)$ formed during oxidation using permanganate may take different forms depending on soil and water conditions as well as where it forms. Much of it is likely to form within the pore space as an amorphous, hydrous, porous form reducing effective porosity available for water flow; this form is expected to have an undetermined density

that is lower than that of dry, solid $\text{MnO}_2(\text{s})$. Additionally, the amorphous, hydrous particles of $\text{MnO}_2(\text{s})$ that form within the pore space may also become lodged in pore throats blocking flow. Further, some may form as a more structured and solid film on soil particle surfaces where it can reduce the pore throat diameter. The effective density parameter accounts for permeability reductions resulting from all three of these mechanisms. The magnitude of permeability reduction occurring as a result of each mechanism is expected to be site specific, depending on soil and water conditions. As a result, it is expected that the effective density parameter may vary between simulations of different site conditions, but should be a constant for all similar conditions within a single simulation. It should also be noted that the relation represented by Equation 3.37 was generated for unconsolidated sand with well-sorted grains and non-wetting DNAPL (Wyllie 1962). If significantly different conditions are to be modeled, a different relation may be necessary. For example, the exponent is changed from 3 to 4 for cemented sandstone (Wyllie 1962).

Because dissolution and oxidation are transient processes where NAPL saturation decreases with time and manganese oxide solids increase with time (i.e. effective porosity and permeability change), the groundwater flow pattern needs to be updated periodically. The more frequent the update of the flow solution (through changes of effective hydraulic conductivity, porosity, NAPL saturation, and manganese oxide volume) the closer the simulation approaches the transient solution. Because the flow and transport solutions are not coupled in this model code, long (time) simulations are broken down to a number of short steady-state flow and transient transport runs that are executed in sequence. The implementation of simulating changing permeability as a result of DNAPL dissolution and chemical oxidation is similar to that described for the natural dissolution module described previously (Equation 3.11).

ISCO Model Code Verification. An important step in developing new model code is verification comparing results from this model code against analytical solutions and/or other (previously verified) numerical codes. After the code has been verified, the next step is testing to demonstrate that a model (utilizing the code) of specific site or experimental conditions can reproduce important processes and effects after being calibrated with an independent set of observations (Refsgaard and Henriksen 2004, Refsgaard and Knudsen 1996, Van Waveren et al. 1999).

Comparison to Analytical Solutions. The model code was verified against one- and two-dimensional analytical solutions incorporating advection, dispersion, and chemical reaction. Although the CORT3D computer model incorporates second-order chemical oxidation, available analytical solutions only incorporate first-order reactions. Additionally, the analytical solutions are for homogeneous systems under uniform flow in the direction of the primary axis.

The CORT3D simulations were set up so that either contaminant or oxidant was present in excess. This means the concentration of the species in excess does not change significantly as the reaction progresses, and the reaction becomes pseudo-first-order with a first-order rate constant (k_1) equal to the second-order rate constant times the molar concentration of the species in excess (Equation 3.38). Equation 3.39 is the one-dimensional solute-transport equation for a finite system with a third-type (or Cauchy) flux boundary at the inlet. Equation 3.40 is the analytical solution from Selim and Mansell (1976), modified by van Genuchten and Alves (1982) and presented in Wexler (1992):

$$k_1 = k_2 [C_{Excess}] \quad (3.38)$$

$$\frac{\partial C}{\partial t} = D_x \frac{\partial^2 C}{\partial x^2} - \bar{v}_x \frac{\partial C}{\partial x} - k_1 C \quad (3.39)$$

$$C(x,t) = C_0 \left\{ \frac{\exp\left[\frac{(\bar{v}_x - U)x}{2D_x}\right] + \frac{(U - \bar{v}_x)}{(U + \bar{v}_x)} \exp\left[\left(\frac{\bar{v}_x + U}{2D_x}\right)x - \frac{UL}{D_x}\right]}{\left[\frac{(U + \bar{v}_x)}{2\bar{v}_x} - \frac{(U - \bar{v}_x)^2}{2\bar{v}_x(U + \bar{v}_x)}\right] \exp\left[\frac{[-UL]}{D_x}\right]}} \right. \\ \left. - 2 \frac{\bar{v}_x L}{D_x} \exp\left[\frac{\bar{v}_x x}{2D_x} - \frac{\bar{v}_x^2 t}{4D_x} - k_1 t\right] \right. \\ \left. \cdot \sum_{i=1}^{\infty} \frac{\beta_i \left[\beta_i \cos\left(\frac{\beta_i x}{L}\right) + \left(\frac{\bar{v}_x L}{2D_x}\right) \sin\left(\frac{\beta_i x}{L}\right) \right]}{\left[\beta_i^2 + \left(\frac{\bar{v}_x L}{2D_x}\right)^2 + \frac{\bar{v}_x L}{2D_x} \right]} \cdot \frac{\exp\left[\frac{-\beta_i^2 D_x t}{L^2}\right]}{\left[\beta_i^2 + \left(\frac{\bar{v}_x L}{2D_x}\right)^2 + \frac{k_1 L^2}{D_x} \right]} \right\} \quad (3.40)$$

with

$$U = \sqrt{\bar{v}_x^2 + 4k_1 D_x} \quad (3.41)$$

where $C(x,t)$ is the concentration at location x and time t , C_0 is the concentration of the species of interest entering at the inlet, \bar{v}_x is the linear pore velocity in the x -direction, D_x is the longitudinal dispersion coefficient, L is the column length, and β_i are the roots of the equation

$$\beta \cot \beta - \frac{\beta^2 D_x}{\bar{v}_x L} + \frac{\bar{v}_x L}{4D_x} = 0 \quad (3.42)$$

The outlet boundary is a second type (or Neumann) specified concentration gradient boundary, with the specified gradient equal to zero. The initial condition is that the concentration of the species of interest is zero at all locations in the column.

Two comparisons were performed for a short, 40cm, column—one with oxidant in excess and one with PCE in excess. In each simulation a unit concentration of the species of interest

was applied at the inlet. A linear pore velocity of 5.0cm/hr, longitudinal dispersion coefficient of 2.0cm²/hr, and pseudo-first order reaction rate constant of 1.362 per hour were used. These parameters are of the same order of magnitude as PCE oxidation experiments performed as part of this research. Figure 3.131 shows the PCE concentration when oxidant is held constant in excess, while Figure 3.132 shows the oxidant concentration when PCE is artificially held constant in excess. In both cases, the CORT3D model results are identical to the analytical solution indicating the model is working correctly.

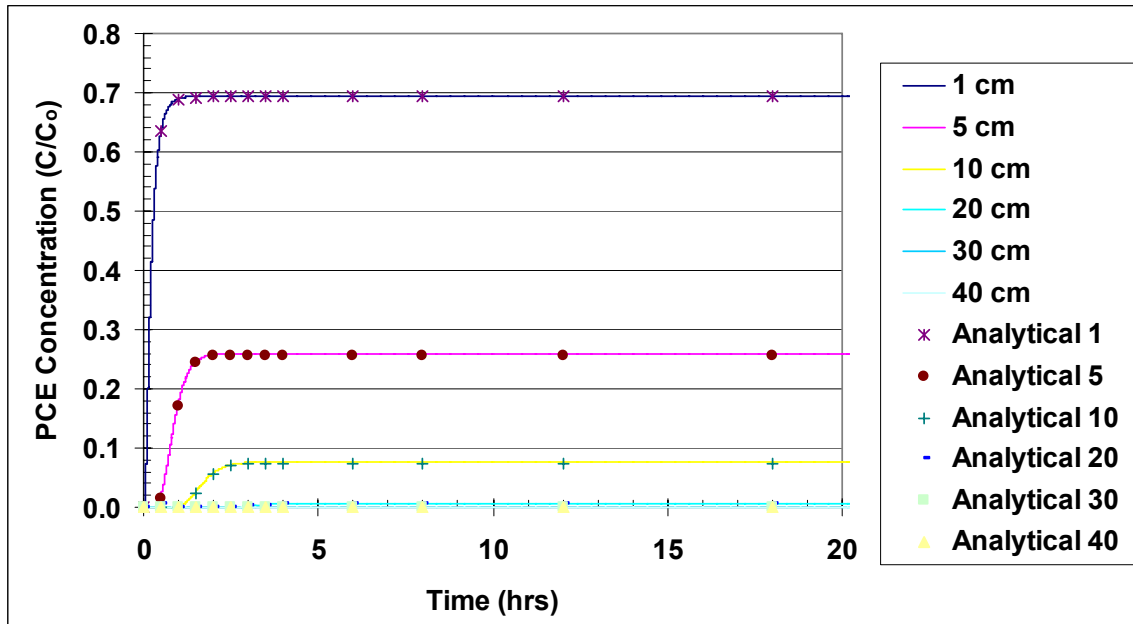


Figure 3.131. Analytical and Model Results for PCE in a Short Column, CORT3D Model Verification

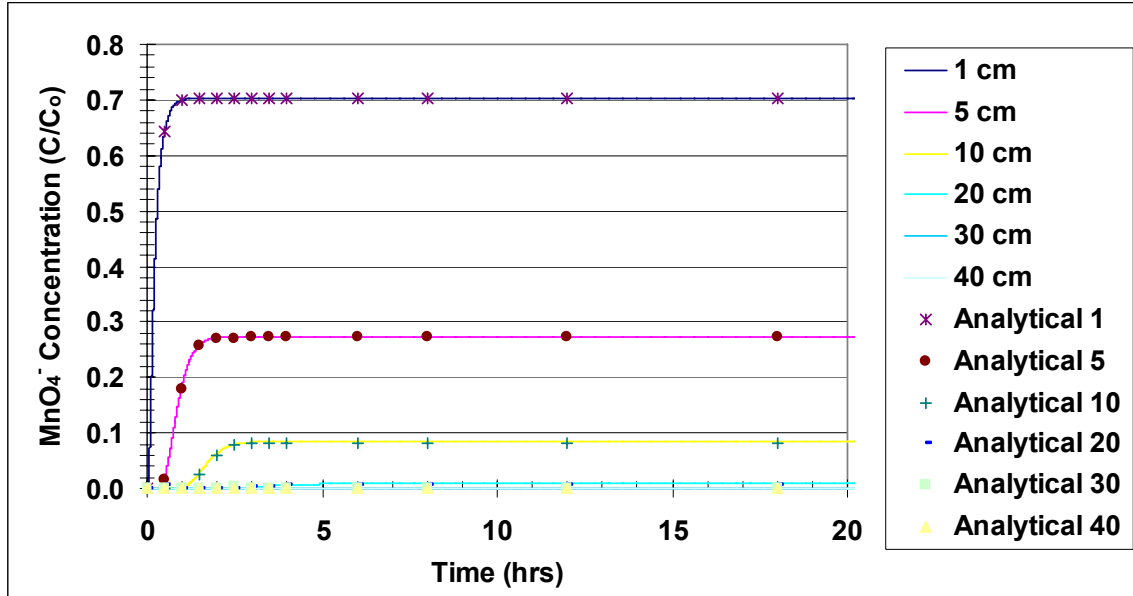


Figure 3.132. Analytical and Model Results for MnO_4^- in a Short Column, CORT3D Model Verification

An additional comparison was made for a much larger one-dimensional case, with a 40m long column, and different conditions to verify the model code works at larger scales. In this simulation, oxidant was held in excess and a unit concentration of PCE was input at the inlet. The linear pore velocity was 0.6m/hr, the longitudinal dispersion coefficient was $0.6\text{m}^2/\text{hr}$, and the pseudo-first-order reaction rate was 0.001 per hour. Again, the model exactly reproduced the analytical solution results.

Next, the model code was verified against a two-dimensional analytical solution for a semi-infinite length, finite width aquifer containing homogenous medium, with constant and uniform groundwater velocity in the x-direction only, and a constant line contaminant source of a finite width at the inlet as illustrated in Figure 3.133. Equation 3.43 shows the governing two-dimensional solute-transport equation. Again the simulation was set up with oxidant in excess to approximate a pseudo-first-order reaction, because the analytical solution is first-order. The analytical solution for this scenario (Equation 3.44) is from Wexler (1992).

$$\frac{\partial C}{\partial t} = D_x \frac{\partial^2 C}{\partial x^2} + D_y \frac{\partial^2 C}{\partial y^2} - \bar{v}_x \frac{\partial C}{\partial x} - k_1 C \quad (3.43)$$

$$C(x, y, t) = C_0 \sum_{n=0}^{\infty} L_n P_n \cos(n\pi y) \cdot \left\{ \exp\left[\frac{x(\bar{v}_x - \beta)}{2D_x}\right] \text{erfc}\left[\frac{x - \beta t}{2\sqrt{D_x t}}\right] + \exp\left[\frac{x(\bar{v}_x + \beta)}{2D_x}\right] \text{erfc}\left[\frac{x + \beta t}{2\sqrt{D_x t}}\right] \right\} \quad (3.44)$$

with

$$L_n = \begin{cases} 1/2 & , n = 0 \\ 1 & , n > 0 \end{cases} \quad (3.45)$$

$$P_n = \begin{cases} \frac{Y_2 - Y_1}{W} & , n = 0 \\ \frac{[\sin(\eta Y_2) - \sin(\eta Y_1)]}{n\pi} & , n > 0 \end{cases} \quad (3.46)$$

$$\eta = \frac{n\pi}{W} \quad , n = 0, 1, 2, \dots \quad (3.47)$$

$$\beta = \sqrt{\bar{v}_x^2 + 4D_x(\eta^2 D_y + k_1)} \quad (3.48)$$

where $C(x,y,t)$ is the concentration at location (x,y) and time t , D_y is the transverse dispersion coefficient, W is the width of the aquifer, Y_1 is the location of the lower edge of the strip source at the inlet, and Y_2 is the location of the upper edge of the strip source. The inlet is a first type (Dirichlet) constant concentration boundary with concentration equal to C_0 for y between Y_1 and Y_2 , and zero elsewhere. The outlet and side boundaries are all second type (Neumann) specified concentration gradient boundaries, with the specified gradient equal to zero.

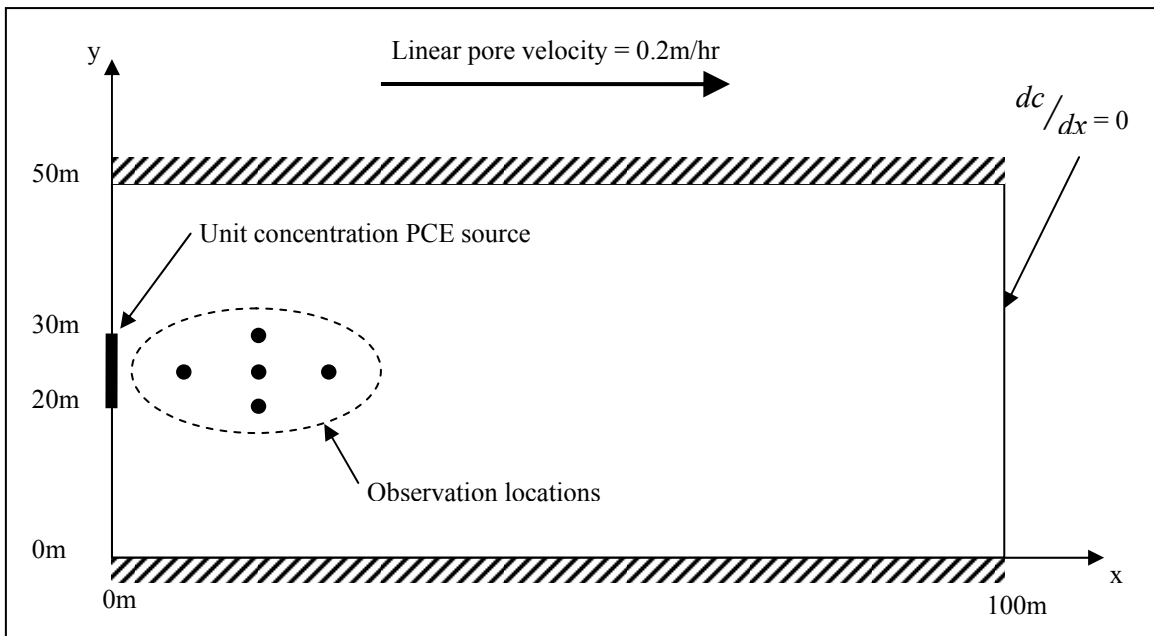


Figure 3.133. Schematic of Two-Dimensional Aquifer Scenario Used to Verify the CORD3D Model

For the comparison, an aquifer 50m wide by 100m long, containing a unit concentration PCE source 10m wide, centered at the inlet was used. A linear pore velocity of 0.2m/hr, longitudinal dispersion coefficient of 0.2m²/hr, transverse dispersion coefficient of 0.02m²/hr, and pseudo-first order reaction rate constant of 1.36x10⁻³ per hour were used. Figure 3.133 is a schematic of the 2D system being simulated. Figure 3.134 shows the PCE concentration when oxidant was held constant in excess. The numbers in the plot legend refer to the x and y location (m).

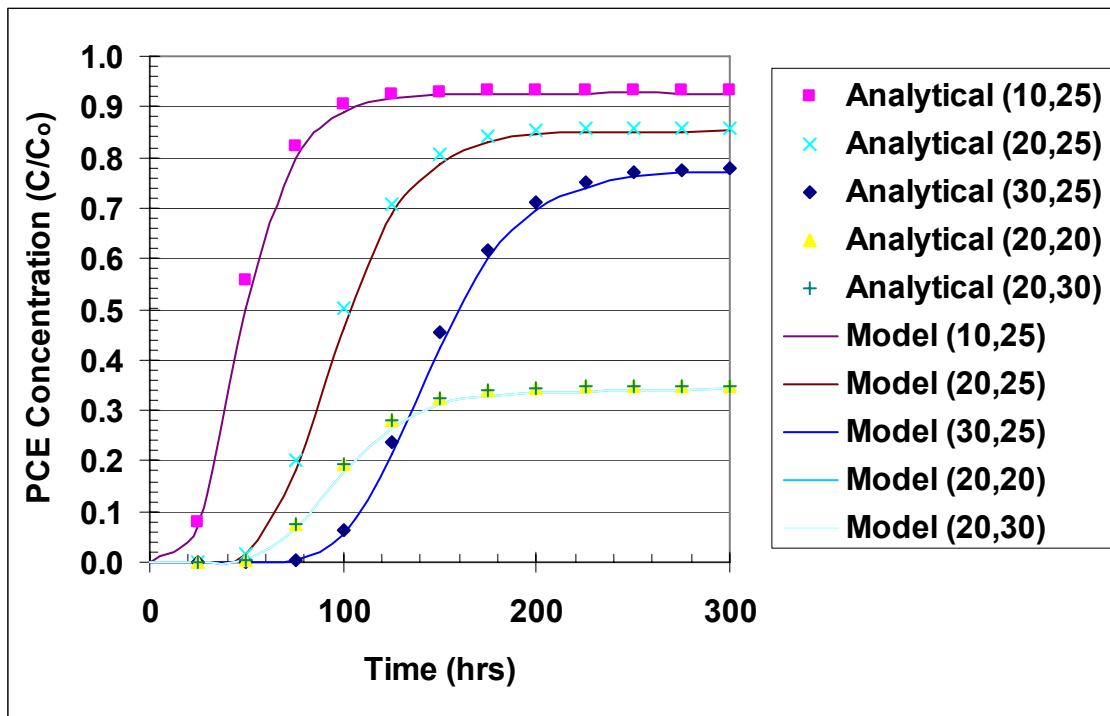


Figure 3.134. Analytical and Model Results for PCE in the Two-Dimensional Verification Exercise of the CORT3D Model

A series of simulations were also performed to verify the revised RT3D diffusion code worked as expected. The new code was used to simultaneously simulate pure diffusion (without a hydraulic gradient, hence absence of advection and mechanical mixing) of three components (PCE, MnO₄⁻, and Cl⁻), and the results were compared to those of running the original RT3D code individually for each of the three component diffusion coefficients. Identical results were produced by the original RT3D and CORT3D model codes, indicating the new effective diffusion code works properly.

3.9.7 Bioremediation model

Numerical modeling of biologically enhanced mass transfer experiments is based on MODFLOW to simulate groundwater flow and RT3D to simulate solute transport. A user-defined reaction module has been developed within RT3D that is capable of simulating abiotic mass transfer from DNAPL coupled with biodegradation. Existing RT3D reaction modules are not sufficient to address biodegradation by a mixed culture of reductive dechlorinators and associated mass transfer from DNAPL to aqueous phases.

Information presented in the refereed literature and results of preliminary experiments were used to identify reaction-transport processes and chemical species that are likely to be considered in modeling mass transfer experiments. A model based on this set of processes and chemical species module also is likely to find wide use in field-scale applications of source-zone bioremediation. The resulting reaction module is based on biodegradation kinetics of a mixed culture that has been studied extensively (Fennell and Gossett, 1998). It has been designed to use a comprehensive set of reaction processes and components. Additional reaction modules have been developed that use simplified subsets of processes and components.

For the comprehensive model, components include the chemicals of concern (PCE and degradation products), biomass, and nutrients such as a carbon source or electron donor that may limit microbe growth. Model components subject to biodegradation include those identified by Fennell and Gossett (Figure 3.135). A single component DNAPL consisting of PCE is assumed to be immobile. The current version of the reaction module also assumes that biomass components are immobile.

Transport of aqueous-phase components occurs by both physical and chemical processes while immobile components are affected solely by chemical processes. Physical processes include advection, hydrodynamic dispersion and source-sink mixing. Mass transfer from aqueous to non-aqueous phase is neglected for PCE breakdown products, carbon substrate, other electron donors and biomass. It also is assumed that entrapped DNAPL does not become remobilized as a separate phase.

Chemical processes simulated in the reaction package include:

1. First-order kinetic dissolution of PCE-NAPL by either of two options: (1) direct input of first-order rate coefficients, or (2) calculation of first-order rate coefficients from hydrodynamic and porous-media properties using a Gilland-Sherwood expression discussed below.
2. Dechlorination of PCE, TCE, DCE, and VC by Monod kinetics including both electron donor (H_2) and electron acceptor (PCE, TCE, DCE, VC) limitations. Zero-order and first-order kinetics also can be simulated with appropriate definition of kinetic parameters.
3. Fermentation of organic acids and alcohols to generate H_2 and acetate. Fermentation to generate non-specific products also is included as a means of simulating loss of primary electron donor for dechlorination.
4. Methanogenesis by both hydrogenotrophic and acetotrophic microbes with equilibrium partitioning of resulting methane between liquid and gas phases.

5. Competition for electron donor (H_2) by dechlorinators and methanogens.
6. Thermodynamic constraints on fermentation, dechlorination and methanogenesis.
7. Biomass growth of separate microbe populations responsible for dechlorination, methanogenesis, fatty-acid fermentation, and alcohol fermentation.
8. Biomass decay and hydrolysis to organic fatty acids by first-order decay.
9. Biomass detachment and loss (first-order process).

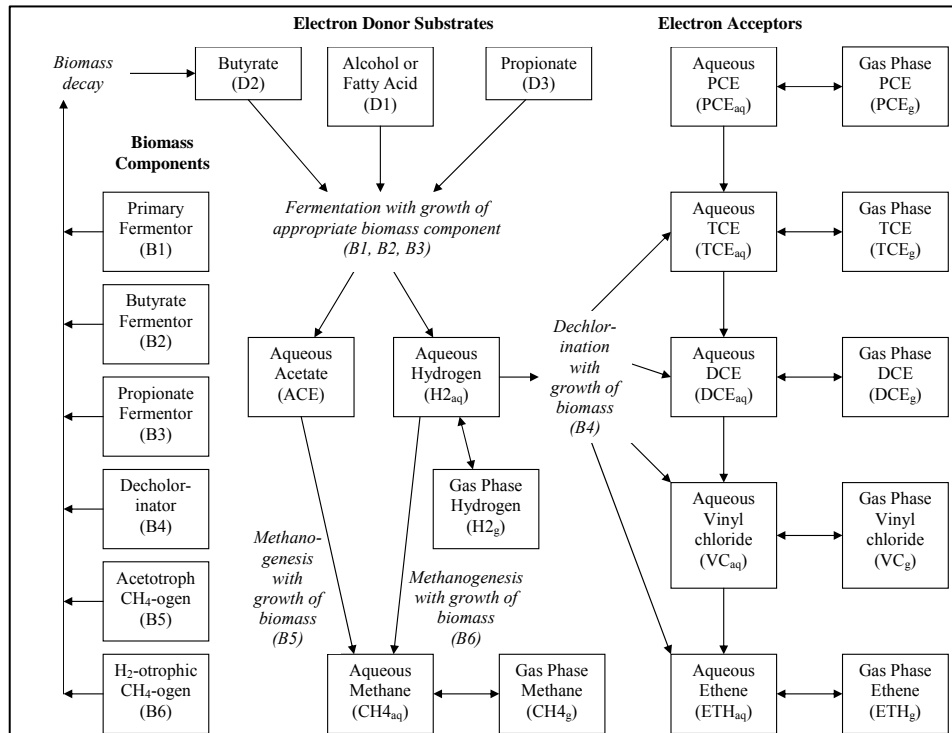


Figure 3.135. Chemical and Biomass Components in the PCE Reductive Dechlorination Model of Fennell and Gossett (1998)

The RT3D reaction module is design to support either of two forms of the Gilland-Sherwood correlation. One form is the abiotic correlation given by Saba and Illangasekare (2000) and Saenton et al. (2002). The second form is a generalized correlation based on an assumption of PCE degradation within water-DNAPL interfacial boundary layers. The latter form of the Gilland-Sherwood correlation currently is the Saba-Illangasekare equation multiplied by the Damkohler number.

In many cases, available data do not justify using such a comprehensive biodegradation model as that of Fennell and Gossett (1998). Therefore, additional reaction modules have been developed. Simplifications were based on expected differences between the batch experiments of

Fennell and Gossett (1998) and those described in this dissertation proposal, as well as results of sensitivity analyses conducted with the full reaction module. Sensitivity analyses using biodegradation parameter estimates similar to those of Fennell and Gossett (1998) were conducted to evaluate the role of fermentation and competition for H_2 in flow cell experiments. Simulation results showed minimal production of methane within PCE source zones. Methanogenesis occurred solely where electron donor transport occurred along flow paths that bypassed source zones. However, occurrence of methanogenesis did not affect rates of mass transfer from DNAPL. Because the primary purpose of the proposed research is to investigate effectiveness of bioremediation in enhancing mass transfer from DNAPL, it was concluded that there is little need to simulate H_2 competition. Simplifications include: (1) removing gas-phase components from the conceptual model, (2) removing propionate and yeast extract as electron-donor substrates for fermentation, (3) removing components related to methanogenesis (methane, acetate and $H_{2,aq}$) along with consideration of fermentation processes, and (4) electron donor substrates were combined as a single component, as were biomass components in Figure 3.135. However, in order to simulate loss of primary electron donor to processes that do not result in dechlorination, fermentation to generate non-specific products was retained in the simplified model. The resulting code was

Code Verification. The validity of the resulting RT3D reaction modules was demonstrated by simulating simple transport problems with known solutions and comparing simulation results with those solutions.

The RT3D reaction module for enhanced mass transfer was developed from a less complex reaction module for simulating DNAPL dissolution (Clement et al., 2003). Clement et al. (2003) demonstrated the validity of their numerical model by simulating a single-species transport problem and comparing the results with an analytical solution for advective-dispersive transport with first-order kinetics (van Genuchten and Alves, 1982). To verify that development of the biodegradation equations did not affect the dissolution model, the test problem presented by Clement et al. (2004) was repeated with the new reaction module.

Verification of the reaction module with respect to the biodegradation equations was undertaken by comparing the RT3D reaction module with solutions obtained with the non-dimensional solute transport model of Brusseau et al. (1999). The Brusseau model solves the one-dimensional equation of advection-dispersion with biodegradation and biomass growth represented by Monod kinetics. Both electron-donor and electron-acceptor availability are modeled and both may limit degradation and growth (i.e. double Monod kinetics). Biomass concentration is assumed to be attached but is represented in terms of an aqueous concentration while biomass concentration in RT3D is represented on a biomass per aquifer-mass basis. Growth yield in the two models also is represented differently but conversion of values between the two models is straightforward. The Brusseau model has been used successfully to simulate results from numerous column experiments involving biodegradation of aqueous-phase contaminants.

For cases where biomass growth and degradation are limited by either the electron donor or the electron acceptor (simple Monod kinetics), Brusseau et al. (1999) presents a sensitivity analysis of contaminant migration and biomass growth as functions of controlling non-dimensional parameters. They presented results of this analysis as a series of non-dimensional “type curves” (Figure 4 in Brusseau et al., 1999). Non-dimensional biodegradation parameters varied during the analysis include:

$$\chi = \frac{M_0}{YC_0} = \frac{\text{initial biomass}}{\text{growth yield} \times \text{boundary concentration}} \quad (3.49)$$

$$\varepsilon_m = \mu_{\max} Y \tau_r = \text{Monod coefficient} \times \text{growth yield} \times \text{residence time}$$

Results of the sensitivity analysis of non-dimensional biodegradation parameters are compared with the Brusseau et al. (1999) model in Figures 3.136 and 3.137. Given uncertainty in the Peclet number used by Brusseau et al. (1999) and the relatively coarse grid spacing of the RT3D simulations, the comparison is considered acceptable. Refining the grid spacing, particularly near the inflow boundary where steep biomass gradients develop, would improve the match.

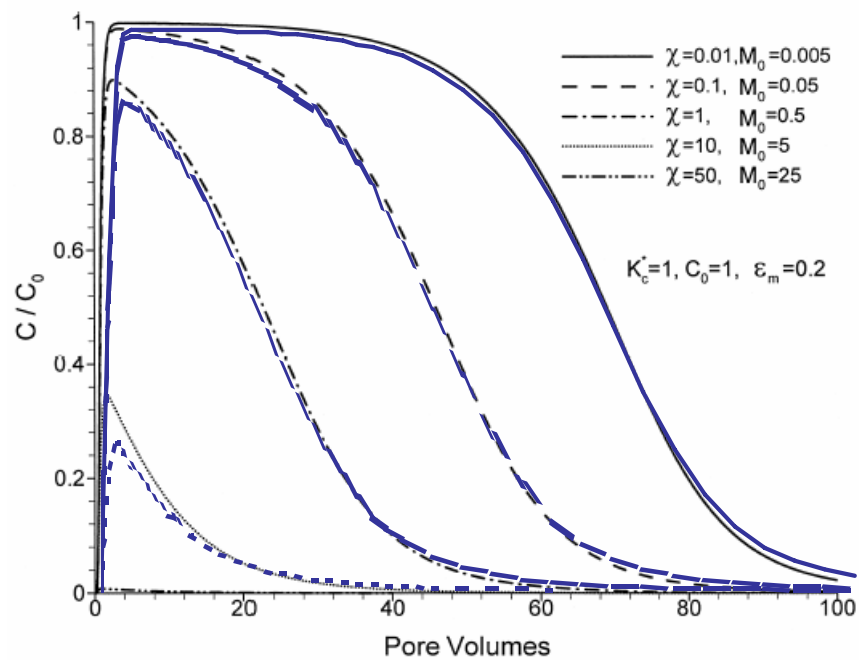


Figure 3.136. Concentration Breakthrough Curves at the Outflow of a Column Obtained with the RT3D (Blue) and Brusseau (Black) Models

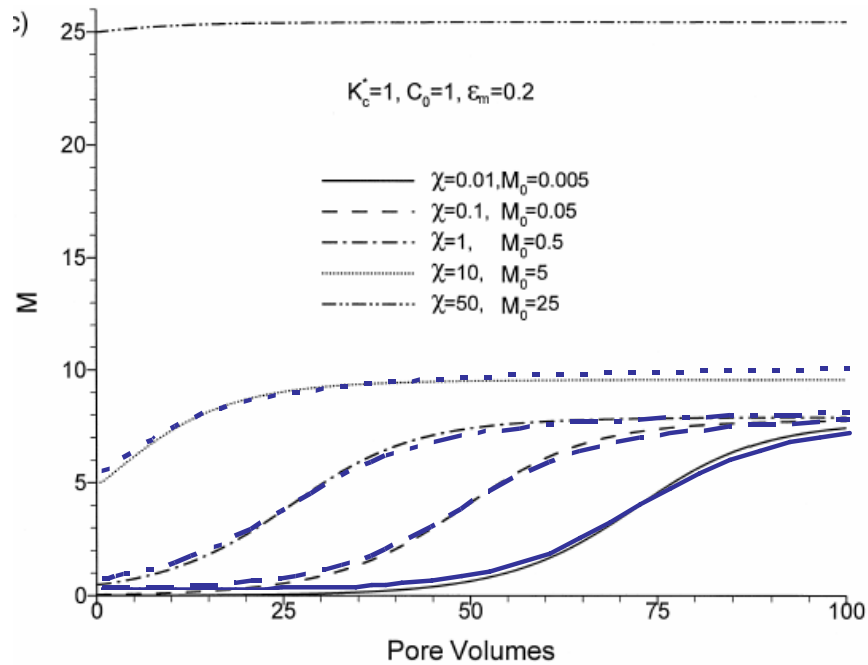


Figure 3.137. Biomass Concentration at the Outflow of a Column Obtained with the RT3D (Blue) and Brusseau (Black) Models

3.10 Design and methods for three dimensional simulation study

Throughout much of this research, experiments and modeling of DNAPL source zone characterization and remediation processes was conducted to achieve an understanding of mass transfer processes and to develop numerical modeling tools and site characterization methods. Very detailed experiments under controlled conditions were required to understand these processes. However, this level of data collection rarely is realistic for field studies. Therefore, a numerical modeling study was conducted with source-zone characterization assuming that only limited data were available at a limited number of locations. The purpose of this effort was to evaluate if it is possible to accurately characterize, design and monitor remediation of NAPL source zones in realistic conditions of data density.

In this section of the report, the capability of aquifer characterization methods and modeling tools was demonstrated by (1) simulating DNAPL distribution, mass transfer, and aquifer response to multiple-tracer tests following an assumed PCE-DNAPL spill in an idealized aquifer with specified hydraulic conductivity distribution, and (2) estimating DNAPL distribution and mass transfer by inverse modeling techniques based on data at 9 randomly selected well locations.

Simulations were based on an assumed heterogeneous unconfined aquifer having width, length, and depth of 15, 15, and 5 m respectively (Figure 3.138). No-flow boundaries were specified at the near and far ends of the aquifer and hydraulic heads were held constant at the left

and right ends of the aquifer. Average hydraulic gradient between the two constant-head boundaries was 10^{-3} . Hydraulic-conductivity distribution within the aquifer was specified as a spatially correlated random field with statistical parameters representing a highly heterogeneous sand aquifer with geostatistical parameters given in Table 3.21. A spill of 872 kg of free-phase PCE (538 L) was assumed to contaminate the aquifer from the top boundary. Simulations were conducted to describe the spatial distribution of DNAPL within the source zone, as well as hydraulic head, and aqueous-phase PCE concentration within the aquifer. A multiple-tracer test was simulated and the spatial and temporal distributions of partitioning tracer concentration were determined. For clarity, simulation results were designated as the IDEAL aquifer characterization.

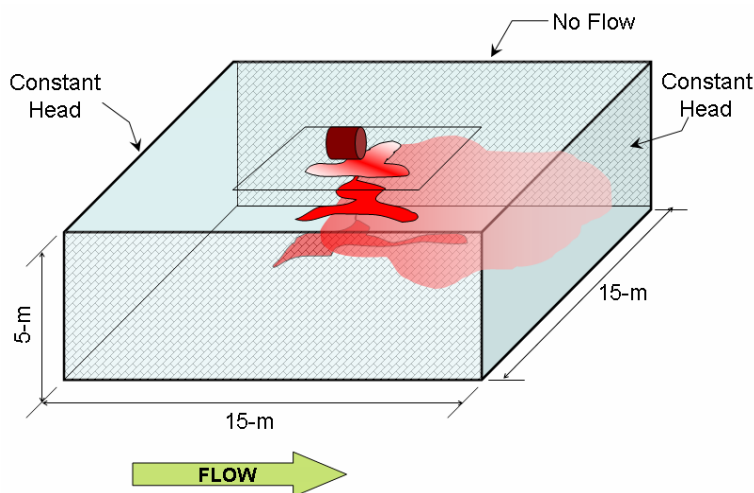


Figure 3.138. Three-Dimensional Hypothetical Aquifer Used in Field-Scale Simulation Study

Estimation of aquifer response based on data at 9 well locations began by assuming no prior information to describe the hydraulic conductivity field and DNAPL entrapment architecture. Borehole lithology, pumping-test response, PCE concentration data, and tracer test response at the 9 locations were then used during model calibration to estimate aquifer-property distribution, plume configuration, and DNAPL source architecture. For clarity, simulation results obtained by inverse modeling were designated as the AQ9 aquifer characterization. After obtaining the AQ9 characterization, SEAR was implemented to demonstrate remediation capabilities.

Numerical simulations were conducted using the following programs: MODFLOW-2000 (Harbaugh et al., 2000), MT3DMS (Zheng and Wang, 1999), RT3D (Clement, 1997). Inverse modeling was conducted using UCODE (Poeter and Hill, 1998) and PEST (Doherty, 1994).

4.0 Results and Accomplishments

This chapter of the report provides detailed interpretation of experimental results and descriptions of models developed from those results to address research objectives. Key findings and accomplishments for specific technical focus areas are summarized. Additional details can be found in a number of theses and dissertations (Saenton, 2003; Kaplan, 2004; Heiderscheidt, 2005; Moreno-Barbaro, 2005; Page, 2005; Glover, 2006)

4.1 Investigation of partitioning tracers

The focus of the tracer research was to evaluate the use of partitioning tracer tests as a tool for characterizing NAPL sources in heterogeneous source zones undergoing remediation. Laboratory studies were conducted at batch, column and large-tank scales to access quantitatively the performance of current tracer methods both before and after remediation. In this way, fundamental processes, hypotheses and data analysis of partitioning tracer methods were investigated. Specific objectives were (1) to identify causes of estimation error, (2) to refine tracer methods, and (3) to obtain information about the architecture of NAPL source zones. The fundamental knowledge gained from these investigations through laboratory investigations under controlled conditions can be used to improve design protocols for field characterization of NAPL entrapment morphologies encountered at geologically complex field sites. Effects of three remediation methods on partitioning-tracer behavior, surfactant flushing, chemical oxidation and bioremediation were evaluated in this research.

4.1.1 Batch tests

Surfactant Flushing. Surfactant treatment showed no significant effect on partitioning behavior and tracer partition coefficients for pure phase DNAPL and a PCE/TCE DNAPL mixture. However, partition coefficients for a field DNAPL mixture decreased with a single surfactant treatment. Partition coefficients for TCE DNAPL are summarized in Table 3.9. Partition coefficients for the DNAPL with a 50/50 mixture of PCE and TCE are summarized in Tables 3.10. Partition coefficients for the field DNAPL are summarized in Tables 3.11. The DMP and hexanol partition coefficients for the field DNAPL changed significantly after multiple surfactant washes. If unrecognized in a column or field application, this change in partition coefficients could significantly affect the accuracy of DNAPL volume estimated following surfactant remediation.

Chemical Oxidation. Tracer partitioning between water and PCE DNAPL that had been treated with a 3 percent solution of KMnO_4 showed interesting behavior. When PCE contacted KMnO_4 for both 48 and 120 hours, tracer partition isotherms were nonlinear (Figure 3.9) and, PCE partition coefficients for all tracers increased. Compared with partition coefficients for PCE DNAPL prior to treatment, partition coefficients were greater at lower tracer concentrations and lower at higher concentrations (Figure 3.10). For oxidant treated TCE DNAPL, there was no significant increase in the tracer partitioning coefficients. The tracer partitioning coefficients for

both PCE DNAPL and TCE DNAPL did not show significant changes after treatment with a 0.3 percent solution of KMnO_4 treated DNAPLs (Table 3.7).

Biological Treatment. Batch tests were conducted to characterize tracer partitioning for 4 tracer solution-DNAPL systems. These systems included (1) fresh DNAPL added to a tracer solution made from water, (2) fresh DNAPL added to a tracer solution made from KB1 nutrient medium that had been autoclaved to prevent biological growth. (3) DNAPL equilibrated with water for selected times, extracted and added to a tracer solution made from water, and (4) DNAPL equilibrated with an actively growing culture of KB-1 for selected times, extracted and added to a tracer solution made with KB1 nutrient medium. In this section of the report, batch systems that included fresh DNAPL are called baseline systems. The system that included DNAPL equilibrated with water is called the water-treated system. The system that included DNAPL equilibrated with the actively growing culture of KB-1 is called the bio-treated system.

Results for baseline DNAPL systems with abiotic nutrient medium indicate an increase in partitioning with nutrient medium compared to pure water (Tables 3.13 and 3.14). However, neither water treatment nor biological treatment of DNAPLs had a significant effect on partitioning coefficients obtained from untreated batch experiments. Partition coefficients for the water-treated systems are shown in Table 3.15. Partition coefficients for the bio-treated systems are shown in Table 3.16. Caution is advised in extending results of the bio-treated batch tests to other conditions. Headspace measurements obtained during biological treatment of DNAPL suggest that no biodegradation occurred during treatment.

4.1.2 Column tests

Surfactant Treatment. Partitioning tracer tests were conducted in two sand-packed columns with either pure TCE or a field DNAPL at residual saturation. Tests conducted before surfactant treatment were able to detect 85 percent of the TCE and 87 percent of the field DNAPL entrapped in the columns. Hexanol, with a relatively lower partition coefficient, gave better estimates than other tracers because Hexanol breakthrough was essentially complete for both column tests within the test period, as indicated by a long tail, while breakthrough of DMP was not complete. Surfactant flushing removed 11.7 mL of TCE from the column with pure TCE DNAPL and 3.44 mL of TCE from the column with the field DNAPL. Total DNAPL removal from the column with the field DNAPL was 8.6 mL.

Partitioning tracer tests conducted after surfactant treatment estimated that 4.4 mL (Hexanol) to 2.96 mL (DMP) of TCE still remained in the column with pure TCE DNAPL. This was 70 to 102 percent of the actual volume estimated based on mass balance. However, for the column with the field DNAPL, partition tracer tests estimated that less than 2.1 ml (Hexanol) to 5.1 ml (DMP) of field DNAPL remain following surfactant treatment. This was 28 to 69 percent of the actual volume estimated based on mass balance. The tracer-test estimates of DNAPL volume depletion are based on an assumption that partitioning coefficients did not change after surfactant treatment. If corrected partition coefficients measured after surfactant treatment in the batch test were used, the tracer-estimated field DNAPL volumes were about 70 to 108% of remaining volumes based on mass balance. This indicates that changes in tracer partition coefficients after surfactant remediation were significant for the field DNAPL. Table 3.18

summarizes residual DNAPL volumes estimated by partition tracer tests for pre and post surfactant flushing.

Biological Treatment. Partitioning tracer tests were conducted in columns. Two column tests were conducted to refine experimental protocols. Redox conditions for subsequent column tests were sufficiently reduced to promote dechlorination. Column 3 was run with residual PCE throughout the entire column, while Columns 4 and 5 were run with residual PCE in the bottom quarter of the column only. Tracer data for the latter three columns were analyzed using the method of moments (Jin et al., 1995) in order to estimate NAPL saturation, mass, and column porosity before and after biological treatment.

Partitioning tracer tests prior to biological treatment gave results that were the same order of magnitude as volumetric estimates but differed by as much as 48 percent (Table 3.20). In most cases the test estimate was lower than the volumetric estimate. Although most tests provided lower estimates of NAPL mass following inoculation and a period of biologically enhanced mass transfer, mass removal estimated from partitioning tracer tests ranged from 3.9 to 51 times higher than that estimated from effluent data. Furthermore, several tests reported higher NAPL mass results after inoculation.

4.1.3 Large-tank experiments

Partitioning interwell tracer tests (PITT) were conducted in two-dimensional large tanks that attempted to emulate real DNAPL spills in order to estimate DNAPL architecture. Tests were conducted in a tank packed with sand having a high degree of spatial heterogeneity, as well as a tank packed with sand having a low degree of spatial heterogeneity. In both experiments, partitioning tracer tests were conducted before and after remediation by surfactant flushing. Descriptions of experimental methods and observed results are provided in section 3.3.3 of this report. Section 3.3.3 also describes the estimation of source-zone architecture by a traditional method of tracer-test analysis called the method of moments (Jin et al., 1995). Application of numerical modeling techniques to the comprehensive data sets obtained during the large-tank tracer tests are described in this section of the report. The objective of the model analysis was to evaluate the performance of PITT by

- Calibrating tracer-test results with a selected numerical model and performing sensitivity analysis of model parameters that may affect effectiveness of partitioning tracer test.
- Evaluating the capability of the selected numerical model for simulation of tracer transport and partitioning behavior
- Comparing the performance of this numerical model to that of the method of moments, and
- Evaluating the influence of source-zone heterogeneity on the effectiveness of PITT.

Comparison Between Inverse Modeling and Method of Moments. Inverse modeling using information contained in the breakthrough curves was used to estimate DNAPL saturation distribution in the source zone. Flow and head observations and tracer-test data collected prior to the DNAPL spill were used for model calibration of flow and transport parameters. MODFLOW (Harbaugh et al., 2000) was used to simulate flow through the large tank. Saturation distribution within the source zone was estimated by solving the transport problem as an inverse problem with experimental breakthrough curves as observed data within a nonlinear least-square regression. MT3D (Zheng and Wang, 2000) was used to simulate transport. The DNAPL phase and partitioning behavior were incorporated in the transport model using the preprocessor MODTRACER developed in this research (Saenton, 2003). Equilibrium partitioning of tracers between DNAPL and water was assumed. The computer program PEST (Doherty, 1994) was used for parameter estimation. The tank was modeled using a finite-difference grid of 106 layers, 154 columns and 2 rows.

For parameter estimation, unknown DNAPL saturations in different areas of the tank were treated as parameters. Observations available for inverse modeling of the high heterogeneity tank consisted of measured relative concentrations of partitioning and conservative tracers collected at sampling arrays A, B and C. Observations in inverse modeling of the low heterogeneity tank consisted of data collected at sampling arrays A and C. Because sampling arrays were downgradient of the source zone, the source zone was reconceptualized as a series of laterally homogeneous but vertically heterogeneous layers. Saturation in each layer was assumed to be an effective uniform value. Figure 4.1 shows the re-conceptualization of the source zone for inverse modeling of the high heterogeneity tank.

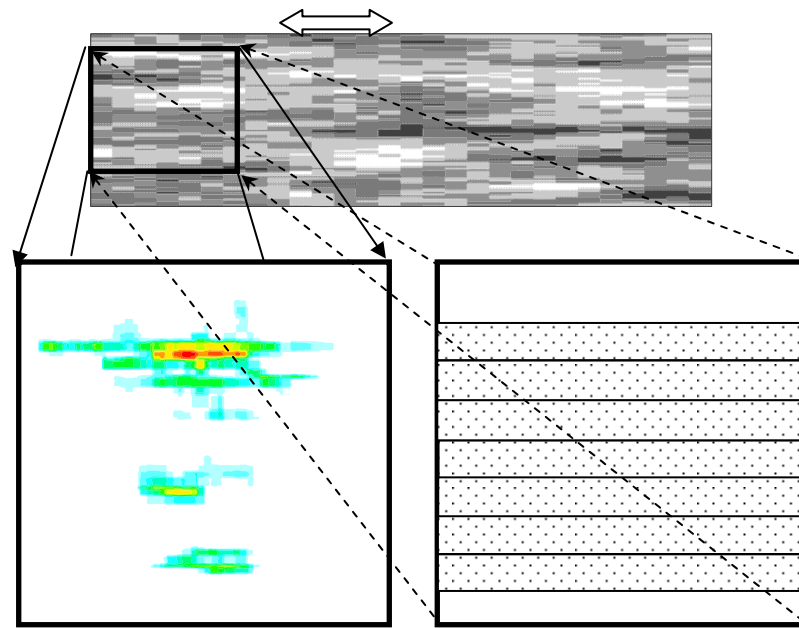


Figure 4.1. Conceptualization of the Source Zone used for Inverse Modeling, Large-Tank Tracer Tests, High Heterogeneity

Heterogeneity within the tanks created a source zone, observed by gamma-attenuation monitoring, that was much more complex than the one conceptualized for inverse modeling. However, only information that was observed during the PITT was used in the inversion problem. This limitation is consistent with conditions that typically would occur at a field site. As a result the source zone conceptualized for inverse modeling was necessarily simplistic. The purpose of inverse modeling was to determine if this information was sufficient to characterize the main features of the source zone that controlled downgradient mass flux. After parameter estimation, the results from the inversion exercise were compared with the exact saturation distribution obtained from gamma attenuation.

The DNAPL architecture obtained by inverse modeling is compared with actual data in Figure 4.2 (high heterogeneity) and Figure 4.3 (low heterogeneity). Results from inverse modeling mimic the vertical distribution of saturation obtained from gamma attenuation. This method of analysis improves the saturation estimation with respect to the traditionally used method of moments. Tracer breakthrough curves analyzed by inverse modeling better captured the DNAPL distribution in the source zone.

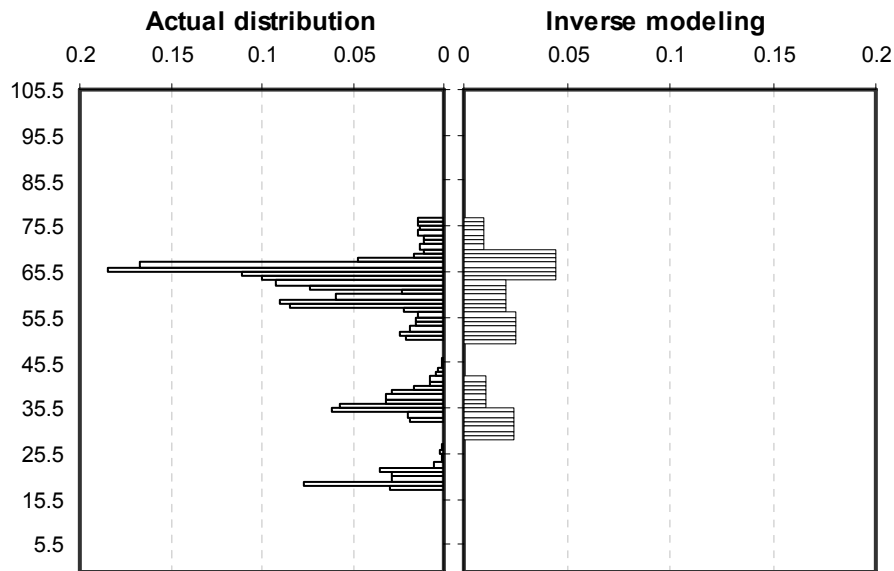


Figure 4.2. Comparison of the Saturation Distributions Obtained by Inverse Modeling and Actual Data, Large Tank Tracer Test, High Heterogeneity

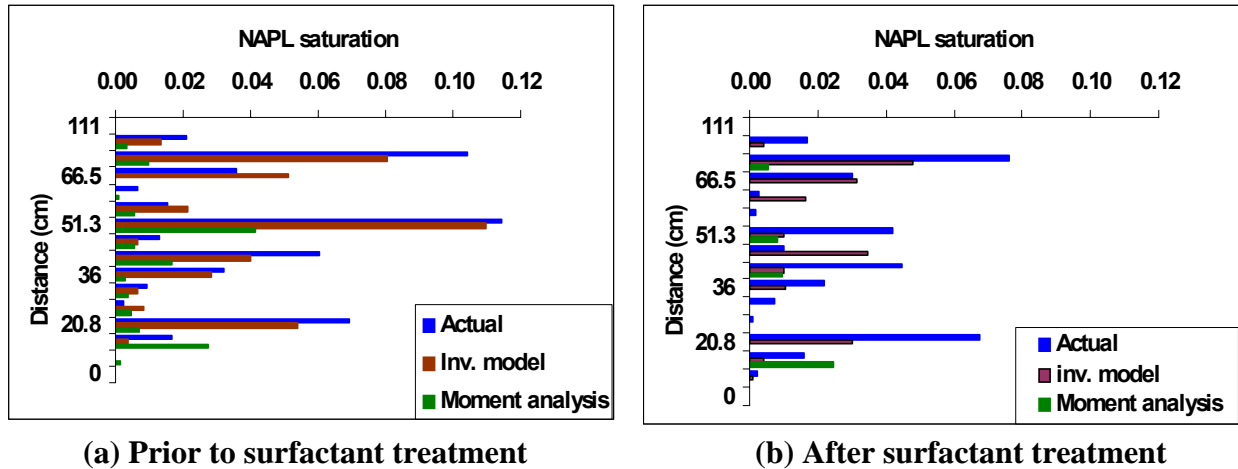


Figure 4.3. Comparison of the Saturation Distributions Obtained by Inverse Modeling, Moment Analysis, and Actual Data, Large Tank Tracer Test, Low Heterogeneity

In the case of the high heterogeneity tank, simulated breakthrough curves at the end of the simulation were compared to experimental data to evaluate whether the model reproduced the long tailing observed in the experimental tracer responses (Figure 4.4). Both curves showed the same time for breakthrough as well as the same degree of spreading. However, DMP simulated values did not provide a good fit when equilibrium was assumed in the analysis. The simulated DMP breakthrough curves showed a single offset instead of the asymmetric and long-tailed curve obtained during experimentation. If local equilibrium is not attained, local equilibrium-based models will predict a breakthrough response that occurs too late and exhibits too little dispersion. This is an indication that the model did not capture the behavior of the tracers and this miscalculation could affect estimates of source saturation.

For the low heterogeneity experiment, both simulated and observed curves show the same time for breakthrough as well as the same degree of spreading (Figure 4.5). Simulated DMP breakthrough curves for almost all sample locations also provided a good fit with the experimental results. This was true for tracer tests conducted both before and after surfactant remediation. These indicate that non-equilibrium effects were not significant at the low level of heterogeneity. As was observed for the high heterogeneity experiment, the results for inverse model replicate the vertical distribution of saturation distribution. Comparison of the moment analysis with actual conditions was not as good.

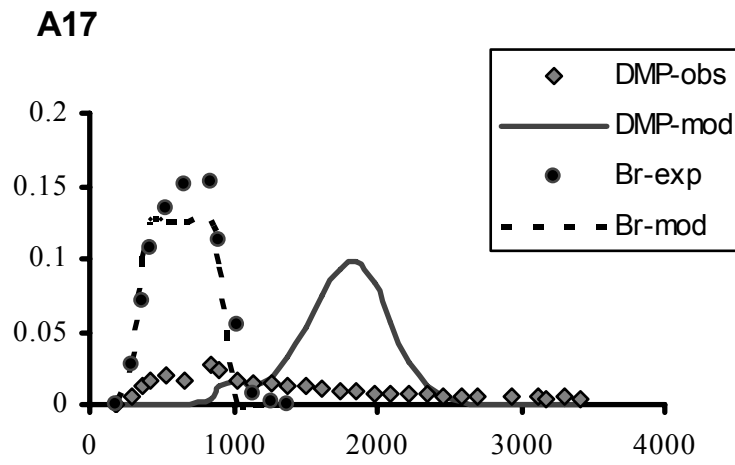
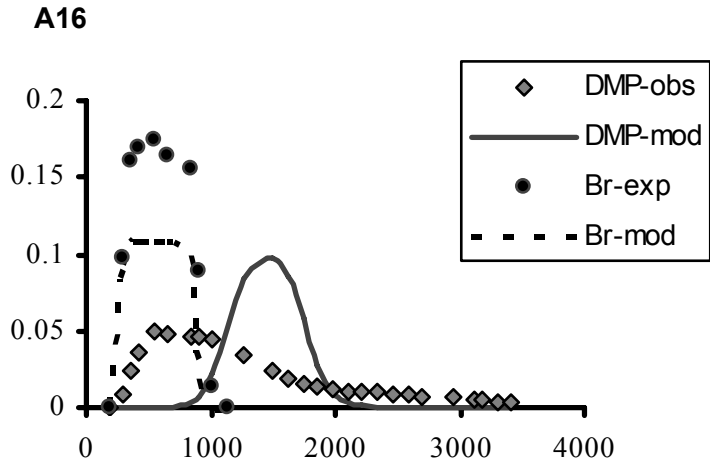
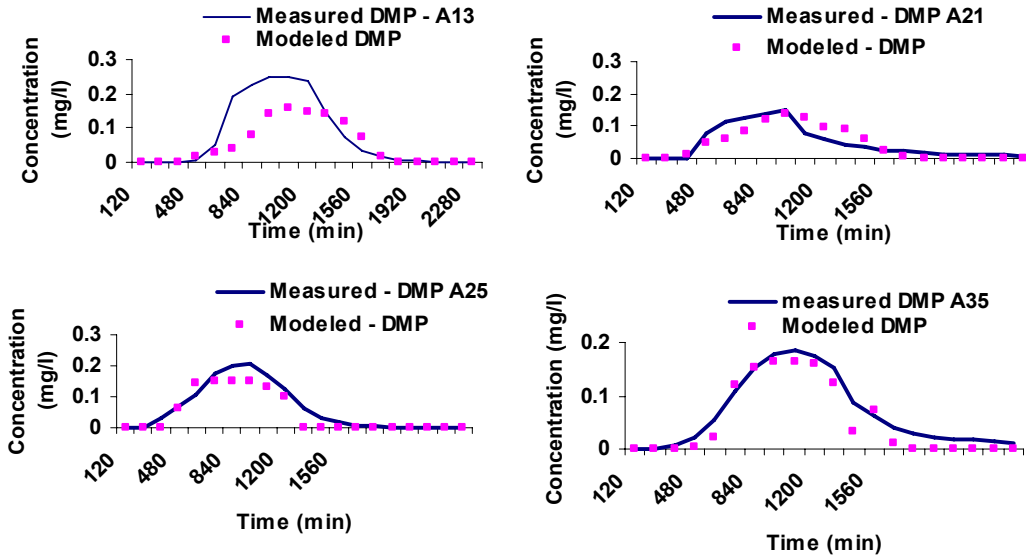
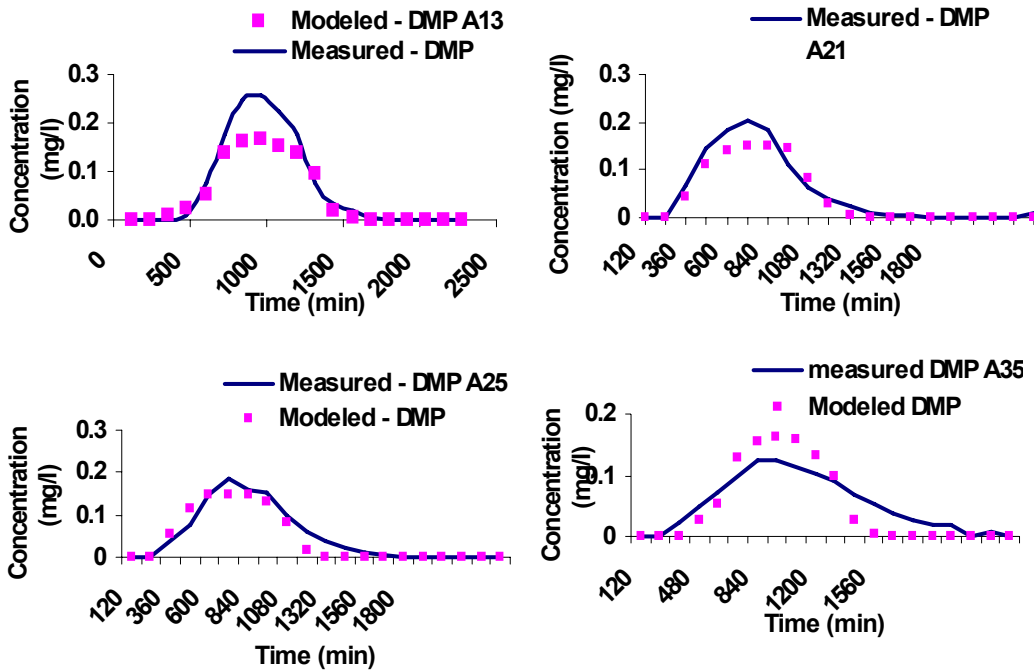


Figure 4.4. Experimental and Simulated Breakthrough Curves for Sample Ports A16 and A17, Large Tank Tracer Test, High Heterogeneity



(a) Prior to surfactant remediation



(b) After surfactant remediation

Figure 4.5. Experimental and Simulated Breakthrough Curves for Selected Sample Ports, Large Tank Tracer Test, Low Heterogeneity

Non-Equilibrium Partitioning. The preceding model analysis of tracer partitioning in the high heterogeneity experiment suggested that non-equilibrium partitioning may affect accuracy of the resulting DNAPL saturation distribution. The issue of non-equilibrium partitioning was addressed using a method proposed by Valocchi (1985). Differences among the simulated and experimental breakthrough curves for DMP are reflected in computed values of moments. Considering that the numerical models provide breakthrough curves that represent local equilibrium and that the experimental data represent breakthrough curves under non-equilibrium behavior, the deviation from equilibrium could be measured using the second moment of the two data sets. ε_2 , the fractional change in the second central moment, is defined as

$$\varepsilon_2 = \frac{\mu_2^K - \mu_2^E}{\mu_2^E} . \quad (4.1)$$

Superscripts K and E refer to the kinetic (i.e. nonequilibrium) and equilibrium models, respectively. The quantity μ refers to the nth central moment

$$\mu_2 = \frac{\int_0^\infty (t - \mu_1)^2 C(t) dt}{\int_0^\infty C(t) dt} \quad (4.2)$$

If the fractional change of the second moment is calculated for the simulated and observed breakthrough curves at all ports (Figure 4.6), large ε_2 values are obtained, representing large deviations from equilibrium. To relax the condition of equilibrium, non-equilibrium coefficients obtained in batch experiments were substituted for the equilibrium values. These values were selectively applied to the areas that were subject to non-equilibrium behavior represented by high values of fractional changes in the second central moments.

Non-equilibrium batch experiments for DMP (Figure 4.7) showed temporal variations in partitioning behavior that could be grouped into three distinctive time periods based on the deviation from equilibrium. These results were used to select partitioning coefficients for the large-tank tracer test. Values of equilibrium partitioning coefficient were modified with effective partition coefficients for portions of the source zone that corresponded to breakthrough curves A16, A17 and A31. Values of $K_{pe}=25$, $K_{pe}=20$ and $K_{pe}=25$ were obtained from Figure 4.7 and applied to source-zone layers S3, S4 and S7 respectively based on the deviation from equilibrium. With the incorporation of K_{pe} the model not only provided an estimate of source zone architecture closer to the actual one (Figure 4.8), it also provided a higher quality regression.

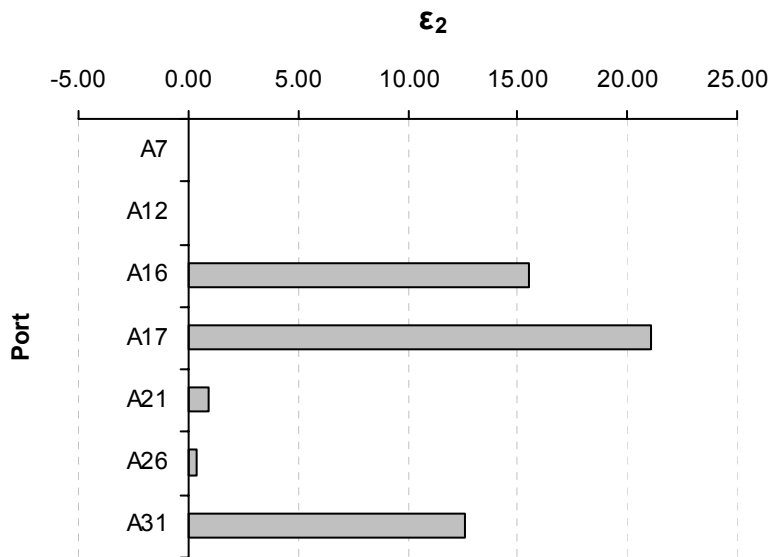


Figure 4.6. Fractional Change of the Second Moment in Sampling Array A, Large Tank Tracer Test, High Heterogeneity

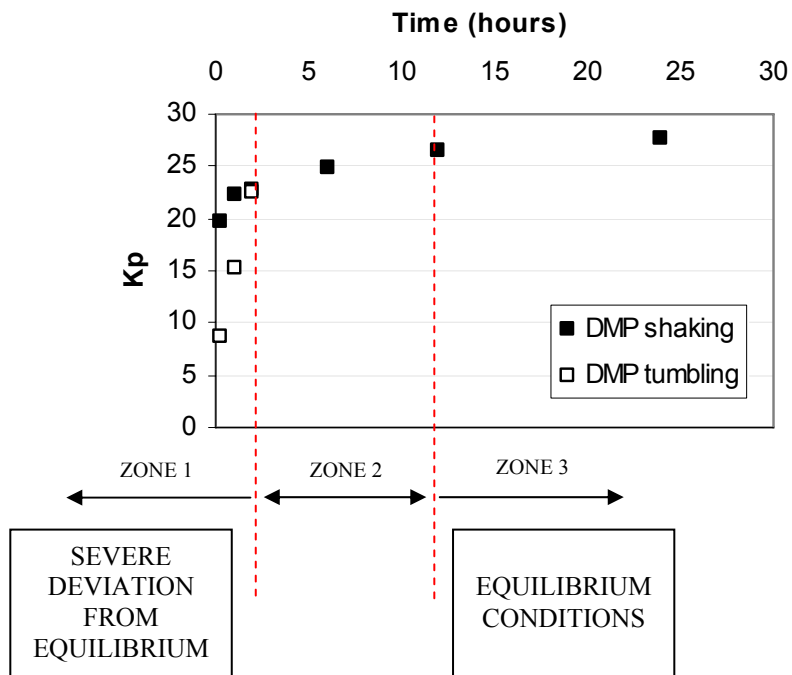


Figure 4.7. K_p as a Function of Time for DMP, Batch Partitioning Tracer Tests

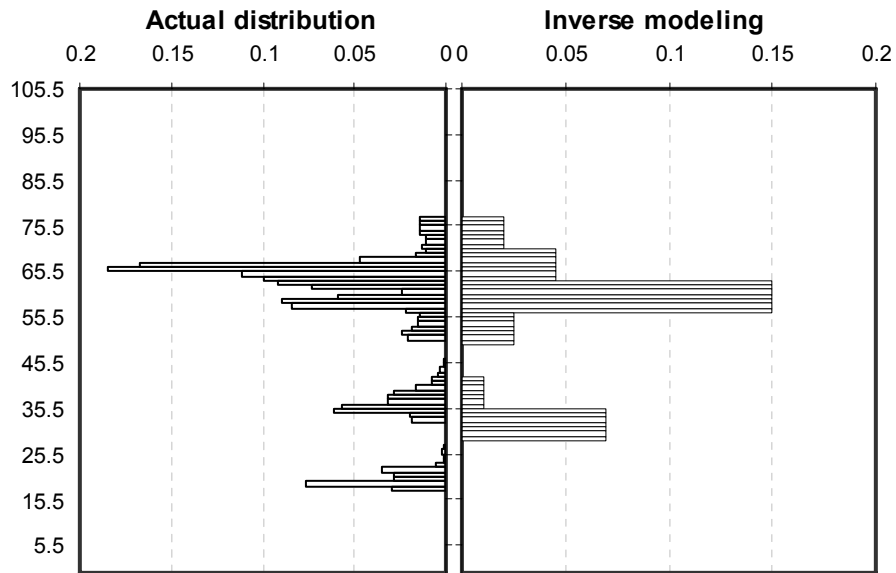


Figure 4.8. Comparison of Observed Saturation Distribution with the Saturation Distribution Obtained by Inverse Modeling with Effective Partitioning Coefficients, Large Tank Tracer Test, High Heterogeneity

The use of ε_2 to assign Kp_e gives rise to two fundamental issues: what is the cut off value for ε_2 to presume rate-limited behavior and how does ε_2 depend on other transport parameters like dispersion. The first is addressed by simply comparing quantitatively fractional change results for all the breakthrough curves and then qualitatively evaluate if these results agree with tailing observed in breakthrough curves. The second issue depends on the accuracy of the transport model. In this scenario, the model was calibrated for flow and transport, so the difference between experimental and simulated DMP breakthrough curves comes only from the saturation distribution and partitioning behavior.

One of the advantages in this correction method is that even though the exact value of Kp_e is not specified for each situation, it allows for a determination of DNAPL distribution in the best and worst case scenario. This is, if equilibrium is assumed in the analysis, the underestimation will reach its highest value. Conversely, if a value of Kp_e far from the equilibrium condition (for example 10) is used in the analysis, the maximum value for the saturation at that location will be obtained. In this way, the method can provide a range of saturation values to account for miscalculations caused by the local equilibrium assumption.

4.1.4 Summary of key results

The effect of a suite of remediation methods (surfactant, chemical oxidation and bioremediation) on partitioning tracer behavior were studied. Equilibrium partitioning behavior for pure TCE or PCE NAPL determined from laboratory experiments was linear and remained

unchanged by remediation. The sole exception to this statement was partitioning behavior for PCE-NAPL following ISCO, which was nonlinear. For NAPL mixtures obtained at field sites, partition coefficients changed following remediation.

This report presented the first experimental study to evaluate the influence of heterogeneity on tracer performance in settings that resemble heterogeneous sites. Since previous work by Moreno and Illangasekare, (2006) demonstrated that extraction wells provide underestimation of the mass under conditions of heterogeneity, only multilevel samplers were used in this study. Multilevel sampling is also the only sampling method that can potentially provide information about the vertical architecture or vertical smearing of DNAPL. Tracer tests in large tanks were conducted at high and low levels of source-zone heterogeneity (section 3.3.3). Observed breakthrough data were analyzed by two distinct methods: the method of moments and numerical modeling coupled with parameter estimation by nonlinear regression techniques.

After collecting tracer breakthrough curves, traditionally used method of moments was applied to determine DNAPL saturation. This method offers limited information about the vertical distribution of DNAPL. It underestimated or overestimated saturation distribution due to the following factors:

1. Flow bypassing due to heterogeneity
2. Monitoring distance from the source zone
3. Source zone architecture (pool or residual)
4. Limited tracer solution accessibility to source zone
5. High detection limit of the analytical instrument.

After method of moments, inverse modeling analysis was conducted. Simulation of tracer tests for two different levels of heterogeneity provided the following conclusions.

1. Inverse model gives better results compared to moment analysis and is a better tool to characterize the source zone architecture both before and after SEAR.
2. Accounting for non-equilibrium behavior in the tracer data analysis does not have a significant effect on the estimation accuracy of tracer concentrations and saturation distribution for low heterogeneous K fields.
3. In the case of high heterogeneity, the non-equilibrium assumption of the partitioning coefficient correctly simulates measured tracer concentrations and saturation distribution.
4. In the scenarios of high and low heterogeneity, the underestimation of PCE mass or the PCE saturation may be due to hydrodynamic inaccessibility of the source zone, rate-limited partitioning (non-equilibrium) of tracer partitioning coefficient or high detection limit of the analytical instrument.
5. Method of moments over or underestimates the vertical saturation profile depending on the tracer flow around the source zone and downstream.

6. Increasing distance of the monitoring wells from the source zone attenuates the signals of the tracers, this leads to inaccurate estimation of source zone vertical architecture and mass.

These studies have shown how tracer tests can overestimate remediation performance in the presence of pools. Divine et al. (2004) discussed the problems encountered using partitioning tracer tests to assess remediation performance when remediation activities were highly effective. He concluded that remediation could result in low remaining saturation distribution that could not be detected by tracer tests. Results from these studies yield the same conclusion for ineffective remediation activities in heterogeneous sites. Because it is difficult for remediation to completely remove pool areas, remaining high saturation zones can be disconnected and difficult to access by tracer flow paths. In this case, pools may not be detected during tracer tests and remediation performance may be severely overestimated.

4.2 Investigation of natural dissolution

Dissolution experiments were conducted at three scales: one-dimensional columns, bench-scale two-dimensional flow cells, and large two-dimensional tanks. Initial experiments were designed to investigate and compare mass transfer characteristics of pure and multi-component field DNAPL. Due to the complex multi-component nature of field DNAPL, mass transfer study of the field DNAPL focused on TCE dissolution. Subsequent dissolution experiments in 1-D column and 2-D test cells and tanks considered dissolution of pure PCE. Data generated from these experiments were used to calibrate and validate mass transfer models and to validate an upscaling method for simulating natural dissolution of entrapped NAPL at larger scales.

The upscaling method used laboratory-scale mass transfer rate coefficients to estimate effective mass transfer coefficients for numerical simulation of DNAPL dissolution at field scales. It was hypothesized that upscaled mass transfer coefficients could be related to geostatistical descriptions of aquifer heterogeneity and spatial DNAPL distribution, as well as laboratory derived mass transfer coefficients. Specifically, the upscaling method involved modifying a laboratory-scale Gilland-Sherwood relationship derived experimentally by incorporating geostatistical parameters that account for soil heterogeneity and NAPL entrapment architecture. Regression analyses and Monte Carlo simulations were used to determine the parameters in the proposed upscaled correlation. The predictive reliability of the upscaled mass transfer correlation was demonstrated through examples.

4.2.1 Column experiments with pure or field DNAPL

Column experiments of natural dissolution with pure PCE DNAPL were described in section 3.4.1. Numerical modeling of these experiments was conducted in order to develop an expression for estimating mass transfer rate coefficients at a column scale. Subsequent modeling of flow-cell and large tank experiments used this expression as a basis for characterizing natural

dissolution of more complex source zones and upscaling the mass transfer process. Specifically, data obtained from the column experiments were analyzed using a numerical model and inverse modeling algorithm to determine empirical parameters in the Gilland-Sherwood correlation given by

$$\text{Sh} = \alpha_1 (\text{Re})^{\alpha_2} (\text{Sc})^{\alpha_3} \left(\frac{\theta_n d_{50}}{\tau L^*} \right)^{\alpha_4} . \quad (4.3)$$

The model was calibrated by fitting breakthrough curves from dissolution experiments for a range of flow conditions. Results from inverse modeling are shown in Table 4.1. Figure 4.9 shows the experimental results and model fit for the three sand types used in the experiments (#70, #30, and #16). The Reynolds number exponent α_2 was the most sensitive parameter indicating that NAPL dissolution largely depends on hydrodynamic conditions in the source zone. In subsequent sections of this chapter, simulation results for column experiments are compared with those of flow cell and large-tank experiments.

Table 4.1. Empirical Gilland-Sherwood Coefficients Resulted from Inverse Modeling of Natural Dissolution Experiments (results shown for three experimental scales)

| Parameter | Column | Bench-Scale Flow Cell | 16-ft Large Tank |
|------------|---------------|--------------------------|---------------------|
| α_1 | 11.871 | 12.41 | 9.74 |
| α_2 | 0.273 | 0.23 | 0.21 |
| α_3 | 0.5 | 0.5 | 0.5 |
| α_4 | 1.282 | 1.28 | 1.12 |

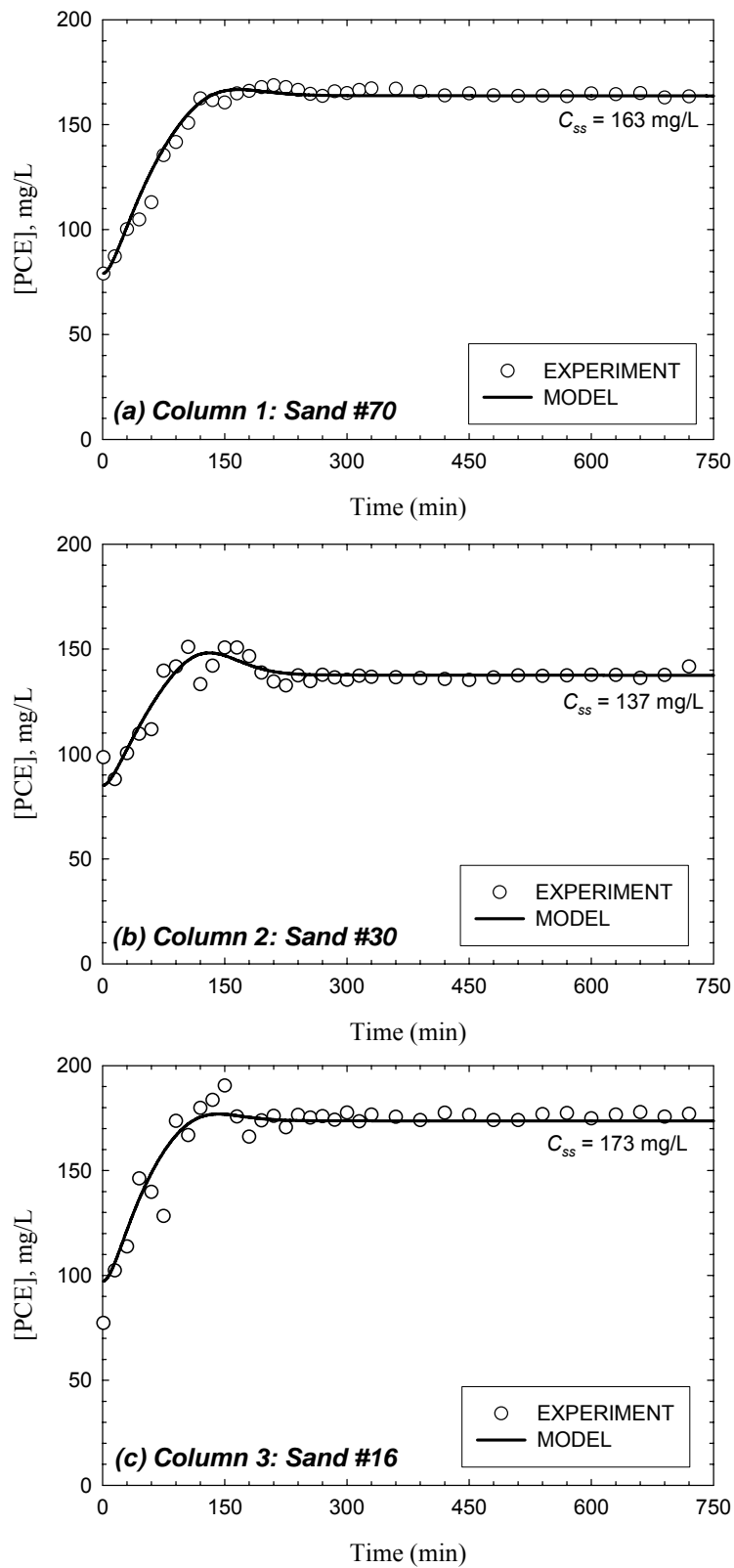


Figure 4.9. Comparison of Observed and Simulated Natural Dissolution of PCE in Column Experiments

4.2.2 Two-dimensional horizontal flow-cell experiments with pure PCE

Flow-cell experiments of natural dissolution with pure PCE DNAPL are described in section 3.4.3. The goal in modeling these experiments was to evaluate the effect of dimensionality on mass transfer coefficients. This was accomplished by comparing coefficient estimates for the flow cell experiments with those estimated from one dimensional column experiments. Separate flow-cell experiments were conducted for packing arrangements with one and two source zones. The 0.65-m × 0.45-m × 0.05-m flow cell was packed with a simple heterogeneous system consisted of a coarse sand lens surrounded by a finer medium. Coarse and fine sands were #16 and #70 (Unimin Corporation), respectively, and their properties were listed in Table 3.24.

Transient and steady-state dissolution of PCE was simulated for natural-dissolution conditions using the natural dissolution model described in section 3.9.2. The empirical parameters α_1 , α_2 , α_3 , and α_4 that appear in the Gilland-Sherwood expression were treated as calibration parameters. The dissolved PCE concentration data from one-source experiment were used for model calibration and the two-source experimental data was reserved for model verification/validation.

(i) **Model Calibration: One-Source Experiment.** The UCODE program (section 3.9.4) was used to evaluate parameter sensitivity prior to calibration. The sensitivity of the Schmidt number exponent was very small compared to the sensitivity of other parameters because the Schmidt number did not vary throughout the experiment. Therefore, it was set to a constant value of 0.5. Values of the Schmidt number exponent reported in literature for both theoretical and experimental studies range from 0.33 to 0.67. The nonlinear regression capabilities of UCODE were then used to calibrate the model. Once the regression converged, UCODE generated linear 95% confidence interval as well as composite scaled sensitivities. Table 4.2 represents the optimized empirical coefficients of the dissolution model with linear 95 percent confidence intervals as well as sensitivities of the final parameter values.

Table 4.2. Optimized Gilland-Sherwood Parameters for Natural Dissolution, Horizontal Flow-Cell Experiments with pure PCE

| Parameter | Value ± 95 percent Confidence Interval | Sensitivity |
|------------|--|--------------|
| α_1 | 12.41 ± 0.713 | 105.7 |
| α_2 | 0.2266 ± 0.0165 | 159.0 |
| α_3 | 0.5 | - |
| α_4 | 1.276 ± 0.279 | 127.4 |

Sensitivity of the Reynolds number exponent α_2 was highest among all parameters. This reflected the strong dependence of mass transfer rate on hydrodynamic conditions. The exponent α_4 for the dimensionless DAPL content ratio $(\theta_n d_{50} / L^* \tau)$ had a relatively high sensitivity. This reflected the importance of DNAPL morphology in mass transfer. The UCODE-generated correlation coefficient matrix indicated that there was no significant correlation among the three parameters. Figures 4.10 to 4.13 illustrate the experimental data and model fit for the one-source experiment. These figures indicate that the natural dissolution model was able to capture the mass transfer characteristics.

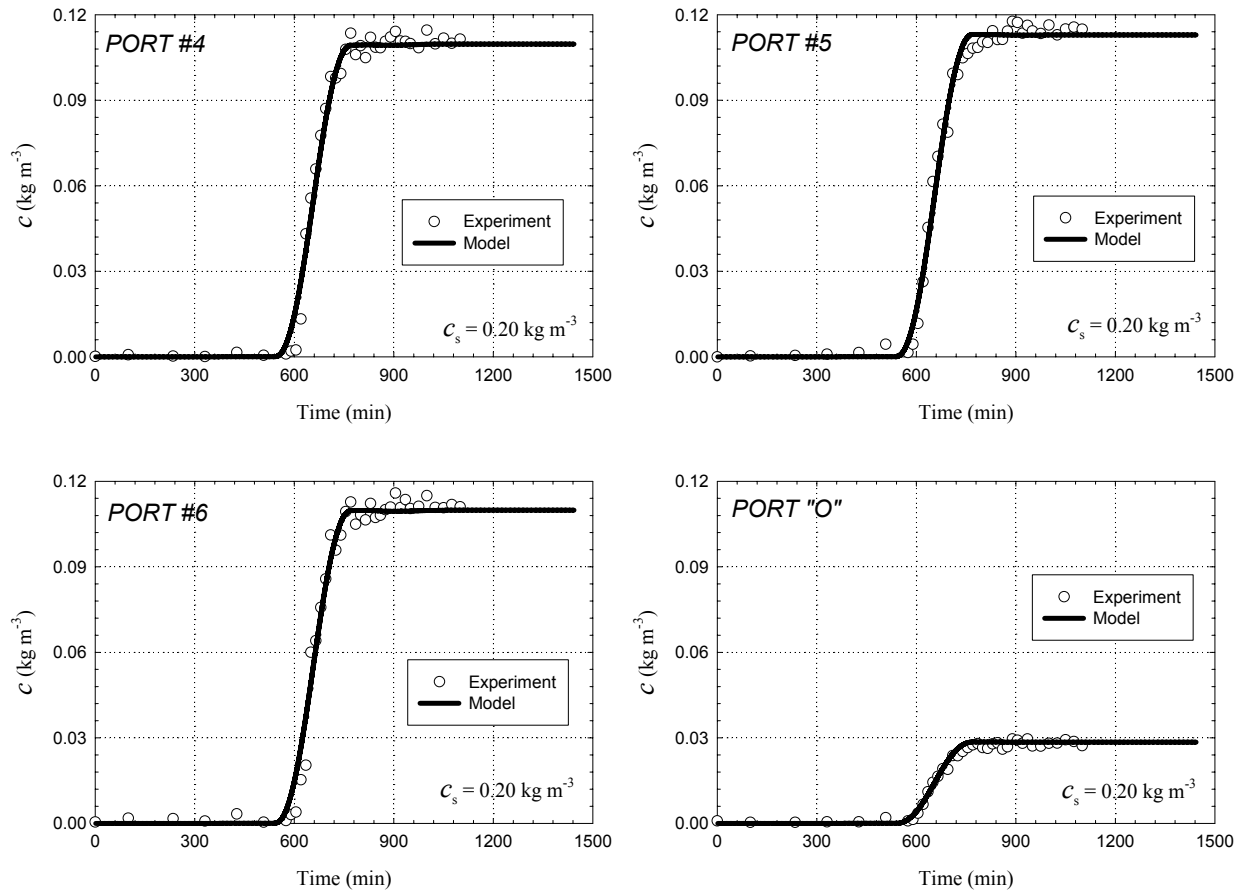


Figure 4.10. Comparison of Observed and Simulated PCE Dissolution under Natural Conditions, Horizontal Flow-Cell Experiments with One Source Zone

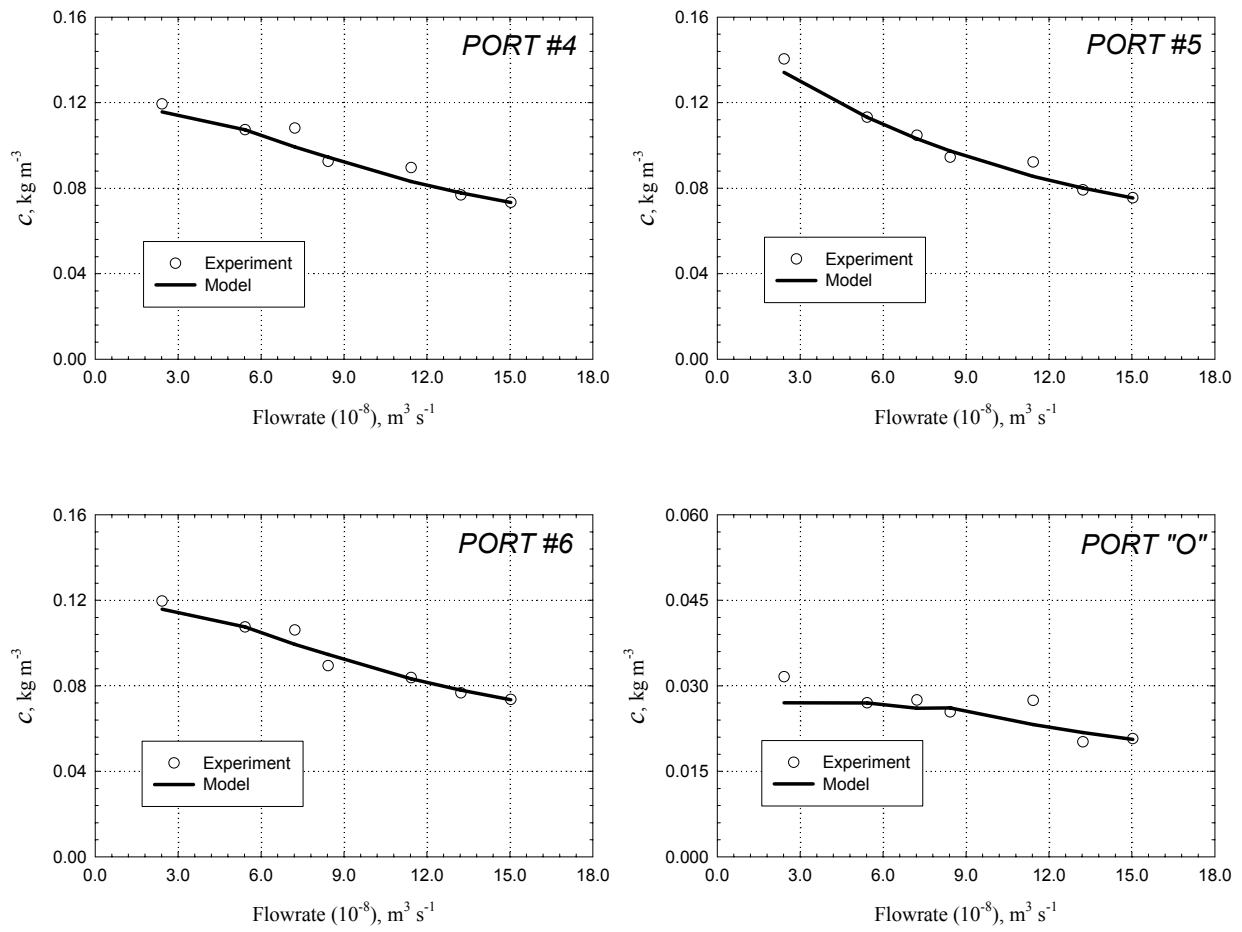


Figure 4.11. Comparison of Observed and Simulated Steady-State PCE Concentration for a Range of Flow Rates, Horizontal Flow-Cell Experiments with One Source Zone

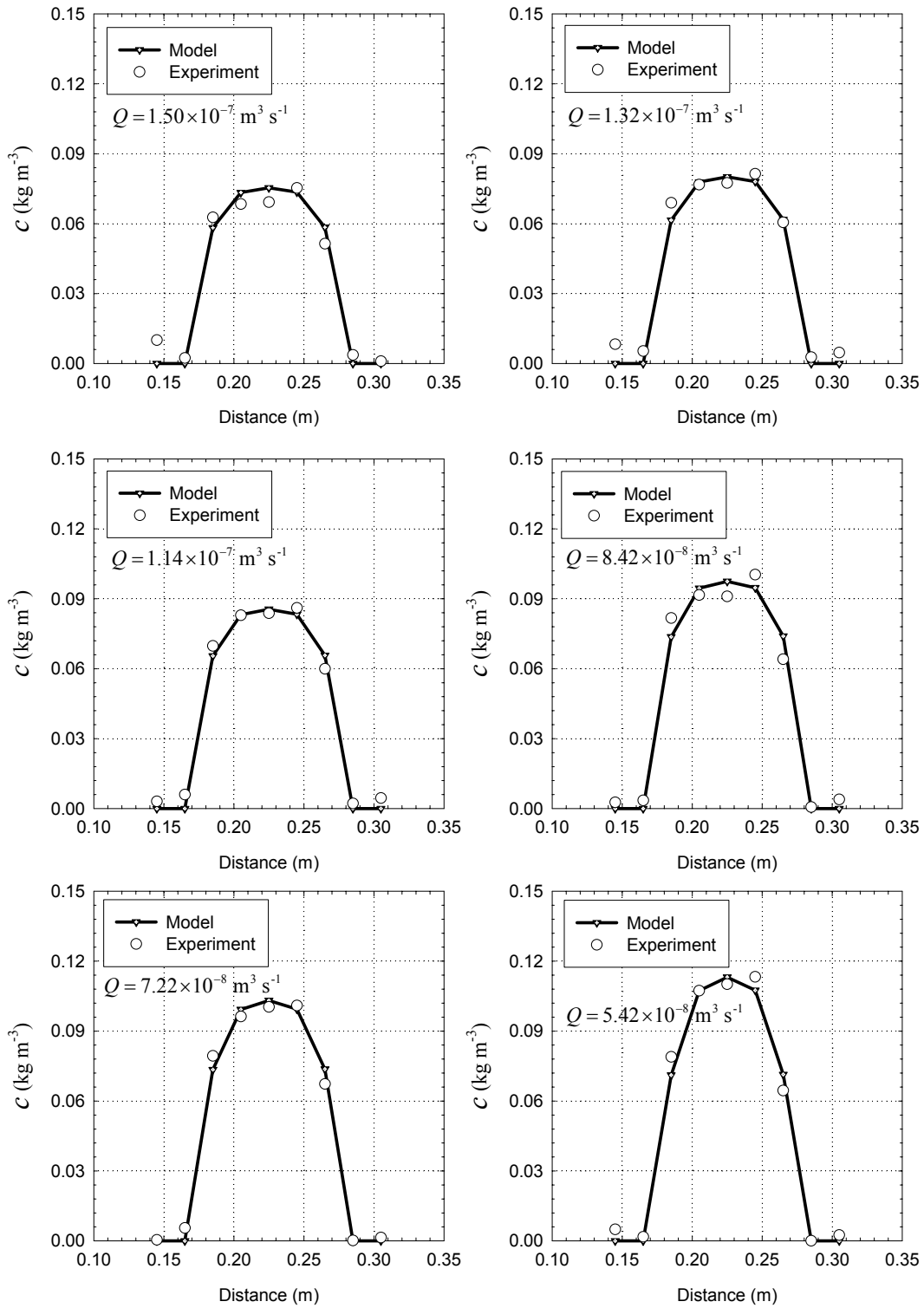


Figure 4.12. Comparison of Observed and Simulated PCE Dissolution Fronts, Horizontal Flow-Cell Experiments with One Source Zone

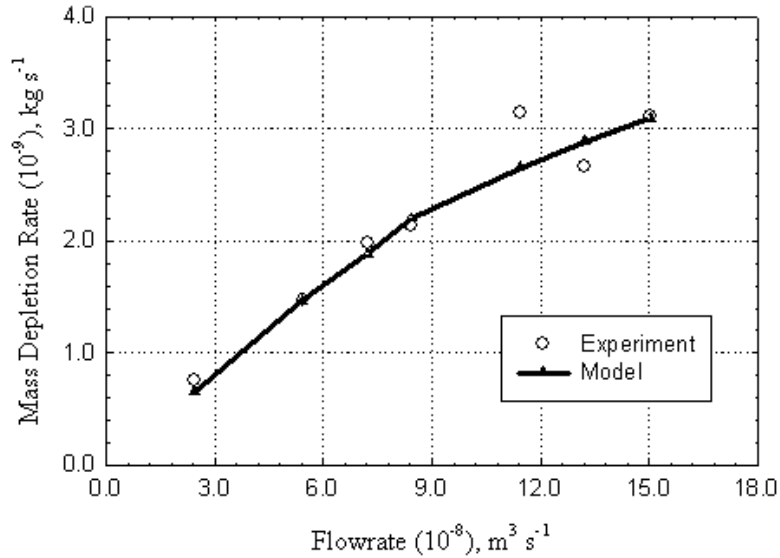


Figure 4.13. Comparison of Observed and Simulated Steady-State Mass Depletion Rates as a Function of Flow Rate, Horizontal Flow-Cell Experiments with One Source Zone

Model Validation: Two-Source Experiment. An independent set of data obtained from the natural dissolution experiment with two PCE DNAPL sources was used to test the validity of the previously calibrated dissolution model. The natural dissolution model was used to predict transient breakthrough curves without further calibration at monitoring port B located immediately downgradient of the sources and port O located to monitor flow-cell effluent. Results were compared with those observed during the experiment (Figure 4.14). The close match suggests that the model for natural dissolution is valid at the scale of the flow cells.

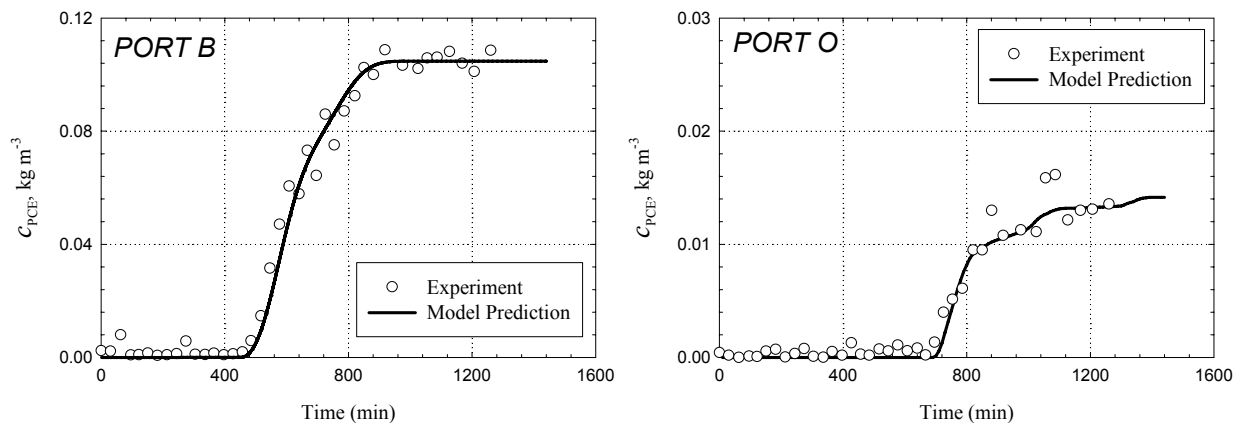


Figure 4.14. Comparison of Observed and Simulated PCE Dissolution under Natural Conditions, Horizontal Flow-Cell Experiments with Two Source Zones

4.2.3 Large-tank experiments of natural dissolution

Two large tank experiments were conducted to evaluate natural dissolution from source zones in complexly heterogeneous porous media. The first experiment was designed with high aquifer heterogeneity (variance of $\ln K = 1.22$) and the second experiment was designed with low aquifer heterogeneity (variance of $\ln K = 0.25$). Detailed descriptions of these experiments are provided in section 3.4.4 of this report.

Natural dissolution tests were conducted in order to (1) confirm the mass transfer model obtained from column and cell studies, (2) validate a methodology for determining entrapped NAPL architecture using mass flux data, and (3) validate a methodology for upscaling models of natural dissolution (Saenton, 2003; Saenton and Illangasekare, 2006).

High Heterogeneity Tank. Prior to modeling natural dissolution, models of water flow and conservative transport were calibrated. Development of the flow and transport models is described in conjunction with the modeling discussion for partitioning tracer tests (section 4.1.3). The natural dissolution model was based on these calibrated flow and transport models. The measured DNAPL saturation distribution was used for initial dissolution modeling (Figure 3.11). Dissolved PCE concentrations measured downstream of the source zone at sampling arrays A, C, and E (16 monitoring ports per array) were used to calibrated the natural dissolution model for empirical Gilland-Sherwood parameters. Calibration was by non-linear regression using the PEST program.

Differences between observed and simulated PCE concentrations generally were acceptably small (Figures 4.21 and 4.16). The correlation coefficient for PCE concentration was 0.936. Optimized Gilland-Sherwood parameters were similar to those obtained by modeling the bench-scale flow-cell experiments but were slightly different from those obtained from the column study (Table 4.1). This result was expected because the size of numerical grid blocks used in large tank and 2-D cell simulations were similar, whereas the grid block size used to analyze the data from column study were smaller.

Low Heterogeneity Tank. Prior to modeling natural dissolution, models of water flow and conservative transport were calibrated. Development of the flow and transport models is described in conjunction with the modeling discussion for partitioning tracer tests (section 4.1.3). The natural dissolution model was based on these calibrated flow and transport models. The measured DNAPL saturation distribution was used for initial dissolution modeling (Figure 3.12). Natural dissolution simulations were developed for a total head difference across the tank of 5.7cm as well as a head difference of 3cm. Dissolved PCE concentrations measured downstream of the source zone were used to calibrated the natural dissolution model for empirical Gilland-Sherwood parameters. Calibration was by non-linear regression using the PEST program.

The simulated and observed PCE concentrations are compared in Figure 4.17 for a head difference of 5.7 cm, and Figure 4.18 for a head difference of 3cm. Optimized parameter values were 12.33, 0.22, 0.51 and 1.11 respectively for α_1 , α_2 , α_3 and α_4 . The optimized alpha values were very similar to those obtained for the bench-scale flow-cell experiment as well as those obtained for the large tank experiment with high heterogeneity.

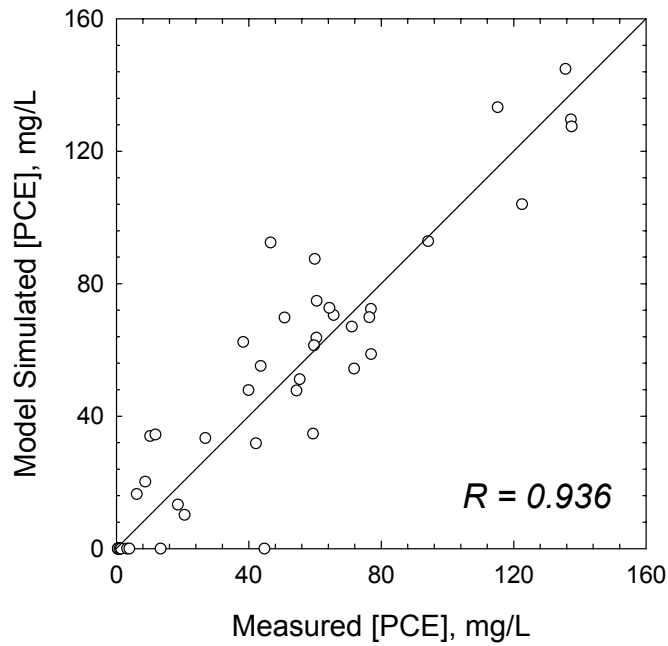


Figure 4.15. Comparison of Observed and Simulated Steady-State PCE Concentration, Large Tank Experiment with High Heterogeneity

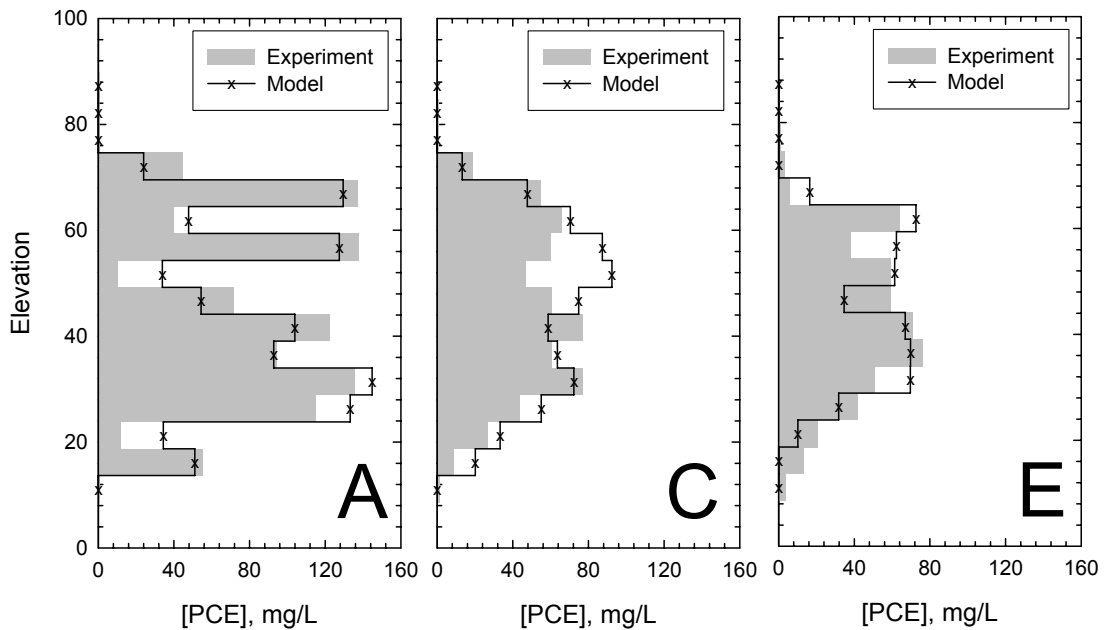


Figure 4.16. Comparison of Observed and Simulated Steady-State PCE Concentration along Three Vertical Sampling Arrays, Large Tank Experiment with High Heterogeneity

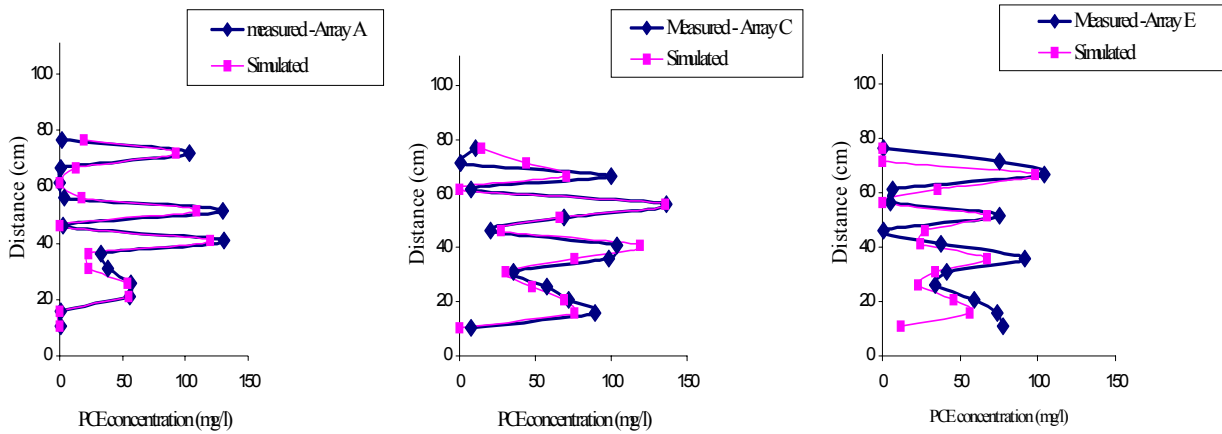


Figure 4.17. Comparison of Observed and Simulated Steady-State PCE Concentration along Three Vertical Sampling Arrays, Large Tank Experiment with Low Heterogeneity and a Total Head Difference of 5.7 cm

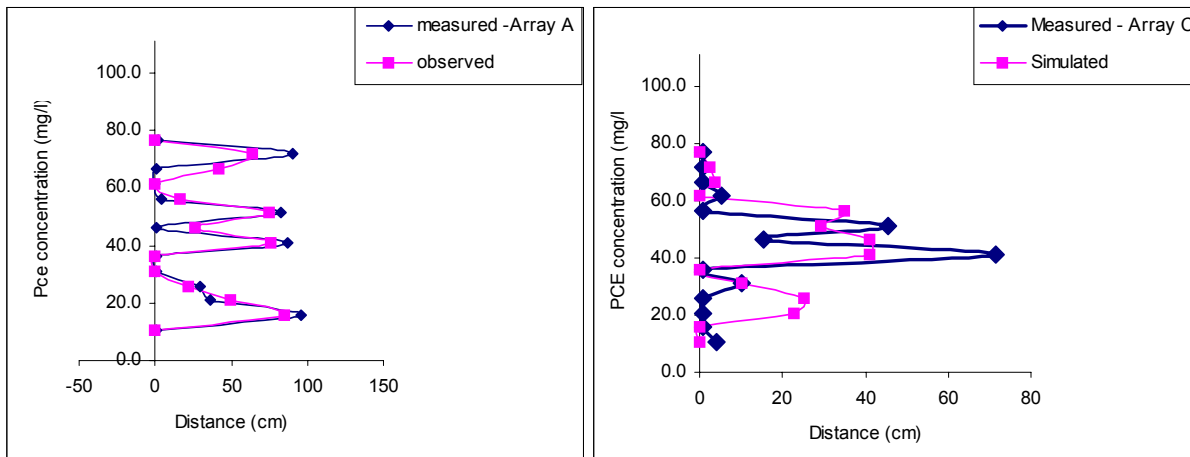


Figure 4.18. Comparison of Observed and Simulated Steady-State PCE Concentration along Two Vertical Sampling Arrays, Large Tank Experiment with Low Heterogeneity and a Total Head Difference of 3 cm

4.2.4 Upscaling natural dissolution

Properties such as pore size, porosity, grain-size distribution, and hydraulic conductivity vary spatially in the subsurface (Gelhar, 1993). This variability significantly affects overall

DNAPL migration, entrapment and dissolution, as well as subsequent transport of dissolved constituents. Groundwater flow through a heterogeneous source zone is governed by the spatial distribution of permeability, reflecting both aquifer characteristics and entrapped DNAPL saturation. Dissolution is largely dependent on the characteristics of the groundwater flow field as well as the spatial configuration of DNAPL. Therefore, mass transfer correlations that predict the DNAPL dissolution in field systems need to include terms that capture the effects of aquifer heterogeneity as well as spatial variations in DNAPL architecture. As it is not feasible to fully characterize this heterogeneity, geostatistical techniques must be used.

Aquifer Heterogeneity. In developing geostatistical models of aquifer heterogeneity, the logarithmic values of hydraulic conductivity of field of soils are usually assumed to be normally distributed (Gelhar, 1993). Letting K denotes hydraulic conductivity, the estimated variance of $\ln K$, denoted by $s_{\ln K}^2$, is

$$s_{\ln K}^2 = \frac{1}{n-1} \sum_{i=1}^n (\ln K_i - \overline{\ln K})^2 \quad (4.4)$$

where $\overline{\ln K}$ is estimated mean $\ln K$ or $\mu_{\ln K}$ which can be calculated by

$$\overline{\ln K} = \frac{1}{n} \sum_{i=1}^n \ln K_i . \quad (4.5)$$

In addition to mean and variance of $\ln K$, a third parameter, referred to as the correlation length (λ), is used to quantify heterogeneity. The correlation length is defined as the maximum distance between two points beyond which no correlation exists in the particular parameter. The correlation length of a system can be obtained from a plot of the semi-variogram defining the distribution of properties within that system (Gelhar, 1993). The semi-variogram $\gamma(h)$ is

$$\gamma(h) = \frac{1}{2n(h)} \sum_{i=1}^{n(h)} [\ln K(x_i + h) - \ln K(x_i)]^2 \quad (4.6)$$

where h is the separation distance between two observation pair, and $n(h)$ is the number of data pairs separated by a distance h . The semi-variogram is a plot between h as an x -axis and $\gamma(h)$ as a y -axis. When an exponential model is fitted to the semi-variogram, the correlation length (λ) is a distance h where $\gamma(h) \approx 0.63s_{\ln K}^2$. The value of $s_{\ln K}^2$ is the variogram sill of the asymptotic h .

DNAPL Entrapment Architecture. Although there has been relatively little study of the effect of DNAPL distribution on mass transfer from entrapped DNAPL in source zones, the findings of Saenton et al. (2002) and Saenton and Illangasekare (2005) strongly support the relative importance of entrapment architecture on net mass flux. In the first study, Saenton et al.

(2002) evaluated the effect of DNAPL entrapment architecture on the effectiveness of mass removal by surfactant enhanced dissolution in heterogeneous formations. When DNAPL source zones contained more pools than residuals, effective clean-up by surfactants was unlikely due to flow bypassing the pools. In the second study, Saenton and Illangasekare (2005) showed that the dissolved mass flux, and hence source longevity depended on DNAPL entrapment architecture. In situations where a larger fraction of the DNAPL was in pools compared to residual zones, mass flux generation was small due to flow bypassing pools. Hence, the source remained active for long periods and contributed to downgradient plumes.

Monte Carlo Simulations. To illustrate the importance of aquifer heterogeneity and DNAPL entrapment architecture on mass transfer, 80 Monte Carlo based numerical simulations of mass transfer were conducted using a hypothetical DNAPL spill in a heterogeneous two-dimensional intermediate-scale test aquifer. The dimensions of the test aquifer were 9.53-m long, 1.02-m high, and 0.05-m thick. The random field consisted of homogeneous and heterogeneous zones (Figure 4.19). Constant-head supplies at both ends were used to maintain a steady hydraulic gradient throughout the simulation. The heterogeneous zone was packed with five sands of different sieve sizes similar to the ones used in the experimental simulations (Table 4.3).

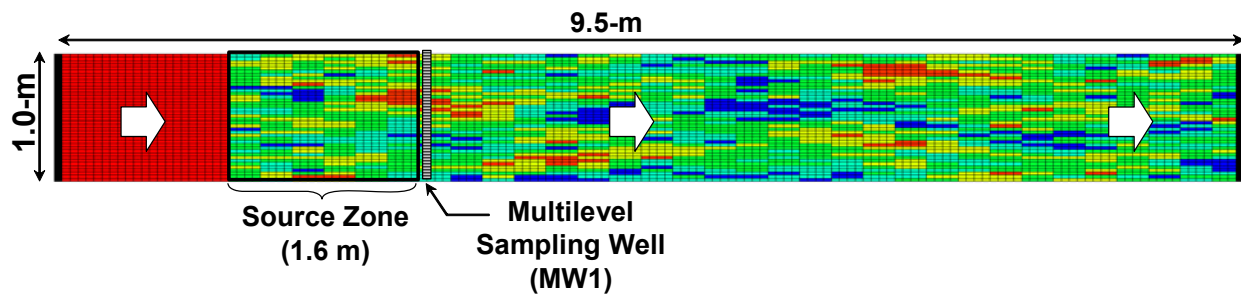


Figure 4.19. Heterogeneous Test Tank used in Monte Carlo Study of Natural Dissolution

Table 4.3. Properties of Sands used to Represent the Random Field, Monte Carlo Study of Natural Dissolution

| Sands | K_s ($\times 10^{-3} \text{ m s}^{-1}$) | d_{50} ($\times 10^{-3} \text{ m}$) | $S_{r,w}$ (-) |
|-------|--|--|------------------|
| #16 | 8.03 | 1.08 | 0.07 |
| #30 | 1.98 | 0.50 | 0.26 |
| #50 | 0.406 | 0.32 | 0.29 |
| #70 | 0.243 | 0.20 | 0.30 |
| #110 | 0.053 | 0.12 | 0.26 |

The heterogeneity was designed as a spatially correlated random field with geostatistical parameters in the range of those determined at field sites (Rehfeldt et al., 1992). The

heterogeneous packing provided a log-normal distribution of hydraulic conductivity with $\overline{\ln K}$ of 4.18 (K is in cm hr^{-1}) and a variance $s_{\ln K}^2$ of 1.22. The correlation lengths in lateral (λ_h) and vertical (λ_v) directions were 0.5 and 0.05 m, respectively. The heterogeneous zone consisted of 1280 cells of 0.25 m in length and 0.025 m in depth which corresponded to 32 columns and 40 layers, and resulted in 16 lateral and 20 vertical correlation lengths.

The DNAPL source architecture was generated from spill simulations using a multiphase flow simulator UTCHEM (Delshad et al., 1996). Spill point in UTCHEM simulations was located at the top center of the source zone. Spill rate and total injected volume were 1.67 L d^{-1} and 1.0 L, respectively. Properties of the DNAPL corresponded to PCE (Table 4.4). Three selected PCE source zone architectures were used in this study (Figures 4.20, 4-21, and 4-22). These three cases were selected from 80 spill simulations to represent different entrapment architecture ranging from highly saturated pools in realization #54 to mostly residuals in realization #11.

As can be seen from the NAPL distribution patterns, PCE source zones consisted of both high saturation pools and residuals. In realization #54, most of the spilled PCE formed pools on top of low permeability layers. On the other hand, most PCE in spill #11 was present as intermediate to low saturation residuals. Spill #1 showed a combination of pools and residuals where both are found throughout the depth of the source zone.

Table 4.4. Properties of PCE DNAPL at 25 °C used in Monte Carlo Simulations of Natural Dissolution

| Property | Value | Unit |
|------------------------------------|-------------------------|-----------------------------|
| Chemical formula | C_2Cl_4 | - |
| Molecular weight [§] | 165.8 | g mol^{-1} |
| Density [§] | 1.62 | g cm^{-3} |
| Aqueous solubility [†] | 200.0 | mg L^{-1} |
| Diffusion coefficient [†] | 8.19×10^{-10} | $\text{m}^2 \text{ s}^{-1}$ |
| Viscosity | $< 10^{-3}$ | Pa s |
| MCL | 0.005 | mg L^{-1} |

[§]Lucius et al. [1992]; [†]U.S. EPA [1996].

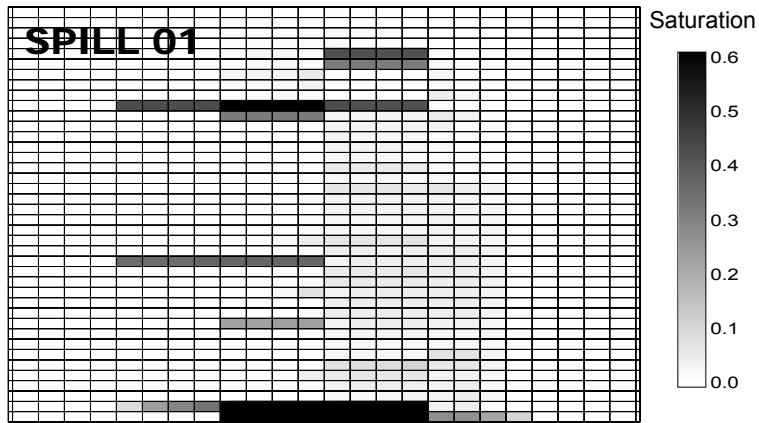


Figure 4.20. PCE Distribution in the Source Zone for Realization #1, Monte Carlo Simulations of Natural Dissolution

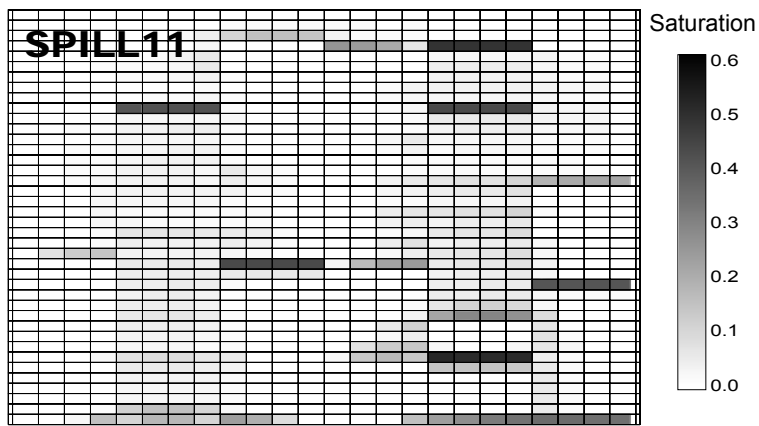


Figure 4.21. PCE Distribution in the Source Zone for Realization #11, Monte Carlo Simulations of Natural Dissolution

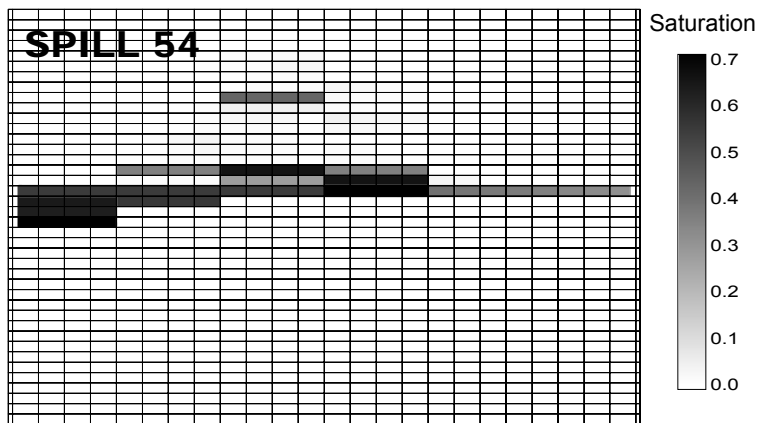


Figure 4.22. PCE Distribution in the Source Zone for Realization #54, Monte Carlo Simulations of Natural Dissolution

To describe source zone architecture quantitatively, the normalized first and second spatial moments of mass distribution of the source zone were calculated. Table 4.5 shows the spatial moments for the three realizations. The normalized second moments in x -, y -, and z -directions were calculated using

$$\hat{M}_{II,x_i} = \frac{\int_V \rho_n \phi_0 S_n (x_i - \bar{x}_i)^2 dV}{\int_V \rho_n \phi_0 S_n dV}, \quad i = 1, 2, \text{ and } 3 \quad (4.7)$$

where x_i refers to the x -, y -, and z -directions, \bar{x}_i refers to the center of mass or normalized first moment, \hat{M}_{I,x_i} of the distributed DNAPL mass in domain V . The centers of mass were calculated using

$$\hat{M}_{I,x_i} = \bar{x}_i = \frac{\int_V \rho_n \phi_0 S_n x_i dV}{\int_V \rho_n \phi_0 S_n dV}, \quad i = 1, 2, \text{ and } 3 \quad (4.8)$$

Table 4.5. Summary of the Spatial Moments Calculated for Realizations 1, 11, and 54, Monte Carlo Simulations of Natural Dissolution

| Spatial Moments | Spill 1 | Spill 11 | Spill 54 |
|-------------------------------------|---------|----------|----------|
| Zero th Moment (g) | 1619.9 | 1620.0 | 1619.7 |
| $\hat{M}_{I,x}$ or \bar{x} (cm) | 79.3 | 64.9 | 56.0 |
| $\hat{M}_{I,z}$ or \bar{z} (cm) | 62.8 | 56.8 | 65.2 |
| $\hat{M}_{II,x}$ (cm ²) | 6282.0 | 9666.0 | 11143.0 |
| $\hat{M}_{II,z}$ (cm ²) | 3703.0 | 3358.0 | 206.0 |

Importance of Entrapment Architecture on Concentration and Mass Flux

Distribution. To illustrate the importance of entrapment architecture on the generation of concentration and mass flux distribution in the vertical direction, a natural dissolution simulation of the entrapped PCE for 80 realizations was conducted. The experimentally validated mass transfer correlation was used in these numerical simulations (Saenton and Illangasekare, 2005). Steady-state downstream concentrations and mass fluxes were analyzed in relation to the entrapment architecture.

Figure 4.23 shows the vertical profile of steady-state PCE concentration and mass flux distributions at several locations downstream of the PCE source for realization #1. Close to the source, the concentration profile exhibited a pattern representing the entrapment architecture where high concentrations were located in zones containing low PCE saturations (residuals).

However, this feature became less evident in profiles located farther downstream where PCE concentration profiles became more uniform due to hydrodynamic mixing. Although the mass flux profile did not exhibit a distinctive pattern, both mass flux and concentration profiles were essential for determining the entrapment architecture (Saenton and Illangasekare, 2004).

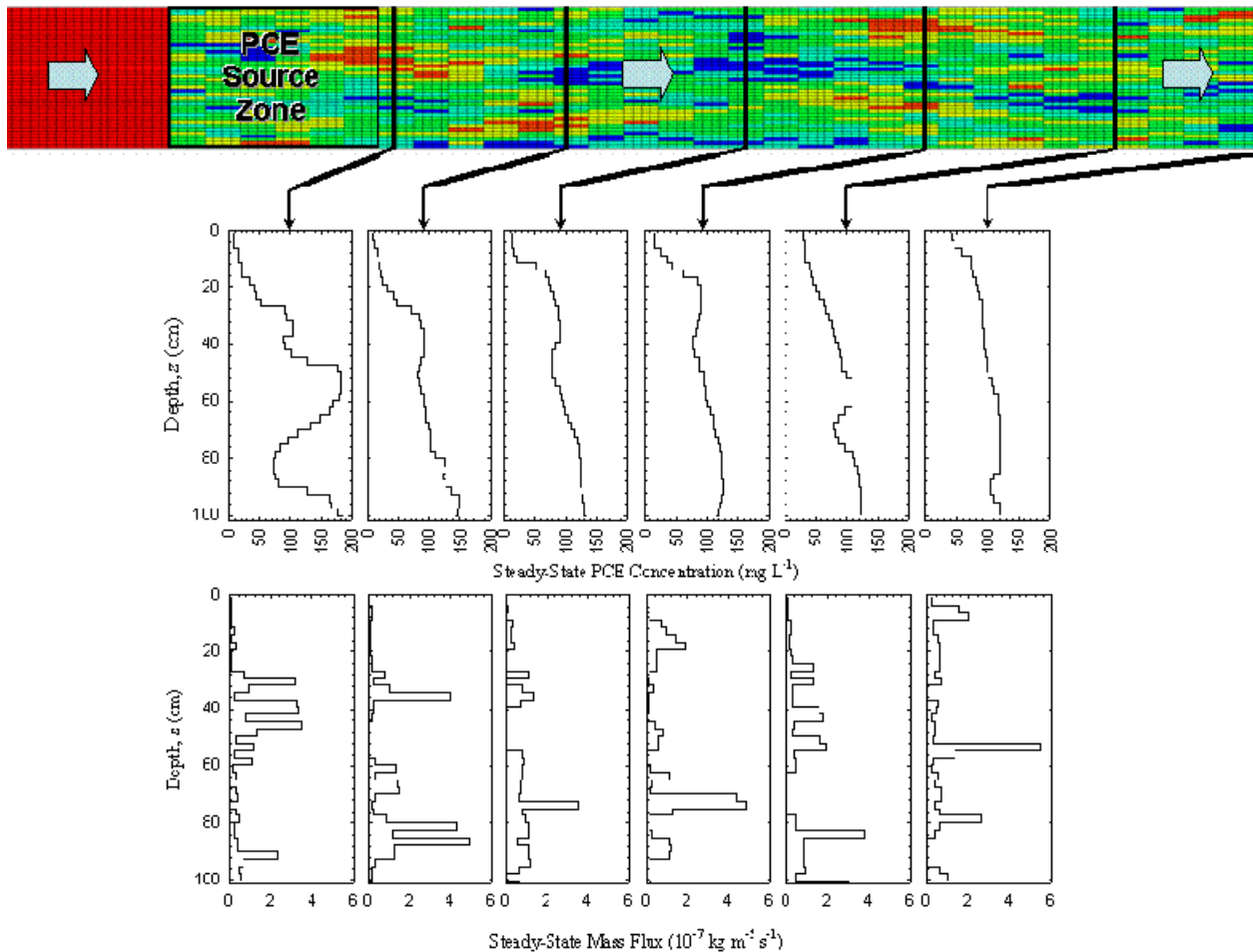


Figure 4.23. Vertical Distribution of Steady-state Dissolved PCE Concentration and Mass Flux Downstream of the Source Zone for Realization #1, Monte Carlo Simulations of Natural Dissolution

Considering results of all 80 realizations, there was no obvious relationship between the total mass flux and the first moments of DNAPL saturation in either x or z directions (Figure 4.24). However, the total mass flux showed a strong dependency with spreading in the vertical direction of DNAPL saturation, $\hat{M}_{II,z}$ (Figure 4-24d). This indicated that mass fluxes were higher for source zones that contained more residuals than pools. For example, mass flux

emanating from the PCE source zone in realization #54, which contained more pools, was an order of magnitude smaller than the flux from entrapment architecture in simulations #1 and #11.

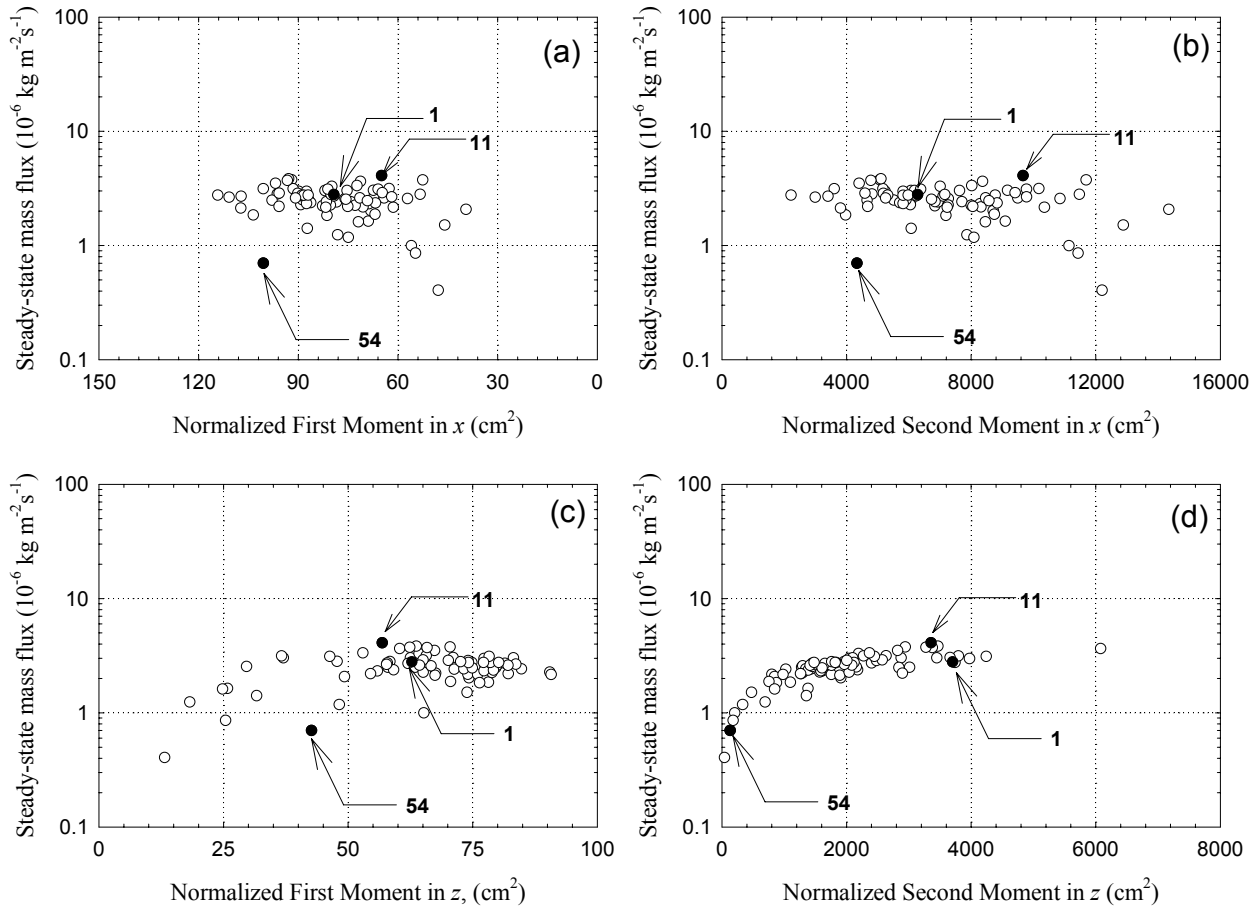


Figure 4.24. Total Steady-State Mass Flux vs. Normalized First (a,c) and Second Moments (b,d) for Realizations 1, 11, and 54, Monte Carlo Simulations of Natural Dissolution

Based on these results and the study by Saenton and Illangasekare (2005), it was concluded that mass flux emanating from the source zone was most sensitive to the normalized second moment of DNAPL saturation in the vertical direction perpendicular to the general ground water flow. Normalized second moment represents degree of smearing of the DNAPL in the vertical direction. The upscaled Gilland-Sherwood expression presented later in this report includes the normalized second moment to account for DNAPL entrapment architecture.

4.2.5 Phenomenological Model for an Upscaleable Mass Transfer Correlation

The development of a modified Gilland-Sherwood expression for upscaling mass transfer is presented in this section. The mass transfer correlation used to estimate mass transfer rate coefficients for column- and bench-scale DNAPL dissolution experiments was modified to include parameters that account for soil heterogeneity and entrapment architecture. These parameters were identified as the mean and variance of the hydraulic conductivity field ($\overline{\ln K}, s_{\ln K}^2$), vertical and horizontal correlation lengths (λ_v, λ_h), and normalized second moments of DNAPL saturation ($\hat{M}_{II,x}$, $\hat{M}_{II,y}$, and $\hat{M}_{II,z}$). An upscaled modified Sherwood number ($\overline{\text{Sh}}$) for estimating NAPL dissolution rates as a function of parameters describing mass flux generation from entrapped DNAPL and hydrodynamic mixing was hypothesized to take the form

$$\overline{\text{Sh}} = \overline{\text{Sh}}_0 \left(\underbrace{s_{\ln K}^2, \overline{\ln K}, \lambda_h, \lambda_v}_{\text{Heterogeneity}}, \underbrace{\hat{M}_{II,x}, \hat{M}_{II,y}, \hat{M}_{II,z}}_{\text{Architecture}} \right), \quad (4.9)$$

where Sh_0 is the local or small-scale mass transfer correlation obtained from fitting the numerical model to column or flow-cell experimental data. This model was given by Saba and Illangasekare (2000) as

$$\text{Sh}_0 = \alpha_1 (\text{Re})^{\alpha_2} (\text{Sc})^{\alpha_3} \left(\frac{\theta_n d_{50}}{\tau L^*} \right)^{\alpha_4}. \quad (4.10)$$

The parameters Re , Sc , θ_n , τ , and L^* are Reynolds number, Schmidt number, volumetric NAPL content, tortuosity factor, and characteristic or dissolution length, respectively. Note that the mass transfer coefficient is related to the Sherwood number by the relationship $k_{La} = D_m \text{Sh}_0 / d_{50}^2$ or $\bar{k}_{La} = D_m \overline{\text{Sh}} / d_{50}^2$ where D_m is the aqueous-phase molecular diffusion coefficient of the dissolved DNAPL. The parameter L^* is equal to the finite-difference grid block size in either x -, or y -, or z -direction depending on dominant ground water flow direction. For example, if the flow in a numerical grid block is generally in the x -direction, the parameter L^* is then set to Δx . A more detailed discussion regarding the characteristic length can be found in Saba and Illangasekare (2000). The empirical parameters $\alpha_1, \alpha_2, \dots, \alpha_4$ are obtained by fitting experimental data to the mass transfer model through inverse modeling.

In order to understand the development of an upscaleable mass transfer correlation, consider a finite-difference grid block having dimensions $\Delta x \times \Delta y \times \Delta z$ with a local Cartesian coordinate system (x', y', z') placed at the top-left corner (Figure 4.25). The $\Delta x \times \Delta y \times \Delta z$ block

is subdivided into smaller sub-blocks where n_x , n_y , and n_z are the number of sub-blocks in x -, y -, and z -direction, respectively. The dimensions of the finite-difference sub-block are δx , δy , and δz , respectively. Within this selected block hydraulic conductivity, porosity, and DNAPL saturation distribution are not uniform. The goal of upscaling is to develop an explicit mathematical expression for \overline{Sh} that can be used to estimate the dissolution rate of entrapped NAPL in the $\Delta x \times \Delta y \times \Delta z$ block.

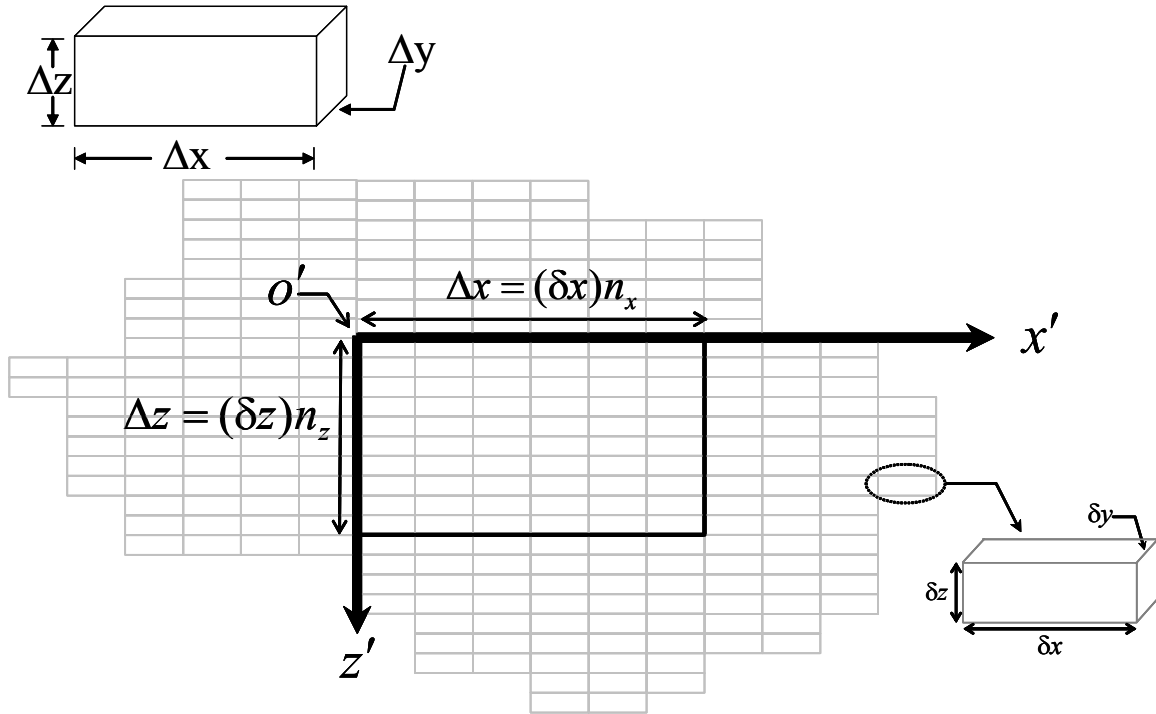


Figure 4.25. Finite-Difference Grid Used in the Upscaling Analysis for Natural Dissolution

An upscaleable mass transfer correlation was hypothesized to be

$$\overline{Sh} = Sh_0 \left(1 + s_{\ln K}^2\right)^{\phi_1} \left[\prod_{i=1}^3 \left(1 + \frac{\Delta x_i}{\lambda_i}\right)^{\phi_{1+i}} \left(\frac{\hat{M}_{II,x_i}}{\hat{M}_{II,x_i}^*}\right)^{\phi_{4+i}} \right]. \quad (4.11)$$

The parameter $s_{\ln K}^2$ is the estimated variance of log-transformed hydraulic conductivity. Δx_i and λ_i are the size of the numerical grid block and the correlation length in the i^{th} direction,

respectively. \hat{M}_{II,x_i}^* denotes the maximum possible normalized second moment of NAPL mass distribution in the i^{th} direction for a $\Delta x \times \Delta y \times \Delta z$ grid block.

If a numerical grid block $\Delta x \times \Delta y \times \Delta z$ is homogeneous with respect to DNAPL saturation, porosity, and hydraulic conductivity, $s_{\ln K}^2 = 0$, $\lambda_i \rightarrow \infty$ and $\hat{M}_{II,x_i} / \hat{M}_{II,x_i}^* = 1$. As a result, the upscaleable modified Sherwood number reduces to the small-scale Sherwood number or Sh_0 . Generally, \hat{M}_{II,x_i}^* is a maximum when NAPL is homogeneously distributed in a grid block. The parameters ϕ_i 's are empirical and need to be determined through model calibration.

The normalized second moment of DNAPL saturation (\hat{M}_{II,x_i}) can be calculated using the following expression which is based on Equation (4.7):

$$\hat{M}_{II,z} = \frac{\sum_{j=1}^{n_x} \sum_{i=1}^{n_y} \sum_{k=1}^{n_z} \rho_n \phi_0 S_n [z'(j,i,k) - \bar{z}']^2 \delta x \delta y \delta z}{\sum_{j=1}^{n_x} \sum_{i=1}^{n_y} \sum_{k=1}^{n_z} \rho_n \phi_0 S_n \delta x \delta y \delta z}, \quad (4.12)$$

where $z'(j,i,k)$ is the location (in the z' -direction) of the centroid of a sub-block ($n_x = j$, $n_y = i$, and $n_z = k$) and, in this case, $z'(j,i,k) = (k - 0.5)\delta z$. Although this calculation uses the z -direction as an example, similar expression can be written for other directions as well. The location of the center of mass \bar{z}' in the local coordinate (x', y', z') is calculated from the expression for first moment (Equation 4.8) as

$$\bar{z}' = \frac{\sum_{j=1}^{n_x} \sum_{i=1}^{n_y} \sum_{k=1}^{n_z} \rho_n \phi_0 S_n z'(j,i,k) \delta x \delta y \delta z}{\sum_{j=1}^{n_x} \sum_{i=1}^{n_y} \sum_{k=1}^{n_z} \rho_n \phi_0 S_n \delta x \delta y \delta z}. \quad (4.13)$$

For uniformly distributed NAPL in a homogeneous domain, the center of mass in the z' -direction (\bar{z}') is located at the center of the grid block or $\bar{z}' = \Delta z/2$, and the normalized second moment in the z' -direction \hat{M}_{II,z_i}^* is calculated from Equation (4.13) as

$$\begin{aligned}
\hat{M}_{II,z}^* &= \frac{\sum_{j=1}^{n_x} \sum_{i=1}^{n_y} \sum_{k=1}^{n_z} \rho_n \phi_0 S_n \left[z'(j,i,k) - \frac{\Delta z}{2} \right]^2 \delta x \delta y \delta z}{\sum_{j=1}^{n_x} \sum_{i=1}^{n_y} \sum_{k=1}^{n_z} \rho_n \phi_0 S_n \delta x \delta y \delta z} \\
&= \frac{\sum_{k=1}^{n_z} \left[\left(k - \frac{1}{2} \right) \Delta z - \frac{1}{2} n_z (\delta z) \right]^2 \delta z}{\sum_{k=1}^{n_z} \delta z} \\
&= \frac{\frac{1}{12} (\delta z)^3 n_z (n_z^2 - 1)}{(\delta z) n_z} \\
&= \frac{1}{12} (\delta z)^2 (n_z^2 - 1).
\end{aligned} \tag{4.14}$$

For very large n_z , the above expression approaches an analytical solution where $\hat{M}_{II,z}^* \rightarrow (\Delta z)^2 / 12$. That is, in a continuous and homogeneous domain with a uniformly distributed DNAPL, the exact normalized second moment based on Equation 4.7 is given as

$$\hat{M}_{II,z}^* = \frac{\int_0^{\Delta x} \int_0^{\Delta y} \int_0^{\Delta z} \rho_n \phi_0 S_n (z' - \Delta z/2)^2 dx' dy' dz'}{\int_0^{\Delta x} \int_0^{\Delta y} \int_0^{\Delta z} \rho_n \phi_0 S_n dx' dy' dz'} = \frac{1}{12} (\Delta z)^2. \tag{4.15}$$

The hypothesized upscaling equation is based partly on an available Gilland-Sherwood correlation for small- or point-scale dissolution (Sh_0) which was obtained by fitting a numerical model to dissolution-experiment data. Source zone heterogeneity and entrapment architecture also are included in the upscaled Gilland-Sherwood correlation given in Equation 4.11. This relationship is incorporated in the numerical dissolution model.

In two-dimensional flow systems, the upscaled Gilland-Sherwood correlation shown in Equation 4.11 can be expanded as

$$\overline{Sh} = Sh_0 \left(1 + s_{\ln K}^2 \right)^{\varphi_1} \left(1 + \frac{\Delta x}{\lambda_x} \right)^{\varphi_2} \left(1 + \frac{\Delta z}{\lambda_z} \right)^{\varphi_3} \left(\frac{\hat{M}_{II,x}}{\hat{M}_{II,x}^*} \right)^{\varphi_4} \left(\frac{\hat{M}_{II,z}}{\hat{M}_{II,z}^*} \right)^{\varphi_5} \tag{4.16}$$

4.2.6 Evaluation of upscaleable mass transfer model with synthetic data

An evaluation of the hypothesized mass transfer correlation was conducted by comparing concentration and mass flux distributions obtained by fine-grid simulations utilizing the small-scale Gilland-Sherwood correlation (section 4.2.4) with those obtained by coarse-grid simulations utilizing the upscaleable mass transfer model. Acceptable matches between fine- and coarse-grid simulations would provide evidence that the hypothesized upscaleable model adequately simulates the mass transfer process. To this end, several coarse grids were utilized in the comparison and inverse modeling with these grids was undertaken utilizing the simulated fine-grid results as observations. Empirical mass transfer correlation parameters ($\phi_1, \phi_2, \dots, \phi_5$ in Equation 4.16) were treated as regression parameters during inverse modeling. As a point of reference, inverse modeling of the coarse grids also was conducted utilizing the small-scale Gilland-Sherwood correlation.

Sets of simulations were conducted for each the three source-zone architectures provided in section 4.2.4 and four hydraulic gradients through the source zone (10^{-5} , 10^{-4} , 10^{-3} and 10^{-2}). For each realization and hydraulic gradient considered, eight simulations were conducted utilizing the grid systems shown in Tables 4.6(a) through 4.6(c). Grid spacing was uniform within each. The finest discretization (No. 1) resulted in 24 columns and 40 layers or 960 grid blocks. It was assumed that each of the grid blocks in the finest discretization was homogeneous in terms of DNAPL saturation, hydraulic conductivity, and porosity. Mass transfer of a block was therefore described by expression for Sh_0 given in Equation 4.10. Empirical parameter values that appear in Equation 4.10 were obtained from modeling results for the bench-scale flow-cell experiment (section 4.2.3, Table 4.2). Inverse modeling was conducted with the remaining grids using the non-linear regression procedures within UCODE to estimate the empirical parameters of the upscaleable mass transfer correlation (Equation 4.16). A total of 696 observations for downstream concentrations and mass fluxes were used in the regression analysis.

Inverse modeling with the coarse grids was accomplished by minimizing squared residuals of concentration and mass flux. In order to compare concentration (\hat{c}_{ss}) and mass flux (\hat{J}_a) simulated with coarse-grid discretizations with those observed from the fine-grid discretization, observed values of concentration (\bar{c}_{ss}) and mass flux (\bar{J}_a) were needed at the coarse-grid scale. Values of \bar{c}_{ss} and \bar{J}_a were derived directly from data obtained from the finest discretization (No. 1) using the following Darcy-flux weighted expressions

$$\bar{c}_{ss} = \frac{\sum_{k=1}^{n_z} q_x(k) c_{ss}(k) \delta x(k) \delta y(k)}{\sum_{k=1}^{n_z} q_x(k) \delta x(k) \delta y(k)}, \text{ and} \quad \bar{J}_a = \sum_{k=1}^{n_z} q_x(k) c_{ss}(k) \delta x(k) \delta y(k). \quad (4.17)$$

Table 4.6(a). Finite-Difference Grids (1-3) Used in Upscaling Analysis for Natural Dissolution

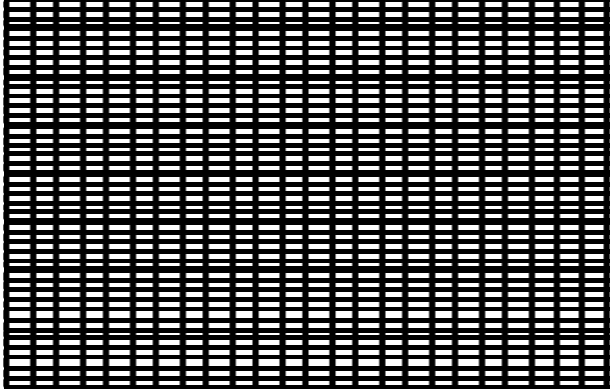
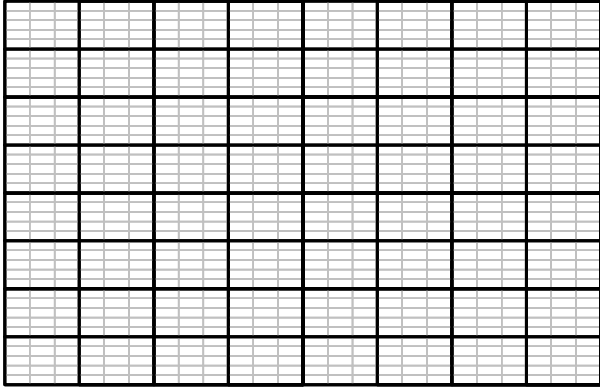
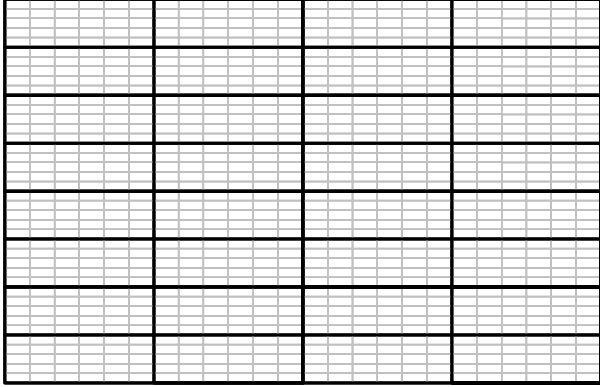
| No. | DNAPL Source-Zone Grid | Discretization Parameters | Model Output |
|-----|---|---|---|
| 1 |  | $N_x = 24$ $N_z = 40$ $n_x = 0$ $n_z = 0$ $\Delta x = 6.35 \text{ cm}$ $\Delta z = 2.54 \text{ cm}$ $\delta x = n/a$ $\delta z = n/a$ $L^* = 1(\delta x)$ | $40 \ c_{ss}$ $40 \ J_a$ (These datasets will be used to calculate \bar{c}_{ss} and \bar{J}_a which are necessary for inverse modeling as observations) |
| 2 |  | $N_x = 8$ $N_z = 8$ $n_x = 3$ $n_z = 5$ $\Delta x = 3(\delta x)$ $\Delta z = 5(\delta z)$ $\delta x = 6.35 \text{ cm}$ $\delta z = 2.54 \text{ cm}$ $L^* = 3(\delta x)$ | <u>Observed Values</u> $8 \ \bar{c}_{ss}$ $8 \ \bar{J}_a$ <u>Simulated Values</u> $8 \ \hat{c}_{ss}$ $8 \ \hat{J}_a$ |
| 3 |  | $N_x = 4$ $N_z = 8$ $n_x = 6$ $n_z = 5$ $\Delta x = 6(\delta x)$ $\Delta z = 5(\delta z)$ $\delta x = 6.35 \text{ cm}$ $\delta z = 2.54 \text{ cm}$ $L^* = 6(\delta x)$ | <u>Observed Values</u> $8 \ \bar{c}_{ss}$ $8 \ \bar{J}_a$ <u>Simulated Values</u> $8 \ \hat{c}_{ss}$ $8 \ \hat{J}_a$ |

Table 4-6(b). Finite-Difference Grids (4-6) Used in Upscaling Analysis for Natural Dissolution

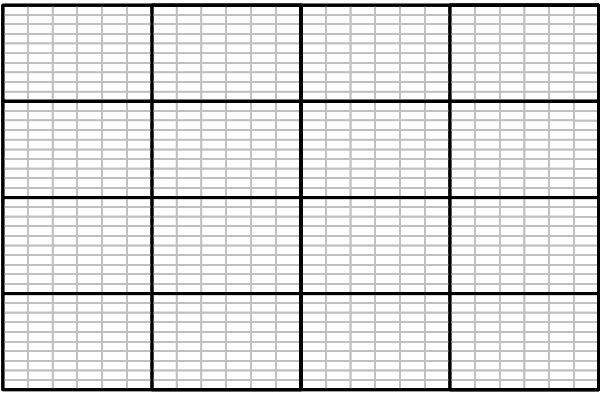
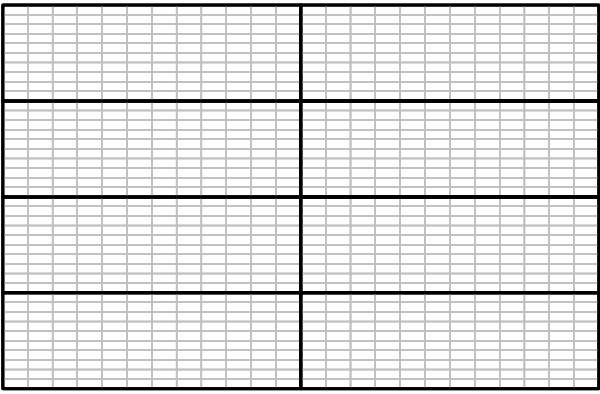
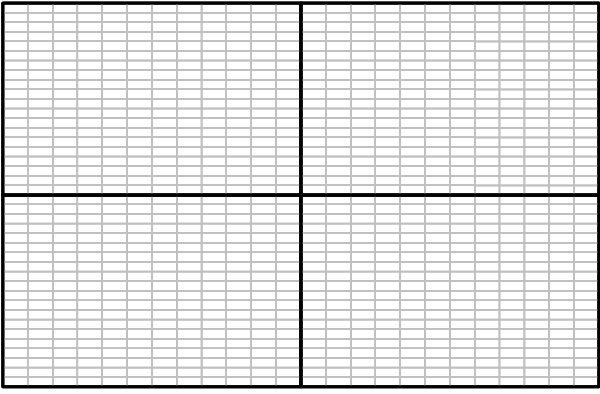
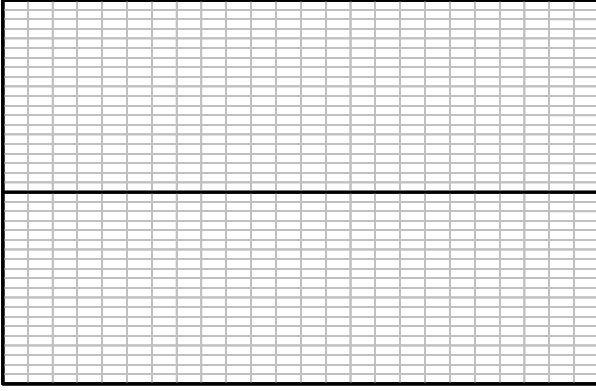
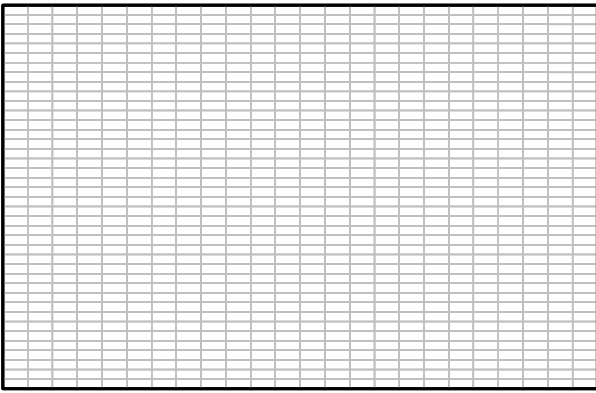
| No. | DNAPL Source-Zone Grid | Discretization Parameters | Model Output |
|-----|---|--|---|
| 4 |  | $N_x = 4$ $N_z = 4$ $n_x = 6$ $n_z = 10$ $\Delta x = 6(\delta x)$ $\Delta z = 10(\delta z)$ $\delta x = 6.35 \text{ cm}$ $\delta z = 2.54 \text{ cm}$ $L^* = 6(\delta x)$ | <u>Observed Values</u> $4 \bar{c}_{ss}$ $4 \bar{J}_a$ <u>Simulated Values</u> $4 \hat{c}_{ss}$ $4 \hat{J}_a$ |
| 5 |  | $N_x = 2$ $N_z = 4$ $n_x = 12$ $n_z = 10$ $\Delta x = 12(\delta x)$ $\Delta z = 10(\delta z)$ $\delta x = 6.35 \text{ cm}$ $\delta z = 2.54 \text{ cm}$ $L^* = 12(\delta x)$ | <u>Observed Values</u> $4 \bar{c}_{ss}$ $4 \bar{J}_a$ <u>Simulated Values</u> $4 \hat{c}_{ss}$ $4 \hat{J}_a$ |
| 6 |  | $N_x = 2$ $N_z = 2$ $n_x = 12$ $n_z = 20$ $\Delta x = 12(\delta x)$ $\Delta z = 20(\delta z)$ $\delta x = 6.35 \text{ cm}$ $\delta z = 2.54 \text{ cm}$ $L^* = 12(\delta x)$ | <u>Observed Values</u> $2 \bar{c}_{ss}$ $2 \bar{J}_a$ <u>Simulated Values</u> $2 \hat{c}_{ss}$ $2 \hat{J}_a$ |

Table 4.6(c). Finite-Difference Grids (7-8) Used in Upscaling Analysis for Natural Dissolution

| No. | DNAPL Source-Zone Grid | Discretization Parameters | Model Output |
|-----|--|--|---|
| 7 |  | $N_x = 1$ $N_z = 2$ $n_x = 24$ $n_z = 20$ $\Delta x = 24(\delta x)$ $\Delta z = 20(\delta z)$ $\delta x = 6.35 \text{ cm}$ $\delta z = 2.54 \text{ cm}$ $L^* = 24(\delta x)$ | <u>Observed Values</u> $2 \bar{c}_{ss}$ $2 \bar{J}_a$ <u>Simulated Values</u> $2 \hat{c}_{ss}$ $2 \hat{J}_a$ |
| 8 |  | $N_x = 1$ $N_z = 1$ $n_x = 24$ $n_z = 40$ $\Delta x = 24(\delta x)$ $\Delta z = 40(\delta z)$ $\delta x = 6.35 \text{ cm}$ $\delta z = 2.54 \text{ cm}$ $L^* = 24(\delta x)$ | <u>Observed Values</u> $1 \bar{c}_{ss}$ $1 \bar{J}_a$ <u>Simulated Values</u> $1 \hat{c}_{ss}$ $1 \hat{J}_a$ |

After optimized parameter estimates were obtained, the upscaleable mass transfer correlation was verified by predictive simulation of NAPL dissolution for another set of entrapment architecture. In this case, PCE spill of realization #16 was selected (Figure 4.26).

During regression, the program UCODE calculated sensitivity coefficients for all parameters. It appeared that the sensitivities for parameters ϕ_2 and ϕ_4 , the exponents of horizontal correlation length and the normalized second moment in the x -direction, respectively, were extremely small compared to sensitivities for other parameters. As a result, the regression analysis did not converge. This insensitivity indicated that the spreading of DNAPL mass in the x -direction as quantified by the normalized second moment ($\hat{M}_{II,x}$) as well as the horizontal correlation length (λ_h) did not significantly affect the mass transfer.

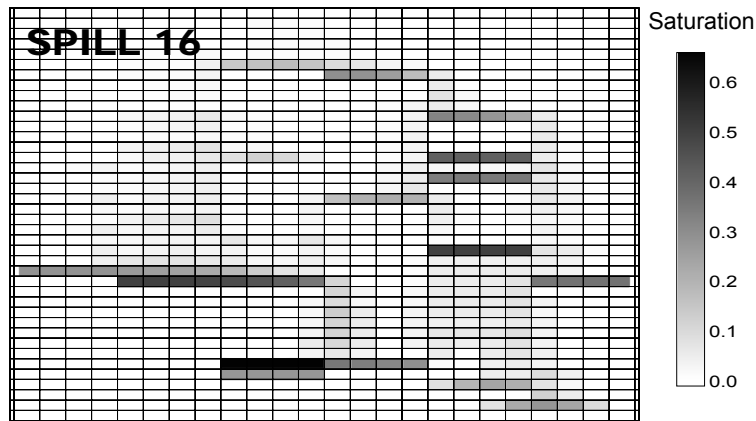


Figure 4.26. PCE DNAPL Distribution for Realization #16, Upscaling Analysis of Natural Dissolution

By setting $\varphi_2 = \varphi_4 = 0$, the x -direction dependent terms in Equation 4.16 were eliminated from the analysis. The simplified mass transfer correlation for upscaling became

$$\overline{\text{Sh}} = \text{Sh}_0 \left(1 + s_{\ln K}^2\right)^{\varphi_1} \left(1 + \frac{\Delta z}{\lambda_z}\right)^{\varphi_3} \left(\frac{\hat{M}_{II,z}}{\hat{M}_{II,z}^*}\right)^{\varphi_5} \quad (4.18)$$

Results of the non-linear regression analysis are presented in Figures 4.27 and 4.28 as plots relating observed and simulated values. The plots at the top of each figure represent simulation results based on the small-scale mass transfer correlation (Sh_0). The plots at the bottom of each figure represent simulation results based on the upscaleable mass transfer correlation ($\overline{\text{Sh}}$). Ideally, if the assumed mass transfer correlation is valid, all data points should fall along the 1:1 line. These results show that both concentration and mass flux are incorrectly estimated when the small-scale Gilland-Sherwood correlation is applied. However, when the correlation is corrected for the variability of hydraulic conductivity as well as the spreading of PCE in the source zone, matches for both concentration and mass flux are much improved.

Table 4.7 lists the optimized empirical parameters with 95 percent confidence intervals and associated parameter sensitivities. The sensitivity for φ_5 is highest indicating that description of vertical spreading of PCE mass, quantified by $\hat{M}_{II,z}$, is necessary for modeling NAPL mass transfer. The variance and vertical correlation length also are important in simulating mass transfer in the upscaled heterogeneous system.

The upscaleable mass transfer correlation was verified by predictive simulations using spill realization #16 (Figure 4.26). The resulting comparison between simulated and observed

mass flux and concentration was acceptable (Figure 4.29). Thus, this two-dimensional, upscaleable mass transfer correlation was verified.

Table 4.7. Optimized Empirical Parameters, Upscaling Analysis of Natural Dissolution

| Parameters | Value \pm 95% Confidence Interval | Sensitivity |
|-------------|-------------------------------------|-------------|
| φ_1 | 1.783 ± 0.763 | 1771.0 |
| φ_3 | 2.350 ± 0.920 | 1378.8 |
| φ_5 | 4.157 ± 0.431 | 2893.2 |

4.2.7 Validation of upscaleable mass transfer model with results of large tank experiment

The large tank natural dissolution experiment with high heterogeneity was simulated with the upscaleable mass transfer model of natural dissolution. The observed DNAPL source zone was discretized into a very fine grid (Figure 4.30, System 1) and observed dissolution data were used to calibrate the mass transfer model by fitting the empirical parameters of the small-scale Gilland-Sherwood correlation. The optimized parameter values are listed in Table 4.1. The source zone was then discretized into five different grid systems consisting of different number of columns (Nx) and layers (Nz) as shown in Figures 4.30 and 4.31. The mass transfer simulations were made for each grid systems using the small-scale and upscaleable Gilland-Sherwood correlations. For simulations with the upscaleable correlation, the inverse modeling algorithm (PEST) was used to determine the empirical parameters φ_1 , φ_3 , and φ_5 . Table 4.8 shows the optimized values of the empirical parameters.

Simulated concentration and mass flux are plotted against observed values for both small-scale and upscaleable Gilland-Sherwood correlations in Figures 4.32 and 4.33. These figures show that the small-scale Gilland-Sherwood correlation was not sufficient to simulate dissolution in the larger grid systems. However, concentration and flux obtained with the upscaleable correlation matched relatively well with observed values.

Table 4.8. Optimization Parameter Estimates for the Upscaleable Gilland-Sherwood Correlation Obtained for the Large-Tank Experiment of Natural Dissolution with High Heterogeneity

| Parameter | Optimized Value |
|-------------|-----------------|
| φ_1 | 1.267 |
| φ_3 | 1.158 |
| φ_5 | 3.112 |

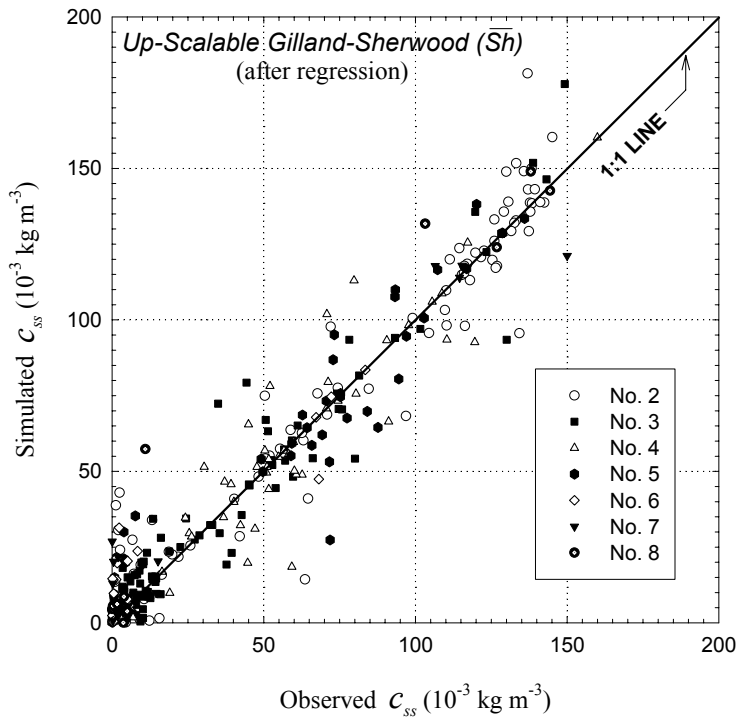
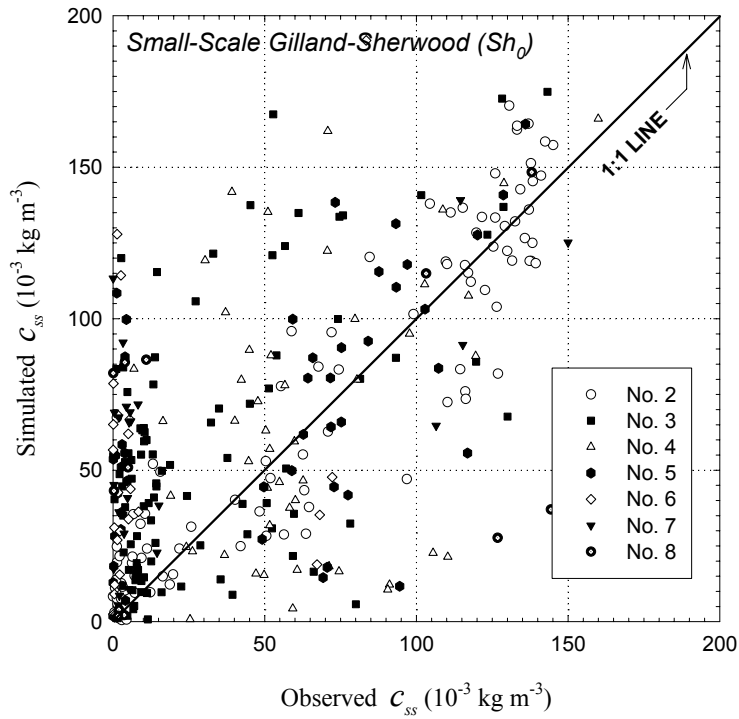


Figure 4.27. Comparison of Observed and Simulated Concentration Using Small-Scale (top) and Upscalable (bottom) Gilland-Sherwood Correlation, Upscaling Analysis of Natural Dissolution

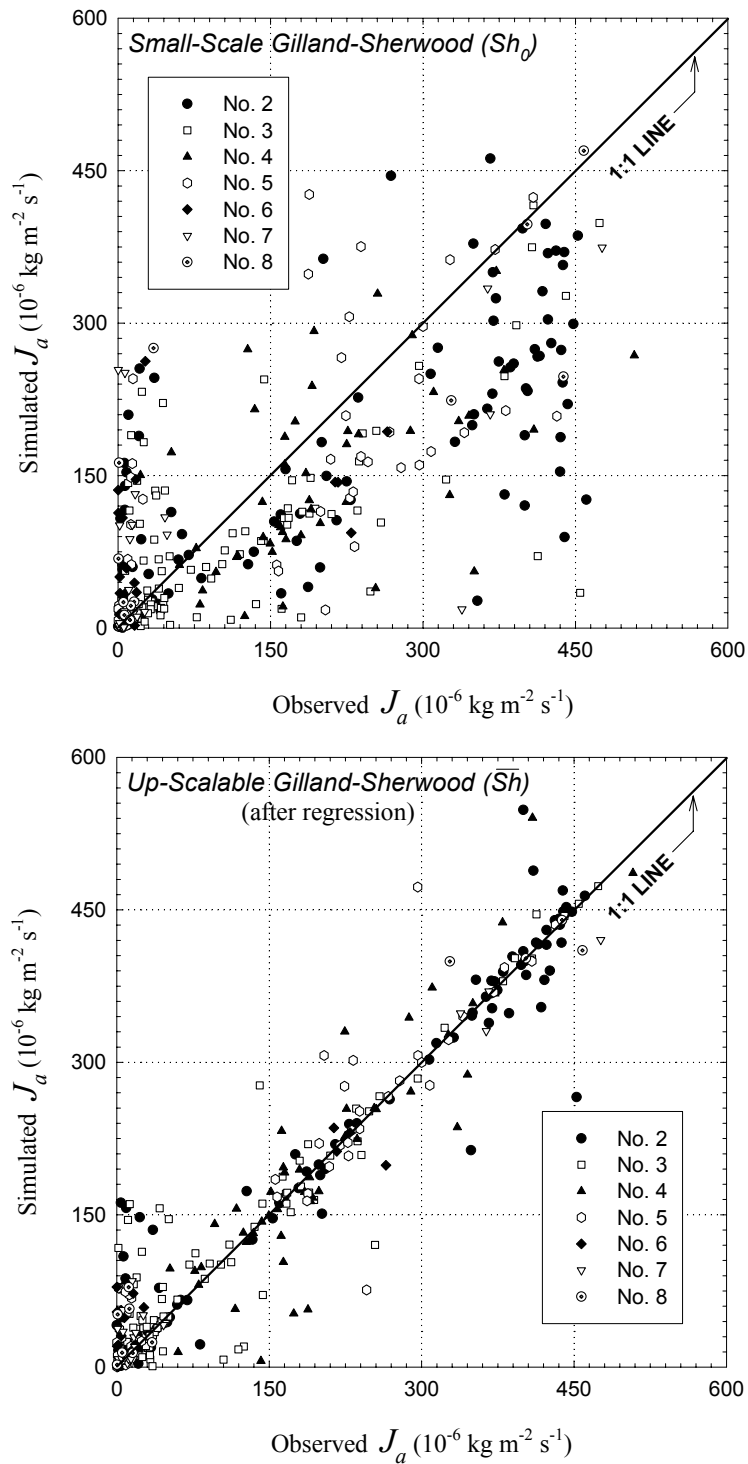


Figure 4.28. Comparison of Observed and Simulated Mass Flux Using Small-Scale (top) and Upscalable (bottom) Gilland-Sherwood Correlation, Upscaling Analysis of Natural Dissolution

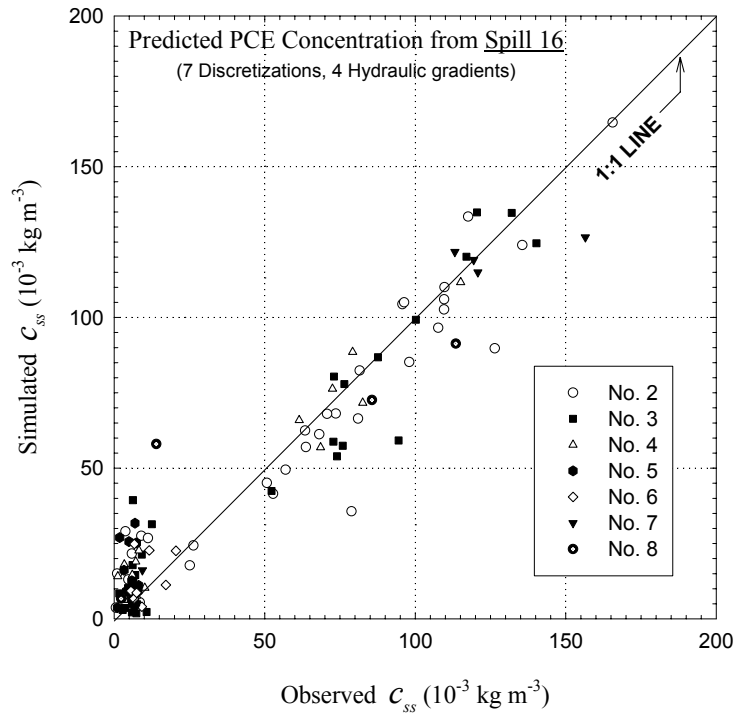
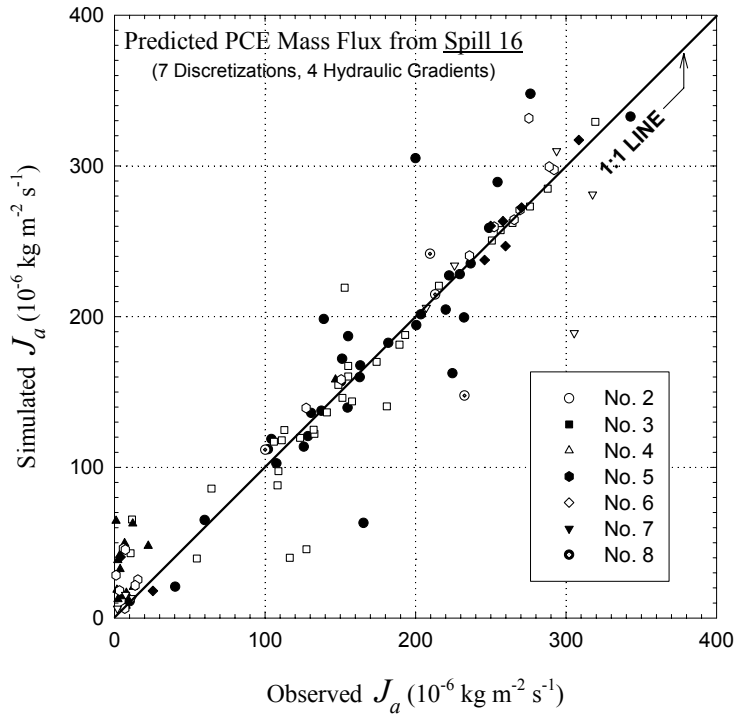


Figure 4.29. Comparison of Observed and Simulated Mass Flux (top) and Concentration (bottom) Using Upscaleable Gilland-Sherwood Correlation for Spill Realization #16, Upscaling Analysis of Natural Dissolution

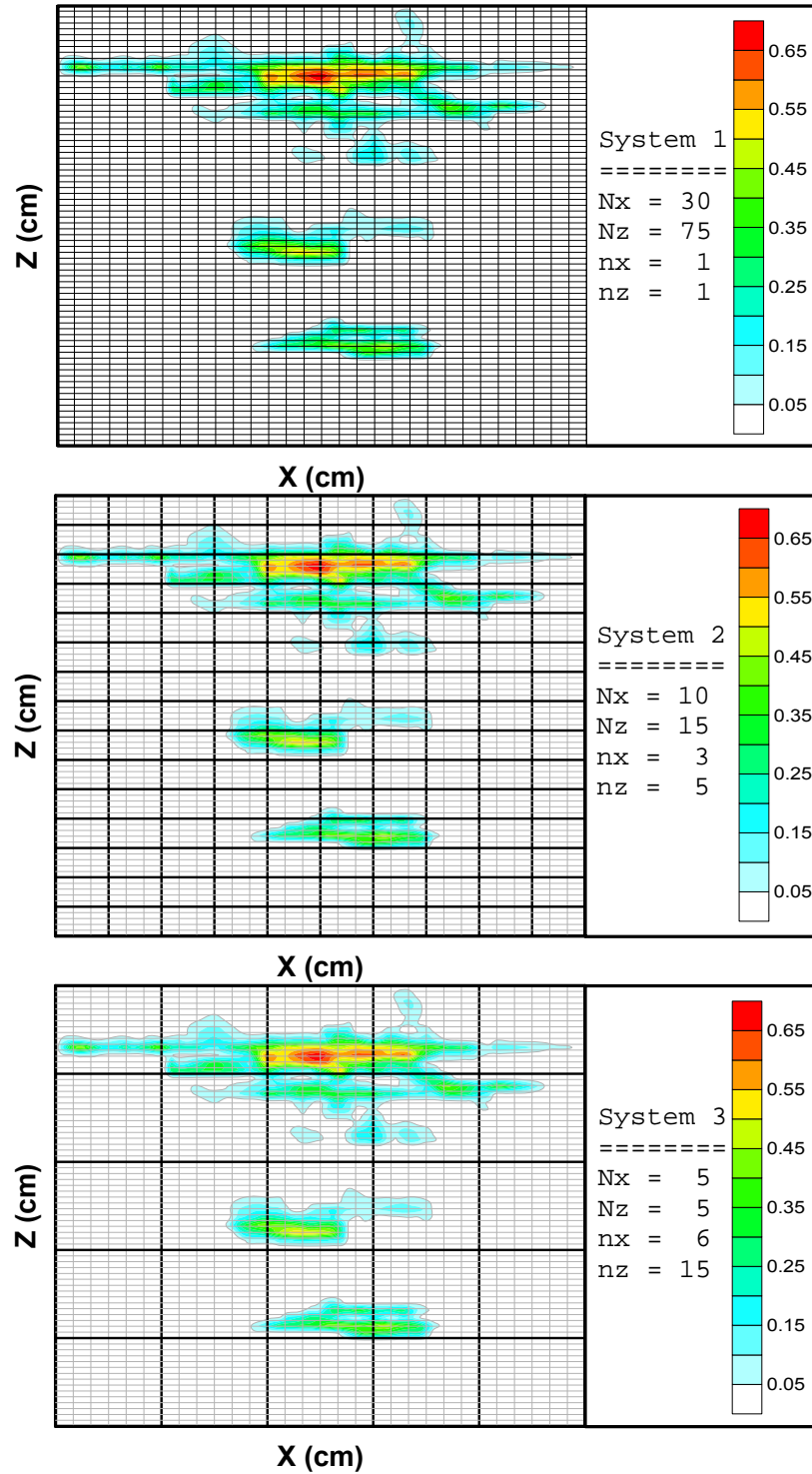


Figure 4.30. Grid Systems 1, 2 and 3 Used in Simulations of Natural Dissolution with the Upscaleable Gilland-Sherwood Correlation, Large Tank Experiment with High Heterogeneity

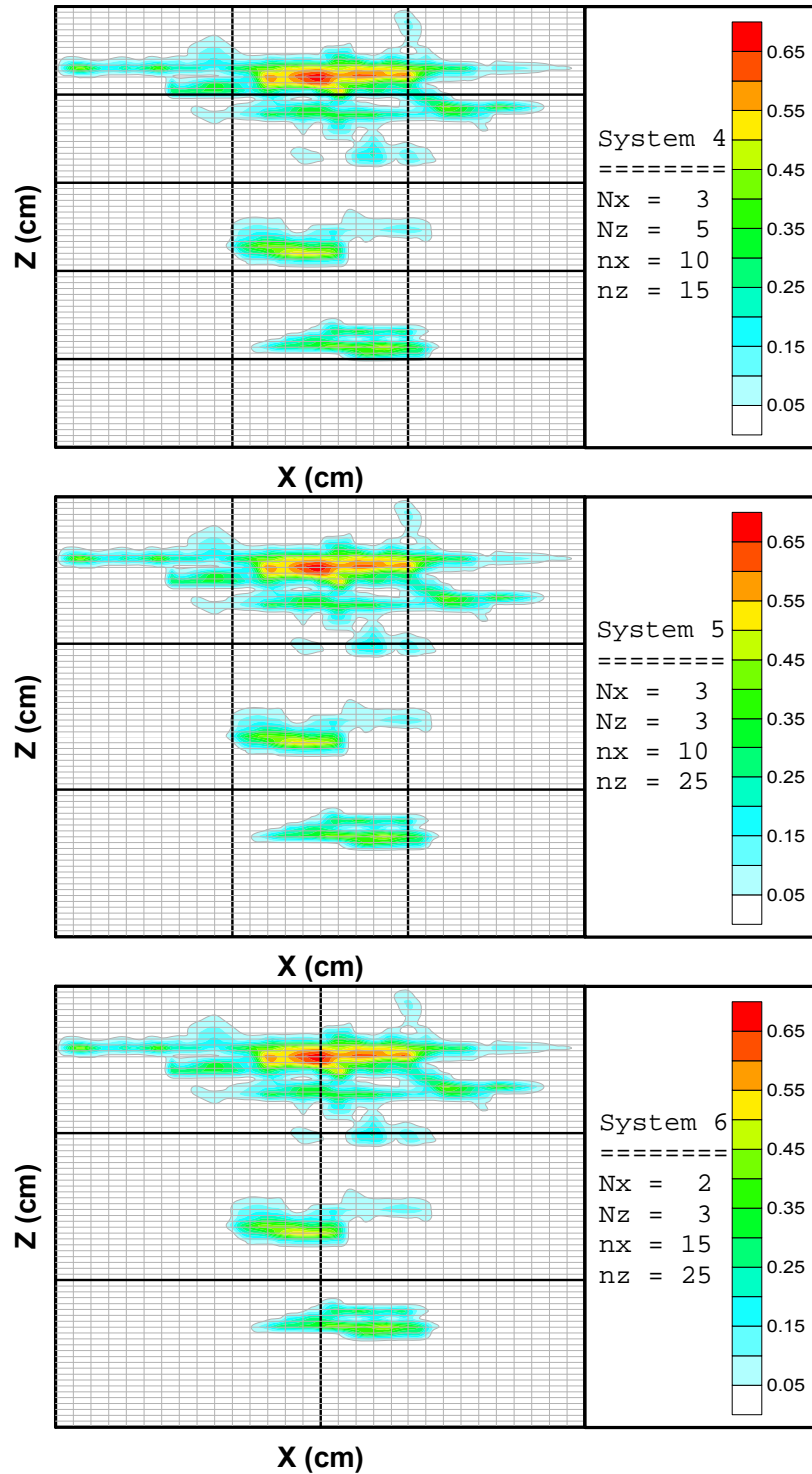


Figure 4.31. Grid Systems 4, 5 and 6 Used in Simulations of Natural Dissolution with the Upscaleable Gilland-Sherwood Correlation, Large Tank Experiment with High Heterogeneity

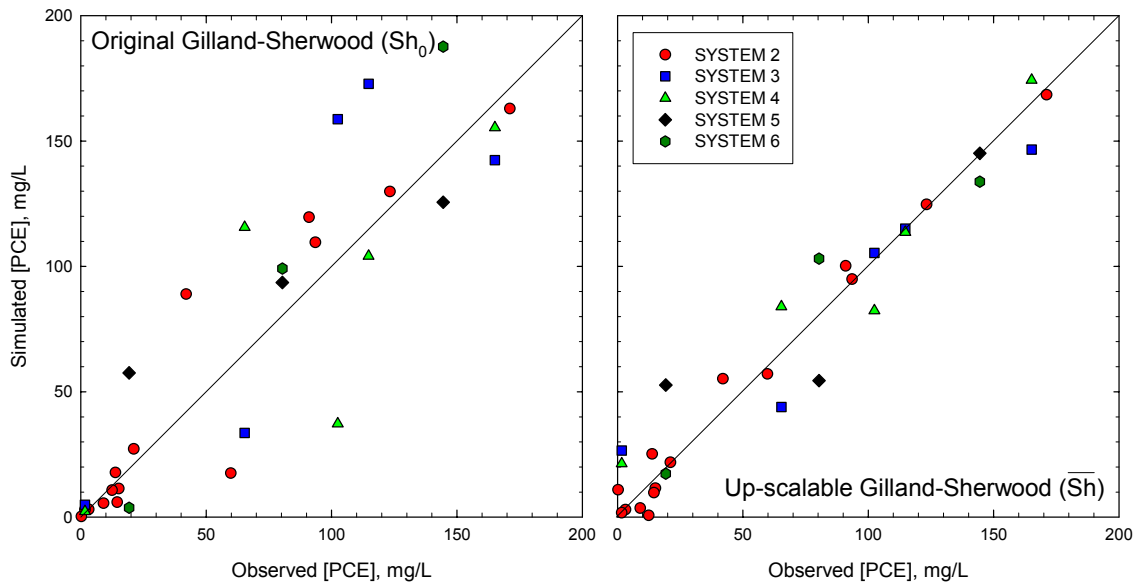


Figure 4.32. Comparison of Observed and Simulated PCE Concentration Using Small-Scale (left) and Upscalable (right) Gilliland-Sherwood Correlation, Large-Tank Experiment of Natural Dissolution with High Heterogeneity

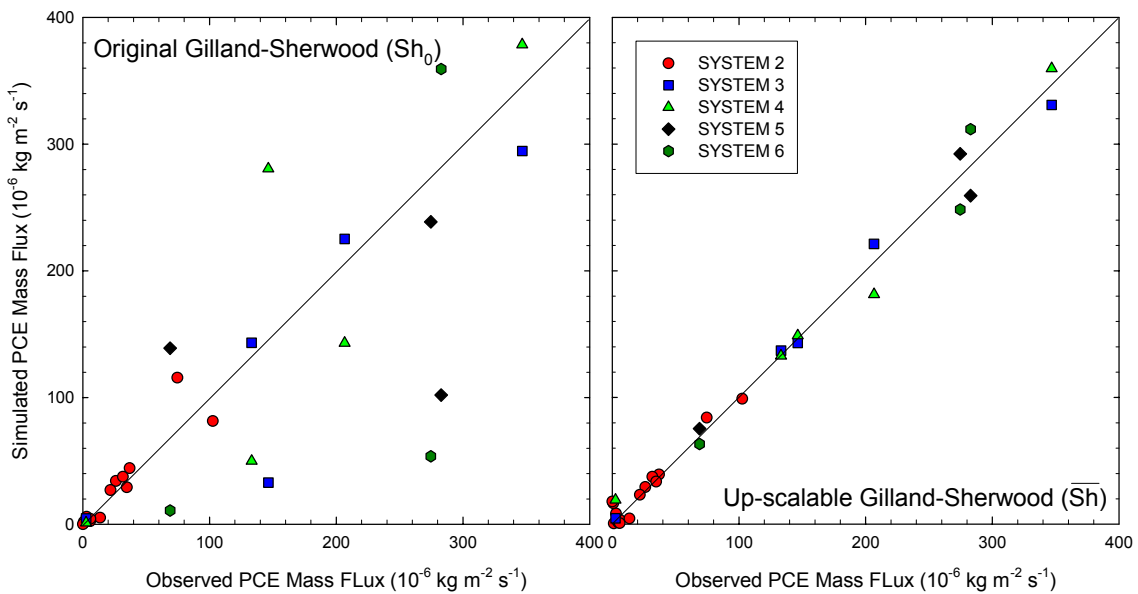


Figure 4.33. Comparison of Observed and Simulated PCE Mass Flux Using Small-Scale (left) and Upscalable (right) Gilliland-Sherwood Correlation, Large-Tank Experiment of Natural Dissolution with High Heterogeneity

4.2.8 Summary of key results

Mass transfer in heterogeneous source zones can be simulated as a kinetic process with effective mass transfer rate coefficients estimated by empirical Gilland-Sherwood correlations. Correlations used to characterize dissolution from pure PCE- or TCE-NAPL are suitable for simulating natural dissolution of NAPL mixtures at field sites. Empirical coefficients in the Gilland-Sherwood correlations obtained from column, two-dimensional flow-cell, and large two-dimensional tank experiments were similar provided finite-difference grid spacings also are similar. This suggests that correlation obtained from bench- scale experiments may be used to simulate dissolution at larger scales.

A numerical modeling approach was developed to upscale mass transfer in simulations with sub-grid heterogeneity or where spatial properties are uncertain. The upscaled Gilland-Sherwood correlation is based on a local-scale Gilland-Sherwood expression in combination with geostatistical descriptions of aquifer-property heterogeneity and DNAPL entrapment architecture. The upscaling technique was verified using natural dissolution data obtained from large-scale 2-D test tank experiments.

Inverse modeling techniques can be used to determine the vertical distribution of NAPL saturation from water samples obtained along vertical profiles downgradient of the source zones. The upscaling technique emphasizes the importance of installing multi-level monitoring wells downgradient of suspected NAPL source zones.

4.3 Investigation of surfactant-enhanced dissolution

The objectives of mass transfer experiments and modeling of surfactant-enhanced aquifer remediation (SEAR) were to evaluate how experimental scale affects SEAR efficiency, and to determine how flow system dimensionality affects SEAR efficiency. Experiments conducted with one-dimensional columns, bench-scale two-dimensional flow cells, and large two-dimensional tanks are described in section 3.5 of the report. This section of the report describes the simulation of these experiments. The theoretical basis for the mass transfer model of surfactant enhanced dissolution was described in section 3.9.2. Simulation results provide a framework for addressing the project objectives. In order to facilitate comparisons across experimental scales, modeling focused on the simulation of SEAR where the DNAPL consisted of pure PCE.

4.3.1 Simulation of column experiment with surfactant-enhanced dissolution model

A column experiment for pure PCE dissolution under surfactant-enhanced conditions with Tween 80 was described in section 3.5.1. Transient breakthrough data for dissolved PCE was used to calibrate a surfactant-enhanced dissolution model. Calibration was accomplished with the inverse modeling algorithm (PEST) to determine empirical parameters in

$$Sh = \beta_0 (Re)^{\beta_1} (Sc)^{\beta_2} \left(\frac{\theta_n}{1 - \theta_n} \right)^{\beta_3} \left(\frac{d_{50}}{L^* \tau} \right)^{\beta_4} \quad (4.19)$$

The resulting model fit is very good (Figure 4.34). Optimized parameters are listed in Table 4.9.

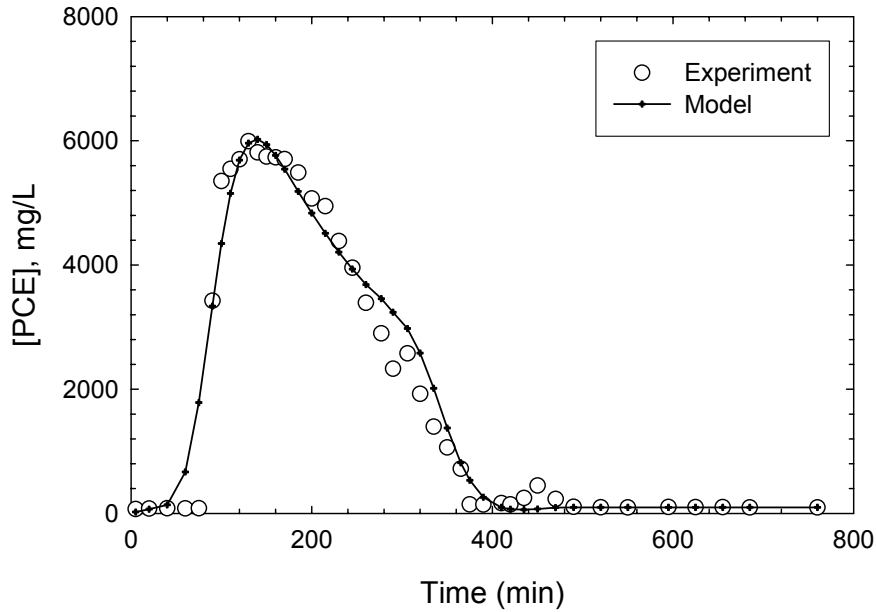


Figure 4.34. Comparison of Observed to Simulated Effluent PCE Concentration, Surfactant-Flushing Column Experiment

Table 4.9. Empirical Parameters of Gilland-Sherwood Expression Obtained by Inverse Modeling, Surfactant-Flushing Column Experiment

| Parameter | Column | Bench-Scale Flow Cell | Large Two-Dimensional Tank |
|-----------|--------|-----------------------|----------------------------|
| β_0 | 0.6425 | 0.526 | 0.447 |
| β_1 | 1.778 | 1.871 | 1.369 |
| β_2 | 0.877 | 0.5 | 0.5 |
| β_3 | 1.566 | 0.189 | 0.241 |
| β_4 | 0.10 | 0.200 | 0.113 |

One Source. The flow cell experiment with one source zone (section 3.5.3) was simulated with the surfactant-enhanced dissolution model. Breakthrough curves for transient PCE concentration were used as a basis for model calibration. The finite-difference grid was the same as the one used to simulate natural dissolution (section 4.2.3). Model calibration was by nonlinear regression using UCODE. The empirical parameters of the Gilland-Sherwood expression (Equation 4.19) were treated as calibration parameters.

The calibrated surfactant-enhanced dissolution model was able to accurately simulate the surfactant flushing breakthrough curves (Figure 4.35). No significant correlation was found among parameters except β_2 and β_4 where the correlation coefficient was $r = 0.74$. This suggests that groundwater flow velocity in this experiment, described in terms of Reynolds number, was closely related to the volumetric NAPL content θ_n in the grid block. The optimized values of β 's are listed in Table 4.9.

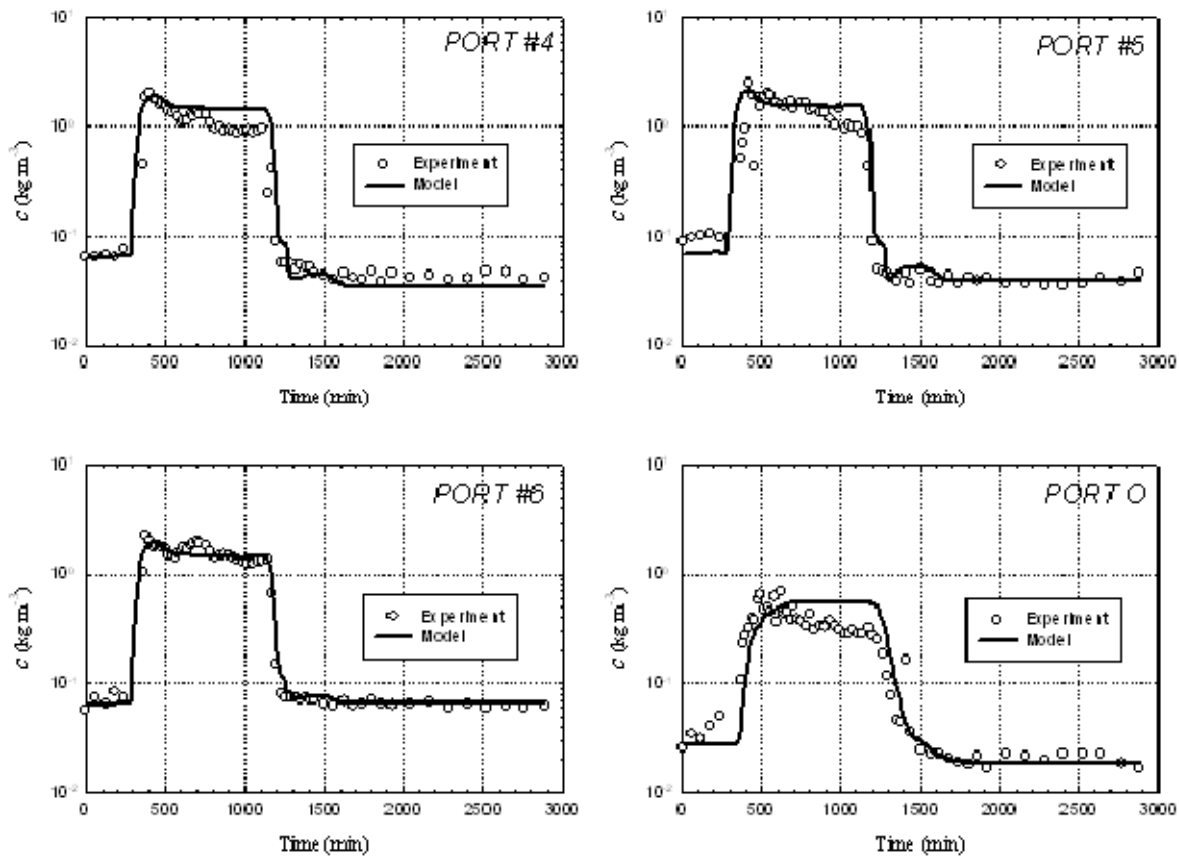


Figure 4.35. Comparison of Observed to Simulated PCE Concentration, Surfactant-Flushing Experiment in a Two-Dimensional Flow Cell with One DNAPL Source Zone

There was a significant difference between SEAR in columns and two-dimensional flow cells for the β_3 parameter, which is the exponent of $\theta_n/(1-\theta_n)$ term. This was attributed to a dimensionality effect. In the column, the surfactant solution was forced to flow through the source zone, removing PCE mass along this pathway. However, in the flow cell, water tended to bypass the source zone and, as a result, contact of the surfactant solution with entrapped DNAPL was more limited. Hence, PCE removal efficiency greatly depended on volumetric DNAPL content because DNAPL content controls the relative permeability of the source zone. At high DNAPL content, relative permeability is small and water will bypass the source.

The sensitivity coefficient for β_4 , the exponent for $\theta_n/(1-\theta_n)$ term, was highest among the four calibrated parameters. This was explained by a rapid change in volumetric NAPL content during enhanced dissolution due to significantly increased PCE solubility in the presence of surfactant. The rapid change in volumetric NAPL content also modified the ground water flow field and, as a result, the sensitivity coefficient associated with the Reynolds number exponent also was large.

Two Sources. The calibrated surfactant-enhanced dissolution model developed from the one-source experiment was used to simulate transient, enhanced dissolution during the two-source PCE experiments described in section 3.5.3. Breakthrough curves for transient PCE concentration were used as a basis for model calibration. The finite-difference grid was the same as the one used to simulate natural dissolution (section 4.2.3). No additional calibration was attempted for this simulation. Simulation results showed that the calibrated parameter estimates obtained from the one-source experiment could successfully simulate the independent set of SEAR data represented by the two-source experiment (Figure 4.36).

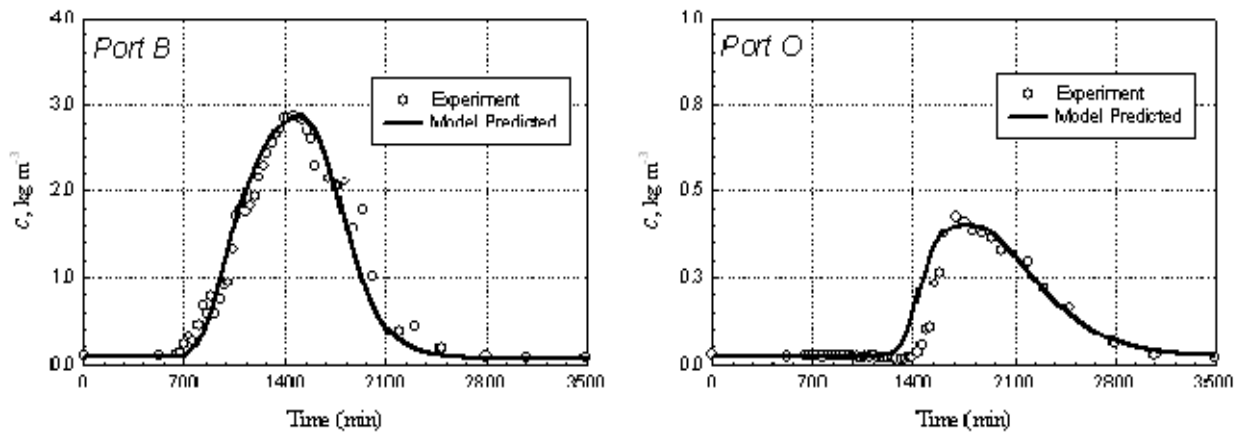


Figure 4.36. Comparison of Observed to Simulated PCE Concentration, Surfactant-Flushing Experiment in a Two-Dimensional Flow Cell with Two DNAPL Source Zones

4.3.2 Large-tank experiment of surfactant-enhanced dissolution

Large-tank experiments with surfactant flushing are described in section 3.5.5. The surfactant-enhanced dissolution model was applied to the large tank experiment with high heterogeneity in order to evaluate the effects of experimental scale on dissolution parameter estimates. Modeling studies of groundwater flow, tracer transport and natural dissolution are described in sections 4.1.3 and 4.2.4 for the large-tank experiment with high heterogeneity are described in 4.1.3 and 4.2.4. The finite-difference grid and boundary conditions for those models also were used to model surfactant-enhanced dissolution. As with the smaller-scale modeling efforts, the large tank model of surfactant-enhanced dissolution was calibrated by nonlinear regression techniques using PEST. The empirical Gilland-Sherwood parameters were treated as calibration parameters.

Results obtained by inverse modeling show a relatively well-estimated breakthrough curves during enhanced dissolution (Figures 4.37 and Figure 4.38). The correlation coefficient between model simulated and observed PCE concentrations was $R = 0.922$. The optimized parameters are provided in Table 4.9. Comparison of parameter values at the column, flow cell and large-tank scales indicate that parameter estimates at one scale are not appropriate for use in simulating surfactant-enhanced dissolution at other scales.

4.3.3 Summary of key results

Effectiveness of surfactant-enhanced remediation decreases as source-zone heterogeneity increases. This was demonstrated by comparing remediation effectiveness for experiments in columns, bench-scale flow cells, and large two-dimensional tanks. In experiments with greater source heterogeneity, groundwater bypassing due to relative permeability contrasts caused removal efficiency to diminish.

The empirical parameters of Gilland-Sherwood correlations during surfactant-enhanced dissolution changed with changes in experimental scale. Parameter estimates showed little change among two-dimensional experiments but were significantly different from column tests. This suggests that Gilland-Sherwood correlations obtained from column tests undergoing surfactant-enhanced remediation may not be appropriate for use in multidimensional experiments or at field sites.

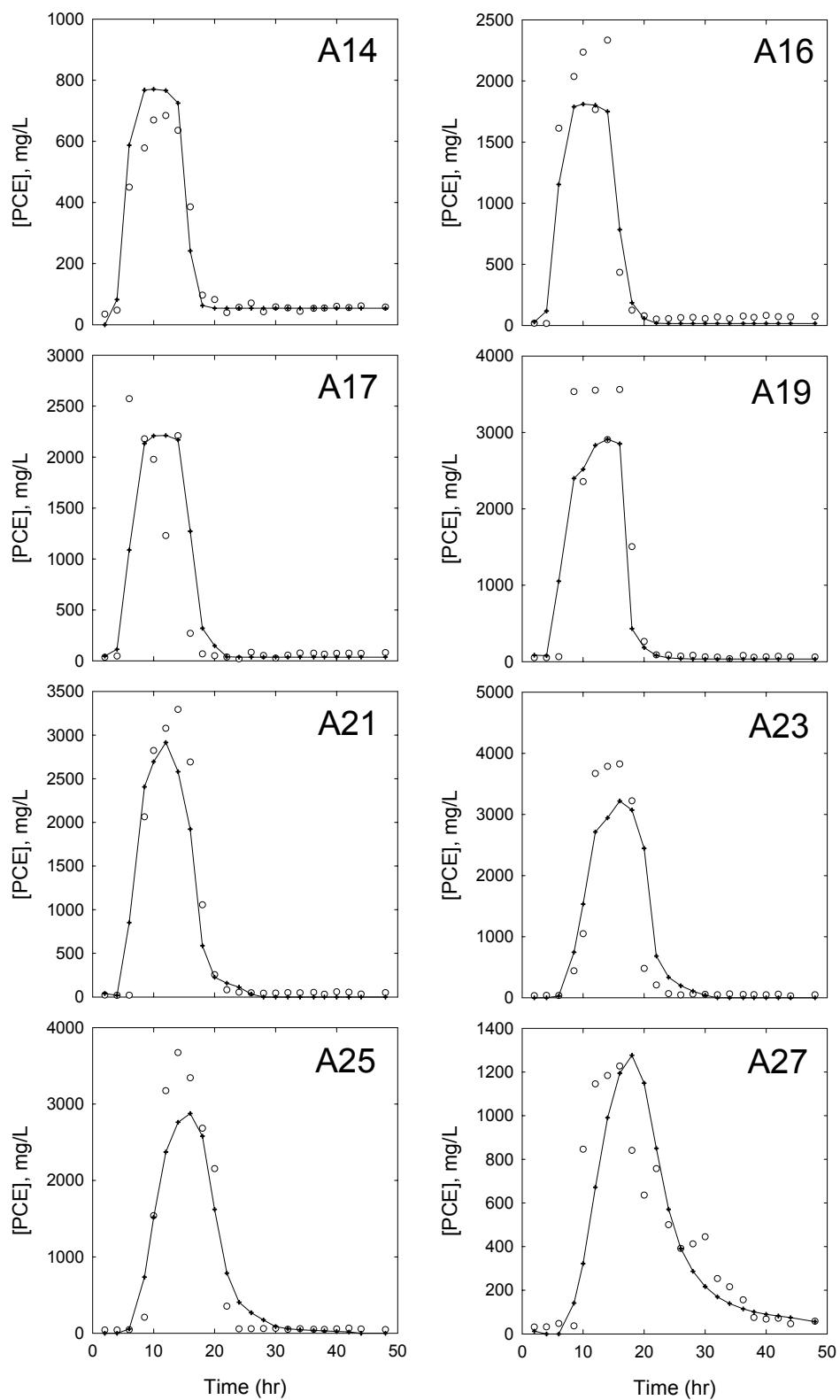


Figure 4.37. Comparison of Observed and Simulated Breakthrough Curves for Sampling Ports A14 to A27, Large-Tank Experiment of Surfactant Flushing with High Heterogeneity

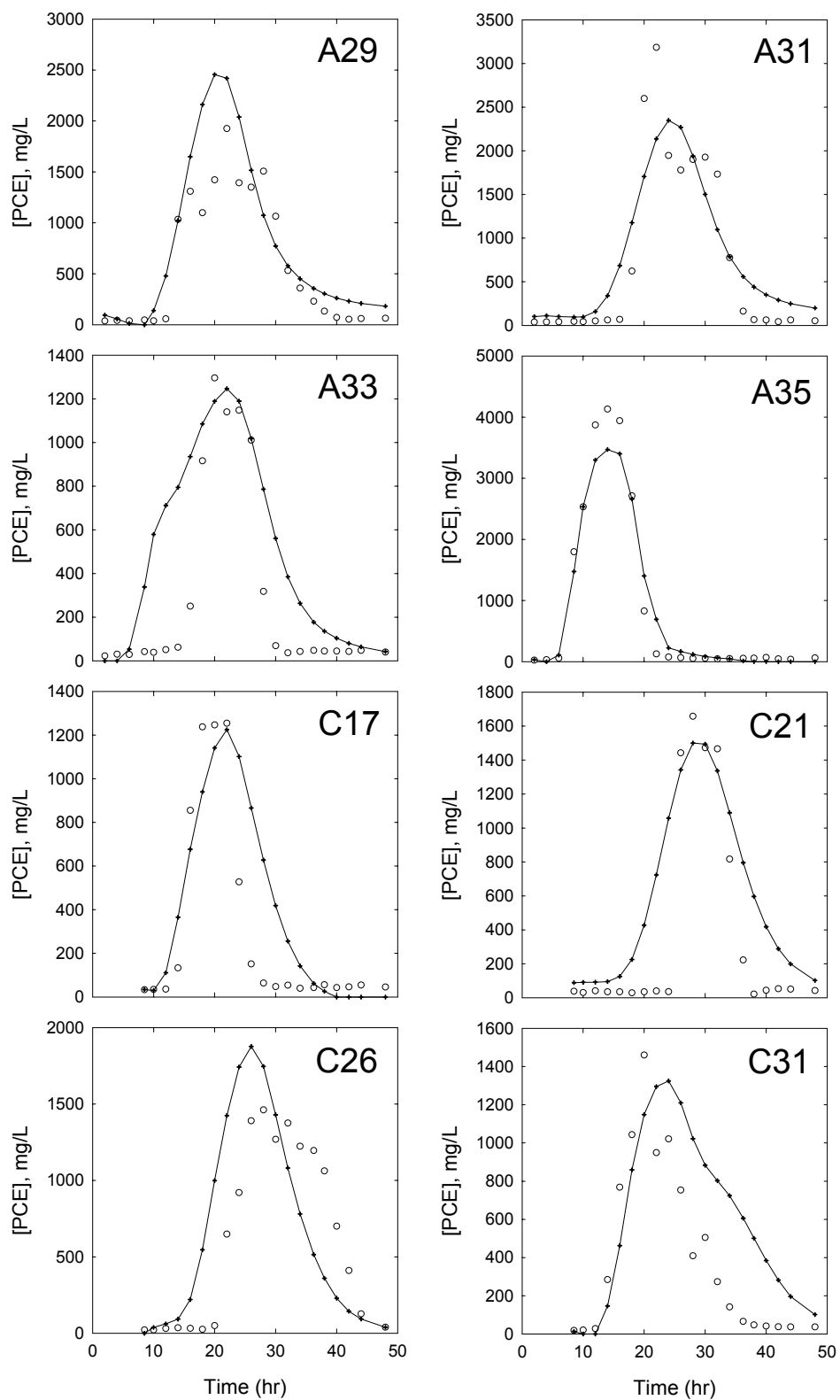


Figure 4.38. Comparison of Observed and Simulated Breakthrough Curves for Sampling Ports A29 to C31, Large-Tank Experiment of Surfactant Flushing with High Heterogeneity

4.4 Investigation of in situ chemical oxidation

In situ chemical oxidation (ISCO) experiments were conducted (1) to evaluate the effect of ISCO on DNAPL source depletion, (2) to evaluate the effect of source zone complexity on ISCO, and (3) to develop comprehensive experimental data sets that can be used for numerical model evaluation and/or validation. Experiments were conducted at a laboratory bench scale using custom-designed flow-through reactor, a two-dimensional intermediate scale using a large flow cell packed with discrete source zones, and a large two-dimensional tank packed with a complex heterogeneous source zone.

In this section of the report, key results and accomplishments of these experiments are presented. Detailed descriptions of experimental data and results are most easily understood when presented in the context of experimental procedures. Therefore the reader is referred to section 3.6 for detailed results. A modeling study of column experiments also is presented that provides additional insight to the effects of ISCO on mass transfer.

4.4.1 Flow-thru reactor (FTR) experiments

The FTR experiments demonstrated that oxidant delivery and DNAPL configuration are important factors in determining an optimal oxidant delivery scenario. Although manganese oxide formation was observed, and sometimes was visually extensive, effects on mass transfer may have been limited by the one-dimensional nature of the experimental setup. It is possible that manganese oxide formation may have a larger impact on mass transfer under two- or three-dimensional flow patterns where water can bypass of the intended DNAPL source zone.

4.4.2 Intermediate-scale cell experiments

This experiment utilized an intermediate-scale two-dimensional cell filled with clean silica sands and a moderately complex PCE DNAPL source zone, under a single set of flow and oxidant delivery conditions. For the conditions investigated, only a small portion of the injected oxidant mass contributed to oxidation of PCE mass. This was attributed to limited mass transfer from DNAPL to aqueous phases within sources or localized bypassing of water within the source zone. Mass transfer limitations appear to have been partly due to the design used in constructing the sources. The design involved using coarse sand in the source and medium to fine sand in the rest of the cell. As a result, the sources had a relatively high hydraulic conductivity and low residual DNAPL saturation. Although oxidation initially tripled the mass depletion rate, the rate dropped as PCE ganglia disappeared and as $\text{MnO}_2(\text{s})$ formed, decreasing DNAPL-water interfacial area and causing water to bypass the sources. In a field situation, DNAPL migrating through a fine subsurface soil may encounter a lens of more coarse sand where it will accumulate as a pool similar to the sources used in this study. In such a situation, if substantial DNAPL mass is present as a pool in the coarse sand, ISCO using permanganate may not be suited to full depletion of the DNAPL source. However, a substantial reduction in mass loading from the DNAPL into the groundwater may still be achieved.

It is possible that the flow velocity through the sources and/or oxidant concentration could be adjusted to optimize the mass depletion rate and minimize the amount of oxidant mass injected. Effects of ISCO on mass depletion and mass depletion rates varied by source as a result of source configuration and location. Mass present as ganglia underwent a large increase in mass depletion rate which appeared to drop off upon ganglia depletion. As oxidation continued, mass depletion rates slowly declined apparently due to manganese oxide formation. Pool 1, located to have minimal interaction with other sources, was the only source not to experience an initial increase in mass depletion rate during oxidation but instead saw a steady decline in mass depletion rate likely due to $\text{MnO}_2(\text{s})$ formation at the DNAPL-water interface. On the other hand, pool 2, located to interact with residual sources above and below it, experienced the greatest rebound of mass depletion rate following oxidation. This appears to be a result of the flow field around that pool that was more complex after oxidation than occurred before oxidation.

Formation and deposition of $\text{MnO}_2(\text{s})$ as a result of PCE oxidation by permanganate affected the porous media, reducing the aqueous permeability in and around DNAPL sources, and resulting in changes to flow patterns. The configuration of the source zones partly determined the effects. A pool with little or no residual around it, in a relatively homogeneous flow field, appeared to benefit from resulting $\text{MnO}_2(\text{s})$ pore-blocking that substantially reduced the mass depletion rate from the pool with relatively little mass removed from the pool. However, a pool with residual around it in a more complex heterogeneous flow field appeared to undergo an increase in mass depletion rate as $\text{MnO}_2(\text{s})$ reduced permeability, complicating flow and increasing mixing at the NAPL-water interface. Additionally, sequential residual zones seemed to have a combined effect where some $\text{MnO}_2(\text{s})$ generated in the first residual was transported a short distance to the second residual to combine with $\text{MnO}_2(\text{s})$ from that source, and magnified impacts in and around the second source. Again, it seemed that flow rate and oxidant concentration could be optimized to maximize mass transfer of PCE from the DNAPL to water phase for oxidation, while minimizing the oxidation rate to slow formation of $\text{MnO}_2(\text{s})$ and move some of the permeability effects down-gradient of the source.

Levels of $\text{MnO}_2(\text{s})$ had to exceed a threshold level before affecting permeability. This threshold was determined to be 0.1g $\text{MnO}_2(\text{s})/\text{kg}$ soil for the conditions of this experiment. It is likely that the threshold will vary depending on system conditions such as flow rates, pore sizes, uniformity of soil particle sizes.

4.4.3 Large-scale tank experiments

Chemical oxidation using permanganate showed potentially significant enhancement of mass-transfer from complex DNAPL sources in heterogeneous flow fields, even in the presence of non-productive oxidant demand. These experiments suggest that a higher degree of subsurface heterogeneity can result in a larger increase in DNAPL mass transfer during oxidation, leading to greater mass depletion. On the other hand, under less heterogeneous conditions oxidation results in a smaller DNAPL mass transfer rate increase but a greater reduction in mass transfer following oxidation. These results are similar to those from the intermediate-scale cell experiment where it was found that the heterogeneous region of the source zone had a larger increase in mass transfer during oxidation, while the less complex region had a greater post-oxidation decrease. Additionally, under higher heterogeneity conditions both scales of

experiments experienced little or no decrease in mass transfer or dissolution of PCE following oxidation despite the buildup of manganese oxide in the source zone.

4.4.4 Modeling study of column experiments

The CORT3D modeling code was used to simulate a series of column experiments documented in literature in order to highlight important ISCO-related processes. The goal of these tests was not to universally validate the modeling code for all conditions, since it is recognized that models of specific scenarios must be individually validated for the specific boundary conditions, performance criteria, and application (Refsgaard and Henriksen 2004, Refsgaard and Knudsen 1996, Van Waveren et al. 1999). Instead, the purpose was to demonstrate that models created using the modeling code capture specific important ISCO-related processes and effects observed in experiments. An additional purpose was to investigate the impact of multiple NOD fractions and generation of manganese oxides on ISCO, as well as the enhancement of mass transfer during oxidation. Where sufficient data were available, the model was calibrated using one set of data and then used to predict observed effects from an independent set of data.

Permeability Effects from Oxidizing TCE DNAPL. A significant feature of CORT3D is ability to simulate changes in permeability resulting from oxidation using permanganate. Schroth et al. (2001) performed a set of column experiments specifically to study the effects of oxidizing TCE DNAPL on porous media permeability. In those experiments, a 95cm x 5.1cm diameter column was packed with high purity silica sand and then a residual TCE DNAPL source zone was created in the first 65cm. TCE DNAPL saturation was measured using dual-energy gamma radiation attenuation to be approximately 17 percent throughout the entire source zone. Once the flushing experiment began, water head drop throughout the column was monitored regularly to assess changes in permeability. A first experiment involved natural dissolution only. A second experiment included flushing with potassium permanganate (790mg/L as KMnO_4), but ended after only 30 hours due to a pump failure. As a result, the CORT3D model code could not be utilized in a prediction scenario. All that could be done was to determine if the model captured the general change in permeability observed in the experiment. Simulating these experiments provided the additional benefit of testing the model for use in simulating TCE oxidation.

Before simulating the experiment, the experimental head data require some discussion. Because this was a column experiment, flow bypassing was not able to occur as pores became blocked due to $\text{MnO}_2(\text{s})$ precipitation. As a result, pressures in the column increased as pores became blocked (Figure 4.39). During the first day of testing, water head increased steadily and the increased pressure gradient physically dislodged precipitates. Similar behavior was reported for column experiments by Reitsma and Randhawa (2002). Such physical dislodgement could have transported manganese oxides along the column ahead of the oxidation reaction front to begin blocking pores that otherwise would not have become blocked. This is suggested by the data where head gradually increases at pressure port T1 between 10-15 hours and then roughly levels off as head begins to gradually increase at T2. The head at T2 initially increased at the same rate that T1 initially increased, and subsequently leveled off. Again, as T2 began to level off, head at T4 began increasing. The leveling off at each location may be due to preferential

channeling that resulted from hydraulic gradients not allowing further blockage of some pores. Development of preferential flow channels may also have advanced the oxidation reaction front (along the channels) faster than if the reaction front advanced uniformly. After one day, water head within the column exceeded the upper limits of the tensiometers and data beyond that time were not reliable. Although the head data beyond 25 hours were not reliable, it does indicate that a substantial increase in hydraulic head occurred. This may be partly due to $\text{MnO}_2(\text{s})$ blockage at the stainless steel column outlet screen.

Despite limitations in the experimental data, the overall permeability reduction process can be discerned. Permeability reductions began later for downgradient locations as the reaction front propagated through the column. Rates of permeability reduction can be estimated from the data prior to apparent dislodgement of $\text{MnO}_2(\text{s})$ particles.

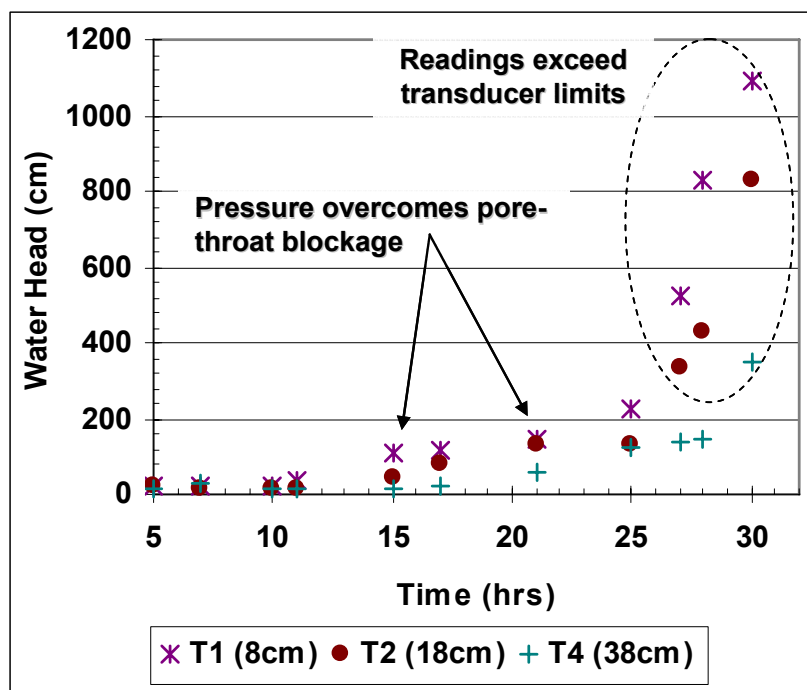


Figure 4.39. Observed Water Head for a Column Experiment with TCE Oxidation (Schroth et al., 2001)

A one-dimensional model was created using a 1 cm finite-difference cell spacing. Boundary conditions consisted of a constant flow inlet ($Q = 21.72 \text{ ml/min}$ for the dissolution experiment and 21.63 mL/min for the oxidation experiment) and a constant head outlet (5 cm). The flow model was calibrated to determine the initial hydraulic conductivity (5.85 cm/min) using head data from the end of the natural dissolution experiment. Next, the dissolution-experimental data were used to estimate parameter values for the Gilland-Sherwood correlation given in section 3.9.6 ($\tau = 2.22$, $\alpha_1 = 59.73$, $\alpha_2 = 6.26$, $\alpha_3 = 0.50$, $\alpha_4 = 0.13$). Parameter estimation was by inverse modeling using the PEST code (Doherty 2003). Simulated and observed effluent

TCE concentration and TCE mass remaining during the natural dissolution experiment are compared in Figure 4.40.

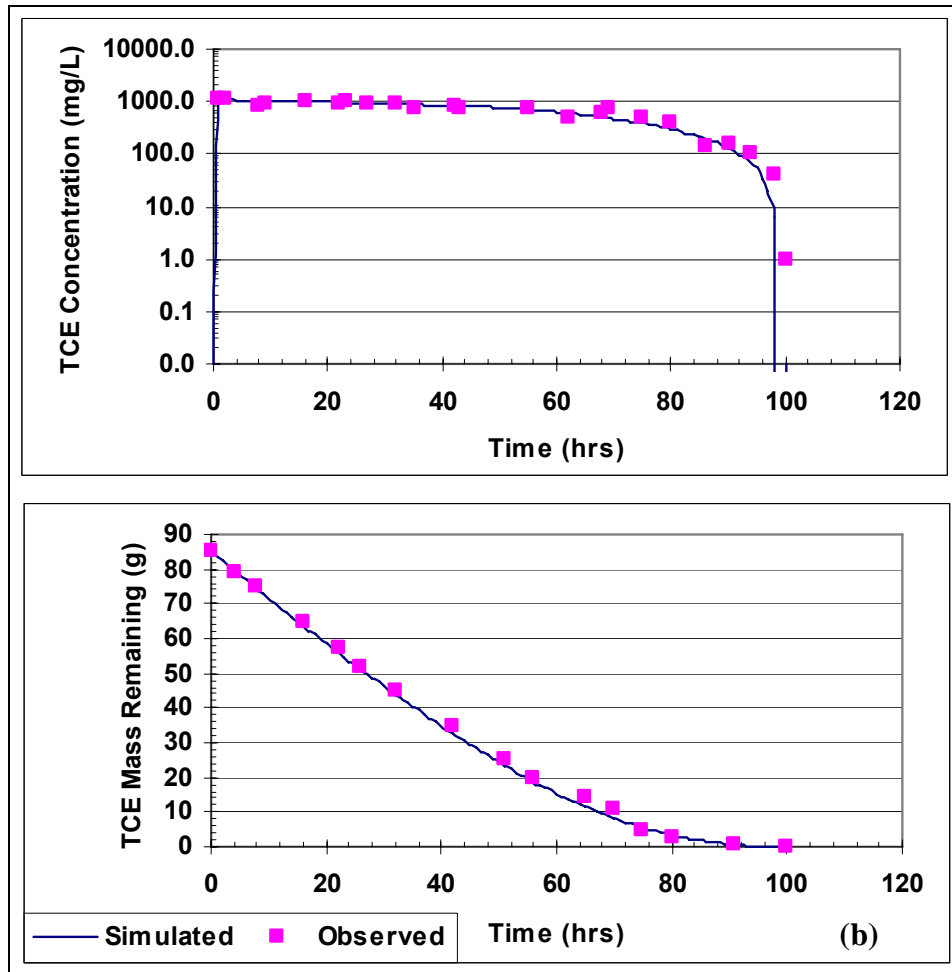


Figure 4.40. Comparison of Observed and Simulated TCE Concentration (a) and TCE Mass Remaining (b) for the Column Dissolution Experiment of Schroth et al. (2001)

The oxidation experiment was simulated using calibrated dissolution parameters and a second-order chemical oxidation kinetic rate for TCE of 39 L/mol-min given by Zhang and Schwartz (2000). The model code converts mass of generated $\text{MnO}_2(\text{s})$ in a model cell to volume based on the effective density of precipitated manganese oxide. However, this effective density is a fitting parameter because the precipitated manganese oxides are a porous, hydrous form having an undetermined density expected to be considerably lower than that of dry, consolidated, manganese oxide solids. The effective density parameter is not an actual density of the precipitated solids as it also accounts for permeability reductions resulting from additional mechanisms including formation of manganese oxide film on the soil particle surfaces reducing

pore throat diameter as well as blockage of some pore throats without significantly reducing pore volume. The optimal $\text{MnO}_2(\text{s})$ effective density for these experimental conditions was found to be 105mg/mL (approximately 48 times less than the density of dry, solid $\text{MnO}_2(\text{s})$).

Figure 4.41 shows the simulated water head (above the effluent) for the same three locations along the column as in Figure 4.39. The simulation was able to capture the general experimental trends in water head observed during the oxidation experiment. These included permeability reduction that developed over time, first near the inlet, with downgradient reductions occurring later. Simulated rates of permeability reduction also were similar to initial rates observed in the experiment.

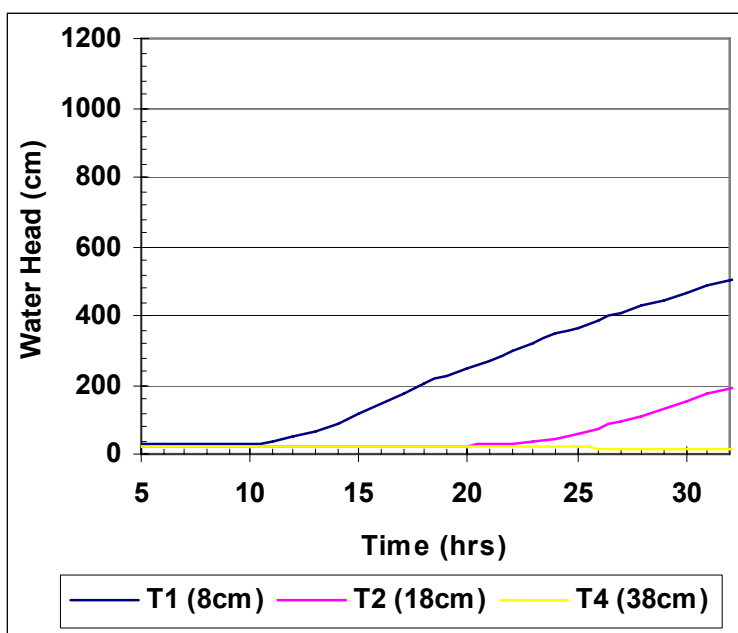


Figure 4.41. Simulated Water Head during TCE Oxidation, Column Experiment of Schroth et al. (2001)

Simulating Oxidation of PCE DNAPL. Column experiments investigating the oxidation of residual PCE DNAPL using potassium permanganate (Schnarr et al., 1998) were simulated. Columns in this experiment were 30cm long with a diameter of 5.2cm, and were filled with fine-grained sand from the Borden test site, Ontario. The organic content of the Borden soil was 0.027 percent by weight and exerted some degree of natural oxidant demand (NOD). However, Schnarr et al. (1998) did not specifically quantify NOD. Approximately one milliliter of PCE was distributed throughout the last 10cm of the column to achieve approximately 1 percent saturation. Two columns received oxidant at 7500mg/L as KMnO_4 and two received oxidant at 10,000mg/L. Flow rates through the columns were established such that one column of each pair had a Darcy velocity of approximately 42 cm/day while the other had a Darcy

velocity of approximately 65cm/day. A fifth column received no oxidant and had a Darcy velocity of 61cm/day. Schnarr et al. (1998) said that although constant flow rates were desired, actual flow rates varied during the experiments and no further details were provided. Only the high flow rate experiments (61-65cm/day) were simulated in the work reported here.

The goal in simulating these experiments was not to reproduce results from the entire experiments, but to determine if specific processes and effects could be captured with the CORT3D model. Additional information about the experiments would be needed to accurately reproduce results such as details about PCE source emplacement, variability of flow rate and possible sorption of PCE to the Borden site soil. Therefore, simulations focused on the ability of the CORT3D model to represent specific mass transfer characteristics including: increased mass transfer from the DNAPL to aqueous phase during oxidation, differences in PCE oxidation and permanganate breakthrough due to the presence of fast vs. slow NOD, simultaneous existence of aqueous PCE and permanganate in effluent, rebound in aqueous PCE concentrations following conclusion of permanganate flushing, and generation of chloride as PCE was destroyed.

A one-dimensional model was created using 1cm finite-difference cell spacing. Boundary conditions consisted of a constant flow inlet and constant head outlet. Data for the column without oxidant was used to estimate values for NAPL dissolution parameters ($\tau= 2.25$, $\alpha_1= 76.51$, $\alpha_2= 0.98$, $\alpha_3= 0.49$, $\alpha_4= 0.75$). Parameter estimation was by inverse modeling using the PEST code (Doherty 2003). Two oxidation experiments were simulated using calibrated dissolution parameters and a second-order chemical oxidation kinetic rate for PCE of 2.7 L/mol-min given by Zhang and Schwartz (2000). The fourth column experiment of Schnarr et al. (1998) with low oxidant and high flow rate was simulated to calibrate NOD parameters (amount and kinetic rates). The third column experiment with high oxidant concentration and high flow rate also was simulated.

Observed and simulated results of the PCE oxidation experiments with low and high oxidant concentrations are shown in Figures 4.42 and 4.43, respectively. Simulations captured desired experimental processes and effects for both experiments. Specifically, delays occurred before PCE concentrations dropped and Cl^- concentrations began to increase. This suggested initial preferential oxidation of fast NOD. A gradual increase in oxidant concentration in effluent also occurred in simulations. This was due to partial oxidant consumption by slow NOD while PCE was oxidized. Simulations resulted in aqueous PCE concentration in the effluent during oxidation that was similar to that of natural dissolution. This occurred even though permanganate was also present in the effluent. Because PCE DNAPL was at the end of the column, travel time from DNAPL source to column effluent was less than the reaction time necessary for complete aqueous PCE oxidation. Chloride generation observed as PCE was destroyed also was replicated by the simulations. Finally, aqueous PCE concentration rebound following oxidation was similar in the simulations to the rebound observed in experiments, especially for the low oxidant concentration experiment.

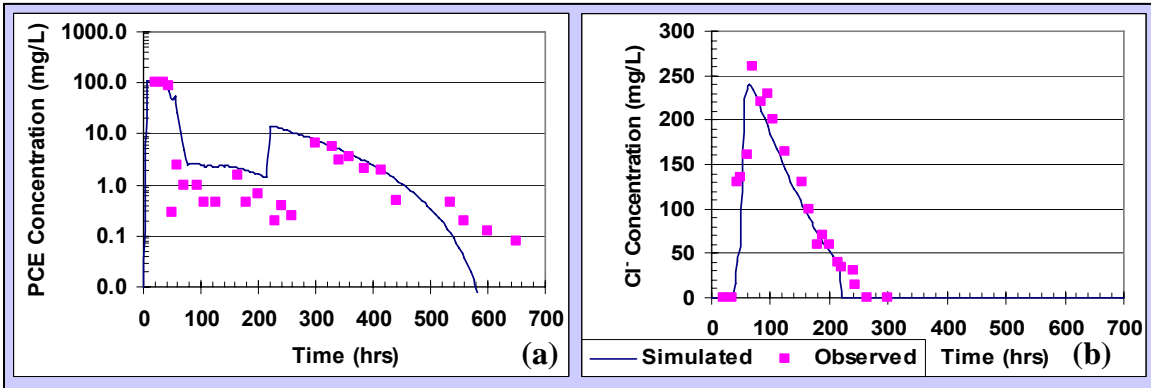


Figure 4.42. Comparison of Simulated and Observed Results for Column Experiments of Schnarr et al. (1998) with PCE Oxidation and Low Oxidant Concentration

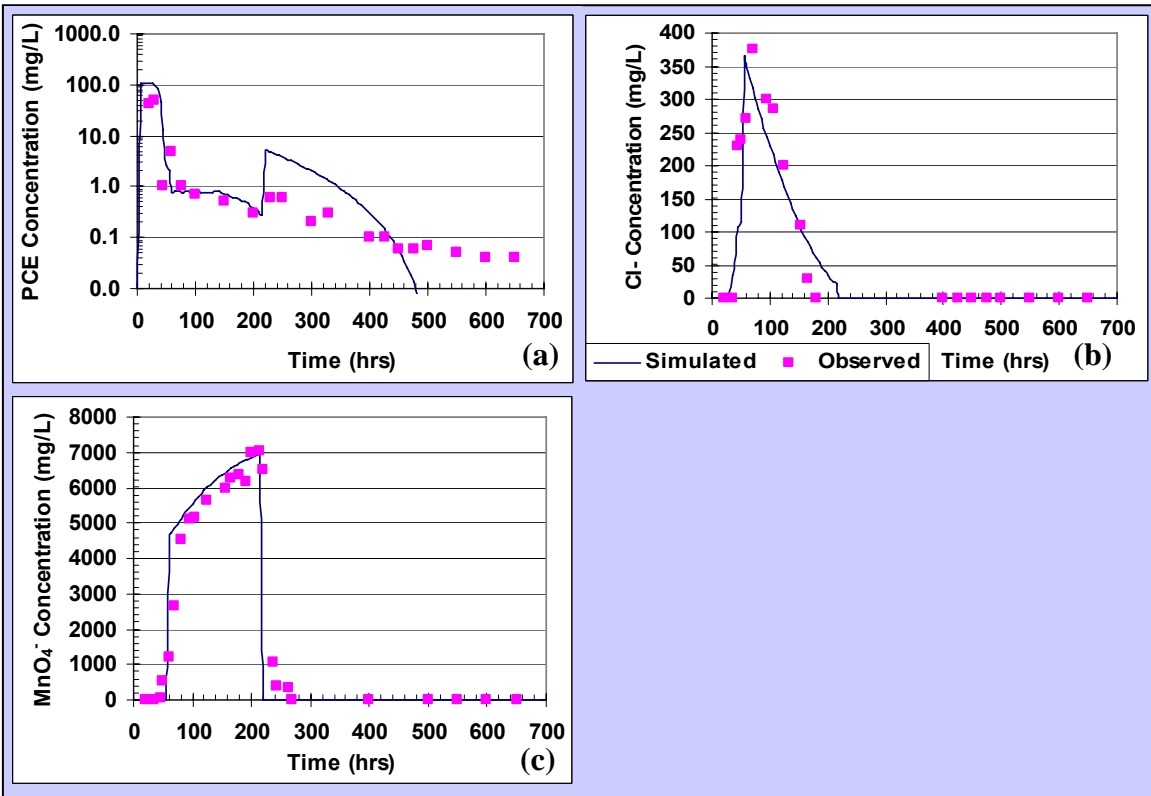


Figure 4.43. Comparison of Simulated and Observed Results for Column Experiments of Schnarr et al. (1998) with PCE Oxidation and High

Both experiments resulted in PCE concentration trends which simulations did not reproduce. Nor did simulations accurately reproduce observed rebounds. There are several possible reasons for departures. First, there may have been differences between simulated and

actual configurations of the DNAPL sources within the columns. Schnarr et al. (1998) did not describe how PCE was emplaced, and experimental results suggest the initial mass may not have been equal between columns or uniform within the source zones. The simulations were constructed assuming equal and uniform sources. Next, sorption of PCE to the field soil and subsequent desorption after the oxidant flush may have occurred during the experiments. Simulations did not incorporate sorption as no sorption data were available. However, Borden soil has been shown to sorb PCE (Ball and Roberts 1991, Mackay et al. 1986, Rivett and Allen-King 2003). Finally, differences may have resulted from fluctuations in the experimental flow rate mentioned by Schnarr et al. (1998) but not quantified. Constant flow rates were assumed in the simulations.

Model calibration of both experiments required that the mass transfer fitting parameter (α_I) be increased during oxidation phase compared to natural dissolution. Increase by a factor of four was required for the high concentration experiment and by a factor of three for the low concentration experiment. The increase over natural dissolution conditions, as well as the difference in magnitude between experiments, may be attributed to the chemical oxidation reaction. A method for calculating changes in mass transfer rate coefficients during oxidation is described in section 3.9.6. Lack of knowledge about the DNAPL-water interfacial area made direct application of this method impossible. Instead, so several assumptions were necessary. Assuming a porosity of 0.41, a uniform distribution of PCE throughout the source zone, one spherical PCE droplet per soil pore, and one-half of each PCE droplet in contact with flowing water, an interfacial area was estimated. The intrinsic mass transfer rate (k_L) was then determined by

$$k_L = \frac{k_{La}V}{A_{mw}} \quad (4.20)$$

The method described in section 3.9.6 was then used to estimate the increase in mass transfer. Results of this calculation are summarized in Table 4.10. The k_{La} computed by CORT3D at the beginning of the simulation was based mass transfer parameter estimates from the calibrated natural dissolution model. Pseudo-first-order kinetic rates for each experiment were calculated from the PCE oxidation rate and specified permanganate concentration. The magnitudes of the increase in α_I required to calibrate the simulations with oxidation were not dramatically different from those shown in Table 4.10. This supported the idea that the increase in α_I was due to chemical oxidation. However, additional research is needed to develop a method for predicting the increase so it does not have to be experimentally determined through inverse modeling.

Table 4.10. Estimation of Expected Mass Transfer Increase due to Oxidation, Column Experiments of Schnarr et al. (1998)

| | Experiment 3 (high oxidant concentration) | Experiment 4 (low oxidant concentration) |
|--|--|---|
| k_{La} during natural dissolution (hr^{-1}) | 0.80 | 0.81 |
| Estimated k_L ($\text{cm}\cdot\text{hr}^{-1}$) | 0.153 | 0.155 |
| Expected ratio of k_{La} during natural dissolution to k_{La} during oxidation | 3.71 | 3.18 |

Simulations were performed to verify that the increased mass transfer was due to oxidation and not due to a physical difference in column experimental conditions. Simulations were conducted (a) utilizing an increased α_1 during oxidation phase, (b) utilizing natural dissolution α_1 during entire simulation, and (c) utilizing increased α_1 during entire simulation. Resulting aqueous PCE (top) and chloride (bottom) concentrations for the three scenarios are presented in Figure 4.45. If the natural dissolution mass transfer coefficient was used for the entire simulation, the model no longer captured the post-oxidation PCE concentration decrease or full chloride production. However, if mass transfer was increased during the entire simulation, as would be the case if physical conditions caused the increase, pre-oxidation dissolution was overestimated so too little PCE remained for oxidation.

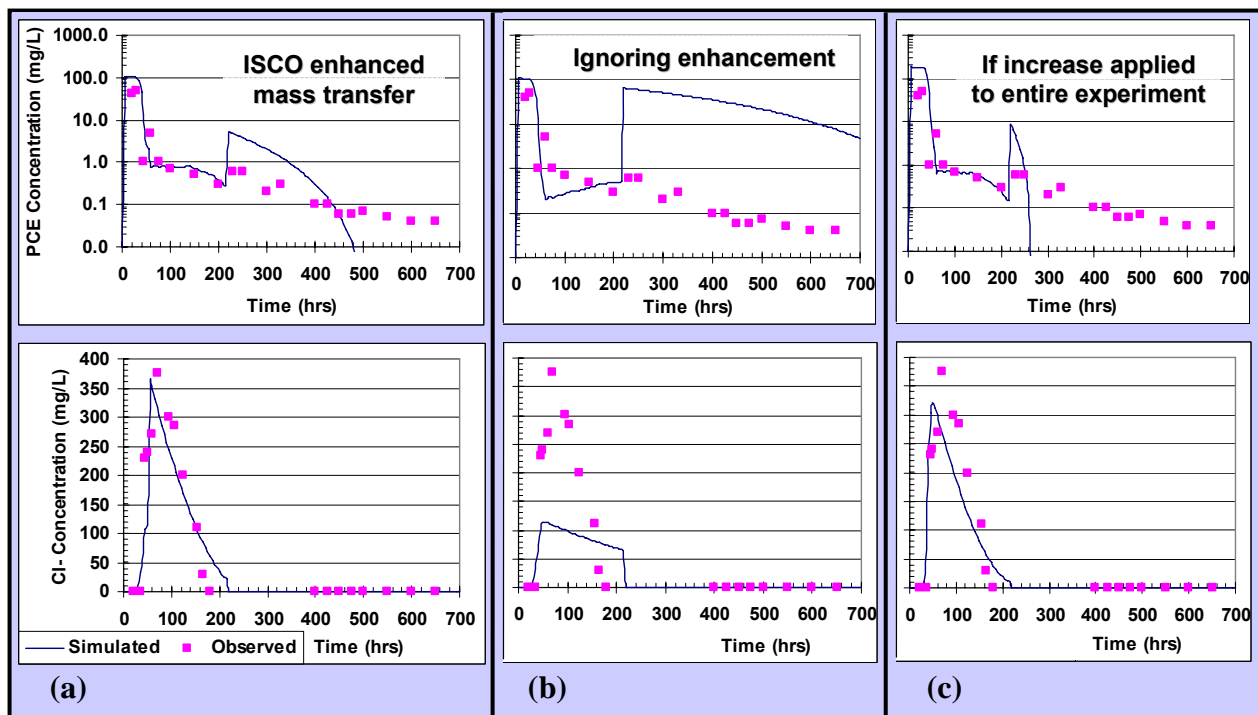


Figure 4.45. Comparison of Simulated and Observed Results for Column Experiments of Schnarr et al. (1998) with Alternative Descriptions of Mass Transfer Enhancement

As noted earlier, the existence of NOD with a very fast kinetic rate accounted for the delayed reduction in PCE concentration and appearance of chloride. However, neither oxidation of this fast NOD nor oxidation of the PCE can account for the delayed increase in oxidant concentrations to the injection concentration. This suggests that a fraction of NOD had a much lower kinetic rate than that which was initially oxidized. This was confirmed by running a simulation without slow NOD and comparing it to the base case simulation with slow NOD (Figure 4.46). When no slow NOD was simulated, the oxidant concentration increased to near injection concentrations as soon as the fast NOD fraction was consumed. PCE concentrations during oxidation were under-predicted as available oxidant was not being reduced due to oxidation of slow NOD. Additional simulations considered other factors and no combination of changing mass transfer parameters, longitudinal dispersivity, or contaminant oxidation rate was able to reproduce the delayed increase in oxidant concentration except for introduction of a slow NOD fraction.

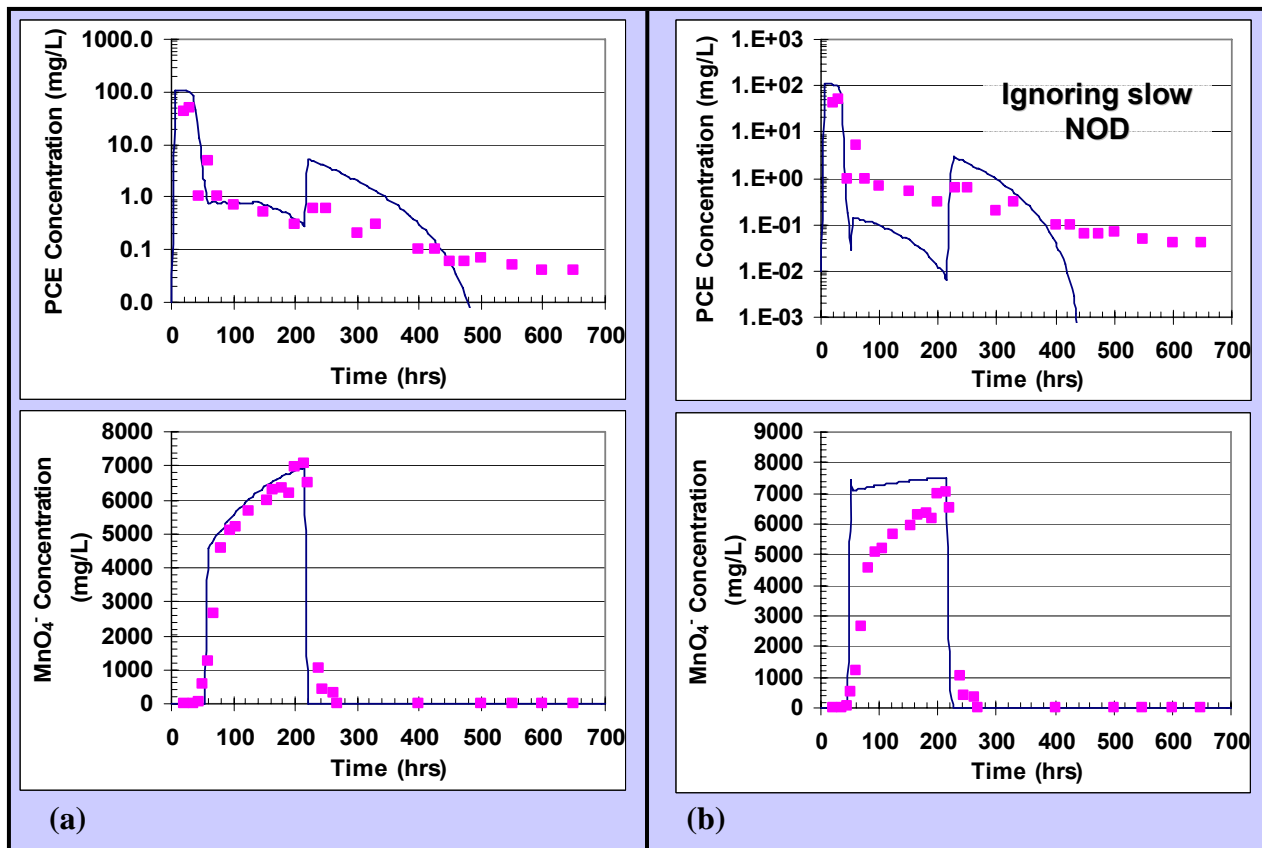


Figure 4.46. Comparison of Simulated and Observed Results for Column Experiments of Schnarr et al. (1998) with Alternative Descriptions of NOD

Additional simulations confirmed the importance of accounting for manganese oxide precipitation in simulations of ISCO using permanganate. When permeability changes due to manganese oxide precipitation were not included, the simulation significantly under predicted

PCE concentrations during oxidation (Figure 4.47). When $\text{MnO}_2(\text{s})$ precipitation was simulated, the generation of manganese oxide reduced effective porosity and consequently permeability. Under constant flow conditions in a column, reductions in effective porosity caused an increase in linear pore velocity and therefore a reduction in travel time through the column to the outlet. As travel time decreased, the residence time for aqueous PCE in contact with permanganate decreased, lowering the amount of PCE that could be oxidized and increasing effluent PCE concentration.

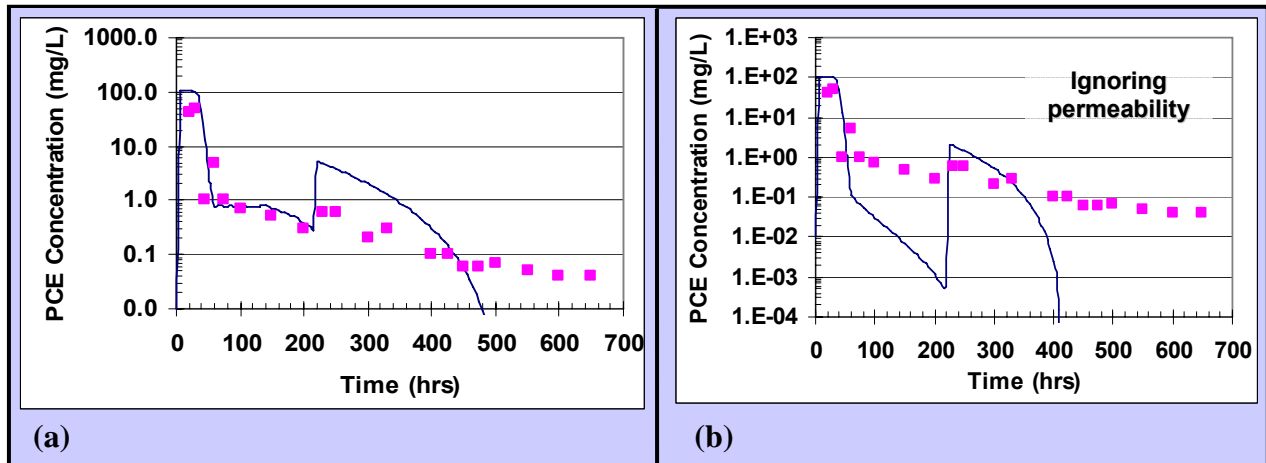


Figure 4.47. Comparison of Simulated and Observed Results for Column Experiments of Schnarr et al. (1998) with Alternative Descriptions of Permeability Changes

4.4.5 Summary of key results

A reactive transport model (CORT3D) based on the widely used RT3D code was developed to simulate effects of in situ chemical oxidation (ISCO) on mass transfer. The model simulates PCE-DNAPL oxidation, TCE-DNAPL oxidation, natural oxidant demand (NOD) based on multiple NOD fractions, kinetic NOD oxidation of each fraction, and permeability reduction due to manganese oxide formation.

In two-dimensional tank experiments with a heterogeneous source, the effectiveness of ISCO depended on the configuration of NAPL. Sources with low ganglia-to-pool ratios resulted in significantly lower mass transport during remediation and less mass depletion.

Heterogeneous NAPL sources underwent a gradual decline in mass depletion rate as oxidation proceeded. Several sources returned to pre-treatment rates of mass depletion as a result of manganese oxide buildup and changes in flow patterns as remediation proceeded. Manganese oxide formation did not noticeably affect permeability until the mass fraction of manganese oxide exceeded $0.1 \text{ mg MnO}_2(\text{s}) / \text{kg}$ aquifer material.

4.5 Investigation of biologically enhanced dissolution

Bioenhanced dissolution experiments were conducted to understand and characterize mass transfer from PCE DNAPL undergoing bioremediation. Experiments at scales ranging from batch to large tanks were conducted to generate accurate data under controlled conditions that are suitable for hypothesis testing, model development and validation. Specific objectives were (1) to determine if biological activity can enhance mass transfer (2) to determine how biological activity changes mass transfer rate coefficients, (3) to identify how experimental scale affects mass transfer during bioremediation, and (4) to develop methods for upscaling models of mass transfer during bioremediation from point scale to multi-dimensional flow fields. These objectives were addressed by conducting experiments at batch, column, flow-cell and large tank scales.

In this section of the report, key results and accomplishments of these experiments are presented. Detailed descriptions of experimental data and results are most easily understood when presented in the context of experimental procedures. Therefore the reader is referred to section 3.7 for detailed results. Modeling studies of bioenhanced dissolution at flow cell and large tank scales added significantly to an understanding of bioenhanced dissolution from DNAPL source zones at high saturation. These modeling studies are presented in detail in this section of the report.

4.5.1 Column experiments

A series of mass transfer experiments were conducted in columns (1 x 12 in.). Column tests were run with residual PCE of approximately 20 percent throughout the entire column, as and with residual NAPL in the bottom quarter of the column only. For each column, mass transfer experiments were conducted under abiotic conditions and following inoculation with the KB-1 culture. Each experiment was conducted until effluent water quality attained steady conditions. Bioenhanced mass flux from NAPL zones has been shown in other studies but most previous column work that investigated mass flux either did not use pure PCE as a DNAPL (Carr and Hughes 1998; Carr et al. 2000; Cope and Hughes 2001; Adamson et al. 2003) or used PCE at a much lower saturation than used in the experiments reported here (Yang and McCarty 2000).

Comparison between the abiotic and biotic runs of all three columns showed that the presence of dechlorinating bacteria enhanced mass flux from the NAPL zone. Although degradation daughter products were observed in effluent of each test, the greatest contributor to increase mass flux during biotic experiments was due to a higher PCE effluent concentration than occurred in abiotic experiments. This may have been due to production of surfactants by the culture, but additional studies are necessary to verify this. Other studies have shown that microorganisms secrete surfactant or emulsifying agents when growing on NAPLs (Einsele et al. 1975). Solubilization caused by these secretions accounts for the utilization of the insoluble substrate at rates greater than their solubilities would predict (Cameotra et al. 1983; Goswami and Singh 1991).

PCE degradation in the column experiments appeared to be first order (data shown in Kaplan, 2004). Rates of PCE degradation in the columns were slower than in batch systems at

relatively low PCE concentration. This is contrary to the findings Major et al. (2002) where KB-1 was used in a field-scale application. Major et al. (2002) found that TCE degradation rates in the field were an order of magnitude higher than those found in batch microcosm studies. However, batch studies and the field study of Major et al. (2002) were conducted at significantly lower PCE concentrations than occurred in effluent from these column experiments. Therefore any inhibitory effects of high PCE concentrations were not observed.

4.5.2 Modeling of flow cell experiments

Flow cell experiments described in section 3.7 showed bioenhanced mass transfer following inoculation by a microbe culture capable of reductive dechlorination. Modeling of these experiments with a reactive-transport model of bioenhanced mass transfer was designed to (1) provide an understanding of how biodegradation enhances mass transfer from DNAPL pools and to (2) evaluate alternative conceptual models of enhanced dissolution.

Modeling Strategy. A conceptual model of bioenhanced mass transfer was developed and tested in a step-wise manner. Several methods for representing DNAPL pool morphology were evaluated during an initial simulation of a dye tracer test and abiotic dissolution test (experiment A6). Subsequent abiotic modeling of experiments with a range of pool saturations and inflow rates focused on estimation of lumped mass transfer rate coefficients (k_{La}). Information from these simulations was used to develop a Gilland-Sherwood correlation for the flow cell. The correlation was constructed from simulation results for four sets of flow cell experiments conducted at moderately high flow rates and was validated by predicting results of subsequent abiotic flow-cell experiments conducted at lower flow rates.

Simulation results for abiotic experiments were then used as a basis for simulations of experiments with bioenhanced mass transfer. The Gilland-Sherwood correlation was used in combination with estimates of degradation kinetic parameters developed previously to evaluate conceptual models of bioenhanced mass transfer. Two experiments in flow cells inoculated with the KB-1 culture were selected for simulation. The first was conducted in a flow cell with average DNAPL saturation of 0.55 and an inflow methanol concentration of 200 mg/L (experiment B1-3). No electron-donor limitation was noted in experimental results. The second was conducted in a flow cell with average DNAPL saturation of 0.25 and an inflow methanol concentration of 82 mg/L (experiment B2-3). Electron-donor limitations in this experiment resulted in lower mass transfer than observed in the first experiment.

A key objective of this study was to determine if bioenhanced dissolution could be simulated with an acceptable degree of confidence using abiotic mass transfer correlations in conjunction with estimates of biodegradation rate coefficients obtained from aqueous-phase batch and flow cell. To address this objective, initial estimates of model parameters were identified on the basis of prior information and the model was calibrated using steady-state concentrations observed in bioenhanced dissolution experiments B1-3 and B2-3. With the exception of abiotic dissolution and biodegradation parameters, most model parameters were tightly constrained by available prior information. Therefore, calibration was used to obtain improved estimates of abiotic dissolution and biodegradation parameters. Sensitivity data for the resulting calibrated models were used to evaluate parameter uncertainty in the close vicinity of

calibrated values. As described later in this section, the difference between initial estimates and calibrated values for abiotic dissolution and biodegradation parameters was small. Therefore, additional sensitivity analysis was conducted with the bioenhanced dissolution model in order to evaluate uniqueness and model robustness over a wide range of parameter values.

Modeling Abiotic Mass Transfer. Alternative representations of saturation distribution within DNAPL source zones were evaluated by simulating an abiotic experiment conducted at a flow rate of 0.084 ml/min in a flow cell designated A6. The average DNAPL saturation of the lower sand in this experiment, determined by gravimetric methods, was 0.45. However, DNAPL distribution, measured by x-ray attenuation methods, was distributed in a heterogeneous manner throughout the source zone (Figure 4.48). Thickness of the transition zone was estimated to be approximately 0.4 cm (Section 3.7.2). Dye tracer tests were conducted and progress through the flow cell was recorded photographically at regular time intervals. The photographic data were not quantitative but did show relative rates of movement along various flow paths. Transport within the DNAPL transition zone was much more rapid than rates of movement within the sand overlying the source zone. Minimal transport occurred through deeper parts of the source zone. The PCE concentration in outflow water was measured. Steady-state PCE concentrations were attained after a cumulative discharge of approximately 3 pore volumes.

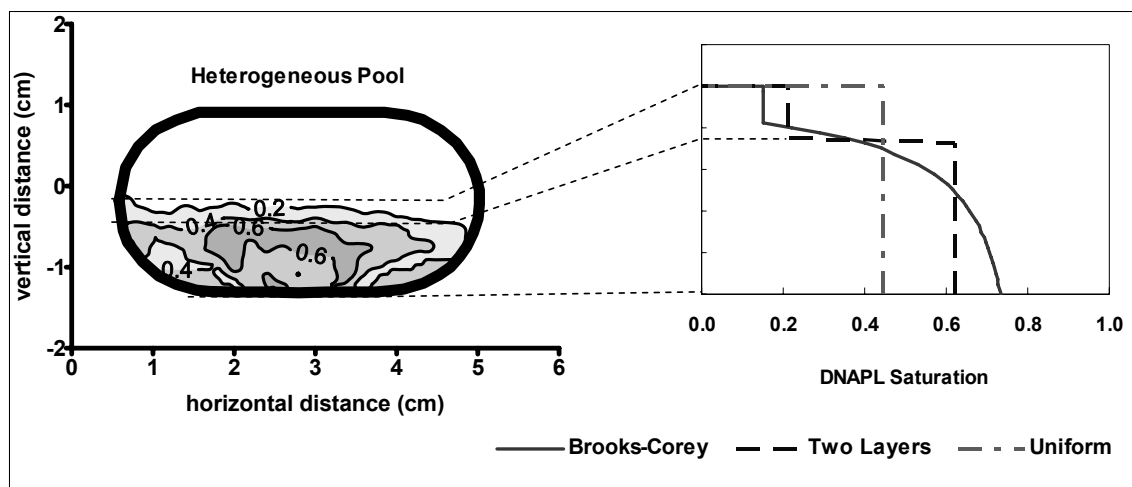


Figure 4.48. Alternative Representations of DNAPL Saturation in Flow-Cell Model of Bioenhanced Dissolution

Abiotic simulations were conducted for each of four source-zone configurations (Figure 4.48). These included: (1) a source zone with saturation that varied spatially in two dimensions (vertical and horizontal) in accordance with x-ray attenuation data, (2) a source zone with vertical heterogeneity described by fitting the Brooks-Corey equation to x-ray data, (3) a two-layer source zone with homogeneous layers representing the transition zone at relatively low saturation and the deeper part of the pool at high saturation, and (4) a source zone with homogeneous saturation. The fourth model of pool morphology is the traditional pool model with sharp boundaries.

Model calibration was attempted for each alternative with the goal of identifying the simplest model of pool saturation that successfully simulated experimental results. The lumped mass transfer rate coefficient (k_{La}) was varied during model calibration. Initial estimates of k_{La} were obtained using the Gilland-Sherwood correlation presented by Saenton (2003) for two-dimensional flow cell experiments with PCE source zones. Model node spacing was 0.2 mm x 0.1 mm x 0.1 mm. Other model parameters were not changed during calibration (Table 4.11). Because no degradation reactions were specified in this simulation, the electron-donor component of the RT3D reaction module was used to represent a conservative tracer.

Table 4.11. Parameter Estimates used in Abiotic Simulations, Flow-Cell Model of Bioenhanced Dissolution

| Parameter | Value | Basis |
|--|--|--|
| Saturated hydraulic conductivity upper sand (Unimin #50 sand) lower sand (Unimin #16 sand) | 2.82 cm/min 42.4 cm/min | Geometric mean of laboratory tests (Illangasekare et al., 1995a; Illangasekare et al., 1995b; Compos, 1998; Saba and Illangasekare, 2000; Barth et al., 2001). |
| Total porosity, DNAPL saturation, flow rate | varied by experiment | Observed experimental results |
| Relative hydraulic conductivity | $k_r = (S_e)^{\frac{2+3\lambda}{\lambda}}$ | $\lambda=1.75$, primary drainage portion of water-retention curve for Unimin #16 sand (scaled from Sakaki et al., 2005). |
| Longitudinal dispersivity | 0.03 cm | Model calibration to 2-D flow-cell dissolution experiments (Saenton, 2003) |
| Dispersivity ratio (transverse to longitudinal) | 0.1 | Model calibration to 2-D flow-cell dissolution experiments (Saenton, 2003) |
| Lumped mass transfer rate coefficient | varied by experiment | Primary calibration parameter. |
| PCE solubility limit | 170 mg/L | Observed experimental result |
| Model grid spacing | 0.02 x 0.01 x 0.01 cm | Resolution comparable to x-ray data. |

Results of conservative tracer transport simulations for each source-zone configuration were compared visually to photographic results of dye tracer tests. Simulations based on the uniform pool model were unable to reproduce the rapid migration rates observed in the upper part of the source zone with minimal transport in the lower part. Simulations based on other pool configurations were able to reproduce the observed behavior. Tracer migration for the two-layer pool model is shown in Figure 4.49.

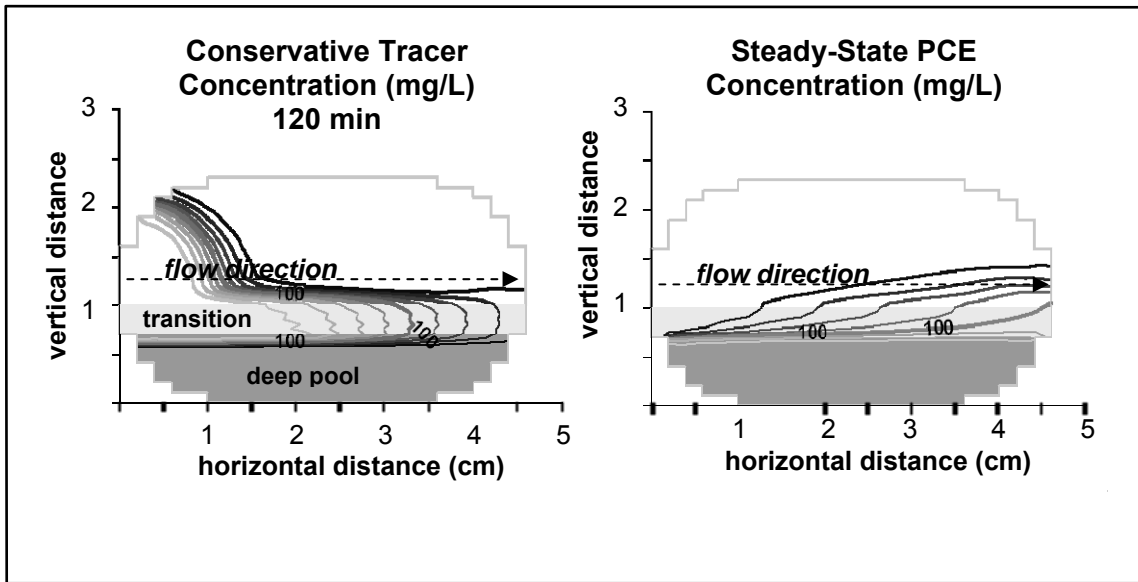


Figure 4.49. Cross Sections of Simulated Tracer Plume and PCE Plume for Abiotic Experiment A6 with Two-Layer Pool Model, Flow-Cell Model of Bioenhanced Dissolution

Simulated steady-state PCE concentration in flow-cell outflow was compared with observed outflow concentration. Changes in PCE concentration observed during the transient portions of mass transfer experiments reflected primarily initial conditions and did not provide a useful calibration criterion for estimation of k_{La} .

Several representations of DNAPL saturation provided calibrations to observed PCE concentration and mass flux within two percent of observed conditions. The simplest of these representations was the two-layer pool model (Figure 4.49). For purposes of describing DNAPL mass transfer at intermediate and field scales, a simple model of pool morphology is preferred. However, simulations with the uniform pool model consistently underestimated PCE concentration and mass flux. With this representation of DNAPL saturation, water flowed primarily through the overlying sand and PCE mass transfer occurred primarily along the upper pool boundary. In contrast, with other pool models, a much greater portion of water flowed through the upper part of the source zone and PCE mass transfer occurred throughout this region.

Simulations were undertaken for 11 additional abiotic flow-cell experiments described in Section 3.7.2 of this report in order to develop an abiotic Gilland-Sherwood correlation for the flow cell. These experiments were conducted at average source-zone saturations of 0.30, 0.45 and 0.67, and flow rates of 0.084, 0.168 and 0.253 mL/min. All simulations were based on the two-layer source-zone morphology. In each case, calibration consisted of varying k_{La} until a suitable match was obtained to observed steady-state PCE mass load in flow-cell outflow (Figure 4.50).

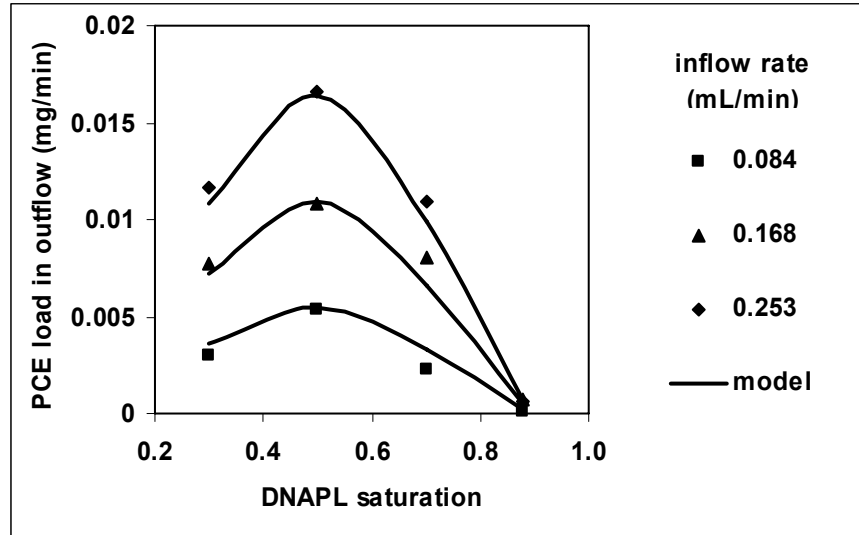


Figure 4.50. Comparison of Simulated and Observed PCE Mass Load for Abiotic Experiments, Flow-Cell Model of Bioenhanced Dissolution

Results of model simulations of abiotic dissolution experiments were used to calculate values of Sherwood number, Reynolds number and DNAPL saturation for the transition zone of each dissolution experiment. For the experimental conditions of the flow cell, many of the parameters in the Gilland-Sherwood correlation of Saenton (2003) remain constant. Therefore, a simplified form of the Gilland-Sherwood correlation was used in a multivariate regression analysis to provide the following result:

$$Sh = 1.77 \times 10^5 (Re)^{1.01} \left(\frac{\theta_N}{\phi} \right)^{6.51} \quad (4.21)$$

Lumped mass transfer rate coefficients (k_{La}) calculated by Equation 4.21 were compared with those calculated by other published Gilland-Sherwood correlations for the experimental conditions used in the flow-cell dissolution experiments. Coefficients calculated by Equation 4.21 consistently were greater than those calculated by correlations of Saba and Illangasekare (2000), and Saenton (2003), but were less than those calculated by the correlation of Nambi and Powers (2003) (Figure 4.51). The published correlations were all developed from flow-cell experiments with a DNAPL source embedded within a two-dimensional flow system. The wide variation in calculated values of k_{La} demonstrates the empirical nature of Gilland-Sherwood correlations.

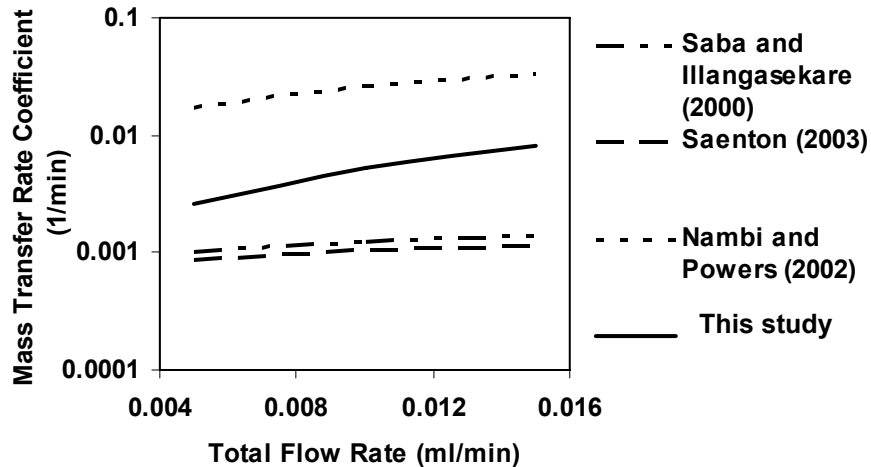


Figure 4.51. Comparison of Gilland-Sherwood Correlations for Flow-Cell Experiments with an Average Source Zone Saturation of 55 Percent, Flow-Cell Model of Bioenhanced Dissolution

Validity of the correlation given in Equation 4.21 was assessed by modeling abiotic experiments conducted in conjunction with biotic flow cell experiments described in later sections of this paper. Inflow solution for experiments used in fitting Equation 4.21 was de-ionized water. In contrast, the validation tests were conducted used an inflow solution of KB-1 growth medium and a specified concentration of methanol. Flow rates for the validation tests also were lower than those used in developing the Gilland-Sherwood correlation. Protocols for conducting the validation simulations were the same as those described previously. Equation 4.21 was used to estimate values of k_{La} appropriate to conditions of the validation experiments. Simulation results matched observed PCE concentration and mass flux when the mass transfer rate coefficient was adjusted slightly upward, well within the 95 percent confidence region associated with the Gilland-Sherwood correlation. Because simulations matching observed conditions could be obtained with small adjustments in k_{La} from those predicted by Equation 4.21, the flow-cell specific Gilland-Sherwood correlation was judged to be effective for a broader set of conditions than was used in correlation development.

Modeling Bioenhanced Mass Transfer. Two experiments in flow cells inoculated with the KB-1 culture were selected for simulation (Table 4.12). Mass transfer during the first, experiment B1-3, was strongly enhanced by biological activity but showing no effect of electron-donor limitation. Mass transfer during the second, experiment B2-3, was not as strongly enhanced by biological activity. While the two experiments were conducted at different DNAPL pool saturations, experimental results for the second suggested that DNAPL mass transfer was affected by low methanol concentration in inflow water which limited biodegradation of PCE.

Table 4.12. Experimental Conditions Used in Flow-Cell Model of Bioenhanced Mass Transfer

| Condition | Experiment B1-3 | Experiment B2-3 |
|---------------------------------|--------------------|--------------------|
| Average saturation | | |
| Transition zone | 0.31 | 0.17 |
| Deep pool | 0.62 | 0.57 |
| Entire source zone | 0.55 | 0.25 |
| Total porosity | 0.37 | 0.40 |
| Volume (mL) | | |
| Upper sand | 13.1 | 12.9 |
| Transition zone | 0.2 | 2.5 |
| Deep pool | 3.5 | 1.4 |
| Inflow | | |
| Flow rate (ml/min) | 0.008 | 0.025 |
| Methanol concentration (mmol/L) | 6.24 | 2.56 |
| Outflow | | |
| PCE (mmol/L) | 0.00603 | 0.144 |
| TCE (mmol/L) | 0.0982 | 0.0342 |
| DCE (mmol/L) | 2.088 | 0.375 |

Simulations were conducted with the two-layer model of DNAPL source zone morphology (transition and high-saturation zones), as well as the model based on Brooks-Corey morphology. Results of the two sets of simulations were very similar. Therefore, results are shown only for the simpler two-layer model.

Initial estimates of hydrodynamic and abiotic dissolution parameters were based on parameter estimates obtained in prior laboratory tests as well as estimates that proved successful in simulating abiotic dissolution (Table 4.13). Saturated hydraulic conductivity for each layer in the model was estimated as the geometric mean of values for Unimin #16 and #50 sand measured in laboratory experiments and estimated in flow-cell models (Illangasekare et al., 1995a; Illangasekare et al., 1995b; Compos, 1998; Saba and Illangasekare, 2000; Barth et al., 2001, Sakaki and Illangasekare, 2006). Total porosity and average DNAPL saturation in the source zones were known from gravimetric measurements during sand packing of the flow cell and prior laboratory tests (Illangasekare et al., 1995a; Sakaki and Illangasekare, 2006). In both experiments, The Brooks-Corey equation was used to estimate saturation distributions based on measured DNAPL injection volumes and values of Brooks-Corey parameters obtained for Unimin #16 sand. The saturation distribution was then used to estimate effective porosity and relative hydraulic conductivity. Dispersivity coefficients were selected to be consistent with the abiotic flow-cell simulations. Mass transfer rate coefficients were estimated on the basis of the Gilland-Sherwood correlation using experimental conditions appropriate to B1-3 and B2-3.

Table 4.13. Prior Information for Parameters of Flow-Cell Model of Bioenhanced Dissolution

| Parameter | Mean | Standard Deviation | Coefficient of Variation (percent) |
|---|---------|--------------------|------------------------------------|
| Porosity, #16 | 0.44 | 0.029 | 6.56 |
| Porosity, #50 | 0.34 | 0.023 | 6.79 |
| Saturated hydraulic conductivity, #16 (cm/min) | 42.4 | 8.78 | 20.7 |
| Saturated hydraulic conductivity, #50 (cm/min) | 2.82 | 0.573 | 20.3 |
| Residual water saturation, #16 | 0.065 | 0.003 | 4.44 |
| $\log[\alpha_0]$ | 5.2470 | 0.2316 | 4.41 |
| α_1 | 1.0054 | 0.0327 | 3.25 |
| α_3 | 6.5059 | 0.3701 | 5.69 |
| k_{La} , transition zone, exp B1-3 | 0.0186 | 0.0146 | 78.4 |
| k_{La} , transition zone, exp B2-3 | 0.00636 | 0.00499 | 78.4 |
| First-order degradation rate coefficient, K_{pce} (1/min) | 0.009 | 0.0073 | 81.1 |
| Ratio of degradation rate coefficients, K_{tce}/K_{pce} | 1.75 | 0.722 | 41.2 |
| ζ_a | 2.052 | 0.199 | 9.69 |

References provided in text.

Effective porosity and relative hydraulic conductivity estimates were not adjusted for effects of biomass clogging. No evidence of clogging was observed during the experiments. Several models of hydraulic-conductivity reduction were applied to flow-cell experimental conditions (Figure 4.52). At the measured biomass concentration of 6×10^{-5} mg C / mg soil, results suggested that effects of bio-clogging were minor. For the colony model of Thullner et al. (2002a and 2002b), biomass may have decreased hydraulic conductivity by approximately 30 percent while results for all other models suggest decreased hydraulic conductivity of 10 percent or less. Because this decrease is less than the uncertainty in hydraulic conductivity, effects of bio-clogging were neglected.

The number of biodegradation model parameters is large. It includes Monod kinetic parameters for PCE, electron donor and each degradation daughter product, as well as reaction stoichiometric coefficients and parameters for electron donor fermentation-loss, biomass growth yield, and decay rate. With such a large number of parameters, meaningful model development relied on prior information to decrease the number of calibration parameters to a minimum. Reasonable constraints on estimates of biodegradation parameters also were consistent with the focus of the study – determining if bioenhanced mass transfer could be estimated on the basis of abiotic Gilland-Sherwood correlations.

Each flow-cell experiment was conducted for the time required to accumulate 20 pore volumes (approximately 5 to 16 days depending on flow rate). Data were not available to evaluate biomass growth during this time period. Therefore, biomass growth was not simulated. Biomass yield coefficient and decay rate were set to zero.

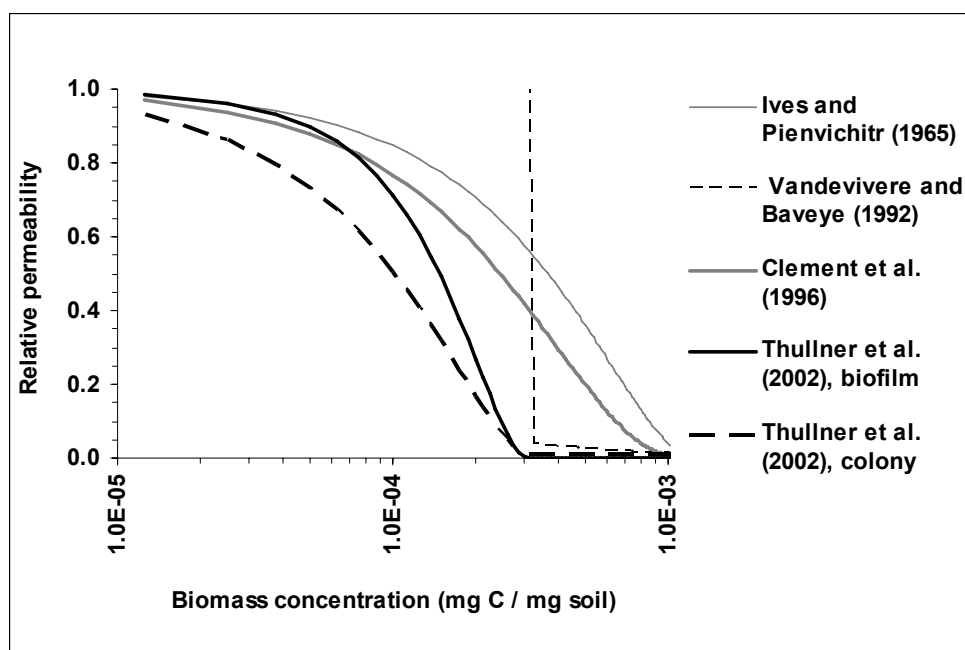


Figure 4.52. Relative Permeability as a Function of Biomass Concentration for Several Biomass-Clogging Models

Empirical stoichiometric coefficients for dechlorination were determined by adjusting methanol utilization data for mixing limitations imposed by hydrodynamics of the flow cell. Abiotic model results indicate that 52 percent of water entering a flow cell moved along flow paths where PCE was present. Methanol that did not mix with PCE was not available to support dechlorination. Therefore, available methanol load was calculated by adjusting inflow methanol load by a factor of 0.52. Results were compared with the PCE degradation product load in flow-cell effluent (Figure 4.53a). Available methanol concentration was calculated by dividing available methanol load by simulated flow rate along paths where PCE was present.

The relationship of PCE degradation product load and available methanol concentration shows three distinct regions (Figure 4.53b). At methanol concentration greater than 3 mmol/L there is no relationship between methanol available for degradation and degradation-product load. In this region, degradation is not limited by the available supply of methanol. The second, at methanol concentrations of 2 to 3 mmol/L, shows a strong linear relationship between available methanol and degradation-product load, suggesting a stoichiometric limitation rather than a rate limitation. The empirical stoichiometric coefficient relating electron acceptor utilization to electron-donor consumption (ζ_a) is given by the slope of this linear relationship. Regression analysis of the linear region shows that 2.1 mmol of degradation product are formed for a unit increase in available methanol. At methanol concentrations less than 2 mmol/L, very limited data suggest that slope decreases with decreasing methanol supply. Therefore, in this range, the rate of TCE and DCE production may be related to methanol concentration.

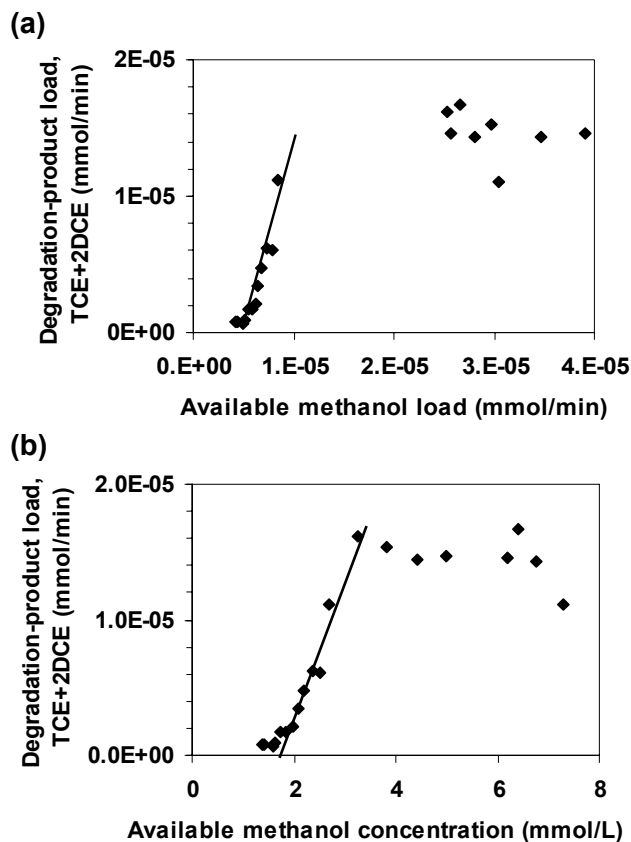


Figure 4.53. Relationship of Degradation-Product Load to (a) Available Methanol Load and (b) Available Methanol Concentration, Flow Cell Experiments of Bioenhanced Dissolution

The RT3D reaction module used in this study does not implicitly simulate methanol fermentation to create H_2 or electron transfer of H_2 to PCE to create TCE. Fermentation to create H_2 can occur by several pathways resulting in loss of reducing power to many reaction byproducts. Nevertheless, the slope obtained by linear regression analysis is consistent with a reaction stoichiometry dominated by methanol fermentation to create formate and H_2 , coupled with electron transfer of H_2 to a chlorinated ethene.

The presence of a non-zero intercept in the linear relationship shown in Figure 4.53 suggests that loss of electron donor due to processes not linked to dechlorination may limit mass transfer or dechlorination at low methanol load. No prior information was available to constrain parameter estimates associated with electron-donor fermentation and loss (Equation 6.11). However, information in Figure 4.52 and Table 4.12 was used to provide an initial estimate for the Monod coefficient ($\tilde{\mu}_m$) equal to 0.3 mg/L/min. This parameter was varied during calibration. The half saturation coefficient (K_{sd}) was set to a low value (0.1 mg/L), resulting in simulation of electron-donor loss and fermentation as a zero-order process. A more complex description of the process is not warranted with existing information.

Estimation of $\tilde{\mu}_m$ was accomplished in the following manner. Figure 4.52 data indicate that the minimum inflow methanol concentration for PCE degradation is 1.81 mmol/L. Using the stoichiometric coefficient for dechlorination estimated previously ($\zeta_a=2.1$), outflow TCE and DCE data for experiment B2-3 (Table 4.12) indicate that 0.37 mmol/L of available methanol was used for dechlorination and 2.19 mmol/L was lost to other processes. The presence of significant PCE in outflow for experiment B2-3 suggests that methanol was not available for degradation in some portion of the flow cell where PCE dissolution was occurring. Nevertheless, a lower limit for $\tilde{\mu}_m > 0.29$ mg/L/min was estimated by assuming that methanol was lost throughout the flow cell and followed a zero-order process.

Data for aqueous-phase PCE degradation by KB-1 have been obtained from batch and porous-media flow-cell experiments (Section 3.7). Within the range of PCE concentration tested (2 to 25 mg/L), degradation followed a first-order rate law with a rate coefficient of 2.55×10^{-5} mg PCE / mg C / min. Biodegradation data for KB-1 are consistent with the Monod model that Nielsen and Kiesling (1999) fit to kinetic data for another mixed culture capable of reductive dechlorination. The Nielsen-Kiesling model is approximately first-order for PCE concentrations less than 50 mg/L. Biodegradation rate data are not available to evaluate KB-1 behavior as PCE concentration approaches solubility. While this may provide justification for using the Nielsen-Kiesling parameter estimates for μ_m and K_{sa} in Equation 6.9, there was little practical need. Initial simulations with the Nielsen-Kiesling parameters showed that simulated concentration of PCE in areas of the flow cell where degradation occurred generally was less than 50 mg/L. Therefore, later simulations were conducted by setting K_{sa} to a large value relative to PCE concentration and setting μ_m such that PCE degradation was modeled as a first-order process. The effective rate coefficient initially was estimated from KB-1 degradation tests and was treated as a calibration parameter.

Kinetic data for KB-1 at μM concentrations suggest that TCE degradation rates for TCE may be 2 to 3 times PCE degradation rates (Duhamel et al., 2002; Major et al., 2002). Because data for TCE in the mmol/L range were not available, Monod coefficients for TCE degradation initially were set equal to those for PCE degradation. The TCE degradation coefficient was treated as a calibration parameter.

Data were not available to estimate the half-saturation coefficient for electron donor (K_{sd}) during dechlorination. However, comparing methanol concentration in experiment B1-3 (6.24 mmol/L) with Figure 4.53b suggested that degradation was not limited by electron donor supply. Therefore, initial simulations of this experiment were conducted by removing electron donor limitations. This tactic proved to be unsuccessful because it permitted PCE degradation to occur throughout the entire depth the DNAPL source zone. As a result, concentration of degradation daughter products in outflow was larger than observed and mass transfer was enhanced to an unrealistic degree. Because Figure 4.53 suggests that PCE degradation is limited at methanol concentrations less than approximately 2mmol/L, subsequent simulations were conducted by setting K_{sd} to a value of 0.03 mmol/L (1mg/L). In this manner, degradation of PCE or TCE was possible only when electron donor was present in a model node. The value of K_{sd} was refined during simulation of experiment B2-3.

A review of coefficients of variation for initial estimates provided in Table 4.13 shows that most model parameters were strongly constrained by prior information. Large coefficients of variation are noted for the mass transfer rate coefficient, PCE degradation rate coefficient and the

ratio of TCE to PCE degradation rate coefficients. Therefore, these three parameters were treated as calibration parameters.

Simulation of experiment B1-3 based on initial estimates of model parameters underestimated observed steady-state mass flux by approximately 8 percent. Differences between simulated and observed concentrations were distributed approximately equally between TCE and DCE. The close comparison between simulated and observed results suggests that the conceptual model of bioenhanced dissolution provided a good representation of actual conditions. An improved match to observed results with less than 3 percent error in mass flux was possible by decreasing the mass transfer rate coefficient a small amount relative to the standard deviation of the initial estimate (Table 4.14). This result supports the hypothesis that a Gilland-Sherwood correlation developed for abiotic conditions provides an appropriate model of DNAPL mass transfer during biodegradation of PCE. Adjusting the PCE and TCE degradation rates from initial estimates did not significantly improve the calibration.

Sensitivity data for the calibrated model of experiment B1-3 are provided in Table 4.15. The model is highly sensitive to variations in the mass transfer rate coefficient and less sensitive to variations in biodegradation rate coefficients. The low sensitivity of the model to degradation rates is consistent with the idea that biodegradation did not limit mass transfer in experiment B1-3.

The calibrated model demonstrates that bioenhanced dissolution can be simulated with an acceptable degree of confidence using abiotic mass transfer correlations in conjunction with estimates of biodegradation rate coefficients obtained from aqueous-phase batch and flow cell. Differences between initial estimates and calibrated values for abiotic dissolution and biodegradation parameters were small. However, additional sensitivity analysis was conducted with the bioenhanced dissolution model in order to evaluate model uniqueness and robustness over a wide range of parameter values. Results of this analysis are presented as plots relating sum of squared residuals to parameter values (Figures 4.54 and 4.55). Residuals are calculated as the difference between simulated and observed concentration for each chlorinated ethene chemical. The sum of squared residuals provides a metric for assessing model match to individual chlorinated ethene compounds as well as overall mass flux of ethenes.

Table 4.14. Values for Calibration Parameters in Bioenhanced Dissolution Model of Flow-Cell Experiment B1-3

| Parameter | Calibrated Value | Calibrated Minus Initial Value (percent of standard deviation of prior information) |
|--------------------|------------------|---|
| k_{La} , (1/min) | 0.0146 | 27.4 |
| Kpce (1/min) | 0.009 | 0 |
| Ktce/Kpce | 0.5 | 173 |

Table 4.15. Sensitivity Coefficients for Calibration Parameters in Bioenhanced Dissolution Model of Flow-Cell Experiment B1-3

| Model Component or Characteristic | Scaled Sensitivity Coefficient with Respect to Model Parameter (dimensionless) | | |
|-----------------------------------|--|-----------|---------------------|
| | k_{La} | K_{pce} | K_{tce} / K_{pce} |
| PCE concentration | 0.996506 | -1.42326 | 0.013711 |
| TCE concentration | 0.69661 | 0.185031 | -1.2514 |
| DCE concentration | 0.405821 | 0.265697 | 0.045906 |
| Mass flux of total ethene | 0.423254 | 0.251758 | -0.01633 |
| Methanol concentration | -0.33716 | -0.21534 | -0.01139 |
| Residual of total ethane | -0.93689 | -0.55728 | 0.036151 |
| Standard error of model | -0.45691 | -0.31191 | -0.10431 |

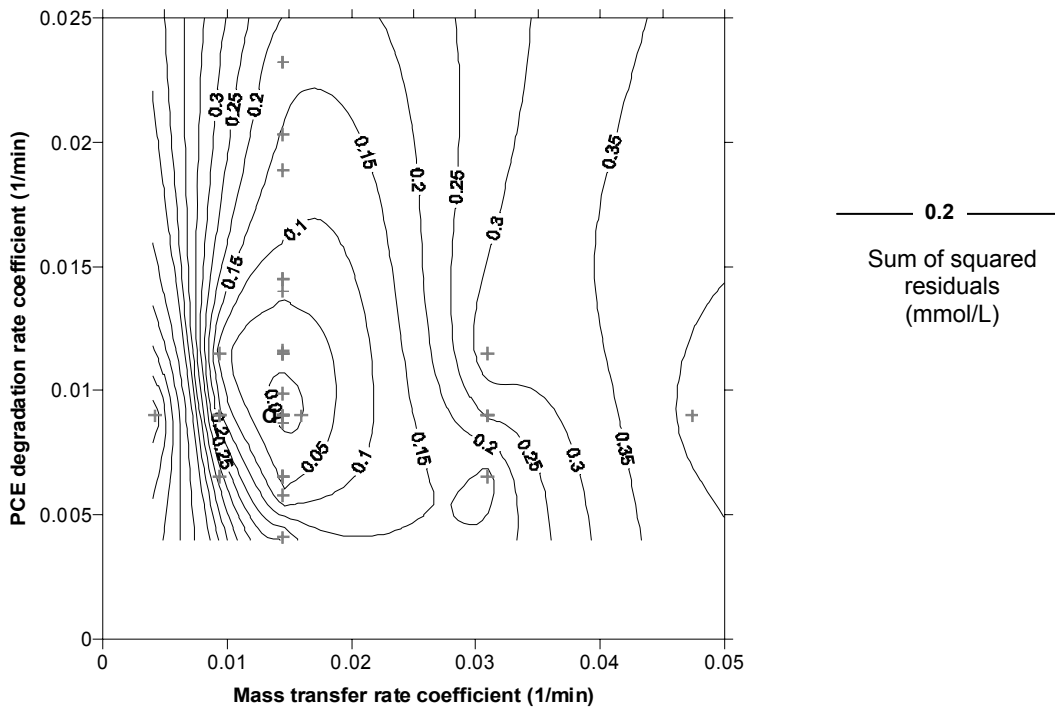


Figure 4.54. Relationship of Sum of Squared Residuals to Mass Transfer Rate Coefficient and PCE Degradation Rate Coefficient, Bioenhanced Dissolution Model of Flow-Cell Experiment B1-3

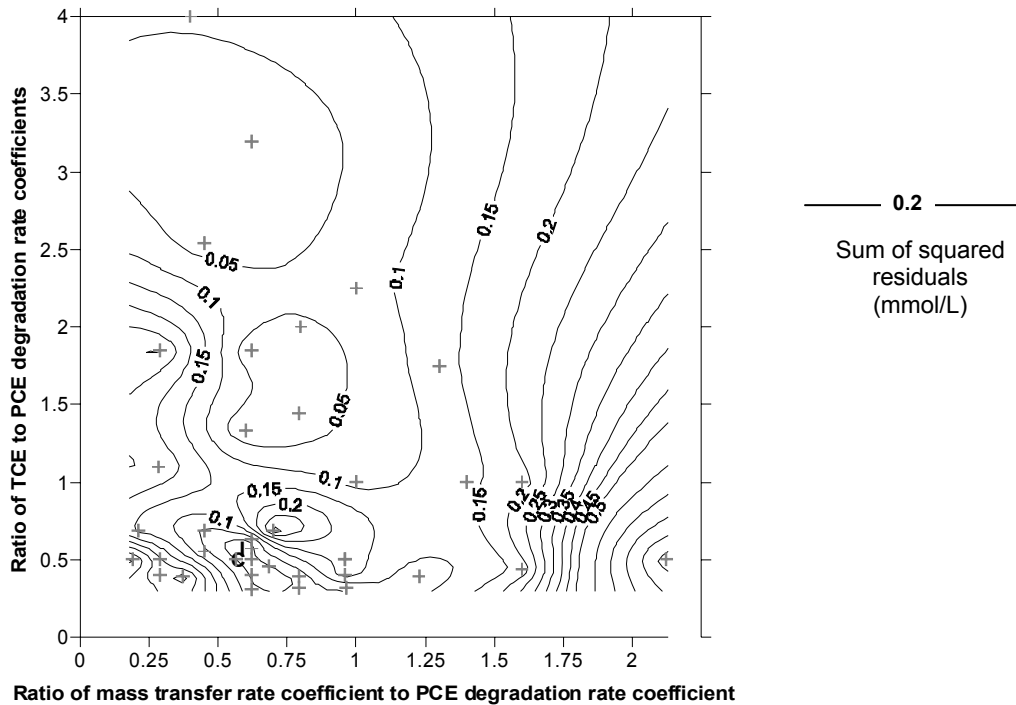


Figure 4.55. Relationship of Sum of Squared Residuals to Calibration Parameter Ratios, Bioenhanced Dissolution Model of Flow-Cell Experiment B1-3

The plot of sum of squared residuals as a function of the mass transfer rate coefficient (k_{La}) and PCE degradation rate coefficient (K_{pce}) shows a single minimum centered at the calibrated values (Figure 4.54). The plot location corresponding to the initial parameter estimates is near the surface minimum. Globally, the model is more sensitive to variations in k_{La} than it is to variations in K_{pce} .

In order to illustrate effects of all three calibration parameters on model response, sum of squared residuals is plotted as a function of parameter ratios (Figure 4.55). This plot shows several minima located at approximately the same value of K_{pce}/k_{La} but at different values of K_{tce}/K_{pce} . This suggests that simulated mass flux is sensitive to the K_{pce}/k_{La} ratio but is insensitive to the value of K_{tce} .

Simulation of experiment B2-3 based on initial estimates of model parameters underestimated observed conditions by approximately 32 percent. Simulated DCE was significantly less than observed DCE while TCE was overestimated and PCE was slightly underestimated. Several calibration parameters were adjusted in an effort to match observed outflow concentrations of PCE, TCE and DCE. Increasing the TCE degradation parameter (K_{tce}) by a factor of 2 provided a value of K_{tce} that is consistent with prior information, as well as providing simulated TCE-DCE concentration ratios that were consistent with observations. Varying other parameters in the Monod expression for dechlorination (μ_m and K_{sd} for PCE degradation; K_{sd} for TCE degradation, and K_{sa}) within reasonable ranges did not decrease simulation residuals. Increasing the Monod coefficient for electron-donor loss ($\tilde{\mu}_m$) without

concurrent adjustment of other parameters shifted the PCE-DCE concentration ratio to match the observed ratio but did not improve match to total mass flux.

An acceptable match was obtained by increasing both $\tilde{\mu}_m$ and the lumped mass transfer rate coefficient (k_{La}). The calibrated estimate of $\tilde{\mu}_m = 0.6$ is 2 times the initial estimate, a reasonable adjustment given the large uncertainty associated with the initial estimate. The calibrated estimate of k_{La} represents a 66 percent increase from the value predicted by the abiotic Gilland-Sherwood correlation but well within the 95 percent confidence limit of the relationship. The small adjustment needed in k_{La} supports the hypothesis that a Gilland-Sherwood correlation developed for abiotic conditions provides an appropriate model of DNAPL mass transfer during biodegradation of PCE.

Sensitivity data for the calibrated model of experiment B2-3 are provided in Table 4.16. The model is sensitive to variations in the electron-donor loss coefficient ($\tilde{\mu}_m$) and the mass transfer rate coefficient. It is less sensitive to variations in biodegradation rate coefficients. The high sensitivity of the model to the electron-donor loss coefficient ($\tilde{\mu}_m$) is consistent with the idea that mass transfer was electron-donor limited in experiment B2-3.

Table 4.16. Sensitivity Coefficients for Calibration Parameters in Bioenhanced Dissolution Model of Flow-Cell Experiment B2-3

| Model Component or Characteristic | Scaled Sensitivity Coefficient with Respect to Model Parameter (dimensionless) | | | |
|-----------------------------------|--|---------|-------------|-----------------|
| | k_{La} | Kpce | Ktce / Kpce | $\tilde{\mu}_m$ |
| PCE concentration | 6.48055 | 4.66504 | 5.07064 | 9.22846 |
| TCE concentration | 1.95339 | 1.54063 | 0.30446 | 0.66404 |
| DCE concentration | -1.3973 | -1.5609 | -1.6266 | -3.9987 |
| Mass flux of total ethene | 0.03431 | -0.3949 | -0.4796 | -1.6685 |
| Residual of total ethane | -0.018 | 0.20772 | 0.25227 | 0.87773 |
| Standard error of model | 0.3039 | 0.25943 | 0.28571 | -0.2961 |

Calibrated model results for both experiments provided insight to the process of bioenhanced dissolution. Most dissolution and biodegradation of PCE in the simulated experiments using calibrated parameter estimates occurred within the DNAPL pool transition zone (Figure 4.56). High DNAPL saturation in deeper portions of the pool decreased hydraulic conductivity and limited migration of methanol. Lacking adequate electron donor to support reductive dehalogenation, biodegradation was limited to the transition zone. Within the transition zone, degradation rates were sufficient to decrease bulk aqueous PCE concentration 1 to 2 orders of magnitude from the concentration that occurred in abiotic systems. As a result, mass transfer was enhanced.

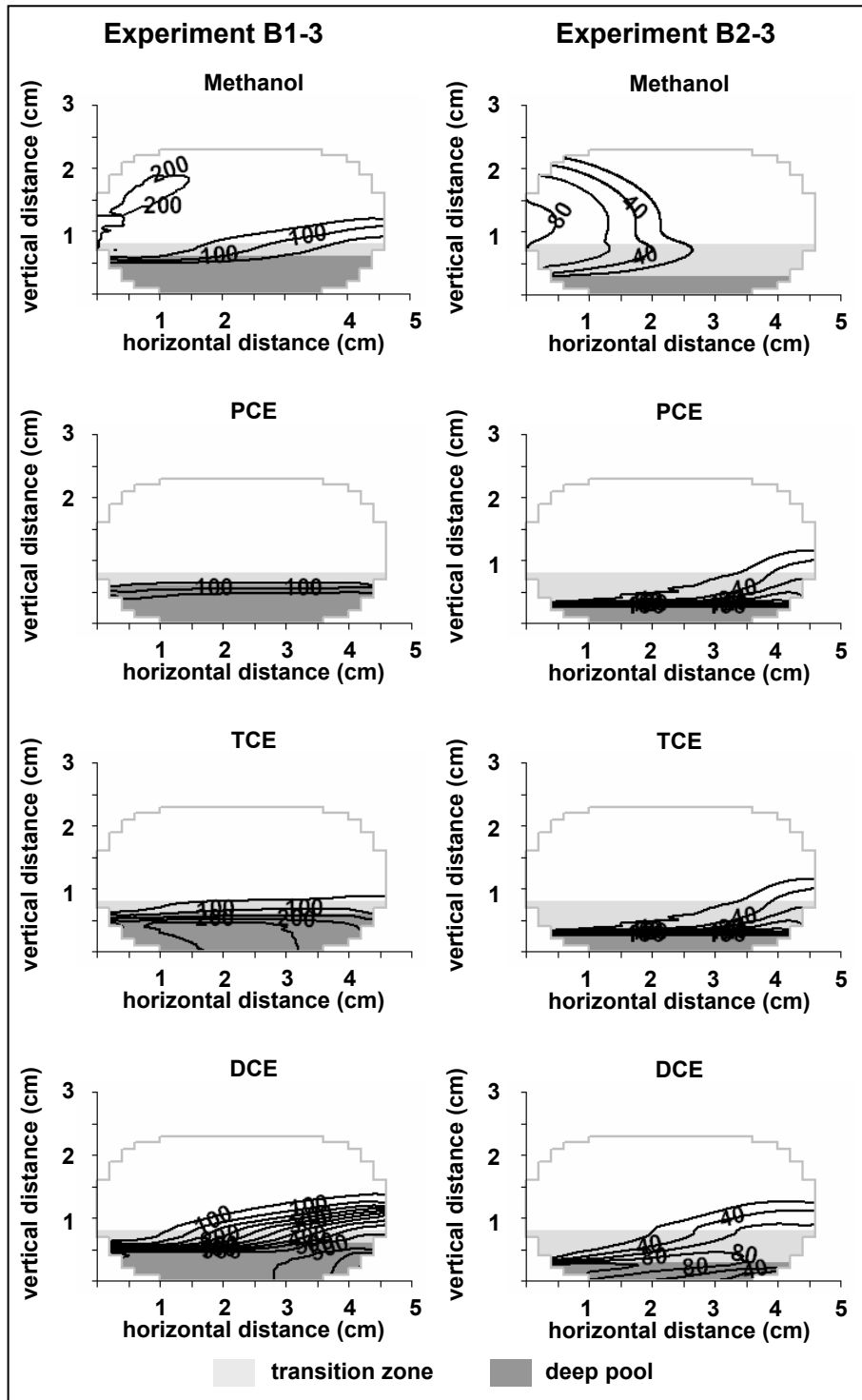


Figure 4.56. Simulated Steady State Concentration Profiles (mg/L), Flow-Cell Model of Bioenhanced Dissolution.

Active biodegradation occurred throughout the transition zone in the simulation of experiment B1-3 but only in the upstream portion of the transition zone in experiment B2-3. Differences in sites of active biodegradation are a direct result of electron-donor availability. In experiment B1-3, methanol loading was sufficient to permit transport throughout the transition zone. As a result, PCE biodegradation decreased bulk aqueous phase PCE concentration, increased dissolution gradients and enhanced mass transfer throughout the transition zone. In contrast, methanol loading in B2-3 was lower than in B1-3. In this case, PCE degradation occurred primarily in the upstream portion of the transition zone. Dissolution gradients and mass transfer also were enhanced solely in the upstream portion of the transition zone. Essentially abiotic mass transfer occurred in downstream portions of the transition zone.

Key Simulation Results. A conceptual model of PCE mass transfer from DNAPL pools has been evaluated by simulating mass-transfer experiments in flow cells containing a high-saturation PCE-DNAPL source zone. Simulation results have provided several insights to conditions and reactive-transport processes that promote bioenhanced mass transfer from DNAPL pools. Key simulation results follow.

1. Bioenhanced dissolution from pools occurs primarily as a result of PCE degradation within saturation-transition zones at pool boundaries. Degradation lowers aqueous PCE concentration near pore-scale DNAPL-water interfaces, increases dissolution gradients and thereby enhances mass transfer.
2. Descriptions of pool morphology accounting for transition zones are needed to adequately model bioenhanced mass transfer. Representing a pool as a zone of uniform saturation with sharp boundaries is not sufficient to reproduce experimental results. While it is important to recognize pool transition zones as distinct from very high saturation portions of pools, it is less important to represent saturation heterogeneity in great detail.
3. Biological enhancement is limited by electron-donor supply within the transition zone. In heterogeneous media with pools that do not completely saturate high-permeability zones, electron-donor transport through transition zones occurs by advection. Electron donor entering a transition zone at the upstream end of a pool mixes with PCE dissolving from DNAPL. In the presence of a suitable microbial culture, degradation occurs and electron-donor supply decreases in downstream portions of the pool. If electron donor is depleted, degradation can not occur. Consequently, enhanced dissolution may occur solely within upstream portions of a pool with essentially abiotic dissolution occurring in downstream portions.
4. Systematic evaluation of model parameters, at least at the flow-cell scale, can lead to reasonable predictions of bioenhanced mass transfer. Specifically, lumped mass transfer rate coefficients (k_{La}) estimated with appropriate abiotic Gilland-Sherwood correlations can be used to represent DNAPL dissolution during biological activity. Biodegradation kinetic parameters obtained from aqueous-phase batch and/or flow-cell tests can be used to represent biodegradation in the close vicinity of DNAPL.

The conceptual model of bioenhanced mass transfer from DNAPL pools presented in this report emphasizes the importance of pool transition zones. In heterogeneous media, pools of DNAPL such as PCE with density significantly greater than water, tend to form as multiple thin

zones (Illangasekare et al., 1995a). At field scales, source-zone characterization of such a DNAPL can represent a difficult challenge. The conceptual model of bioenhanced mass transfer further highlights the importance of meeting this challenge. Clearly, detailed mapping of thin pool-transition zones over wide areas will not be a practical solution in the foreseeable future. Modeling approaches will be needed that recognize the competing needs to aggregate information at larger scales while providing physically meaningful description of processes within transition zones.

Processes leading to bioenhanced mass transfer in pool transition zones are essentially the same as those leading to enhanced dissolution from DNAPL sources at residual saturation. The simulations presented in this study suggest that data needed to parameterize these processes are minimal. Data needs include information typically available to characterize a groundwater flow system and abiotic dissolution prior to remediation. Descriptions of lumped mass transfer rate coefficients developed from pre-remediation data are applicable to mass transfer during bioremediation. If estimated from an abiotic Gilland-Sherwood correlation that was developed from laboratory data, scaling issues addressed in applying the result to field problems of abiotic dissolution are the same issues that would apply to field problems of bioenhanced dissolution.

Similarly, information needed to characterize biodegradation kinetics of plume remediation is the same information that would be needed to characterize source-zone bioremediation. Aqueous-phase kinetic testing by batch, column and flow-cell techniques typical is conducted to account for site-specific characteristics that could affect plume bioremediation. While aqueous-phase concentrations in source zones may differ from those of downstream plumes, simulation results presented in this study suggest that testing of this type also is sufficient to characterize biological processes in the vicinity of DNAPL.

Concentrations of PCE and degradation products in downstream plumes often are very low and biokinetic testing may focus on degradation behavior when supply of these chemicals is limiting. In contrast, supply of PCE is less likely to limit degradation rates in DNAPL source zones. Supplying adequate electron donor to sustain active biodegradation is likely to be a challenge. Heterogeneous source-zone architecture may divert electron donor from entrapped DNAPL, and methanogenesis or other processes upstream of source zone may result in loss of electron donor. Therefore, characterization of biokinetic behavior in source zones will require that greater attention be placed on electron-donor limitations during biokinetic testing.

Adapting the conceptual model to field-scale problems will require that several challenges be addressed. Nevertheless, linking biodegradation to abiotic dissolution within pool-transition zones provides a straightforward description of bioenhanced mass transfer that builds directly on information needed for source-zone characterization. Additional data needs related to biodegradation processes are essentially the same as data needed for application of biotechnologies to aqueous-phase plume remediation.

4.5.3 Modeling of large-tank experiments

Simulations at flow-cell scales suggested that bioenhanced dissolution from DNAPL pools can be modeled by coupling abiotic dissolution with aqueous-phase biodegradation. In this section of the report the bioenhanced dissolution model is extended to intermediate scales.

Techniques for modeling abiotic dissolution at intermediate and field scales, based on a scale-dependent Gilland-Sherwood correlation (Saba and Illangasekare, 2000; Saenton and others, 2002), are used to simulate abiotic dissolution experiments in the CF tank. Detailed description of these experiments was provided in section 3.7.3 of this report. Aqueous-phase biodegradation is then modeled as a local-scale process using estimates of kinetic parameters derived at batch and flow-cell scales. Finally, a method for upscaling the model of bioenhanced dissolution is demonstrated.

Groundwater Flow and Abiotic Dissolution. Steady-state simulation of abiotic dissolution experiments in the CF tank required iteration between flow and solute transport models in an effort to match both observed head and PCE aqueous-phase concentration distributions. Parameter estimates for groundwater flow and abiotic solute transport were obtained directly from test data and are summarized in Table 4.17. Hydraulic conductivity was modeled with a single value for each sand type and was treated as the sole calibration parameter for groundwater-flow simulation. Effective porosity and longitudinal dispersivity were estimated from results of tracer tests and were not varied during calibration. The ratio of transverse to longitudinal dispersivity was assumed to be 0.1 in accordance with ratios used successfully in tank experiments with similar sands (Barth et al., 2001; Fernandez-Garcia et al., 2002; Moreno-Barbero, 2005). Mass transfer rate coefficients were estimated on the basis of the Gilland-Sherwood correlation given in equation 3.16. Initial estimates of the correlation coefficients $\alpha_0, \alpha_1, \alpha_2, \alpha_3$ were obtained from a calibrated model of PCE dissolution experiments with high-saturation sources (Saenton, 2003). The rationale for treating these coefficients as calibration parameters is provided below.

Simulations of abiotic dissolution in small flow cells indicated that the distribution of DNAPL saturation within a pool could be represented adequately by accounting for vertical variations in saturation while averaging horizontal variations. At a minimum, successful model calibration required that flow-cell source zones be represented as two homogeneous layers; one with high DNAPL saturation and an overlying layer representing the pool transition zone with DNAPL near residual saturation. Representing source-zone heterogeneity in greater detail did not significantly improve the quality of calibration. Representing the pool as a single homogeneous region of high saturation did not result in adequate calibration. Moreno-Barbero (2005) represented source-zone DNAPL morphology by a similar set of horizontal layers (residual zone, transition zone, and deep pool) when modeling partitioning tracer tests conducted in two-dimensional flow cell experiments.

Consistent with this conclusion, the source zones in the CF tank were represented in flow and solute transport simulations as varying solely in the vertical direction as shown in Figure 3.107. Effective porosity and hydraulic-conductivity estimates for the source zone also were varied solely in the vertical direction. Effective-porosity profiles were obtained by adjusting effective porosity obtained from tracer tests (Table 4.17) in accordance with the saturation profiles given in Figure 3.107. Relative hydraulic conductivity profiles were obtained by fitting the Brooks-Corey retention function (Corey, 1994) to the average saturation profiles and using the resulting estimate of pore-size distribution parameter in the Corey relative permeability equation.

Table 4.17. Parameter Estimates Used to Simulate Groundwater Flow and Abiotic Dissolution in the CF Tank, Large Tank Experiments of Bioenhanced Dissolution

| Parameter | Value |
|---|-----------|
| Model node spacing, Δz , Δx , Δy (cm) | 1 x 2 x 5 |
| Saturated hydraulic conductivity (cm/min) | |
| #16 sand | 42.4 |
| #30 sand | 8.4 |
| #50 sand | 2.82 |
| #70 sand | 2.37 |
| #110 sand | 0.892 |
| Brooks-Corey pore size distribution parameter (λ) | |
| Drainage | 1.72 |
| Imbibition | 0.620 |
| Residual water saturation | 0.15 |
| Maximum water saturation | 0.85 |
| Effective porosity, water saturated | 0.50 |
| Lateral dispersivity | 1 |
| Ratio of transverse to lateral dispersivity | 0.1 |
| Gilland-Sherwood coefficients | |
| α_0 – upper source | 192 |
| α_0 – lower source | 64 |
| α_1 | 0.2266 |
| α_2 | 0.5 |
| α_3 | 0.997 |

Estimates of saturated hydraulic conductivity for each sand type (Table 4.17) were obtained from values determined in previous laboratory experiments for clean sands (Illangasekare et al., 1995; Compos, 1998; Saba and Illangasekare, 2000; Barth et al., 2001; Sakaki and Illangasekare, 2006). As described in section 3.7.3, efforts to control redox conditions in the tank prior to the dissolution experiments resulted in precipitate accumulation, particularly in coarse-grained sands (#30 and #16). As a result, *in situ* values of hydraulic conductivity were expected to be less than laboratory-test estimates obtained for clean sands. Consistent with this expectation, successful calibration required a hydraulic-conductivity estimate for the coarse-grained #30 sand that was approximately half the initial estimate. Calibrated estimates of hydraulic conductivity for other sands were very similar to the initial estimates.

Solute transport simulations based on initial estimates of Gilland-Sherwood empirical coefficients ($\alpha_0, \alpha_1, \alpha_2, \alpha_3$) significantly underestimated observed PCE concentration downgradient of sources. Initial estimates were obtained from dissolution experiments for source zone lengths approximately half the length used in the CF tank experiment. The likely explanation for low simulated PCE concentrations with initial estimates of Gilland-Sherwood coefficients is that estimated median grain-size diameter (d_{50}) and flow-path tortuosity (τ) used in the Gilland-Sherwood expression were incorrect. The d_{50} appears in both the Sherwood number (Sh) and the dimensionless saturation ratio (Θ) and is used as a surrogate for pore size. In this paper, d_{50} was estimated from data for clean sand and tortuosity was assumed to be consistent with estimates used successfully simulations of similar tank experiments. However,

during efforts to control redox conditions of the tank, significant precipitates accumulated within the #16 sand lenses that formed the sources. Precipitates may have altered both the median pore size and flow-path tortuosity.

Because existing information provided no basis for adjusting d_{50} and τ for precipitates, the empirical coefficients α_0 and α_3 were adjusted in a trial-and-error fashion to improve the calibration. Large adjustments were required to calibrate α_0 , reflecting the fact that d_{50} appears in the Sherwood number as a squared term (Table 4.17). Differences in the calibrated α_0 for the two sources may reflect differences in precipitate accumulation. Based on visual observation, precipitates accumulated to a greater degree in the upper source. The calibrated estimates of α_0 are consistent with this observation. Only minor adjustment was required to calibrate α_3 .

Simulated steady-state distribution of PCE generally compared well with observed PCE at the end of the abiotic dissolution experiment (Figure 4.57). The most significant exception to this conclusion occurred in the vicinity of water samples obtained from fine-grained sand near the downgradient end of the upper unit. In this area, simulated results overestimated observed PCE aqueous-phase concentration distribution. Efforts to improve the calibration by adjusting the hydraulic properties of the fine-grained sand were not effective. One possibility for the discrepancy may be that steady-state conditions had not been fully established in the fine-grained material by the end of the experiment.

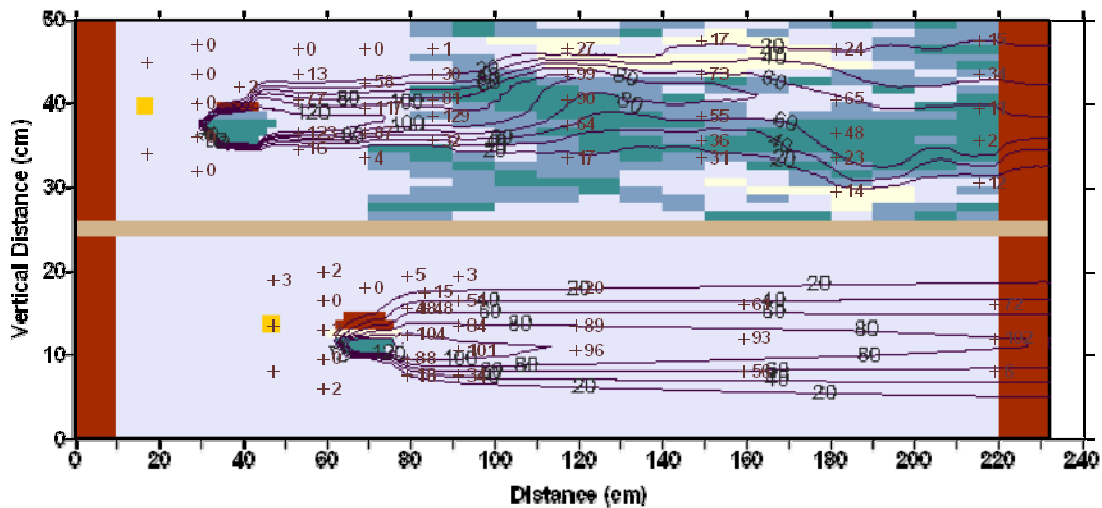


Figure 4.57. Simulated Steady-State PCE Concentration in the CF Tank during Abiotic Dissolution, Large Tank Experiments of Bioenhanced Dissolution

Abiotic mass flux of PCE calculated along profiles immediately downgradient of the sources illustrates the importance of transition zones in dissolution from pools (Figure 4.58 and Table 4.18). To facilitate comparison with subsequent simulation results for bioenhanced mass transfer, PCE concentration values have been converted to units of mmol/L. Simulated abiotic mass flux was greatest along flow paths that traverse the transition zone. Overall, abiotic mass flux in the upper unit was greater than in the lower unit.

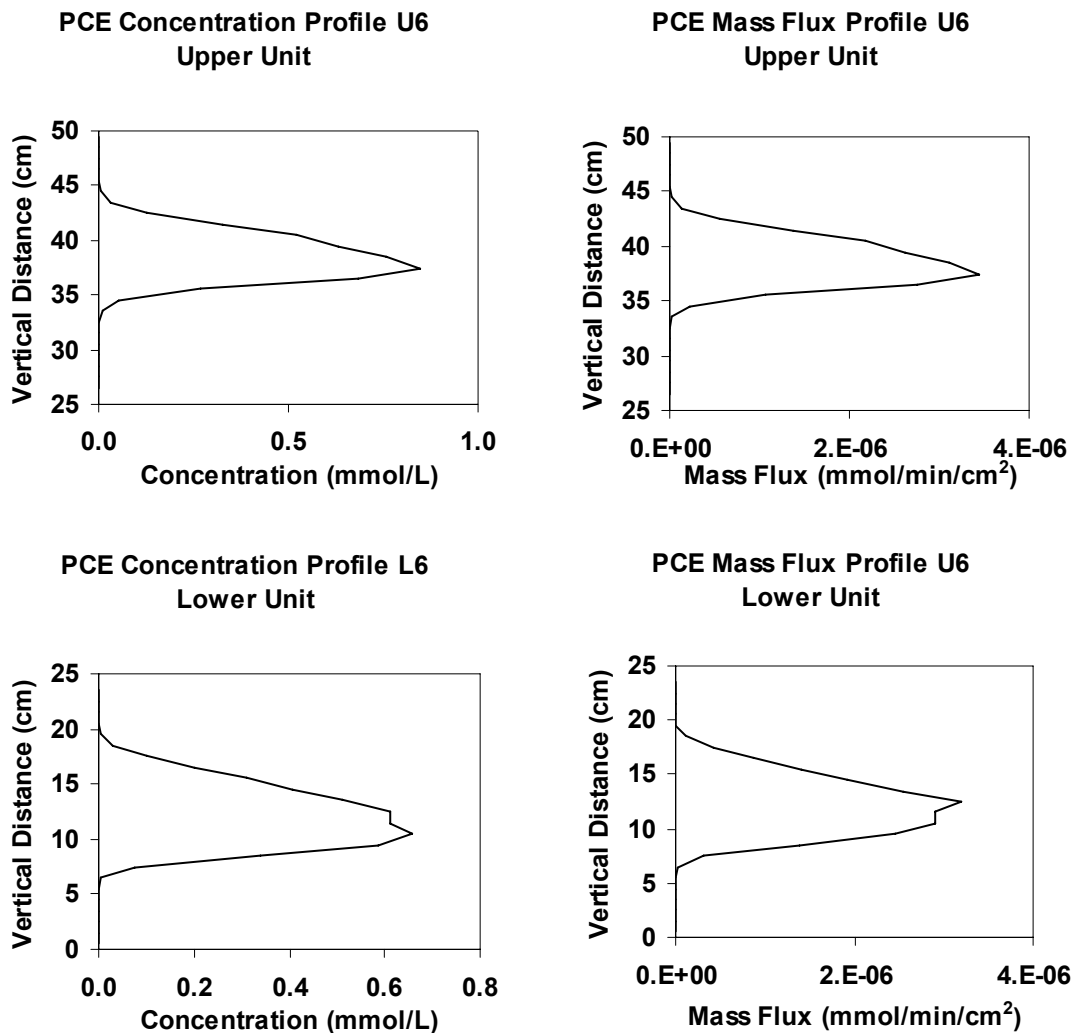


Figure 4.58. Simulated PCE Concentration and Mass Flux Profiles Downgradient of DNAPL Sources during Abiotic Dissolution in the CF Tank, Large Tank Experiments of Bioenhanced Dissolution

Table 4.18. Mass Flux of Aqueous Phase Ethene Chemicals in the CF Tank, Large Tank Experiments of Bioenhanced Dissolution

| Experimental Conditions | Profile U6, Upper Source (mmol/min/cm ²) | Profile L6, Lower Source (mmol/min/cm ²) |
|---|--|--|
| Abiotic | 1.46 x 10 ⁻⁷ | 1.67 x 10 ⁻⁷ |
| Biotic, 11 source pore volumes after inoculation | 4.66 x 10 ⁻⁷ | 6.27 x 10 ⁻⁷ |
| Biotic, 20 source pore volumes after inoculation | 1.66 x 10 ⁻⁷ | 2.54 x 10 ⁻⁷ |
| Biotic, 20 source pore volumes after inoculation (simulated concentrations from base scenario) | 3.39 x 10 ⁻⁷ | 2.78 x 10 ⁻⁷ |

Cross sectional area of experiments was 120 cm². All flux calculations based on simulated groundwater flow rates.

Observed aqueous-phase mass fluxes after 15 and 30 days of bioenhanced dissolution also are presented in Table 4.18. Bioenhanced mass flux was calculated by combining groundwater flux estimated by modeling with observed aqueous-phase concentrations of PCE and degradation products. Gas production was observed during bioenhanced dissolution experiments immediately downstream of sources. Mass flux associated with gas production is not included in the results presented in Table 4.18. Therefore, results presented in Table 4.18 represent minimum mass flux that may have occurred during bioenhanced dissolution. Nevertheless, results show that biological activity significantly increased mass transfer.

Bioenhanced Dissolution. Simulations of bioenhanced dissolution experiments were undertaken with the goals of extending the flow-cell scale conceptual model of bioenhanced dissolution to intermediate scales, and testing a protocol for using batch and flow-cell estimates of bio-kinetic parameters to describe bioenhanced dissolution at intermediate scales. Specifically, it is hypothesized that bioenhanced dissolution can be modeled by coupling abiotic dissolution kinetics parameterized by an intermediate-scale Gilland-Sherwood correlation with local-scale biodegradation processes parameterized from results of independent aqueous-phase batch, column and small flow-cell experiments.

Results of the tank experiments provided several complications to fully meeting these objectives. Several secondary processes not considered in the flow-cell-scale conceptual model affected mass transfer during the tank experiments. The relative importance of these reaction processes evolved throughout the bioenhanced dissolution experiments. Although results were consistent qualitatively with the flow-scale conceptual model of bioenhanced dissolution, spatial and temporal patterns of electron donor, PCE, and degradation products had not attained steady-state conditions. Changes in gas accumulation patterns upstream and within sources suggest that processes of electron-donor fermentation and loss to sulfate reduction and methanogenesis became important as the experiments progressed. Gas accumulation also occurred downstream of sources suggesting phase partitioning of more volatile PCE degradation products (ethene, vinyl chloride). Gas accumulation and migration was particularly significant in the upper unit of the CF tank. Evidence of changing bioactivity and lag in dechlorination also was noted in the lower unit of the CF tank.

Consequently, the intermediate-scale experiments did not provide data sets suitable for model validation. In this paper, simulation focused on techniques for integrating available descriptions of reactive-transport processes into a coherent representation of bioenhanced mass transfer that would be useful in assessing feasibility and effectiveness of source-zone bioremediation at intermediate and field scales. Rather than rely on model calibration (fitting a model to measured bioenhanced dissolution data), parameters describing bioenhanced dissolution processes were estimated from independent information in an effort to explain as much experimental variability as possible. Detailed model calibration for the tank experiments would require information not yet available. For example, understanding of gas composition and fermentation waste products that do not contribute to dechlorination (e.g. methane, sulfide, acetate) are not available. Additional sampling and analysis of the CF tank has been undertaken as part of another research project in an effort to improve the available database. Biomass distribution and composition also will be determined by destructively coring the tank.

A sensitivity analysis was conducted to evaluate if independently derived estimates of bio-kinetic parameters associated with dechlorination could be used with confidence to simulate bioenhanced dissolution at intermediate scales. The analysis consisted of a set of RT3D transient simulations with selected values of bio-kinetic degradation parameters derived from batch, column and flow cell experiments in aqueous systems without DNAPL. Biomass distribution was assumed to be uniformly distributed throughout the source zone at a concentration consistent with that of the KB-1 cultures used to inoculate the tanks. Biomass growth and transport were not considered. Estimates of hydrodynamic and abiotic dissolution parameters were based directly on parameter estimates that proved successful in simulating abiotic dissolution.

Rather than attempt to simulate loss of electron donor (methanol) to processes such as sulfate reduction and methanogenesis that have not been characterized, inflow methanol concentration was adjusted from the observed 200 mg/L to a simulated value of 80 mg/L. This concentration provided a methanol load equal to the methanol load observed along a vertical profile immediately downgradient of sources plus the methanol used to support observed dechlorination. In calculating the methanol used to support dechlorination, a stoichiometric coefficient of 2.1 was assumed. This value was obtained from results of flow-cell experiments.

The number of biodegradation model parameters required by the RT3D reaction module is large and includes Monod kinetic parameters for PCE, electron donor and each degradation daughter product. In simulating flow-cell experiments of bioenhanced dissolution, it was possible to simplify the number of parameters by recognizing that PCE and TCE concentrations within the flow cell were within ranges where degradation was effectively first order. The same strategy was adapted for selecting degradation parameter estimates in this paper. Simulations were conducted by setting Monod half-saturation coefficients (K_{sa}) to a large value relative to electron-acceptor concentration and setting the maximum specific growth rate coefficient (μ_m) such that degradation was first order with respect to electron acceptor. Consistent with the approach used in simulations at the flow-cell scale, the Monod half-saturation constant for electron donor (K_{sd}) was 0.03 mmol/L (1 mg/L). In this manner, dechlorination was possible only when electron donor was present in a model node.

Bio-kinetic parameter estimates used in the sensitivity analysis were obtained from results of aqueous-phase batch experiments conducted with the KB-1 culture by numerous researchers (Bloom et al., 2000; Duhamel et al., 2002; Kaplan, 2004; Slater et al., 2000) as well as simulation results for the flow-cell scale experiments of bioenhanced dissolution. Rate

coefficients estimated from small-scale experiments show a wide range of variability and great care must be taken when comparing results of experiments conducted under different conditions. For example, reported degradation rates vary in response to the electron acceptor used during culture enrichment. Methods used to measure biomass concentration during batch tests also vary and may not be directly comparable.

Considering only experiments conducted with KB-1 cultures enriched and maintained with methanol as primary electron donor and either PCE or TCE as primary electron acceptor, ratios of first-order degradation coefficients show relatively consistent patterns (Table 4.19). These degradation coefficient ratios also are consistent with those reported by Major et al. (2002) for a field-scale test.

Table 4.19. Estimated Ratios of Effective First Order Degradation Coefficients for Chlorinated Ethenes

| Chlorinated Ethenes | Ratio of Degradation Coefficients |
|---------------------|-----------------------------------|
| TCE / PCE | 2 to 3 |
| DCE / TCE | 0.25 to 0.5 |
| VC / DCE | 0.2 to 1.0 |

Four sets of degradation-coefficient estimates were selected for reactive-transport simulations (Table 4.20). Estimates were selected on the basis of ratios shown in Table 4.19 in combination with estimates of effective first-order degradation coefficients for PCE and TCE that were successful in modeling bioenhanced dissolution in flow-cell experiments. Estimates used in three simulations, designated as the low middle and high scenarios, were obtained directly from the range of ratios presented in Table 4.19. The fourth, designated as the base scenario, represents a qualitative assessment based on experience gained maintaining and using the KB-1 culture for a period of 2-3 years. Estimates used in the base scenario also are consistent with Table 4.19.

Table 4.20. Estimates of Effective First-Order Degradation Coefficients Used in Sensitivity Analysis of Bioenhanced Dissolution in the CF Tank

| Simulation Scenario | PCE (1/min) | TCE (1/min) | DCE (1/min) | VC (1/min) |
|---------------------|-----------------------|-----------------------|-----------------------|-----------------------|
| Base | 6.6×10^{-3} | 1.32×10^{-2} | 3.3×10^{-3} | 1.1×10^{-3} |
| Low | 3.3×10^{-3} | 6.6×10^{-2} | 1.65×10^{-3} | 6.6×10^{-4} |
| Middle | 6.6×10^{-3} | 1.65×10^{-2} | 4.95×10^{-3} | 2.92×10^{-3} |
| High | 1.32×10^{-2} | 3.96×10^{-2} | 1.32×10^{-2} | 1.32×10^{-2} |

Thirty-day transient simulations of bioenhanced dissolution experiments in the CF tank were conducted assuming no lag in biological activity. Near steady-state conditions were established in both upper and lower units after approximately 15 days. As discussed previously, processes such as gas accumulation and electron-donor loss that may have contributed to the observed non-steady response after 30 days were not included in this simulation. Empirical methods for simulating lags in biological activity (Li et al., 2001) also were not included in the simulation. Therefore, the rapid convergence on steady-state conditions that occurred during the simulations was not unexpected.

Steady-state simulation results are presented as vertical profiles of concentration at two locations downgradient of sources in the upper and lower units of the CF tank (Figures 4.59 and 4.60). Plume centers shown in these profiles correspond with flow paths that traversed pool transition zones. Total mass flux in the upper unit was significantly greater for all simulation scenarios than in the lower unit. This was consistent with mass flux observed under abiotic conditions. Simulated mass flux with biological enhancement greatly exceeded abiotic mass flux for all scenarios considered. Within the upper unit, a secondary but notable portion of total ethene concentration (PCE + TCE + DCE + VC + ethene) was in the form of PCE, reflecting electron-donor limitations within the sources. In the lower unit, simulated PCE concentration was minimal.

Differences in concentration profiles of total degradation products were small among the four simulation scenarios (Figure 4.59 and 4.60). Vertical profile plots constructed for individual degradation products showed greater variation, particularly along plume centers (data not shown), but had little effect on overall simulated mass flux leaving sources. As expected, total aqueous-phase concentration of degradation products calculated by simulation did not compare well with observed experimental results, particularly along plume centers. Observed experimental results reflected effects of gas accumulation and migration.

Conditions for gas formation and accumulation in the experiments were evaluated by identifying critical aqueous-phase concentrations of degradation products needed to form a distinct gas phase. For a specified chemical and aqueous-phase concentration, gas-phase partial pressure was calculated by Henry's Law. For a gas-phase to be present, the sum of theoretical partial pressures for all degradation products must exceed the sum of water pressure and air-displacement pressure for the sand. Water pressure increased with depth below the piezometric surface and was measured during the experiments. Air-displacement pressure for the #50 sand located downgradient of source areas has been measured in independent laboratory tests (Sakaki and Illangasekare, 2006).

The principal degradation product driving gas formation in the CF tank experiments was ethene. Comparison of critical ethene concentration required for gas formation with results of the sensitivity analysis (Figure 4.61) showed depth intervals where gas formation was expected. Within the upper unit, gas formation was predicted for all simulation scenarios throughout much of the simulated ethene plume. Gas formation in the lower unit was predicted over a narrower depth range for some, but not all, simulation scenarios. These simulation results were consistent with the observed accumulation of significant gas in the upper unit downgradient of the source. Gas formation in the lower unit downgradient of the source was not observed.

If a gas phase was present, PCE and all degradation products would tend to partition in accordance with Henry's coefficients and observed aqueous-phase concentrations would differ from those predicted by a model that does not consider gas accumulation and migration. Visual comparison of predicted intervals for gas formation (Figure 4.60) with vertical profiles of total degradation products (Figures 4.58 and 4.59) show that simulations did not match observed experimental results in depth intervals where gas formation was predicted. The match was much better outside these depth intervals.

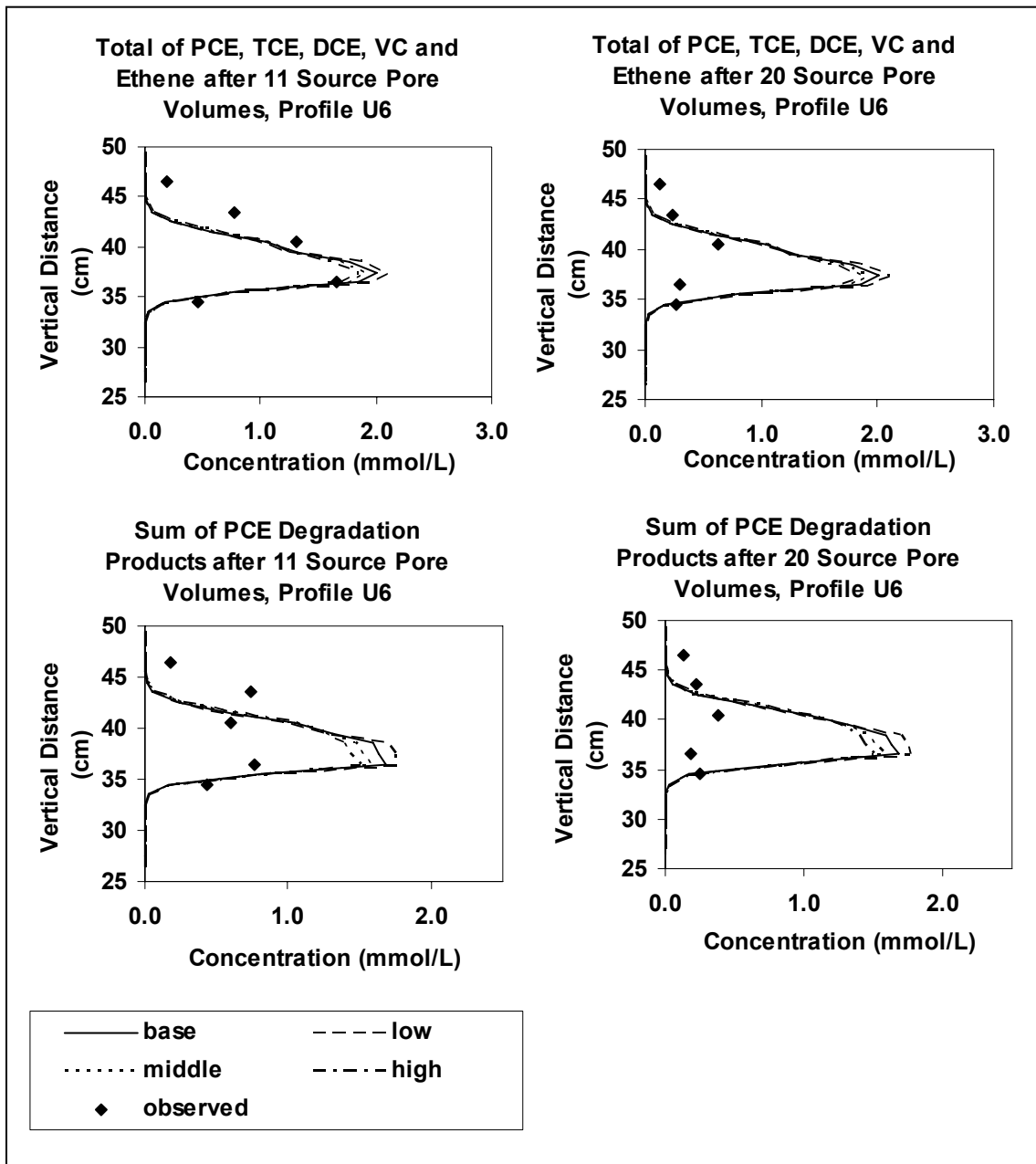


Figure 4.59. Concentration Profiles in Upper Unit, CF Tank, for Four Simulation Scenarios, Large-Tank Modeling of Bioenhanced Dissolution

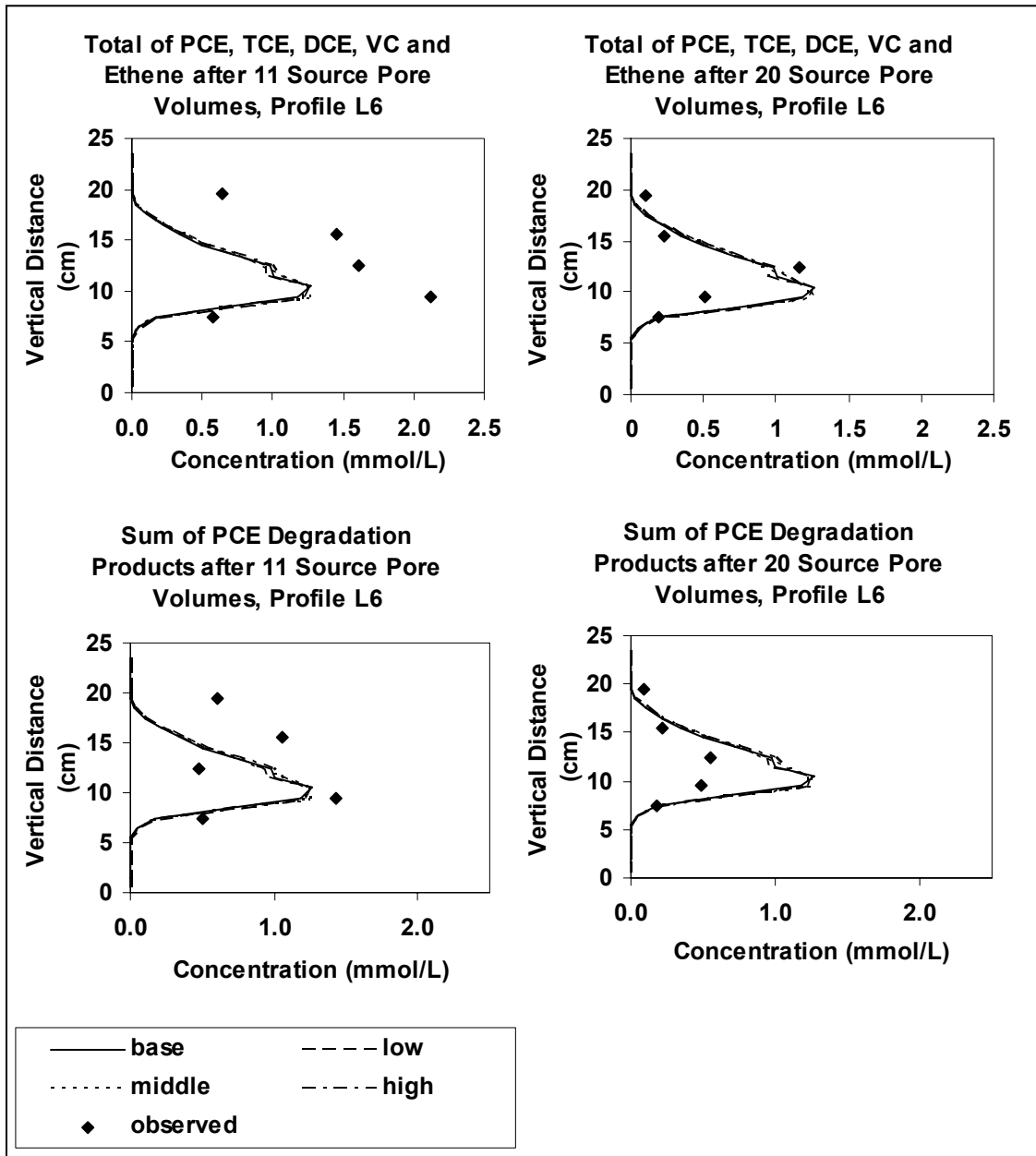


Figure 4.60. Concentration Profiles in Lower Unit, CF tank, for Four Simulation Scenarios, Large-Tank Modeling of Bioenhanced Dissolution

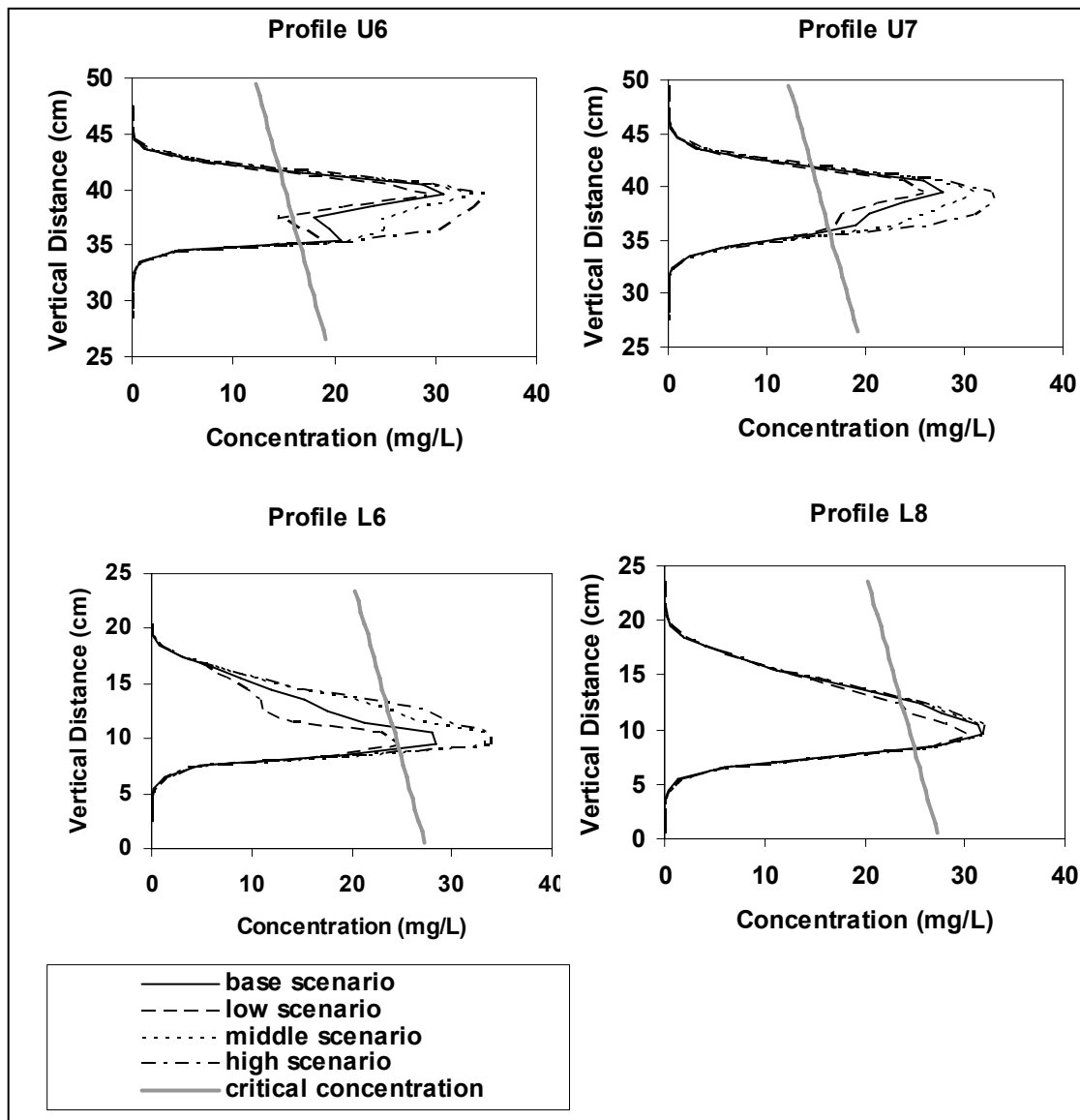


Figure 4.61. Comparison of Critical Ethene Concentration for Gas Formation with Simulated Ethene Concentration after 11 Source Pore Volumes, Large Tank Modeling of Bioenhanced Dissolution

Several models have been proposed to simulate gas accumulation and transport coupled with reactive transport. These include multiphase reactive transport models such as T2VOC (Falta, 2000), kinetic models of gas bubble formation and transport (Holoher et al., 2003), and equilibrium geochemical models of gas formation (van Breukelen et al., 2004). Data requirements for each are large and limit application to one-dimensional analyses, or sites and experiments with extensive gas-phase data.

The flow-cell scale conceptual model of bioenhanced dissolution was represented numerically as an RT3D reaction module that did not simulate gas accumulation and migration. The RT3D model simulates reactive transport processes in a single mobile fluid phase – water. Therefore, accurate representation of gas accumulation and migration is not possible within RT3D. However, two simplified approaches to simulating gas formation within the context of RT3D were evaluated.

One approach was based on assumptions that gas partitioning can be treated as an equilibrium process with gas accumulation occurring as an immobile phase. These assumptions are readily incorporated within RT3D simulations with the use of a retardation coefficient. This approach is more typically used in RT3D to simulate equilibrium sorption processes. Details of this approach are provided in the Ph.D. thesis of Glover (2006).

Efforts to simulate the bioenhanced dissolution experiments with equilibrium gas partitioning proved unsuccessful. Although simulated aqueous-phase concentrations downstream of source areas were less than simulated without gas partitioning, equilibrium gas partitioning did not significantly improve the match to observed experimental results. Simulated gas saturations also were significantly greater than residual saturation measured in independent laboratory tests (Sakaka and Illangasekare, 2006). Under these conditions, gas would not be retained as an immobile phase but would rise through the sand. This is consistent with observed gas migration and accumulation at overlying confining units during the experiments.

The second approach to modeling gas formation within RT3D was based on the assumption that gas partitioning can be treated as a first-order mass transfer process (Holocher et al., 2003). Holocher et al. (2003) found that gas bubble formation was controlled by hydrostatic pressure, molecular diffusion coefficients and ambient aqueous-phase concentration. Details of this approach are provided in the Ph.D. thesis of Glover (2006). An RT3D reaction module that includes kinetic gas partitioning was developed and used to simulate the bioenhanced dissolution in the CF tank. The RT3D reaction module does not simulate gas migration. Rather, it removes mass in the form of gas bubbles from the simulation as they are formed.

Efforts to simulate bioenhanced dissolution in the CF tank with kinetic gas partitioning provided some improvement over the equilibrium approach and simulations without gas formation in matching observed experimental results (Figure 4.62). However, large differences remained in the upper unit at vertical distance of 36.5 cm and in the lower unit for the sum of degradation products at vertical distances of 9.5 cm and 12.5 cm. Overall, the RT3D reaction module used in this study was poorly suited to detailed simulation of gas accumulation and migration. Nevertheless, for purposes of remediation technology screening, the kinetic mass transfer expression provided a first approximation for gas-phase partitioning. Simulation results correctly identified experimental conditions that resulted in gas formation. Because gas composition consisted primarily of ethene and vinyl chloride generated downstream of DNAPL sources, errors in simulating gas accumulation were judged to have minimal effect on simulated mass transfer from source zones.

While not definitive, modeling results suggest that bio-kinetic parameter estimates used in the sensitivity analysis provided reasonable predictions of bioenhanced dissolution. More definitive evidence that local-scale estimates of bio-kinetic parameters may be used successfully in intermediate-scale models will require improved understanding of gas composition, gas accumulation and migration.

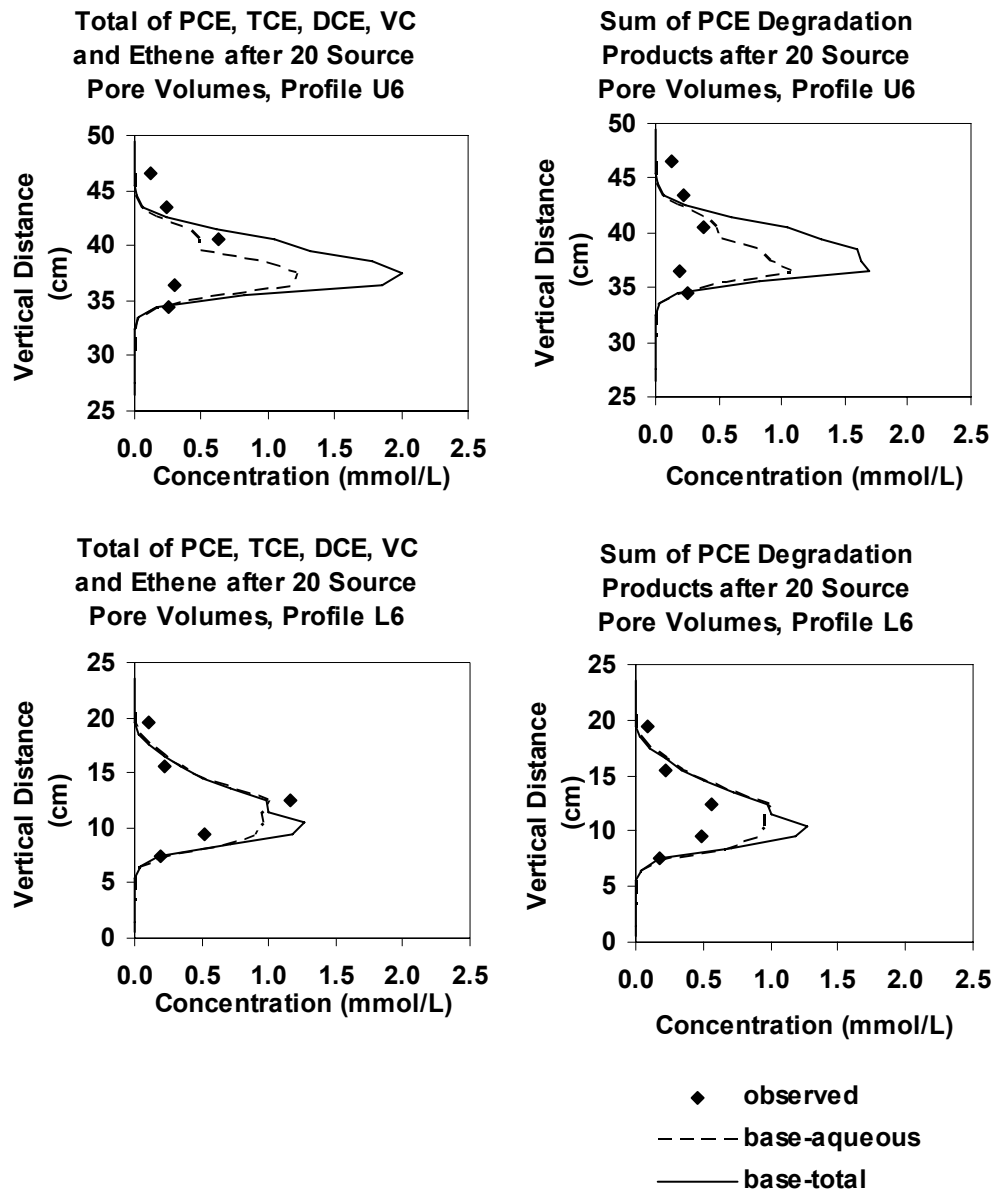


Figure 4.62. Concentration Profiles in the CF Tank for the Base Scenario with Kinetic Gas Partitioning, Large Tank Bioenhanced Dissolution Experiments

Sub-Grid Representation of Pool Morphology. Detailed simulations of flow cell experiments and results of intermediate-scale tank experiments have shown that biologically enhanced dissolution occurs primarily within saturation transition zones in the upper portion of DNAPL pools. Within deeper portions of pools, DNAPL saturation is sufficiently high to minimize advective and hydrodynamic transport. Because advection in the deeper portions of a pool is minimal, mass transfer between the transition zone and deeper portions is very slow and

is likely to be controlled by diffusion at the interface between the two zones. As a result, mixing of electron donor supplied at upgradient locations with PCE dissolving from the DNAPL phase is effectively limited to the transition zone. Because mixing of electron donor and acceptor is required for biodegradation, biological activity also is effectively limited to the transition zone.

Several strategies for representing sub-grid heterogeneity have been developed. In many situations, estimates of groundwater flow and solute transport parameters at large scales can be obtained with an averaging strategy that is effective in simulating overall system response at specified downgradient locations (de Marsily, et al., 2005). Strategies also have been developed that use second order moments of sub-grid heterogeneity in an attempt to account for underlying geostatistical structure and preferential channeling (Saenton and Illangasekare, 2005; de Marsily et al., 2005). Dual-domain approaches have found application to a variety of transport problems (Falta, 2000; Sun et al., 1999).

The description of biological activity within a pool is conceptually similar to dual domain approaches. Although the analogy is not exact, the dual-domain approach is used in this study because it provides a relatively simple means of testing the upscaling hypothesis given previously in this section of the thesis. Extension of the RT3D model to simulate reactive transport in dual-domain systems is straightforward (Sun et al., 1999). Limitations associated with the dual-domain approach are discussed later in this section.

In dual-domain approaches, the aquifer is conceptualized as aggregated porous media consisting of parallel pore sequences. Advective and hydrodynamic dispersive transport is assumed to be relatively rapid in one sequence and relatively slow in the second sequence. Within the second sequence, diffusion often is considered to be the dominant transport process. To upscale the bioenhanced dissolution model within the framework of the dual-domain approach, mixing required to drive biodegradation is assumed to occur solely within the advective sequence or domain (Figure 4.63). Reactions are not assumed to occur in the diffusive sequence or domain.

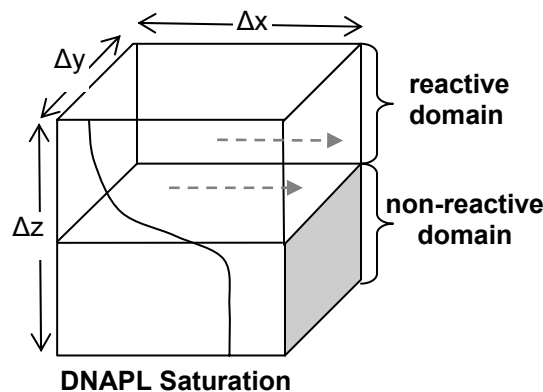


Figure 4.63. Schematic Diagram of Sub-Grid Heterogeneity Due to Pool Morphology

The mathematical equations used for describing dual porosity systems are very similar to those describing bioenhanced dissolution in a single domain, but with a few subtle differences. In the single domain model, DNAPL is defined as an immobile phase component. In the dual

domain model, the DNAPL component is divided into two components, one representing the DNAPL concentration or saturation in the transition zone and the second representing the DNAPL concentration or saturation in the non-reactive deep pool (\tilde{C}_{pool}). As with the single domain model, both DNAPL components are considered to be immobile.

With this definition of model components, the governing equations for modeling contaminant transport in a dual-domain system can be written as

$$\frac{\partial C_k}{\partial t} = \frac{\partial}{\partial x_i} \left(D_{ij} \frac{\partial C_k}{\partial x_j} \right) - \frac{\partial}{\partial x_i} (v_i C_k) + \frac{q_s}{\phi} C_{S_k} \pm r_k, \quad k = 1, 2, \dots, m \quad (4.22)$$

$$\frac{\rho_b}{\phi} \frac{d\tilde{C}_{im}}{dt} = \pm \tilde{r}_{im}, \quad im = 1, 2, \dots, (n - m) \quad (4.23)$$

$$\frac{\rho_b}{\phi_{nr}} \frac{d\tilde{C}_{pool}}{dt} = \tilde{r}_{pool}, \quad (4.24)$$

where n is the total number of components, m is the total number of aqueous-phase mobile components, im is the total number of immobile components, C is the aqueous-phase concentration of the k th component in the reactive domain [ML^{-3}], \tilde{C} is the solid-phase concentration of the im th component in the reactive domain [MM^{-1}], \tilde{C}_{pool} is the solid-phase concentration of PCE-DNAPL in the non-reactive domain [MM^{-1}], D_{ij} is the hydrodynamic dispersion coefficient of the reactive domain [L^2T^{-1}], v is the pore velocity in the reactive domain [LT^{-1}], q_s is the volumetric flux of water per unit volume of aquifer that represents sources and sinks [T^{-1}], ϕ is the effective porosity of the reactive domain, C_s is the source-sink concentration [ML^{-3}], r represents aqueous-phase reaction rate terms (mass of species removed or produced per unit void volume per unit time) [$ML^{-3}T^{-1}$], ρ_b is the bulk density of the porous media [ML^{-3}], \tilde{r} represents solid-phase reaction rate terms [$MM^{-1}T^{-1}$], and \tilde{r}_{pool} represents mass transfer of PCE from non-reactive to reactive domains.

Many of the parameters in Equations 4.22-4.24 are defined with reference either to the reactive domain or the non-reactive domain. Defining the parameters in this manner permits simulation of rates of advection, residence time within a finite-difference cell, and concentrations that more accurately reflect conditions within transition zones. As a result, reaction rates are simulated with a greater degree of accuracy than would be possible with upscaling strategies based on spatial averaging.

Equations 4.22 and 4.23 are modified to describe biodegradation reactions occurring in the mobile phase as well as rate-limited mass transfer from DNAPL in the transition zone. However, for simplicity, these terms are not emphasized in this discussion.

Mass transfer of PCE from non-reactive DNAPL to aqueous phase occurs by dissolution from DNAPL and diffusion of aqueous phase PCE from the non-reactive pool into the adjacent transition zone. Because saturation of the pool is very high and relative permeability is very low,

aqueous phase PCE within the non-reactive pool tends to approximate aqueous solubility. Development of a detailed model of these coupled processes within the non-reactive portion of the pool is beyond the scope of this project. Instead, the RT3D reaction module developed for this study models mass transfer from the non-reactive pool as a first-order kinetic process. The mass transfer expression is

$$\tilde{r}_{pool} = -k_{Lp}(C^* - C_{pce}) \quad (4.25)$$

where k_{Lp} is an empirical rate coefficient and C^* is the equilibrium aqueous phase concentration of PCE [ML^{-3}]. Sun et al. (1999) and Falta (2000) use similar empirical approaches to model mass transfer in dual-domain systems.

As commonly applied, each pore sequence or domain in a dual-domain approach is conceptually visualized as a continuum which occupies the entire spatial domain of a model cell. Mass transfer between domains is then modeled on a volumetric basis. In applying the dual domain concept to bioenhanced pool dissolution, mass transfer between domains occurs across the macroscopic surface area separating transition zone (reactive domain) from deep pool (non-reactive domain).

An RT3D user-defined reaction module was developed to setup the reaction equation. The details of the reaction module are provided in the Ph.D. thesis of Glover (2006).

Evaluation of Upscaling Strategy. The intermediate-scale tank experiments provided a qualitative assessment of the conceptual model for bioenhanced dissolution from pools. However, accurate quantitative simulation was not possible due to gas formation and accumulation processes. Therefore, simulations of the tank experiments do not provide an appropriate framework for evaluating the proposed upscaling strategy.

Instead, an evaluation based on a numerical experiment has been conducted to evaluate the upscaling strategy. Hypothetical DNAPL abiotic and bioenhanced dissolution experiments in two dimensions were simulated using very fine node spacing where DNAPL saturation profiles were represented in detail (Figure 4.64). Results were compared with simulations conducted with a coarse grid where DNAPL saturation was represented using the dual-domain approach. Abiotic dissolution and hydraulic properties for the coarse-grid simulations were adjusted in accordance with the scale dependent Gilland-Sherwood correlation and the dual-domain formulation. However, estimates of biodegradation rate coefficients were not adjusted from those used in fine-grid simulations. Simulation times were sufficient to establish steady-state conditions and steady-state results from fine- and coarse-grid simulations were compared. Comparison provided a test of the upscaling hypothesis that reliable predictions of mass flux at intermediate and field scales can be based on local-scale measurements of bio-kinetic parameters provided that hydrodynamic and abiotic dissolution parameters are upscaled by an appropriate method.

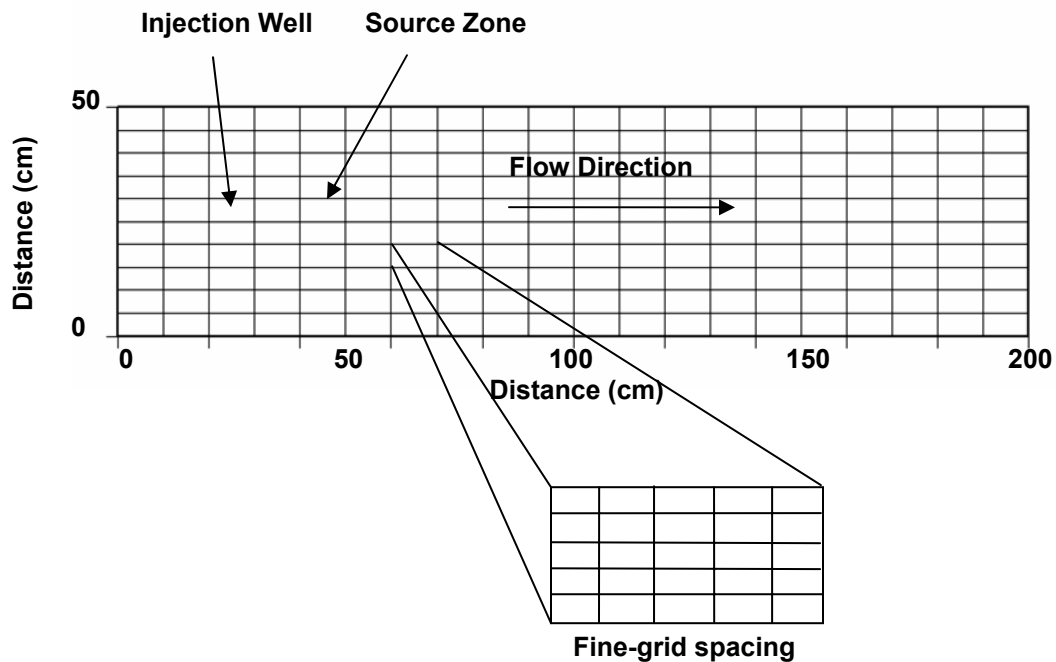


Figure 4.64. Aquifer System and Finite Difference Grids Used to Evaluate Upscaling Strategy for Bioenhanced Dissolution

The fine-grid spacing provided sufficient detail to simulate vertical variations in pool saturation without treating the pool as a dual-domain system. Node spacing was 2 cm in flow direction by 1 cm in vertical. A DNAPL source zone 10 cm in flow direction by 5 cm in vertical was established. Abiotic dissolution experiments were simulated for three scenarios (Table 4.21) using hydraulic properties and abiotic Gilland-Sherwood correlations that were consistent with conditions observed in the lower unit of the CF intermediate-scale tank experiment (Table 4.17). The lower unit consisted of a homogeneous unit (#50 sand) with a coarse-grained inclusion of #16 sand that was used to create a PCE-DNAPL source zone. Simulation generated a synthetic data set of PCE concentration at cross sections located a short distance downgradient of the source zone. Concentrations were generated by flux averaging concentrations along in adjacent nodes to give an effective concentration at the coarse-grid scale. Bioenhanced dissolution experiments were simulated for each flow-system scenario using four sets of biodegradation rate coefficients that represent the range of parameter estimates obtained from laboratory kinetic tests in aqueous-phase batch and flow cells (Table 7.20). The four sets of coefficients were designated as the base, low, middle and high parameter sets. This designation is consistent with the designations used in sensitivity analyses presented previously in this section.

Table 4.21. Flow-System and Source-Zone Characteristics Used to Evaluate Upscaling Strategy for Bioenhanced Dissolution

| System Characteristic | | Simulation Scenario | | |
|--|-------------------------------------|---------------------|---------|---------|
| | | A | B | C |
| Average saturation of source zone | | 0.60 | 0.60 | 0.40 |
| Transition zone | Thickness (cm) | 2 | 2 | 4 |
| | Saturation | 0.30 | 0.30 | 0.30 |
| | Effective porosity | 0.28 | 0.28 | 0.28 |
| | Relative permeability | 0.2266 | 0.2266 | 0.2266 |
| Pool | Effective porosity | 0.8 | 0.8 | 0.8 |
| | Relative permeability | 0.08 | 0.08 | 0.08 |
| | | 0.00123 | 0.00123 | 0.00123 |
| Upgradient inflow rate (cm ³ /min/cm) | | 1.00 | 0.25 | 1.00 |
| Injection well | Flow rate (cm ³ /min/cm) | 0.20 | 0.05 | 0.20 |
| | Methanol concentration (mg/L) | 100 | 100 | 100 |

A coarse node spacing of 10 cm in the flow direction and 5 cm in the vertical was selected for simulations. With this spacing, the entire DNAPL source zone was represented by one finite-difference cell, providing a meaningful test of the dual-domain strategy for upscaling. Abiotic dissolution experiments were simulated for the three flow-system scenarios used in the fine-grid simulations (Table 4.21). Hydraulic properties and abiotic Gilland-Sherwood correlations also were consistent with those used in the fine-grid simulations. Because the Gilland-Sherwood correlation includes a length parameter for node spacing, values of k_{La} differed between the fine- and coarse-grid simulations.

The dual-domain model used in the coarse-grid simulations includes an empirical mass transfer rate coefficient (k_{Lp}) to model transfer of PCE from the non-reactive portion of the DNAPL pool to the reactive transition zone. Initial simulation of abiotic dissolution with this parameter value set to zero significantly underestimated PCE concentration recorded as the synthetic data set. Therefore, calibration of the coarse-grid abiotic model was undertaken to match fine-grid data.

Bioenhanced dissolution experiments were simulated with the coarse grid using the four sets of biodegradation rate coefficients applied in the fine-grid simulations. No adjustments were made to these parameter estimates.

Simulation results for two sets of simulations were compared by plotting concentration obtained with fine- and coarse-grid models at vertical profiles located downgradient of the source zone. Ideally, if the proposed upscaling strategy was correct, all data would fall along a line with 1:1 slope. Comparison of steady-state PCE concentrations show that the dual-domain strategy for upscale provided an accurate representation of fine-grid simulation results (Figure

4.65). The standard error of abiotic residuals was 0.0245 mmol/L. No trends in residuals with increasing concentration were noted.

Comparison of total ethene concentrations show that the dual-domain strategy for upscaling, coupled with laboratory-scale estimates of biodegradation parameters provided an acceptable representation of fine-grid simulation results (Figure 4.66). The standard error of residuals for biotic simulations was 0.0399 mmol/L. While this is larger than the standard error of abiotic residuals, the overall match between fine-and coarse-grid simulations is acceptable. Residuals for biotic simulations with increasing concentration show a slight tendency of the coarse-grid simulation to underestimate mass flux at high total ethene concentrations.

Results of this study suggest that a dual-domain strategy for upscaling bioenhanced dissolution from pools may be appropriate. Predictions of mass flux from a single DNAPL pool undergoing bioremediation were considered to be acceptable using laboratory-scale measurements of biodegradation parameters in conjunction with abiotic dissolution parameters appropriate for coarse node spacing. More rigorous tests of this strategy are needed before the strategy is accepted for use at field scales. For example, an evaluation with node spacing greater than those used in this study would be appropriate. Model evaluation with actual rather than synthetic data also would be appropriate. More complex source zone architectures need to be assessed, as does the effect of uncertainty in pool characterization. An empirical approach was used in this study to model mass transfer from non-reactive portions of pools to transition zones. A model based on an improved physicochemical theory of mass transfer would be appropriate.

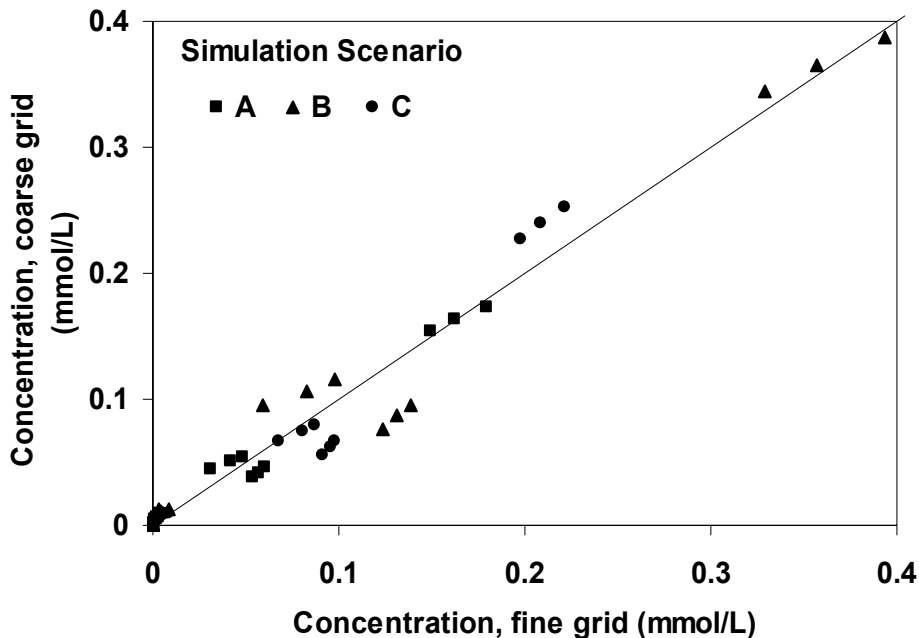


Figure 4.65. Comparison of PCE Concentrations Simulated with Abiotic Dissolution Model Using Fine and Coarse Grids, Upscaling Simulations of Bioenhanced Dissolution

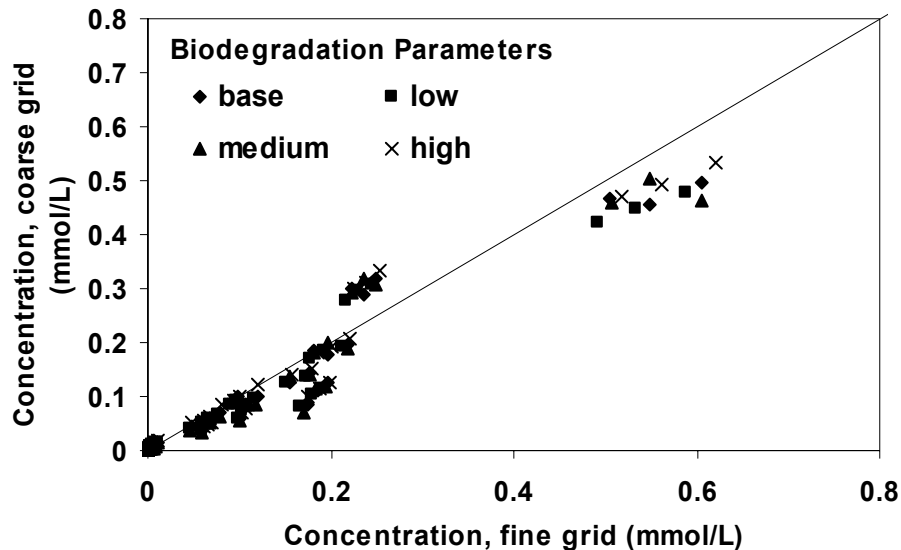


Figure 4.66. Comparison of Total Ethene Concentrations Simulated Using Fine and Coarse Grids, Upscaling Simulations of Bioenhanced Dissolution

4.5.4 Summary of key results

Column, flow-cell and large-tank experiments showed significantly enhanced mass transfer from DNAPL sources with an average saturation of 60 percent or less. Bioenhanced dissolution occurred by biodegradation of PCE within source zones to less chlorinated but toxic daughter products with rapid degradation to nontoxic ethene in adjacent downgradient areas.

A conceptual and numerical model of bioenhanced DNAPL dissolution based on the widely used RT3D code was developed and applied successfully to experimental results. The resulting model is suitable for use as a remediation screening tool at sites contaminated with chlorinated DNAPL.

In sources dominated by pools, accurate simulation of bioenhanced dissolution requires inclusion of saturation transition zones at pool boundaries. Bioenhanced dissolution depends on an adequate supply of electron donor within pool transition zones. Electron-donor advection within transition zones promotes rapid PCE degradation, lower aqueous-phase PCE concentrations, enhanced dissolution gradients, and increased rates of pool depletion. Therefore, recognition of transition-zone hydrodynamics is critical to characterization and modeling of bioenhanced dissolution.

Simulations of experimental results showed that scale-dependent Gilland-Sherwood correlations developed for pre-remediation conditions are suitable for simulating bioenhanced dissolution. Biodegradation is a local-scale process that can be modeled with parameter estimates

derived at batch or column scales. A numerical simulation study suggests that dual-domain approaches can be effective for addressing sub-grid heterogeneity associated with pool transition zones.

4.6 Investigation of thermal treatment

Mass transfer during thermal treatment was characterized and modeled as a kinetic process with effective mass transfer rate coefficients estimated by Gilliland-Sherwood correlations. Research focused on understanding how thermal treatment affects solubility of PCE-DNAPL and empirical coefficients of Gilliland-Sherwood correlations. Hot-water flooding was selected for study as representative of the broader range of thermal technologies. Results presented here were obtained with batch and column experiments. Research to upscale these results to multi-dimensional flow systems in flow cells and large tanks is continuing.

Column experiments with PCE-DNAPL at residual saturation were conducted for a range of temperatures typically used in thermal technologies. Variations in temperature resulted in large variations in effluent concentration of aqueous-phase PCE. Higher temperature resulted in higher PCE concentration. Variations in flow rate also affected PCE concentration, but this effect was secondary to that of temperature. This implies that thermal-treatment designs may be optimized for temperature with optimization for flow rate being a secondary goal.

Temperature affects fluid viscosity and diffusion coefficients and therefore directly affects several dimensionless numbers used as a basis for Gilliland-Sherwood correlations. Statistical analysis of changes in empirical coefficients with temperature demonstrated that the use of Gilliland-Sherwood correlations developed at one temperature can be used to simulate mass transfer at greater temperatures.

4.7 Three dimensional simulation of mass transfer during remediation

Much of the research presented in this report has focused on understanding of mass transfer processes and development of numerical modeling tools and site characterization methods. A very thorough characterization was required to understand these processes. However, this level of data collection and analysis typically is unrealistic for field studies. In this numerical modeling study, an analysis of characterization techniques was conducted assuming that only limited data at a limited number of locations were available. The capability of aquifer characterization methods and modeling tools was demonstrated by (1) simulating DNAPL distribution, mass transfer, and aquifer response to multiple-tracer tests following an assumed PCE-DNAPL spill in an idealized aquifer with specified hydraulic conductivity distribution, and (2) estimating DNAPL distribution and mass transfer by inverse modeling techniques based on data at 9 randomly selected well locations. DNAPL removal by SEAR technology was then simulated.

Simulations were based on an assumed heterogeneous unconfined aquifer having width, length, and depth of 15, 15, and 5 m respectively (Figure 4.67). No-flow boundaries were specified at the near and far ends of the aquifer and hydraulic heads were held constant at the left

and right ends of the aquifer. Average hydraulic gradient between the two constant-head boundaries was 10^{-3} . Hydraulic-conductivity distribution within the aquifer was specified as a spatially correlated random field with statistical parameters representing a highly heterogeneous sandy aquifer (Table 3.21). A spill of 872 kg of free-phase PCE (538 L) was assumed to contaminate the aquifer from the top boundary. Simulations were conducted using UTCHEM (Delshad et al., 1996) to describe the spatial distribution of DNAPL within the source zone, as well as hydraulic head, and aqueous-phase PCE concentration within the aquifer. A multiple-tracer test was simulated and the spatial and temporal distributions of partitioning tracer concentration were determined. For clarity, simulation results were designated as the IDEAL aquifer characterization.

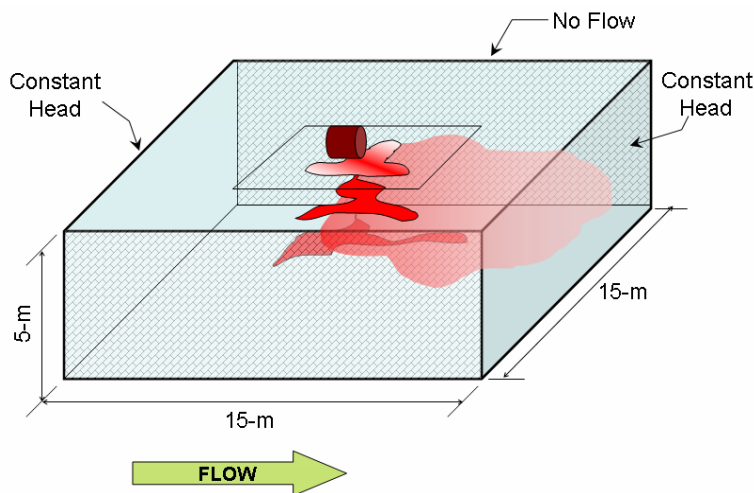


Figure 4.67. Hypothetical Aquifer Used in Three-Dimensional Study of Mass Transfer

Estimation of aquifer response based on data at a limited number of well locations began by assuming no prior information to describe the hydraulic conductivity field and DNAPL entrapment architecture. Borehole lithology, pumping-test response, PCE concentration data, and tracer test response at the 9 locations were then used during model calibration to estimate aquifer-property distribution, plume configuration, and DNAPL source architecture. For clarity, simulation results obtained by inverse modeling were designated as the AQ9 aquifer characterization. After obtaining the AQ9 characterization, SEAR was implemented to demonstrate remediation capabilities.

Numerical simulations were conducted using the MODFLOW-2000 (Harbaugh et al., 2000), MT3DMS (Zheng and Wang, 1999), and RT3D (Clement, 1997). Inverse modeling was conducted using UCODE (Poeter and Hill, 1998) and PEST (Doherty, 1994).

4.7.1 IDEAL aquifer characterization

Random Field Generation. The hydraulic conductivity field was designed as a spatially correlated random field with statistical parameters representing a highly heterogeneous sandy aquifer. A random field was generated corresponding to a log-normal distribution of hydraulic

conductivity with average $\ln K$ of 4.18 (K is in m/day) and variance $s_{\ln K}^2$ of 1.22. The correlation lengths in lateral (λ_h) and vertical (λ_v) directions were 5.0 and 1.0 m, respectively. The heterogeneous zone consisted of a finite-difference grid of 100 columns, 100 rows and 50 layers ($\Delta x = \Delta y = 0.15$ m, $\Delta z = 0.1$ m). The random field hydraulic conductivity selected for use in this study (Figure 4.68) was generated using a turning band algorithm (Tompson et al., 1989). Specific storage and specific yield were assumed to be homogeneous at 10^{-4} m⁻¹ and 0.2, respectively. Porosity was assumed to be uniformly 0.4 and dispersivity was assumed to be zero since a small grid size was used

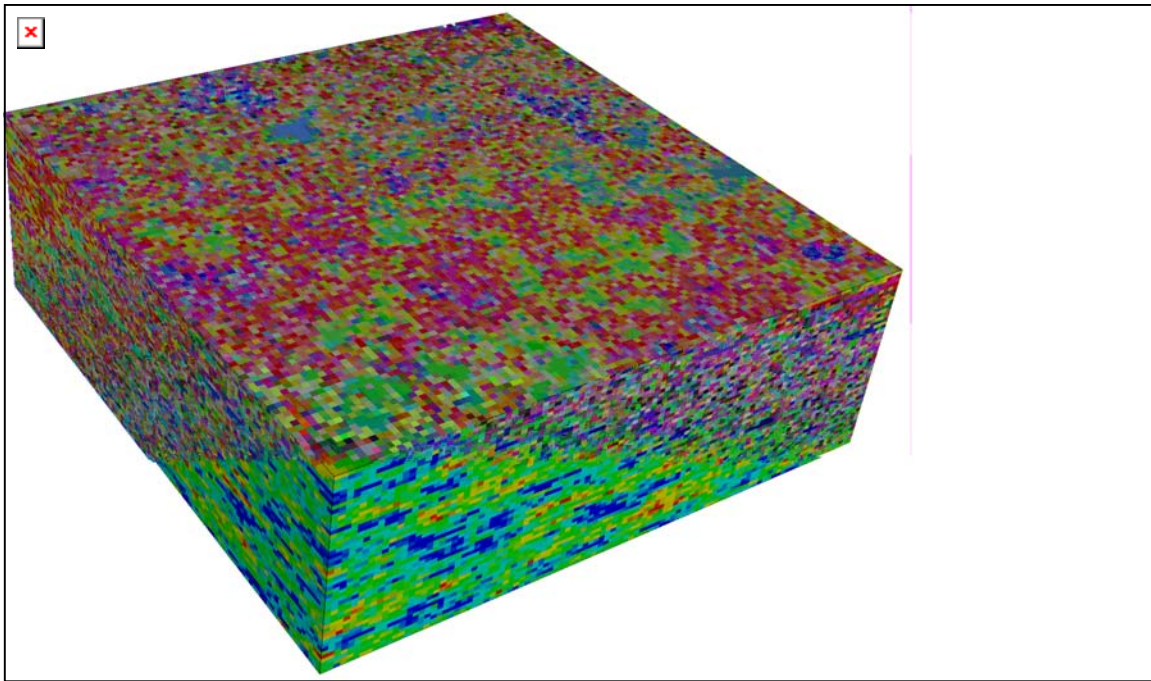


Figure 4.68. Hydraulic Conductivity Distribution for IDEAL Simulations, Three-Dimensional Study of Mass Transfer

PCE Spill Simulation. The PCE-DNAPL source was created within a 3m x 3m x 3m zone located at the center of the aquifer domain. Within this subdomain, the permeability field was discretized into five categories representing five sands used throughout this research (Table 3.6, #16, #30, #50, #70, and #110). Brooks and Corey relative permeability saturation and capillary pressure saturation relations were used to describe constitutive relations for multi-phase flow. A spill of PCE-DNAPL was simulated using the three dimensional multiphase, multi-component flow and transport simulator UTCHEM (Delshad et. al, 1996). A total of 538 L of PCE was injected at the top center of the subdomain through 32 wells of 4 cm depth and allowed to distribute for 1 day. No flow boundaries were maintained along the sides, top, and bottom of the subdomain. Constant pressure and saturation were specified for the left and right boundaries respectively. The resulting distribution of DNAPL is shown in Figure 4.69.

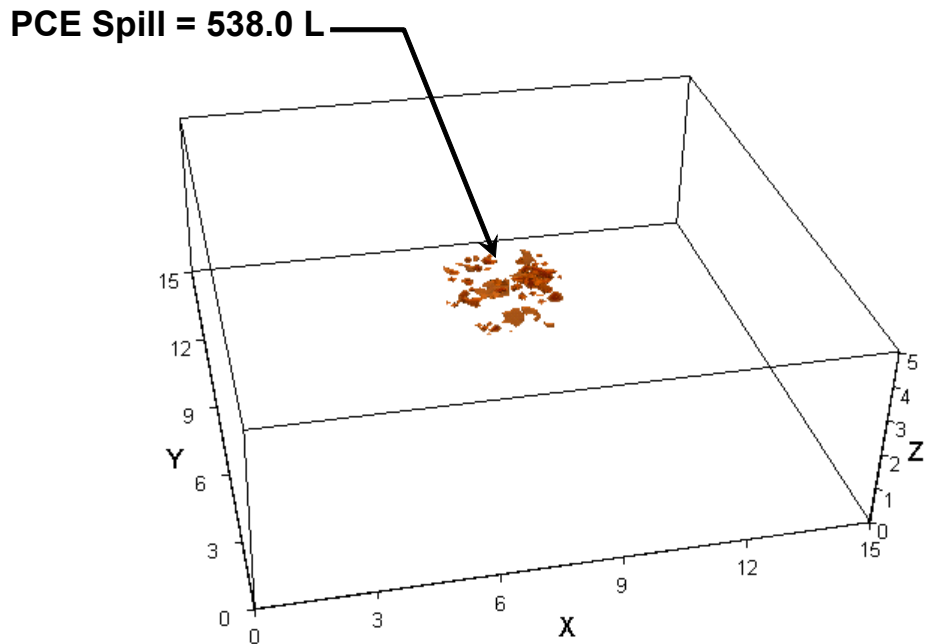


Figure 4.69. PCE DNAPL Distribution Based on UTCHEM Simulation, Three-Dimensional Study of Mass Transfer

Natural Dissolution. Simulations were conducted to generate a steady-state dissolved PCE plume (Figure 4.70). The dissolved-phase PCE plume for natural dissolution in the IDEAL aquifer was obtained by using mass transfer correlations described in Equation 3.16 and the values of α_1 - α_4 listed in Table 4.1. This concentration plume was used to identify PCE concentration at well locations used in inverse modeling and to provide a basis of comparison with estimated plume configuration for the AQ9 aquifer characterization. In Figure 4.70, monitoring wells colored white indicate 0.0 mg/L PCE concentration whereas the observation wells colored red indicate a non-zero PCE concentration. Monitoring wells located downstream of the DNAPL source detect dissolved PCE in groundwater.

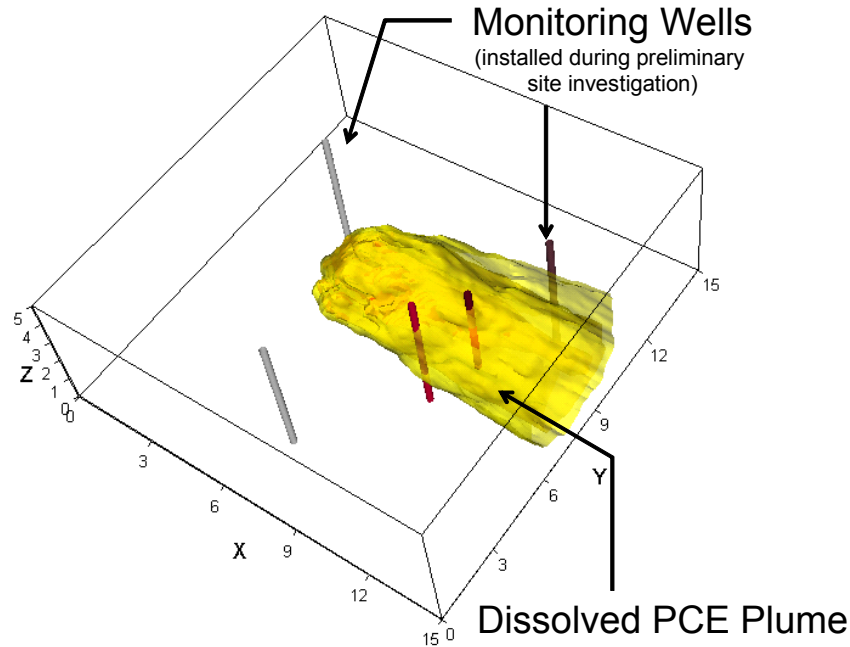


Figure 4.70. Locations of Observation Wells and Steady-State Dissolved PCE Plume, Three-Dimensional Study of Mass Transfer

Pumping Tests. Pumping test simulations were conducted using MODFLOW-2000 program with the Multi-Node Well (MNW1) package (Halford and Hanson, 2002). Pumping test simulations were conducted using four wells (Figure 4.71). One well was pumped during each test with the remaining three wells serving as observation wells. Time-drawdown data at the observation wells were analyzed using the type-curve matching program WTAQ (Barlow and Moench, 1999). In this way, average hydraulic conductivity and specific yield/storage values were obtained. These values were used as initial estimates for inverse modeling during AQ9 aquifer characterization.

Figures 4.72 and 4.73 show water-table contours at an intermediate time for pumping tests at PW1 and OW4. In each test, the simulated pumping rate was $25\text{m}^3/\text{day}$. Early time-drawdown data at observation wells were analyzed using WTAQ program (Barlow and Moench, 1999) and resulting estimates of average hydraulic conductivity, specific yield, and specific storage were used in subsequent inverse modeling as initial parameter values. Figures 4.74 and 4.75 illustrate the type-curve matches obtained for PW1 and OW4.

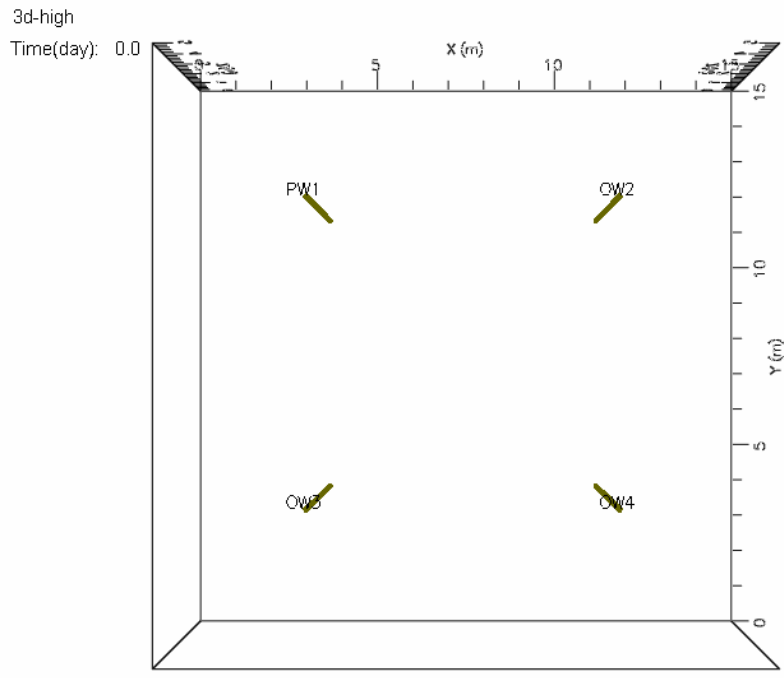


Figure 4.71. Locations of Pumping and Observation wells, Three-Dimensional Study of Mass Transfer

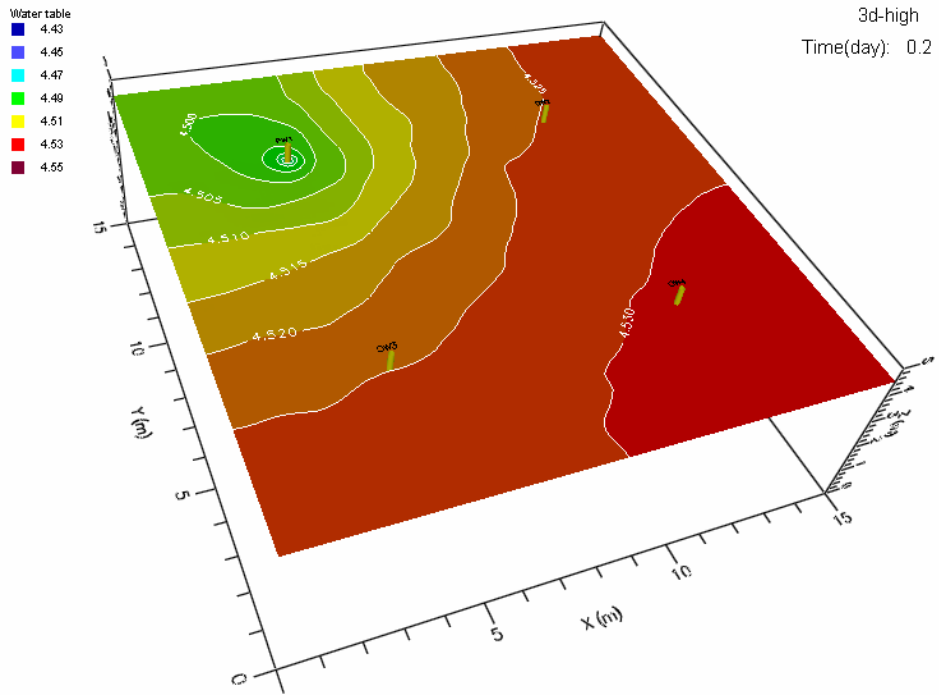


Figure 4.72. Water-Table Configuration for IDEAL Simulation After 0.2 Days of Pumping at PW1, Pumping Rate is 25 m³/day, Three-Dimensional Study of Mass Transfer

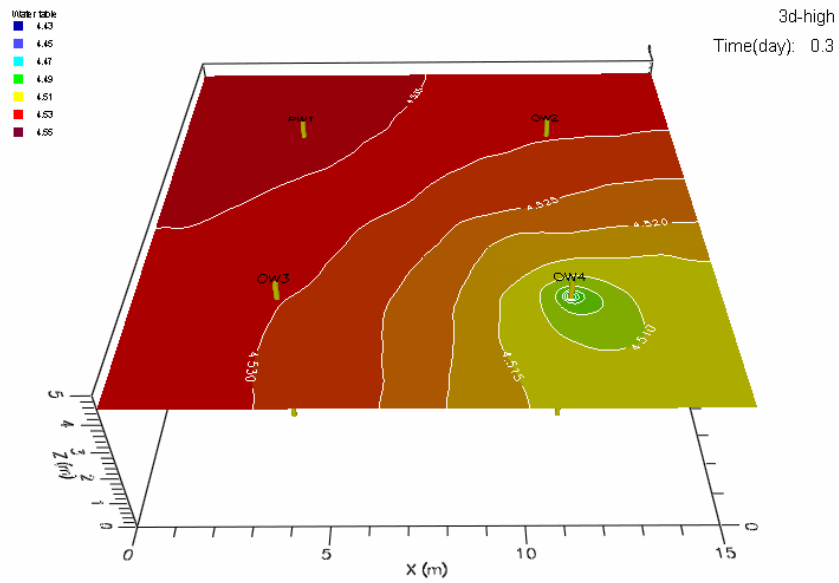


Figure 4.73. Water-Table Configuration for IDEAL Simulation After 0.2 Days of Pumping at OW4, Pumping Rate is 25 m³/day, Three-Dimensional Study of Mass Transfer

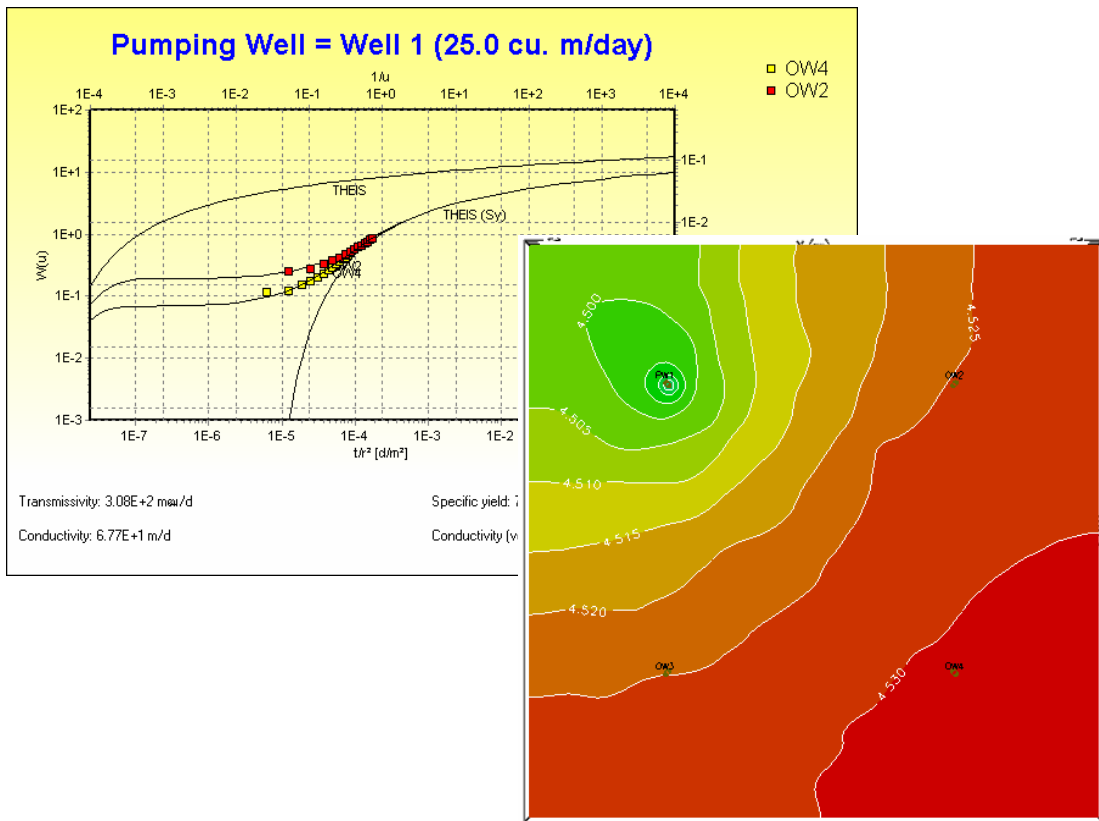


Figure 4.74. Type-Curve Matching for Pumping Well PW1, Three-Dimensional Study of Mass Transfer

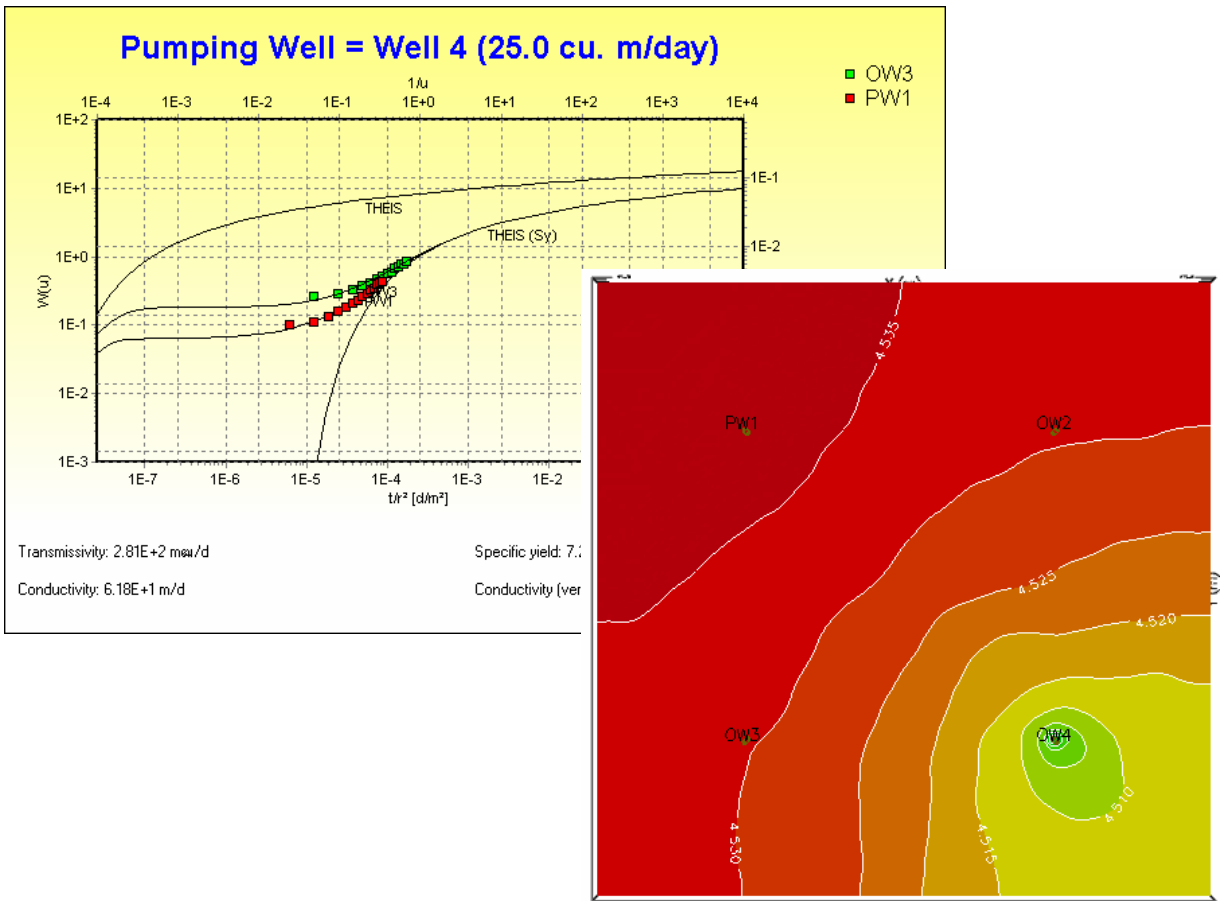


Figure 4.75. Type-Curve Matching for Pumping Well OW4, Three-Dimensional Study of Mass Transfer

Multiple Tracer Test. A multiple tracer test was simulated using bromide as a conservative tracer and 2,2-dimethyl-3-pentanol or DMP as a partitioning tracer. Simulation of DMP transport was conducted using an equilibrium partition coefficient (K_p) of 27.5. Injection and extraction wells were located upstream and downstream of the DNAPL source zone (Figure 4.76). The simulated tracer test was conducted using a 1000-mg/L bromide and 500.0-mg/L DMP solution injected at a rate of 25 m³/day for two days in a steady-state flow field. The tracer solution was then replaced by clean water while the injection rate remained constant. Total simulation time was 58 days.

Simulations were conducted using MODFLOW and MT3DMS programs to generate transient bromide and DMP breakthrough curves at several monitoring locations (Figure 4.76). The MODTRACER (Saenton, 2003) pre-processor program was used to generate files necessary for simulating NAPL/water partitioning phenomena of DMP. For purposes of AQ9 aquifer characterization described later, breakthrough concentrations were recorded daily at selected multi-level sampling locations.

Both bromide and DMP breakthrough curves were analyzed using the method of temporal moments to obtain PCE saturation at various locations. Resulting PCE saturation data (Figures 4.77 and 4.78) were used as initial estimates for subsequent AQ9 aquifer

characterization. Breakthrough curves of both tracers in the extraction well (Figure 4.79) were analyzed and only 229.7 L of PCE was detected. This represented an underestimation of actual PCE by 42.7 percent.

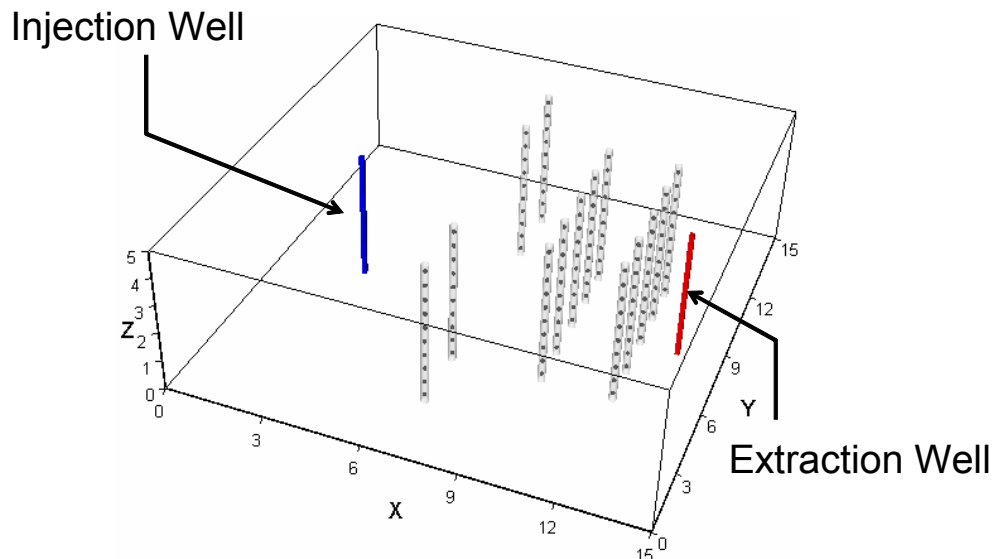


Figure 4.76. Multi-Level Sampling Wells and Injection-Extraction System used in the Multiple Tracer Test, Three-Dimensional Study of Mass Transfer

4.7.2 AQ9 aquifer characterization

Aquifer characterization at actual sites is not possible to the level of detail provided by the IDEAL simulations of the previous section. Instead, aquifer characterization must be based on a limited set of observations. The objective of this section is to estimate aquifer response based on data at a limited number of well locations. As often occurs at actual sites, efforts to characterize aquifer response began by assuming no prior information was available to describe the hydraulic conductivity field and DNAPL entrapment architecture. Borehole lithology, pumping-test response, PCE concentration data, and tracer test response at the 9 locations were then used during model calibration to estimate aquifer-property distribution, plume configuration, and DNAPL source architecture.

Borehole Lithology. Nine borehole logs were randomly selected (Figure 4.80) and soil types were recorded. It was assumed that well-log analysis provided geological information that could be correlated to soil hydraulic conductivity. Hydraulic conductivity (K) estimates from well-log analyses were considered to be initial estimates for subsequent refinement. The histogram of initial estimates was log-normally distributed (Figure 4.81). The continuous $\ln K$ distribution indicated by a Gaussian fit to the histogram was divided into five categories corresponding to the five soil types noted in the borehole logs. Estimates of hydraulic conductivity as well as soil-storage parameters for each soil type were refined during subsequent inverse modeling of pumping test data.

AQ9 aquifer modeling began by constructing a uniform grid system (50 row, 50 columns, and 25 layers) and estimating the distribution of soil types throughout the model domain. Soil-type data at the 9 boreholes were used with the *t-progs* algorithm of the GMS 5.0 program to interpolate the distribution of soil types throughout the model domain. Figure 4.82 shows examples of soil distribution in layers 6 and 12, and Figure 4.83 illustrated the 3-D distribution of soil in this AQ9 aquifer after interpolation by *t-progs* was completed.

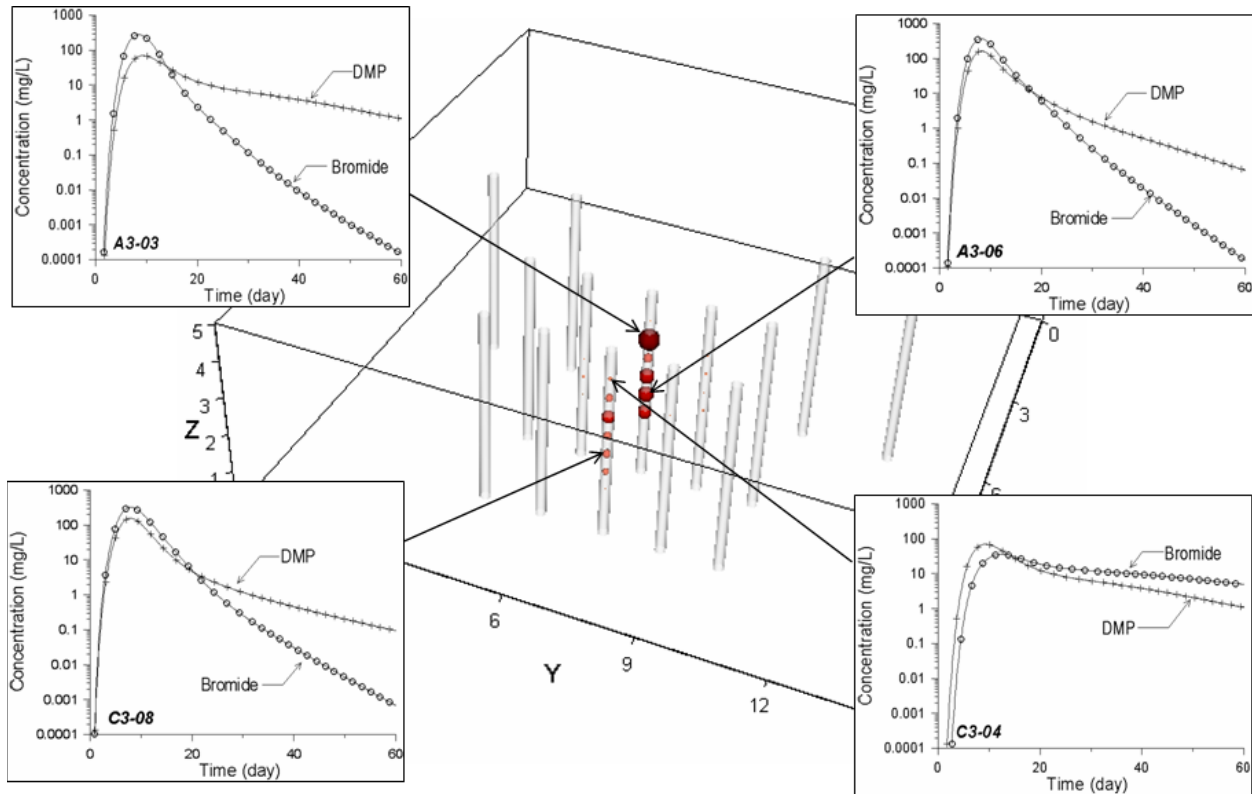


Figure 4.77. Examples of Breakthrough Curves at Two Multi-Level Sampling Wells, Three-Dimensional Study of Mass Transfer. Larger Sphere Indicates Higher PCE Saturation Calculated by the Method of Moments.

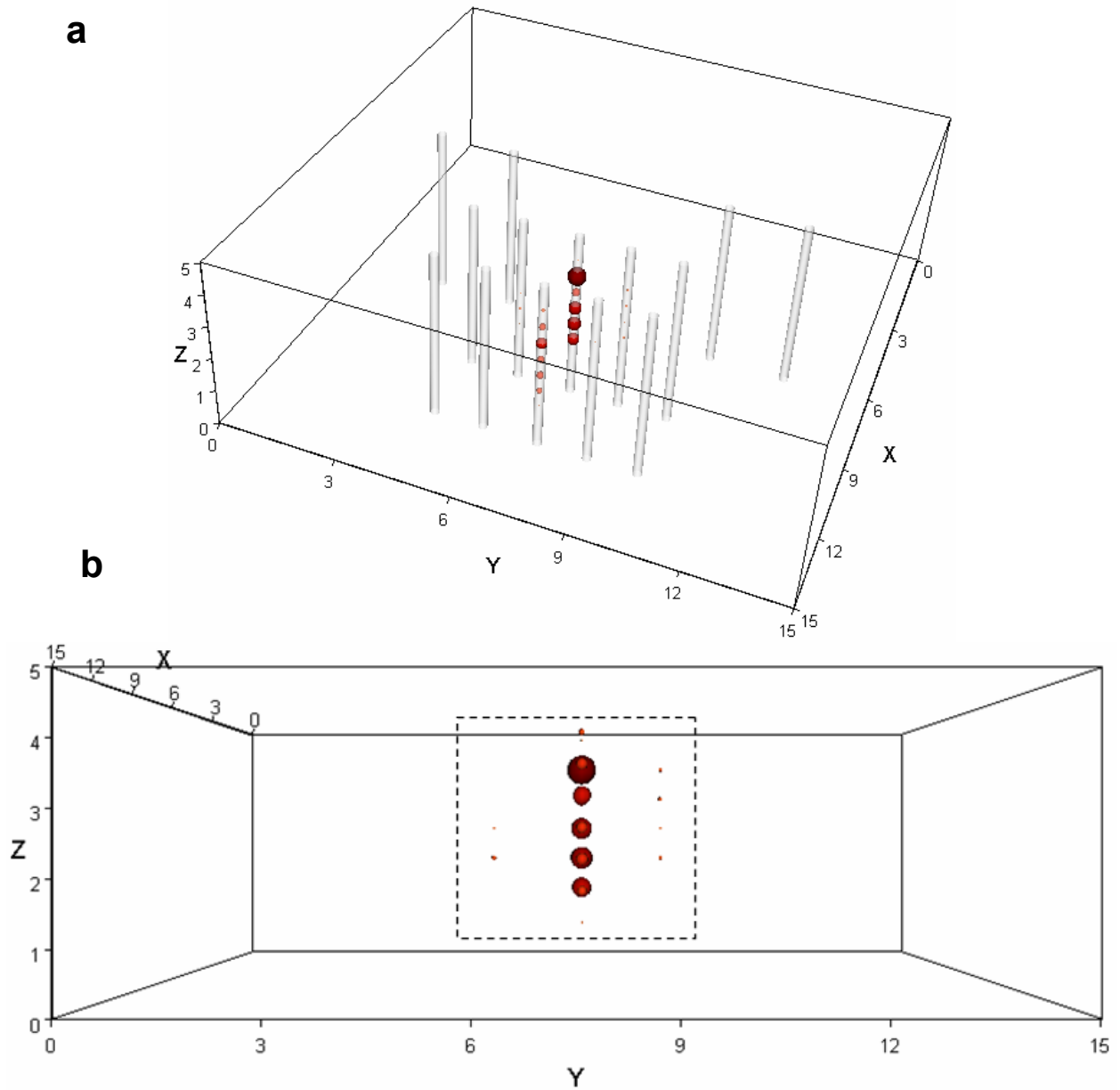


Figure 4.78. Point Estimates of PCE Saturation Based on the Method of Moments Analysis (a) 3-D View, and (b) View from Downstream, Three-Dimensional Study of Mass Transfer

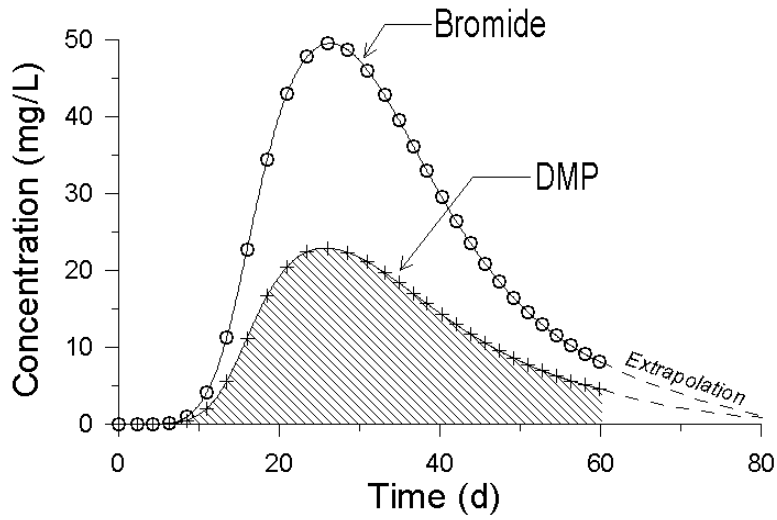


Figure 4.79. Tracer Breakthrough Curves at the Extraction Well, Three-Dimensional Study of Mass Transfer

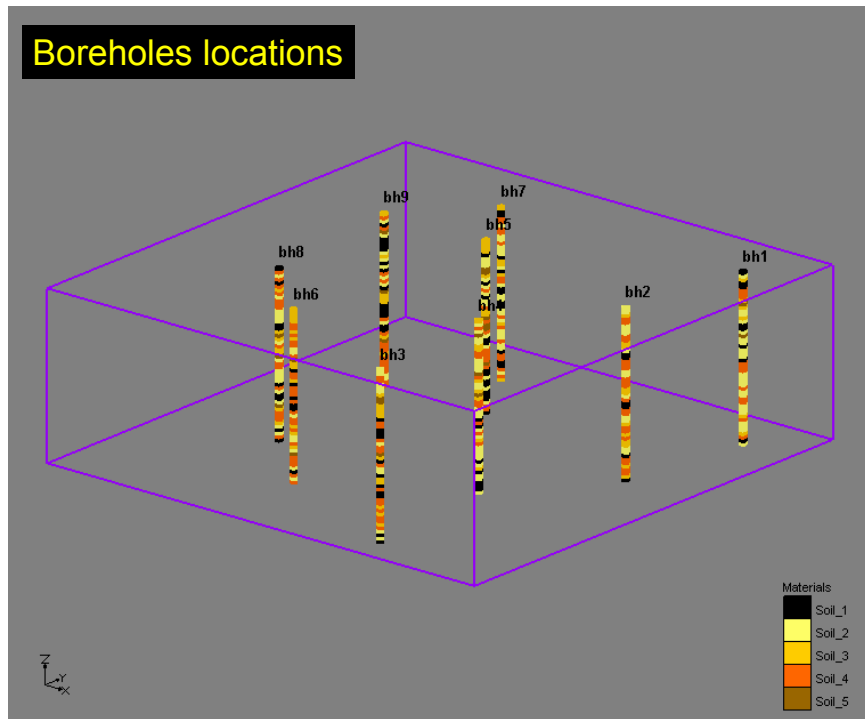


Figure 4.80. Borehole Logs of Soil Types and Spatial Distribution of Boreholes Used in AQ9 Aquifer Characterization, Three-Dimensional Study of Mass Transfer

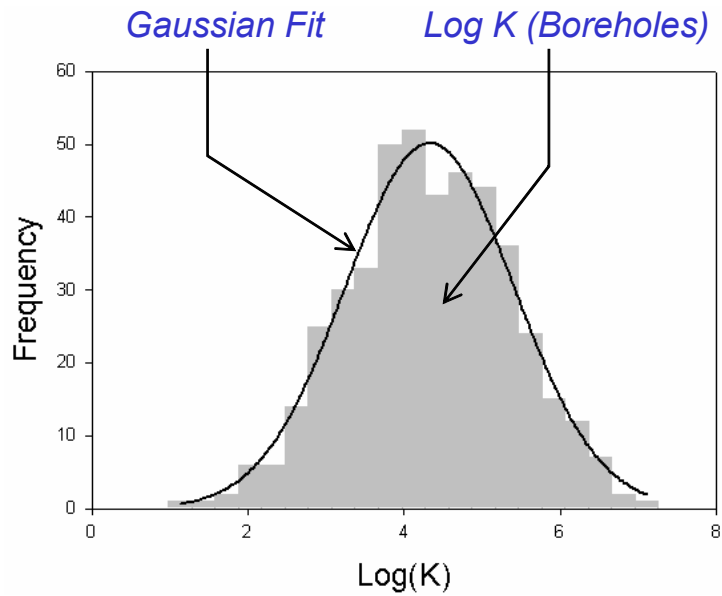


Figure 4.81. Histogram of Log Hydraulic Conductivity Obtained from Borehole Well-Log Analysis, Three-Dimensional Study of Mass Transfer

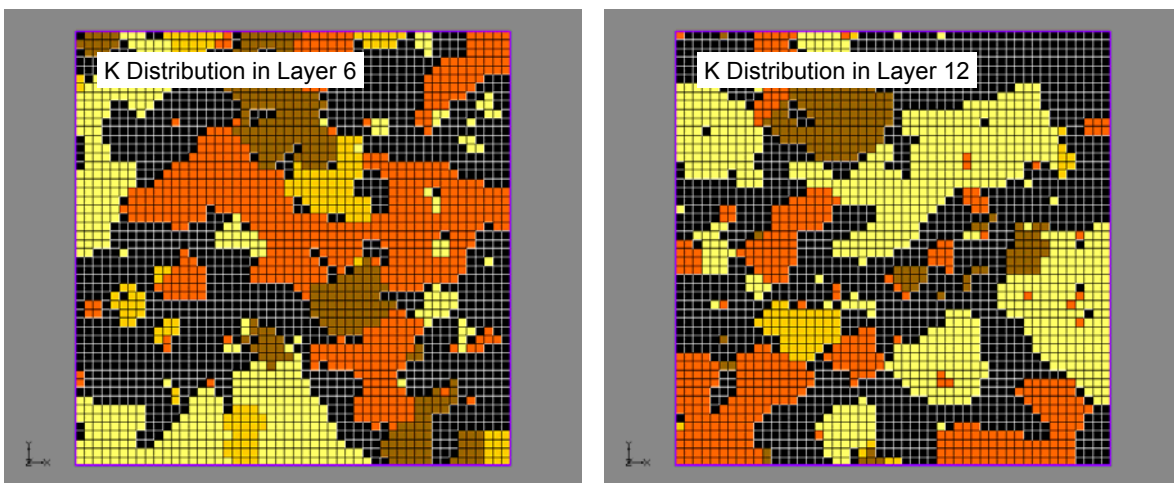


Figure 4.82. Example distributions of soil materials in layers 6 and 12, AQ9 Aquifer Characterization, Three-Dimensional Study of Mass Transfer

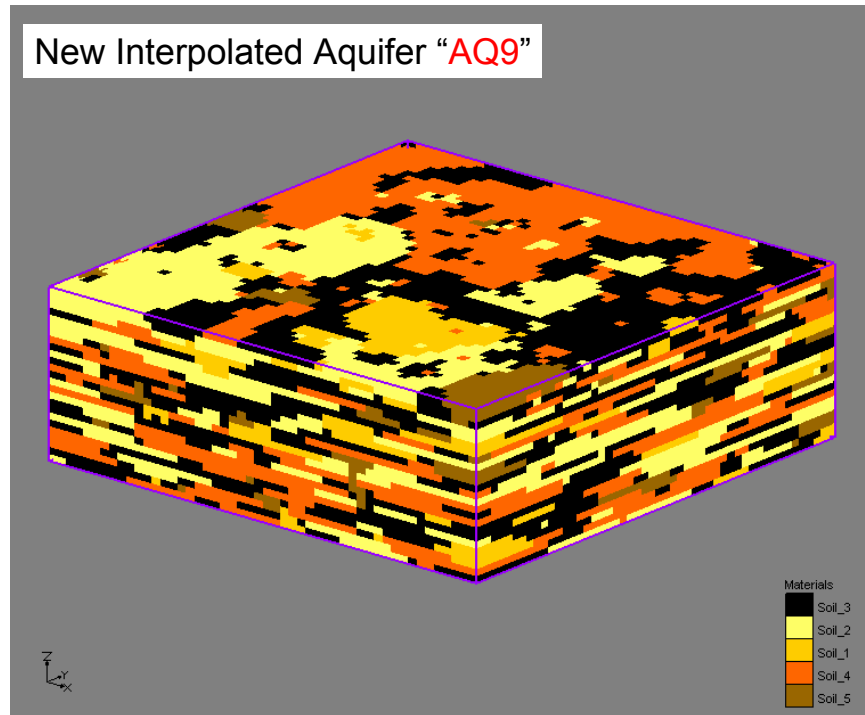


Figure 4.83. Soil-Type Distribution, AQ9 Aquifer Characterization, Three-Dimensional Study of Mass Transfer

Flow Parameter Calibration. After the soil-type distribution for the AQ9 aquifer was obtained, four pumping tests were simulated using MODFLOW-2000 with the MNW1 package. For each test, the inverse modeling algorithm PEST was coupled with this MODFLOW simulation in order to match measured time-drawdown data extracted from the IDEAL aquifer simulation for the 9 well locations. Estimated parameters included hydraulic conductivity, specific storage, and specific yield for each of the five soils. Initial estimates for these parameters were input based on results of type-curve matching described previously. During inverse modeling, parameter values were varied on the basis of the soil-type distribution giving a total of 15 parameters. Figure 4.84 show model simulated and observed time-drawdown data in the pumping well for the four tests after calibration with PEST. Optimized parameter values are listed in Table 4.22.

Transport Parameter Calibration. After flow parameters of the AQ9 aquifer were estimated, bromide tracer tests were simulated. The inverse modeling algorithm PEST was coupled with this simulation in order to match bromide breakthrough curves extracted from the IDEAL aquifer simulation at the 9 boreholes. Estimated parameters included effective porosity and effective dispersivity of each of the five soils. Optimized parameter values for the transport model are listed in Table 4.23. The optimized values for $\alpha_{T,h}/\alpha_L$ and $\alpha_{T,v}/\alpha_L$ are 1.0 and 0.351, respectively.

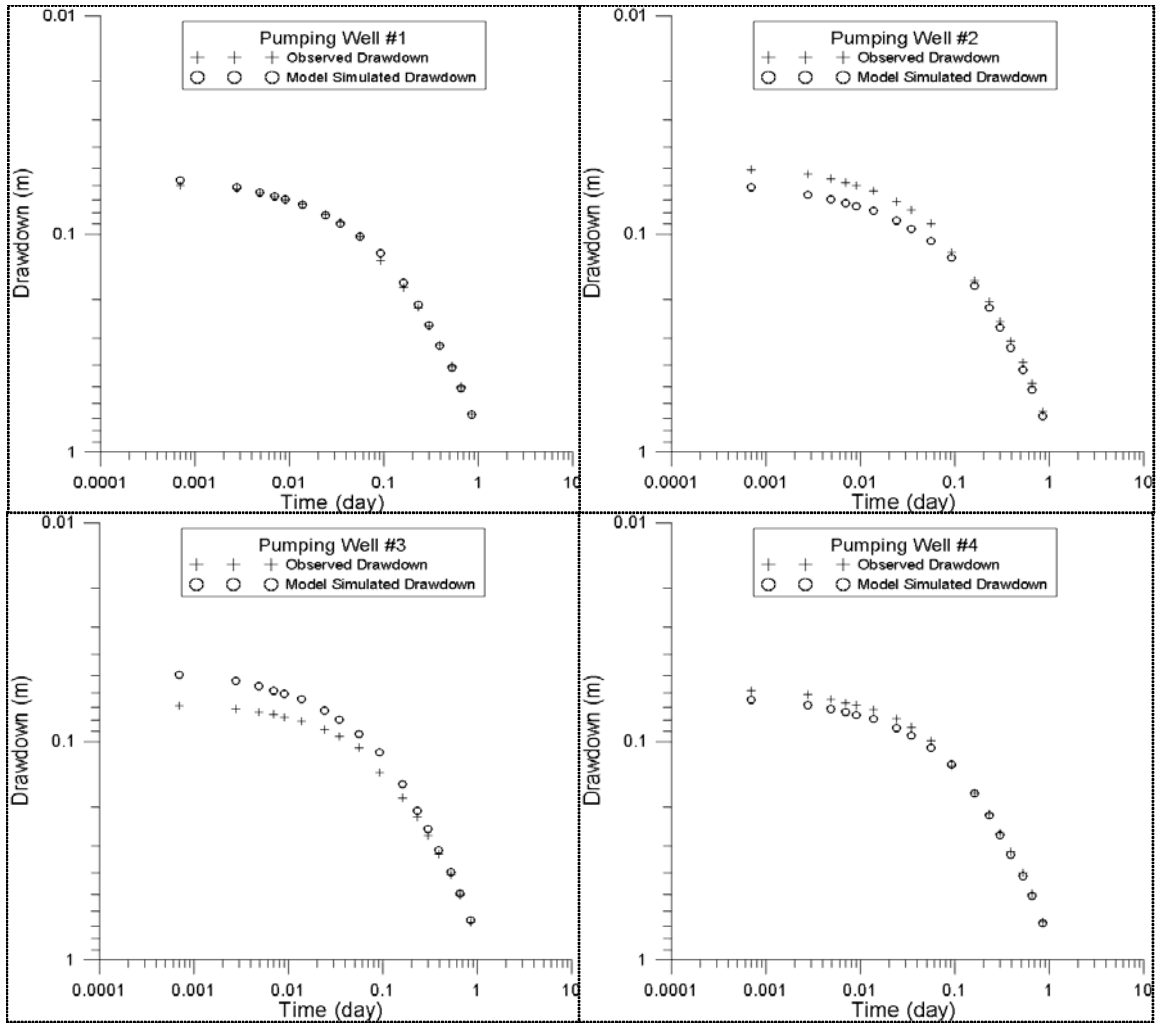


Figure 4.84. Observed (IDEAL) and Simulated (AQ9) Time-Drawdown Plots for Pumping Tests, Three-Dimensional Study of Mass Transfer

Table 4.22. Calibrated Flow Parameters, AQ9 Aquifer Characterization, Three-Dimensional Study of Mass Transfer

| Soil Type | K (m/d) | S_s (m^{-1}) | S_y |
|-----------|---------|-----------------------|-------|
| 1 | 1.65 | 1.02×10^{-6} | 0.196 |
| 2 | 38.6 | 5.05×10^{-4} | 0.176 |
| 3 | 97.3 | 1.72×10^{-6} | 0.100 |
| 4 | 140.6 | 1.00×10^{-6} | 0.307 |
| 5 | 326.5 | 1.09×10^{-6} | 0.100 |

Table 4.23. Calibrated Transport Parameters, AQ9 Aquifer Characterization, Three-Dimensional Study of Mass Transfer

| Soil Type | Effective Porosity | Effective Dispersivity (m) |
|-----------|--------------------|----------------------------|
| 1 | 0.352 | 1.0×10^{-10} |
| 2 | 0.281 | 1.0×10^{-10} |
| 3 | 0.304 | 1.86×10^{-1} |
| 4 | 0.484 | 1.98×10^{-2} |
| 5 | 0.550 | 2.10×10^{-1} |

PCE Source Zone Characterization. To determine NAPL entrapment architecture, partitioning tracer tests were simulated using MODTRACER coupled with the inverse modeling algorithm PEST. DMP breakthrough curves extracted from the IDEAL simulation at the 9 boreholes were used as observation data during inverse modeling. In order to optimizing PCE saturation, it was necessary to identify a source-zone boundary. Average NAPL saturation from tracers test (Figure 4.78) and observed steady-state PCE concentration (Figure 4.85) were used to estimate an approximate source-zone size as 3.5 m long (*y*-direction) and 3.75 m deep (*z*-direction). It was also assumed that the extent of NAPL in *x*-direction was similar to the extent in the *y*-direction. Figure 4.86 show the NAPL saturation distribution or entrapment architecture determines by inverse modeling. Total PCE volume was calculated to be 441.6 L. This was 82.1 percent of the total NAPL mass present in the IDEAL aquifer.

Based on the estimated entrapment architecture, natural dissolution was simulated and downstream PCE concentrations at the locations in the monitoring arrays were compared to observed values. Mass transfer rate coefficients were estimated using the Gilland-Sherwood expression with parameter values given in Table 4.1. These values also were used to generate the IDEAL aquifer distribution of mass flux. Therefore, inverse modeling served to evaluate uncertainty associated with NAPL entrapment architecture. No calibration was required for the dissolution model. Figure 4.87 compares steady-state dissolved PCE plume from both IDEAL and AQ9 aquifers.

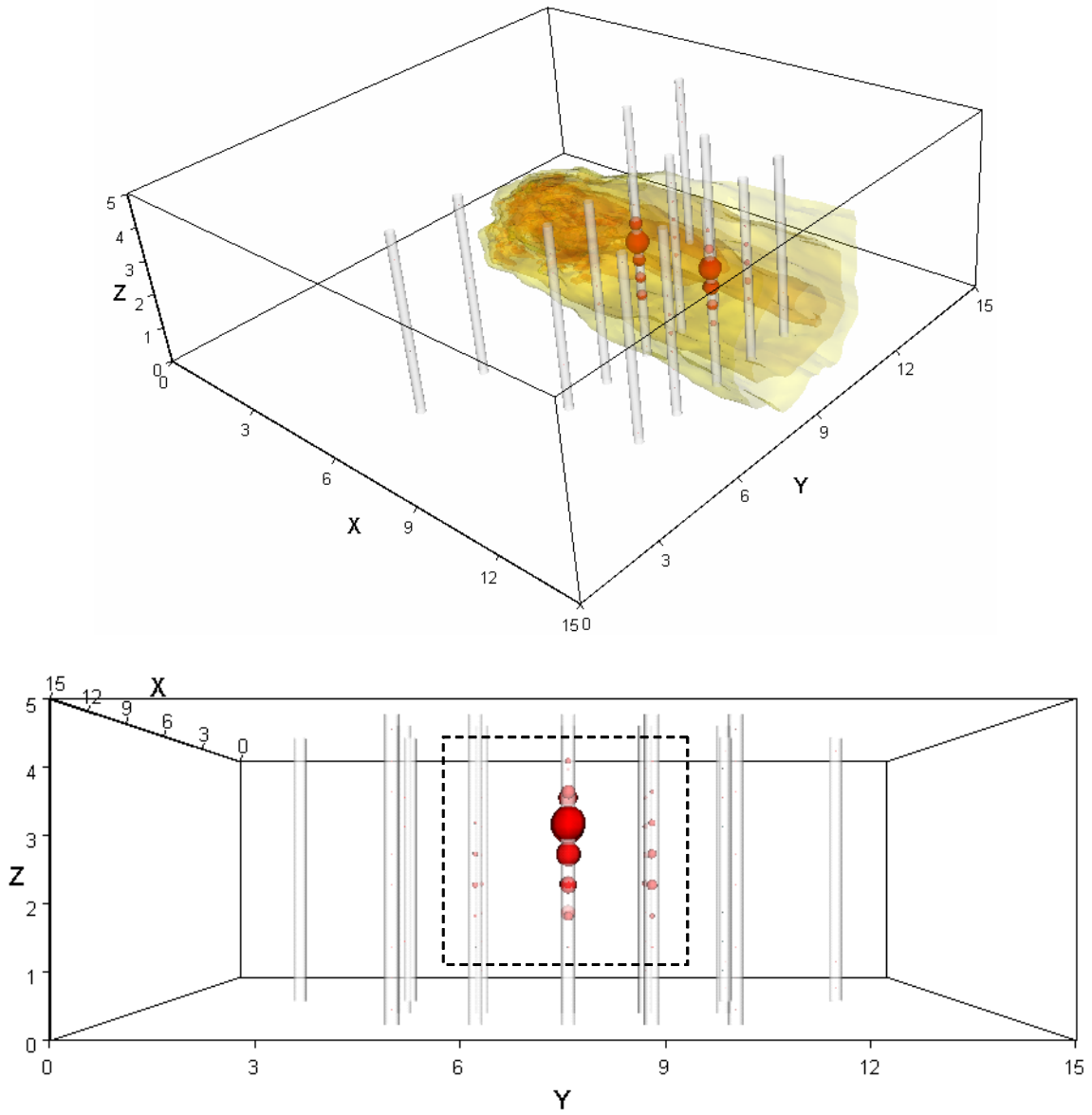


Figure 4.85. Measured Steady-State PCE Concentration at Sampling Wells (red spheres), Three-Dimensional View (top) and View from Downstream (bottom), Three-Dimensional Study of Mass Transfer

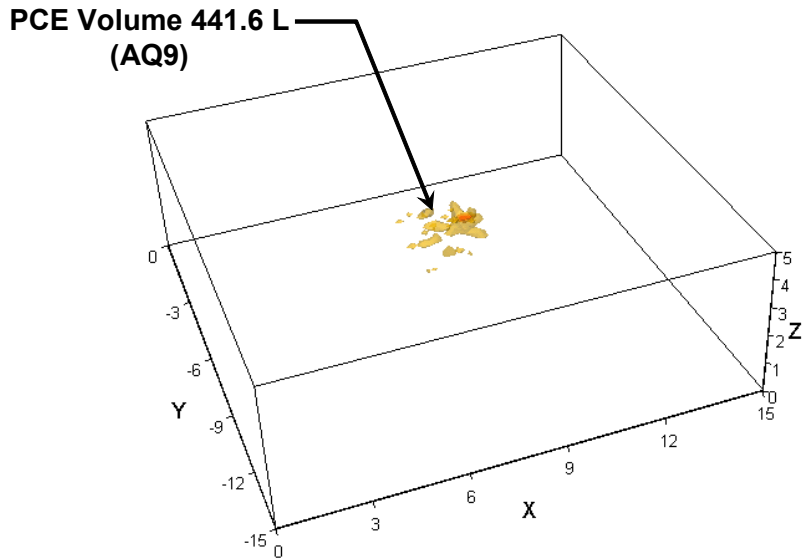


Figure 4.86. PCE Source Zone Estimated by Inverse Modeling, AQ9 Aquifer Characterization, Three-Dimensional Study of Mass Transfer

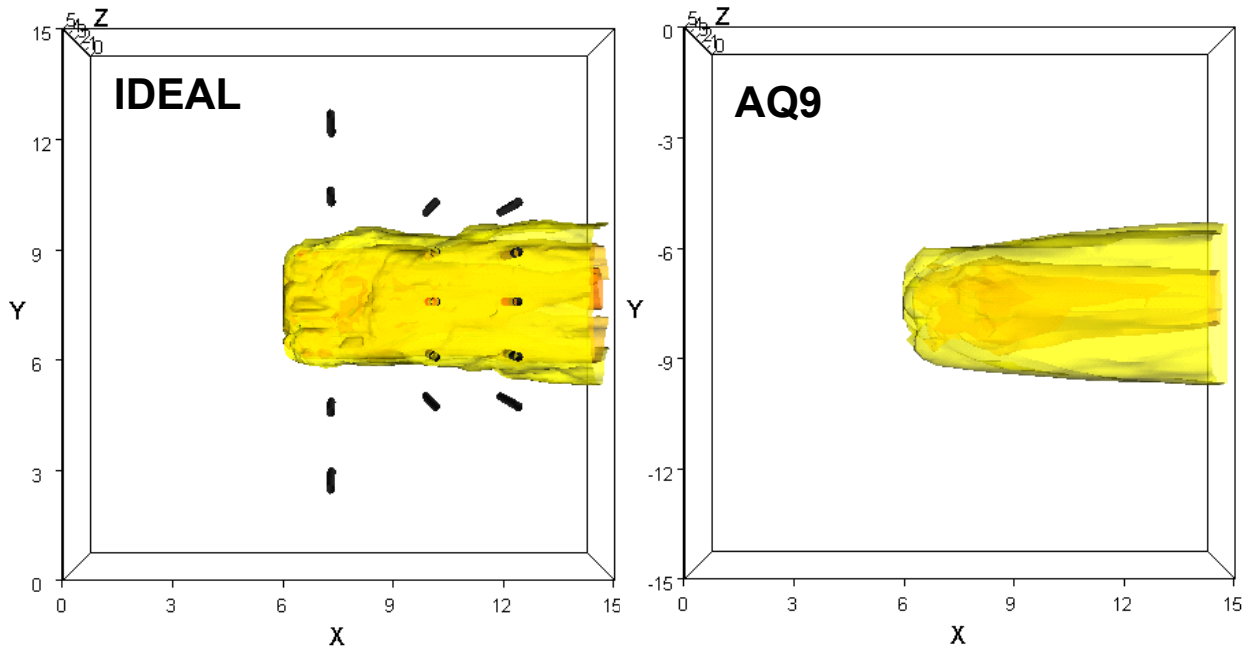


Figure 4.87. Comparison of steady-state dissolved PCE plume from the IDEAL and AQ9 Aquifer Characterizations, Three-Dimensional Study of Mass Transfer

Remediation Simulation. Surfactant-enhanced remediation (SEAR) was simulated for the AQ9 aquifer characterization. Because no simulation of SEAR was performed for the IDEAL aquifer, results could not be compared to evaluate effects of data uncertainty on remediation effectiveness. However, the simulation does provide an indication of SEAR effectiveness in heterogeneous source zones.

Prior to simulating SEAR, particle tracking simulations were conducted and a surfactant-delivery system was designed. As a result, the source zone estimated during AQ9 aquifer characterization was fully contained within capture zone of the designed delivery scheme (Figure 4.88).

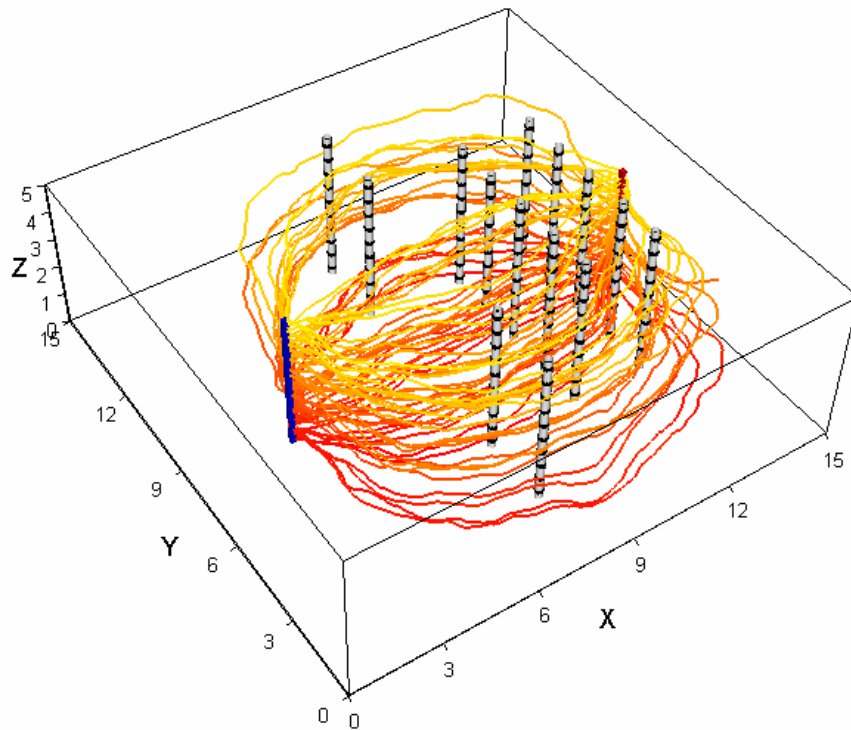


Figure 4.88. Particle Tracking Simulation of the Surfactant Delivery System, AQ9 Aquifer Characterization, Three-Dimensional Study of Mass Transfer

Simulated remediation involved continuous injection of a 50.0 g/L Tween-80 surfactant solution. Injection rate was 25.0 m³/day. Water was extracted at the same rate at a single well downstream of the source zone. PCE mass in the source zone and the concentration of dissolved PCE in extracted water were recorded as a function of time (Figure 4.89). Results indicated that a long period of surfactant injection was required before remediation was effective in removing the majority of PCE NAPL. SEAR was not very effective in removing NAPL mass at early simulation time due to effects of surfactant solution preferentially bypassing high saturation portions of the source zone. No simulation of post-remediation conditions was conducted.

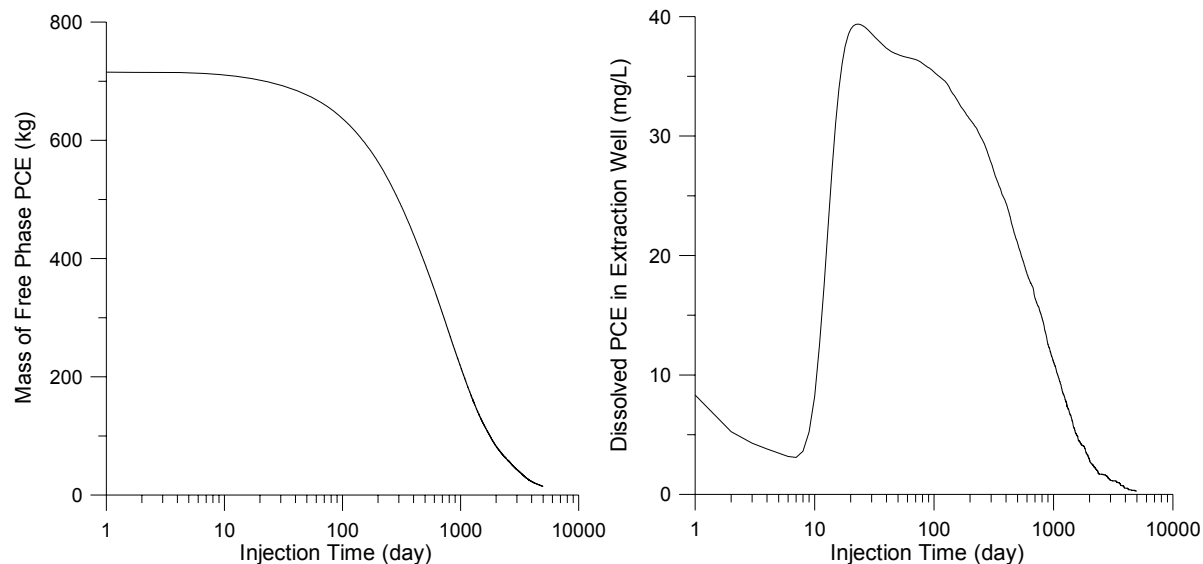


Figure 4.89. SEAR Simulation Results, AQ9 Aquifer Characterization, Three-Dimensional Study of Mass Transfer

4.7.3 Summary of key results

A numerical experiment demonstrated the ability to characterize mass transfer from a heterogeneous source in conditions with limited data. Key findings of this research project in conjunction with inverse modeling techniques were used to evaluate DNAPL mass distribution and mass depletion on the basis of hydraulic and chemical data at a limited number of wells located downgradient of the source. In the heterogeneous geological setting considered, characterization of source-zone configuration, mass transfer and remediation effectiveness required an understanding of plume and tracer distribution transverse to the primary direction of groundwater flow. In field settings, this type of data would be obtained by constructing monitoring wells as multi-level samplers.

5.0 Conclusions and Implications

Characterizing and modeling mass transfer from a heterogeneous DNAPL source and predicting effectiveness of source remediation can be a daunting task. This is particularly true when resources to map source heterogeneity and downgradient plume configuration are limited. The research presented in this report provides a technical defensible basis for addressing this task using pre-remediation mass-flux information supplemented by limited laboratory-scale study of remediation processes. Conceptual and numerical models of pre- and post-remediation mass transfer and partitioning tracer behavior were developed for several remediation technologies using bench-scale experimental results. These models were developed within the framework of widely used groundwater flow and reactive transport codes. Controlled experiments in large tanks provided large high-quality data sets for model validation at intermediate scales. The model validation studies support the use of these models in evaluating mass transfer during remediation at field scales. Additional research based on controlled field-scale experiments that provide high-quality data sets for model validation would prove beneficial.

5.1 Key accomplishments

A strategy for evaluating mass transfer from heterogeneous sources was developed that can simplify and decrease the amount of site data needed for source-zone characterization and remediation. At the same time, research results point to the importance of using monitoring wells as multi-level samplers to accurately understand mass transfer from heterogeneous sources and to generate required data input for inverse modeling techniques. The accuracy of these techniques is greatest in sources dominated by residual saturation (high ganglia-to-pool ratios) and declines in sources where pools predominate.

Common trends and patterns occur in the key research results presented in this report. These trends are listed below.

- For ISCO, bioremediation and thermal treatment, Gilland-Sherwood correlations describing pre-remediation mass transfer processes can be used with acceptable accuracy to predict mass transfer during and after remediation.
- Procedures for upscaling estimates of mass-transfer rate coefficients from bench to intermediate scales were developed and evaluated. For pre-remediation dissolution, the upscaled Gilland-Sherwood correlation is based on a local-scale Gilland-Sherwood expression in combination with geostatistical descriptions of aquifer-property heterogeneity and DNAPL entrapment architecture. For bioremediation and ISCO, upscaling of pre-remediation dissolution and hydrodynamic processes is required while no upscaling is required to parameterize reaction processes.
- Accurate characterization of mass transfer and tracer partitioning in sources dominated by pools requires simulation of hydrodynamics and remediation processes within saturation transition zones at pool boundaries.

- Flow paths through heterogeneous sources can be highly irregular resulting in water bypassing some high-saturation zones. For surfactant-enhanced remediation, ISCO, and bioremediation, this can limit delivery of chemicals to sites of active DNAPL dissolution and reaction, and adversely impact remediation effectiveness. Research to develop protocols for optimizing delivery of reactants in highly heterogeneous sources is needed.

A three-dimensional simulation study addressed the application of this research to field problems with limited data at a limited number of monitoring wells. In the heterogeneous geological setting considered, characterization of source-zone configuration, mass transfer and remediation effectiveness required an understanding of plume and tracer distribution transverse to the primary direction of groundwater flow. In field settings, this type of data would be obtained by constructing monitoring wells as multi-level samplers.

Experiments and model analyses presented in this report have shown that accurate description of mass-transfer characteristics and source depletion requires an understanding of source-zone architecture and porous-media heterogeneity. Treating a heterogeneous source zone as an equivalent homogeneous zone results in assessments of source remediation effectiveness that are highly uncertain. For example, preferential flow paths that are common in heterogeneous source zones, particularly those with high-saturation pools, have a pronounced effect on down gradient mass flux. However, preferential flow paths would not be modeled if a source zone is conceptualized as homogeneous.

The approach used throughout this research was to develop characterization and modeling methods that minimize the amount of extra field-scale data needed to characterize mass transfer. For example, this research demonstrates that estimates of many model parameters describing mass-transfer processes before, during and after remediation at field scale can be obtained from laboratory studies of small-scale systems using appropriate upscaling techniques. However, as demonstrated by a three-dimensional simulation study using a limited number of monitoring wells, characterization of mass transfer in a heterogeneous source zone requires a geostatistical description of soil types and knowledge of the spatial distribution of aqueous-phase contaminant in the plume down gradient of the source zone. Description of vertical variations in down gradient contaminant concentration are particularly important.

At many sites, existing borehole logs can provide information on the geostatistical nature of a porous media. Methods are also available to use tracer tests to estimate geostatistical parameters. However, well completions suitable for multi-level sampling rarely are available. In these situations, decisions regarding the characterization of source-zone architecture and down gradient mass flux, as well as remediation strategies, must be made with the realization that uncertainty in decisions can be high. If risks associated with this uncertainty are unacceptable, there is little alternative to collecting plume information with the aid of multi-level sampling wells.

5.2 Limitations

This research emphasized experiments and modeling at a variety of scales to characterize DNAPL source zone architecture and mass transfer in heterogeneous porous media undergoing

remediation. Although the number and scope of these experiments was large and has provided significant insight to source-zone characterization and mass transfer, no set of experiments can model all possible conditions at field sites. Therefore, it is important to recognize limitations inherent in these experiments.

Flow rates for large-tank experiments were selected on the basis of the remediation technique that was being evaluated. For surfactant flushing and chemical oxidation, field-scale remediation is likely to involve relatively rapid water movement within a forced-gradient system. Therefore, flow rates for surfactant and chemical-oxidation experiments were selected to be representative of a forced-gradient system that develops in response to relatively rapid injection upgradient of the source area. Specifically, flow rates were selected that provided average pore-water velocities in the range of 1.0 to 4.5 m/day. Because high flow rates typical of forced gradient systems were used, caution must be used in applying results of surfactant and chemical-oxidation experiments to natural-gradient flow systems. For experiments involving bioremediation much slower flow rates typical of natural gradients were used. Tests with biological activity were conducted at an average pore-water velocity of 0.20 to 0.24 m/day. These flow rates are consistent with typical field conditions during bioremediation.

Column and small flow cell experiments were performed using a wide range of flow rates. A primary goal of most of these experiments was to develop Gilland-Sherwood expressions for estimating mass transfer rate coefficients that would apply over a wide range of Reynolds number.

Experiments were conducted using a range of sandy materials. Use of sandy materials with minimal background organic content permitted research to focus on processes affecting mass transfer from DNAPL in heterogeneous material without complicating factors associated with sorption or clay-surface chemistry. Materials with low permeability, such as silt and clay, are common at hazardous waste sites. Therefore, caution should be used in extending research results presented in this report to sites dominated by low permeability material. For example, low permeability material can act as a long term source for contaminants by processes of diffusive transport. This continuing source can remain active long after a separate non-aqueous phase has fully dissolved. The process of back diffusion from low-permeability material such as clay and fine silt is not addressed by this research.

The sands used in heterogeneous tank experiments described in this research provided a three order-of-magnitude range in hydraulic conductivity with the very fine sand providing an estimate of 0.126 cm/min. Although this lower value is 5 to 10 times greater than values typically associated with clay, the fine sand performed functionally in a manner that was very similar to more fine-grained sediments. Irregular flow paths developed in tank experiments with preferential flow occurring through coarse-grained sands and minimal water movement through the fine-grained sands. DNAPL architectures created during spill experiments showed long-term entrapment at high saturation in coarse-grained lenses connected by thin vertical zones of residual saturation in fine-grained sediments.

Heterogeneity in flow paths and DNAPL distribution affects the ability to deliver partitioning tracer, surfactant, chemical oxidant, and bioremediation substrates to DNAPL source zones. This behavior is reflected in the upscaling knowledge and methods developed in this research. At a heterogeneous field site that includes low-permeability material, problems

associated with delivery of chemicals to a source zone may be even more significant. Nevertheless, results of this research provide a framework for addressing this problem.

5.3 Application of results to source-zone remediation and future research

Research described in this report has provided results that are particularly relevant to the practice of source remediation. These observations are provided in the following list.

1. Although partitioning interwell tracer tests (PITT) have been used to characterize source-zone depletion due to remediation at field sites, controlled experiments in heterogeneous porous media with known DNAPL distribution have shown that this method provides little accurate information to describe source-zone heterogeneity where knowledge of vertical distribution of DNAPL is needed. The method proved inaccurate due to hydrodynamic inaccessibility of pools for tracer partitioning.
2. Empirical Gilland-Sherwood correlations developed from column experiments can be used to simulate natural dissolution at larger scales by incorporating appropriate parameters of the multi-dimensional flow field. The upscaling method developed in this research is based on a local-scale Gilland-Sherwood expression in combination with geostatistical descriptions of aquifer heterogeneity and DNAPL entrapment architecture.
3. Effectiveness of surfactant-enhanced remediation decreases as source-zone heterogeneity increases. In experiments with greater source heterogeneity, groundwater bypassing due to relative permeability contrasts caused DNAPL mass removal efficiency to diminish significantly. Gilland-Sherwood correlations obtained from column tests undergoing surfactant-enhanced remediation are not appropriate to parameterize mass transfer in multidimensional flow systems at field sites.
4. A reactive transport model based on the widely used RT3D code was developed to simulate effects of in situ chemical oxidation (ISCO) on mass transfer. The model simulates PCE-DNAPL oxidation, TCE-DNAPL oxidation, natural oxidant demand (NOD) based on multiple NOD fractions, kinetic NOD oxidation of each fraction, and permeability reduction due to manganese oxide formation.
5. Effectiveness of ISCO depends on DNAPL source-zone architecture. Sources with low ganglia-to-pool ratios result in significantly lower mass transport during remediation and less mass depletion. Mass depletion rates from heterogeneous DNAPL sources undergo a gradual decline as oxidation proceeds due to manganese oxide buildup and changes in flow patterns. Manganese oxide formation does not noticeably affect permeability until the mass fraction of manganese oxide exceeded $0.1 \text{ mg MnO}_2(\text{s}) / \text{kg}$ aquifer material.
6. A reactive transport model based on the RT3D code was developed to simulate effects of bioenhanced DNAPL dissolution. In sources dominated by pools, accurate simulation of bioenhanced dissolution requires inclusion electron donor transport and mixing in saturation transition zones at pool boundaries. A numerical simulation study suggests that dual-domain approaches can be effective for addressing sub-grid heterogeneity associated with pool transition zones.

7. Research results suggest that evaluations of bioenhanced dissolution at field scales should focus on understanding the complexities of abiotic dissolution and electron-donor delivery in heterogeneous systems. Scale-dependent Gilland-Sherwood correlations developed to describe mass transfer prior to remediation are suitable for simulating bioenhanced dissolution. Biodegradation is a local-scale process that can be modeled with parameter estimates derived at batch or column scales.

Experiments and modeling described in this report also have provided insight to needs for continued research. Critical observations are provided in the following list.

1. Inverse modeling techniques developed in this research can be used to determine the vertical distribution of NAPL saturation from water samples obtained along vertical profiles downgradient of the source zones. The technique emphasizes the importance of installing multi-level monitoring wells downgradient of suspected NAPL source zones. This suggests the need to develop monitoring methods that are different from the conventional methods that are used at most DNAPL sites.
2. Flow paths through heterogeneous sources can be highly irregular resulting in water bypassing some high-saturation zones. This can limit deliver of chemicals to sites of active DNAPL dissolution and reaction, and adversely impact remediation effectiveness. Research to develop protocols for optimizing delivery of reactants in highly heterogeneous sources is needed.
3. Much of the experimentation and modeling described in this report focused on mass transfer from single-component DNAPL. Research to extend results to source zones with multi-component DNAPL typical of many field sites is appropriate.
4. This research focused on characterization of DNAPL architecture and mass transfer in heterogeneous porous media dominated by sandy material. Investigations of mass transfer during remediation are needed for geologic settings dominated by low-permeability and fractured material.
5. Research conclusions presented in this report were supported primarily by experiments and modeling of two-dimensional flow systems. Although extension of these results to three-dimensional field scales was demonstrated, validation of research results in heterogeneous three-dimensional systems is needed by performing controlled intermediate-scale experiments.
6. The intermediate scale experiments and modeling performed as part of this research permitted detailed control and measurement of DNAPL architecture, aquifer heterogeneity, and flow patterns. In this manner, processes affecting DNAPL depletion during source-zone remediation could be evaluated systematically and critical data needs for scaling conceptual and numerical models to field problems could be identified. Testing of conceptual and numerical models at field scales is equally important. In addition to model testing and validation, well instrumented and carefully designed field-scale tests may highlight key processes that either were not considered in laboratory tests or were of secondary importance.

References

- Abriola, L. M., T.J. Dekker, and K.D. Pennell (1993) Surfactant enhanced solubilization of residual dodecane in soil columns, 2, mathematical modeling, *Environ. Sci. Technol.*, 27(12), 2341-2351.
- Adams, E. E. and L. W. Gelhar (1992) Field study of dispersion in a heterogeneous aquifer, 2, Spatial moments analysis, *Water Resour. Res.*, 28(12), 3293–3307.
- Adamson D.T., J.M. McDade, and J.B. Hughes (2003) Inoculation of a DNAPL source zone to initiate reductive dechlorination of PCE. *Environ. Sci. Technol.*, 37, 2525-2533.
- Allison S.B. (1988) Analysis of field tracers for reservoir description, M.S. Thesis, University of Texas at Austin.
- Allison S.B., G.A. Pope, and K. Sepehrnoori (1991) Analysis of field tracers for reservoir description, *J. Petrol. Sci. Engrg.*, 5, 173-186.
- Annable, M.D., P.S.C. Rao, K. Hatfield, W.D. Graham, A.L. Wood, and C.G. Enfield (1998) Partitioning tracers for measuring residual NAPL: field-scale test result, *J. Environ. Engrg.*, 124, 901-908.
- ATSDR (2003) 2003 CERCLA Priority List of Hazardous Substances, Agency for Toxic Substances and Disease Registry, Division of Toxicology, U.S. Dept. of Health and Human Services, October 2003, <http://www.atsdr.cdc.gov/clist.html>.
- ATSDR (2004) Medical management guidelines (MMGs) for tetrachloroethylene, Agency for Toxic Substances and Disease Registry, Division of Toxicology, U.S. Dept. of Health and Human Services, May 2004, <http://www.atsdr.cdc.gov/MHMI/mmg18.html>.
- Ball, W.P. and P.V. Roberts (1991) Long term sorption of halogenated organic chemicals by aquifer materials: 1. Equilibrium, *Environ. Sci. Technol.*, 25(7), 1223-1236.
- Barlow, P.M., and A.F. Moench (1999) WTAQ – a computer program for calculating drawdowns and estimating hydraulic properties for confined and water-table aquifers, U.S. Geological Survey Water-Resources Investigations Report 99-4225, 74 p.
- Barth, G., M. Hill, T. Illangasekare, and H. Rajaram (2001) Predictive modeling of flow and transport in a two-dimensional intermediate-scale, heterogeneous porous medium, *Water Resour. Res.*, 37(10), 2503-2512.
- Baveye, P., P. Vandevivere, B.L. Hoyle, P.C. DeLeo, and D.S. de Lozada (1998) Environmental impact and mechanisms of the biological clogging of saturated soils and aquifer materials, *Crit. Rev. Environ. Sci. Technol.*, 28(2), 123-191.
- Bear, J. (1972) *Dynamics of Fluids in Porous Media*, American Elsevier Publishing Company, Dover, NY, 764 pp.
- Bedient, P.B., HS Rifai, CJ Newell (1999) *Ground Water Contamination: Transport and Remediation*, Prentice Hall PTR Upper Saddle River, NJ
- Bird, R., E. Stewart, and E. Lightfoot (1960) *Transport Phenomena*, John Wiley, New York.

- Bloom, A., G. DeLong, R. Lyon, A. Buell, and R. Gwinnet (2005) In situ accelerated anaerobic biodegradation of a chlorinated source area, Proceedings of the Eight International Symposium on In Situ and On-Site Bioremediation, Battelle Press, Baltimore, MD, June 2005.
- Boggs, J. M., Adams, E. E. (1992) Field study of dispersion in a heterogeneous aquifer, 4, investigation of adsorption and sampling bias, *Water Resour. Res.*, 28(12), 3325-3336.
- Bradford, S.A., T.J. Phelan, and L.M. Abriola (2000) Dissolution of residual tetrachloroethylene in fractional wettability porous media: correlation development and application, *J. Contam. Hydrol.*, 45, 35-61.
- Bradford, S.A., K. M. Rathfelder, J. Lang, and L. M. Abriola (2003), Entrapment and dissolution of DNAPLs in heterogeneous porous media, *J. Contam. Hydrol.*, 67, 133– 157.
- Brooks, M.C., M. D. Annable, P. S. C. Rao, K. Hatfield, J. W. Jawitz, W. R. Wise, A. L. Wood, and C. G. Enfield (2002) Controlled release, blind tests of DNAPL characterization using partitioning tracers, *J. Contam. Hydrol.*, 59 187– 210.
- Brooks, R.H., and A.T. Corey (1966) Properties of porous media affecting fluid flow, *J. Irrig. Drain. Engrg.*, 92(2), 61-88.
- Brown C. L., G.A. Pope, L.M. Abriola, and K. Sepehrnoori (1994) Simulation of surfactant-enhanced aquifer remediation, *Water Resour. Res.*, 30(11), 2959-2977.
- Brusseau, M.L., L.H. Xie, and L. Li (1999) Biodegradation during contaminant transport in porous media: 1. mathematical analysis of controlling factors, *J. Contam. Hydrol.*, 37, 269-293.
- Cameotra, S. S., H. D. Singh, et al. (1983) Mode of uptake of insoluble solid substrates by microorganisms. II: Uptake of solid n-alkanes by yeast and bacterial species, *Biotechnol. Bioengr.* 25(12), 2845-2956.
- Carr, C. S. and J.B. Hughes (1998) Enrichment of high-rate PCE dechlorination and comparative study of lactate, methanol and hydrogen and electron donors to sustain activity, *Env. Sci. Technol.*, 32, 1817-1824.
- Carr, C.S., S. Garg, and J.B. Hughes (2000) Effect of dechlorinating bacteria on the longevity and composition of PCE-containing nonaqueous phase liquids under equilibrium dissolution conditions, *Environ. Sci. Technol.*, 34(6), 1088-1094.
- Chu, M., P.K. Kitanidis, and P.L. McCarty (2003) Effects of biomass accumulation on microbially enhanced dissolution of a PCE pool: a numerical simulation, *J. Contam. Hydrol.*, 65, 79-100.
- Clement, T.P. (1997) A modular computer code for simulating reactive multi-species transport in 3-D groundwater systems, PNNL-11720, Pacific Northwest National Laboratory, Richland WA, 59 p.
- Clement, T.P. (2002) What's new in RT3D version 2.5, Pacific Northwest National Laboratory, Richland WA, 20 p.

- Clement, T.P., T.R. Gautam, K.K. Lee, and M.J. True (2004) Modeling coupled NAPL-dissolution and rate-limited sorption reactions in biologically active porous media, *Biorem. J.*, 8(1-2), 47-64.
- Clement, T.P., B.S. Hooker, and R.S. Skeen, R.S. (1996) Macroscopic models for predicting changes in saturated porous media properties caused by microbial growth, *Ground Water*, 34(5), 934-942.
- Clement, T.P., Y. Sun, B.S. Hooker, and J.N. Petersen (1998) Modeling multispecies reactive transport in ground water, *Ground Water Monit. Rem.*, 18(2), 79-92.
- Cline, S.R., O.R. West, N.E. Korte, F.G. Gardner, R.L. Siegrist, R.L., and J.L. Baker (1997) KMnO₄ chemical oxidation and deep soil mixing for soil treatment, *Geotech. News*, 15(5), 25-28.
- Compos, R. (1998) Hydraulic conductivity distribution in a DNAPL entrapped zone in a spatially correlated random field, M.S. thesis, University of Colorado, Boulder, CO.
- Conrad, S.H., R.J. Glass, and W.J. Peplinski (2002) Bench-scale visualization of DNAPL remediation processes in analog heterogeneous aquifers: surfactant floods and in situ oxidation using permanganate, *J. Contam. Hydrol.*, 58(1-2), 13-49.
- Cope, N. and J.B. Hughes (2001) Biologically-enhanced removal of PCE from NAPL source zones, *Environ. Sci. Technol.*, 35(10), 2014-2021.
- Corey, A.T. (1994) *Mechanics of Immiscible Fluids in Porous Media*, Water Resources Publications, Highlands Ranch, CO, 252 p.
- Crimi M. and R.L. Siegrist (2004) Experimental evaluation of in situ chemical oxidation activities at the Naval Training Center (NTC) site, Orlando, Florida, Naval Facilities Engineering Command, Port Hueneme CA, 64 pp.
- Cussler, E.L. (1997) *Diffusion: Mass Transfer in Fluid Systems*, Cambridge University Press, 580 p.
- Dai D., F. T. Barranco Jr., and T.H. Illangasekare (2001) Partitioning and interfacial tracers for differentiating NAPL entrapment configuration: column-scale investigation, *Environ. Sci. Technol.*, 35, 4894-4899.
- Delshad, M., G.A. Pope, and K. Sepehrnoori (1996) A compositional simulator for modeling surfactant enhanced aquifer remediation, *J. Contam. Hydrol.*, 23(1-2), 303-327.
- de Marsily, Gh., F. Delay, J. Goncalves, Ph. Renard, V. Teles, and S. Violette (2005) Dealing with spatial heterogeneity, *Hydrogeol. J.*, 13, 161-183.
- Dennis, P., E. Hood, and D. Major (2005) Impacts of chemical oxidation and bioaugmentation on microbial population, diversity, and dechlorinating activity, Proceedings of the Eight International Symposium on In Situ and On-Site Bioremediation, Battelle Press, Baltimore, MD, June 2005.
- Divine, C.E., J.E. McCray, L.M. Wolf Martin, W.J. Blanford, D.J. Blitzer, M.L. Brusseau, and T.B. Boving (2004) Partitioning tracer test as a remediation metric: case study at Naval Amphibious Base Little Creek, Virginia Beach, Virginia, *Remediation*, Spring issue, 7-31.

- DiStefano, T. D., J. M. Gossett, et al. (1992) Hydrogen as an electron donor for dechlorination of tetrachloroethene by an anaerobic mixed culture, *Appl. Environ. Microbiol.*, 58(11), 3622-3629.
- Doherty, J. (2003) Manual for PEST 7.0, Watermark Numerical Computing, Brisbane Australia, 279 p.
- Duhamel, M., S.D. Wehr, L. Yu, H. Rizvi, D. Seepersad, S. Dwaratzek, E.E. Cox, and E.A. Edwards (2002) Comparison of anaerobic dechlorinated enrichment cultures maintained on tetrachloroethene, trichloroethene, cis-dichloroethene and vinyl chloride, *Water Res.*, 36, 4193-4202.
- Dwarakanath, V, K. Kostarelos, G.A. Pope, D. Shotts, and W.H. Wade WH. (1999) Anionic surfactant remediation of soil columns contaminated by nonaqueous phase liquids, *J. Contam. Hydrol.*, 38, 465-488.
- Edwards, E. A. and E. E. Cox (1997) Field and laboratory studies of sequential anaerobic-aerobic chlorinated solvent biodegradation, Fourth International Symposium on In Situ and On-Site Bioreclamation, New Orleans, LA, Battelle Press.
- Edwards, E. A., and D. Grbic-Galic (1994) Anaerobic degradation of toluene and o-xylene by a methanogenic consortium, *Appl. Environ. Microbiol.*, 60, 313-322.
- Efroymsen, R.A., and M. Alexander (1994) Role of partitioning in biodegradation of phenanthrene dissolved in nonaqueous-phase liquids, *Environ. Sci. Technol.*, 28(6), 1172-1179.
- Elder, C., P. Zeeb, D. Larson, and D. Wanty (2005) Full-scale implementation of anaerobic bioaugmentation in an aerobic aquifer, Proceedings of the Eight International Symposium on In Situ and On-Site Bioremediation, Battelle Press, Baltimore, MD, June 2005.
- Falta, R.W. (2000) Numerical modeling of kinetic interphase mass transfer during air sparging using a dual-media approach, *Water Resour. Res.*, 36(12), 3391-3400.
- Feenstra, S. and J.A. Cherry (1996) Diagnosis and assessment of DNAPL sites, in J.F. Pankow and J.A. Cherry (Eds.) *Dense Chlorinated Solvents and Other DNAPLs in Groundwater: History, Behavior, and Remediation*, Waterloo Press, Portland, OR, 395-473.
- Fennell, D.E., and J.M. Gossett (1998) Modeling the production of and competition for hydrogen in a dechlorinating culture, *Environ. Sci. Technol.*, 32(16), 2450-2460.
- Fernandez-Garcia, D., X. Sanchez-Vila, and T. H. Illangasekare (2002) Convergent-flow tracer tests in heterogeneous media: combined experimental–numerical analysis for determination of equivalent transport parameters, *J. Contam. Hydrol.*, 57, 129–145.
- Ferre, T., T. Binley, Geller, J., E.H. Hill, III, T.H. Illangasekare (2005), Hydrogeophysical Case Studies at the Lab Scale, in Y. Rubin and S. Hubbard (Eds.) *Hydrogeophysics*, Springer Verlag, Dordrecht, The Netherlands, 441-466.
- Fetzner, S. (1998) Bacterial dehalogenation, *Appl. Microbiol. Biotechnol.*, 50, 633-657.
- Freedman, D. L. and J. M. Gossett (1989) Biological reductive dechlorination of tetrachloroethylene and trichloroethylene to ethylene under methanogenic conditions, *Appl. Environ. Microbiol.*, 55, 2144-2151.

- Freyberg, D.L. (1986) A natural gradient experiment on solute transport in a sandy aquifer, 2, spatial moments and the advection and dispersion of nonreactive tracers, *Water Resour. Res.*, 22(13), 2031–2046.
- Gago, J.L., G. Middleton, E.H. Hill, III, and T.H. Illangasekare (2002) Real time monitoring of NAPL sources using photon attenuation techniques on chlorinated solvents, Geological Society of America, 2002 Denver Annual Meeting, October 27-30, 2002.
- Gates-Anderson, D.D., Siegrist, R.L., and Cline, S.R. (2001) Comparison of potassium permanganate and hydrogen peroxide as chemical oxidants for organically contaminated soils, *J. Environ. Engrg.*, 127(4), 337-347.
- Gelhar, L. (1993) *Stochastic Subsurface Hydrology*, Prentice-Hall, Englewood Cliffs, New Jersey.
- Geller, J., and J. Hunt (1993) Mass transfer from non-aqueous phase organic liquids in water saturated porous media, *Water Resour. Res.*, 29(4), 833-845.
- Glaze, W.H., and J.-W. Kang (1988) Advanced oxidation processes for treating groundwater contaminated with TCE and PCE: laboratory studies, *J. Am. Water Works Assoc.*, 88(5), 57-63.
- Glover, K.C. (2006) Microbe-enhanced dissolution of non-aqueous phase tetrachloroethene in naturally heterogeneous subsurface source zones: a multiscale study, Ph.D. dissertation, Environ. Sci. Engrg., Colorado School of Mines, Golden, CO, 297p.
- Gossett, J. M. (1987), Measurement of Henry's Law Constants for C1, and C2 Chlorinated Hydrocarbons, *Environ. Sci. Technol.*, 21(2), 202-208.
- Goswami, P., and H. D. Singh (1991) Different modes of hydrocarbon uptake by two *Pseudomonas* species, *Biotechnol. Bioenrg.*, 37(1), 1-11.
- Harbaugh, A.W., E.R. Banta, M.C. Hill, and M.G. McDonald (2000) MODFLOW-2000, the U.S. Geological Survey modular ground-water model—User guide to modularization concepts and the ground-water flow process model: U.S. Geological Survey Open-File Report 00-92, 130 p.
- Heiderscheidt, J.L. (2005) DNAPL source zone depletion during in situ chemical oxidation (ISCO): experimental and modeling studies, Ph.D. Thesis, Colorado School of Mines, Golden, Colorado, 295p.
- Hendrickson, E.R., J.A. Payne, R.M. Young, M.G. Starr, M.P. Perry, S. Fahnestock, D.E. Ellis, and R.C. Ebersole (2002) Molecular analysis of Dehalococcoides 16S ribosomal DNA from chloroethene-contaminated sites through North America and Europe, *Appl. Environ. Microbiol.*, 68(2), 485-495.
- Heron, G., S. Carroll, et al., 2005. Full-Scale Removal of DNAPL Constituents Using Steam-Enhanced Extraction and Electrical Resistance Heating, *Ground Water Monit. Rem.*, 25(4), 92-107.
- Heron, G., T. H. Christensen, et al. (1998) Soil heating for remediation of dissolved trichloroethylene in low-permeable soil, Battelle Press, Columbus, OH.

- Hess, K. M., S.H. Wolf, and M.A. Celia (1992) Large-scale natural gradient tracer test in sand and gravel, Cape Cod, Massachusetts, 3, Hydraulic conductivity variability and calculated macrodispersivities, *Water Resour. Res.*, 28(8), 2011-2027.
- Hill, E. H. III, L. L. Kupper, et al. (2002) Evaluation of path-length estimators for characterizing multiphase systems using polyenergetic x-ray absorptiometry, *Soil Science*, 167(11), 703-719.
- Hood, E. (2000) Permanganate Flushing of DNAPL Source Zones: Experimental and Numerical Investigation. Ph.D. Dissertation, University of Waterloo, Waterloo, ON. 243 p.
- Holocher, J., F. Peeters, W. Aeschbach-Hertig, W Kinselbach, and R. Kipfer (2003) Kinetic model of gas bubble dissolution in groundwater and its implications for the dissolved gas composition, *Environ. Sci. Technol.*, 37(7), 1337-1343.
- Holzmer, F J; Pope, G A; Yeh, L (2000) Surfactant-enhanced aquifer remediation of PCE-DNAPL in low-permeability sand, Proceedings of the Second International Conference on Remediation of Chlorinated and Recalcitrant Compounds, Monterey, CA, 22-25 May 2000, 187-193.
- Huang, K., G.E. Hoag, P. Chheda, B.A. Woody, and G.M. Dobbs (1999) Kinetic study of oxidation of trichloroethylene by potassium permanganate, *Environ. Engrg. Sci.*, 16(4), 265-274.
- Huang, K., G.E. Hoag, P. Chheda, B.A. Woody, and G.M. Dobbs (2001) Oxidation of chlorinated ethenes by potassium permanganate: a kinetics study, *J. Haz. Mater.*, 87(1-3), 155-169.
- Huang, K., G.E. Hoag, P. Chheda, B.A. Woody, and G.M. Dobbs (2002) Kinetics and mechanism of oxidation of tetrachloroethylene with permanganate, *Chemosphere*, 46(6), 815-825.
- Hunt, J., N. Sitar, and K. Udell (1988) Nonaqueous phase liquid transport and cleanup: 1. Analysis of mechanisms, *Water Resour. Res.*, 24(8), 1247-1258.
- Ibaraki, M. and F.W. Schwartz, (2001) Influence of natural heterogeneity on the efficiency of chemical floods in source zones, *Ground Water*, 39(5), 660-666.
- Illangasekare, T.H., E.J. Armbruster III, and D.N. Yates (1995a) Non-aqueous-phase fluids in heterogeneous aquifer—experimental study, *J. Environ. Engrg.*, 121(8), 571-579.
- Illangasekare, T.H., J.L. Ramsey, K.H. Jensen, and M. Butts (1995b) Experimental study of movement and distribution of dense organic contaminants in heterogeneous aquifers: an experimental study, *J. Contam. Hydrol.*, 20(1-2), 1-25.
- Imhoff, P. T., A. Frizzell, et al. (1997) Evaluation of thermal effects on the dissolution of a nonaqueous phase liquid in porous media, *Environ. Sci. Technol.*, 31(6), 1615-1622.
- Imhoff, P.T., M.H. Arthur, and C.T. Miller (1998) Complete dissolution of trichloroethylene in saturated porous media, *Environ. Sci. Technol.*, 32(16), 2417-2424.
- Imhoff, P. T., M. W. Farthing, et al. (2003) Modeling NAPL dissolution fingering with upscaled mass transfer rate coefficients, *Adv. Water Resour.*, 26(10), 1097-1111.

- Imhoff, P.T., P.R. Jaffe, and G.F. Pinder (1994) An experimental study of complete dissolution of a nonaqueous phase liquid in saturated porous media, *Water Resour. Res.*, 30(2), 307-320.
- Isalou, M., B.E. Sleep, and S.N. Liss (1998), Biodegradation of high concentrations of tetrachloroethene in a continuous flow column system, *Environ. Sci. Technol.*, 32, 3579-3585.
- Jackson R.E. (2001) DNAPL remediation: which 'new paradigm' will prevail?, *Ground Water Monit. Rem.*, 21(3), 54-58.
- Jawitz J.W., M.D. Annable, and P.S.C. Rao (1998) Field implementation of a Winsor Type I surfactant/Alcohol mixture for in situ solubilization of a complex LNAPL as a single phase microemulsion, *Environ. Sci. Technol.*, 32, 523-530.
- Jin, M.Q., M. Delshad, V. Dwarakanath, D.C. Mckinney, G.A. Pope, K. Sepehrnoori, C.E. Tilburg, and R.E. Jackson (1995) Partitioning tracer test for detection, estimation, and remediation performance assessment of subsurface nonaqueous phase liquids, *Water Resour. Res.*, 31(5), 1201-1211.
- Johnson, T., and J. Pankow (1992) Dissolution of dense chlorinated solvents into groundwater: 2. source functions for pools of solvent, *Environ. Sci. Technol.*, 26(5), 896-901.
- Jury, W.A., W.R. Gardner, and W.H. Gardner (1991) *Soil Physics*, 5th ed., John Wiley & Sons, New York, NY, 328 p.
- Kaplan, A. (2004) The effects of chlorinated ethene biodegradation on mass transfer from DNAPL and alcohol tracer partitioning coefficients, M.S. Thesis, Colorado School of Mines, Environmental Science and Engineering Division.
- Kaslusky, S. F., and K. S. Udell (2002) A theoretical model of air and steam co-injection to prevent the downward migration of DNAPLs during steam-enhanced extraction, *J. Contam. Hydrol.*, 55(3-4), 213-232.
- Kaslusky, S. F., and K. S. Udell (2005) Co-injection of air and steam for the prevention of the downward migration of DNAPLs during steam enhanced extraction: An experimental evaluation of optimum injection ratio predictions, *J. Contam. Hydrol.*, 77(4), 325-347.
- Kavanaugh, M. C., P. Rao, et al. (2003) The DNAPL remediation challenge: is there a case for source depletion?, Cincinnati, U.S. Environmental Protection Agency, National Risk Management Research Laboratory.
- Khachikian, C., and T. Harmon (2000) Non-aqueous phase liquid dissolution in porous media: Current state of knowledge and research needs, *Transport in Porous Media*, 38(1), 3-28.
- Krumholz, L.R., R. Sharp, and S.S. Fishbain (1996) A freshwater anaerobe coupling acetate oxidation to tetrachloroethylene dehalogenation, *Appl. Environ. Microbiol.*, 62(11), 4108-4113.
- Kueper, B., W. Abbot, and G. Farquhar (1989) Experimental observations of multiphase flow in heterogeneous porous media, *J. Contam. Hydrol.*, 5(1), 83-95.
- Kueper, B.H., and E.O. Frind (1991a) Two-phase flow in heterogeneous porous media, 1, model development, *Water Resour. Res.*, 27(6), 1049-1057.

- Kueper, B. H., and E. O. Frind (1991b) Two-phase flow in heterogeneous porous media, 2, model application, *Water Resour. Res.*, 27(6), 1059-1070.
- Kueper, B.H., D. Redman, R.C. Starr, S. Reitsma, and M. Mah (1993) A field experiment to study the behavior of tetrachloroethylene below the water table; spatial distribution of residual and pooled DNAPL. *Ground Water*, 31(5), 756-766.
- Lackovic, J.A. and A.R. Zlotnick (2005), Targeted bioremediation program to remediate halogenated VOCs in a brackish alluvial aquifer, Proceedings of the Eight International Symposium on In Situ and On-Site Bioremediation, Battelle Press, Baltimore, MD, June 2005.
- Lee, E.S., Y. Seol, Y.C. Fang, and F.W. Schwartz (2003) Destruction efficiencies and dynamics of reaction fronts associated with the permanganate oxidation of trichloroethylene, *Environ. Sci. Technol.*, 37(11), 2540-2546.
- Li, X.D., and F.W. Schwartz (2000) Efficiency problems related to permanganate oxidation schemes. in G.B. Wickramanayake, A.R. Gavaskar, and A.S.C. Chen (Eds.), *Chemical Oxidation and Reactive Barriers*, Battelle Press, Columbus, OH, 41-48.
- Loeffler, F.E., J.M. Tiedje and R.A. Sanford (1999) Fraction of electrons consumed in electron acceptor reduction and hydrogen thresholds as indicators of halorespiratory physiology, *Appl. Environ. Microbiol.*, 65(9), 4049-4056.
- Lucius, J., G. Olhoeft, P. Hill, and S. Duke (1992) Properties and Hazards of 108 Selected Substances. U.S. Geological Survey, Open-File Report 92-527 September, 1992.
- Lunn, S.R.D., and B.H. Kueper (1999) Risk reduction during chemical flooding: preconditioning DNAPL density in situ prior to recovery by miscible displacement, *Environ. Sci. Technol.* 33, 1703–1708.
- Macbeth T.W., D.E. Cummings, S. Spring, L.M. Petzke, K.S. Sorenson, Jr. (2004) Molecular characterization of a dechlorinating community resulting from in situ biostimulation in a Trichloroethene-Contaminated Deep, Fractured Basalt Aquifer and Comparison to a Derivative Laboratory Culture, *Appl. Environ. Microbiol.*, 70(12), 7329–7341.
- Macbeth T.W., and K.S. Sorenson, Jr. (2005) Molecular characterization of a TCE-dechlorinating field community and implications for bioremediation performance, Proceedings of the Eight International Symposium on In Situ and On-Site Bioreclamation, Battelle Press: Baltimore, MD, June 2005.
- Mackay, D. M., D. L. Freyberg, P. L. McCarty, P. V. Roberts and J. A. Cherry (1986) A natural gradient experiment on solute transport in a sand aquifer: I. approach and overview of plume movement, *Water Resour. Res.*, 22(13), 2017-2030.
- MacDonald, J.A, and M.C. Kavanaugh (1994) Restoring contaminated groundwater: an achievable goal?, *Environ. Sci. Technol.*, 28, 362A-368A.
- Mackay, D.M., and J.A. Cherry (1989) Groundwater contamination: pump-and-treat remediation, *Environ. Sci. Technol.*, 23(6), 630-636.
- Mackay, D.M., D.L. Freyberg, P.V. Roberts, and J.A. Cherry (1986) A natural gradient experiment on solute transport in a sand aquifer: 1. approach and overview of plume movement, *Water Resour. Res.*, 22(13), 2017-2029.

- MacKinnon, L.L. and N.R. Thomson (2002) Laboratory-scale in situ chemical oxidation of a perchloroethylene pool using permanganate, *J. Contam. Hydrol.*, 56(1-2), 49-74.
- Major, D.W., M.L. McMaster, E.E. Cox, E.A. Edwards, S.M. Dworatzek, E.R. Hendrickson, M.G. Starr, J.A. Payne, and L.W. Buonamici (2002) Field demonstration of successful bioaugmentation to achieve dechlorination of tetrachloroethene to ethene, *Environ. Sci. Technol.*, 36(23), 5106-5116.
- Morrill P.L., G. Lacrampe-Couloume, G.F. Slatara, B.E. Sleep, E.A. Edwards, M.L. McMaster, D.W. Major, and B. Sherwood Lollar (2005) Quantifying chlorinated ethene degradation during reductive dechlorination at Kelly AFB using stable carbon isotopes, *J. Contam. Hydrol.*, 76, 279-293.
- Martin J.P., J.F. Horst, and F. Lenzo (2005) Full-scale ZVI and molasses for reductive dechlorination of PCE DNAPL in fractured bedrock, Proceedings of the Eight International Symposium on In Situ and On-Site Bioremediation, Battelle Press, Baltimore, MD, June 2005.
- Mason, AR, and BH Kueper (1996) Numerical simulation of surfactant flooding to remove pooled DNAPL from porous media, *Environ. Sci. Technol.*, 30(11), 3205 -3215.
- Mayer, A., and C. Miller (1996) The influence of mass transfer characteristics and porous media heterogeneity on non-aqueous phase dissolution, *Water Resour. Res.*, 32(6), 1551-1567.
- Maymo-Gatell, X., V. Tandoi, J.M. Gossett, and SH. Zinder (1995) Characterization of an H₂-Utilizing Enrichment Culture that Reductively Dechlorinates Tetrachloroethene to Vinyl Chloride and Ethene in the Absence of Methanogenesis and Acetogenesis, *Appl. Environ. Microbiol.*, 61(11): 3928-3933.
- McDonald, M.G., and A.W. Harbaugh (1988) A modular three-dimensional finite-difference ground-water flow model, U.S. Geological Survey Techniques of Water-Resources Investigations, book 6, chap. A1, 586 pp.
- McGuire, T.M., J.M. McDade, and C.J. Newell (2006) Performance of DNAPL source depletion technologies at 59 chlorinated solvent-impacted sites, *Ground Water Monit. Rem.*, 26(1), 73-84.
- Meinardus H.W., V. Dwarakanath, J. Ewing, G.J. Hirasaki, R.E. Jackson, M. Jin, J.S. Ginn, J.T. Londergan, C.T. Miller, and G.A. Pope (2002) Performance assessment of NAPL remediation in heterogeneous alluvium, *J. Contam. Hydrol.*, 54, 173-193.
- Mercer, J., and R. Cohen (1990) A review of immiscible fluids in the subsurface: Properties, models, characterization and remediation, *J. Contam. Hydrol.*, 6, 107-163.
- Miller, C., M. Poirier-McNeil, and A. Mayer (1990) Dissolution of trapped non-aqueous phase liquids: Mass transfer characteristics, *Water Resour. Res.*, 23(11), 2783-2793.
- Miller, M.E. (2005) Biostimulation of anaerobic dechlorination: strategy and results at four sites, Proceedings of the Eight International Symposium on In Situ and On-Site Bioremediation, Battelle Press, Baltimore, MD, June 2005.
- Millington, R.J., and J.P. Quirk (1959) Permeability of porous media, *Nature*, 183, 387-388.

- Millington, R.J. and J.P. Quirk (1961) Permeability of porous solids, *Trans. Faraday Soc.*, 57, 1200-1207.
- Moreno-Barbero, E. (2005) Evaluation of the partition interwell tracer test and extension to determine DNAPL architecture in heterogeneous media, Ph.D. dissertation, Environ. Sci. Engrg., Colorado School of Mines, Golden, CO.
- Moreno-Barbero, E. and T.H. Illangasekare (2006) Influence of dense nonaqueous phase liquid pool morphology on the performance of partitioning tracer tests: evaluation of the equilibrium assumption, *Water Resour. Res.*, 42, W04408, doi:10.1029/2005WR004074.
- Morrill P.L., G. Lacrampe-Couloume, G.F. Slatara, B.E. Sleep, E.A. Edwards, M.L. McMaster, D.W. Major, and B. Sherwood Lollar (2005) Quantifying chlorinated ethene degradation during reductive dechlorination at Kelly AFB using stable carbon isotopes, *J. Contam. Hydrol.*, 76, 279– 293.
- Mravik, S.C., R.K. Sillan, A.L. Wood, and G.W. Sewel (2003) Field evaluation of the solvent extraction residual biotreatment technology, *Environ. Sci. Technol.*, 37, 5040-5045.
- Nambi, I. (1999) Dissolution of non-aqueous phase liquids in heterogeneous subsurface systems, Ph.D. thesis, Clarkson University, Potsdam, New York.
- Nambi, I.M., and S.E. Powers (2003) Mass transfer correlations for nonaqueous phase liquid dissolution from regions with high initial saturations, *Water Resour. Res.*, 39(2), 1030, doi:10.1029/2001WR00067.
- National Research Council (1994) Alternatives to Ground Water Cleanup, National Academy Press, Washington, DC.
- NATO/CCMS (North Atlantic Treaty Organization/Committee on the Challenges of Modern Society) (2003) Evaluation of demonstrated and emerging technologies for the treatment and clean up of contaminated land and groundwater (phase III), USEPA Rep. No. EPA/542/R-02/010, U.S. EPA, Washington D.C., 291 p.
- Nelson, M.D., B.L. Parker, T.A. Al, J.A. Cherry, J.A., and D. Loomer (2001) Geochemical reactions resulting from in situ oxidation of PCE-DNAPL by KMnO₄ in a sandy aquifer, *Environ. Sci. Technol.*, 35(6), 1266-1275.
- Newmark, R.L., and R.D. Aines (1997) Dumping pump and treat; rapid cleanups using thermal technology, National spring meeting and petrochemical exposition of the American Institute of Chemical Engineers (AIChE) and Plant operations and design conference, Houston, TX, United States, March 10-13, 1997, Houston, TX.
- Nielsen, B. R., and J.D. Keasling (1999) Reductive dechlorination of chlorinated ethenes by a culture enriched from contaminated groundwater, *Biotechnol. Bioengr.*, 62, 160-165.
- Ortega-Calvo, J.J., I. Birman, and M. Alexander (1995) Effect of varying the rate of partitioning of phenanthrene in nonaqueous-phase liquids on biodegradation in soil slurries, *Environ. Sci. Technol.*, 29(9), 2222-2225.
- Page, J.W.E. (2005) A mass flux and partitioning tracer concept for DNAPL source zone characterisation, Ph.D. dissertation, University of Cambridge, Cambridge, England.

- Pankow, J.F. and J.A. Cherry (1996) *Dense Chlorinated Solvents and Other DNAPLs in Groundwater: History, Behavior, and Remediation*, Waterloo Press, Portland, OR, 525 p.
- Pennell, K.D., M. Jin, L.M. Abriola, G.A. Pope (1994) Surfactant-enhanced remediation of soil columns contaminated by residual tetrachloroethylene, *J. Contam. Hydrol.*, 16, 35–53.
- Parker, B.L., J.A. Cherry, S.W. Chapman, and M.A. Guilbeault (2003) Review and analysis of chlorinated solvent dense non-aqueous phase liquid distributions in five sandy aquifers, *Vadose Zone J.*, 2(2), 116-137.
- Parker, J.C. and E. Park (2004) Modeling field-scale dense nonaqueous phase liquid dissolution kinetics in heterogeneous aquifers, *Water Resour. Res.*, 40, W05109, doi:10.1029/2003WR002807.
- Poeter, E., and M. Hill (1998) Documentation of UCODE, a computer code for universal inverse modeling, U.S. Geological Survey Water Resources Investigation Report 98-4080.
- Pope, G. A., M. Jin, V. Dwarakanath, B.A. Rouse, and K. Sepehrnoori (1994) in T. Bjørnstad, G.A. Pope (Eds.), Partitioning tracer tests to characterize organic contaminants, Proceedings of the Second Tracer Workshop, Center for Petroleum and Geosystems Engineering, The University of Texas at Austin, November 14-15, 1994.
- Powers, S. E., L.M. Abriola, and W.J. Weber (1992) An experimental investigation of nonaqueous phase liquid dissolution in saturated subsurface systems: steady state mass transfer rates, *Water Resour. Res.*, 28(10), 2691-2705.
- Powers, S.E., L.M. Abriola, and W.J. Weber (1994) An experimental investigation of nonaqueous phase liquid dissolution in saturated subsurface systems: transient mass transfer rates, *Water Resour. Res.*, 30(2), 321-332.
- Rao, P. S. C., M. D. Annable, et al. (1997) Field-scale evaluation of in situ cosolvent flushing for enhanced aquifer remediation, *Water Resour. Res.*, 33(12), 2673-2686.
- Rao S.P.R., M.D. Annable, and H. Kim (2000) NAPL source zone characterization and remediation technology performance assessment: recent developments and applications of tracer techniques, *J. Contam. Hydrol.*, 45, 63-78.
- Refsgaard, J.C., and H.J. Henriksen (2004) Modelling guidelines—terminology and guiding principles, *Adv. Water Resour.*, 27(1), 71-82.
- Refsgaard, J.C., and J. Knudsen (1996) Operational validation and intercomparison of different types of hydrological models, *Water Resour. Res.*, 32(7), 2189-2202.
- Rehfeldt, K.R., J.M. Boggs, and L.W. Gelhar (1992) Field study of dispersion in a heterogeneous aquifer, 3, geostatistical analysis of hydraulic conductivity, *Water Resour. Res.*, 28(12), 3309–3324.
- Reis, J.C., and A.M. Acock (1994) Permeability reduction models for the precipitation of inorganic solids in Berea sandstone, *In Situ*, 18(3), 347-368.
- Reitsma, S., and M. Marshall (2000) Experimental study of oxidation of pooled NAPL, in G.B. Wickramanayake, A.R. Gavaskar, and A.S.C. Chen (Eds.), *Chemical Oxidation and Reactive Barriers*, Battelle Press, Columbus, OH. 25-32.

- Reitsma, S., and J. Randhawa (2002) Experimental investigation of manganese dioxide plugging in porous media, in A.R. Gavaskar, and A.S.C. Chen (Eds.), Proceedings of the 3rd International Conference on Remediation of Chlorinated and Recalcitrant Compounds, Monterey CA, May 2002, Battelle Press, Columbus, OH, 2C-39.
- Rivett, M.O., and R.M. Allen-King (2003) A controlled field experiment on groundwater contamination by a multicomponent DNAPL: dissolved-plume retardation, *J. Contam. Hydrol.*, 66(1-2), 117-146.
- Saba, T.A. (1999) Upscaling of mass transfer from entrapped NAPLs under natural and enhanced conditions, Ph.D. Dissertation, University of Colorado, Boulder CO, 204 p.
- Saba, T.A. and T.H. Illangasekare (2000) Effect of ground-water flow dimensionality on mass transfer from entrapped non-aqueous phase liquid contaminants, *Water Resour. Res.*, 36(4), 971-979.
- Sabatini D.A., R.C. Knox, and J.H. Harwell (1995) *Emerging Technologies in Surfactant-Enhanced Subsurface Remediation*, ACS symposium series No.594. American Chemical Society, Washington, DC, 1-8.
- Sabatini D.A., R.C. Knox, J.H. Harwell, and B. Wu (2000) Integrated design of surfactant enhanced DNAPL remediation: efficient supersolubilization and gradient systems, *J. Contam. Hydrol.*, 45, 99-121.
- Saenton, S. (2003) Prediction of mass flux from DNAPL source zone with complex entrapment architecture: Model development, experimental validation, and up-scaling, Ph.D. Thesis, Colorado School of Mines, Golden, Colorado.
- Saenton, S. and T. Illangasekare. (2005) Evaluation of the effect of partial removal of NAPL mass on plume concentrations: Experimental and numerical model investigations, *J. Contam. Hydrol.*, Submitted.
- Saenton, S., T. Illangasekare, K. Soga, and T. Saba (2002) Effect of source zone heterogeneity on surfactant enhanced NAPL dissolution and resulting remediation endpoints, *J. Contam. Hydrol.*, 53(1-2), 27-44.
- Sakaki, T. and T.H. Illangasekare (2006) Tempe-cell based static capillary pressure – saturation relationships for sands: Conventional averaging method vs. point measurement, 26th Annual AGU Hydrology Days, Fort Collins, CO, March 20-22, 2006.
- Schirmer, M., J.W. Molson, E.O. Frind, and J.F. Barker (2000) Biodegradation modelling of a dissolved gasoline plume applying independent laboratory and field parameters, *J. Contam. Hydrol.*, 46, 339– 374.
- Schnarr, M., C. Truax, G. Farquhar, E. Hood, T. Gonully, and B. Stickney (1998) Laboratory and controlled field experimentation using potassium permanganate to remediate trichloroethylene and perchloroethylene DNAPLs in porous media, *J. Contam. Hydrol.*, 29(3), 205-224.
- Schroth, M.H, M. Oostrom, T.W. Wietsma, and J.D. Istok (2001) In situ oxidation of trichloroethene by permanganate: effects on porous medium hydraulic properties, *J. Contam. Hydrol.*, 50(1-2), 79-98.

- Schwille, F. (1988) *Dense Chlorinated Solvents in Porous and Fractured Media*, Lewis Publishers, Chelsea, MI, translated by J.F. Pankow, 146 p.
- Seagren, E.A., B.E. Rittmann, and A.J. Valocchi (2002) Bioenhancement of NAPL pool dissolution: experimental evaluation, *J. Contam. Hydrol.*, 55(1-2), 57-85.
- Seguiti, F., K. Smith, W. Abdullah, E. Petrovskis, F. Loeffler, and K. Pennell (2005) Bioaugmentation to remediate a TCE site, Proceedings of the Eight International Symposium on In Situ and On-Site Bioremediation, Battelle Press, Baltimore, MD, June 2005.
- Seitz, S. (2004) Experimental evaluation of mass transfer and matrix interactions during in situ chemical oxidation relying on diffusive transport, MS Thesis, Colorado School of Mines, Golden, CO, 125 p.
- Selim, H.M. and R.S. Mansell, R.S. (1976) Analytical solutions of the equation for transport of reactive solutes through soils, *Water Resour. Res.*, 12(3), 528-532.
- Seol, Y., H. Zhang, and F.W. Schwartz (2003) A review of in situ chemical oxidation and heterogeneity, *Environ. Engrg. Geosci.*, 9(1), 37-49.
- Sharma, P.K., and P.L. McCarty (1996) Isolation and characterization of a facultatively aerobic bacterium that reductively dehalogenates tetrachloroethene to cis-1,2-dichloroethene, *Appl. Environ. Microbiol.*, 62(3), 761-765.
- Sherwood, T.K., R.L. Pigford, and C.R. Wilke (1975) *Mass Transfer*, McGraw-Hill, New York, NY, 677 p.
- Shiau, B-J, D.A. Sabatini, and J.H. Harwell (1994) Solubilization and microemulsification of chlorinated solvents using direct food additive (edible) surfactants, *Ground Water*, 32, 561-569.
- Siegrist, R.L., K.S. Lowe, L.C. Murdoch, T.L. Case, and D.A. Pickering (1999) In situ oxidation by fracture emplaced reactive solids, *J. Environ. Engrg.*, 125(5), 429-440.
- Siegrist, R.L., M.A. Urynowicz, M.L. Crimi, and K.S. Lowe (2002) Genesis and effects of particles produced during in situ chemical oxidation using permanganate, *J. Environ. Engrg.*, 128(11), 1068-1079.
- Siegrist, R.L., M.A. Urynowicz, O.R. West, M.L. Crimi, and K.S. Lowe (2001) *Principles and Practices of In Situ Chemical Oxidation Using Permanganate*, Battelle Press, Columbus, OH, 348 p.
- Slater, G. F., B.S. Lollar, B.E. Sleep, and E.A. Edwards (2001) Variability in carbon isotopic fractionation during biodegradation of chlorinated ethene: Implications for field applications. *Env. Sci. Technol.*, 35, 901-907.
- Sleep, B. E. and Y. Ma (1997) Thermal variation of organic fluid properties and impact on thermal remediation feasibility, *J. Soil Contam.*, 6(3), 281-306.
- Smith, L. A. and R. E. Hinchee (1993) *In Situ Thermal Technologies for Site Remediation*, Lewis Publishers, Boca Raton, Florida.
- Soga K., J.W.E. Page, and T.H. Illangasekare (2004) A review of NAPL source zone remediation efficiency and the mass flux approach, *J. Hazard. Mater.*, 110(1-3):13-27.

- Song, D.L., M.E. Conrad, K.S. Sorenson, and L. Alvarez-Cohen (2002) Stable carbon isotope fractionation during enhanced in situ bioremediation of trichloroethene, *Environ. Sci. Technol.*, 36, 2262–2268.
- Stewart, R. (1965) Oxidation by permanganate, in K.B. Wiberg, (Ed.), *Oxidation in Organic Chemistry*, Part A, Chap. 1, Academic Press, New York, NY. 1-68.
- Stroo, H.F., M. Unger, C.H. Ward, M.C. Kavanaugh, C. Vogel, A. Leeson, J.A. Marqusee, and B.P. Smith (2003) Remediating chlorinated solvent source zones, *Environ. Sci. Technol.*, 37(11), 224A-230A.
- Struse, A.M., R.L. Siegrist, H.E. Dawson, and M.A. Urynowicz (2002) Diffusive transport of permanganate during in situ oxidation, *J. Environ. Engrg.*, 128(4), 327-334.
- Sudicky, E. A. (1986) A natural gradient experiment on solute transport in a sandy aquifer: spatial variability of hydraulic conductivity and its role in the dispersion process, *Water Resour. Res.*, 22(13), 2069–2082.
- Sun, Y., J.N. Petersen, J. Bear, T.P. Clement, and B.S. Hooker (1999) Modeling microbial transport and biodegradation in a dual-porosity system, *Transport in Porous Media*, 35(1), 49-65.
- Tandoi, V., T.D. DiStefano, P.A. Bowser, J.M. Gossett, and S.H. Zinder (1994) Reductive dehalogenation of chlorinated ethenes and halogenated ethanes by a high-rate anaerobic enrichment culture, *Environ. Sci. Technol.*, 28, 973-979.
- Thullner, M., L. Mauclair, M.H. Schroth, W. Kinzelbach, and J. Zeyer (2002a) Interaction between water flow and spatial distribution of microbial growth in a two-dimensional flow field in saturated porous media, *J. Contam. Hydrol.*, 58, 169–189.
- Thullner, M., J. Zeyer, and W. Kinzelbach, W. (2002b) Influence of microbial growth on hydraulic properties of pore networks, *Transport Porous Media*, 49, 99–122.
- Tompson, A. F. B., R. Ababou, and L. W. Gelhar (1989) Implementation of the three-dimensional turning bands random field generator, *Water Resour. Res.*, 25(10), 2227–2243.
- Tyn, M.T., and W. F. Calus (1975) Temperature and concentration dependence of mutual diffusion coefficients of some binary liquid systems, *J. Chem. Engrg. Data*, 20(3), 310-316.
- Udell, K.S. (1997) Thermally enhanced removal of liquid hydrocarbon contaminants from soils and groundwater, in C.H. Ward, J.A. Cherry, and M.R. Scalf (Eds.), *Subsurface Restoration*, Ann Arbor Press, Chelsea, Michigan, 251-270.
- Udell, K. S., R. D. Aines, et al. (1994) Application of steam injection and electrical heating for enhanced in situ soil and ground water treatment, *Ground Water*, 32(5), 840-841.
- Udell, K. S., and M. T. Itamura (1998) *Removal of Dissolved Solvents from Heated Heterogeneous Soils during Depressurization*, Battelle Press, Columbus, OH.
- Udell, K. S., and R. L. McCarter (1998) *Steam Enhanced Extraction of Wood Treatment Chemicals from Soils*, Battelle Press, Columbus, OH.

- Udell, K. S., N. Sitar, et al. (1988) A pilot study of steam injection for the removal of semi-volatile contaminants from soil, *Eos, Transactions*, American Geophysical Union, 69(44), 1206.
- Unger, A.J.A., E.A. Sudicky, and P.A. Forsyth (1995) Mechanisms controlling vacuum extraction coupled with air sparging for remediation of heterogeneous formations contaminated by dense nonaqueous phase liquids, *Water Resour. Res.*, 31, 1913-1925.
- Urynowicz, M.A. (2000) Dense non-aqueous phase trichloroethene degradation with permanganate ion, Ph.D. Dissertation, Colorado School of Mines, Golden CO. 166 pp.
- Urynowicz, M.A., and R.L. Siegrist (2000) Chemical degradation of TCE DNAPL by permanganate, in G.B. Wickramanayake, A.R. Gavaskar, and A.S.C. Chen, A.S.C. (Eds.), *Chemical Oxidation and Reactive Barriers*, Battelle Press, Columbus, OH, 75-82.
- USEPA (1992) Dense non-aqueous phase liquids—A workshop summary, USEPA Rep. No. EPA/600/R-92/030, Office of Research and Development, Washington D.C., 78 p.
- USEPA (1993) Evaluation of the likelihood of DNAPL presence at NPL sites, USEPA Rep. No. EPA/540/R-93/073, Office of Solid Waste and Emergency Response, Washington D.C., 114 p.
- USEPA (1995) National primary drinking water regulations, Retrieved March 03, 2006 from <http://www.epa.gov/ogwdw/dwh/c-voc.html>.
- USEPA (1996) Soil screening guidance: technical background document, USEPA Rep. No. EPA/540/R-95/128, July 1996.
- USEPA (1998) In Situ Remediation Technology: In situ chemical oxidation, USEPA Rep. No. EPA/542/R96/005, Office of Solid Waste and Emergency Response, Washington D.C., 39 p.
- USEPA (2004b) Discussion paper--Cleanup goals appropriate for DNAPL source zones, USEPA, Office of Solid Waste and Emergency Response, Washington D.C., 16 p., http://gwtf.cluin.org/docs/options/dnapl_goals_paper.pdf.
- USHHS (2002) Report on carcinogens, tenth edition, U.S. Department of Health and Human Services, Public Health Service, National Toxicology Program, December 2002, <http://ehp.niehs.nih.gov/roc/toc10.html>.
- Valocchi, A.J. (1985) Validity of the local equilibrium assumption for modeling sorbing solute transport through homogeneous soils, *Water Resour. Res.*, 21(6), 808-820.
- van Breukelen, B.M., J. Griffioen, W.F.M. Roling, and H.W. van Verseveld (2004) Reactive transport modeling of biogeochemical processes and carbon isotopic geochemistry inside a landfill leachate plume, *J. Contam. Hydrol.*, 70, 249-269.
- van der Ham, A. G. J. and H. J. H. Brouwers (1998) Modeling and experimental investigation of transient, nonequilibrium mass transfer during steam stripping of a nonaqueous phase liquid in unsaturated porous media, *Water Resour. Res.*, 34(1), 47-54.
- van Genuchten, M.T. (1980) A closed-form equation for predicting the hydraulic conductivity of unsaturated soils, *Soil Sci. Soc. Am. J.*, 44, 892-898.

- van Genuchten, M.T., and Alves, W.J. (1982) Analytical solutions of the one-dimensional convective-dispersive solute transport equation, U.S. Department of Agriculture Technical Bulletin 1661, 151 p.
- Van Waveren, R.H., S. Groot, H. Scholten, F.C. Van Geer, J.H.M. Wosten, R.D. Koeze, and J.J. Noort (1999) Good modeling practice handbook, STOWA Report 99-05, Utrecht, RWS-RIZA, Lelystad, The Netherlands.
- Vella, P.A., and Veronda, B. (1994) Oxidation of trichloroethylene: A comparison of potassium permanganate and Fenton's Reagent, Proceedings of the 3rd International Symposium, Chemical Oxidation: Technologies for the Nineties, Vol. 3., Vanderbilt University, Nashville, TN, Feb 1993, Technomic Publishing, Lancaster, PA, 62-73.
- Vidumsky, J.E., D.E. Ellis, J. Wetherington, and F. Gheorghiu (2005) Natural biodegradation of chlorinated solvents in a high-concentration source area, Proceedings of the Eight International Symposium on In Situ and On-Site Bioremediation, Battelle Press, Baltimore, MD, June 2005.
- Vogel, T.M., C.S. Criddle, and P.L. McCarty (1987) Transformation of halogenated aliphatic compounds, *Environ. Sci. Technol.*, 21(8), 722-736.
- Vogel, T.M., and P.L. McCarty (1987) Rate of Abiotic Formation of 1,1-Dichloroethylene from 1,1,1-trichloroethane in groundwater, *J. Contam. Hydrol.*, 1, 299-308.
- Voudrias, E.A., and M.-F. Yeh (1994) Dissolution of a toluene pool under constant and variable hydraulic gradients with implications for aquifer remediation, *Ground Water*, 32, 305-311.
- Wexler, E. (1992) Analytical solutions for one-, two-, and three-dimensional solute transport in ground-water systems with uniform flow, U.S. Geological Survey Techniques of Water-Resources Investigations, vol. 3, chap. B7, 198 p.
- Wyllie, M.R.J. (1962) Relative permeability, in T.C. Frick (Ed.), *Petroleum Production Handbook, Reservoir Engineering, Vol. II*, McGraw-Hill, New York, NY.
- Yan, E.Y., and F.W. Schwartz (1999) Oxidative degradation and kinetics of chlorinated ethylenes by potassium permanganate, *J. Contam. Hydrol.*, 37(3), 343-365.
- Yan, E.Y., and F.W. Schwartz (2000) Kinetics and mechanisms for TCE oxidation by permanganate, *Environ. Sci. Technol.*, 34(12), 2535-2541.
- Yang, Y., and P.L. McCarty (2000) Biologically enhanced dissolution of tetrachloroethene DNAPL, *Environ. Sci. Technol.*, 34(14), 2979-2984.
- Yang Y. and P.L. McCarty (2002) Comparison between donor substrates for biologically enhanced tetrachloroethene DNAPL dissolution, *Environ. Sci. Technol.*, 36, 3400-3404.
- Zhang, H., and F.W. Schwartz (2000) Simulating the in situ oxidative treatment of chlorinated ethylenes by potassium permanganate, *Water Resour. Res.*, 36(10), 3031-3042.

- Zheng, C., and P.P. Wang (1999) MT3DMS: A modular three-dimensional multispecies transport model for simulation of advection, dispersion, and chemical reactions of contaminants in groundwater systems, documentation and user's guide. Contract report SERDP-99-1, U.S. Army Engineer Research and Development Center Project 1294, Vicksburg, MS.
- Zhou, M., and R.D. Rhue (2000) Screening Commercial Surfactants Suitable for Remediating DNAPL Source Zones by Solubilization, *Environ. Sci. Technol.*, 34(10), 1985-1990.

Appendix 1 – Large Tank Experiments with High Heterogeneity

A1.1 Introduction

Experiments were performed in a large tank constructed to represent a test aquifer with a high degree of soil heterogeneity (variance of $\log K = 1.22$). In this experiment, data needed to study partitioning tracer behavior, natural dissolution, surfactant enhanced dissolution and in situ chemical oxidation was generated. Multiple tracer tests were performed prior to and after natural dissolution, surfactant flushing, and chemical oxidation.

The large tanks experiments generated a large amount of data (tracer and solute concentration data collected at 30 sampling ports for 4 to 5 days, at 2 hour intervals). Data analysis included (1) head-and-flow characterization, (2) transport model calibration, (3) natural dissolution after a DNAPL spill, (4) natural dissolution after surfactant flushing, and (5) multiple tracer data (pre- and post-remediation) using methods of moments, (6) multiple tracer data using method of inverse modeling, (7) surfactant flushing data, and (8) chemical oxidation data.

A1.2 Packing

Tank setup is shown in Figure A1.1 and Figure A1.2. The dimension of this large tank is 16-ft×4-ft×2-in. Wall units used in a previous experiment were cleaned and re-assembled. A 0.25-inch thick tempered glass was attached to one of the polycarbonate wall unit in the part of the tank where the DNAPL source zone was created. The tank was packed using the five different sands, corresponding to sieve sizes #16, #30, #50, #70, and #110, in a heterogeneous zone. A homogeneous zone of #8 sand was located upgradient of the expected source area. The homogeneous zone was used to provide uniform injection of tracers and other solution during remediation. Six pairs of array for head monitoring and sampling and one array for injection of tracer and treating reagents were installed. Each array has 40 ports every inch. Electrically controlled constant-head devices were used to maintain the hydraulic heads at both ends, and to provide hydraulic gradient to generate the groundwater flow through the test tank.



Figure A1.1. Large-Scale Two-Dimension Test Tank

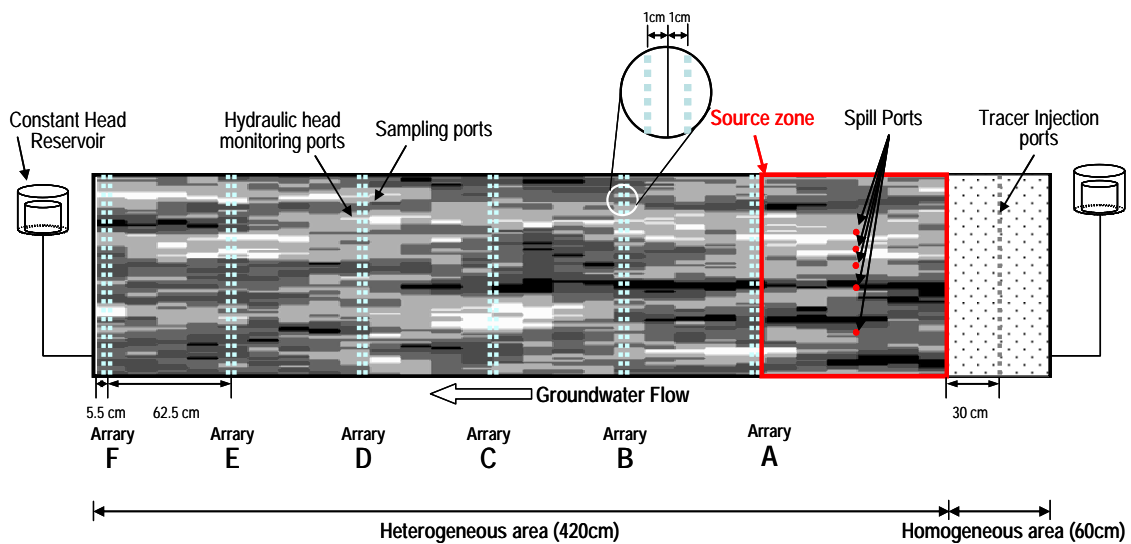


Figure A1.2. Design for Experimental Tank Showing Heterogeneous Packing, Constant Head Devices, Head Monitoring Ports, and Sampling Ports

A heterogeneous packing configuration was selected for the 16-ft test tank to represent a highly heterogeneous field. The parameters of the packing were: (1) mean of $\ln K$ (K in m/day) of 4.18, (2) variance of 1.22, (3) horizontal correlation length of 0.5 m and (4) vertical correlation length of 0.05 m. This packing produced an anisotropy ratio of 10. Random heterogeneous hydraulic-conductivity fields were generated using the turning bands algorithm

resulting in a continuous distribution of $\ln K$ (log-normally distributed). Then, the continuously distributed K field was discretized into five sands, corresponding to sieve sizes #16, #30, #50, #70, and #110, in a manner that preserved the theoretical $\ln K$ and variance $\sigma_{\ln K}^2$ values. Categories were associated with laboratory sands having known hydraulic properties (based on data obtained from column studies). Multiple random field realizations were generated using these design parameters. A realization suitable for entrapping a heterogeneous DNAPL source zone was then selected for packing the tank. The chosen configuration included zones within the target source area for DNAPL injection that were likely to produce a complex entrapment morphology while minimizing the possibility of vertical DNAPL migration to the bottom of the tank.

The tank was filled by hand according to the design. Filling involved placing individual sand volumes of approximately 80 cm^3 into the tank with the aid of a 5 cm PVC pipe. In this manner, individual sand lenses approximately 15 cm long and 1 cm high were placed at the desired locations. By dropping the sand through the PVC pipe as the pipe was moved laterally along a 15 cm track, a discrete 'blocky' geometry was avoided and more realistic sand contacts were established. The resulting individual sand units were tapered at their boundaries rather than having sharp vertical fronts (Figure A1.3). Water level in the tank was raised as the tank was filled in an effort to eliminate trapped air. However, the heterogeneous nature of the resulting capillary fringe resulted in air entrapment at several locations. After packing was completed, entrapped air was removed by flushing the system for an extended period with de-aired water.

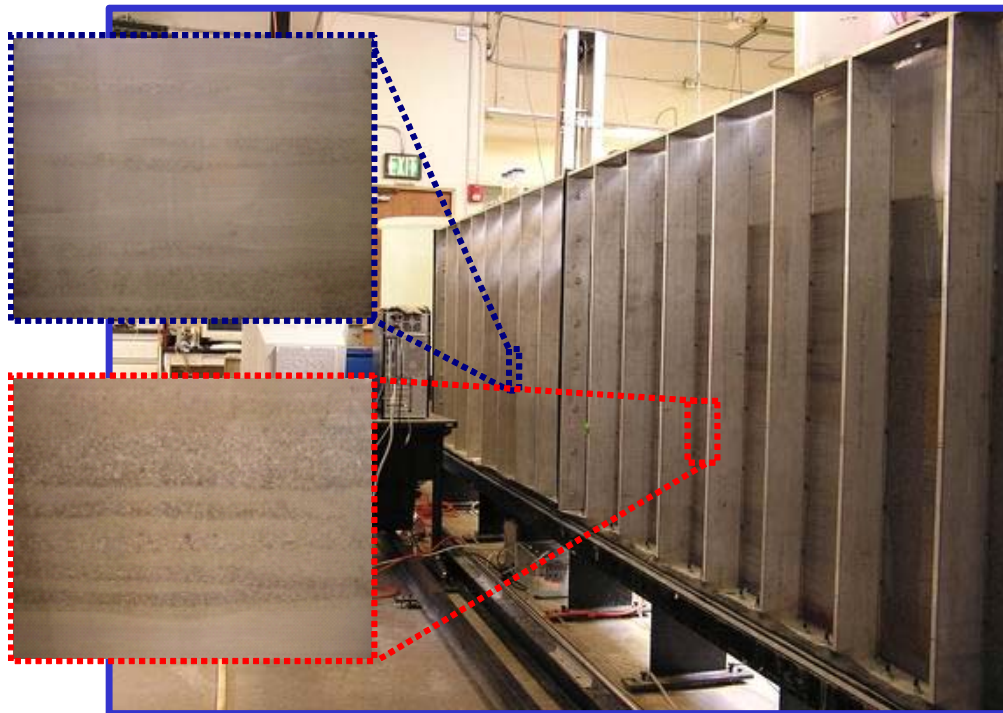


Figure A1.3. Large Tank after Sand Packing Showing Close-up View of Individual Sand Lenses

The final distribution of sands within the tank was mapped and compared to heterogeneity specified in the design. The actual distribution of sands was used in subsequent interpretation of flow and transport experiments.

A1.3 Gamma Scanning

A gamma-ray attenuation system was used to scan the source zone prior to and after PCE spill. The difference in gamma-ray intensity (i.e. photons counted) was used to quantitatively evaluate DNAPL saturation distribution. It took approximately 8 days to scan the entire source zone area (an area of approximately 70-cm×60-cm).

A determination of the gamma-ray attenuation coefficients was completed for water, surfactant (Tween-80) and PCE-DNAPL (Table A1.1). The attenuation coefficient is a characteristic value of a material indicating how gamma rays will be attenuated during penetration) of used in all experiments was completed. These values are used in the calculation of PCE saturation in the source zone before and after treatment based on the expression

$$I = I_0 \exp(-\mu t)$$

where I and I₀ are number of photons that transmit with and without absorber, respectively. The parameter μ is attenuation coefficient, and t is the path length. The value of NAPL saturation is directly related to this path length.

Table A1.1. Gamma-Ray Attenuation Coefficient of Chemicals Used in the Experiment

| Chemicals | Attenuation Coefficient (cm ⁻¹) |
|---------------|--|
| Water | 0.2034 ± 0.000822 |
| Tween-80 (5%) | 0.203405 ± 2.98764×10 ⁻⁵ |
| PCE* | 0.64239 ± 0.003787 |

*Red-dyed tetrachloroethene using Sudan IV.

A1.4 Flow and transport characterization

A1.4.1 Head and flow measurements

Hydraulic heads were monitored at 46 locations using an automated pressure transducer (Figure, Table). The automated pressure transducer is illustrated in Figure A1.2. Figure shows hydraulic heads in the monitoring ports for an overall head difference between two constant head reservoirs of 5.7 cm. Monitoring points located on the same vertical line show slightly different hydraulic heads due to heterogeneity of the hydraulic conductivity field. The hydraulic head showed slight daily variations by the amount of about 2 mm because the water body expanded and extracted as a results of room temperature variation. Flow measurements throughout the experiment showed a steady flow rate of 62.93 ± 0.50 mL/min for the head drop of 5.7 cm. Figure shows flow measurements during experiment.

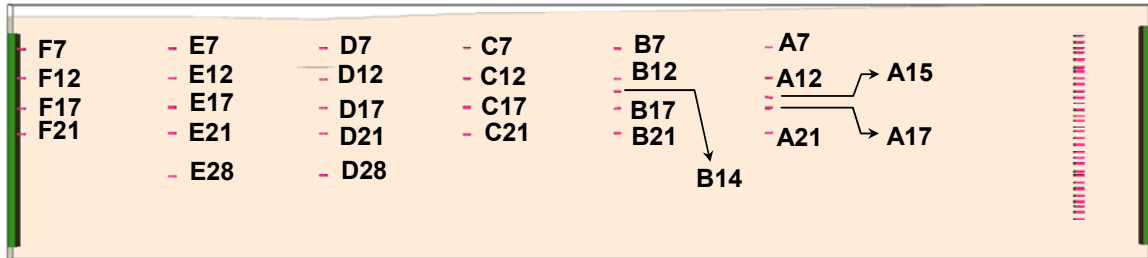


Figure A1.4. Head Monitoring Locations in the Test Tank

Table A1.2. Summary of Monitoring Locations

| Vertical Distance from Top of Tank (in) | | | | | | | |
|---|--------------|-------------------------|-------------------------|-------------------------|--------------------------|-------------------------|--------------------------|
| Injection Ports | Spill Ports | Array A | Array B | Array C | Array D | Array E | Array F |
| 5, 10, 15, 20, 25, 30, 35 | 3, 8, 17, 22 | 6, 12, 18 26, 30, 35 | 7, 10, 14 18, 23, 33 | 7, 12, 16 23, 29, 35 | 12, 15, 21 28, 35, 38 | 8, 16, 21 28, 32, 35 | 10, 14, 16 23, 28, 32 |

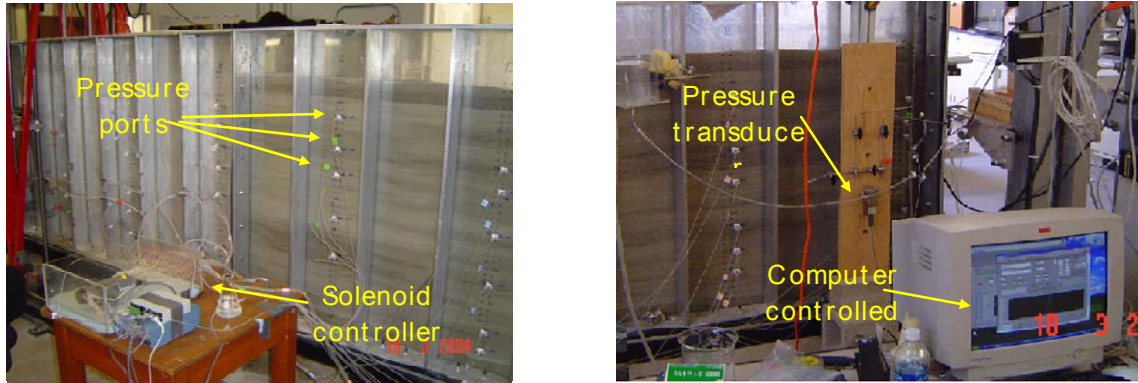


Figure A1.2. Pressure Transducer System.

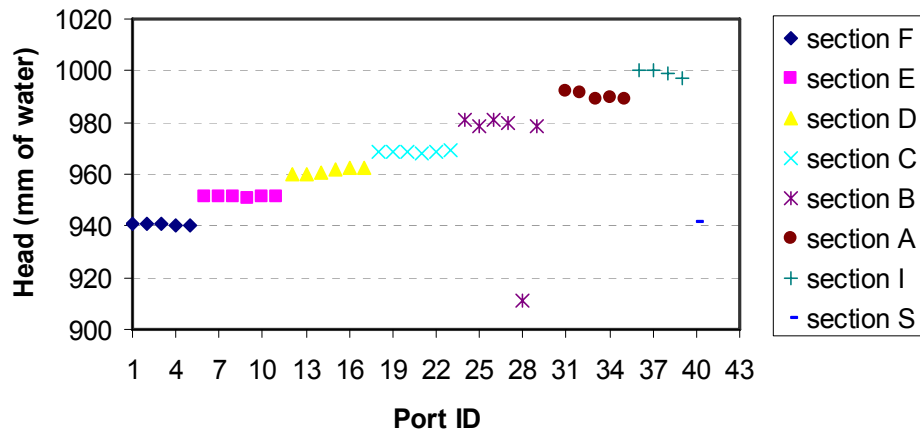


Figure A1.6. Example of Steady-State Head Measurements (head drop = 5.7 cm)

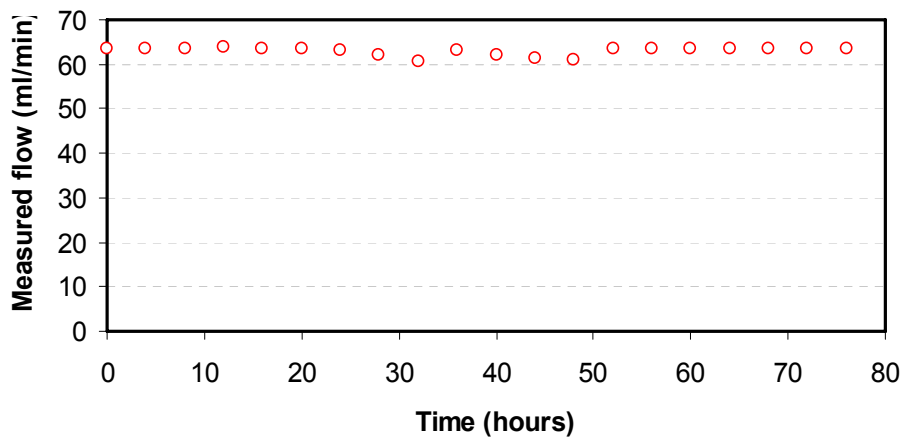


Figure A1.7. Example of Flow Measurements (head difference = 5.7 cm)

A1.4.2 Pre-spill tracer test

A bromide and partitioning tracer test was conducted on March 22nd, 2004 prior to the DNAPL spill. The objectives of this experiment were:

1. To evaluate the uniformity of tracer injection through all the ports,
2. To evaluate if the partitioning tracers were subject to retardation due to sorption into the soil,
3. To test design parameters of the tracer test for post spill characterization: concentration of tracer, flow rate, injection time, sampling frequency and total sampling time, and
4. To obtain a conservative tracer data set for estimation of transport parameters using numerical models.

A solution of 500 ppm of Bromide, 300 ppm of hexanol and 300 ppm of DMP was injected in the tank using a multi-syringe pump. The total flow rate of water through the tank was controlled using two constant head reservoirs with a head difference of approximately 8 cm. The flow rate of the injected solution was 0.25 mL/min per port. Since the multi-syringe pump allows for injection in 32 ports, the total injection flow was 8 mL/min. The duration of the tracer slug was 10 hours. Samples were taken manually in 28 locations located in 6 different arrays as specified in Figure A1.2. To reduce the sampling volume, 0.5-mL inserts were placed in 2.5-mL vials. A total of 596 samples were generated during the experiment and analyzed by gas and ion chromatography. The results are shown in Figure A1.3 to Figure A1.10.

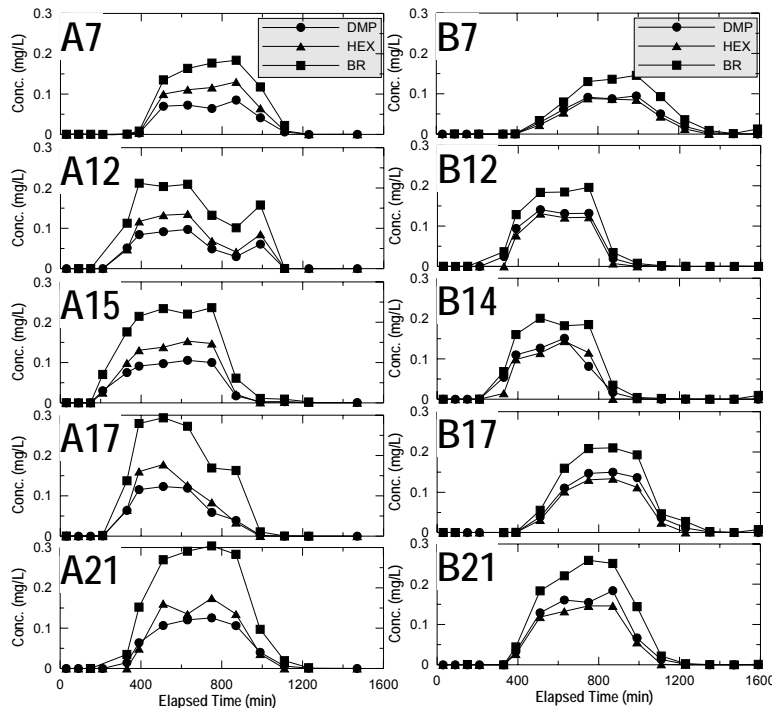


Figure A1.3. Tracer Test Result for Sample Arrays A and B

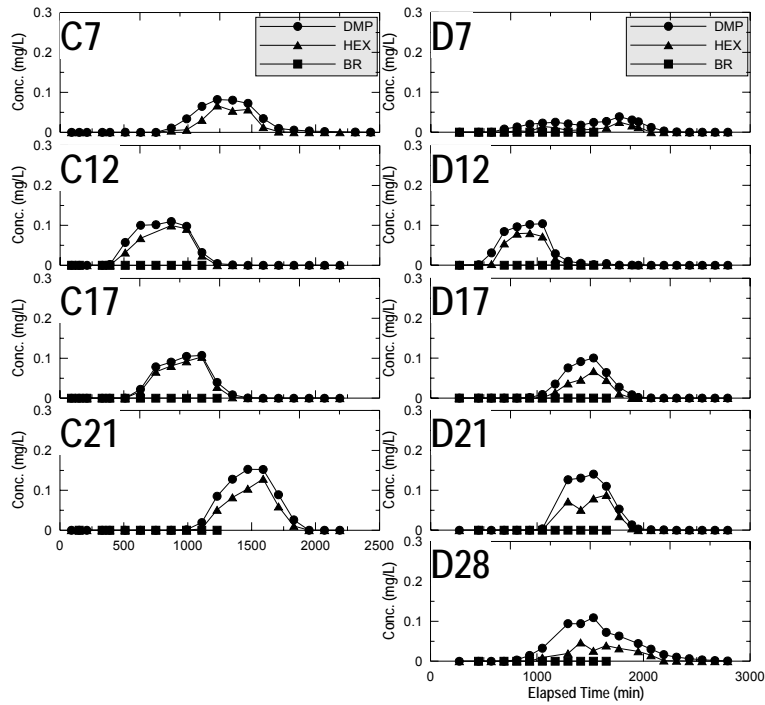


Figure A1.4. Tracer Test Results for Sample Arrays C and D

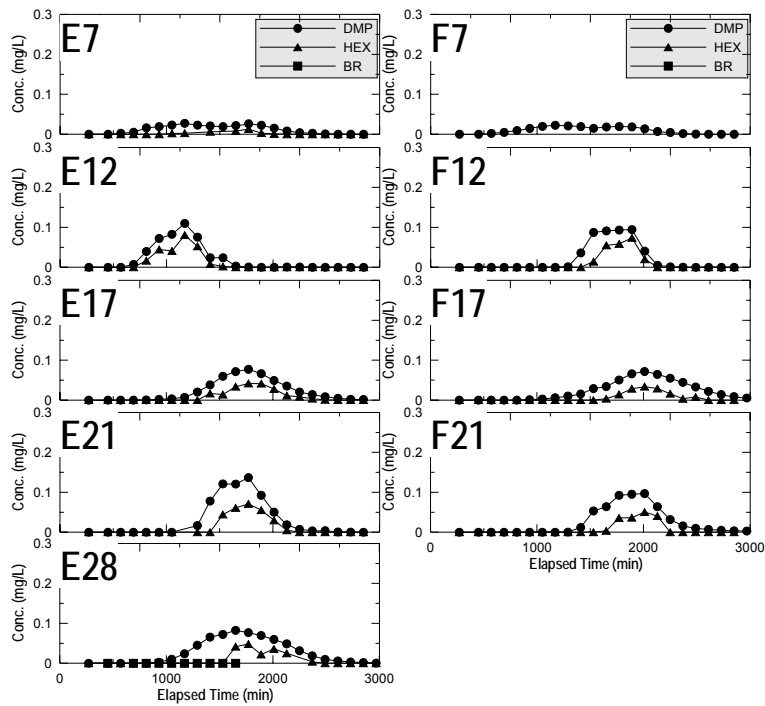


Figure A1.5. Tracers test result for ports in arrays E and F.

As observed in data from sample array A, some discrepancies between bromide and the partitioning tracers were observed. Since there was no NAPL in the tank, it was expected to obtain the same breakthrough curves from all the tracers. These discrepancies can be a result of the volatilization of the alcohols. The initial concentration of the tracer solution for analysis was not collected until 24 hours after injection, so this also could have decreased the concentrations of alcohols in the solution. To evaluate if the difference in concentration values between the different tracers affected the travel time, the first centralized moments were calculated. As shown in the Figure A1.6, the center of mass remained the same so these differences didn't affect retardation values obtained from partitioning tracers.

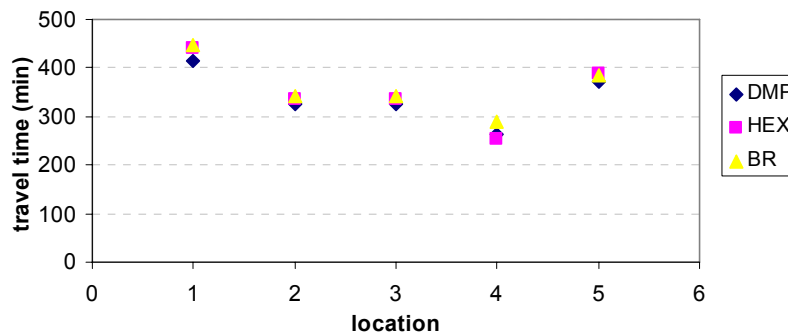


Figure A1.6. Travel Times Obtained from Breakthrough Curves of Three Different Tracers at Sample Array A

Based on the above tracer results, the following conclusions were drawn.

1. The tracer front was fairly uniform in the vertical direction.
2. No retardation of partitioning tracers was observed due to sorption into the soil.
3. Design parameters including concentration of tracer, flow rate, injection time, sampling frequency and total sampling time provided adequate results for the objectives of the test.
4. The set of tracer data set was suitable for estimation of transport parameters used in numerical models.

A1.4.3 PCE-DNAPL spill

A total of 586.7 mL of PCE-DNAPL dyed with red Sudan IV (0.01%) was injected in the source zone through five ports (Figure A1.7). The amounts injected into each port are listed in Table A1.3. PCE was injected under constant head of PCE using a Mariotte bottle.

Table A1.3. Volume of PCE Injected into Each Injection Port

| Source Zone | Volume Injected (mL) |
|--------------|----------------------|
| 1 | 272.0 |
| 2 | 71.9 |
| 3 | 41.4 |
| 4 | 93.3 |
| 5 | 93.2 |
| Total | 586.7 |

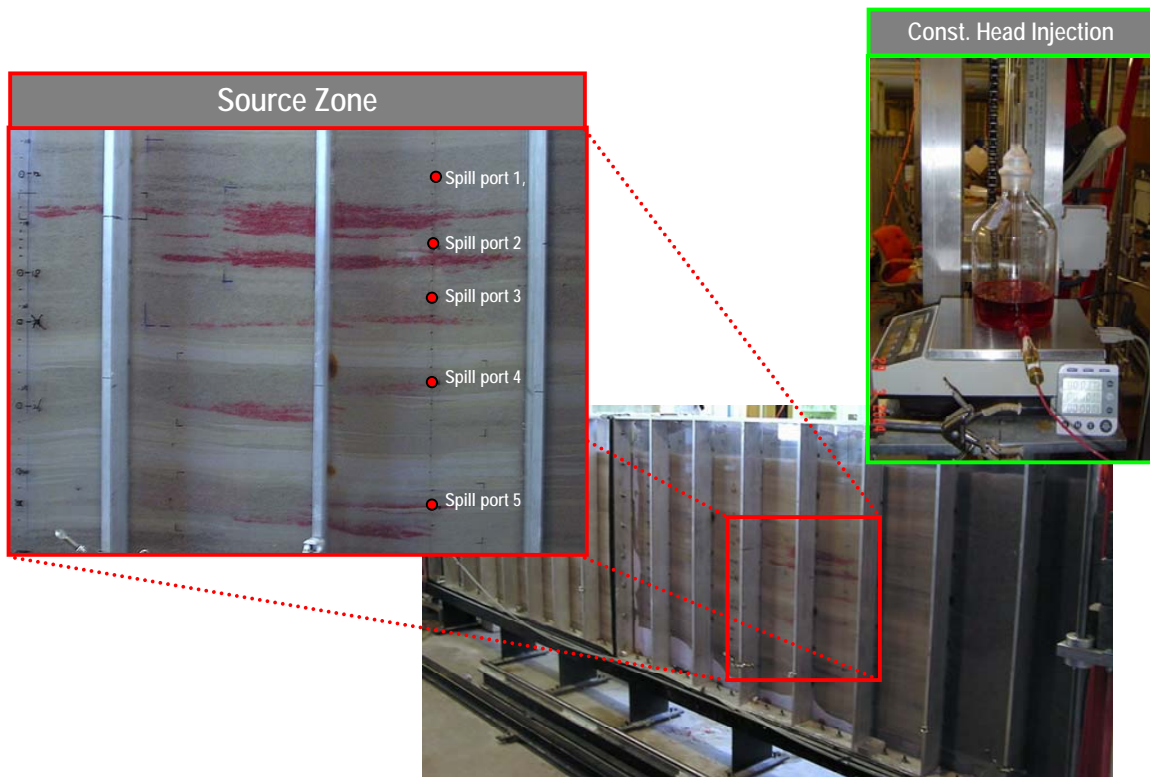


Figure A1.7. Spill device, location, and final NAPL distribution

A1.4.4 Gamma-ray scanning

The gamma attenuation system was used to scan the PCE entrapment zone after the spill was completed and static conditions had been achieved (i.e. after no further NAPL migration was observed). The gamma system took approximately 8 days to complete the scan and the saturation distribution from the signal is illustrated in Figure A1.8. The result was comparable to visual observation. Mass balance was approximately 97 percent.

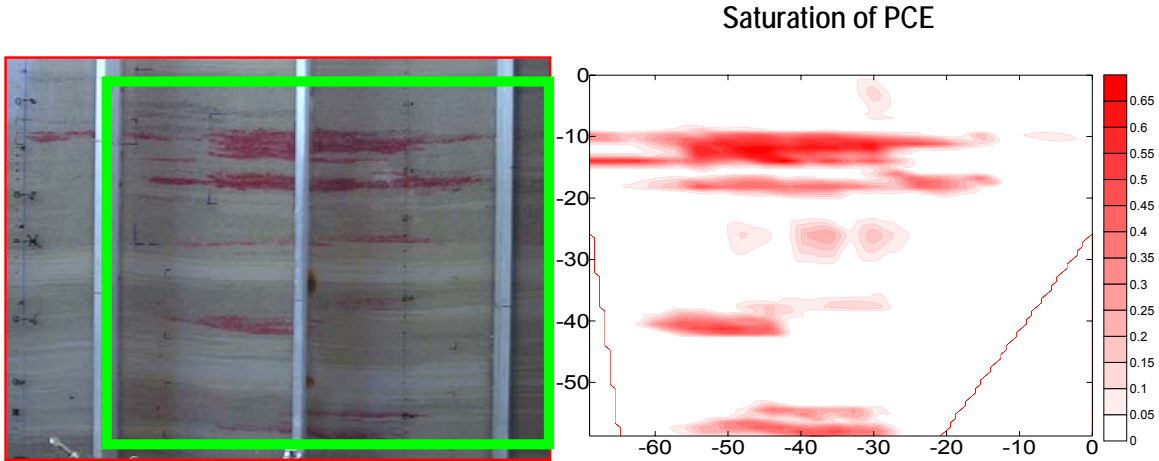


Figure A1.8. PCE Saturation Distribution Obtained from Gamma Attenuation System

A1.5 Natural Dissolution

A1.5.1 Steady-state natural dissolution experiment

Once the static PCE entrapment architecture had been established, four different hydraulic gradients were applied to the test tank. Aqueous samples were taken at every other port (in the vertical direction) for three arrays (A, C, and E). The example shown below (Figure 3.36) illustrates the distribution of PCE concentration in the vertical direction for head difference of 8 cm.

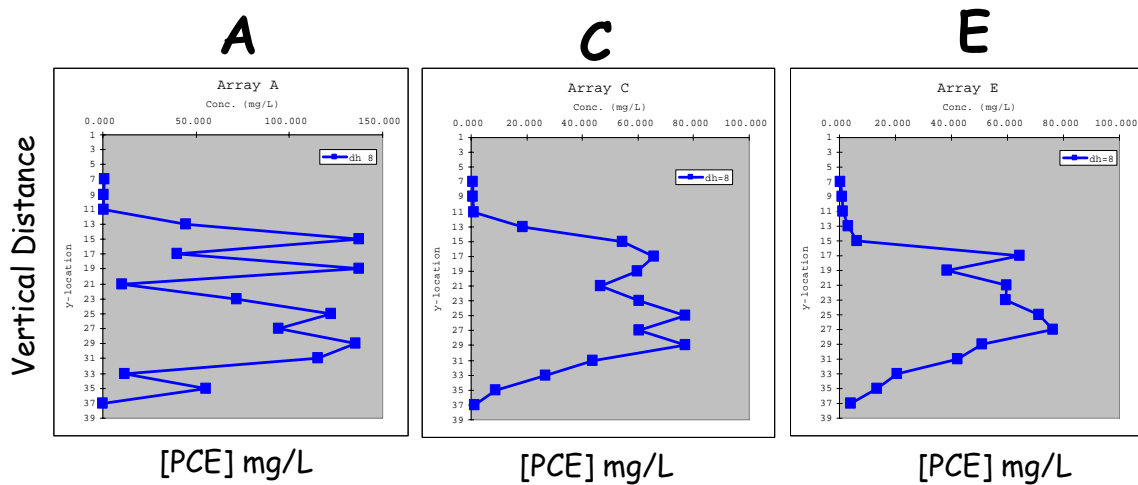


Figure A1.9. PCE Concentration Distribution at Sampling Arrays A, C and E

A1.5.2 Pre-treatment multiple tracers test

The objective of this experiment was to develop data to validate techniques that could delineate and determine DNAPL saturations in heterogeneous entrapment configurations. Previous experiments in this research study had been conducted to quantify estimation errors of partitioning tracers and to improve existing tracer technologies. This experiment was used to validate these improvements in tracer protocols. To aid in the discussion of tracer tests, each experiment in the tank was assigned a task ID (Table A1.5).

Table A1.1. Chronology of Experiments for the Large Tank with High Heterogeneity

| Task ID | Description |
|----------------|---|
| Scanning 0 | Gamma scan prior to spill |
| PITT 0 | Blank tracer test to check design parameters, background retardation and to obtain transport parameters for model calibration |
| PCE spill | 586.7 ml of PCE were spilled into the tank |
| Scanning 1 | Gamma scan to determine saturations |
| PITT 1 | Partitioning tracer test to determine DNAPL architecture |
| SEAR | Surfactant flushing |
| Scanning 2 | Gamma scanning to determine new saturations after remediation |
| PITT 2 | Partitioning tracer test to determine DNAPL architecture and remediation performance |

Results from experiment PITT 0 showed that there was no background retardation of any tracer in the system. Breakthrough curves also demonstrated that the injection pump was generating flow patterns in the domain that resulted in a uniform tracer front in the homogeneous zone before tracer entered the heterogeneous zone. The locations of injection and extraction ports was found to be suitable for future tracer tests since the tracer front swept the entire area associated with the source zone. The data obtained in PITT 0 also showed the influence of heterogeneity reflected in the variability in breakthrough curve shapes collected at the same vertical location.

After the spill of PCE, the saturations of PCE in the source zone were determined using gamma attenuation. Results from Scanning 0 and Scanning 1 were combined to obtain NAPL saturation using differencing methods (Saba, 1999). Figure A1.8 shows the comparison between the final visual distribution of PCE and the contours defined from gamma attenuation. The PCE spread downwards and laterally within the coarser layers around the injection ports until it reached the finer layers (#110 sand) where it spread laterally.

After scanning of the source zone, PITT 1 was conducted. The same design parameters used for PITT 0 were applied in this test. A total of 900 samples were collected during this experiment. The total time of the experiment was increased to 4 days since it was expected to obtain a delay of the partitioning tracer transport due to the presence of DNAPL.

A1.5.3 Method of moments

After analysis of the samples using gas and ion chromatography, the relative concentration of all the tracers was plotted over time (Figure A1.10). During data analysis, the ion chromatograph experienced some technical difficulties, which caused the loss of some bromide samples. This technical problem resulted in bromide breakthrough curves that were inexistent or incomplete. Before the data were examined using method of moments, the breakthrough curves were analyzed qualitatively to evaluate signatures or features that contain information about the vertical architecture of the system.

In Figure A1.10, the breakthrough curves collected in array A are represented. All the locations captured some retardation by the partitioning tracers. The breakthrough curves collected during PITT 1 demonstrated the presence of high saturation zones of PCE. Tailing observed in A16 and A17 indicates that the DNAPL is not distributed uniformly since a uniform distribution would produce a simple offset (Brooks et al., 2002; Jawitz et al. 1998b). This feature could also be the result of non equilibrium conditions that reflect permeability contrasts in the source zone. These permeability contrasts will control the local velocities, and tracer may not spend enough residence time to partition with all the DNAPL mass.

In these scenarios of high heterogeneity and rate limited partitioning, the retardation is manifest in the tailing portion of the breakthrough curve and may not be entirely captured due to the detection limit of the analytical instruments. The tail was extrapolated using an exponential decay function (Pope et al., 1994; Annable et al., 1997) in the cases where truncation was observed (A16 and A17). The issue of tailing becomes more problematic as the distance from the source zone increases. In array F most of the observation data are close to the detection limits and tailing was not captured.

After qualitative analysis of the breakthrough curves, arrival times of all the tracers were calculated using methods described by (Jin et al., 1995). The saturation values obtained at each location are represented in Table A1.2.

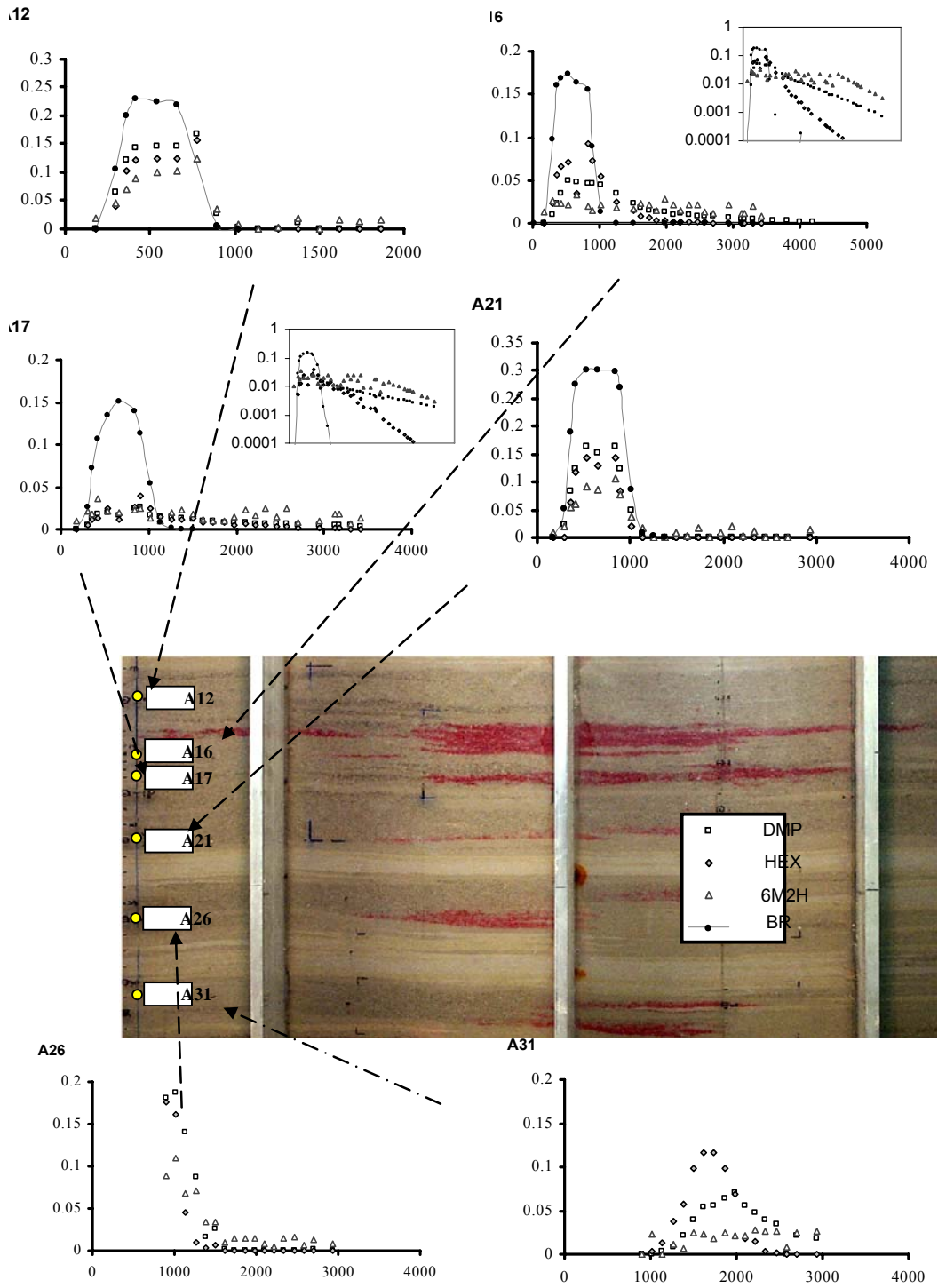


Figure A1.10. Breakthrough Curves Collected at Sampling Array A

Table A1.2. Saturation Values Obtained Using Method of Moments for all Sampling Ports

| PORT | SATURATION | | |
|------|------------|--------|--------|
| | DMP | HEX | 6M2H |
| A7 | 0.0038 | 0.0121 | 0.0049 |
| A12 | 0.0027 | 0.0041 | 0.0048 |
| A16 | 0.0703 | 0.0800 | 0.0374 |
| A17 | 0.0646 | 0.1352 | 0.0267 |
| A21 | 0.0019 | | 0.0085 |
| A26 | 0.0185 | | 0.0144 |
| A31 | 0.0121 | | 0.0022 |

| PORT | SATURATION | | |
|------|------------|--------|--------|
| | DMP | HEX | 6M2H |
| B7 | 0.0003 | | 0.0111 |
| B12 | 0.0016 | | 0.0165 |
| B14 | 0.0142 | 0.0058 | 0.0156 |
| B17 | 0.0207 | 0.0177 | 0.0105 |
| B21 | 0.0437 | 0.0527 | 0.0238 |
| B26 | 0.0012 | | 0.0051 |
| B31 | 0.0121 | 0.0149 | 0.0031 |

| PORT | SATURATION | | |
|------|------------|--------|--------|
| | DMP | HEX | 6M2H |
| C7 | 0.0005 | 0.0084 | 0.0049 |
| C12 | 0.0087 | | 0.0161 |
| C17 | 0.0136 | 0.0004 | 0.0070 |
| C21 | 0.0081 | 0.0045 | 0.0029 |
| C26 | 0.0234 | 0.0256 | 0.0138 |
| C31 | 0.0360 | 0.0765 | 0.0146 |

| PORT | SATURATION | | |
|------|------------|--------|--------|
| | DMP | HEX | 6M2H |
| D7 | 0.0023 | | 0.0097 |
| D12 | | | |
| D17 | 0.0111 | 0.0036 | 0.0035 |
| D21 | 0.0110 | | 0.0013 |
| D28 | 0.0083 | | 0.0024 |

| PORT | SATURATION | | |
|------|------------|-----|--------|
| | DMP | HEX | 6M2H |
| E7 | 0.0001 | | 0.0084 |
| E12 | | | |
| E17 | 0.0085 | | 0.0024 |
| E21 | 0.0037 | | 0.0003 |
| E28 | 0.0042 | | 0.0034 |

| PORT | SATURATION | | |
|------|------------|-----|--------|
| | DMP | HEX | 6M2H |
| F7 | 0.0141 | | |
| F12 | | | 0.0028 |
| F17 | 0.0073 | | 0.0015 |
| F21 | 0.0114 | | 0.0018 |

When the lateral distance from the source zone increases, retardation values became smaller. This is because the signal attenuates by mixing and the resulting saturation is the average value of the increasingly large swept zone. Figure A1.16 shows the average saturation values obtained at each array, the error bars in the y axis represent the variability of the values obtained from all the ports located in the array. Array A (the closest to the source zone) has more variability since the ports collected strong signals with information about the vertical architecture of source zone. As the distance from the source zone increases, the signal attenuates and the information about vertical architecture dissipates (low variability in array F). This figure shows the importance of well location in the design of the PITT.

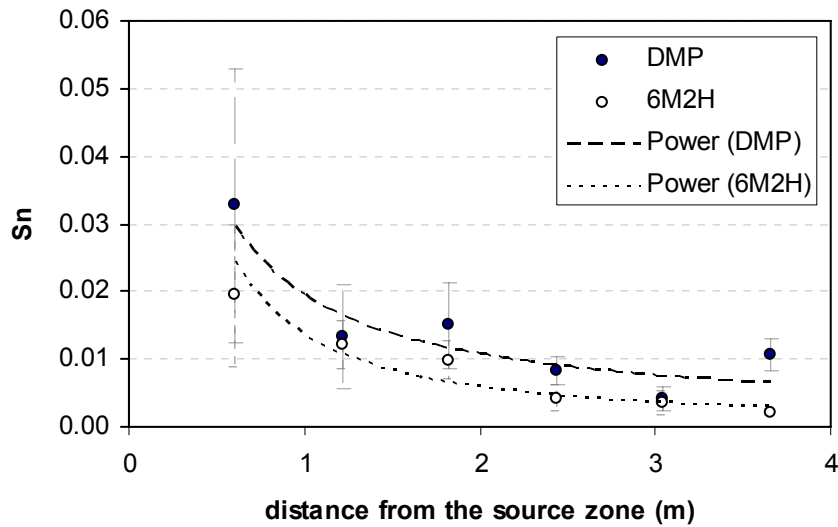


Figure A1.16. Saturation Values Obtained with Increasing Distance from the Source Zone

After the first tracer test to characterize DNAPL, surfactant-enhanced aquifer remediation (SEAR) was applied to the two-dimensional tank. SEAR is design to enhance the solubility of the DNAPL phase by reducing the interfacial tension between the NAPL and water phases. For this particular investigation, the purpose was to obtain a new distribution of PCE with the use of surfactants; rather than to evaluate the remediation performance of the SEAR technology. It was expected that the surfactants would remove most of the DNAPL that was accessible along flow paths. After remediation, it was expected that most DNAPL in residual form would have been removed and most of the pools would prevail.

The gamma was applied after SEAR and a PITT was conducted again (PITT 2). In this way, not only the performance of the PITT to determine architecture was evaluated but also the performance of PITT as a tool to determine the effectiveness of the remediation was assessed. PITT 2 was carried out with the same design parameters as PITT 1 and 0. The qualitative observation of breakthrough curves showed a lack of tailing in all the locations. From the contours obtained by gamma attenuation, it was known that high saturations zones of PCE were still present (Figure A1.11).



Figure A1.11. Final Distribution of PCE and Contours Obtained from Gamma Data after SEAR

It was hypothesized that tracer flow through high saturation portions of the source zone would be limited, due to a large permeability contrast. Therefore it was expected that tracer retardation would not be reflective of most of the PCE mass remaining after SEAR. Test results showed that most of the DNAPL mass had been removed, when in reality significant DNAPL remained (Figure A1.18). This suggests that tracers did not detect DNAPL saturation that was not accessible along flowpaths.

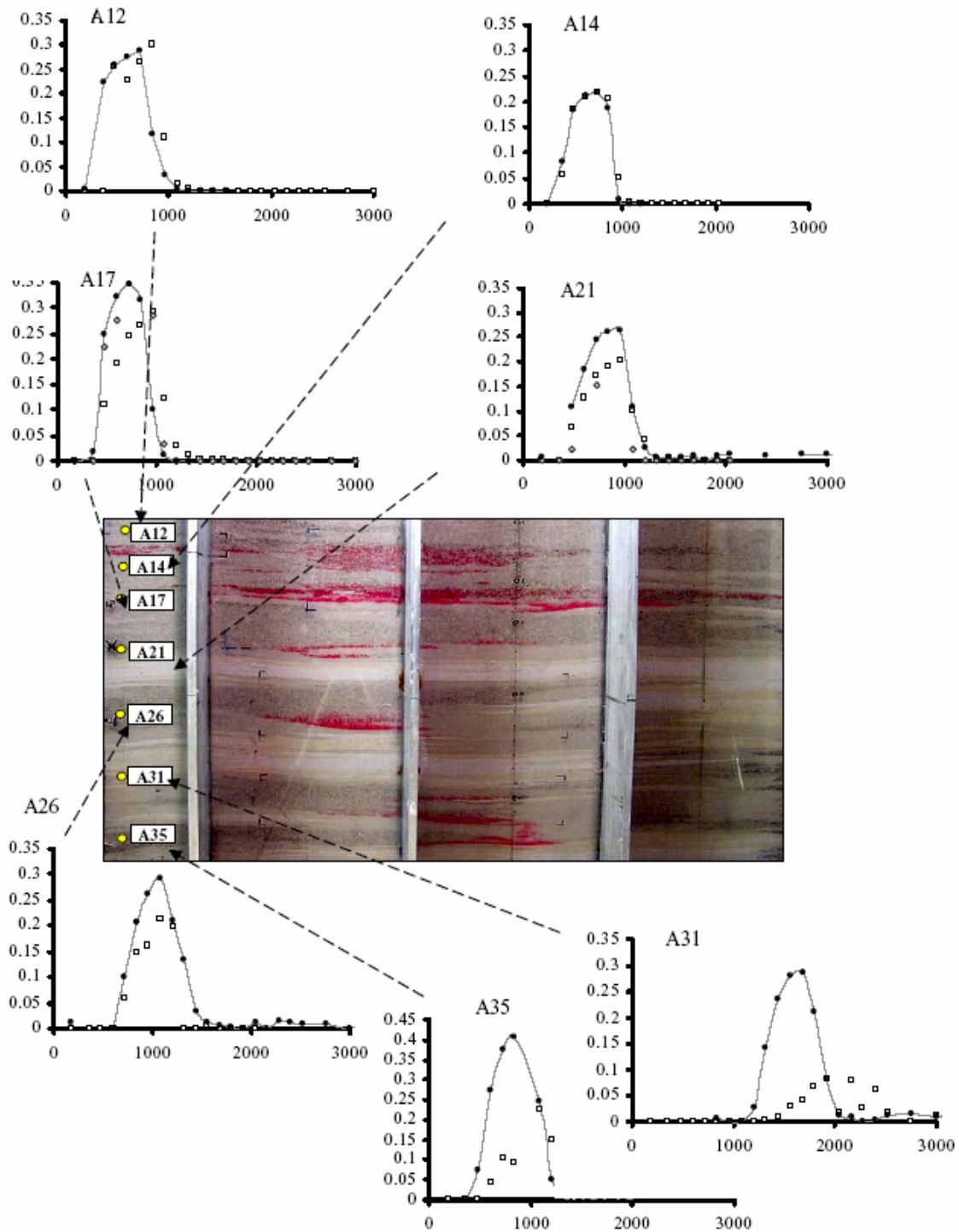


Figure A1.12. DMP Breakthrough Curves Collected at Array A after Surfactant Flushing

After qualitative analysis of the breakthrough curves, arrival times of all the tracers were calculated using numerical integration following the same procedures use in PITT 1. The difference between the saturations obtained from PITT 2 and the saturations obtained from PITT

1 should hypothetically represent the PCE removed by the SEAR technology.

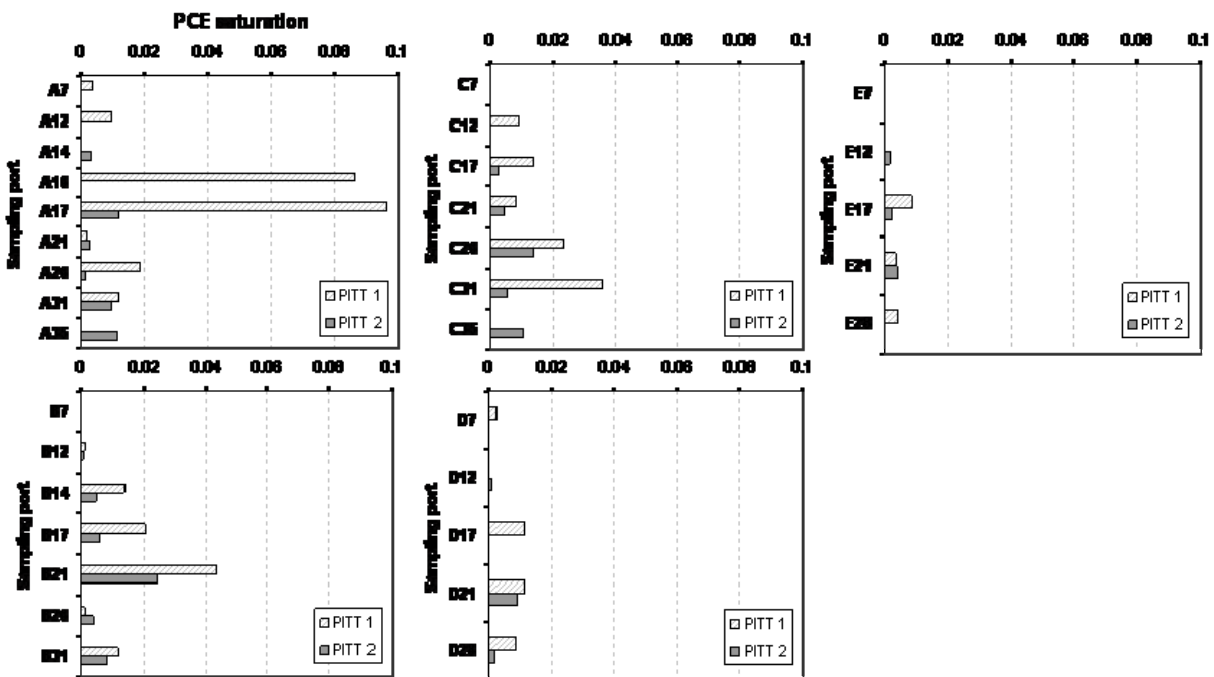


Figure A1.13 represents saturation results from both tests, each graph show results for each of the arrays. On first inspection, array A and B show a relevant decrease on saturation in the portions of the source zone that contain most of the PCE mass (between 14 and 17). However, as it can be observed in the pictures there is a considerable amount of PCE remaining in those portions where PITT showed a decrease in saturation (A16 and A17).

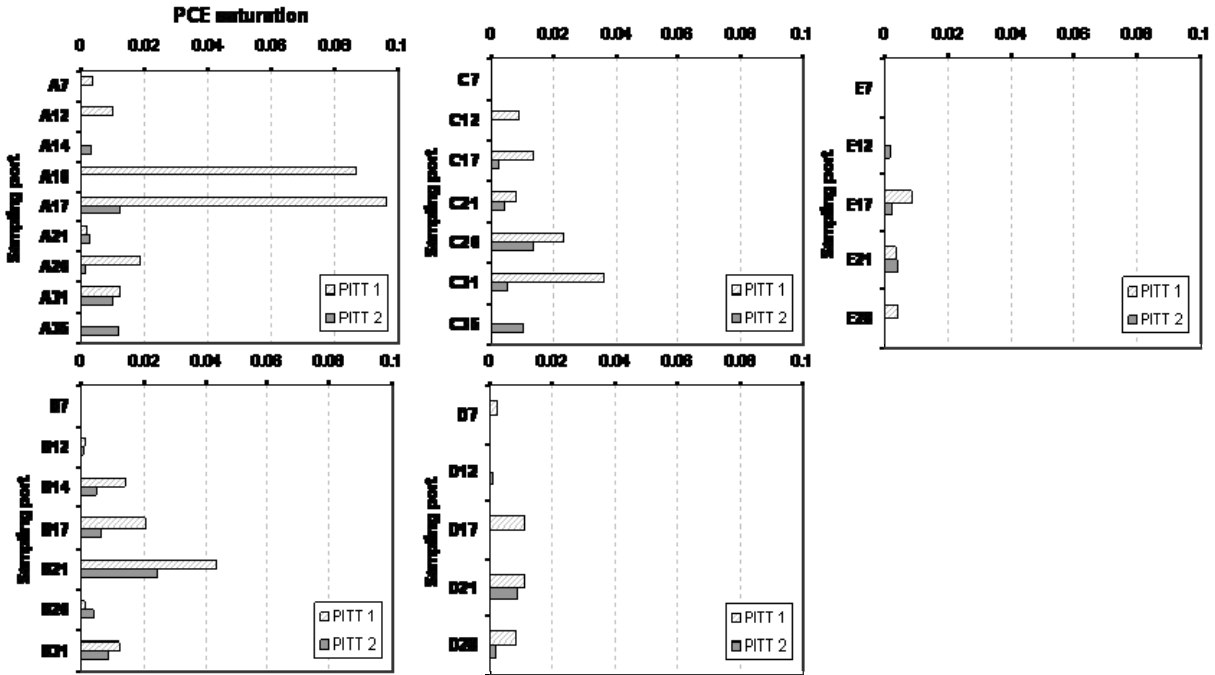


Figure A1.13. Saturation Obtained from PITT 1 and PITT 2 at all Sampling Arrays

A1.6 Surfactants

A 50.0 g/L surfactant (Tween-80; non-ionic food-grade surfactant) solution was injected into the test tank in the injection array (32 injection ports) for 10 hours. The aqueous samples were taken every two hours at arrays A and C. The plume concentration was monitored for four consecutive days. Figure 3.61 shows breakthrough curves of PCE concentration for monitored ports at arrays A and C. Figure 3.62 shows a vertical profile of PCE concentration in array A. The peak concentration of PCE is as high as 4000 mg/L which is 20 times larger than the aqueous solubility limit ($C_s = 200$ mg/L). Based on mass balance calculation from both the effluent breakthrough curve and the gamma detection, total PCE removal is approximately 24%.

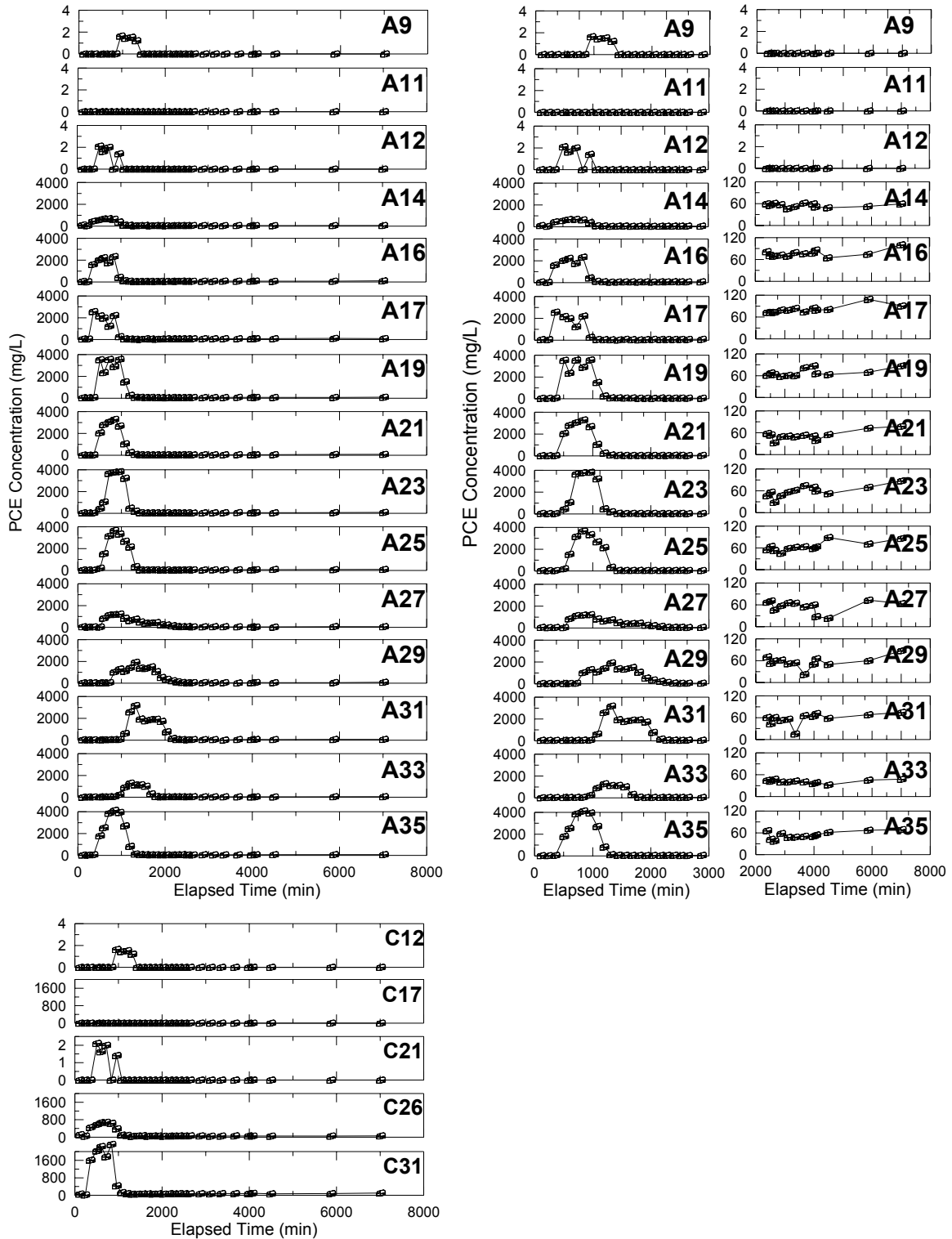


Figure A1. Error! No text of specified style in document. 14. Breakthrough Curves Obtained from Surfactant-Enhanced Dissolution Experiment, Sampling Arrays A and C

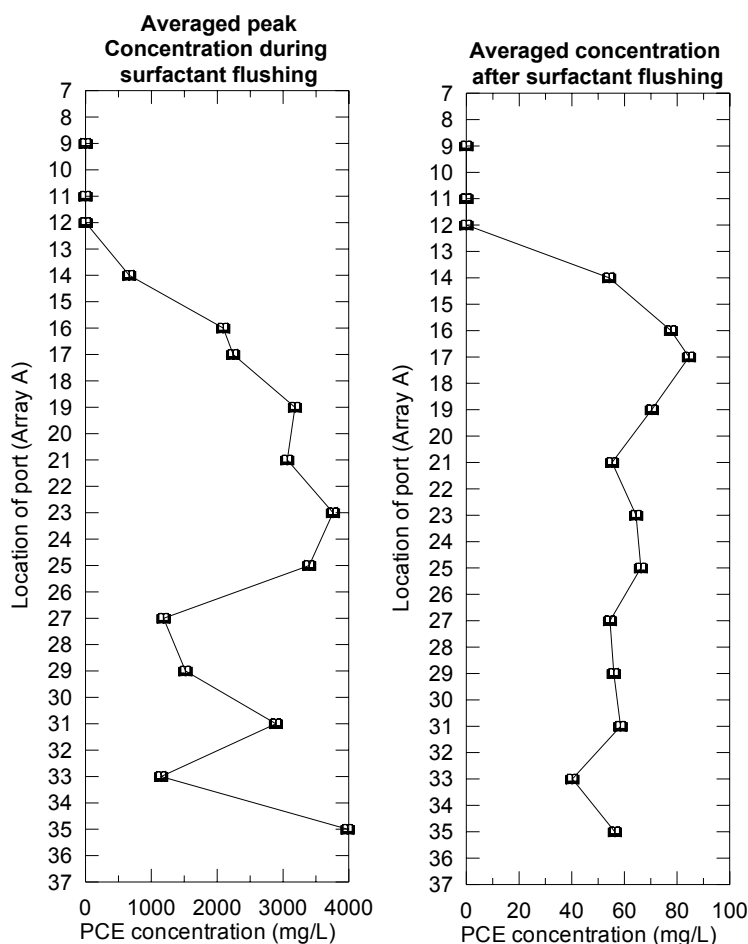


Figure A1.15. Vertical Profile of PCE Concentration Distribution at Sampling Array A Measured During and After Surfactant Flushing Experiment

A1.7 Chemical oxidation

An oxidation experiment was conducted in the large tank. At the time of the experiment, the tank contained approximately 400 g of PCE in a source zone with saturations ranging from suspended residual to pools. The oxidation experiment followed a series of natural dissolution, surfactant enhanced dissolution, and partitioning tracer tests. Tween-80 had been used as the surfactant, and despite two weeks of flushing with clean water following surfactant flushing, Tween-80 was still present up to 1000 mg/L. Tween-80 is readily oxidized by permanganate and exerted a non-productive oxidant demand similar to NOD. As a result, increased manganese oxide generation was expected. In fact, during oxidation, significant generation of immobile manganese oxides was observed (Figure A1.22).



Figure A1.16. Large-Scale Tank during Chemical Oxidation.

In the chemical oxidation experiment, an 8,000 mg/L solution of potassium permanganate (KMnO_4) was injected into the test tank through 32 injection ports. The total injection rate was $8.0 \text{ cm}^3/\text{min}$ while the total effluent was maintained at approximately $70.0 \text{ cm}^3/\text{min}$. Aqueous samples were taken every 3-5 hours for 4 days at arrays A and C. Samples were analyzed for (1) permanganate concentration using UV-Vis detector, (2) chloride ion concentration using Ion Chromatograph, (3) pH using pH-meter, and (4) PCE concentration using Gas Chromatograph. Figure A1.17 and Figure A1.18 show PCE and permanganate concentration at arrays A and C and the effluent, respectively. Figure A1.19 shows a close-up comparison of PCE and KMnO_4 concentrations during injection. The drop in PCE concentration clearly indicates the removal of aqueous phase PCE from oxidation reaction. In addition, significant amount of manganese dioxide ($\text{MnO}_{2(s)}$) precipitates were also observed in the source zone as well as downstream of the source. The precipitates were both deposited and transported downstream. The transported particles sometimes clogged the effluent line and created the pressure built-up. As a result, the effluent rate drops periodically. It was required to purge the effluent line very frequently to maintain constant flow during experiment.

Despite the build-up of manganese oxides (Figure A1.26), mass transfer from the DNAPL was enhanced as shown in Figure A1.20. This figure shows the mass of PCE removed from the tank via dissolution and oxidation, as measured at the effluent. The tank utilized a constant head inlet, so the injection didn't increase overall flow through the tank. Oxidant injection began at time 0, and ended at 1 day. The slope of the dissolved PCE line decreased as a result of oxidation, while the slopes of the oxidized and total PCE lines were much greater than the dissolved PCE line was originally. This indicates that mass-transfer from the DNAPL had been enhanced by the presence of oxidant. Chemical oxidation using permanganate showed potentially significant enhancement of mass transfer from a DNAPL source, even in the presence of non-productive oxidant demand.

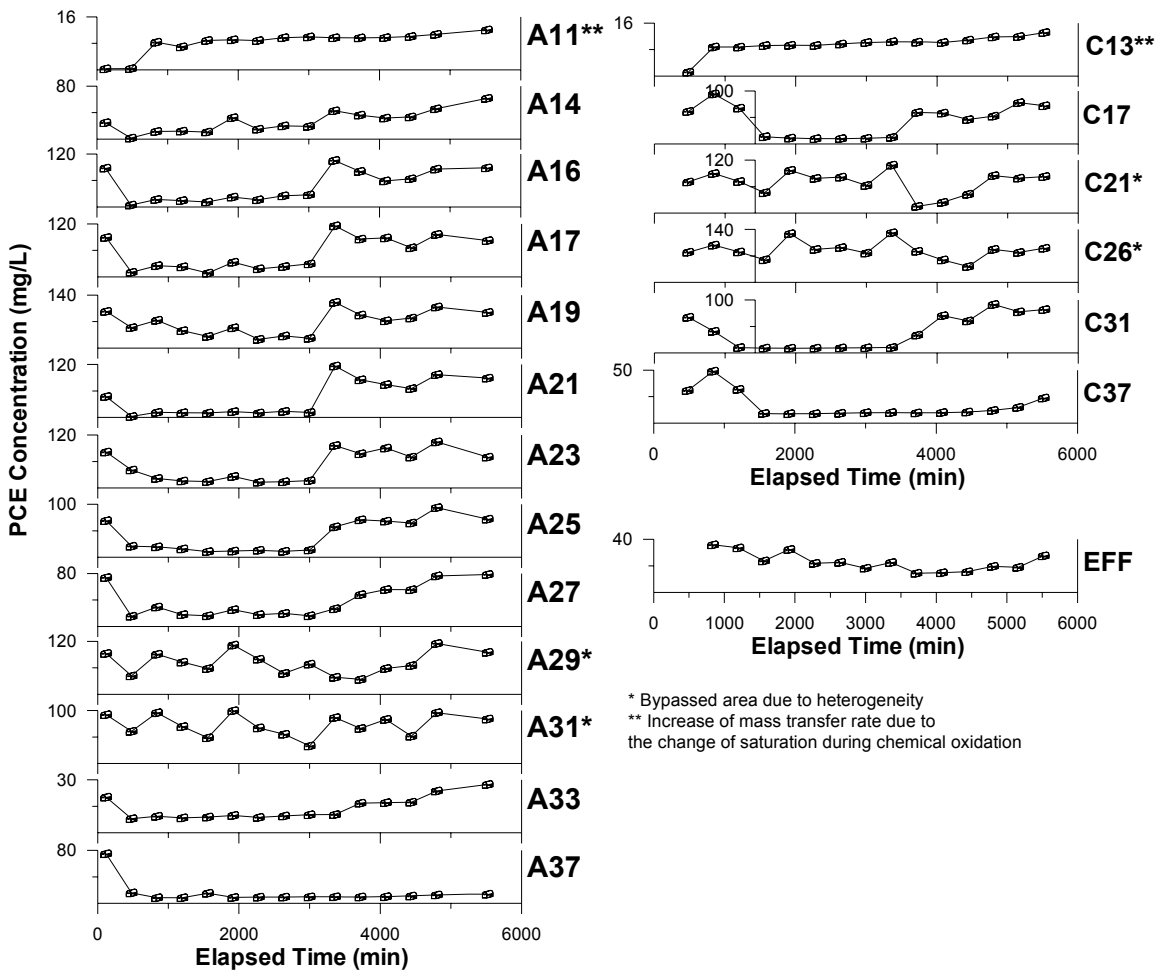


Figure A1.17. PCE Concentration During Chemical Oxidation Experiment.

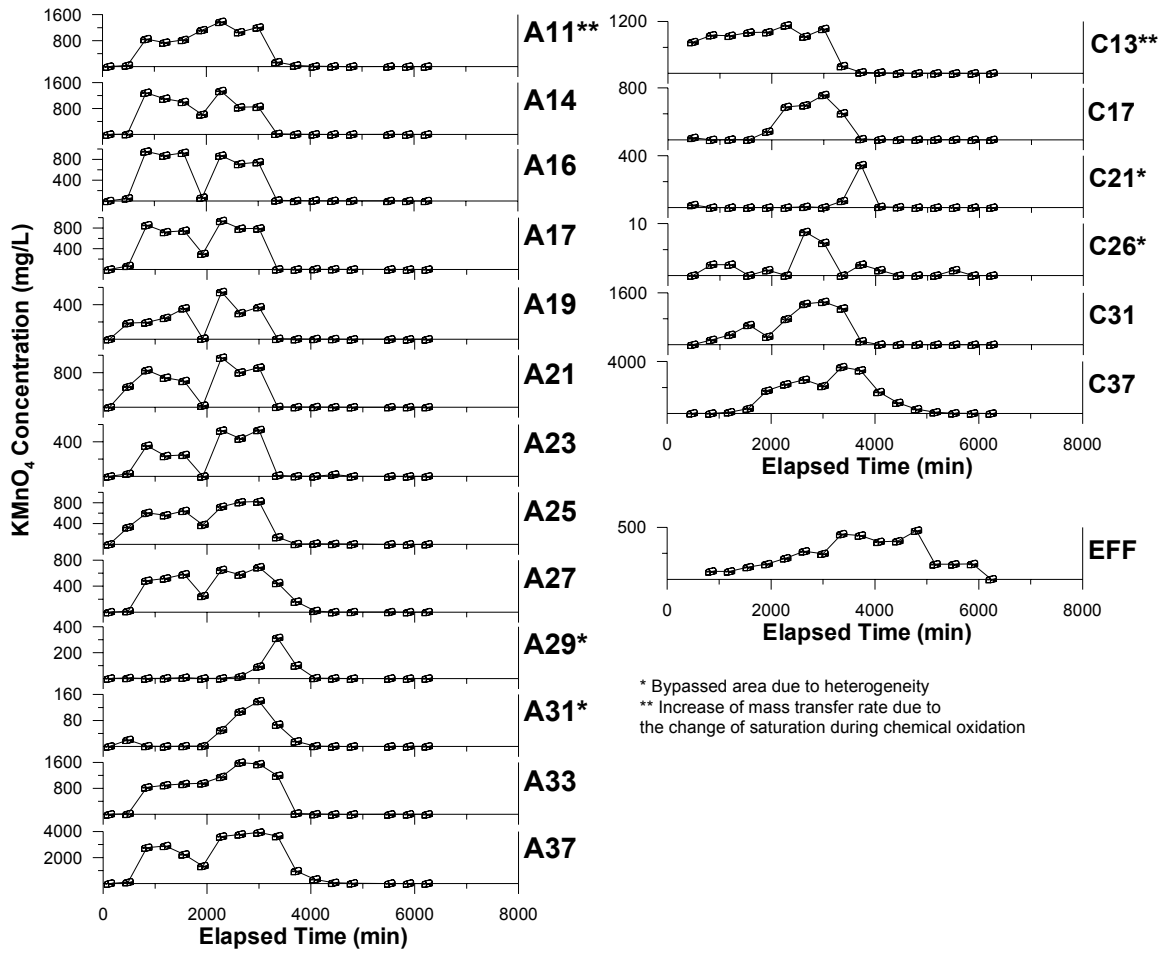


Figure A1.18. Permanganate Concentration during Chemical Oxidation Experiment

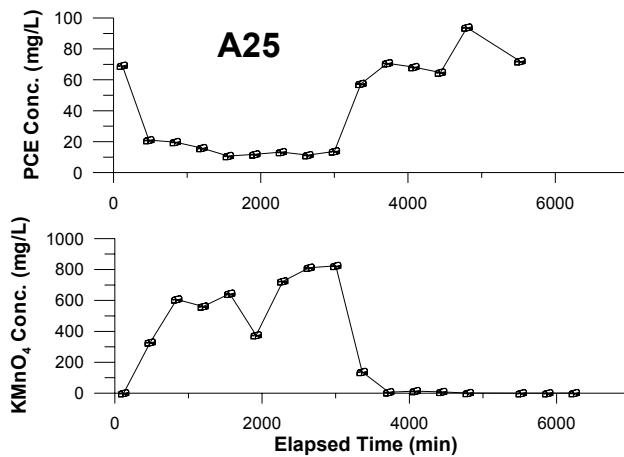


Figure A1.19. Comparison of PCE and KMnO_4 Concentration at Sample Port A25 during Chemical Oxidation Experiment

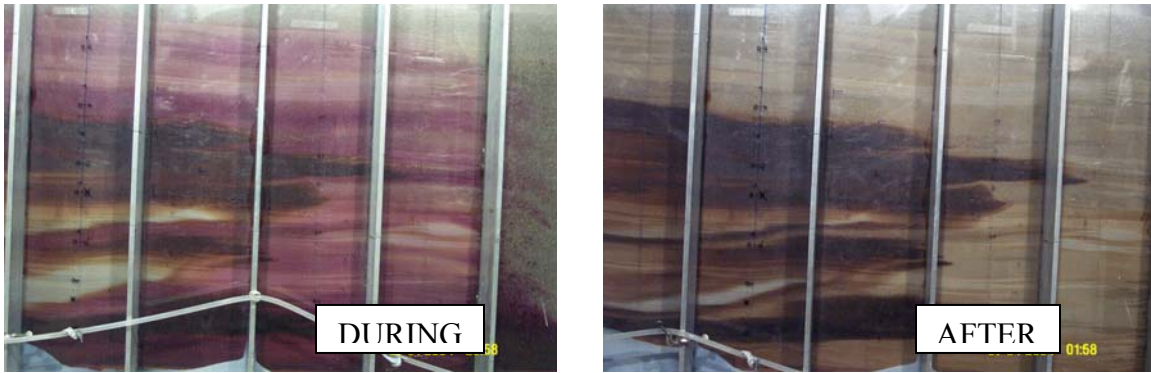


Figure A1.26. Source Zone During and After Chemical Oxidation Experiment

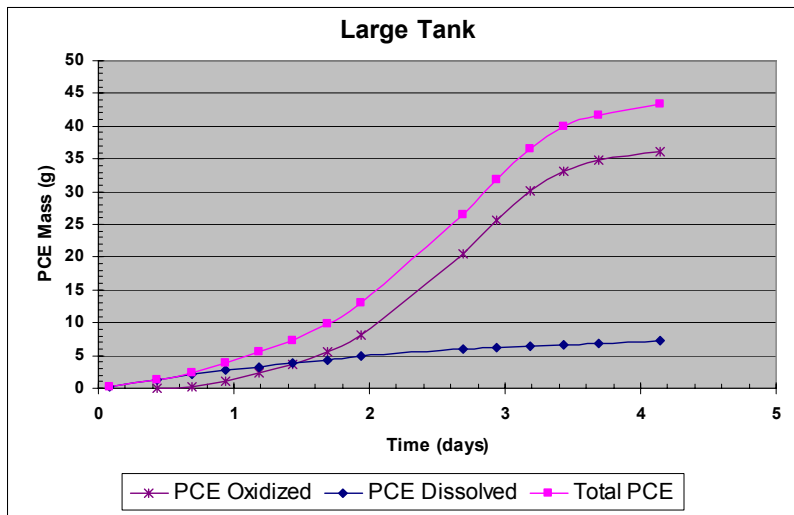


Figure A1.20. Cumulative PCE Mass Removed from Large Tank with High Heterogeneity

Appendix 2 – Large Tank Experiments with Low Heterogeneity

A2.1 Introduction

This chapter discusses the second set of large tank experiments. These experiments were conducted in a tank that was packed to represent a test aquifer with a low degree of heterogeneity (variance of $\log K = 0.25$). Investigations focused on DNAPL source remediation by surfactant enhanced dissolution and in situ chemical oxidation. The experiments generated a large amount of data including tracer and solute concentration data collected for 4 to 5 days, at 2 hour intervals during natural dissolution. Natural dissolution was monitored after the initial DNAPL spill and after surfactant flushing. Multiple tracer tests were performed both before and after remediation.

A2.2 Packing and initial scanning

At the end of the large tank experiments with high heterogeneity (Appendix 1), the tank was emptied of sand, water and DNAPL. Following repairs and reassembly, Experiments with low heterogeneity were initiated. Figure A2.1 shows the schematic of tank setup, locations of arrays and sampling ports.

Random heterogeneous hydraulic-conductivity fields were generated using the turning bands algorithm, resulting in continuous distributions of $\ln K$ (log-normally distributed). The parameters used in this design were: (1) mean of $\ln K$ (K in m/day) 4.18, (2) variance of 0.25, (3) horizontal correlation length of 0.5 m and (4) vertical correlation length of 0.05 m. These statistics produced an anisotropy ratio of 10. Multiple random field realizations were generated using these design parameters and one realization was selected for packing. The continuously distributed K field was discretized into five sands (#16, #30, #50, #70, and #140) where the theoretical $\ln K$ and variance $\sigma_{\ln K}^2$ values were preserved. The chosen configuration included zones within the target source area for DNAPL injection that were likely to produce a complex entrapment morphology while minimizing the possibility of vertical DNAPL migration to the bottom of the tank.

The tank was filled using the same procedure as described for large tank experiments with high heterogeneity (Appendix 1). The tank was packed using five different-sized sands for heterogeneous zone. The upstream part of the source zone was packed homogeneously with sand #8. The injection array was in the center of a homogeneous section to facilitate mixing and uniform vertical distribution through 32 ports. Six pairs of array for head monitoring and sampling, and one array for injection of tracer and treating reagents were installed. Each array had 40 ports every inch.

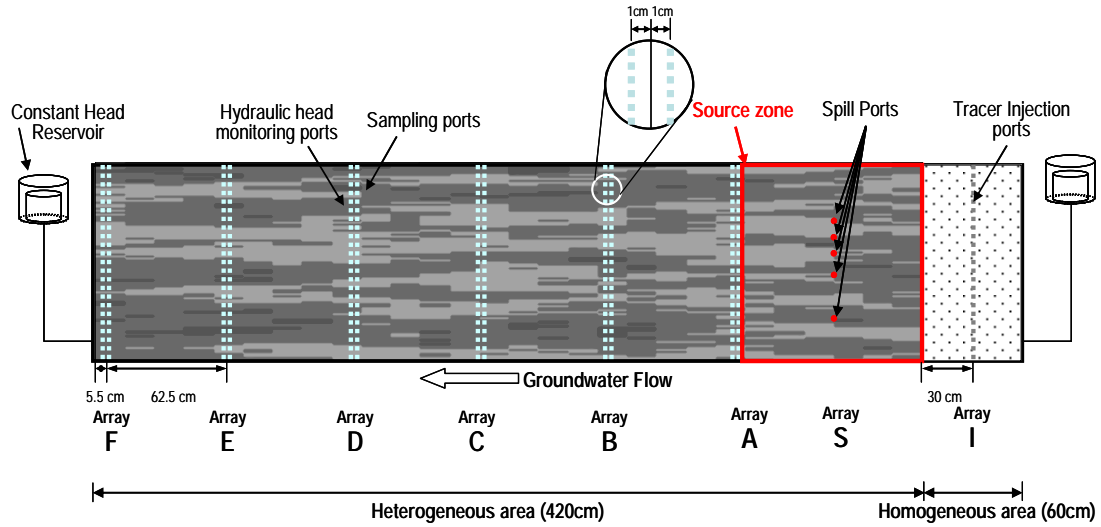


Figure A2.1. Design for Experimental Tank Showing Heterogeneous Packing, Constant Head Devices, Head Monitoring Ports, and Sampling Ports

Gamma-ray attenuation system was used to scan the source zone prior to and after PCE spill. The difference in gamma-ray intensity (i.e. photons counted) was used to quantitatively evaluate DNAPL saturation distribution.

A2.3 Flow and transport characterization

Hydraulic heads were monitored at 48 locations using automatic pressure transducer. The monitoring locations are listed in Table A2.1. The tank included influent and effluent end wells connected to constant head reservoirs to maintain a specified hydraulic gradient through the tank. Head and flow measurements were measured for a hydraulic head difference of 10cm, 8cm, 5.7 cm, and 3cm. The flow through the experiment showed a steady flow rate of 77.77 ml/min, 58.75 ml/min, 38.06 ml/min, and 17.73 ml/min respectively for head drops of 10cm, 8cm, 5.7 cm, and 3cm. Figure A2.1 shows head measurements during experiment for a head drop of 10 cm.

Table A2.1. Summary of Head Monitoring Locations.

| Vertical Distance from Top of Tank (in) | | | | | | | |
|---|-----------------|-------------------------------|-------------------------|-------------------------|--------------------------|-------------------------|--------------------------|
| Injection Array | Source Array | Array A | Array B | Array C | Array D | Array E | Array F |
| 5, 10, 15 20, 25, 30 35 | 4, 12, 15 23 | 6, 12, 14 16, 18, 26 35 | 7, 10, 14 18, 23, 33 | 7, 12, 16 23, 29, 35 | 12, 15, 21 28, 35, 38 | 8, 16, 21 28, 32, 35 | 10, 14, 16 23, 27, 32 |

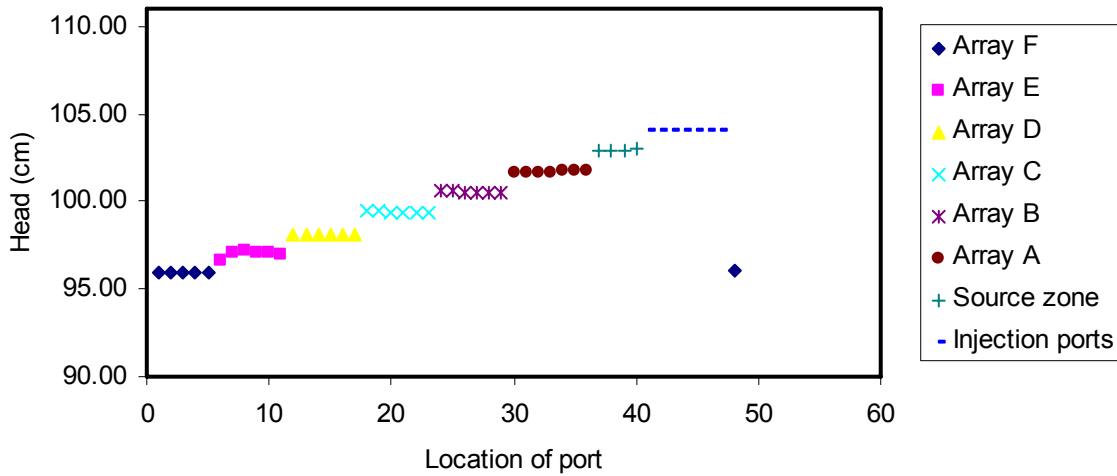


Figure A2.2 Head Measurements for a Head Drop of 10 cm

(b) A2.4 PCE spill, gamma scanning, natural dissolution, and pre-surfactant multiple tracer test

Analytical grade PCE (>99% purity), colored with 0.01% of Sudan IV hydrophobic organic red dye was used as the DNAPL. A total of 284.1 ml of PCE was injected in the source zone through four ports. The amounts injected into each port are listed in Table A2.2. PCE was injected under constant head of PCE using a Mariotte bottle. Figure A2.3 shows the location and final distribution of the NAPL in the tank.

Table A2.2. Volume of PCE Injected into each Injection Port

| Source/Port | Volume (ml) |
|-------------|-------------|
| 1/4 | 61 |
| 2/13 | 103.1 |
| 3/17 | 60 |
| 4/14 | 60 |
| Total | 284.10 |



Figure A2.3. Spill Device, Location, and Final NAPL Distribution

A2.4.1 Gamma-ray scanning

The gamma attenuation system was used to scan the PCE entrapment zone after the spill was completed and static condition had been achieved. The gamma system took approximately 8 days to complete the scan and the saturation distribution from the signal is illustrated in Figure A.2.3. The result was comparable to visual observation. Mass balance was approximately 85 percent.

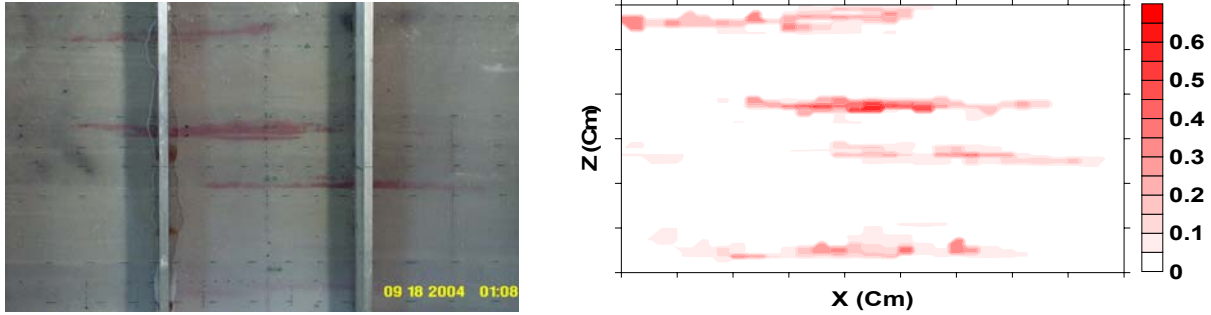


Figure A2.3. PCE Saturation Distribution Obtained from Gamma Attenuation System and Photograph of the Source Zone

A2.4.2 Natural Dissolution

Once the static PCE entrapment architecture had been established, three different hydraulic gradients were applied to the test tank and the concentration of PCE was monitored at different locations. Aqueous samples were taken at every other port (in the vertical direction) for three arrays (A, C, and E) and the PCE concentrations were determined by gas chromatography. Figure A2.4 shows the distribution of PCE concentration in the vertical direction for three different head drops.

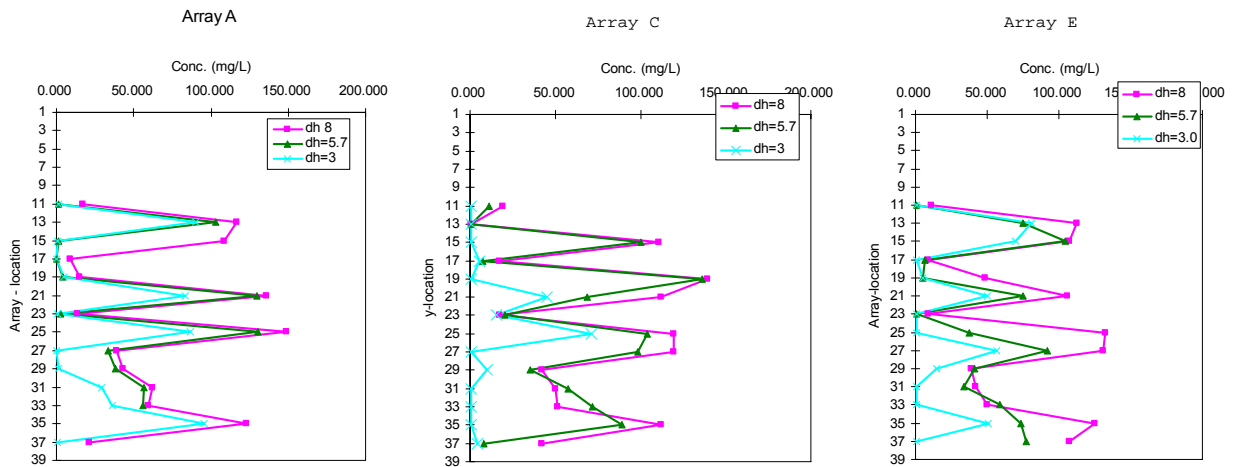


Figure A2.4. PCE Concentration Distribution in the Test Tank in Arrays A, C and E

A2.4.3 Pre-surfactant multiple tracer test

Since the results from tracer tests in the high heterogeneity tank showed that there was no background retardation of any of the tracers in the system, the background tracer test was not conducted before DNAPL injection.

A multiple tracer test was performed after the source zone was created and scanned. The test was performed in conjunction with monitoring for natural dissolution. Because this tracer test evaluated conditions prior to surfactant remediation the test was called the pre-surfactant PITT. Table A2.3 provides a summary of pre-surfactant PITT. Samples were taken at an interval of 2hrs for first 40hrs and 4hrs interval in the rest of the experiment. Total duration of the experiment was 80 hours. The samples collected were analyzed by gas chromatography and ion chromatography for tracer concentrations.

Table A2.3. Summary of Pre-Surfactant PITT

| Parameters | Experiment 2 |
|-------------------------------------|--|
| Tracers used | Bromide, DMP, HEX |
| Duration of injection | 11 hrs |
| Head difference | 8 cm |
| Injection rate | 32 ports @ 0.25 ml/min |
| Sampling ports | A11, A13, A15, A17, A19, A21, A23, A25, A27, A29, A31, A33, A35, A37 C11, C13, C15, C17, C19, C21, C23, C25, C27, C29, C31, C33, C35, C37 |
| Initial tracer concentration (mg/l) | Br = 605.2, DMP= 905.4, and HEX= 770.1 |

Figure A2.5 shows the breakthrough curves collected at array A. Curves for all sample locations show some retardation by the partitioning tracers. Differences in tailing observed in A13, A21, A25, and A35 indicated that DNAPL was not distributed uniformly. The saturation distribution of the source zone was evaluated using method of moments. Table A2.4 and Figure A2.6 show the actual saturation measured by gamma scanning and the saturation obtained from method of moments. These show the method of moments over and under estimate at some locations. As lateral distance of the observation well from the source zone increased, retardation values became smaller (Figure A2.7). This occurred because the tracer signal attenuated by mixing and calculated saturation was based on an increasingly large swept volume. This figure shows the importance of well location in the design of the PITT.

Table A2.4. Saturation of PCE Using Method of Moments at Array A and C

| Location | Actual | DMP | HEX | Location | DMP |
|----------|----------|----------|----------|----------|-----------|
| A11 | 2.45E-02 | 3.14E-03 | 2.19E-02 | C11 | -1.13E-04 |
| A13 | 1.00E-01 | 9.77E-03 | 5.45E-02 | C13 | 1.89E-03 |
| A15 | 3.56E-02 | 3.32E-04 | 4.48E-02 | C15 | 5.79E-03 |
| A17 | 2.00E-03 | 1.01E-03 | 5.17E-02 | C17 | -5.79E-04 |
| A19 | 7.00E-03 | 5.48E-03 | 1.03E-01 | C19 | 7.31E-03 |
| A21 | 1.59E-01 | 4.12E-02 | 5.19E-02 | C21 | 5.08E-03 |
| A23 | 1.44E-02 | 5.47E-03 | 0.00E+00 | C23 | 1.04E-03 |
| A25 | 3.67E-02 | 1.67E-02 | 6.52E-02 | C25 | 3.45E-03 |
| A27 | 5.19E-02 | 2.83E-03 | 6.35E-02 | C27 | 6.18E-03 |
| A29 | 5.90E-03 | 3.85E-03 | 6.98E-02 | C29 | 6.63E-04 |
| A31 | 1.72E-03 | 4.59E-03 | 8.84E-02 | C31 | 6.69E-04 |
| A33 | 7.22E-02 | 7.02E-03 | 1.08E-01 | C33 | 1.26E-03 |
| A35 | 1.10E-02 | 2.75E-02 | 4.43E-02 | C35 | 9.35E-03 |
| A37 | 0.00E+00 | 1.49E-03 | 1.47E-02 | C37 | 4.56E-03 |

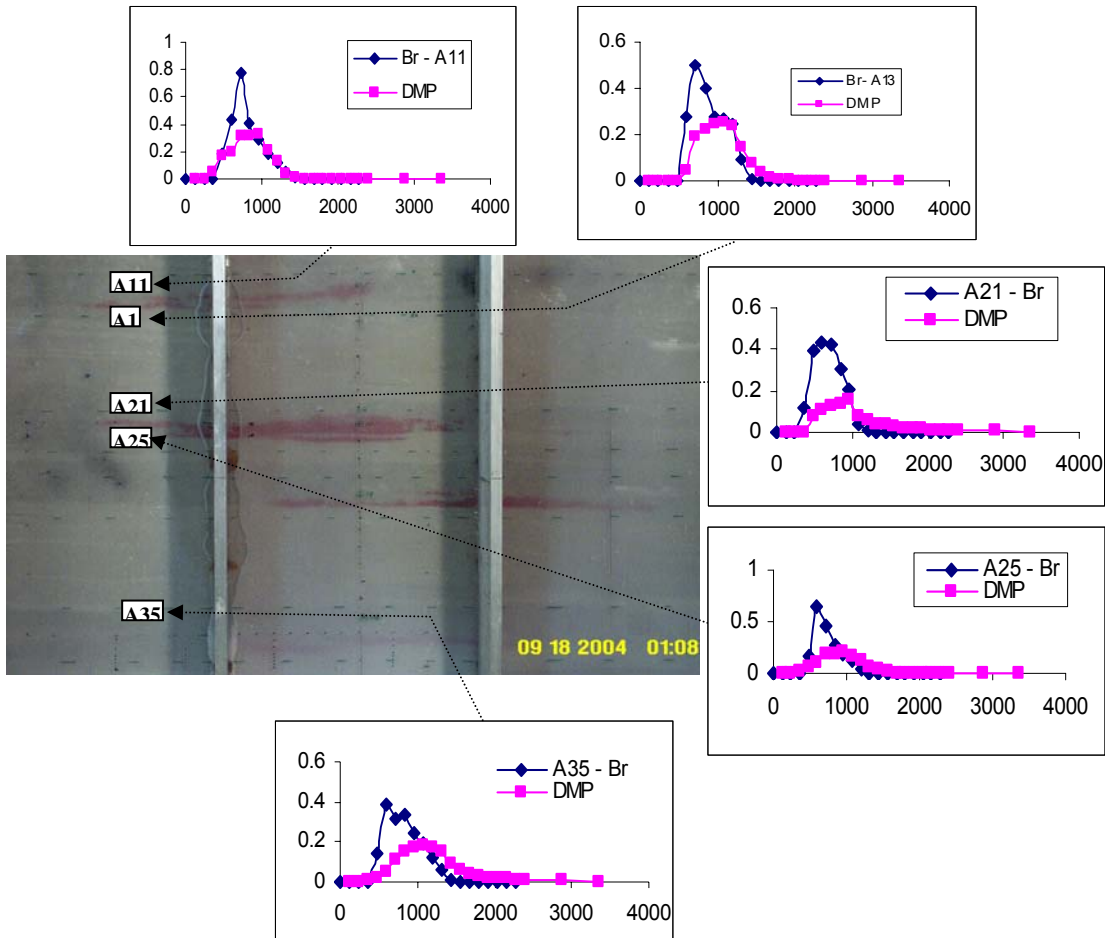


Figure A2.5. Breakthrough Curves Collected at Array A

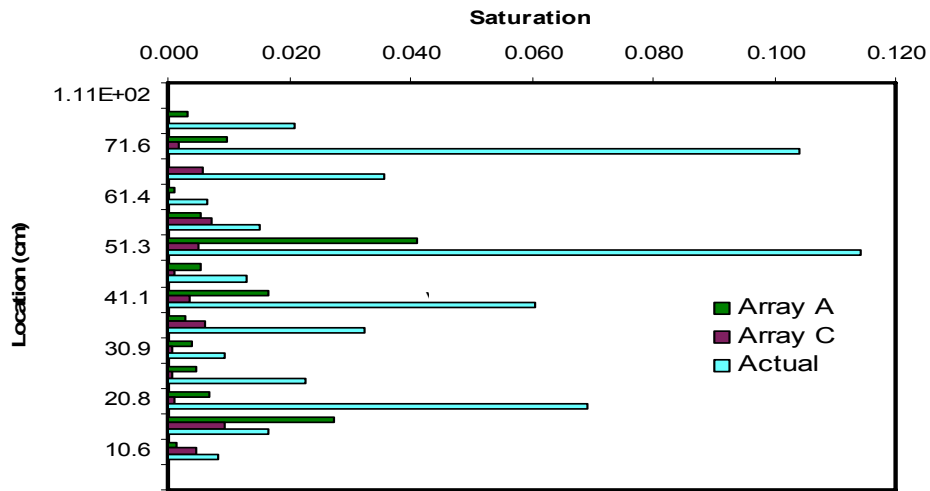


Figure A2.6. Actual Saturation Obtained from Gamma and Saturation by Method of Moments at Different Locations

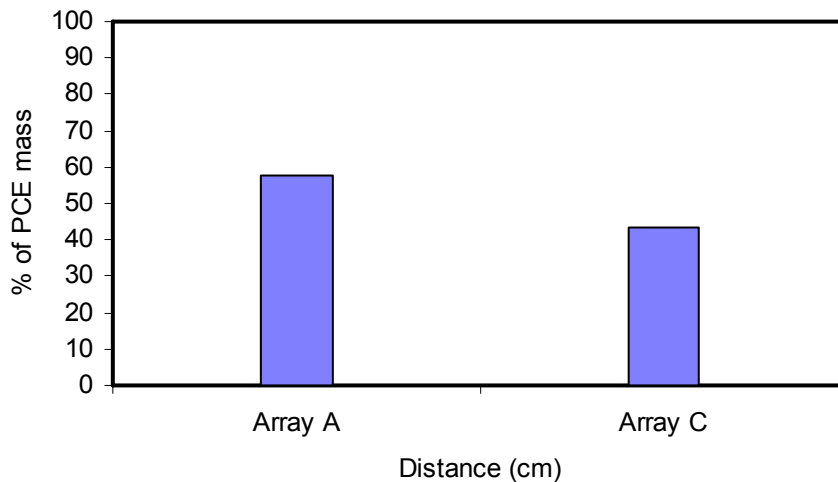


Figure A2.7. Percentage PCE Mass Identified at Different Locations

A2.5 Surfactant enhanced remediation and dissolution

Once the multiple tracer tests were finished, surfactant flushing was performed by flushing 50.0 g/L Tween-80 through the tank, 57.0 ml/min for 11.75hrs through the injection

ports. Aqueous samples were taken at every two hours at arrays A, C, and at effluent. The plume concentration was monitored for four consecutive days. Figure A2.8 shows breakthrough curves of PCE concentration for monitored ports at arrays A, C, and at the tank effluent. The peak concentration of PCE is as high as 7000 mg/l which is much larger than the aqueous solubility under natural conditions ($C_s = 200$ mg/L). The injected surfactants removed approximately 5 percent of PCE mass entrapped in the residually saturated zone (based on both visual observation and gamma scan). No remobilization of PCE mass in the source zone during surfactant flushing was observed. PCE concentrations at the effluent after surfactant flushing reached slightly higher steady state concentrations compared with concentrations before SEAR. This steady state concentration was below solubility.

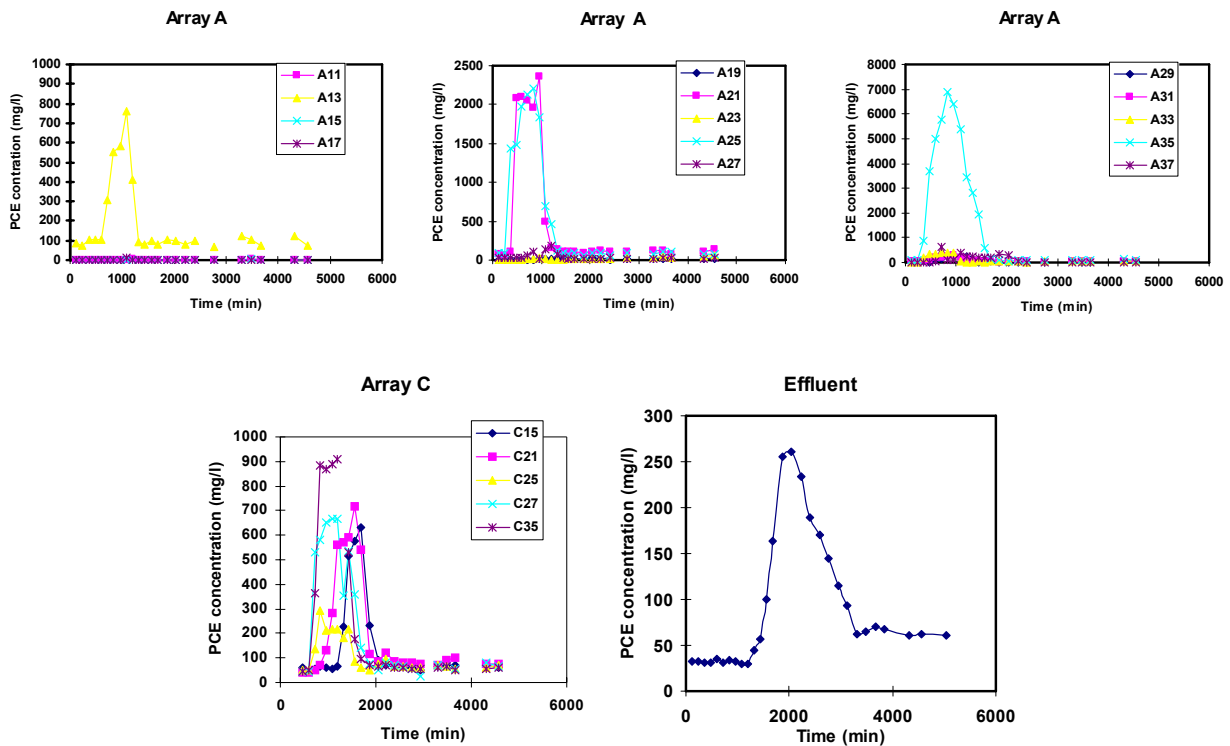


Figure A2.8. Breakthrough Curves Obtained from Surfactant-Enhanced Dissolution Experiment for Arrays A and C and at the Tank Effluent

Once the surfactant enhanced remediation observations were finished, post-remediation dissolution was conducted in the tank for three values of head difference (3.0cm, 5.7 cm and 8cm). Figure A2.9 shows the PCE concentration distribution at array A measured before and after the SEAR. This figure also shows the vertical PCE concentration at array A during enhanced dissolution.

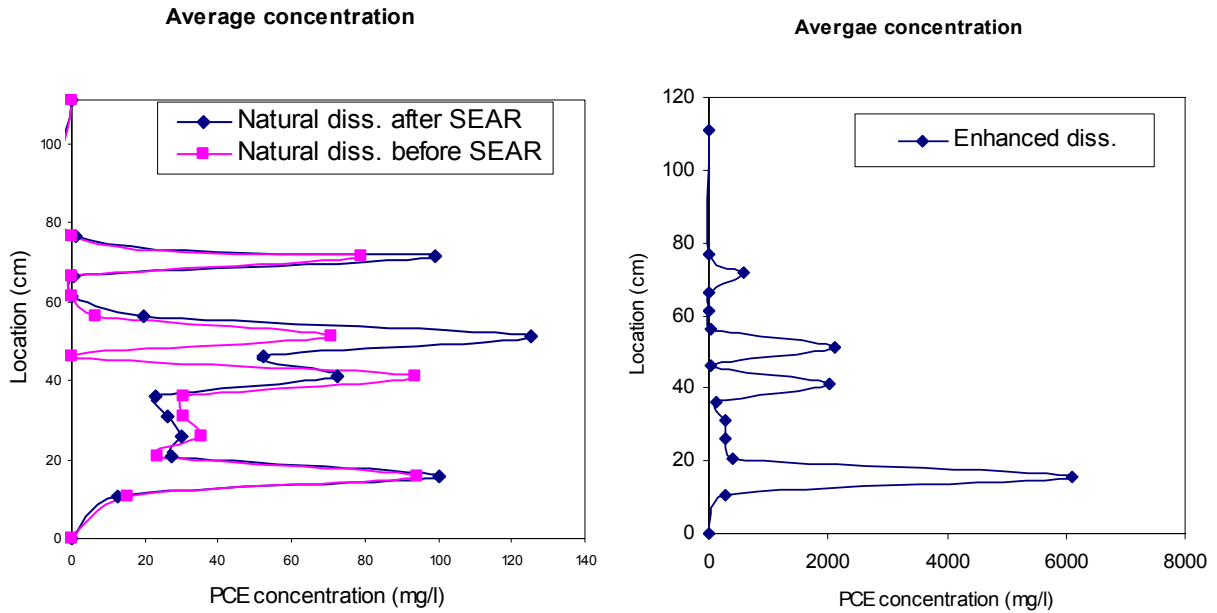


Figure A2.9. Vertical Profile of PCE Concentration at Array A Measured before, during and after Surfactant Flushing

A2.6 Gamma Scanning and Post-Surfactant Multiple Tracer Test

Once surfactant remediation and subsequent dissolution monitoring were complete, the source zone was scanned by gamma attenuation methods to determine the new architecture of the source zone. Figure A2.10 compares the visual observation with results of the gamma scanning. At some locations residual PCE was present. However, most of the PCE remained as pools.

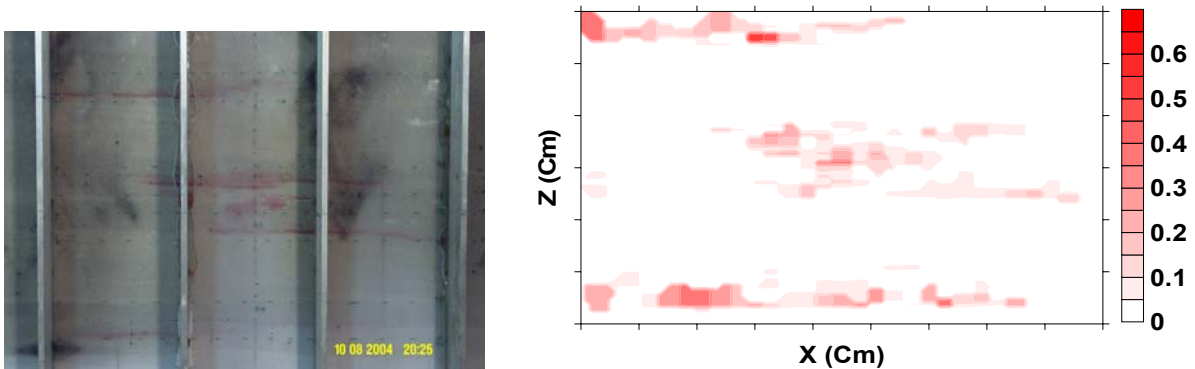


Figure A2.10. Final Distribution of PCE and Contours Obtained from Gamma Data after SEAR

A PITT also was conducted with the same design parameters as used in the pre-surfactant PITT. Figure A2.11 shows the DMP and bromide breakthrough curves obtained during the experiment. After qualitative analysis of the breakthrough curves, arrival times of all the tracers were calculated using numerical integration. The difference between saturation obtained after remediation (PITT 2) and saturation obtained prior to remediation (PITT 1) should hypothetically represent the PCE removed by the SEAR technology. Figure A2.12 represents saturation results from both tests. On first inspection, array A shows a relevant decrease on saturation in the portions of the source zone. However, as it can be observed in the pictures there is a considerable amount of PCE remaining in those portions where PITT showed a decrease in saturation.

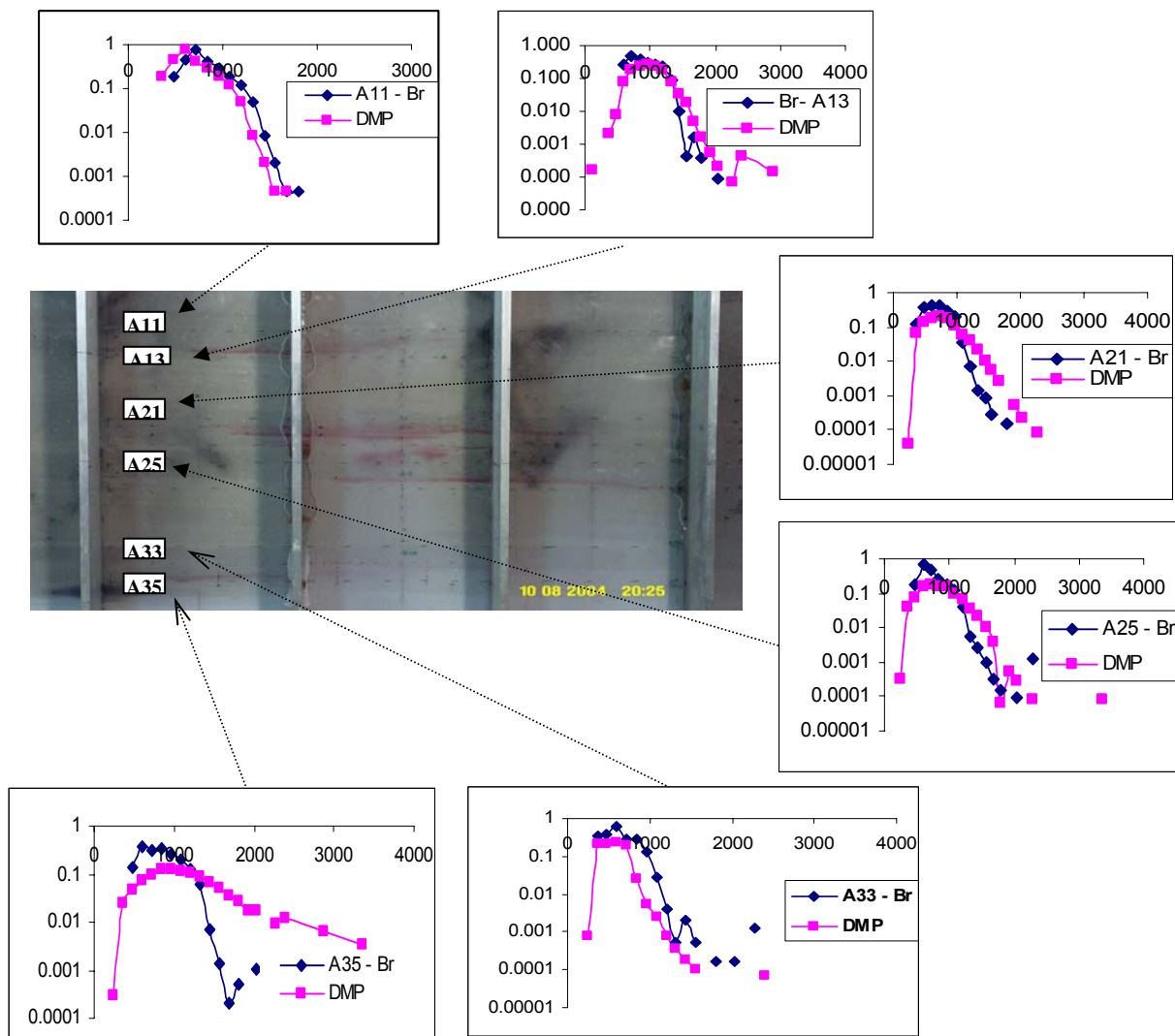


Figure A2-11: Breakthrough Curves Collected at Array A after Surfactant Flushing

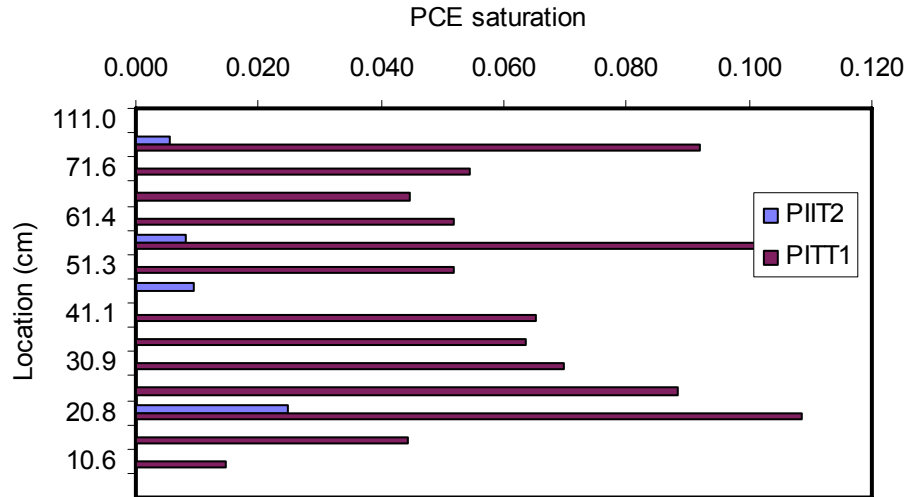


Figure A2.12. Saturation Estimated by PITT prior to SEAR (PITT1) and after SEAR (PITT2)

(i)

(ii)A2.7 Chemical oxidation in large tanks

A chemical oxidation experiment was conducted in the large tank with low heterogeneity. This experiment was the last one completed in the tank before sand, water and DNAPL were removed and the tank was reconditioned. A detailed description of this experiment is provided in section 3.6.3 of this report.

Appendix 3 – Large Tank Experiments with Multiple Hydrogeologic Units

A3.1 Introduction

The first two sets of large-tank experiments were conducted in tanks packed to represent test aquifers with high and low degrees of soil heterogeneity (variance of $\log K = 1.22$ and 0.25 , respectively). In those experiments, data needed to study surfactant enhanced dissolution and in situ chemical oxidation were generated. The final packing of the large tank was designed to support experiments involving bioremediation and thermal treatment. In order to accommodate the different research needs of these technologies, and to focus more closely on mass transfer characteristics of DNAPL entrapped at specified saturations, the large tank was packed with three hydraulically isolated hydrogeologic units. Each unit was packed with two lenses of coarse-grained sand suitable for creating DNAPL sources of specified saturation. In two units, the downgradient section of the tank was packed as homogeneous porous media. In the third unit, the downgradient section was packed as a randomly heterogeneous porous medium.

A3.2 Packing

The final set of large-tank experiments was conducted using the same tank assembly that was used in previous experiments (Appendices 1 and 2). Three confined aquifer units (upper, middle, and lower aquifer) were packed in a tank (Figure A3.1a). Aquifers were hydraulically isolated by confining unit of very low hydraulic conductivity. The confining units consisted of overlying layers of #140 sand, a continuous Teflon sheet, clay, another Teflon sheet, and #140 sand. Each aquifer has two source zones which are created with elliptical lenses of #16 and #30 sand. The lens of #30 sand was placed in the lower part of each aquifer unit and the lens of #16 sand was placed in the upper part in each aquifer unit.

Downgradient of the source zones, the upper aquifer was packed with a heterogeneous hydraulic-conductivity field (Figure A3.1b). Homogeneous fields of #70 sand were packed within the lower two aquifers downgradient of the source zone. In all three aquifers, #70 sand was packed around source zone lenses and #8 sand is packed in upstream portion of the tank. Statistical properties of the heterogeneous portion of the upper aquifer were average $\ln(K)$ of 4.18 and variance $\ln(K)$ of 1.22. Twenty-two columns and 33 layers composed of 5 different sands (#16, #30, #50, #70, #110) were used to pack the heterogeneous portion of the tank. All sands are wet-packed using the techniques described previously for large tank experiments (Appendix 1). Sampling arrays also were identical to those used in previous large tank experiments.

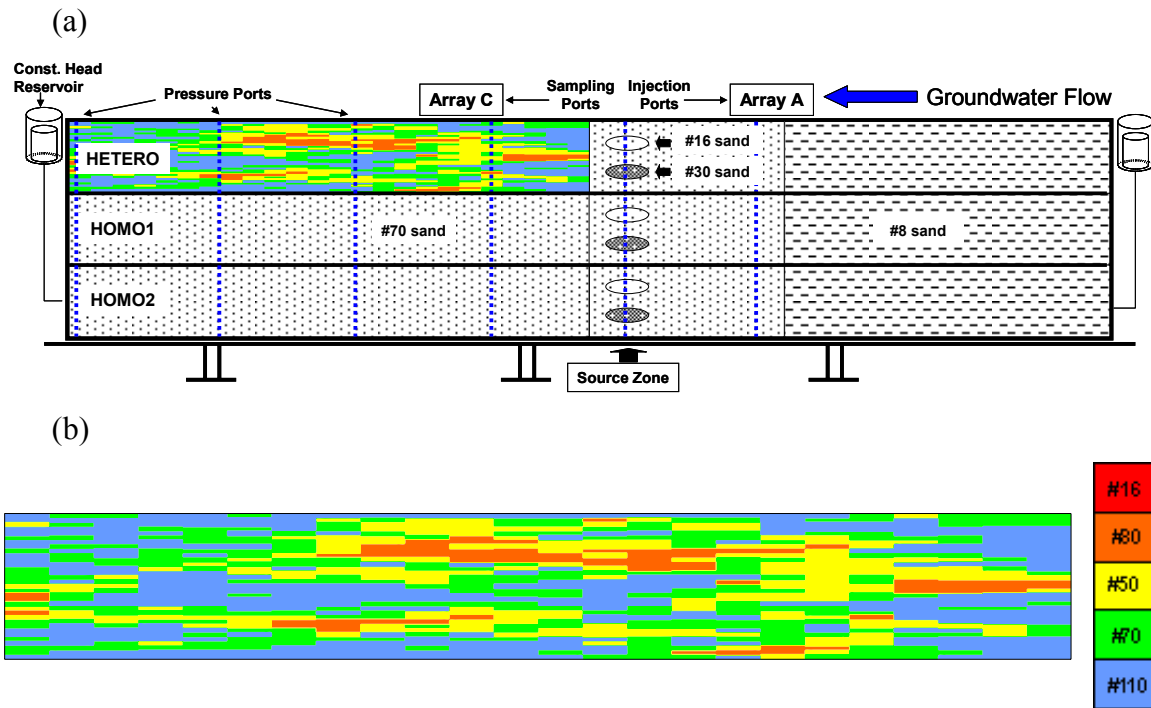


Figure A3.1. Tank Assembly for the Third Set of Large-Tank Experiments (a) and Heterogeneous Distribution of Sands Used in the Upper Aquifer (b)

A3.3 Flow and transport characterization

After packing was completed, pressure head was monitored using 48-channel automated pressure transducer system. Head difference between both ends of the tank was maintained at 6 cm during monitoring.

A dye tracer test was conducted to monitor flowpaths that developed in response to selected tracer injection rate and to validate hydraulic isolation between aquifer units. Dye tracer tests also were useful to determine sampling locations during subsequent partitioning tracer tests. A divergent-convergent flow field was created within each aquifer by injecting upstream (Array A) and extracting downstream (Array C) of the planned source areas. Injection and withdrawal was by a multi-channel peristaltic pump. Pictures taken during the dye tracer test showed that there was no movement between aquifers (Figure A3.2). Photographs also showed that most of the injected tracers were captured by extraction ports even though flow rates differed among the aquifer units. Results of the dye tracer test were used to determine flow rates and sampling locations for subsequent tests.

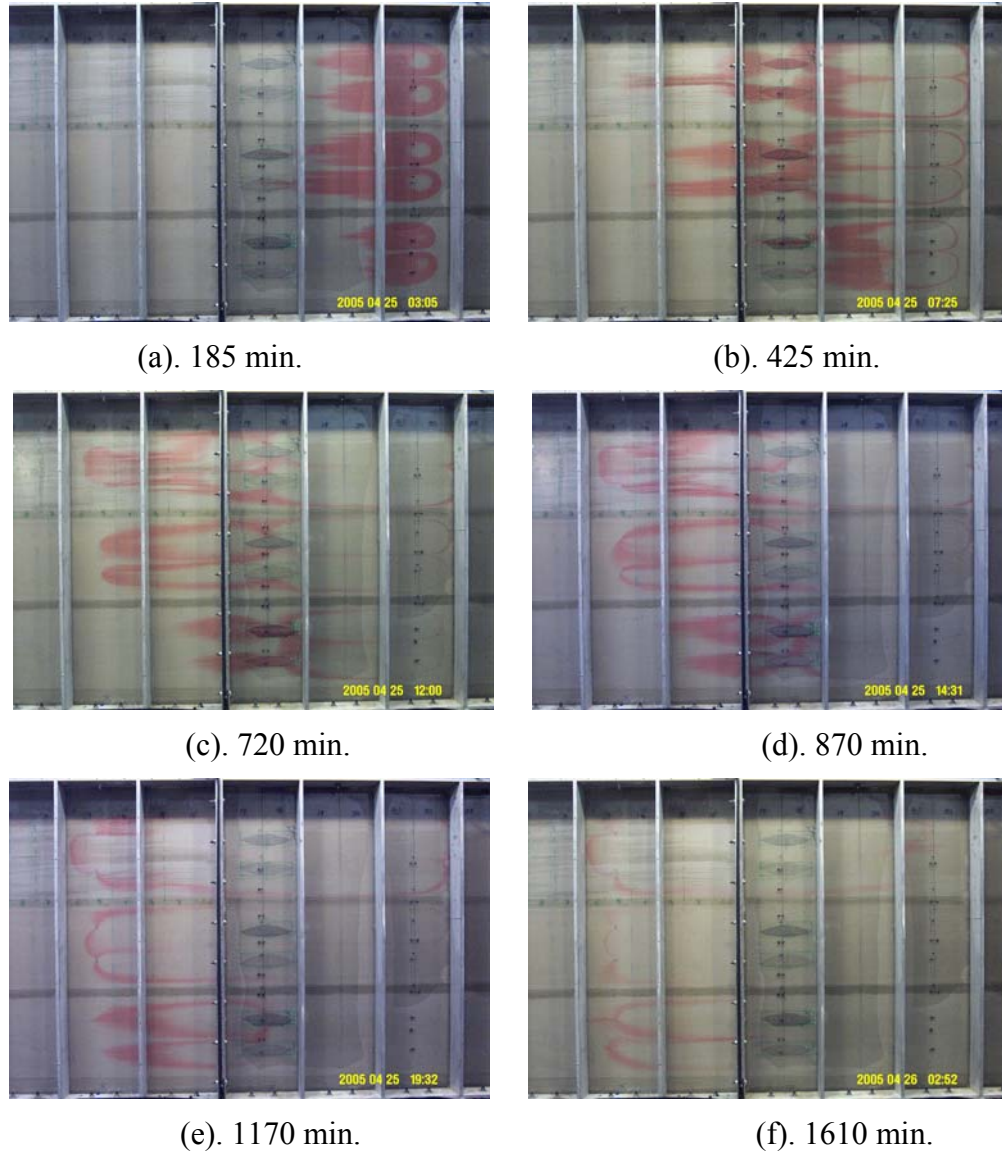


Figure A3.2. Photographs Taken during the Dye Tracer Test

A tracer test using partitioning and non-partitioning tracers was performed before injecting PCE-DNAPL to estimate solute transport parameters. Bromide and 2,4-Dimethyl-3-Pentanol (DMP) was used for non-partitioning and partitioning tracer, respectively. Generally, partitioning tracer tests are performed with several partitioning tracers having different values of partition coefficient. However, in this test, only one partitioning tracer ($K_{DMP}=28.96$) was used to save time and efforts in sample analysis. Partitioning tracer tests in previous tanks had shown that data obtained using DMP provided adequate partitioning for the estimation of saturation. The partitioning tracer test was conducted using the same divergent-convergent flow field as was used for the dye tracer test. Total injection rate for the three aquifers was 3.15 mL/min. Injection and extraction ports are listed in Table A3.1.

Table A3.1. Injection and Extraction Ports for Partitioning Tracer Tests

| Layer | Source Lens and Sand Type | Injection Ports | Extraction Ports |
|---------------|---------------------------|-----------------|------------------|
| Heterogeneous | HE-#16 | A2 | C3 |
| | HE-#30 | A7 | C7 |
| Homogeneous_1 | HO1-#16 | A16 | C16 |
| | HO1-#30 | A21 | C21 |
| Homogeneous_2 | HO2-#16 | A30 | C30 |
| | HO2-#30 | A35 | C35 |

A3.4 PCE-DNAPL injection

PCE was injected into source zone lenses using a Mariotte bottle under constant head while pictures were automatically taken for visual monitoring. Injected mass was monitored quantitatively using a digital scale controlled by computer. PCE was dyed with SUDAN IV at a concentration of 0.01 percent. PCE was injected near the top of the each lens until saturation in the lens was very large. After injection, PCE was withdrawn to make a source zone of a specified average saturation. Source zones in the heterogeneous and homogeneous_1 aquifers had similar net amounts of injected PCE (80.45 ± 0.26 g). Net amounts of injected PCE in the lower homogeneous_2 aquifer varied with source zones HO2-#16 and HO2-#30 containing 120.1 g and 120.5 g, respectively. The intent of this injection pattern was to create source zones in the heterogeneous and homogeneous_1 aquifers having similar values of residual-to-pool ratio (RP ratio) but with different type of downstream porous media while source zones in the two homogeneous aquifers had different RP ratios but the same type of downstream porous media.

A3.5 Gamma attenuation scanning

Source zones were scanned using the gamma-ray attenuation system before and after the injection of PCE to measure the saturation distribution of PCE. Gamma attenuation data scanned before the injection of PCE were used as background data for saturation calculations. Figure A3.3 shows that the visually observed distribution of PCE-DNAPL compared favorably with saturation distributions determined from gamma attenuation data.

The saturation distribution measured after conducting a partitioning tracer test (PITT1) also is shown in Figure A3.3. Comparison of saturation distributions before and after PITT1 suggested that enhanced dissolution of PCE may have occurred during the test. The high flow velocity and tracer concentration used in the test appeared to dissolve PCE rapidly from areas at residual saturation. Dissolution also appeared to occur first at the upstream edge of the source zones.

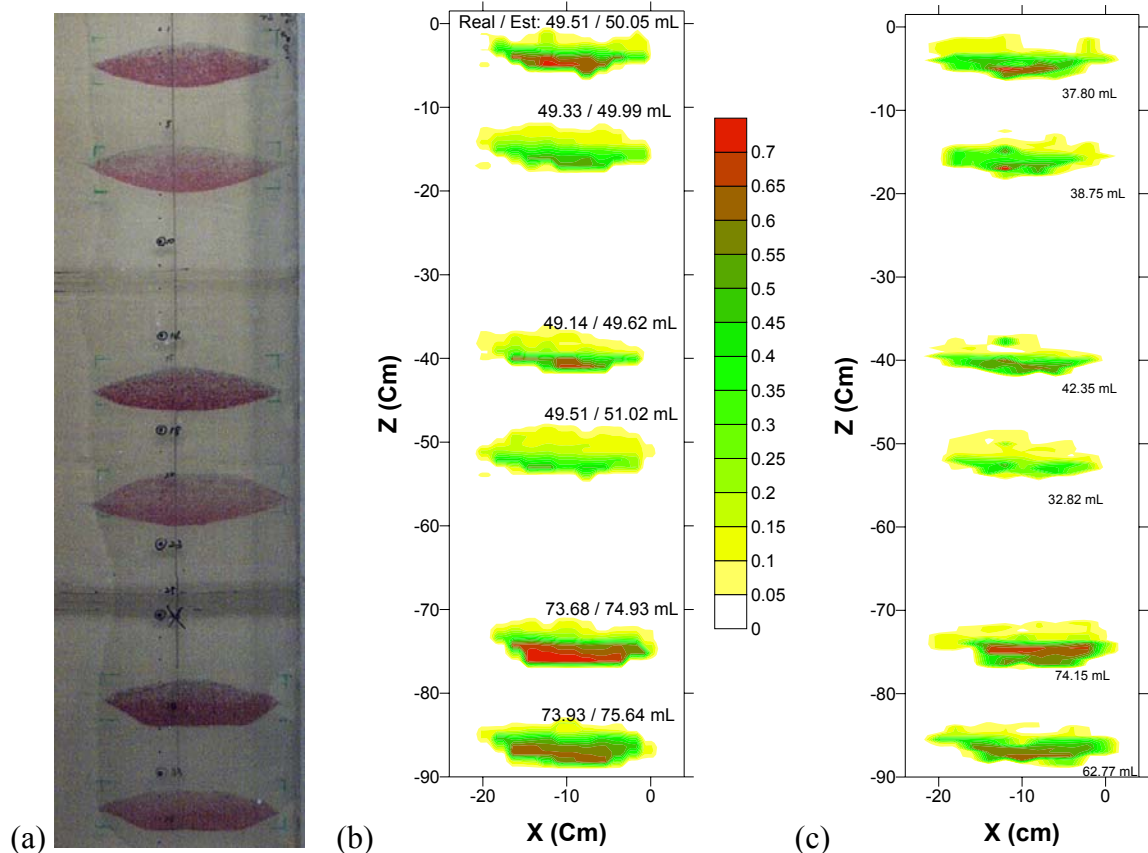


Figure A3.3. Visual Distribution of PCE in Source Zones (a), and Saturation Distribution Determined from Gamma Attenuation Scans after DNAPL Spill (b) and after PITT1(c)

A3.6 Partitioning tracer tests

A dipole partitioning tracer test with pulse injection was conducted after the PCE-DNAPL spill and gamma scanning. This test was labeled as PITT1. Bromide and DMP with concentration of 250 mg/L were used as non-partitioning and partitioning tracers. Injection and extraction ports and pumping rate were the same as those used in dye tracer tests. Samples were collected at a large number of sampling ports in order to refine the vertical profile of saturation.

Results of this tracer test were inconclusive. At most sampling ports, breakthrough curves for partitioning and non-partitioning tracers were very similar. This reflects the high injection rates used in the test. Because results were inconclusive, data are not shown in this report.

To find out the influence of dipole partitioning tracer test on redistribution or remobilization of PCE DNAPL, source zone was scanned again using gamma attenuation system after the dipole partitioning tracer test.

A dipole partitioning tracer test with injection over an extended time period was conducted. This test was labeled as PITT2. Bromide and DMP with concentration of 250 mg/L

were used as non-partitioning and partitioning tracer and injection and extraction rates of 1.05 ml/min were used. Injection continued until the concentration of tracer at monitoring ports downgradient of the source zones reaches injection concentration. Tracer solution was injected into the injection ports in Array A for 39 hours and 25 minutes. Following tracer injection, clean water injection continued until the concentration of tracer at the monitoring wells returned to background concentration.

A3.7 Source zone bioremediation experiments

An extensive series of source-zone bioremediation experiments was conducted in the middle unit of this large tank. A recycle flow system with injection upgradient and withdrawal downgradient of the source zones was used in these experiments. Detailed descriptions and results of the experiments are provided in section 3.7.3. Experiments included

1. A gamma scan to determine initial saturation distribution,
2. Development of redox conditions in the aquifer suitable for reductive dehalogenation,
3. Monitoring of pressure distribution and natural dissolution at a slow flow rate typical of field sites,
4. A gamma scan to determine changes in saturation after natural dissolution monitoring,
5. Inoculation of the source zones with KB-1, a mixed culture of microbes capable of reductive dehalogenation at high PCE concentrations,
6. Monitoring of bio-enhanced dissolution, and
7. A gamma scan to determine changes in saturation due to bioenhanced dissolution.

Appendix 4 – List of Publications

The following publications were prepared as a part of research described in this report.

Peer-Reviewed Journal Articles

1. Glover, K.C., and T.H. Illangasekare (2006) Biologically-enhanced mass transfer of tetrachloroethene from DNAPL pools: a dual-domain approach for upscaling model parameters, *Ground Water*, in preparation.
2. Glover, K.C., T.H. Illangasekare, and J. Munakata-Marr (2006) Biologically-enhanced mass transfer of tetrachloroethene from DNAPL pools: effect of biological activity on mass transfer rate coefficient, *J. Contam. Hydrol.*, in preparation.
3. Glover, K.C., J. Munakata-Marr, and T.H. Illangasekare (2006) Biologically-enhanced mass transfer of tetrachloroethene from DNAPL pools: experimental evaluation and influence of pool morphology, *Environ. Sci. Technol.*, re-submitted for publication with revisions.
4. Glover, K.C., J. Munakata-Marr and T.H. Illangasekare (2006) Biologically-enhanced mass transfer of tetrachloroethene from DNAPL pools: large tank experiments, *Bioremediation J.*, in preparation.
5. Heiderscheidt, J.L., M. Crimi, T.H. Illangasekare, R.L. Siegrist, and M.A. Singletary (2006) Optimization of full-scale permanganate ISCO system design: II. Numerical study to evaluate oxidant transport. *J. Environ. Engrg.*, in preparation.
6. Heiderscheidt, J.L., T.H. Illangasekare, and R.L. Siegrist (2006) Large-scale 2D experimental investigation of in situ chemical oxidation of complex DNAPL source zones in heterogeneous aquifer by permanganate. *Vadose Zone J.*, in preparation.
7. Heiderscheidt, J.L., T.H. Illangasekare, and R.L. Siegrist (2006) Chemical oxidation reactive transport in 3D (CORT3D) numerical model development and testing. *Water Resour. Res.*, in preparation.
8. Heiderscheidt, J.L., R.L. Siegrist, and T.H. Illangasekare (2006) Intermediate-scale 2D experimental investigation of in situ chemical oxidation of complex DNAPL source zones by permanganate. *Environ. Sci. Technol.*, in preparation.
9. Kaplan, A., and J. Munakata-Marr (2006) Biodegradation of Tetrachloroethene in Residual DNAPL Source Zones: Effects on Mass Transfer, in preparation.
10. Moreno-Barbero, E., and T.H. Illangasekare (2006) Simulation and performance assessment of partitioning tracer tests in heterogeneous aquifers. *Environ. Engrg. Geosci.*, XI(4), 395-404.

11. Moreno-Barbero, E., and T.H. Illangasekare (2006) Influence of dense nonaqueous phase liquid pool morphology on the performance of partitioning tracer tests: evaluation of the equilibrium assumption. *Water Resour. Res.* 2006, 42, W04408, doi:10.1029/2005WR004074.
12. Moreno-Barbero, E., S. Saenton, Y. Kim, and T.H. Illangasekare (2006) Influence of DNAPL source zone architecture on the performance of partitioning tracer tests: Intermediate scale investigation. *Vadose Zone Journal*, in review.
13. Page, J.W., K. Soga, K. and T.H. Illangasekare (2006) The significance of heterogeneity on mass flux from DNAPL source zones: an experimental investigation, *J. Cont. Hydrology*, in review.
14. Saenton, S., and T.H. Illangasekare (2006) Evaluation of the effect of partial removal of NAPL mass on plume concentrations: Experimental and numerical model investigations, *J. Contam. Hydrol.*, accepted for publication.
15. Saenton. S., and T.H. Illangasekare (2006) Up-scaling of mass transfer rate coefficient for the numerical simulation of DNAPL dissolution in heterogeneous aquifers. *Water Resour. Res.*, accepted for publication.
16. Saenton, S., T.H. Illangasekare, K. Soga, and T.A. Saba (2002) Effects of source zone heterogeneity on surfactant enhanced NAPL dissolution and resulting remediation endpoints. *Journal of Contaminant Hydrology*, 59(1-2): 27-44.
17. Soga, K., J.W.E. Page, and T.H. Illangasekare (2004) A review of NAPL source zone remediation efficiency and the mass flux approach, *J. of Hazardous Waste*, 110, 13-27.

MS/PhD Theses

1. Glover, K.C. (2006) Microbe-enhanced dissolution of non-aqueous phase tetrachloroethene in naturally heterogeneous subsurface source zones: a multiscale study, Ph.D. Thesis, Colorado School of Mines, Golden, Colorado, U.S.A., 297p.
2. Heiderscheidt, J.L. (2005) DNAPL source zone depletion during in situ chemical oxidation (ISCO): experimental and modeling studies, Ph.D. Thesis, Colorado School of Mines, Golden, Colorado, U.S.A., 295p.
3. Kaplan, A. (2004) The effects of chlorinated ethene biodegradation on mass transfer from DNAPL and alcohol tracer partitioning coefficients, M.S. Thesis, Colorado School of Mines, Golden, CO, 99p.
4. Kulasooriya, I.H. (2005) Remediation of dense non-aqueous phase liquids using surfactant flushing; mass flux approach, Ph.D. dissertation, University of Cambridge, Cambridge, England, 188p.
5. Moreno-Barbero E. (2005) Evaluation of the partition interwell tracer test and extension to determine DNAPL architecture in heterogeneous media, Ph.D. Thesis, Colorado School of Mines, Golden, Colorado, U.S.A., 218p.

6. Page, J.W.E. (2005) A mass flux and partitioning tracer concept for DNAPL source zone characterisation, Ph.D. dissertation, University of Cambridge, Cambridge, England, 199p.
7. Saenton, S. (2003) Prediction of mass flux from DNAPL source zone with complex entrapment architecture: model development, experimental validation, and up-scaling. Ph.D. Thesis. Colorado School of Mines, Golden, CO.

Conference/Symposium Proceedings

1. Gago, J., and T. Illangasekare (2006) Validation of isothermal Gilland-Sherwood type model under non-isothermal conditions, Proceedings of International Conference "MODFLOW and More 2006," Golden, CO, May 22-24, 2006, p. 584-588.
2. Glover, K.C., T.H. Illangasekare, and J. Munakata Marr (2006) Biologically enhanced mass transfer of PCE from DNAPL pools: influence of pool morphology on reactive transport processes, Proceedings of International Conference "MODFLOW and More 2006," Golden, CO, May 22-24, 2006, p. 195-199.
3. Heiderscheidt J.L., T.H. Illangasekare, R.L. Siegrist, M. Crimi (2004). Use of Chemical Oxidation to Reduce Rate-Limited Matrix Diffusion of PCE from Low Permeability Materials and Effects on Natural Oxidant Demand. The Third International Conference on Oxidation and Reduction Technologies for In Situ Treatment of Soil and Groundwater. Oct. 24-28. San Diego, California.
4. Illangasekare, T.H., and S. Saenton (2004) Application of stochastic methods in the study of fluid flow, solute transport, and multiphase fluid behavior in heterogeneous porous media. S. B. Weerakoon (Editor) In, Proceedings of the Tenth Asian Congress of Fluid Mechanics. University of Peradeniya, Sri Lanka, May 17–21, 2004.
5. Illangasekare, T.H., S. Saenton, D. Dai, and Q. Moore (2002) Modeling for determination of pre- and post-remediation prediction of dissolved contaminant concentration downstream of NAPL source zones. S.M. Hassanizadeh, R.J. Schotting, W.G. Gray, and G.F. Pinder (Editors). In, Proceedings of XIVth International Conference on Computational Methods in Water Resources (CMWR XIV), Vol. 1, pp. 843-850 (Developments in Water Science #47), June 23-28, 2002, Delft, The Netherlands.
6. Illangasekare, T.H., S. Saenton, Y.-C. Kim, K. Glover, J. Heiderscheidt, E. Moreno-Barbero, J. Munakata Marr, R. Siegrist, and K. Soga (2006) Pre and post-treatment mass flux emission for DNAPL source zones – modeling, up-scaling and characterization, Proceeding of KSEEG 2006 spring meeting, Korea Society of Economic and Environmental Geology (KSEEG).
7. Kaplan, A., K. Glover, T. Illangasekare, and J. Munakata Marr (2004) DNAPL Biodegradation Effects on Mass Transfer and Partitioning Tracer Behavior. In, Proceedings of 4th International Conference on Remediation of Chlorinated and Recalcitrant Compounds, Monterey, California, U.S.A., May 24-27, 2004.

8. Kim, Y., S. Saenton, E. Moreno-Barbero and T. H. Illangasekare, 2006, DNAPL source zone distribution characterization using partitioning tracer test in heterogeneous aquifer, Proceeding of KSEEG 2006 spring meeting, Korea Society of Economic and Environmental Geology (KSEEG), p.204-206.
9. Mathew, M., E. Moreno-Barbero, and T. H. Illangasekare (2006) Simulation and performance assessment of partitioning tracer test (PITT) in permeability correlated aquifers, Proceedings of International Conference "MODFLOW and More 2006," Golden, CO, May 22-24, 2006, p. 673-677.
10. Moreno-Barbero, E. and T. H. Illangasekare, 2003. Evaluation of estimation errors of partitioning tracer tests for source zones with DNAPL pools, E.P. Poeter, C. Zheng, M.C. Hill, and J. Doherty (Editors) In, Proceedings of MODFLOW and More 2003: Understanding through Modeling, Vol. 1, pp. 321-326. Golden, Colorado, U.S.A., September 16-19, 2003.
11. Moreno-Barbero, E., S. Saenton, and T.H. Illangasekare (2004) Potential use of partitioning tracer and mass flux emission data to characterize DNAPL source zone architecture. In, Proceedings of 4th International Conference on Remediation of Chlorinated and Recalcitrant Compounds (Part 1B Innovative Characterization Approaches), Monterey, California, U.S.A., May 24-27, 2004.
12. Saenton, S., and T.H. Illangasekare (2003) Determining the entrapment architecture in the DNAPL source zone using downgradient mass flux measurements: A combined numerical and stochastic study. E.P. Poeter, C. Zheng, M.C. Hill, and J. Doherty (Editors) In, Proceedings of MODFLOW and More 2003: Understanding through Modeling, Vol. 2, pp. 615-619. Golden, Colorado, U.S.A., September 16-19, 2003.
13. Saenton, S., and T.H. Illangasekare (2003) Evaluation of benefits of partial source zone treatment using intermediate-scale physical model testing and numerical analysis: Preliminary Studies. Kono, Nishigaki, and Komatsu (Editors).In, Proceedings of the International Symposium on Groundwater Problems Related to Geo-Environment, 25-35 pp. Okayama, Japan, May 28-30, 2003.
14. Saenton, S. and T.H. Illangasekare (2004) Determination of DNAPL entrapment architecture using experimentally validated numerical codes and inverse modeling. In, Proceeding of the Computational Methods in Water Resources 2004 International Conference, Chapel Hill, North Carolina U.S.A., June 13-17, 2004.

Published Technical Abstracts

1. Dai, D., S. Saenton, and T.H. Illangasekare (2003) Natural and surfactant enhanced dissolution of field DNAPLs, Paper presentation at AGU Hydrology Days, March 31-April 2, 2003. Fort Collins, Colorado, USA.
2. Gago, J.L., G. Middleton, Hill, E.H., III, and T. Illangasekare (2002) Real time monitoring Of NAPL sources using photon attenuation techniques on chlorinated solvents, Geological Society of America Abstracts with Programs, 34(6), 2002 Annual Meeting, Denver, CO, October 27-30, 2002.

3. Glover, K.C., E.H. Hill, III, and T.H. Illangasekare (2002) High-resolution monitoring of NAPL saturation in heterogeneous porous media: application of x-ray attenuation techniques to chlorinated solvents and a nontoxic surrogate, Geological Society of America Abstracts with Programs, 34(6), 2002 Annual Meeting, Denver, CO, October 27-30, 2002.
4. Glover, K.C., A. Hoenke, T.H. Illangasekare, and J. Munakata Marr (2003) Microbially influenced mass transfer from entrapped pools of non-aqueous phase tetrachloroethene: preliminary results of small flow-cell experiments, 23rd Annual AGU Hydrology Days, Fort Collins, CO, March 31 – April 2, 2003
5. Glover, K., and A. Kaplan (2004) Microbe-enhanced mass transfer from PCE entrapped in porous media: experiments and modeling, SERDP & ESTCP DNAPL Source Zone Technical Review Panel Meeting, December 1–2, 2004. Washington, D.C., U.S.A.
6. Glover, K., T.H. Illangasekare, and J. Munakata Marr (2006) Biologically enhanced mass transfer of PCE from DNAPL pools: model development and evaluation at intermediate scales, 27th Annual AGU Hydrology Days, Fort Collins, CO, April, 2006.
7. Glover, K., J. Munakata Marr, and T.H. Illangasekare (2006) Biodegradation-enhanced mass flux from tetrachloroethene (PCE) pools: upscaling studies, International and European Symposium on Environmental Biotechnology, Leipzig, Germany, July 9-13 2006.
8. Heiderscheidt, J. (2004), Development and testing of numerical model for in-situ chemical oxidation of PCE using permanganate, SERDP & ESTCP DNAPL Source Zone Technical Review Panel Meeting, December 1–2, 2004. Washington, D.C., U.S.A.
9. Heiderscheidt, J.L., T.H. Illangasekare, and R.L. Siegrist (2003) Use of chemical oxidation to reduce rate-limited matrix diffusion of PCE from low permeability material – a numerical study, 23rd Annual AGU Hydrology Days, Fort Collins, CO, March 31 – April 2, 2003
10. Heiderscheidt, J.L., T.H. Illangasekare, and R.L. Siegrist (2005) Experimental investigation of in-situ chemical oxidation of complex DNAPL source zones by permanganate, Eos Trans. AGU, 86(52), Fall Meet. Suppl., Abstract H23A-1409, AGU Fall Meeting, December 2005, San Francisco, California U.S.A.
11. Illangasekare, T.H. (2002) Evaluation of benefits of partial source zone treatment using intermediate-scale physical model testing and numerical analysis, Geological Society of America, Fall Annual Meeting. Abstracts with Programs, Vol. 83, no. 12, September 2002.
12. Illangasekare, T H, (2002) Partial source zone treatment at DNAPL contaminated sites: issues of heterogeneity, characterization, mass transfer and up-scaling, Eos Trans. AGU, 83(47), Fall Meet. Suppl., Abstract H21E-07 INVITED, AGU Fall Meeting, December 2002, San Francisco, California U.S.A.
13. Illangasekare, T.H. (2003) Issues of heterogeneity, characterization, mass transfer and up-scaling associated with partial source zone treatment at DNAPL contaminated sites, Paper presentation at AGU Hydrology Days, March 31-April 2, 2003. Fort Collins, Colorado, USA.

14. Illangasekare, T. H. (2005) From Laboratory To The Field: Intermediate Scale Testing, A Necessary Step. Invited, American Geophysical Union, Spring Meeting, New Orleans May 2005.
15. Illangasekare, T.H. K. Jensen, I. Javandal, I., and A.S. Mayer (2005) Chapter on “Migration and Distribution” in “Soil and Groundwater Contamination: Nonaqueous Phase Liquids”, Ed. A. S. Mayer and S.M. Hassanizadeh, Water Resources Monograph 17, American Geophysical Union.
16. Illangasekare, T.H., M. Mathew, S. Saenton, K. Glover, J. Heiderscheidt, Y.-C. Kim, J. Gago, J. Munakata Marr, K. Soga, and R. Siegrist (2005) Improving the understanding of mass transfer from entrapped DNAPL source zones undergoing remediation – validation of prediction tools and characterization methods, SERDP and ESTCP Partners in Environmental Technology Technical Symposium & Workshop, Washington, D.C., Nov. 29-Dec. 1, 2005.
17. Illangasekare, T.H., E. Moreno-Barbero, and E. Hill (2003) Study of DNAPL Pool Morphology Using X-ray Attenuation to Evaluate Limitations of Partitioning Tracer Method in Complex Entrapment Architecture. Poster presentation in the American Geophysical Union Fall Meeting, December 8-12, 2003.
18. Illangasekare, T.H., and S. Saenton (2005) Up-scaling of mass transfer from entrapped DNAPL sources From laboratory to field – experimental validation of an empirical approach, Eos Trans. AGU, 86(52), Fall Meet. Suppl., Abstract H21H-07 INVITED, AGU Fall Meeting, December 2005, San Francisco, California U.S.A.
19. Illangasekare, T.H., S. Saenton, J. Heiderscheidt, K. Glover, Y.-C. Kim, M. Mathew, J. Gago, J. Munakata Marr, K. Soga, and R. Siegrist (2004) Decision tool for management of source zones contaminated with DNAPL, SERDP and ESTCP Partners in Environmental Technology Technical Symposium & Workshop, Washington, D.C., Dec 1-2, 2004.
20. Illangasekare, T.H., S. Saenton, Y.-C. Kim, and D. Rodriguez (2004) Role of aquifer heterogeneity on mass flux emission from DNAPL entrapment zones, Eos Trans. AGU, 85(47), Fall Meet. Suppl., Abstract H43H-01 INVITED, American Geophysical Union Fall Meeting, December 13–17, 2004, San Francisco, California U.S.A.
21. Kaplan, A.R., K.C. Glover, J. Munakata-Marr, and T.H. Illangasekare (2005), Effect of PCE biodegradation on mass transfer from entrapped DNAPL, Proceedings of the Eight International Symposium on In Situ and On-Site Bioreclamation, Battelle Press, Baltimore, MD, June 2005.
22. Kim, Y.-C., S. Saenton, K.K. Lee, and T.H. Illangasekare (2003), Mass transfer characteristics of entrapped DNAPL during surfactant flushing in two dimensional flow field , 23rd Annual AGU Hydrology Days, Fort Collins, CO, March 31 – April 2, 2003
23. Kim, Y.-C., S. Saenton, E. Moreno-Barbero, and T.H. Illangasekare (2004) Pre- and post-treatment characterization of DNAPL source zone architecture in heterogeneous aquifers using mass flux and tracer data, Eos Trans. AGU, 85(47), Fall Meet. Suppl., Abstract H31B-0378, American Geophysical Union Fall Meeting, December 13–17, 2004, San Francisco, California U.S.A.

24. Mathew, M, T.H. Illangasekare, F. Fagerlund, F. and A. Niemi (2005) Sensitivity of Model Parameter in the Predication of DNAPL Infiltration and Redistribution in Heterogeneous Porous Media, poster presentation at the American Geophysical Union, Fall Meeting, San Francisco, December, 2005.
25. Moreno-Barbero, E., D. Dai, and T.H. Illangasekare, T.H. (2003) Influence of pool morphology on the performance of the PITT DNAPL characterization, Paper presentation at AGU Hydrology Days, March 31-April 2, 2003. Fort Collins, Colorado, USA.
26. Moreno-Barbero, E., S. Saenton, D. Dai, and T.H. Illangasekare (2002) Evaluation of the partitioning interwell tracer technique for possible characterization of DNAPL pools. Poster presentation in the 2002 Geological Society of America (GSA) Denver Annual Meeting, Denver, Colorado, U.S.A. Geological Society of America, October 27–30, 2002.
27. Saenton, S. (2004) Mass transfer from entrapped DNAPL sources undergoing remediation: Characterization methods and prediction tools. SERDP & ESTCP DNAPL Source Zone Technical Review Panel Meeting, December 1–2, 2004. Washington, D.C., U.S.A.
28. Saenton, S., and T.H. Illangasekare (2003) Consequences of incomplete remediation of the DNAPL-contaminated aquifers: Intermediate-scale experiments and numerical modeling studies. Paper presentation at AGU Hydrology Days, March 31 – April 2, 2003. Fort Collins, Colorado, U.S.A.
29. Saenton, S., and T.H. Illangasekare (2003) Uncertainty in characterization of source zone DNAPL entrapment architecture using mass flux measurements due to geologic heterogeneity, *Eos Trans. AGU*, 85(47), Fall Meet. Suppl., Abstract H21E-0899, American Geophysical Union Fall Meeting, December 8–12, 2003, San Francisco, California U.S.A.
30. Saenton, S., T.H. Illangasekare, and D. Dai (2002) Upscaling of mass transfer from entrapped DNAPL zones: An experimental and a modeling study. Poster presentation in the 2002 Geological Society of America (GSA) Denver Annual Meeting, Denver, Colorado, U.S.A. Geological Society of America, October 27–30, 2002.
31. Siegrist, RL., M. Crimi, J.M. Marr, and T.H. Illangasekare (2005) Reaction and Transport Process Controlling In Situ Chemical Oxidation, Poster at Partners in Environmental Technology. Technical Symposium and Workshop, SERDP/ESTCP Conference, Washington DC.

Invited Presentations and Workshops

1. Illangasekare, T.H. (2002) Dissolution of nonaqueous phase liquids in heterogeneous aquifers, NSF Sponsored Pan American Advanced Study Institute, Rio DeJaniro, Brazil, July 2002.
2. Illangasekare, T.H. (2002) Behavior and remediation of nonaqueous phase waste chemicals in the subsurface, Workshop Sponsored by the Geological Society of Japan and Kajima Corporation, Tokyo Japan, August 2002.
3. Illangasekare, T.H. (2002) Behavior and remediation of NAPLs in the subsurface, Okayama University, Okayama, Japan. August 2002.

4. Illangasekare, T.H. (2002) Characterization of sites contaminated with nonaqueous phase liquids, *Frontiers In Geophysics*, Sponsored by Army Research Office, Water ways Experiment Station, Vicksburg, Mississippi.
5. Illangasekare, T.H. (2002) Source zone remediation of DNAPL sites: physical modeling to investigate role of heterogeneity and demonstrate the need for up scaling, *Subsurface Conference* sponsored by INEL and INRL, Boise Idaho, November 2002.
6. Illangasekare, T.H. (2003) AFCEE source zone initiative- technical assistance to F.E. Warren, NAS Fort Worth & AFP 4, AFCEE 2003 Technology Transfer Workshop, San Antonio, Texas, February 2003.
7. Illangasekare, T.H. (2004) Dissolved mass emission from DNAPL source zones with complex entrapment architecture, Dept. of Agriculture and Biosciences, Texas A& M University, College Station, October 2004.
8. Illangasekare, T.H. (2004) Dissolved mass emission from DNAPL source zones with complex entrapment architecture, Dept. of Civil Engineering, University of Texas at Austin, October 29, 2004.
9. Illangasekare, T.H. (2004) Dissolved mass emission from DNAPL source zones with complex entrapment architecture, Dept. of Petroleum Engineering, University of Texas at Austin, June 7, 2004.
10. Illangasekare, T.H. (2004) Dissolved mass emission from DNAPL source zones with complex entrapment architecture, Dept. of Earth Science, University of Waterloo, Ontario, Canada, July 6, 2004.
11. Illangasekare, T.H. (2004) Dissolved mass emission from DNAPL source zones with complex entrapment architecture, Dept. of Chemical Engineering, Yale University, 2004.
12. Illangasekare, T.H. (2004) Application of Stochastic Methods in Heterogeneous Porous Media, Asian Institute of Technology, Bangkok, Thailand, May 25, 2004.
13. Illangasekare, T.H. (2004) Dissolved mass emission from DNAPL source zones with complex entrapment architecture, Distinguished Lecture Series, Dept. of , University of California at Davis, January 29, 2004.
14. Illangasekare, T.H. (2004) Characterization of NAPL Retention Volumes in Heterogeneous Aquifers, Invited talk at Gordon Research Conference on Flow and Transport in Permeable Media, Queen's College, Oxford, July 11-16, 2004
15. Nakels, D and T.H. Illangasekare (2004) Use of TarGost results to develop relationship between NAPL subsurface architecture and groundwater impacts, EPRI Workshop on New Tool Box Approach for Innovative Characterization of NAPLs at MPG sites, Cambridge, MA., June 23, 2004.